Universitat de Girona

ISOMERISM AND C-H, C-C, O-O, C-O BOND ACTIVATION STUDIES BY TRANSITION METALS

Albert POATER I TEIXIDOR

ISBN: 84-689-9111-2
Dipòsit legal: GI-677-2006

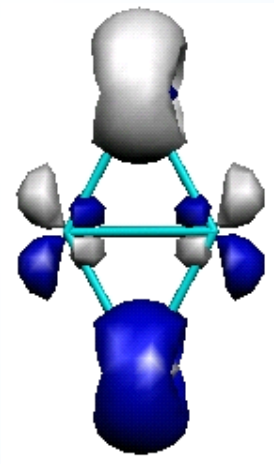

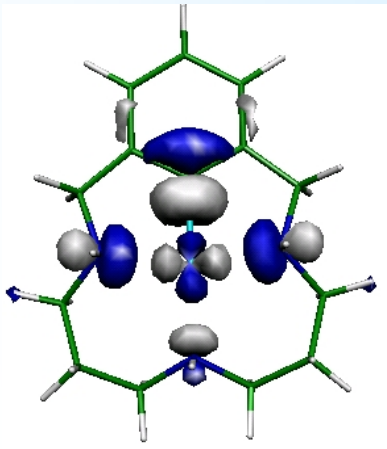

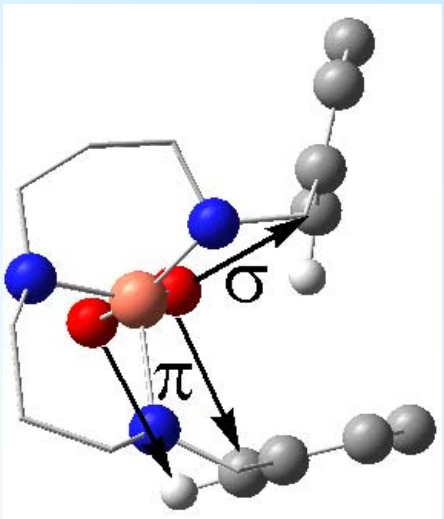

Universitat de Girona

Isomerism and C-H, C-C, O-O, C-O bond activation studies by transition metals

Institut de Química Computacional

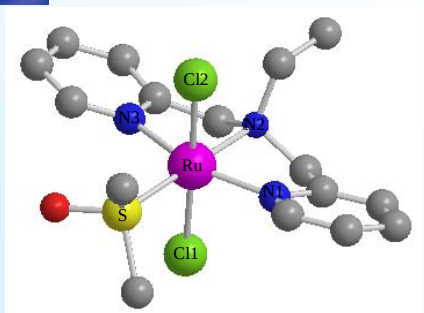

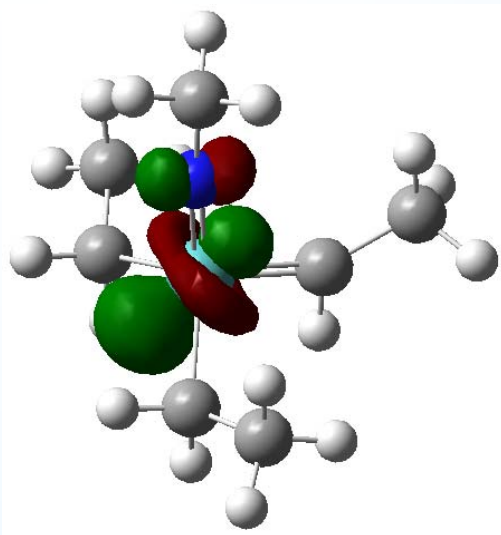

ALBERT POATER TEIXIDOR

Thesis directed by:
Prof. Dr. Miquel Duran
Prof. Dr. Miquel Solà

Institut de Química Computacional
Departament de Química
Facultat de Ciències
Universitat de Girona

Thesis:

Isomerism and C-H, C-C, O-O, C-O bond activation studies by transition metals

Albert Poater Teixidor

Directed by:

Prof. Dr. Miquel Solà i Puig
Prof. Dr. Miquel Duran i Portas

Títol: Isomerism and C-H, C-C, O-O, C-O bond activation studies by transition metals

Nom: Albert Poater Teixidor

Miquel Solà i Puig, professor Catedràtic d'Universitat de l'àrea de Química Física de la Universitat de Girona, i Miquel Duran i Portas, professor Catedràtic d'Universitat de l'Àrea de Química Física de la Universitat de Girona, certifiquem que:

L'Albert Poater Teixidor, llicenciat en Química per la Universitat de Girona, ha realitzat sota la nostra direcció, a l'Institut de Química Computacional i al Departament de Química de la Facultat de Ciències de la Universitat de Girona, el treball d'investigació titulat:

"Isomerism and C-H, C-C, O-O, C-O bond activation studies by transition metals"

que es presenta en aquesta memòria per optar al grau de Doctor en Química.

I perquè consti a efectes legals, signem aquest certificat.

Girona, 16 de març de 2005

Prof. Dr. Miquel Solà i Puig Prof. Dr. Miquel Duran i Portas

Al meu entorn,
Família, cor i amics

Al meu avi

Table of Contents

Table of contents

PART I: Introduction

Chapter I: Prologue

This computational thesis directed by Prof. Miquel Duran and Prof. Miquel Solà started indeed in the summer of 2000 with an experimental work carried out in the group of Prof. Antoni Llobet of the Universitat de Girona. Later on, in the same group I spent several months doing research on Ru chemistry and I did a doctorate course entitled "Simulation of experiments". Part of the results obtained during this period has been reported in the only publication that I have involving only experimental work.[1] X. Sala finished the experimental project. Nevertheless after one year we decided to perform calculations to complement the experimental results. Prof. M. Duran and Prof. M. Solà supervised my progress, and I followed the doctoral courses of the "Computational and Theoretical Chemistry" Ph. D. as a teacher of the Chemistry Department. The aim of my Ph. D. Thesis was to use the available theoretical methods to provide help and understanding for the experimental work. As a consequence, I have not focused my research in a single topic. Rather, I have been permanently in contact with different experimental groups, with special emphasis for my former experimental group, i. e., the group of Prof. Antoni Llobet. During the first year in the theoretical group of Prof. Duran and Solà, I got a contract and at the same time I was charged to carry out calculations based on the understanding of the behavior of some monoatomic and diatomic copper complexes.[2-8] In November 2001 I visited the theoretical group of Prof. A. Toro-Labbé in Santiago de Chile (Chile) and the collaboration in the subject of copper clusters has been followed at least till now.[9,10]

In 2002 I received a four-year grant from the spanish "Ministerio de Educación y Cultura" that allowed me to center my work only in research.

New collaborations with experimental groups of the Universitat de Girona appeared. First, with the group of Dr. A. Polo, treating the isomerism problems of Ni complexes.[11] Later we have collaborated together again in the field of platinum complexes.[12,13]

Another aim was to be able to get insight into some properties of ruthenium complexes. The experimental research of X. Sala[14] and J. Mola,[15,16] directed by Prof. A. Llobet, Dr. M. Rodríguez, and Dr. I. Romero, was the starting point.

Other minor projects have given me a view of problems unknown *a priori* for me. Dr. M. A. Martínez introduced me in antitumoral agents, with experimental work carried out by Dr. S. Moradell.[17] Furthermore the collaboration with Prof. N. Martín allowed me to work with fullerenes.[18]

In 2004 I did a four-month stay in the CNRS theoretical group of Prof. O. Eisenstein in Montpellier, where I developed some theoretical projects, and, directed by Dr. X. Solans-Monfort, Dr. E. Clot, and Prof. O. Eisenstein, I made the prediction of novel and better Schrock catalysts.[19-21]

The study of copper complexes has been done in collaboration with A. Company, Dr. M. Costas, Dr. X. Ribas, Dr. R. Xifra, and Prof. A. Llobet.[2-8] This study has been the main subject of the present thesis. Nevertheless, the understanding in other subjects has allowed me improving my knowledge of the experimental problems that can be solved by theoretical tools. Moreover, the good synergy between the experimental and theoretical groups has been a key factor to finish successfully the projects.

The title of the thesis, “Isomerism and C-H, C-C, O-O, C-O bond activation studies by transition metals” is general and tries to summarize nearly all the work that has been done during the last five years. The thesis is organized as follows. In the first part there is the prologue and a section called Theoretical Methods that includes a general overview of the computational methods used, and different techniques that help to better understand the properties and reactivity of the studied molecules. The second part includes six chapters related to copper complexes, and the third part two chapters about copper clusters. The fourth part includes four chapters related to ruthenium complexes. Part V, with three chapters, collects the computational results of the work done in the theoretical group of Prof. O. Eisenstein. The last part of the thesis collects several works done in collaboration with different experimental groups. Furthermore, at the end of the thesis there are some general conclusions.

Each chapter of Parts II to V in the thesis has the following structure. First, apart from an initial Abstract that resumes very synthetically the work done in the chapter, I give an Introduction to introduce the field of the study, after this there is the Computational Details section that includes all the programs and the applications used in the

calculations. After this I include and discuss the results of my research, being often summarized by the Conclusion section. I have extracted all the computational part of each paper already written either published or not, and I have inserted it in this thesis. Some experimental results, not done by me, are included to get insight in the problem that I had to solve computationally. Each thesis chapter involves the work reported in a paper or two papers depending on the case.

1. Synthesis, structure, and redox properties of a new aqua ruthenium complex containing the tridentate [9]aneS_3 and the didentate 1,10-phenanthroline ligands. X. Sala, A. Poater, I. Romero, M. Rodríguez, A. Llobet, X. Solans, T. Parella, T. M. Santos, *Eur. J. Inorg. Chem.* **2004**, 612-618.
2. Fine-tuning the electronic properties of highly stable organometallic Cu^{III} complexes containing monoanionic macrocyclic ligands R. Xifra, X. Ribas, A. Llobet, A. Poater, M. Duran, M. Solà, T. D. P. Stack, J. Benet-Buchholz, B. Donnadieu, J. Mahía, T. Parella, *Chem. Eur. J.* **2005**, *11*, 5146-5156.
3. Cu(II) Hexaaza Macrocyclic Dinuclear Complexes Obtained from the Reaction of their Cu(I) Derivates and Molecular Oxygen. An Example of How Subtle Ligand Variations Can Lead to Major Differences in Reactivity. M. Costas, X. Ribas, A. Poater, J. M. López-Balvuena, R. Xifra, A. Company, M. Duran, M. Solà, A. Llobet, M. Corbella, M. A. Usón, J. Mahía, X. Solans, X. Shan, J. Benet-Buchholz, *Inorg Chem.* **2006**, in press.
4. O_2 chemistry of dicopper complexes with alkyltriamine ligands. comparing synergetic effects on O_2 binding. A. Company, D. Lamata, A. Poater, M. Solà, E. Rybak-Akimova, L. Que, X. Fontrodona, T. Parella, A. Llobet, M. Costas, *Inorg. Chem*., submitted.
5. Intramolecular aromatic reactivity of Cu(II) hexaaza macrocyclic dinuclear complexes obtained from the reaction of their Cu(I) derivates and molecular oxygen. A. Poater, M. Costas, X. Ribas, M. Duran, M. Solà, A. Llobet, to be written.
6. Regiospecific C-H activation: reversible H/D exchange promoted by Cu^{I} complexes with triazamacrocyclic ligands. X. Ribas, R. Xifra, T. Parella, A. Poater, M. Solà, A. Llobet, *Angew. Chem. Int. Ed.*, accepted.
7. C-C bond activation in square planar triazamacrocyclic Cu complexes. R. Xifra, X. Ribas, A. Poater, T. Parella, A. Llobet, M. Solà, to be written.

8. Regiospecific intramolecular C-H bond activation promoted by transition metal complexes with triazamacrocyclic ligands. A. Poater, X. Ribas, R. Xifra, M. Duran, A. Llobet, M. Solà, to be written.
9. Molecular structure and bonding of copper cluster monocarbonyls Cu_nCO (n = 1-9). A. Poater, M. Duran, P. Jaque, A. Toro-Labbé, M. Solà, *J. Phys. Chem. B*, in press.
10. Molecular structure and bonding of anionic, cationic, and neutral copper and sodium cluster monocarbonyls M_nCO (n = 1-9). A. Poater, M. Duran, A. Toro-Labbé, M. Solà, to be written.
11. Stereodiscrimination in phosphanylthiolato nickel(II) complexes. J. Duran, A. Polo, J. Real, J. Benet-Buchholz, A. Poater, M. Solà, *Eur. J. Inorg. Chem.* **2003**, 4147-4151.
12. Diastereoisomerism in platinum(II) 2-phosphino complexes J. Duran, A. Polo, J. Real, A. Poater, M. Solà, J. Benet-Buchholz, to be submitted.
13. Comparison of the diastereoisomerism in platinum(II) 2-phosphino and 2-aminothiolato complexes J. Duran, A. Polo, J. Real, A. Poater, M. Solà, J. Benet-Buchholz, to be submitted.
14. New Ru^{II} complexes containing C2 didentate chiral 1,2-bis(oxazolinyl)benzene ligands. Structure and atropisomeric discrimination. X. Sala, E. Plantalech, I. Romero, M. Rodríguez, A. Llobet, A. Poater, M. Duran, M. Solà, S. Jansat, M. Gómez, T. Parella, H. Stoeckli-Evans, J. Benet-Buchholz, *Chem. Eur. J.* **2006**, in press.
15. Synthesis, structure, spectroscopic, and catalytic properties of new ruthenium complexes containing the N-tridentate "*bpea*" and phosphine ligands. J. Mola, I. Romero, M. Rodríguez, A. Llobet, T. Parella, J. M. Campelo, D. Luna, J. M. Marinas, T. Parella, A. Poater, M. Duran, M. Solà, to be submitted.
16. Synthesis, structure, spectroscopic, and catalytic properties of ruthenium(II) isomeric complexes containing dimethyl sulfoxide, chloro, and the N-tridentate "*bpea*" ligands. J. Mola, I. Romero, M. Rodríguez, A. Llobet, T. Parella, J. Benet-Buchholz, X. Fontrodona, A. Poater, M. Solà, M. Duran, to be submitted.
17. Trinuclear Pt(II) compound with short Pt-Pt-Pt contacts. An analysis of the influence of π–π stacking interactions on the strength and length of the Pt-Pt bond. A. Poater, S. Moradell, E. Pinilla, J. Poater, M. Solà, M. A. Martínez, A. Llobet, *Dalton Trans*. **2006**, 1188-1196.

18. Regioselective intramolecular Pauson-Khand reactions of C_{60}: An electrochemical study and theoretical underpinning. N. Martín, M. Altable , S. Filippone, A. Martín-Domenech, A. Poater, M. Solà, *Chem. Eur. J.* **2005**, *11*, 2716-2729.
19. Efficient d^0 olefin metathesis catalysts: which metal, which metal, which ligands? A. Poater, X. Solans-Monfort, E. Clot, C. Copéret, O. Eisenstein, to be submitted.
20. Structural and dynamic properties of molybdenum and tungsten-based olefin metathesis catalysts, $M(=NR^1)(=CHR^2)(X)_2$. A. Poater, X. Solans-Monfort, E. Clot, C. Copéret, O. Eisenstein, to be submitted.
21. The role of the cyclo-metallacycles of Mo, W, and Re in the reactivity of metathesis catalysts. X. Solans-Monfort, A. Poater, E. Clot, C. Copéret, O. Eisenstein, to be written.

Chapter II: *Theoretical Methods*

INTRODUCTION INDEX

A) Introduction to Quantum Chemistry

In the early 1930's, the advent of the new quantum concepts to the study of atomic and molecular systems initiated the field of computational and theoretical chemistry. Some semi-empirical approximations were developed like the Hückel model for calculations of the orbital energies of conjugated organic molecules making use of empirical parameters. First principles quantum mechanical methods are, on the other hand, aimed at solving the Schrödinger equation with neither approximations nor additional parameters. That is, to solve equation (1) *ab initio*:

$$H\Psi = E\Psi \tag{1}$$

$$H = -\frac{1}{2}\sum \nabla_i^2 - \sum_{i=1}^{N}\sum_{A=1}^{M}\frac{Z_A}{r_{iA}} + \sum_{i=1}^{N}\sum_{j>i}^{N}\frac{1}{r_{ij}} \tag{2}$$

where H is the full time-independent electronic Hamiltonian. The first term is the electronic kinetic energy, the second one is the electron-nucleus coulombic attraction, and the third one accounts for the electron-electron repulsion. Even though theoreticians realized that the exact solution of (1) is only attainable for monoelectronic systems, so only when Ψ describes the motion of one electron (hydrogen-like systems). However, the interest on monoelectronic systems among the scientific community is rare, and the efforts to obtain accurate results for polielectronic systems started soon. Therefore, approximate methods were developed in order to obtain an estimation for the energy of the system and other molecular properties. In a way, especially in a first stage of this new theory, the main problem was the complicated way to find the solution to the equations arising from that theory. The fundamentals for the modern methods of computation were established during the 1930-50's. Since the decade of 1960's, with the introduction of the primitive computing machines, the development of more and more efficient algorithms for solving the equations involved in the motion of electrons allowed to obtain the first relevant results.[1-4]

B) Density functional theory (DFT)

The most characteristic method of the quantum mechanics to solve the Schrödinger equation is the Hartree-Fock approach.[2-5] By this method, the electronic correlation due to the Coulomb hole (two electrons with different spin can be at the same time in the same position in the space, but with reduced probability) is not introduced explicitly. Nevertheless, the Fermi hole (two electrons with the same spin cannot be at the same time in the same position in the space) is well described, because the wave function is built from a Slater determinant. In order to improve the

Hartree-Fock wave function it is necessary to introduce the electronic correlation due to the Coulomb hole by different methods, known as post-Hartree-Fock methods.[2-5] The easiest way to achieve these purposes is from the perturbation theory (Mϕller-Plesset, MP); or by introducing additional determinants promoting occupied orbitals towards unoccupied ones (configuration interaction, CI).

The main problem that these post-Hartree-Fock methods like MP2, MP3, MP4, CISD, CCSD, and CCSD(T) present is their expensive computational cost, because they scale about orders of N^5, N^6, N^7, N^6, N^6, and N^7, respectively, where N is the number of particles. Furthermore, they present the additional problem that by augmenting the precision of the method it is necessary to use a larger basis set. Therefore, the chemical precision is only available for small systems, with less than 10 heavy atoms. However, great advances during these recent years have been done.

The Hohenberg-Kohn theorem,[6] starting point of the density functional theory (DFT),[1a,3-5] establishes that the wave function of the ground state of an electronic system is a functional of the electronic density. Therefore, it is only necessary to know the density to calculate all the properties of a system. As the density, $\rho(r)$, contains all the information of the system, the chemical reactivity can be represented as changes of $\rho(r)$.

In 1965, the spectroscopist Bright-Wilson said that the idea was not so surprising as it could seem initially: ”well, the total electron density defines the number of electrons in the system: the cusps in the density define the nuclear coordinates; the derivative of the density at the cusp defines the nuclear charge at that cusp and thus the configuration of the elements in the molecules; therefore, the system is fully defined”.[7]

The physicians were the first ones to apply the DFT to simplify the quantum mechanics and to study the solid state. This first simplification consists of that the wave function (Ψ) depends on the $3N$ spatial coordinates of each electron, while the density only on 3. Nevertheless, it presents the inconvenience that the exact mathematical formula that gives the relationship between the energy with the electronic density is not known, and it is necessary to use approximations.[1a] Thomas,[8] Fermi[9], and Dirac[10] were the first ones to try to express the kinetic and potential energy as function of the density.

The fact that DFT scales formally with an order of N^4, and only with density fitting as N^3, and that it introduces potentially all the electronic correlation at a lower computational cost than the conventional *ab initio* methods has allowed to study large organometallic and bioinorganic systems. Therefore, during these last years, DFT has become the most used methodology in the study of the ground state of the molecules with medium or large size.[11]

The large impact of the computational chemistry was reflected in 1998 by the Nobel Prize of Chemistry awarded to professors Walter Kohn[12] and John A. Pople.[13] The first one was the one who created the DFT, and the second is recognized by the implementation of *ab initio* methods.

Another important branch generated from DFT theory has been conceptual DFT.[1a,14,15] The creator of this theory is Robert G. Parr and it is based on the idea that the electronic density is the fundamental tool to describe the electronic states of atoms and molecules. Conceptual DFT has allowed giving a mathematical definition to a series of chemical concepts as electronegativity and hardness.

A big part of the theoretical chemistry related on reactivity is based on the concept of the Frontier Molecular Orbitals (FMO), introduced by Fukui,[16] especially the lowest unoccupied molecular orbital (LUMO) and the highest occupied molecular orbital (HOMO). The interaction between these orbitals often allows us to obtain a good description of the reactivity and the stereoselectivity of the reactions. The FMO theory says that the attack of an electrophilic species will take place where there is more density of the HOMO, while the attack of a nucleophilic species will take place in a region with higher density of the LUMO. Parr and coworkers have demonstrated that nearly all the frontier molecular theory can be rationalized from the DFT.

In the conceptual DFT, the chemical reactivity is quantitatively studied by using a set of chemical reactivity indices (hardness, Fukui functions, electrophilicity,…). Furthermore, these indices have been useful to define and redefine other chemical reactivity principles as the hard-soft acid-base principle (HSAB),[17] the electronegativity equalization principle by Sanderson (EEP),[18] the maximum hardness principle (MHP)[17,19] and the minimum polarizability principle (MPP).[20]

The conceptual DFT is a useful tool to obtain quantitative information about the chemical reactivity and it presents the additional advantage that in spite of the reactivity indices are developed from DFT, they can be used for DFT and non DFT calculations (semi-empirical, HF or post-HF).

Hohenberg-Kohn theorems

1st Theorem:"Any observable of a non degenerated ground state can be calculated, in principle exactly, from the electronic density of the ground state; which means that any observable can be written as a functional of the electronic density of the ground state".[6]

It can be demonstrated by reductio ad absurdum that from a density given, the external potential, $v(r)$, (the potential created at one position of the space by the nucleus plus any other external field, either electric or magnetic), is absolutely determined, except for an additive constant. Thus, if the density determines the number of electrons, from $\int\rho(r)dr=N$, and $v(r)$ according the first Hohenberg-Kohn theorem, the $\rho(r)$ can also determine the hamiltonian (except for an additive constant) and the wave function of the ground state. By extension, all the observable properties of the ground state, including the kinetic energy of the electrons, the coulombic repulsion between electrons can be expressed as density functionals. Take for instance, in the case of the total energy of a system:

$$E_v[\rho(\vec{r})] = T[\rho(\vec{r})] + V_{Ne}[\rho(\vec{r})] + V_{ee}[\rho(\vec{r})] \quad (+V_{NN}) \quad , \tag{3}$$

where $T[\rho]$ is the electronic kinetic energy, $V_{Ne}[\rho]$ the electronic-nucleus potential energy, $V_{ee}[\rho]$ is the electron-electron potential energy and V_{NN} the nucleus-nucleus potential energy. $T[\rho]$ and $V_{ee}[\rho]$ do not depend on the external potential. Nevertheless, they are universal functionals, and therefore, can be included inside of the so-called Hohenberg and Kohn functional, $F_{HK}[\rho(r)]$:

$$E_v[\rho] = \int \rho(\vec{r})v(\vec{r})d\vec{r} + F_{HK}[\rho(\vec{r})] \quad (+V_{NN}) \quad . \tag{4}$$

$\rho(r)$ must accomplish two conditions: be N-representable ($\int\rho(r)dr=N$) and v-representable (given a $\rho(r)$ it exists a $v(r)$ that can generate the density). The N-representability of a density is easily checked. However, to be sure that the density is v-representable is more complicated, so much that there are some cases presenting trial reasonable densities that are not able to be found from any external potential.

2nd Theorem:"The electronic density of a non degenerated ground state can be calculated, in principle exactly, determining the density that minimized the ground state energy".[6]

This also can be reformulated as a trial density will give always a higher energy with respect to the exact energy for the ground state. The minimization of the energy functional, $\delta E_v[\rho]=0$, gives the ground state energy. The wave function that we must minimize is built using the method of the Lagrange non determined multipliers and introducing the *N*-representability condition, $\int \rho(\vec{r})d\vec{r} - N = 0$:

$$\delta\left[E_v[\rho(\vec{r})] - \mu\left(\int \rho(\vec{r})d\vec{r} - N\right)\right] = 0 \tag{5}$$

where μ, the non determined Lagrange multiplier, is the chemical potential. The derivative of a functional $F[\rho]$ is defined as:

$$\delta F = F\left[\rho(\vec{r}) + \delta\rho(\vec{r})\right] - F\left[\rho(\vec{r})\right] = \int \frac{\delta F}{\delta\rho(\vec{r})}\delta\rho(\vec{r})d\vec{r} \quad , \tag{6}$$

and therefore,

$$\int \frac{\delta E_v\left[\rho(\vec{r})\right]}{\delta\rho(\vec{r})}\delta\rho(\vec{r})d\vec{r} - \mu\int \delta\rho(\vec{r})d\vec{r} = 0 \quad , \tag{7}$$

where adding the terms,

$$\int\left[\frac{\delta E_v\left[\rho(\vec{r})\right]}{\delta\rho(\vec{r})} - \mu\right]\delta\rho(\vec{r})d\vec{r} = 0 \quad . \tag{8}$$

Eq (8) proportionates the minimization condition and allows obtaining the value of μ in the minimum. Finally, if eq. (4) is introduced in eq. (8) we obtain the Fundamental equation of DFT or Euler equation:

$$\mu = \frac{\delta E_v\left[\rho(\vec{r})\right]}{\delta\rho(\vec{r})} = v(\vec{r}) + \frac{\delta F_{HK}\left[\rho(\vec{r})\right]}{\delta\rho(\vec{r})} \quad . \tag{9}$$

C) Basis set

In 1951, Roothaan[21] introduced the use of a set of spatial basis functions to solve the differential equations of the HF approximation. Thus, the differential equations were converted into a set of algebraic equations that could be solved by matrix techniques. A given basis set is formed by an ensemble of functions that describe the motion of the electrons in space. The choice of the basis set is very important since it governs the correct functioning of the machinery

of calculation. Lots of basis sets are available nowadays. They were developed with the aim of improving the behavior of electrons by stressing some characteristics. Two types of functions are commonly used. Their mathematical differences are of much importance in the computational implementation. The Slater-type orbitals (STO) are defined, in general, as

$$\varphi^{STO} = Nx^l y^m z^n e^{-\xi r} \tag{10}$$

Whereas Gaussian-type orbitals (GTO) are

$$\varphi^{GTO} = Nx^l y^m z^n e^{-\xi r^2} \tag{11}$$

x, y, and z describe the angular part of the orbital, and the ξ factor, which affects the exponential radial function, fixes how much contracted the orbital is. The only difference between STO's and GTO's is the dependence with respect to r of the exponential term. Even though, this has dramatic implications in the treatment of data. GTO's enables the efficient calculation of molecular multicenter integrals by an analytical procedure. On the other hand, STO's are more adequate for numerical integration since no efficient analytical algorithms are known yet. Even though, and as a general rule, the accuracy achieved by a single STO is similar to that of about three GTOs. This fact arises from the behavior of each type of orbital in the vicinity of the nuclei and in the $r \to 0$ region. STO's are advantageous from this point of view since they reproduce very well the necessary conditions of electronic behavior around a nucleus. They are actually the exact solutions of the Schrödinger equations for the hydrogen atom. Contrarily to wavefunction-based methods, where Gaussian-type functions are commonplace because of the advantages they offer to the calculation of four-centre-two-electron integrals, there is no need of combinations of functions to reproduce the cusp behavior at $r \to 0$.

Every basis set can be classified in terms of quality. It depends on the number of functions describing each atomic orbital. The larger the number of functions, the better the basis set accuracy. The exponential factor ξ governs how much diffuse is each function. The second characteristic describes the angular part of the function, that is, the complexity of the nodal structure of φ_i. For a better description of the electronic structure, φ_i's with different values of ξ and polarization functions may be used. Of course, the more extended the basis is, the more time-demanding the calculation becomes, but the better the result is.

D) The Kohn-Sham approach

Almost all the modern DFT-based applications make use of the DFT formulation of Kohn and Sham (KS).[22] It was postulated the existence of an auxiliary system of noninteracting electrons moving in an external and unique potential, $\upsilon_S(r)$. This potential has the property of yielding exactly the same density than the interacting system. In addition, that exact wavefunction for this reference system is a Slater determinant. The exact energy may be written as

$$E = \int -\frac{1}{2}\nabla^2(\vec{r}_1)\gamma(\vec{r}_1,\vec{r}_{1'})d\vec{r}_1 + \int \rho(\vec{r})v(\vec{r})d\vec{r} + \frac{1}{2}\int \vec{r}_{12}^{\ -1}\Gamma(\vec{r}_1,\vec{r}_2)d\vec{r}_1 d\vec{r}_2 \qquad (12)$$

where $\Gamma(\vec{r}_1,\vec{r}_2)$ is the probability density of finding two electrons at $\vec{r}_1$ and $\vec{r}_2$. It is decomposed into the uncorrelated part, $\rho(\vec{r}_1)\upsilon(\vec{r}_2)$, and the remainder that accounts for the exchange and correlation parts of the correlated probability.

From this formulation we obtain the KS orbitals, in which the optimization of the density is straightforward since it is derived after solving a set of one-electron equations. The problem at this point is that the exact mathematical form connecting the energy and the total electronic density is yet unknown. Hence, approximations should be introduced in order to have an analytic expression to be evaluated. The primitive XC part of E[ρ] is the central battlefield of theoreticians that try to improve the performance of the model.

Local Density Approximation. Being the central model that gave birth to the DFT, it is the simplistic but surprisingly good uniform electron gas approximation (or homeogeneous gas model) proposed in the middle 1920's by Thomas and Fermi.[23] Such a model can be mathematically formulated as an energy functional that accounts for the local value of ρ at each point in space (regardless of any other one). For the homogeneous gas approximation, the first analytic expression obtained for the electron correlation part was reported in the early 80's by Vosko, Wilk, and Nusair (VWN)[24] which fitted energy values obtained from Monte Carlo simulations by Ceperley and Alder.[25] The exchange part of this functional was approximated, in a simple form, with the Xα method of Slater[26]

$$E_{X\alpha}[\rho] = -\frac{9}{8}\left(\frac{3}{\pi}\right)^{\frac{2}{3}}\alpha\int \rho(\vec{r}_1) - \frac{4}{3}d\vec{r}_1 \qquad (13)$$

where α is a semi-empirical adjustable parameter. The XC part of the energy functional within the Local Density Approximation (LDA) consists in these two parts

$$E_{XC}^{LDA} = E_X^{X\alpha} + E_C^{VWN} \tag{14}$$

Generalised Gradient Approximation. The modestly accurate results of the LDA applied to molecules forced the search of more accurate expressions for describing the motion of electrons. The central idea is to take into account not only the value of the electron density at each point in space but also what is the value of its first derivative. This constitutes the so-called non-local or generalised gradient approximations, GGA. These gradient corrections are added to the local definition of X and C, thus redefining the E_{XC} and, in most of the cases, improving the performance of the model. In general, the gradient corrections are functionals of the density and of its first derivative:

$$E_{XC}^{NLDA}[\rho] = \int f(\rho, \nabla\rho) d\vec{r} \tag{15}$$

The density gradient is typically included in the form $\frac{|\nabla\rho|^2}{\rho^{\frac{4}{3}}}$.

The non-local term, NLDA, together with the LDA part of the XC leads to mathematical expressions for the corrected $E_{XC}^{GGA}[\rho]$ functionals

$$\begin{aligned} E_C^{GGA}[\rho] &= E_C^{LDA}[\rho] + E_C^{NLDA}[\rho] \qquad \text{for correlation} \\ E_X^{GGA}[\rho] &= E_X^{LDA}[\rho] + E_X^{NLDA}[\rho] \qquad \text{for exchange} \end{aligned} \tag{16}$$

All the efforts concerned with the development of DFT are aimed at improving and testing the exchange and correlation corrections for the NLDA part. There is an inherent problem beneath the current status of the model. Provided that the exact form of $E[\rho]$ is unknown, we cannot say much about the performance of the new functionals until they are tested with chemical systems. So, there is no systematic way to get better functionals and, a priori, a new formulation of the E_{XC} part is not better than a previous one. There are many XC expressions in the literature.[27] The functionals enjoying a widespread acceptance nowadays are the Becke[28] exchange functional and the Perdew[29] and Perdew-Wang[30] correlation functionals, like the Lee-Yang-Parr[31] (LYP) for correlation that combined with the Becke's three-parameter method (B3),[32] led to the popular

B3LYP exchange-correlation functional. They were introduced with the aim of including the exact exchange energy as a contribution from the correct HF exchange. This latter mathematical approach has proven to be accurate for many systems, although somewhat more time demanding than non-hybrid XC functionals like the BP86 or the BPW91. This is so since the calculation of the two-electron integrals in the HF exchange is avoided.

E) Details of DFT

Compared to HF-based methods, the way to account for the correlation effects in the framework of the DFT does not pass through enlarging the trial wavefunction. It is the unknown Hamiltonian that is improved, indeed.

Total Molecular Energies. The analysis of molecular energies obtained by different functionals is not absolute due to the fact that the variational principle is not applicable in the framework of the DFT (the exact functional connecting E and ρ is unknown), it is impossible to know a priori whether a simpler functional does not imply a worse energy, therefore there is not such a direct connection in DFT energies.

Molecular Geometries. LDA and GGA geometries are supposed to give better geometries with respect to HF ones. The available experimental data reflect this. Equilibrium geometries computed by LDA tend to underestimate bond distances GGA overcorrects LDA and slightly overestimates the Metal-Ligand (M-L) distances, which is an effect of the inherent deficiencies in the treatment of electron correlation.

Electronic Properties. DFT gets rid of electrons as the basic unit. Instead, it is based on a gas of electrons. Even though, the current formalism in use, the Kohn-Sham approach, forced the implementation in density functional-based methods of molecular orbitals containing the electrons, the KS orbitals that are connected to the density via

$$\rho(r) = \sum_i \left|\varphi_{i,KS}\right|^2 \qquad (17)$$

Although the physical significance of the KS orbitals is not clear, their use in the context of the density functional scheme has been spread and their application for rationalizing chemical phenomena is routinely used.

Chemists are being familiarized with the discussion of properties related with the Highest Occupied Molecular Orbital (HOMO) and the Lowest Unoccupied Orbital (LUMO) and their

spatial shape. The HOMO-LUMO gap, i. e. the energetic separation between both orbitals, is an indicator of the stability of the compound.

DFT energy is not variational with υ_{XC}. The HF method was formulated within the framework of an exact Hamiltonian, and in this case the variational principle is applicable. The only way to improve DFT is formulating better *XC* potentials.

The single-determinant nature of DFT cannot handle complex electronic configurations. Post-HF techniques are the tool to be used in such cases, but they are quite more expensive.

Highly negatively charged molecules display artificially upshifted occupied molecular orbitals. In general, HOMO-LUMO gaps are smaller at the DFT level than in the HF approximation.

The electronic correlation is introduced at low cost for DFT, whereas including correlation to the HF method is very expensive.

DFT mainly works with ρ while HF with the wavefunction, which is not an observable as ρ.

Summarizing, before the eighties, the conventional ab initio methods were the only way to include correlation effects in quantum calculations. DFT represents nowadays an alternative way for introducing the electronic correlation effects for solving the electronic Schrödinger equation. DFT methods are known as good for calculating systems of medium and large size at low computational cost, and the accuracy reached is generally comparable to the expensive post-HF methods.

F) DFT descriptors

The fundamental equation of the chemical change

In the canonic ensemble the Hamiltonian of a system only depends on the number of electrons and the external potential, therefore, $E = E[N, \nu(r)]$. An expansion of the energy functional by Taylor series gives:

$$dE = \left(\frac{\partial E}{\partial N}\right)_{\nu(r)} dN + \int \left(\frac{\delta E}{\delta \nu(\vec{r})}\right)_N \delta\nu(\vec{r}) d\vec{r} \quad + \ldots \quad . \tag{18}$$

But, also according to the first HK theorem $E_v = E_v[\rho(r)]$:

$$dE = \int \left(\frac{\delta E}{\delta \rho(\vec{r})} \right)_{v(r)} \delta\rho(\vec{r}) d\vec{r} + \int \left(\frac{\delta E}{\delta v(\vec{r})} \right)_{\rho(r)} \delta v(\vec{r}) d\vec{r} \quad + \ldots \quad . \tag{19}$$

Including eq. (9) and eq. (19) we obtain:

$$dE = \mu dN + \int \left(\frac{\delta E}{\delta v(\vec{r})} \right)_{\rho(r)} \delta v(\vec{r}) d\vec{r} \quad + \ldots \quad . \tag{20}$$

Comparing eq. (18) and eq. (20):

$$\mu = \left(\frac{\partial E}{\partial N} \right)_{v(r)} = \left(\frac{\delta E}{\delta \rho(\vec{r})} \right)_{v(r)} \quad . \tag{21}$$

In eq. (4) it is seen that the electron-nucleus potential is the unique part of the electronic energy that depends on the external potential. Therefore, studying how changes the electronic energy changing *v(r)* and keeping constant the density, eq. (4) turns out to be:

$$dE = \int \delta v(\vec{r}) \rho(\vec{r}) d\vec{r} \quad , \tag{22}$$

If the same conditions are applied to eq. (19):

$$dE = \int \left(\frac{\delta E}{\delta v(\vec{r})} \right)_{\rho(r)} \delta v(\vec{r}) d\vec{r} \quad , \tag{23}$$

comparing eq. (22) and eq. (23):

$$\rho(\vec{r}) = \left(\frac{\delta E}{\delta v(\vec{r})} \right)_{\rho(r)} \quad . \tag{24}$$

Introducing eq. (24) in eq. (20), the fundamental equation of the chemical change is achieved:

$$dE = \mu dN + \int \rho(\vec{r}) \delta v(\vec{r}) d\vec{r} \quad + \ldots \quad . \tag{25}$$

Finally, comparing eq. (25) and eq. (18):

$$\rho(\vec{r}) = \left(\frac{\delta E}{\delta v(\vec{r})} \right)_{N} = \left(\frac{\delta E}{\delta v(\vec{r})} \right)_{\rho(r)} \quad . \tag{26}$$

If in the energy expansion by Taylor series of eq. (18) the second order terms are included:

$$\begin{aligned} dE = \mu dN + \int \rho(\vec{r}) \delta v(\vec{r}) d\vec{r} \quad + \frac{1}{2} \left(\frac{\partial^2 E}{\partial N^2} \right)_{v(r)} dN^2 + \frac{1}{2} \int \left(\frac{\delta^2 E}{\delta v(\vec{r}) \delta v(\vec{r}')} \right)_{N} \delta v(\vec{r}) \delta v(\vec{r}') d\vec{r} d\vec{r}' + \\ \int \left(\frac{\delta^2 E}{\delta v(\vec{r}) \partial N} \right) \delta v(\vec{r}) dN d\vec{r} + \quad \ldots \quad , \end{aligned} \tag{27}$$

It is possible to define the following functions:

$$\eta = \left(\frac{\partial^2 E}{\partial N^2}\right)_{v(r)} = \left(\frac{\partial \mu}{\partial N}\right)_{v(r)} \quad , \tag{28}$$

$$\chi(\vec{r},\vec{r}') = \left(\frac{\delta^2 E}{\delta v(\vec{r})\delta v(\vec{r}')}\right)_N \quad \text{and} \tag{29}$$

$$f(\vec{r}) = \left(\frac{\delta^2 E}{\delta v(\vec{r})\partial N}\right) = \left(\frac{\delta \mu}{\delta v(\vec{r})}\right)_N = \left(\frac{\partial \rho(\vec{r})}{\partial N}\right)_{v(r)} \quad , \tag{30}$$

where η is the hardness,[33] $\chi(r,r')$ is the lineal response function[34] and $f(r)$ the Fukui function.[35] Now eq. (27) reads:

$$dE = \mu dN + \int \rho(\vec{r})\delta v(\vec{r})d\vec{r} \quad + \frac{1}{2}\eta dN^2 + \frac{1}{2}\int \chi(\vec{r},\vec{r}')\delta v(\vec{r})\delta v(\vec{r}')d\vec{r}d\vec{r}' + \int f(\vec{r})\delta v(\vec{r})dNd\vec{r} + \quad \ldots \tag{31}$$

Figure II-1 represents a summary of the derivatives of the electronic energy with respect to the external potential and the number of electrons found in the canonic ensemble.

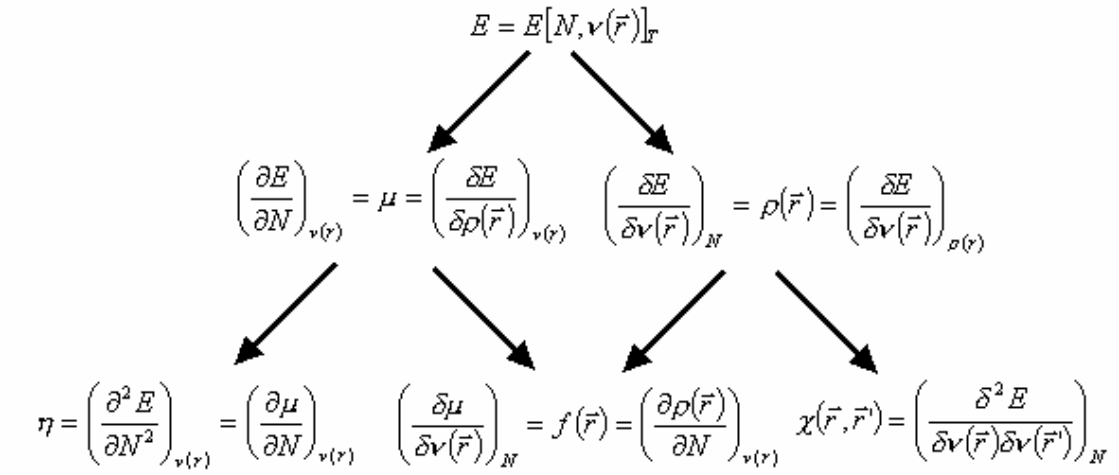

Figure II-1: Scheme of the derivates of the electronic energy obtained in the canonic ensemble. The arrows towards the right mean derivatives with respect to the external potential, while the arrows towards the left corresponds to the derivatives with respect to the number of electrons.

For the grand canonical ensemble, the same approach leads to the following derivatives:

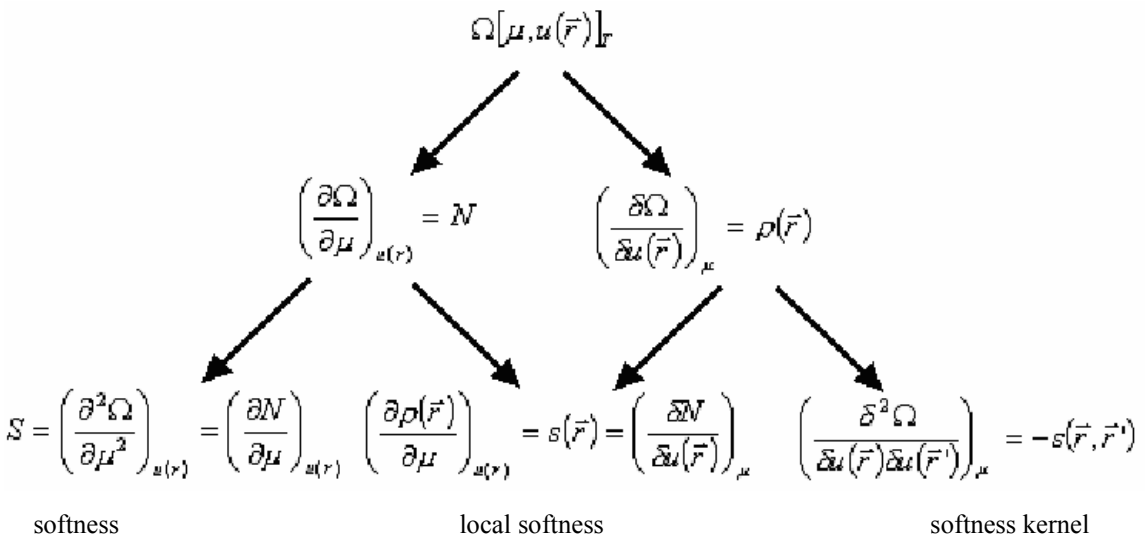

Figure II-2: Scheme of the relationships that are obtained with the grand canonic ensemble. The arrows towards the left correspond to the derivatives with respect to the chemical potential, while the arrows towards the right mean derivatives with respect to the potential *u(r)*, which is defined as $u(r) = v(r) - \mu$, where $v(r)$ is the external potential and μ is the chemical potential.

The grand canonical ensemble is defined as:[36]

$$\Omega[\rho(\vec{r})] = \Omega[\mu, u(\vec{r})]_T = E[\rho(\vec{r})] - N\mu \quad , \tag{32}$$

In the following part of this introduction these reactivity indexes will be studied in detail, splitting them in two large groups: global, characteristic of all a whole molecule or system; and local, they present a different value in any position of the space [*g(r)*].

Global properties

1.Chemical potential and electronegativity

In the DFT field, chemical potential (μ) is defined as the first derivative of the electronic energy with respect to the number of electrons while keeping constant the external potential:[37]

$$\mu = \left(\frac{\partial E}{\partial N}\right)_{v(r)} \quad , \tag{33}$$

where μ has the same physical meaning as the chemical potential in the classical thermodynamics of the macroscopic systems (it measures the tendency of the electrons of escaping of a considered system).[38] The main inconvenience that presents the calculation of the derivatives of the electronic energy with respect to the number of electrons (chemical potential,

hardness, Fukui functions…) is that the energy is not a continuous function with the number of electrons.[39,40] If in eq. (33) the finite differences approximation is used:

$$\mu = \left(\frac{\partial E}{\partial N}\right)_{v(r)} \cong \frac{\Delta E}{\Delta N} = \frac{E(N+1) - E(N-1)}{(N+1) - (N-1)} = \frac{(E(N) - A) - (E(N) + I)}{2} \quad , \tag{34}$$

where A is the electronic affinity [*E(N)-E(N+1)*] and *I* the ionization potential [*E(N-1)-E(N)*]. As the external potential must be kept constant, the values *A* and *I* are vertical, which mean adding or extracting electrons of the system, but keeping the same equilibrium geometry.

$$\mu \cong -\frac{(A+I)}{2} = -\chi_M \quad , \tag{35}$$

where χ_M is the Mulliken electronegativity. The electronegativity (χ) is the capacity of an atom or a molecule to attract electrons. Eq. (35) can be simplified using the Koopmans' theorem,[41] which equals to the electronic affinity and the ionization potential to the negative of the LUMO and HOMO energies, respectively.

$$-\mu = \chi_M \cong \frac{(A+I)}{2} \cong -\frac{\varepsilon_{HOMO} + \varepsilon_{LUMO}}{2} \quad . \tag{36}$$

2.Hardness and softness

The first observations that made the hardness concept appear were done by Berzelius, who observed that some metals in the nature are present as sulfurs, while other ones as oxides or carbonates. In 1963, Ralph G. Pearson introduced in the chemical world the concept of hard and soft Lewis acids and basis,[42,43] but it was not till 1983 after working together with Robert G. Parr that a mathematical expression for the hardness was obtained.[33]

The hardness (η) is a measure of the resistance of a system to modify its electronic configuration.[17] In the DFT formalism, the hardness can be defined as the second partial derivative of the energy with respect to the total number of electrons of the system keeping the external potential constant.

$$\eta = \left(\frac{\partial \mu}{\partial N}\right)_{v(r)} = \left(\frac{\partial^2 E}{\partial N^2}\right)_{v(r)} \quad . \tag{37}$$

If the finite differences approximation is applied in eq. (37):

$$\eta = \left(\frac{\partial \mu}{\partial N}\right)_{v(r)} = \left(\frac{\partial^2 E}{\partial N^2}\right)_{v(r)} \cong E(N+1) + E(N-1) - 2E(N) \quad , \tag{38}$$

Operating and introducing the ionization potential and the electronic affinity concepts:

$$\eta \cong E(N+1)+E(N-1)-2E(N)=\big(E(N)-A\big)+\big(E(N)+I\big)-2E(N)=I-A \quad , \qquad (39)$$

and finally introducing the Koopmans' theorem:[41]

$$\eta \cong I-A \cong \varepsilon_{LUMO}-\varepsilon_{HOMO} \quad . \qquad (40)$$

Experimentally, the hardness can be calculated from the reaction energy of the following disproportion reaction:

$$2X_{(g)} \rightarrow X^{-}{}_{(g)}+X^{+}{}_{(g)} \qquad \eta=\Delta E=I-A \quad . \qquad (41)$$

The higher the ΔE, the harder the considered species is. Experimentally, it has been obtained $\Delta E>0$ for all the known species, which means that $\eta>0$.

These last years, lots of efforts have been made to find alternative ways to evaluate the hardness.[44-51]

The inverse of the hardness is the softness (S):[17]

$$S=\frac{1}{\eta}=\left(\frac{\partial N}{\partial \mu}\right)_{v(r)} \quad . \qquad (42)$$

Different authors have studied the relationship between the softness and the polarizability (α), and empirically it has been found that $\alpha^{1/3}$ is a linear function of the softness.[52-54]

3.Global Electrophilicity index

The global electrophilicity index was proposed by Parr, Von Szentpaly, and Liu. It associated to the power of an atom or a molecule to capture electrons.[55] Considering a system as a model of an electrophilic species inside a sea of free electrons and settling the saturation conditions of the species, it is achieved that the stabilization energy of the system is equal to $-\mu^2/2\eta$. Therefore, eq. (43) is a measure of the system electrophilicity.

$$\omega=\frac{\mu^2}{2\eta} \qquad (43)$$

Application of the global properties

1.Hard and soft acid basis principle

Pearson in his article *J. Am. Chem. Soc.* **1963**, *85*, 3533 (the thirteenth article most cited of JACS in its 125 years of history) introduced in the world of the chemistry the hard and soft acids and the hard and soft bases concepts, all together with the hard and soft acid bases principle (HSAB):

"The hard acids prefer to be coordinated with hard bases, while the soft acids tend to be coordinated with soft bases, either from the thermodynamic or the kinetic points of view."

Soft bases: Electron donator species easily oxidable that presents a high polarizability and a low electronegativity. Examples: I^-, Br^-, and H^-.

Hard bases: Electron donator species not easily oxidable that presents a low polarizability and a low electronegativity. Examples: F^-, OH^-, and H_2O.

Soft acid: Electron acceptor species that holds a small charge density. Examples: Rb^+, Cu^+, and Fe^+.

Hard acid: Electron acceptor species that holds an important charge density. Examples: H^+, Li^+, and Fe^{3+}.

An example of controlled reaction by HSAB principle can be:

$$\text{Ex}: \quad \underbrace{Li^+}_{\text{hard}}\underbrace{I^-}_{\text{soft}} \quad + \quad \underbrace{Ag^+}_{\text{soft}}\underbrace{F^-}_{\text{hard}} \quad \rightarrow \quad Li^+F^- \quad + \quad Ag^+I^- \tag{44}$$

One of the most interesting applications of the HSAB in the organic chemistry world has been the nucleophilic substitutions, though this principle can be applied to a number of other chemical branches as the coordination compounds, solute interactions with solvent, and catalysis.[17]

In 1983, Parr and Pearson demonstrated theoretically the HSAB principle.[33] In the formation of one AB diatomic molecule where the external potential is kept constant, the behavior of the chemical potentials of the systems A and B is described as:

$$\mu = \mu^0 + \left(\frac{\partial \mu^0}{\partial N}\right)_{v(r)} \Delta N = \mu^0 + \eta^0 \Delta N \quad , \tag{45}$$

$$\mu_A = \mu_A^0 + \eta_A^0 \Delta N_A \quad and \tag{46}$$

$$\mu_B = \mu_B^0 + \eta_B^0 \Delta N_B \quad , \tag{47}$$

where the superindex 0 is referred to the properties before the bond formation. For the created molecule $\mu_A=\mu_B$; thus equaling eq. (46) and eq. (47) and taking in account that $\Delta N_A=-\Delta N_B$, the following conclusion is achieved:

$$\Delta N = \frac{\mu_B^0 - \mu_A^0}{\eta_B^0 + \eta_A^0} \quad , \tag{48}$$

where B is the species with the highest chemical potential (Lewis bases) and A the species with the lowest chemical potential (Lewis acid). According to eq. (48), the difference between both chemical potentials facilitates the electronic transfer, while the sum of the hardness blocks it. Low η values mean highly reactive species (high η values mean high stability). The increase of energy of this process is given by:

$$\Delta E = \Delta E_A + \Delta E_B = \mu_A^0 \Delta N_A + \frac{1}{2}\eta_A^0 \Delta N_A^2 + \mu_B^0 \Delta N_B + \frac{1}{2}\eta_B^0 \Delta N_B^2 \quad , \tag{49}$$

if the condition $\Delta N_A=-\Delta N_B$, is applied and the result of eq. (48) is introduced, we obtain:

$$\Delta E = \Delta N\left(\mu_A^0 - \mu_B^0\right) + \frac{1}{2}\Delta N^2\left(\eta_A^0 + \eta_B^0\right) = -\frac{\left(\mu_B^0 - \mu_A^0\right)^2}{\eta_A^0 + \eta_B^0} + \frac{1}{2}\frac{\left(\mu_B^0 - \mu_A^0\right)^2}{\left(\eta_A^0 + \eta_B^0\right)^2}\left(\eta_A^0 + \eta_B^0\right) \quad , \tag{50}$$

and finally,

$$\Delta E = -\frac{1}{2}\frac{\left(\mu_B^0 - \mu_A^0\right)^2}{\eta_A^0 + \eta_B^0} = -\frac{1}{2}\frac{\left(\Delta\mu^o\right)^2}{\eta_B^0 + \eta_A^0} = -\frac{1}{2}\frac{\left(\Delta\mu^o\right)^2 S_A^0 S_B^0}{S_A^0 + S_B^0} \quad , \tag{51}$$

If the interaction of one soft acid with a soft bases is considered, $\left(\eta_A^0 + \eta_B^0\right)$ will present a small value and for a given $\Delta\mu$ highly stabilized ΔE values are obtained. On the other hand, if the interaction of one hard acid with one hard bases is taken in account, for a given $\Delta\mu$, the value of $\left(\eta_A^0 + \eta_B^0\right)$ is large; and therefore, ΔE is not very stabilizing, which does not agree with the chemical experience. This means that a second effect in the formation of the chemical bond must be considered. While the soft acids and bases tend to form covalent bonds, the hard acids and bases form ionic bonds and in eq. (51) lacks the inclusion the part of electrostatic stabilization, that in the case of hard acids or bases is very important.[56]

2. Maximum hardness principle (MHP)and minimum polarizability (MPP):

"Molecules always tend to a maximum hardness state"

The maximum hardness principle was formulated by Pearson in 1987,[57] and four years later theoretically demonstrated by Parr and Chattaraj.[20] This demonstration is based on the combination of the statistical mechanics with the density functional theory. The external potential, the chemical potential, and the temperature must be constant.[58,59]

Taking into account the inverse relationship between the hardness and the polarizability,[52-54] Chattaraj and Sengupta formulated the minimum polarizability principle.[20]

"Molecules tend to a state of minimum polarizability"

The application of these principles is more limited, due to the fact that the restriction of the constant external potential and the chemical potential is very strict and in the chemistry world most of the processes mean changes in the nucleus positions. However, the relaxation of these principles is possible and these two principles have been successfully applied to the study of the molecular vibrations,[60-62] internal rotations,[63] proton transfer reactions,[64] and different types of reactions.[65] There are some chemical processes that do not agree with the MHP and the MPP because of the large changes in the chemical potential and the external potential occur along the reaction coordinate.[66]

3. Electrophilicity:

In an analogous way to the MHP and the MPP, the minimum electrophilicity principle has been formulated.[67] Furthermore, the electrophilicity has been used with success to understand the reactivity and behavior of carbenes,[68] cycloaddition reactions,[69] and the interactions of the electrophiles with solvents.[70]

Local Properties

1.Fukui function

The Fukui function is a reactivity index that connects the concepts of the molecular frontier orbitals of Fukui with the DFT. It was defined by Yang and Parr[35] as:

$$f(\vec{r}) = \left(\frac{\delta\mu}{\delta v(\vec{r})}\right)_N = \left(\frac{\partial\rho(\vec{r})}{\partial N}\right)_{v(r)} \quad , \quad \int f(\vec{r})d\vec{r} = 1 \quad . \tag{52}$$

The Fukui function defines the local changes in the electronic density of a system, due to a perturbation in the total number of electrons; therefore, it reflects the character of a molecule to

accept or give electrons to another system. For a molecule or an atom, the derivative in eq. (52) is not continuous with respect to the number of electrons.[40] Because of this, Parr and Yang created three definitions of the Fukui functions: $f^{+}(\vec{r})$, $f^{-}(\vec{r})$, and $f^{0}(\vec{r})$ corresponding to the reactivity index that describes the attack to the system by a nucleophile, an electrophile or a radical:

$$f^{+}(\vec{r}) = \left(\frac{\partial \rho(\vec{r})}{\partial N} \right)^{+}_{v(r)} \quad , \tag{53}$$

$$f^{-}(\vec{r}) = \left(\frac{\partial \rho(\vec{r})}{\partial N} \right)^{-}_{v(r)} \quad , \quad and \tag{54}$$

$$f^{0}(\vec{r}) = \frac{1}{2}\left(f^{+}(\vec{r}) + f^{-}(\vec{r}) \right) \quad , \tag{55}$$

where the superindex +, –, and 0 refer to the right, left, and central derivatives, respectively. If the technique of the finite differences used in the chemical potential and the hardness is applied to eqs. (53)-(55) and using the theory of the frontier orbitals of Fukui, we find:

$$f^{+}(\vec{r}) \cong \rho_{N+1}(\vec{r}) - \rho_{N}(\vec{r}) \cong \rho_{LUMO}(\vec{r}) \quad , \tag{56}$$

$$f^{-}(\vec{r}) \cong \rho_{N}(\vec{r}) - \rho_{N-1}(\vec{r}) \cong \rho_{HOMO}(\vec{r}) \quad and \tag{57}$$

$$f^{0}(\vec{r}) \cong \frac{1}{2}\left[\rho_{N+1}(\vec{r}) - \rho_{N-1}(\vec{r}) \right] \cong \frac{1}{2}\left[\rho_{HOMO}(\vec{r}) + \rho_{LUMO}(\vec{r}) \right] \quad . \tag{58}$$

These Fukui functions are defined in order to give null or positive values for most of the points in space ($\rho_{N+1}(r) > \rho_{N}(r) > \rho_{N-1}(r)$).

$$f^{+}(\vec{r}) = \lim_{\Delta N \to 0} \frac{\rho_{N+\Delta N}(\vec{r}) - \rho_{N}(\vec{r})}{\Delta N} \quad . \tag{59}$$

This last statement would be certain in the limit $\Delta N \to 0$, but in the definition of the Fukui functions it has been used $\Delta N = 1$. This considerable change in the electronic density distribution can produce a relaxation of the corresponding anion, producing a decrease of the electronic density in some points, even though the increase of one unit in the total number of electrons.

For the attack of a nucleophile to an electrophile, if there are two possible sites to be attacked, the attacking reactive will prefer to approach where the Fukui function is maximum. According to eq. (52), an external potential change where the Fukui function is maximum means a maximum chemical potential change. And this also means a reduction of the energy.

In 1986, Yang and Mortier defined the condensed Fukui functions by integrating eqs. (56)-(58) over the atomic regions:[71]

$$f^{+}{}_{k} = q_k(N+1) - q_k(N) \quad , \tag{60}$$

$$f^{-}{}_{k} = q_k(N) - q_k(N-1) \qquad and \tag{61}$$

$$f^{0}{}_{k} = \frac{1}{2}\left[q_k(N+1) - q_k(N-1)\right] \quad , \tag{62}$$

where $q_k(N)$, $q_k(N+1)$, and $q_k(N-1)$ are the charges of the atom *k* calculated in the system with *N*, *N+1*, and *N-1* electrons, respectively. The main problem that these equations present is that they give different values of Fukui functions depending on the definition of the charge used (Mulliken,[72] CHELPG,[73] NPA,[74] AIM,[75] Hirshfeld[76] or others). The Hirshfeld charges[77] are particularly interesting because they give positive condensed Fukui functions in most cases. Roy[77e), f), g)] has attributed the existence of negative condensed Fukui functions to the relaxation of the density of the cation and the anion, and the incorrect split of the charges.

2. Local softness and hardness:

Yang and Parr defined in 1985 the concept of the local softness as:[78]

$$s(\vec{r}) = \left(\frac{\partial\rho(\vec{r})}{\partial\mu}\right)_{v(r)} \quad , \tag{63}$$

applying the chain rule and taking into account eqs. (42) and (52) the following expression is derived:

$$s(\vec{r}) = \left(\frac{\partial\rho(\vec{r})}{\partial N}\right)_{v(r)}\left(\frac{\partial N}{\partial\mu}\right)_{v(r)} = f(\vec{r})S \quad , \tag{64}$$

which gives the following relationship:

$$\int s(\vec{r})d\vec{r} = S\int f(\vec{r})d\vec{r} = S \quad , \tag{65}$$

where *S* is the global softness. Eq. (65) shows that *s(r)* and $f(r)$ contain the same information, but Geerlings suggested that the local softness containing the global softness of the system could be a useful tool to explain the intermolecular reactivity. If eqs. (60)-(62) are applied to eq. (64) the local condensed softnesses are obtained:

$$s^{+}{}_{k} = \left[q_k(N+1) - q_k(N)\right]S \quad , \tag{66}$$

$$s^{-}{}_{k} = \left[q_k(N) - q_k(N-1)\right]S \quad and \tag{67}$$

$$s^0{}_k = \frac{1}{2}[q_k(N+1) - q_k(N-1)]S \quad . \tag{68}$$

According to local HSAB, if two molecules react, the atoms that will interact will be those having more similar local hardness or softness.

The local hardness[79] is defined as:

$$\eta(\vec{r}) = \left(\frac{\partial \mu}{\partial \rho(\vec{r})}\right)_{v(r)} \quad , \tag{69}$$

and presents the property:

$$\eta = \int \eta(\vec{r}) g(\vec{r}) d\vec{r} \quad , \tag{70}$$

where *g(r)* is any normalized function, thus any function that integrates to 1, for instance $\rho(r)/N$, ρ_{HOMO}, ρ_{LUMO}, or the Fukui functions. The relationship that relates the local hardness and softness is:

$$\int \eta(\vec{r}) s(\vec{r}) d\vec{r} = 1 \quad . \tag{71}$$

3. Local electrophilicity:

Chattaraj[80] defined the local electrophilicity as:

$$\omega_k^\alpha = \omega f_k^\alpha = \frac{\mu^2}{2\eta} f_k^\alpha \quad , \tag{72}$$

where α can be +, -, or *0* and presents the same meaning as in the Fukui functions and *k* refers to the atom of the studied molecule.

G) Energy Decomposition Analysis (EDA)

The bonding interactions between the molecular fragments A and B in a molecule AB have been analyzed with the energy decomposition scheme of the program package ADF[81,82] which is based on the Energy Decomposition Analysis (EDA) method of Morokuma[83] and the Extended Transition State (ETS) partitioning scheme of Ziegler and Rauk.[84] The bond dissociation energy ΔE between the fragments A and B is partitioned into several contributions which can be identified as physically meaningful quantities. First, ΔE, also called BE (Binding Energy) is separated into two major components ΔE_{prep} and ΔE_{int}:

$$\Delta E = \Delta E_{prep} + \Delta E_{int} \tag{73}$$

ΔE_{prep} is the energy which is necessary to promote the fragments A and B from their equilibrium geometry and electronic ground state to the geometry and electronic state which they have in the compound AB. ΔE_{int} is the instantaneous interaction energy between the two fragments in the molecule. The latter quantity is the focus of the bonding analysis.

The first term of Eq. (73), ΔE_{prep},[85] is the energy needed to prepare the fragments for the A-B bond formation. In the case of fragments that do not present singlet state as multiplicity ground state this term must be corrected by an additional term. Therefore, ΔE_{prep} includes a distortion from the geometry of the fragment in its ground state to its geometry in the combined compound as well as an electronic promotion to the state with singlet multiplicity if this is not already the electronic ground state configuration of the fragment. This additional term to form the ΔE_{prep} is sometimes called ΔE_{excit}.

The interaction energy ΔE_{int} can be divided into three main components:

$$\Delta E_{int} = \Delta E_{elstat} + \Delta E_{Pauli} + \Delta E_{orb} \quad (74)$$

ΔE_{elstat} gives the electrostatic interaction energy between the fragments which are calculated with a frozen electron density distribution in the geometry of the complex. ΔE_{Pauli} gives the repulsive interactions between the fragments which are caused by the fact that two electrons with the same spin can not occupy the same region in space. The term comprises the four-electron destabilizing interactions between occupied orbitals. ΔE_{Pauli} is calculated by enforcing the Kohn-Sham determinant of AB, which results from superimposing fragments A and B, to be orthonormal through antisymmetrization and renormalization. The stabilizing orbital interaction term ΔE_{orb} is calculated in the final step of the analysis when the Kohn-Sham orbitals relax to their final form. The latter term can be further partitioned into contributions by the orbitals which belong to different irreducible representations of the point group of the interaction system.

The three terms given in eq. (74) have a physical clear interpretation. The two terms ΔE_{elstat} and ΔE_{Pauli} are sometimes added to a single term ΔE^{o} which is then called the “steric energy term”.[86] ΔE^{o} can have positive or negative values and it should not be identified with the steric interaction which is often used to explain the repulsive interactions of bulky substituents. Since ΔE_{elstat} is usually attractive and ΔE_{Pauli} repulsive, the two terms often nearly cancel each other and the focus of the discussion of the bonding interactions then rests on the orbital interaction term

ΔE_{orb}. Frenking et al. suggest that ΔE_{elstat} should be used to estimate the strength of the electrostatic bonding and ΔE_{orb} for the covalent bonding.[87] Thus, information about the ionic/covalent character of the bond can be obtained from the ratio $\Delta E_{elstat}/\Delta E_{orb}$. It is necessary to be aware of the fact that ionic bonding is a term which originally comes from VB (valence bond) theory and thus, it has conceptually a different meaning than electrostatic attraction. In this context, the names ionic bonding and electrostatic attraction are used for the same quantity, *i. e.* ΔE_{elstat} as defined in the energy partitioning scheme.

The suggestion to identify ΔE_{elstat} and ΔE_{orb} with electrostatic and covalent bonding may be criticized because the former term is calculated using the frozen charge distribution of the interacting fragments.[87] This means that the effects of charge polarization are completely adsorbed by the ΔE_{orb} term. The latter expression contains also a component which clearly does not come from covalent bonding between the fragments. It is the relaxation of the orbitals which is caused by the electrostatic effect of the other fragment. This effect becomes obvious when one fragment has orbitals which have a symmetry that the other fragment does not have. In such cases there is no orbital mixing possible and thus, no covalent interactions which come from these orbitals take place. Nevertheless, the energy levels of the occupied orbitals will change due to electrostatic effects. The associated energy change will appear as part of ΔE_{orb} and thus, it will be interpreted as covalent bonding. It follows that the energy decomposition analysis (EDA) underestimates the electrostatic component and overestimates covalent bonding.

Some procedures to solve the above mentioned problems and artifacts have been thought. A possible way to estimate polarization effects has been suggested in the original work of Kitaura and Morokuma.[83] These authors suggested that the orbital mixing term shall be divided into intrafragment and interfragment contributions. This has been criticized, however, because the former contribution always contains components which come from interfragment mixing due to the basis set superposition between the fragments.[88] The error will even become worse when the basis set is improved because the terms do not converge to definite limits with the extension of basis sets.[89]

Frenking[87] proposed to use eq. (74) with the three terms ΔE_{elstat}, ΔE_{Pauli}, and ΔE_{orb} in an unmodified way because (i) the interpretation is straightforward and the three terms have a

physical meaning; (ii) the terms are mathematically well defined, can be used with any quantum chemical method and they converge to definite limits with the extension of basis sets; (iii) the results appear reasonable when they are compared to previous interpretations; (iv) the results indicate that there seems to be no major errors which are introduced by the fact that polarization effects are only covered by ΔE_{orb} and by the inclusion of orbital relaxation in the latter term.

Furthermore, the ΔE_{orb} which stems from the stabilizing 2-orbital-2-electron interactions between occupied and virtual orbitals of the two fragments in their prepared states, can further be split into contributions from the different symmetry representations as

$$\Delta E_{orb} = \sum_i \Delta E_{\Gamma_i} \tag{75}$$

H) Mayer Bond Order (MBO)

The ideas of bond order and valence are key to our everyday understanding of chemistry and chemical processes. They are implicit in every chemical structure that is drawn and are central to the teaching of inorganic chemistry at all levels. Whilst quantum theory and modern ideas of electronic structure provide a quantitative rationalization of chemical bonding and structure, useful chemical notions such as atomic charge, valence, and bond order for which no quantum mechanical operator can be deduced lose focus and status.

The expectation of the chemist is that the order of a bond is related to the strength and hence to the length of the bond. Pauling and co-workers[90] suggested a simple function to reflect the expected correlation between bond order and length,

$$B_{AB} = \exp\left(\frac{-(r - r_0)}{b}\right) \tag{76}$$

which suggests that the bond order increases or decreases exponentially as the bond length, r, decreases or increases with respect to the length of a reference single bond, r_0. The latter may or may not be known so that r_0 as well as the parameter b are fitted empirically. This requires knowledge of the order of a bond at a number of different lengths. The Pauling correlation is extensively used in the bond valence model. In this approach, the bond valences about an atom sum up to give the absolute amount of the atom's oxidation state. By assigning classical values to the bonds in the simplest systems, the bond valences in more complicated molecules are determined by fitting to the Pauling or related formula.

A number of methods or prescriptions for the calculation of bond order from molecular orbital calculations have been proposed. Probably the simplest is that proposed by Coulson[91] for π-orbitals at the Hückel level. In this definition, the bond order between atoms A and B is simply given by,

$$B_{AB} = \sum_i c_{iA} c_{iB} \tag{77}$$

where c_{iA} is the coefficient of the atomic orbital φ_A on atom A in the i^{th} doubly occupied molecular orbital θ_i,

$$\theta_i = \sum_i c_{iA} \varphi_A \tag{78}$$

and normalization is implicit in the definition of the coefficients. The Coulson bond orders in a molecule, given by eq. (77), are the off-diagonal terms of the matrix P whose elements are given in general as,

$$P_{st} = \sum_i^{occupied} n_i c_{rs} c_{rt} \tag{79}$$

where the summation is over the molecular orbitals with occupation numbers n_i. P is known as the density matrix as the electron density ρ is,

$$\rho(\vec{r}) = \sum_s \sum_t P_{st} \varphi_s \varphi_t \tag{80}$$

In a zero-overlap model such as Hückel theory, the diagonal elements are the atomic charges and the total number of electrons in the molecule is given by their sum. P is often also referred to as the bond-order matrix. In calculations beyond the simple minimal basis Hückel approach, the summation in eq. (78) for the molecular orbital involves a number of orbitals on each atomic centre. The bond order definition given in eq. (77) must be generalized by summing over each of the off-diagonal terms in P involving the orbitals of each atom,

$$B_{AB} = \sum_s^{onA} \sum_t^{onB} P_{st} \tag{81}$$

An alternative definition of bond order due to Wiberg[92] is also based on the P matrix and is applicable to NDO-type theories where the atomic orbital basis forms an orthonormal set. The Wiberg bond order uses the square of the off-diagonal elements of P,

$$B_{AB}^{Wiberg} = \sum_s^{onA} \sum_t^{onB} P_{st}^{\,2} \tag{82}$$

This definition leads to intrinsically positive bond orders between all atoms in a molecule. Wiberg bond orders are closer to classical bond valences and are implemented in many semi-empirical electronic structure codes. In ab initio molecular orbital theories, a basis set of non-orthogonal atomic orbitals is generally used and overlap is included. The total number of electrons in a molecule is given by integrating eq. (80) over all space,

$$N = \sum_{s} P_{ss} + \sum_{s} \sum_{t \neq s} P_{st} S_{st} \tag{83}$$

where S is the atomic orbital overlap matrix. The off-diagonal matrix elements of PS are known as Mulliken overlap populations and are, by analogy with the Coulson definition, often taken as a measure of the contribution from each pair of orbitals to the strength of the chemical bonds. Mayer[93] has suggested a method for calculating bond orders from the P matrix,

$$B_{AB}^{Mayer} = \sum_{s}^{onA} \sum_{t}^{onB} (\mathrm{PS})_{\mathrm{st}} (\mathrm{PS})_{\mathrm{ts}} \tag{84}$$

The Mayer definition can be seen as an extension of the Wiberg index. This leads to the classical integer values for homonuclear diatomics when minimal or small basis sets are used. Non-integer values are found for larger basis sets and in more complicated molecules and these reflect the ionic character of the bonds as well as delocalization and multicentre effects. Mayer bond orders are a valuable tool in the analysis of the bonding in main group[94] and transition metal[95] systems. The insight that can be obtained into the strength and nature of the bonding using the Mayer bond order has been demonstrated by a number of case studies in this thesis, drawn from a variety of areas of the periodic table.

The relationship of the Mayer bond order to the Mulliken population is clear from the definitions given above. The basis set dependence of the Mulliken population analysis is well known, although Mayer[93] has also shown that its form is fully consistent with the molecular orbital approach rather than an arbitrary choice. The basis set dependence of the Mayer bond order has been less thoroughly studied.

Lendvay[96] has studied the predictions of the Mayer definition for C–C, C–O and C–H bonds and found that the Pauling formula describes the correlation extremely well. It may be noted that the dependence of the Mayer bond order on bond length does not arise from the inclusion of orbital overlap in its definition. When a non-orthogonal basis set is used, the normalization of the

molecular orbital leads to orbital coefficients that are dependent on the atomic orbital overlaps. The calculation of the Coulson or Wiberg bond orders using the molecular orbitals generated using such a basis set then introduces this overlap dependence. The multiplication of the P and S matrices removes this dependence in the Mayer definition, as may be simply demonstrated for a molecule such as H_2. The variation in the order of the bond between atoms A and B with its length in a set of molecules containing a variety of substituents on the two atoms thus reflects the redistribution of electron density and the differing electronic demands of the molecular fragments.

Orbital symmetry plays a central role in bonding theory based on the concepts of molecular orbital models. As well as aiding the computational efficiency of electronic structure codes, it has a strong influence on the teaching and description of covalent bonding. Thus, bonding interactions are often separated into σ, π, and δ-interactions even in molecules where these labels are inappropriate. The synergistic roles of σ-donation and π-acceptance by ligands such as CO and olefins in organometallic compounds of many different shapes are used, for example, as a powerful tool for the understanding and prediction of molecular properties. Symmetry allows the chemist to build up the complex electron density in a molecule and decompose the bonding into the orbital contributions from fragments.

The definition of the P matrix, given in eq. (79), may be rewritten by grouping together the occupied orbitals into symmetry types Γ,

$$P = \sum_{\Gamma}^{sym\ \ types} P^{\Gamma} \tag{85}$$

Similarly, the PS matrix may be rewritten as a sum over symmetry types,

$$PS = \left(\sum_{\Gamma} P^{\Gamma} \right) S = \sum_{\Gamma} (PS)^{\Gamma} \tag{86}$$

The Mayer bond order given in eq. (78) then becomes,

$$B_{AB}^{Mayer} = 2 \sum_{r}^{onA} \sum_{t}^{onB} \left(\sum_{\Gamma_i} PS_{st}^{\Gamma_i} \right) \left(\sum_{\Gamma_i} PS_{ts}^{\Gamma_i} \right) \tag{87}$$

As long as the orbitals s and t, centred on atoms A and B respectively, only occur in one common symmetry species at most, there are no cross-terms arising from the two summations in brackets in eq. (87). In this case, the bond order is given as a sum over symmetry species,

$$B_{AB}^{Mayer} = \sum_{\Gamma} B_{AB}^{\Gamma} \tag{88}$$

This is the case in many complexes for the bonds to the central element. In these systems, the atomic orbitals of the central element each span a single symmetry species. Each atomic orbital on the central atom only occurs in molecular orbitals with ligand orbitals of one symmetry type. 'Cross terms' in eq. (87) of the type $(P^{\Gamma_i} S)_{st}$ $(P^{\Gamma_j} S)_{ts}$ are zero unless i = j. The Mayer bond order can then be broken down into its contributions from orbitals of each symmetry type.

Eq. (88) does not apply when s and t occur in more than one symmetry species. This may be the case in high symmetry molecules if there is more than one atom of type A and of type B. The two atoms in a homonuclear diatomic, for example, are equivalent by symmetry. Each orbital on atom A occurs in molecular orbitals of two symmetry types labelled as g and u. The equivalent orbital on atom B occurs in the same two symmetry types. The cross terms in eq. (87) are non-zero. It is similarly not possible to compute the contributions by symmetry type to the C–H or C–C bond orders in the benzene molecule as there are six equivalent C and six equivalent H atoms.

Even in these cases, some information about the contributions can still be obtained by summing over sets of symmetry types. In the homonuclear diatomic, there are no atomic orbitals which occur in both σ and π molecular orbitals. No cross terms therefore occur in the summation if the PS^{Γ} matrices are added together for the g and u parts of the σ, π, δ, . . . orbitals. Similarly, in the benzene ring, there is a complete separation of the atomic orbitals into those symmetric and asymmetric with respect to the σ_h plane and thus the in-plane and out-of-plane contributions to the C–C bonding can be obtained. The most useful separation into σ and π bond orders is thus possible.

In molecules with low symmetry, there is often only one symmetry equivalent atom of each type and this problem is not relevant. In such molecules, however, the small number of symmetry species reduces the relevance of symmetry in understanding the bonding and the usefulness of the decomposition.

I) Time Dependent Density Functional Theory (TDDFT)

Time dependent density functional theory (TDDFT) has been shown to be a reliable quantum mechanical method for the calculation of molecular response properties such as excitation energies,[97-100] dynamic polarizabilities[98,101,102] and van der Waals dispersion coefficients[103] TDDFT has also been used to calculate the first order susceptibility of solids.[104]

The advantage of TDDFT compared to most other quantum methods is that TDDFT has a high accuracy, is time efficient, and can be applied to large systems.

Time-dependent density functional theory[105] provides a formally rigorous extension of Hohenberg–Kohn–Sham density-functional theory, to the situation where a system, initially in its ground stationary state, is subject to a time-dependent perturbation modifying its external potential υ. This allows for the description of various time-dependent phenomena, such as atoms and solids in time-dependent electric or magnetic fields. In addition, TDDFT provides an efficient way to calculate the dynamic polarizability, required to describe the optical properties of matter.

The first step in the development of the theory is to demonstrate the existence of an unique correspondence between the time dependent one-body density $\rho(\mathbf{r}, t)$ and the time-dependent potential $\upsilon(\mathbf{r}, t)$. This mapping is proven in the Runge–Gross theorem,[106] which can be considered as the time-dependent generalization of the Hohenberg–Kohn theorem. Then, a corresponding Kohn–Sham construction of the theory can be used that leads to a set of practical equations for the calculations:

$$i\frac{\partial}{\partial t}\psi_i(\vec{r},t) = \left[-\frac{\nabla^2}{2} + \upsilon_{eff}(\vec{r},t)\right]\psi_i(\vec{r},t) \tag{89}$$

where $\psi_i(\mathbf{r}, t)$ are the time-dependent Kohn–Sham orbitals which constructs the one-body density:

$$\rho(\vec{r},t) = \sum_{i=1}^{N}\left|\psi_i(\vec{r},t)\right|^2 \tag{90}$$

As in ordinary Kohn–Sham DFT, it is used an auxiliary system of non-interacting electrons subject to a $\upsilon_{eff}(\mathbf{r}, t)$ potential which is chosen such that the density built from these Kohn–Sham orbitals is the same as the density of the original interacting system. If the exact time-dependent

Kohn–Sham potential is known $\upsilon_{eff}(\mathbf{r}, t)$, then the equations stated above would lead to the exact one-body density. This $\upsilon_{eff}(\mathbf{r}, t)$ potential can be divided in different contributions which read as follows:

$$\upsilon_{eff}(\vec{r},t) = \upsilon_{ext}(\vec{r},t) + \upsilon_{Hartree}(\vec{r},t) + \upsilon_{XC}(\vec{r},t) \tag{91}$$

where $\upsilon_{Hartree}(\mathbf{r}, t)$ accounts for the classical electrostatic interaction between electrons

$$\upsilon_{Hartree}(\vec{r},t) = \int d\vec{r}' \frac{\rho(\vec{r}',t)}{|\vec{r}-\vec{r}'|} \tag{92}$$

and the external potential $\upsilon_{ext}(\mathbf{r}, t)$ accounts for the interaction of the electrons with the nuclei (whose positions could change dynamically) and any other external potential that is dependent on time. For example if one wants to study the optical absorption of a molecule subject to the effect of a laser of a given frequency the external potential would be

$$\upsilon_{ext}(\vec{r},t) = \upsilon_{nuclei}(\vec{r},t) + \upsilon_{laser}(\vec{r},t) = -\sum_{\alpha} \frac{Z_\alpha}{|\vec{r}-\vec{R}_\alpha(t)|} + Ef(t)\sin(\omega t)\vec{r}\alpha \tag{93}$$

where $\upsilon_{laser}(\mathbf{r}, t)$ accounts for the laser field in the dipole approximation and $f(t)$ is a function that controls the laser pulse.

Finally, $\upsilon_{xc}(\mathbf{r}, t)$ needs to be defined. The time-dependent exchange-correlation potential can be formally defined as the functional derivative of the exchange-correlation part of the quantum mechanical action of the electronic system A_{XC}.

$$\upsilon_{XC}(\vec{r},t) = \frac{\delta A_{XC}}{\delta \upsilon(\vec{r},t)} \tag{94}$$

In contrast to ordinary DFT, approximations to $\upsilon_{xc}(\mathbf{r}, t)$ are still in their infancy. The majority of the existing functionals make use of the adiabatic approximation,[107,108] which allows the use of the existing time-independent exchange-correlation functionals. The approximations is as follows, let us assume that $\overline{\upsilon}[\rho]$ is an approximation to the ground-state exchange-correlation potential, then the adiabatic time-dependent exchange-correlation potentials is written as:

$$\upsilon_{XC}^{adiabatic}(\vec{r},t) = \overline{\upsilon}[\rho(\vec{r})]_{\rho=\rho(t)} \tag{95}$$

That is, the adiabatic approximation consists of using the same exchange-correlation potential as in the time-independent theory but evaluated with the electron density at time t, $\rho(\mathbf{r}, t)$. The functional is local in time, and this is of course a quite dramatic approximation. In cases where the temporal dependence is large, like interactions with strong lasers pulses with matter, one

should go beyond the present approximation. Apart from approximations to the exchange-correlation potential, the scheme described so far is perfectly general and can be applied to essentially any time-dependent situation. Nevertheless, in practice two different regimes are considered. In the case that the time dependent potential is weak, linear-response theory can be applied to solve the problem.[109-113] On the contrary, if the time-dependent potential is strong a full solution of the Kohn–Sham equations is required.[108,114]

J) Aromaticity

Aromaticity is a concept of central importance in physical organic chemistry.[115-119] It has been very useful in the rationalization of the structure, stability, and reactivity of many molecules. Even though this concept was introduced 137 years ago,[120] it has no precise and generally well-established definition yet. Aromaticity is not an observable, and therefore, not being a directly measurable quantity, it must be defined by convention. According to Schleyer and Jiao,[118] aromatic systems are conjugated cyclic π-electron compounds that exhibit a cyclic electron delocalization leading to bond length equalization, abnormal chemical shifts and magnetic anisotropies, as well as energetic stabilization.

Because of the importance of aromaticity in chemistry, there have been many attempts to rationalize and quantify this property, and to derive a universal quantitative measure of aromaticity. However, because of its multiple manifestations, there is no single quantitative definition of aromaticity collectively accepted yet. The evaluation of aromaticity is usually based on the classical aromaticity criteria, namely, structural, magnetic, energetic, and reactivity-based measures.[119-121]

The structure-based measures of aromaticity rely on the idea that important manifestations of aromaticity are equalization of bond lengths and symmetry.[122] Among the most common structural-based indices of aromaticity, one of the most effective[122] is the harmonic oscillator model of aromaticity (HOMA) index, defined by Kruszewski and Krygowski as:[123,124]

$$HOMA = 1 - \frac{\alpha}{n}\sum_{i=1}^{n}\left(R_{opt} - R_i\right)^2 \tag{96}$$

where n is the number of bonds considered, and α is an empirical constant fixed to give HOMA = 0 for a model nonaromatic system, and HOMA = 1 for a system with all bonds equal to an

optimal value R_{opt}, assumed to be achieved for fully aromatic systems. R_i stands for a running bond length.

Magnetic indices of aromaticity are based on the π-electron ring current that is induced when the system is exposed to external magnetic fields. Historically, characteristic proton NMR chemical shifts and the exaltation of magnetic susceptibility (Λ) have been important magnetic criteria to quantify aromaticity.[121,122,125] The exaltation is defined as the difference between the true diamagnetic susceptibility χ_M and the one calculated by an additive scheme using atom and bond increments $\chi_{M'}$, as:

$$\Lambda = \chi_{\mathbf{M}} - \chi_{\mathbf{M'}} \tag{97}$$

The exaltations are negative (diamagnetic) for aromatic compounds and positive (paramagnetic) for antiaromatic compounds. The ring-current intensities have been also used as a criterion for aromaticity.[126,127] More recently, a new and widely used aromatic index, the nucleus independent chemical shift (NICS), has been proposed by Schleyer and co-workers.[118,128] It is defined as the negative value of the absolute shielding computed at a ring center or at some other interesting point of the system. Rings with large negative NICS values seem to be indicative of aromatic character. The more negative the NICS values, the more aromatic the rings are.

Finally, energetic-based indices of aromaticity make use of the fact that conjugated cyclic π-electron compounds are more stable than their chain analogues,[117,129] while reactivity-based indices exploit the fact that aromatic compounds prefer substitution to addition reactions to retain their π-electron structure.[130] The most common used measure among energetic-based indices is the aromatic stabilization energy (ASE), calculated as the energetic effect of an imaginary homodesmotic reaction.[131-133]

Also as aromaticity criteria based on electron delocalization, one can use the *para*-delocalization index (PDI)[134,135] and the aromatic fluctuation index (FLU).[136] The PDI is obtained employing the delocalization index (DI)[137-139] as defined in the framework of the atoms in molecules (AIM) theory of Bader.[140-142] The PDI is an average of all DI of *para*-related carbon atoms in a given six-membered ring (6-MR). Calculation of these DIs at the DFT level of theory cannot be performed exactly[143] because the electron-pair density is not available at this level of

theory. As an approximation, one can used the Kohn-Sham orbitals obtained from DFT to calculate Hartree-Fock-like DIs:[143]

$$\Lambda = \chi_{\mathrm{M}} - \chi_{\mathrm{M}'}\ \delta(A,B) = 4\sum_{i,j}^{N/2} S_{ij}(A)S_{ij}(B) \tag{98}$$

The summations in Eq. (98) run over all the N/2 occupied molecular orbitals. S_{ij}(A) is the overlap of the molecular orbitals *i* and *j* within the basin of atom A. Eq. (98) does not account for electron correlation effects. In practice, the values of the DIs obtained using this approximation are generally closer to the Hartree-Fock values than correlated DIs obtained with a configuration interaction method.[143] On the other hand, the FLU index[136] is based on the fact that aromaticity is related to the cyclic delocalized circulation of π electrons, and it is constructed not only considering the amount of electron sharing between contiguous atoms, which should be substantial in aromatic molecules, but also taking into account the similarity of electron sharing between adjacent atoms. It is defined as:[136]

$$\mathrm{FLU} = \frac{1}{\mathrm{n}}\sum_{\mathrm{A-B}}^{\mathrm{RING}}\left[\left(\frac{\mathrm{Flu(A\rightarrow B)}}{\mathrm{Flu(B\rightarrow A)}}\right)^{\alpha}\left(\frac{\delta(\mathrm{A,B})-\delta_{\mathrm{ref}}(\mathrm{A,B})}{\delta_{\mathrm{ref}}(\mathrm{A,B})}\right)\right]^2 \tag{99}$$

with the sum running over all adjacent pairs of atoms around the ring, *n* being equal to the number of members in the ring, $\delta_{ref}(C,C)=1.4$ (the $\delta(C,C)$ value in benzene at the HF/6-31G(d) level),[136] α=1 for $\mathrm{FLU(A\rightarrow B)>FLU(B\rightarrow A)}$ and α=-1 otherwise, and the fluctuation from atom A to atom B reading as follows:

$$Flu(A\rightarrow B) = \frac{\delta(A,B)}{\sum_{B\neq A}\delta(A,B)} = \frac{\delta(A,B)}{2(N(A)-\lambda(A))} \tag{100}$$

where $\delta(A,B)$ is the DI between basins of atoms A and B, $N(A)$ is the population of basin A, and $\lambda(A)$ is the number of electrons localized in basin A. FLU is close to 0 in aromatic species. The higher the FLU values, the less aromatic the rings.

K) Atoms in Molecules (AIM) theory

The Atoms in Molecules (AIM) theory partitions the charge density of a molecule (see Figure II-3), $\rho(\mathbf{r})$, in its atomic fragments. This allows the partition of the molecular properties in atomic contributions. Only from the topology of the electronic density, AIM theory can solve the

conflict between the classical molecular description by atoms connected by bonds and the quantum mechanics description of the molecules, in which the bonds or the molecular connectivity are not observables and cannot be obtained directly from the wavefunction. On the other hand, being based on observable quantities as the first or second order densities, it allows avoiding a lot of problems associated with other methods that are based on the analysis of molecular orbitals, that are not physical observables.

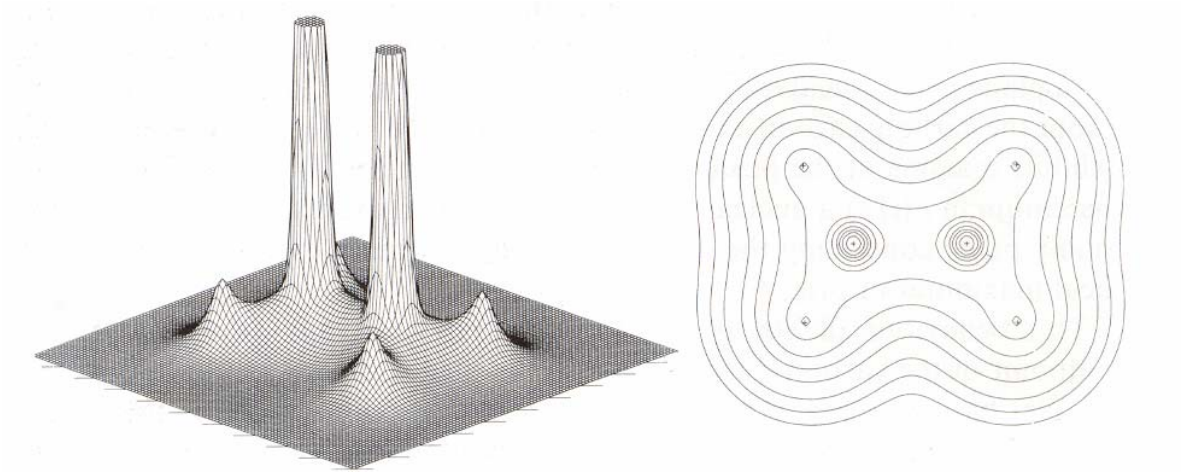

Figure II-3. Representation of the electronic charge density of the ethylene molecule in the plane that contains the nucleus. In the left diagram, the density value is shown as a projection over the geometrical plane; the right diagram corresponds to the contour plot of $\rho(\mathbf{r})$.[141]

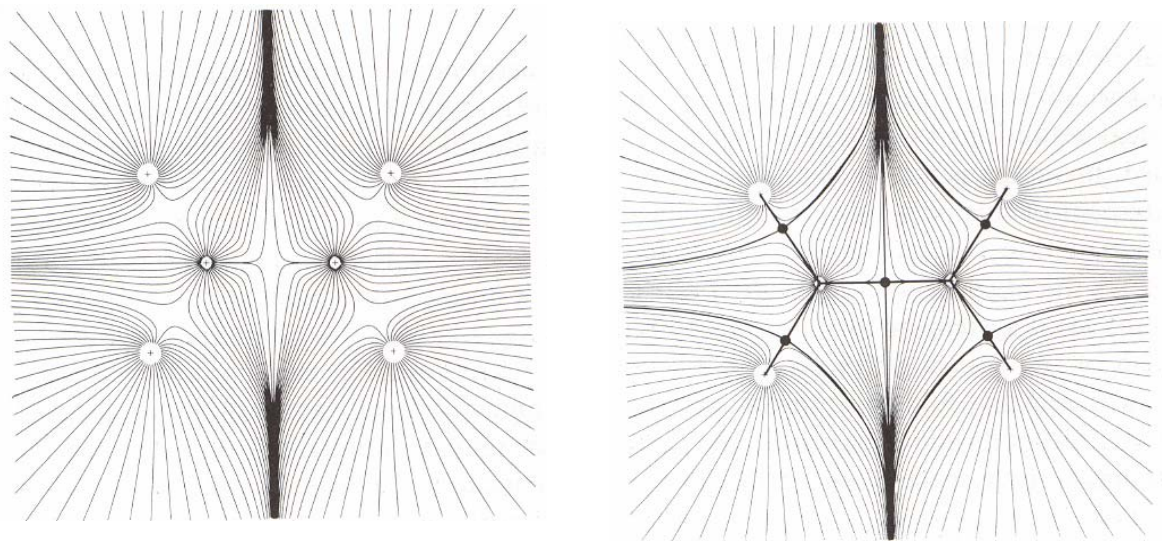

Figure II-4. Gradient maps of the charge density for the plane that contains the nucleus of the ethylene molecule. Each line represents a trajectory of $\nabla\rho(\mathbf{r})$. In the left map are shown only the trajectories that finish in the positions of the nucleus. The right one adds the trajectories that start and finish in the critical points (3,-1).

It is necessary to start by the condition of null flux, that allows the partition of one molecule in atoms. Within this partition, an atom can be defined as an open quantic subsystem, delimited in the tridimensional space by a surface of null flux in the vector of gradient of the electronic density (see Figure II-4),

$$\nabla\rho(\vec{r})\cdot n(\vec{r}) = 0, \forall \vec{r} \in S(\vec{r}) \qquad (101)$$

being $S(\mathbf{r})$ the surface that delimitates the system and $n(\mathbf{r})$ the normal vector to this surface in point $\mathbf{r}$. For an extended system with respect to the whole space, this condition is accomplished in the infinite, where $\nabla\rho(\mathbf{r})$ tends to 0. When this condition is applied to the density of a molecule, the regions of the space delimited by these surfaces of null flux are named atomic basins. In general, an atomic basin is always found associated to each atomic nucleus of the molecule, though there can be exceptions to this rule.[144] The mean values of the properties of a subsystem delimited according to eq. (101) can be determined using the same expressions employed for the isolated system, but restraining the integration in the space of the atomic basin. Delimiting a subsystem according to the condition of null flux, one can be sure of maintaining the hermitic character of the operators and that the virial theorem is accomplished, in the same way as for an isolated system.

A topological analysis of the monoelectronic density allows identifying several critical points in the molecule. A critical point is defined as a point in the space where the first derivatives of $\rho(\mathbf{r})$ are null. The critical points can be classified according to the Hessian values in the same point, diagonalized properly. The rang, ω, is the number of curvatures different from 0 in the Hessian matrix, and the signature, σ, is the algebraic sum of the signs of these curvatures. According to this nomenclature, the types of critical points of rang 3, normally found in the first order density, are:

(3,-3). Attractor. In these points all the curvatures of the Hessian are negative, i. e., we have a maximum of the density. Although the condition of the nuclear cusp, the maxima of the density at the atomic nucleus do not accomplish strictly the requirements for a point (3,-3), the nuclear

maxima can be considered as attractors. An only attractor or point (3, -3) for each atomic basin is always found. Therefore an atom can be defined as the union of an attractor with its basin.

(3,-1). Bond critical point. In these points, the density has a positive curvature in one direction and two negative curvatures in the other two. This kind of points is found between separated atoms by surfaces of null flux; the fact that two atoms share a bond point and an interatomic surface is the condition to consider that they are bonded. Furthermore, the values of the electronic density and the other properties in a bond critical point give valuable information about the type of interaction between both atoms (see Figure II-5).

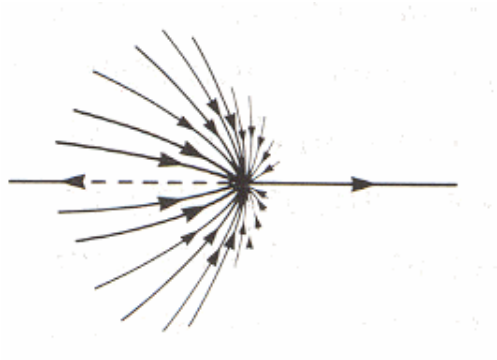

Figure II-5. Representation of the trajectories that finish in a critical point (3,-1) and define the interatomic surface, with the ones defined by the bond path.

(3,+1) Ring critical point. One critical point has two positive curvatures of the density and a negative one. This type of critical points is found in the centre of the rings (see Figure II-6).

(3,+3). Cage point. It corresponds to a minimum in the electronic density. As the name indicates, a cage point can be found only if there are a group of bonded atoms forming a closed cage among them. Take for instance the centre of the C_{60}.

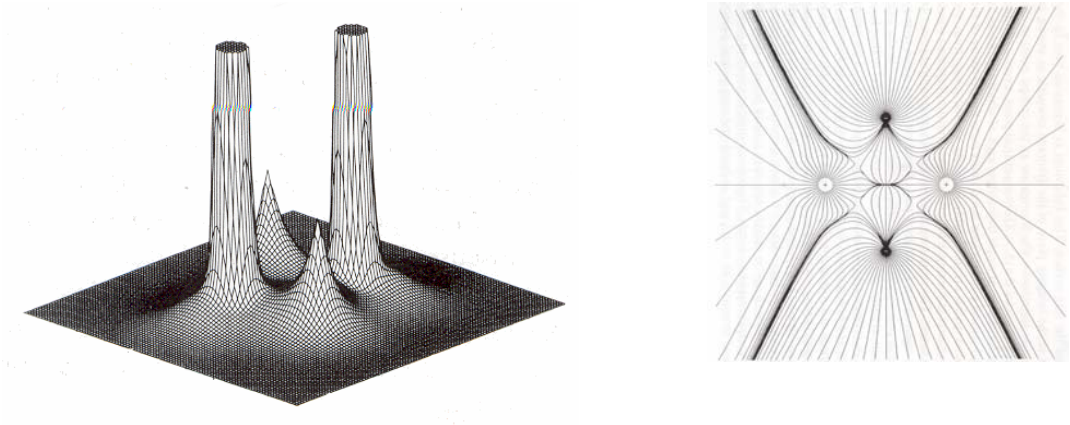

Figure II-6. On the left, relief map of the electronic charge density of the molecule of diborane, in the plane that contains the two boron atoms and the two bridge protons. On the right, the map for the gradient of the electronic density, showing the trajectories originated at the infinite or in the central ring critical point. (3,+1).

In the critical points of order 2 (see Figure II-7) the curvature of the density is null in one direction. There are three possible critical points of order 2: (2,-2), (2,0), and (2,+2). In fact, it is more suitable to name them critical rings, because it is the shape that they present. On the other hand, the two possible structures of order 1 can also be named critical rings: (1,-1) and (1,+1). Although no critical ring in monoelectronic densities has been found, these structures are usual in the topologies of the intracular or extracular densities with cylindrical or spherical symmetry, even for easy systems, mainly when the Coulomb correlation is taken into account.[145,146]

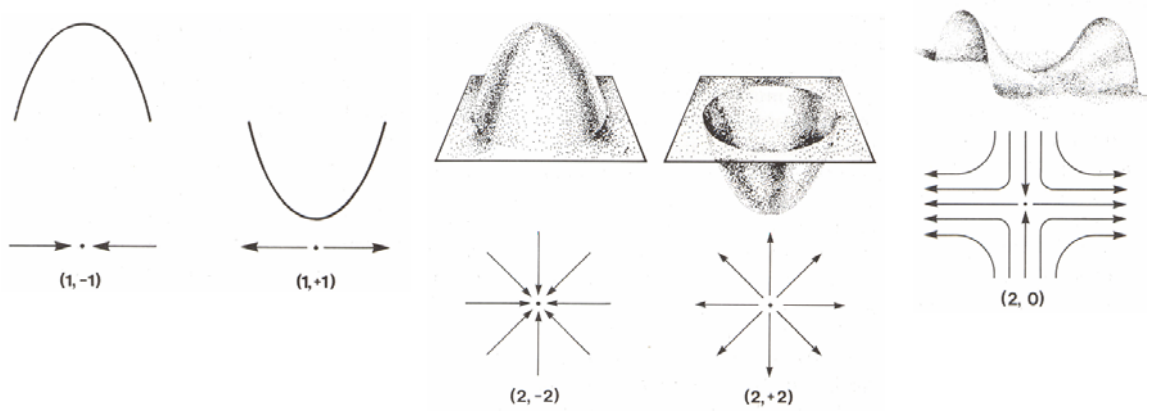

Figure II-7. Representation of maxima and minima in one and two dimensions, and one chair point.[141]

The study of the derivative functions of the monoelectronic density also bring interesting data. For example following the flux lines of the density gradient,

$$\nabla\rho(\vec{r}) = \left(\frac{\partial\rho(\vec{r})}{\partial x}, \frac{\partial\rho(\vec{r})}{\partial y}, \frac{\partial\rho(\vec{r})}{\partial z} \right) \tag{102}$$

it is possible to establish the molecular connectivity: if two atoms are bonded between them, there must exist gradient lines that connect one bond critical point, the same for the two atoms with each attractor. Following these gradient lines for all the attractors, it is possible to generate a molecular plot that indicates how the atoms of the molecule are bonded. The gradient lines that

are not originated from the point (3,-1), can start from points as (3,+1) or (3,+3), or from the infinite.

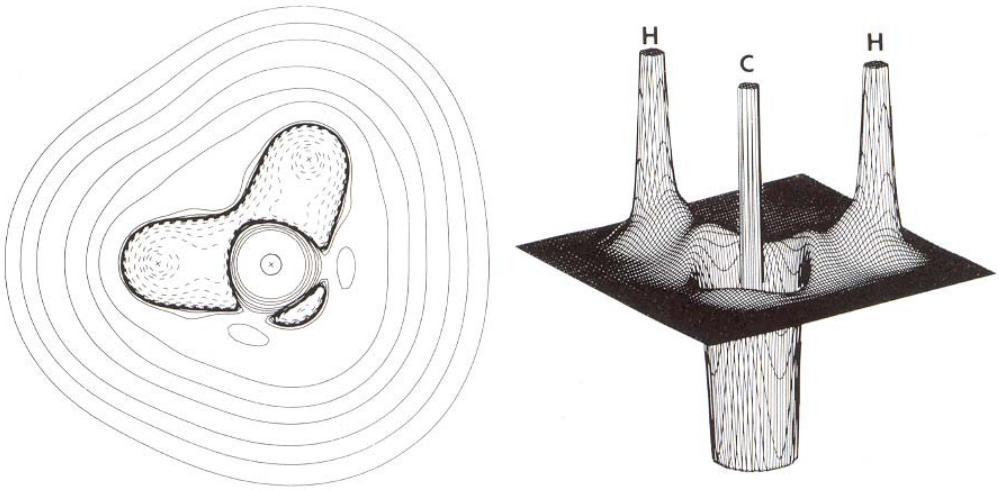

Figure II-8. Contour maps and relief for the Laplacian of the CH_4 molecule in the plane that contains the HCH nucleus. The continuous contour lines represent positive values of $\nabla^2\rho$, while the discontinuous lines give negative values. The relief map gives the negative Laplacian function.

Another interesting function is the density Laplacian (see Figure II-8), $\nabla^2\rho(\mathbf{r})$, that is defined as

$$\nabla^2\rho(\vec{r}) = \frac{\partial^2\rho(\vec{r})}{\partial x^2} + \frac{\partial^2\rho(\vec{r})}{\partial y^2} + \frac{\partial^2\rho(\vec{r})}{\partial z^2} \tag{103}$$

The sign of the density Laplacian indicates where the electronic density accumulates (negative sign), or where it depletes (positive sign). The study of the topology of $\nabla^2\rho(\mathbf{r})$ reveals important information that is not evident in $\rho(\mathbf{r})$.[147,148] Take for instance, the structure of shells in isolated atoms and molecules that is reflected in $\nabla^2\rho(\mathbf{r})$. The value of $\nabla^2\rho(\mathbf{r})$ in a bond critical point helps to define the character of the interaction between the bonded atoms connected to this critical point. A negative value means that there is an accumulation of the electronic density in the bond region, and it is characteristic of atoms with an interaction of open shell or covalent interaction. Nevertheless, a positive value means that there is a depletion of charge in this region, and it is characteristic of closed shell, as ionic or van der Waals interactions. Furthermore, the accumulations of charge due to non-bonded electronic pairs are also identifiable in the function $\nabla^2\rho(\mathbf{r})$.

Apart from the monoelectronic density, the bielectronic density also plays a key role in the AIM theory. It is useful to determine the localization of the electronic pairs of the molecule. The degree of localization and delocalization of the electrons in the different points of the space can be appreciated visually by Fermi hole density plots,[149-153] that describes the probability of finding one electron of the same spin at $\vec{r}_2$ when a certain reference electron is placed at $\vec{r}_1$ position..

From the bielectronic density, the localization ($\lambda(A)$) and delocalization ($\delta(A,B)$) atomic index can also be defined, showing the degree of electronic share between different atoms of a molecule.[154]

References

1. a) R. G. Parr, W. Yang. *Density Functional Theory of Atoms and Molecules*. Oxford University Press. New York, 1989. b) R. M. Dreizler, E. K. U. Gross. *Density Functional Theory: An Approach to the Many-Body Problem*. Springer-Verlag. Berlin, 1990. c) W. Koch, M. C. Holthausen. *A Chemist's Guide to Density Functional Theory*, 2nd edition, Wiley, Weinheim, 2001.
2. A. Szabo, N. S. Ostlund. In *Modern Quantum Chemistry*, Dover Publications, Inc.: New York, 1982.
3. F. Jensen. In *Introduction to Computational Chemistry*, Wiley, New York, 1998.
4. C. J. Cramer. In *Essentials of Computational Chemistry*, Wiley, New York, 2003.
5. B. O. Roos, P. Widmark. In *European Summerschool in Quantum Chemistry Book I, II, and III*, Lund University: Lund, 2000.
6. P. Hohenberg, W. Kohn, *Phys. Rev. B* **1964**, *136*, 864-871.
7. E. Bright-Wilson. In *Structural Chemistry and Biology*, conference 1968.
8. L. H. Thomas, *Proc. Cambridge Philos Soc.* **1927**, *23*, 542-548.
9. E. Z. Fermi, *Phys.* **1928**, *48*, 73-79.
10. P. A. M. Dirac, *Proc. Cambridge Philos. Soc.* **1930**, *26*, 376-385.
11. M. Torrent, M. Solà, G. Frenking, *Chem. Rev.* (Washington, D. C.) **2000**, *100*, 439-493.
12. W. Kohn, *Rev. Mod. Phys.* **1999**, *71*, 1253-1266 (Nobel Lecture).
13. J. A. Pople, *Rev. Mod. Phys.* **1999**, *71*, 1267-1274 (Nobel Lecture).
14. H. Chermette, *J. Comput. Chem.* **1999**, *20*, 129-154.

15. P. Geerlings, F. De Proft, W. Langenaeker, *Chem. Rev.* (Washington, D. C.) **2003**, *103*, 1793-1873.
16. a) K. Fukui, T. Yonezawa, H. Shingu, *J. Chem. Phys.* **1952**, *20*, 722-725. b) K. Fukui, T. Yonezawa, C. Nagata, H. Shingu, *J. Chem. Phys.* **1954**, *22*, 1433-1442.
17. R. G. Pearson. In *Chemical Hardness: Applications from Molecules to Solids*; Wiley-VCH: Weinheim, 1997.
18. a) R. T. Sanderson, *Science* **1951**, *114*, 670-672. b) R. T. Sanderson. In *Chemical Bonds and Bond Energy*, Academic Press: New York, 1976.
19. R. G. Parr, P. K. Chattaraj, *J. Am. Chem. Soc.* **1991**, *131*, 1854-1855.
20. P. K. Chattaraj, S. Sengupta, *J. Phys. Chem*. **1996**, *100*, 16126-16130.
21. C. C. J. Roothaan, *Rev. Mod. Phys*. **1951**, *23*, 69-89.
22. W. Kohn, L. Sham, *J. Phys. Rev. A*. **1965**, *140*, 1133-1138.
23. a) L. H. Thomas, *Proc. Camb. Phil. Soc*. **1927**, *23*, 542-548. b) E. Fermi, Rend. *Accad. Lincei*. **1927**, *6*, 602-607.
24. S. H. Vosko, L. Wilk, M. Nusair, *Can. J. Phys*. **1980**, *58*, 1200-1211.
25. D. M. Ceperley, B. J. Alder, *Phys. Rev. Lett*. **1980**, *45*, 566.-569.
26. J. C. Slater. *Quantum Theory of Molecules and Solids*. Vol. 4. McGraw-Hill, New York, 1974.
27. a) J. P. Perdew, K. Burke, M. Ernzerhof, *Phys. Rev. Lett*. **1996**, *77*, 3865-3868. b) M. Filatov, W. Thiel, *Mol. Phys*. **1997**, *91*, 847-859. c) M. Filatov, W. Thiel, *Int. J. Quant. Chem.* **1997**, *62*, 603-616. d) F. A. Hamprecht, A. J. Cohen, D. J. Tozer, N. C. Handy, *J. Chem. Phys*. **1998**, *109*, 6264-6271.
28. a) A. D. Becke, *J. Chem. Phys* **1986**, *84*, 4524-4529. b) A. D. Becke, *Phys. Rev. A* **1988**, *38*, 3098-3100.
29. a) J. P. Perdew, *Phys. Rev. B* **1986**, *33*, 8822-8824. b) J. P. Perdew, *Phys. Rev. B* **1986**, *34*, 7406-7406.
30. J. P. Perdew, Y. Wang, *Phys. Rev. B* **1986**, *33*, 8800-8802.
31. C. Lee, W. Yang, R. G. Parr, *Phys. Rev. B* **1988**, *37*, 785-789.
32. A. D. Becke, *J. Chem. Phys*. **1993**, *98*, 5648-5652.
33. R. G. Parr, R. G. Pearson, *J. Am. Chem. Soc.* **1983**, *105*, 7512-7516.
34. M. J. Stott, E, Zaremba, *Phys. Rev.* A **1980**, *21*, 12-23.
35. R. G. Parr, W. Yang, *J. Am. Chem. Soc.* **1984**, *106*, 4049-4050.
36. R. G. Parr, J. L. Gázquez, *J. Phys. Chem.* **1993**, *97*, 3939-3940.

37. R. G. Parr, R. A. Donnelly, M. Levy, W. E. Palke, *J. Chem. Phys.* **1978**, *68*, 3801-3807.
38. W. Kohn, A. D. Becke, R. G. Parr, *J. Phys. Chem.* **1996**, *100*, 12974-12980.
39. T. T. Nguyen-Dang, R. F. W. Bader, H. Essén, *Int. J. Quantum Chem.* **1982**, *22*, 1049-1058.
40. J. P. Perdew, R. G. Parr, M. Levy, J. L. Balduz Jr., *Phys. Rev. Lett.* **1982**, *49*, 1691-1694.
41. T. Koopmans, *Physica* (Utrecht) **1934**, *1*, 104-113.
42. R. G. Pearson, *J. Am. Chem. Soc.* **1963**, *85*, 3533-3539.
43. R. G. Pearson, *Science* **1966**, *151*, 172-177.
44. R. Balawender, L. Komorowski, *J. Chem. Phys.* **1998**, *109*, 5203-5211.
45. T. Mineva, E. Sicilia, N. Russo, *J. Am. Chem. Soc.* **1998**, *120*, 9053-9058.
46. J. Cioslowski, M. Martinov, *J. Chem. Phys.* **1994**, *101*, 366-370.
47. R. F. Nalewajski. In *Chemical Hardness*; K. D. Sen, Ed.; Structure and Bonding 80; Springer-Verlag: Berlin, 1993; p. 194.
48. B. G. Baekelandt, W. J. Mortier, R. A. Schoonheydt. In *Chemical Hardness*; K. D. Sen, Ed.; Structure and Bonding 80; Springer-Verlag: Berlin, 1993; p. 187.
49. S. K. Ghosh, *Chem. Phys. Lett.* **1990**, *172*, 77-82.
50. P. K. Chattaraj, A. Cedillo, R. G. Parr, *J. Chem. Phys.* **1995**, *103*, 7645-7646.
51. S. Liu, F. De Proft, R. G. Parr, *J. Phys. Chem.* A **1997**, *101*, 6991-6997.
52. L. Komorowski, *Chem. Phys.* **1987**, *114*, 55-71.
53. A. Vela, J. L. Gázquez, *J Am. Chem. Soc.* **1990**, *112*, 1490-1492.
54. T. K. Ghanty, S. K. Ghosh, *J. Phys. Chem.* **1993**, *97*, 4951-4953.
55. R. G. Parr, L. Von Szentpaly, S. Liu, *J. Am. Chem. Soc.* **1999**, *121*, 1922-1924.
56. a) P. K. Chattaraj, *J. Phys. Chem. A* **2001**, *105*, 511-513. b) P. K. Chattaraj, B. Gómez, E. Chamorro, J. Santos, P. Fuentealba, *J. Phys. Chem. A* **2001**, *105*, 8815-8820.
57. R. G. Pearson, *J. Chem. Educ.* **1987**, *64*, 561-567.
58. G. H. Liu, R. G. Parr, *J. Chem. Phys.* **1997**, *106*, 5578-5586.
59. P. W. Ayers, R. G. Parr, *J. Am. Chem. Soc.* **2000**, *122*, 2010-2018.
60. R. G. Pearson, W. E. Palke, *J. Phys. Chem.* **1992**, *96*, 3283-3285.
61. G. Makov, *J. Phys. Chem.* **1995**, *99*, 9337-9339.

62. a) S. Pal, N. Vaval, R. Roy, *J. Phys. Chem.* **1993**, *97*, 4404-4406. b) P. K. Chattaraj, P. Fuentealba, P. Jaque, A. Toro-Labbé, *J. Phys. Chem. A* **1999**, *103*, 9307-9312.

63. a) G. I. Cárdenas-Jirón, J. Lahsen, A. Toro-Labbé, *J. Phys. Chem.* **1995**, *99*, 5325-5330. b) T. Uchimaru, A. K. Chandra, S. Kawahara, K. Matsumura, S. Tsuzuki, M. Mikami, *J. Phys. Chem. A* **2001**, *105*, 1343-1353. c) R. Parthasarathi, J. Padmanabhan, V. Subramanian, B. Maiti, P. K. Chattaraj, *J. Phys. Chem. A* **2003**, 107, 10346-10352. d) J. Cadet, A. Grand, C. Morell, J. R. Letelier, J. L. Moncada, A. Toro-Labbé, *J. Phys. Chem. A* **2003**, *107*, 5334-5341. e) P. K. Chattaraj, S. Gutiérrez-Oliva, P. Jaque, A. Toro-Labbé, *Molecular Physics* **2003**, *101*, 2841-2853.

64. P. Jaque, A. Toro-Labbé, *J. Phys. Chem. A* **2000**, *104*, 995-1003.

65. a) D. Datta, *J. Phys. Chem.* **1992**, *96*, 2409-2410. b) T. Kar, S. Scheiner, *J. Phys. Chem.* **1995**, *99*, 8121-8124. c) P. K. Chattaraj, A. Cedillo, R. G. Parr, E. M. Arnett, *J. Org. Chem.* **1995**, *60*, 4707-4714. d) T. K. Ghanty, S. K. Ghosh, *J. Phys. Chem.* **1996**, *100*, 12295-12298. e) A. Toro-Labbé, *J. Phys. Chem. A* **1999**, *103*, 4398-4403. f) P. Pérez, A. Toro-Labbé, *J. Phys. Chem. A* **2000**, *104*, 1557-1562. g) P. K. Chattaraj, P. Fuentealba, B. Gómez, R. Contreras, *J. Am. Chem. Soc.* **2000**, *122*, 348-351. h) U. Hohm, *J. Phys. Chem. A* **2000**, *104*, 8418-8423. i) P. Jaque, A. Toro-Labbé, *J. Chem. Phys.* **2002**, *117*, 3208-3218. j) T. K. Ghanty, S. K. Ghosh, *J. Phys. Chem. A* **2002**, *106*, 4200-4204.

66. a) E. Sicilia, N. Russo, T. Mineva, *J. Phys. Chem. A* **2001**, *105*, 442-450. b) T. Kar, S. Scheiner, A. B. Sannigrahi, A. B. *J. Phys. Chem. A* **1998**, *102*, 5967-5973. c) M. Solà, A. Toro-Labbé, *J. Phys. Chem. A* **1999**, *103*, 8847-8852. d) L. T. Nguyen, T. N. Le, F. De Proft, A. K. Chandra, W. Langenaeker, M. T. Nguyen, P. Geerlings, *J. Am. Chem. Soc.* **1999**, *121*, 5992-6001. e) B. Gómez, P. K. Chattaraj, E. Chamorro, R. Contreras, P. Fuentealba, *J. Phys. Chem. A* **2002**, *106*, 11227-11233. f) B. Gómez, P. Fuentealba, R. Contreras, *Theor. Chem. Acc.* **2003**, *110*, 421-427. g) L. T. Nguyen, F. De Proft, M. T. Nguyen, P. Geerlings, *J. Org. Chem.* **2001**, *66*, 4316-4326.

67. E. Chamorro, P. K. Chattaraj, P. Fuentealba, *J. Phys. Chem. A.* **2003**, *107*, 7068-7072.

68. a) M. Cases, G. Frenking, M. Duran, M. Solà, *Organometallics* **2002**, *21*, 4182-4191. b) J. Pérez, *J. Phys. Chem. A* **2003**, *107*, 522-525.

69. a) L. R. Domingo, J. Aurell, P. Pérez, R. Contreras, *J. Phys. Chem. A* **2002**, *106*, 6871-6875. b) L. R. Domingo, M. Arnó, R. Contreras, P. Pérez, *J. Phys. Chem. A* **2002**, *106*, 952-961. c) L. R. Domingo, J. Aurell, P. Pérez, R. Contreras, *J. Org.*

Chem. **2003**, *68*, 3884-3890. d) L. R. Domingo, J. Andrés, *J. Org. Chem.* **2003**, *68*, 8662-8668.

70. a) P. Pérez, A. Toro-Labbé, R. Contreras, *J. Am. Chem. Soc.* **2001**, *123*, 5527-5531. b) F. Aparicio, R. Contreras, M. Galván, A. Cedillo, *J. Phys. Chem. A* **2003**, *107*, 10098-10104.
71. W. Yang, W. J. Mortier, *J. Am. Chem. Soc.* **1986**, *108*, 5708-5711.
72. R. S. Mulliken, *J. Chem. Phys.* **1955**, *23*, 1833-1840.
73. C. M. Breneman, K. B. Wiberg, *J. Comput. Chem.* **1990**, *11*, 361-373.
74. A. E. Reed, L. A. Curtiss, F. Weinhold, *Chem. Rev.* **1988**, *88*, 899-926.
75. R. F. W. Bader. *In Atoms in Molecules: a Quantum Theory*; Clarendon Press: Oxford, 1990.
76. F. L. Hirshfeld, *Theor. Chim. Acta* **1977**, *44*, 129-138.
77. a) J. Cioslowski, M. Martinov, S. T. Mixon, *J. Phys. Chem*. **1993**, *97*, 10948-10951. b) F. De Proft, J. M. L. Martin, P. Geerlings, *Chem. Phys. Lett.* **1996**, *256*, 400-408. c) S. Arulmozhiraja, P. Kolandaivel, *Mol. Phys.* **1997**, *90*, 55-62. d) F. Gilardoni, J. Weber, H. Chermette, T. R. Ward, *J. Phys. Chem. A* **1998**, *102*, 3607-3613. e) R. K. Roy, S. Pal, K. Hirao, *J. Chem. Phys.* **1999**, *110*, 8236-8245. f) R. K. Roy, K. Hirao, S. Pal, *J. Chem. Phys.* **2000**, *113*, 1372-1379. g) R. K. Roy, K. Hirao, S. Krishnamurty, S. Pal, *J. Chem. Phys.* **2001**, *115*, 2901-2907.
78. W. Yang, R. G. Parr, *Proc. Natl. Acad. Sci. USA* **1985**, *82*, 6723-6726.
79. M. Berkowitz, S. K. Ghosh, R. G. Parr, *J. Am. Chem. Soc.* **1985**, *107*, 6811-6814.
80. P. K. Chattaraj, B. Maiti, U. Sarkar, *J. Phys. Chem.A* **2003**, *107*, 4973-4975.
81. F. M. Bickelhaupt, E. J. Baerends, Rev. Comput. Chem., ed. K. B. Lipkowitz and D. B. Boyd, Wiley-VCH, New York, 2000, vol. 15, p. 1.
82. G. te Velde, F. M. Bickelhaupt, E. J. Baerends, S. J. A. van Gisbergen, C. Fonseca Guerra, J. G. Snijders, T. Ziegler, *J. Comput. Chem*. **2001**, *22*, 931-967.
83. a) K. Morokuma, *J. Chem. Phys.* **1971**, *55*, 1236-1244. b) K. Kitaura, K. Morokuma, *Int. J. Quantum Chem.* **1976**, *10*, 325-340.
84. T. Ziegler, A. Rauk, *Theor. Chim. Acta* **1977**, *46*, 1-10.
85. O. González-Blanco, V. Branchadell, K. Monteyne, T. Ziegler, *Inorg. Chem*. **1998**, *37*, 1744-1748.
86. Selected examples: a) T. Ziegler, V. Tschinke, A. D. Becke, *J. Am. Chem. Soc*. **1987**, *109*, 1351-1358. b) T. Ziegler, V. Tschinke, C. Ursenbach, *J. Am. Chem. So*c. **1987**,

109, 4825-4837. c) J. Li, G. Schreckenbach, T. Ziegler, *J. Am. Chem. Soc.* **1995**, *117*, 486-494. d) A. W. Ehlers, E. J. Baerends, F. M. Bickelhaupt, U. Radius, *Chem. Eur. J*. **1998**, *4*, 210-221.

87. M. Lein, A. Szabó, A. Kovács, G. Frenking, *Faraday Discussions* **2003**, *124*, 365-378.
88. J. Cioslowski. In Encyclopedia of Computational Chemistry, e., P. v. R. Schleyer, N. L. Allinger, P. A. Kollmann, T. Clark, H. F. Schaefer III, J. Gasteiger, Wiley, Chichester, 1998, vol. 2, p. 892.
89. a) R. F. Frey, E. R. Davidson, *J. Chem. Phys*. **1989**, 90, 5555-5562. b) S. M. Cybulski, S. Scheiner, *Chem. Phys. Lett*. **1990**, *166*, 57-64. c) M. Martinov, J. Cioslowski, Mol. Phys. **1995**, *85*, 121-129.
90. a) L. Pauling, *J. Am. Chem. Soc*. **1947**, *69*, 542-553. b) L. Pauling. *The Nature of the Chemical Bond*, Cornell University Press, New York, 1960.
91. a) C. A. Coulson, *Proc. R. Soc. London, Ser. A* **1939**, *169*, 413-428. b) C. A. Coulson, *Proc. R. Soc. London, Ser. A* **1951**, *207*, 91-101. c) C. A. Coulson, Valence, 2nd ed., Oxford University Press, London, 1961.
92. K. B. Wiberg, *Tetrahedron* **1968**, *24*, 1083-1096.
93. I. Mayer, *Chem. Phys. Lett*. **1983**, *97*, 270; I. Mayer, *Int. J. Quantum Chem*. **1984**, *26*, 151-154.
94. a) A. J. Bridgeman, N. Harris, N. A. Young, *Chem. Commun*. **2000**, 1241-1242. b) A. J. Bridgeman, N. A. Nielsen, *Inorg. Chim. Acta* **2000**, *303*, 107-115. c) A. J. Bridgeman, J. Rothery, *J. Chem. Soc., Dalton Trans*. **1999**, 4077-4082. d) A. J. Bridgeman, J. Rothery, *Inorg. Chim. Acta* **1999**, *288*, 17-28. e) A. J. Bridgeman, Polyhedron, **1998**, *17*, 2279-2288. f) A. J. Bridgeman, *J. Chem. Soc., Dalton Trans*. **1997**, 2887-2893. g) A. J. Bridgeman, *J. Chem. Soc., Dalton Trans.* **1997**, 1323-1329.
95. a) A. J. Bridgeman, J. Rothery, *J. Chem. Soc., Dalton Trans*. **2000**, 211-218. b) A. J. Bridgeman, *J. Chem. Soc., Dalton Trans*. **1996**, 2601-2607. c) A. J. Bridgeman, *J. Chem. Soc., Dalton Trans*. **1997**, 4765-4771. d) A. J. Bridgeman, C. H. Bridgeman, *Chem. Phys. Lett*. **1997**, *272*, 173-177. e) A. J. Dridgeman, G. Cavigliasso, L. R. Ireland, J. Rothery, *J. Chem. Soc, Dalton Trans.* **2001**, 2095-2108.
96. G. Lendvay, *THEOCHEM* **2000**, *501*, 389-393.

97. P. Th. van Duijnen. “Embedding in Quantum Chemistry: the Direct Reaction Field Approach”. In New Challenges in Computational Quantum Chemistry, R. Broer, P. J. C. Aerts, P. S. Bagus, Eds., Dept. of Chemical Physics and Material Science, 1994.
98. P. Th. van Duijnen A. H. de Vries, *Int. J. Quant. Chem*. **1995**, *29*, 523-532.
99. P. Th. van Duijnen, A. H. de Vries, *Int. J. Quant. Chem*. **1996**, *60*, 1111-1132.
100. P. Th. van Duijnen, M. Swart, *J. Phys. Chem. A* **1998**, *102*, 2399-2407.
101. P. Th. van Duijnen, M. Swart, F. Grozema. “QM/MM Calculation of Hyper-Polarizabilites with the DRF Approach”. In ACS Symposium Series 712, ACS, **1998**, 220-232.
102. P. Th. van Duijnen, F. C. Grozema, M. Swart, *J. Mol. Str. Theochem* **1999**, *464*, 193-200.
103. R. W. J. Zijlstra, F. C. Grozema, M. Swart, B. L. Feringa, P. Th. van Duijnen, *J. Phys. Chem. A* **2001**, *105*, 3583-3590.
104. A. H. Juffer. PhD Thesis: On the Modelling of Solvent Mean Force Potentials-From Liquid Argon to Solvated Macromolecules. Rijksuniversiteit Groningen, The Netherlands, 1993.
105. M. A. L. Marques, E. K. U. Gross, *Annu. Rev. Phys. Chem.* **2004**, *55*, 427-455.
106. E. Runge, E. K. U. Gross, *Phys. Rev. Lett.* **1984**, *52*, 997-1000.
107. E. K. U. Gross, W. Kohn. In: S.B. Trickey, Editors, *Advances in Quantum Chemistry*, Academic Press, San Diego (1990) p. 255.
108. M. A. L. Marques, E. K. U. Gross. In: C. Fiolhais, F. Nogueira, M. Marques, Editors, *A Primer in Density-Functional Theory, vol. 620*, Springer, Berlin (2003), p. 144.
109. C. Jamorski, M. E. Casida, D. R. Salahub, *J. Chem. Phys.* **1996**, *104*, 5134-5147.
110. M. E. Casida, C. Jamorski, K. C. Casida, D. R. Salahub, *J. Chem. Phys.* **1998**, *108*, 4439-4449.
111. M. Petersilka, U. J. Gossmann, E. K. U. Gross, *Phys. Rev. Lett.* **1996**, *76*, 1212-1215.
112. T. Grabo, M. Petersilka, E. K. U. Gross, *J. Mol. Struct. (Theochem)* **2000**, *501-2*, 353-367.
113. M. Petersilka, E. K. U. Gross, K. Burke, *Int. J. Quantum Chem.* **2000**, *80*, 534-554.

114. A. Castro, M. A. L. Marques, J. A. Alonso, G. F. Bertsch, A. Rubio, *Eur. J. Phys. D* **2004**, *28*, 29211-29218.

115. P. v. R. Schleyer, *Chem. Rev*. **2001**, *101*, 1115-1117.

116. J. Garrat. *Aromaticity*, John Wiley & Sons, New York, 1986.

117. V. I. Minkin, M. N. Glukhovtsev, B. Y. Simkin. *Aromaticity and Antiaromaticity: Electronic and Structural Aspects*, John Wiley & Sons, New York, 1994.

118. P. v. R. Schleyer, H. Jiao, *Pure Appl. Chem*. **1996**, *68*, 209-219.

119. T. M. Krygowski, M. K. Cyrañski, Z. Czarnocki, G. Häfelinger, A. R. Katritzky, *Tetrahedron* **2000**, *56*, 1783-1796.

120. A. Kekulé, Bull. *Soc. Chim. Fr.* (Paris) **1865**, *3*, 98-111.

121. A. R. Katritzky, K. Jug, D. C. Oniciu, *Chem. Rev*. **2001**, *101*, 1421-1449.

122. T. M. Krygowski, M. K. Cyrañski, *Chem. Rev.* **2001**, *101*, 1385-1419.

123. J. Kruszewski, T. M. Krygowski, *Tetrahedron Lett*. **1972**, 3839-3842.

124. T. M. Krygowski, *J. Chem. Inf. Comp. Sci*. **1993**, *33*, 70-78.

125. F. De Proft, P. Geerlings, *Chem. Rev.* **2001**, *101*, 1451-1464.

126. P. Lazzeretti. *Progress in Nuclear Magnetic Resonance Spectroscopy*, Vol. 36 (Eds.: J. W. Emsley, J. Feeney, L. H. Sutcliffe), Elsevier, Amsterdam, 2000, pp. 1-88.

127. J. A. N. F. Gomes, R. B. Mallion, *Chem. Rev*. **2001**, *101*, 1349-1383.

128. P. v. R. Schleyer, C. Maerker, A. Dransfeld, H. Jiao, N. J. R. van Eikema Hommes, *J. Am. Chem. Soc*. **1996**, *118*, 6317-6318.

129. S. W. Slayden, J. F. Liebman, *Chem. Rev*. **2001**, *101*, 1541-1566.

130. M. Bühl, A. Hirsch, *Chem. Rev.* **2001**, *101*, 1153-1183.

131. P. George, M. Trachtman, C. W. Bock, A. M. Brett, *J. Chem. Soc., Perkin Trans 2* **1977**, 1036-1047.

132. M. N. Glukhovtsev, P. v. R. Schleyer, *Chem. Phys. Lett*. **1992**, *198*, 547-554.

133. C. H. Suresh, N. Koga, *J. Org. Chem*. **2002**, *67*, 1965-1968.

134. J. Poater, X. Fradera, M. Duran, M. Solà, *Chem. Eur. J.* **2003**, 9, 400-406.

135. J. Poater, X. Fradera, M. Duran, M. Solà, *Chem. Eur. J*. **2003**, *9*, 1113-1122.

136. E. Matito, M. Duran, M. Solà, *J. Chem. Phys.* **2005**, *122*, 014109-014116.

137. R. F. W. Bader, in O. Chalvet, R. Daudel, S. Diner, J. P. Malrieu (Eds.), *Localization and delocalitzation in quantum chemistry*; Reidel: Dordrecht, 1975, p. 15.

138. X. Fradera, J. Poater, S. Simon, M. Duran, M. Solà, *Theor. Chem. Acc*. **2002**, *108*, 214-224.

139. X. Fradera, M.A. Austen, R.F.W. Bader, *J. Phys. Chem. A* **1999**, *103*, 304-314.

140. R. F. W. Bader, *Acc. Chem. Res.* **1985**, *18*, 9-15.

141. R. F. W. Bader, *Atoms in Molecules: A Quantum Theory*; Clarendon: Oxford, 1990.

142. R. F. W. Bader, *Chem. Rev*. **1991**, *91*, 893-928.

143. J. Poater, M. Solà, M. Duran, X. Fradera, *Theor. Chem. Acc*. **2002**, *107*, 362-371.

144. W. L. Cao, C. Gatti, P. J. McDougall, R. F. W. Bader, *Chem. Phys. Lett.* **1987**, *141*, 380-385.

145. J. Cioslowski, *J. Chem. Phys*. **1999**, *111*, 3401-3409.

146. J. Cioslowski, G. H. Liu, *J. Chem. Phys.* **1999**, *110*, 1882-1887.

147. R. P. Sagar, A. C. T. Ku, V. H. Smith, *J. Chem. Phys.* **1988**, *88*, 4367-4374.

148. R. F. W. Bader, R. J. Gillespie, P. J. McDougall, *J. Am. Chem. Soc*. **1988**, *110*, 7329-7336.

149. W. L. Luken, *Croat. Chem. Acta* **1984**, *57*, 1283-1294.

150. W. L. Luken, D. N. Beratan, *Theor. Chim. Acta* **1982**, *61*, 265-276.

151. R. J. Gillespie, D. Bayles, J. Platts, G. L. Heard, R. F. W. Bader, *J. Phys. Chem. A* **1998**, *102*, 3407-3414.

152. R. F. W. Bader, G. L. Heard, *J. Chem. Phys.* **1999**, *111*, 8789-8798.

153. R. F. W. Bader, M. E. Stephens, *J. Am. Chem. Soc.* **1975**, *97*, 7391-7399.

154. X. Fradera, M. A. Austen, R. F. W. Bader, *J. Phys. Chem. A* **1999**, *103*, 304-314.

PART II: Copper Complexes

Chapter III: *Regiospecific C-H Activation: Reversible H/D Exchange Promoted by Cu^{I} Complexes with Triazamacrocyclic Ligands*

Regiospecific C-H Activation: Reversible H/D Exchange Promoted by Cu^{I} Complexes with Triazamacrocyclic Ligands

Abstract

The first example of an isotopic reversible and regiospecific H/D exchange promoted by Cu^{I} is analyzed using density functional methods. The reaction only proceeds by using weakly-coordinating deuterated solvents bearing an acidic proton source such as acetone-d^6 or methanol-d^4. The kinetics of the reaction, studied in both directions (H/D and D/H exchange) by the experimental group of Llobet et al. is the key factor to propose a molecular mechanism in accordance to all experimental and theoretical data.

Introduction

Selective C-H bond activation by metals under mild conditions is a major subject of research targeting the final functionalization of organic substrates.[1] The characterization of the usually unstable intermediates of the C-H bond activation prior to functionalization is crucial for the mechanistic comprehension of the reaction.[2] Different mechanisms, such as oxidative addition, electrophilic metalation or agostic bonding, have been proposed in extensive work published for second and third row transition metal (TM)-catalyzed C-H activation of aromatic or aliphatic compounds (i. e, Pd and Pt,[3] and Ru, Rh, and Ir[4]). However, much less work is found with first row transition metals (e. g. Ni,[4c,5] Co,[6] Fe,[7] Mn[8]) and even less for the biologically relevant Cu metal.[9] Llobet et al.[10] recently reported an example of intramolecular aromatic C-H activation by Cu^{II} undergoing a disproportionation reaction where an aryl-Cu^{III} species was characterized as a reaction product.[11] The reactivity of five triazamacrocyclic ligands (see Scheme III-1) in front of Cu^{I} studied by ^{1}H,^{2}H-NMR, ESI-MS was reported. In this chapter, DFT calculations are carried out to shed light on the mechanism of this reaction.

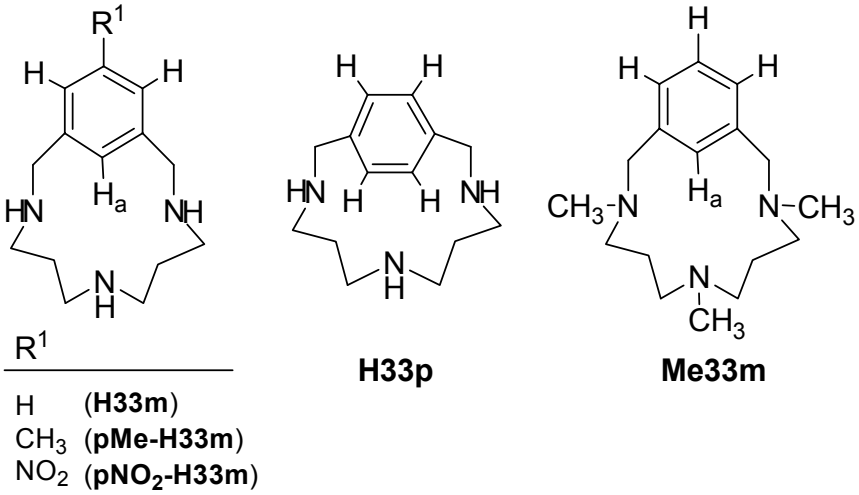

Scheme III-1. Ligands used for Cu^{I} complexation.

The reaction of ligands H33m, pMe-H33m and pNO_2-H33m (Schemes III-1 and -2) with one equivalent of $[Cu^{I}(CH_3CN)_4]PF_6$ in CD_3CN under N_2 afforded the formation of the corresponding Cu^{I} complex. These complexes show very similar ^{1}H-NMR spectra compared to the free ligands. On the contrary, by using acetone-d^6 we observed a gradual decay of the singlet corresponding to H_a on the ^{1}H-NMR spectra, without other integration changes in the rest of the signals. The ESI-MS spectra of deuterated acetone solutions showed a peak at m/z = $[Cu^{I}(R^{1}\text{-H33m})]^{+}$ +1, compared to the peak at m/z = $[Cu^{I}(R^{1}\text{-H33m})]^{+}$ for CD_3CN solutions, clearly suggesting a substitution of H_a by a deuterium atom (Scheme III-2).

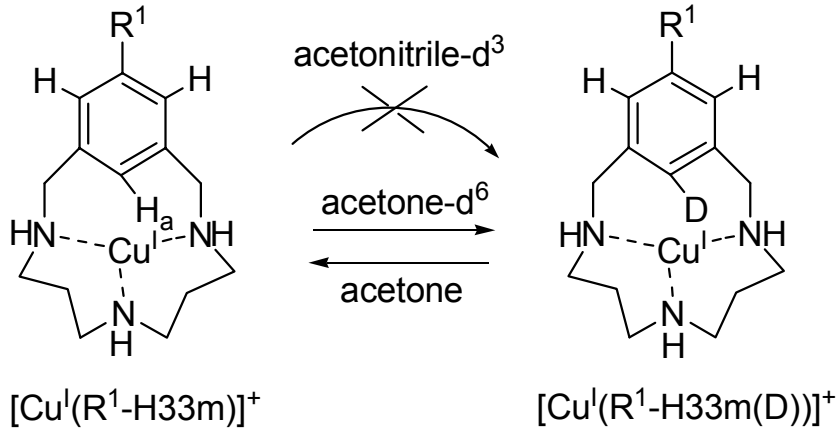

R^{1} = H (**H33m**), CH_3 (**pMe-H33m**), NO_2 (**pNO_2-H33m**)

Scheme III-2. Solvent-dependent reversible isotopic exchange.

This result was confirmed by the demetalation of the deuterated complex by adding an excess of 1,10-phenanthroline (phen) to form the highly stable $[Cu^{I}(phen)_2]^+$ complex, the free deuterated ligand remaining in solution. Chromatographic purification of the deuterated ligand afforded the H33m(D), pMe-H33m(D) and pNO_2-H33m(D) ligands, which were characterized by $^1H,^2H$-NMR and ESI-MS, confirming the regiospecific deuteration at the inner-macrocyclic aromatic position.

The kinetics of the H/D exchange reaction in the R^1-H33m systems were studied by following the decay of the H_a signal in the ^1H-NMR spectrum, respectively.[10] The three ligands were chosen in order to study the influence of the electronic effect exerted by the different R^1 substituents on the isotopic exchange reaction. The decay of the signal intensity was adjusted to a pseudo-first-order kinetics and the reaction rates ($k_{obsH\text{-}D}$) are listed in Table III-1. The deuterium atom comes from the acetone-d^6 (see discussion below), so the pseudo-first-order kinetics are explained by the large excess of deuterium source. In order to extract kinetic information, the Kinetic Isotope Effects (KIE) were measured by preparing the Cu^I complexes of the pure deuterated ligands, that allowed the authors to follow the decay of the deuterium signal. For that purpose ^2H-NMR experiments of the $[Cu^{I}(R^1\text{-H33m(D)})]^+$ complexes in non-deuterated acetone were performed. Apart from the gradual disappearance of the aromatic deuterium singlet, a triplet corresponding to monodeuterated acetone (CH_2DCOCH_3) at 2.05 ppm was increasing following also first-order kinetics with the same rates (see Figure III-1 and Table III-1), finally obtaining the complexes with the original protio ligands.

		$[Cu^{I}(H33m)]^+$	$[Cu^{I}(pMe\text{-}H33m)]^+$	$[Cu^{I}(pNO_2\text{-}H33m]^+$
1	$k_{obsH\text{-}D}$ (min^{-1})[a]	0.0144(5)	0.0134(2)	0.00033(1)
2	$k_{obsD\text{-}H}$ (min^{-1})[b]	0.0164(4)	0.0165(8)	0.000054(5)
3	overall KIE	0.88	0.81	6.1

[a] from ^1H-NMR studies in CD_3COCD_3; [b] from ^2H-NMR studies in CH_3COCH_3 for monodeuterated $[Cu^{I}(R^1\text{-H33m(D)})]^+$ complexes.

Table III-1. Kinetic data of the H/D ($k_{obsH\text{-}D}$) and D/H ($k_{obsD\text{-}H}$) isotopic substitution at 300 K adjusted to a first-order rate law.

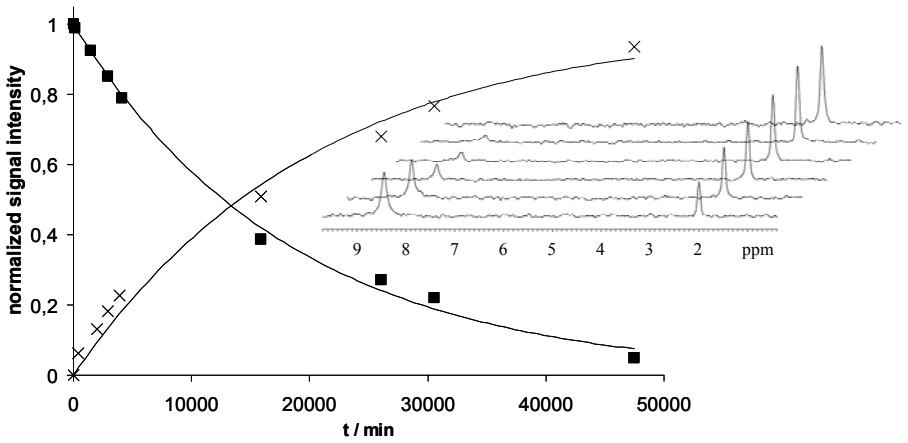

Figure III-1. Plot of normalized signal intensity vs time of the decay of aromatic D signal at 8.45 ppm (■) and the growing of the CDH_2COCH_3 signal at 2.05 ppm (**x**) for the $[Cu^{I}(pNO_2\text{-H33m(D)})]^+$ complex in CH_3COCH_3 (inset shows the ^{2}H-NMR spectra evolution over time).

In order to gain more insight into the nature of this C-H activation, the isotopic exchange reaction for the H33m system in different deuterio solvents was studied. The reaction proceeds in CD_3OD,[12] but it does not proceed in CD_3CN or CD_2Cl_2 clearly manifesting the need of an acidic D atom.

The H/D exchange was followed by ^{1}H-NMR for complex $[Cu^{I}(pMe\text{-H33m})]^+$ at different concentrations of acetone-d^6 in an innocent solvent such as CD_2Cl_2 (and fixing the concentration of complex), thus finding also first order kinetics with respect to acetone.

The kinetics in pure acetone-d^6 indicates a pseudo-first-order reaction for all systems, with roughly two orders of magnitude faster rates ($k_{obsH\text{-}D}$) for H33m and pMe-H33m compared to pNO_2-H33m (Table III-1, entry 1). However, when the aromatic D/H exchange is studied in pure non-deuterated acetone for the respective deuterated ligands (Table III-1, entry 2), the $k_{obsD\text{-}H}$ values are about three orders of magnitude higher. These data result in the observation of an inverse KIE for H33m and pMe-H33m systems, whereas a direct KIE for pNO_2-H33m is observed, manifesting the presence of radically different rate-determining steps (rds) (Table III-1, entry 3). It is important to note here that the addition of H^- to $[Cu^{III}(H33mC)]^{2+}$ complex yields quantitatively the corresponding $[Cu^{I}(H33m)]^+$ complex.[13] Furthermore, the existence of inverse isotopic

effects for the breaking of Rh^{III}-H bonds has been well documented in the literature.[14] On the other hand, the presence of free D^+ caused the decomposition of the complex.[15]

Computational details

The reported calculations were carried out by using the Amsterdam density functional (ADF) package developed by Baerends *et al*.[16-18] and vectorized by Ravenek.[19] The numerical integration scheme employed was that of te Velde and Baerends.[20] Both geometry optimizations and energy evaluations were performed with ADF 2000.02[21] using a generalized gradient approximation (GGA) that includes the GGA exchange correction of Becke[22] and the GGA correlation correction of Perdew.[23] Optimizations were done for the neutral closed-shell singlet ground-state structures and also for open-shell triplet states to verify that the open-shell triplet state is always higher in energy than the closed-shell singlet one. For geometry optimizations we have used an uncontracted triple-ς basis set for describing 3s, 3p, 3d, 4s, and 4p orbitals of copper. For carbon (2s, 2p), nitrogen (2s, 2p), oxygen (2s, 2p), and hydrogen (1s), double-ς basis sets were employed. The two sets were augmented by an extra polarization function.[24,25] Electrons in lower shells were treated within the frozen core approximation.[16] A set of auxiliary s, p, d, f, and g functions, centered in all nuclei, was introduced in order to fit the molecular density and Coulomb potential accurately in each SCF cycle.[26]

Results

DFT geometry optimizations in the gas phase were carried out for the free H33m ligand, the $[Cu^{I}(H33m)]^+$ complex, and the same Cu^{I} complex starting with two axially coordinated molecules of acetonitrile, acetone or methanol.

The geometry optimization of the free H33m ligand in its closed-shell singlet ground state (see Scheme III-3) yields a C1-H_a bond distance of 1.092 Å. This bond length is equal to the rest of aromatic C-H bonds, thus indicating no activation of this bond.

We have also optimized the structure of the metallic complexes depicted in Scheme III-3, all having a closed-shell singlet ground state structure. In all cases, the triplet is more than 40 kcal·mol^{-1} less stable. To simulate the interaction in the solvent phase in a

realistic approach, we completed the coordination sphere of the metal by adding two solvent molecules at the two axial positions available. Thus, we performed the geometry optimization of the complexes with two molecules of acetonitrile, acetone, and methanol attached to the copper atom. All final optimized structures are depicted in Figure III-2. The main geometrical parameters of the studied species are displayed in Tables III-2 and -3. The atoms have the labels of Scheme III-3.

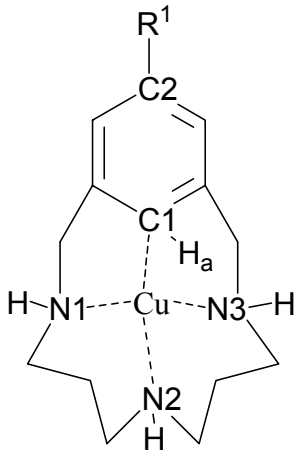

Scheme III-3. Scheme of the $[(R^1\text{-H33m})Cu^I]^+$ (R^1= H, Me, NO_2) complexes that have been structurally optimized.

Ligand H33m	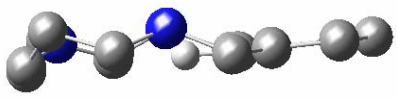
$[(H33m)Cu^I]^+$	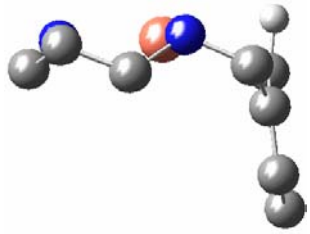
$[(pMe\text{-}H33m)Cu^I]^+$	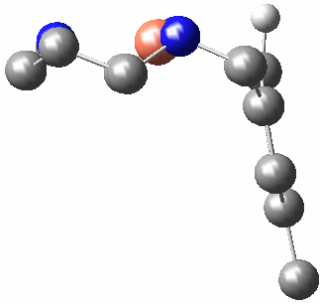

$[(pNO_2\text{-H33m})Cu^I]^+$	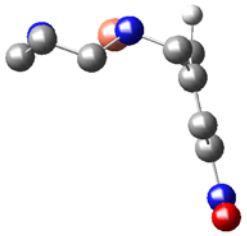
$[(H33m)Cu^I(CH_3CN)_2]^+$	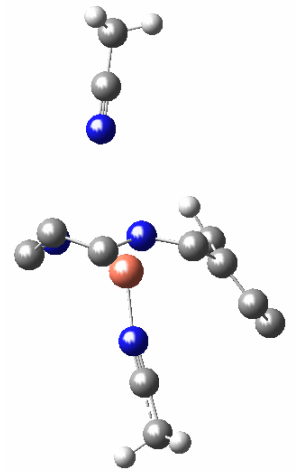
$[(H33m)Cu^I(acetone)_2]^+$	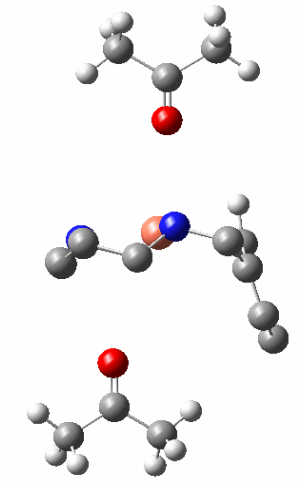
$[(H33m)Cu^I(CH_3OH)_2]^+$	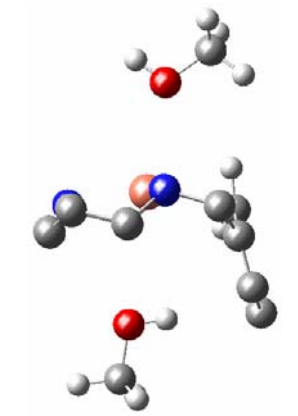

Figure III-2. Optimized geometries of the calculated molecules (some hydrogen atoms have been omitted for clarity).

R^1	Solvent	Complex	C1-H_a	Cu-C1	Cu-H_a	Cu-N1 Cu-N2 Cu-N3	Cu-Solvent (up)	Cu-Solvent (down)	Cu-C1-H_a	Cu-C1-C2	C2-C1-H_a	N2-Cu-C1	N1-Cu-N3	N1-Cu-N2 N2-Cu-N3
H	/	[H33m]	1.092	/	/	/	/	/	/	/	178.0	/	/	/
H	/	$[(H33m)Cu^I]^+$	1.098	2.249	2.285	2.205 2.068 2.204	/	/	77.8	113.8	168.3	156.3	162.1	101.6 101.6
CH_3	/	$[(pMe\text{-}H33m)\ Cu^I]^+$	1.098	2.214	2.259	2.216 2.064 2.221	/	/	78.1	115.3	166.6	164.0	156.5	101.4 101.2
NO_2	/	$[(pNO_2\text{-}H33m)\ Cu^I]^+$	1.097	2.225	2.285	2.172 2.077 2.176	/	/	79.0	115.3	165.7	165.0	156.9	101.2 101.1
H	CH_3CN	$[(H33m)Cu^I$ $(CH_3CN)_2]^+$	1.091	2.434	2.456	2.248 2.112 2.253	3.923	1.907	81.3	106.4	175.4	136.4	124.4	97.8 97.6
H	Acetone	$[(H33m)Cu^I$ $(acetone)_2]^+$	1.098	2.261	2.269	2.157 2.067 2.176	3.280	3.838	76.4	115.1	168.5	166.6	155.8	101.5 101.9
H	CH_3OH	$[(H33m)Cu^I$ $(CH_3OH)_2]^+$	1.096	2.324	2.271	2.167 2.078 2.171	2.908	3.489	73.6	115.7	170.7	155.5	159.0	102.1 102.3

Table III-2. Main geometrical parameters. (Distances are given in Å and angles in degrees).

R^1	Solvent	Complex	d(plane3N-Cu)	d(phenyl-H_a)	∠ phenyl-C1-H_a	∠ plane3N-phenyl
H	/	[H33m]	/	0.036	2.0	1.8
H	/	$[(H33m)Cu^I]^+$	0.074	0.270	11.8	86.0
CH_3	/	$[(pMe\text{-}H33m)\ Cu^I]^+$	0.099	0.302	13.4	83.4
NO_2	/	$[(pNO_2\text{-}H33m)\ Cu^I]^+$	0.096	0.318	14.4	82.3
H	CH_3CN	$[(H33m)Cu^I$ $(CH_3CN)_2]^+$	0.942	0.150	4.9	56.3
H	Acetone	$[(H33m)Cu^I$ $(acetone)_2]^+$	0.100	0.266	11.6	81.0
H	CH_3OH	$[(H33m)Cu^I$ $(CH_3OH)_2]^+$	0.024	0.221	9.4	84.5

Table III-3. Dihedral angles between most relevant planes. The plane defined as phenyl includes the six carbon atoms of the phenyl unit. The plane 3N is defined by the three N atoms (Distances are given in Å and angles in degrees).

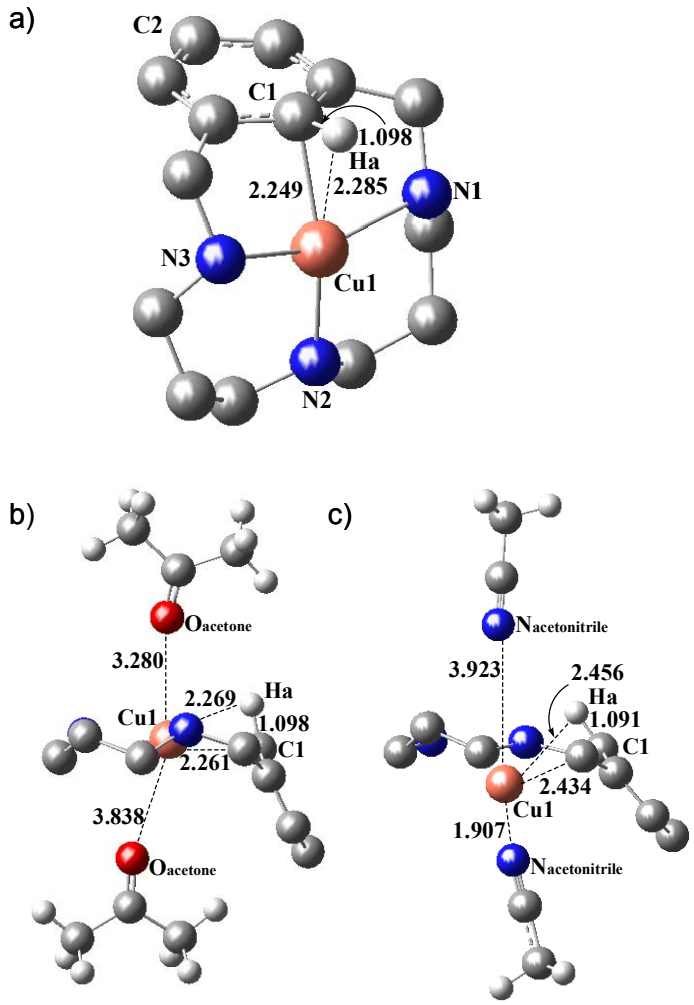

Figure III-3. DFT geometry optimization for the $[Cu^{I}(H33m)]^{+}$ complex showing a) the Cu···CH_a agostic bond in the absence of solvent molecules, b) the complex with two axially coordinated CH_3COCH_3 molecules (the agostic interaction with C-H_a persists) and c) the complex with one coordinated CH_3CN molecule and a second uncoordinated CH_3CN (no agostic interaction observed). All distance values are given in Å.

An agostic interaction between the Cu^{I} and the C-H_a bond is found for complex $[Cu^{I}(H33m)]^{+}$, with an enlargement of the C-H_a bond (1.098 Å) compared to the free ligand (1.092 Å), and an angle of 11.8º between the C-H_a bond and the plane of the aromatic ring (Figure III-3a). In the case of introducing acetone and methanol molecules, both axial molecules remain mostly uncoordinated (d_{Cu-O} > 2.9 Å) and the Cu center is kept in the macrocyclic plane (defined as the best fitted plane that contains the N atoms of the ligand, see Figure III-3b) enabling the agostic interaction between the Cu^{I} and the aromatic C-H_a (this bond is elongated by 0.006 and 0.004 Å with respect

to the free ligand in the presence of acetone and methanol molecules, respectively). In the case of CH_3CN, the Cu^I center is released out of the macrocyclic plane adopting a distorted tetrahedral geometry and coordinates to one CH_3CN molecule, while the other axial solvent molecule remains mainly uncoordinated with a very weak contact (see Figure III-3c). Indeed, the C-H_a bond length and C2-C1-H_a angle are unaffected compared to the free ligand, thus no agostic interaction is found.

Consistent with all the data exposed and taking into account the first-order kinetics with respect to complex and acetone, the mechanism outlined in Scheme III-4 can be proposed. Initially acetone-d^6 in its enolic form coordinates to the metal center with the agostic interaction (species A),[27] then it follows an oxidative type of addition to yield a formal H^- bonded to a Cu^{III} center (species B;[28] rds for pNO_2-H33m in agreement with a direct KIE), followed by the H/D exchange (species C; rds for H33m and pMe-H33m, in agreement with an inverse KIE) to finally generate the $[Cu^I(H33m(D))]^+$ complex with incorporated deuterium atom. Indeed, the difficulty to reach the Cu^{III} oxidation state for the complex with the strongly electron-withdrawing NO_2 group with regard to the complexes containing pMe-H33m and H33m has been shown recently by ourselves[11b] and agrees with the mechanism proposed. In addition, the higher stability of the Cu^{III} complex containing the pMe-H33m ligand with electron-donating group with regard to the H33m ligand, will generate more stable B type of species (with a stronger Cu-H bond) and thus will end up having lower rates for the former (Table III-1). However, the stronger Cu-H bond generates a slightly larger isotopic inverse effect on the H/D process and thus will lead to a lower KIE value for the pMe-H33m system.

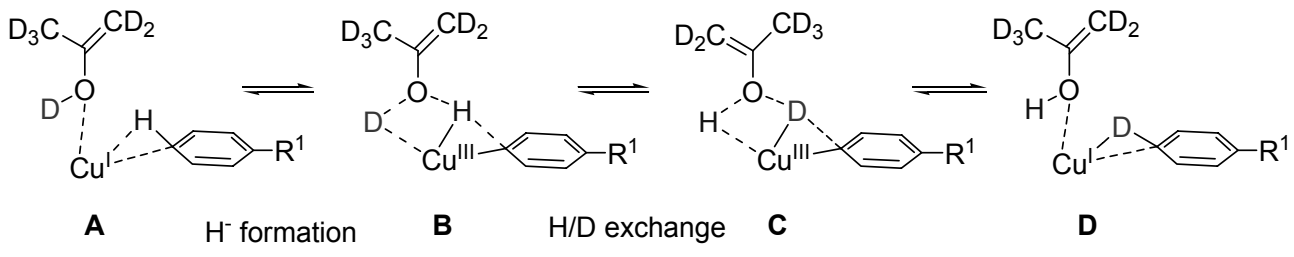

Scheme III-4. Proposed H/D exchange mechanism.

The precise macrocyclic coordination environment is essential for the reaction to take place, and this is evidenced by absence of H/D exchange in the sterically hindered

$[Cu^{I}(H33p)]^{+}$ system, (compared to H33m, ligand H33p in Scheme III-1 is the *para*-substitution instead of *meta*- on the aromatic ring) where despite there are two inner-macrocycle aromatic C-H bonds, no reaction takes place. The $[(H33p)Cu^{I}]^{+}$ complex is depicted in Figure III-4. On the other hand, the $[Cu^{I}(Me33m)]^{+}$ system does not undergo isotopic exchange in acetone-d^6. The reason for that is the stabilization of low oxidation states of the Cu center due to N-methylation as described by Meyerstein and Bernhardt,[11b,29] thus precluding the formation of high oxidation intermediates and therefore in line with the mechanistic proposal.

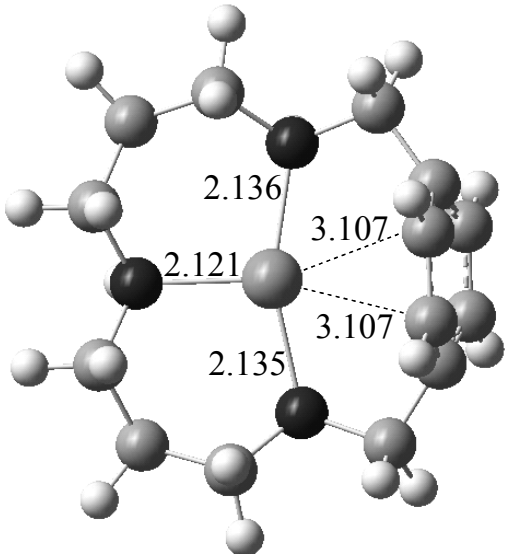

Figure III-4. Geometry optimization of complex $[(H33p)Cu^{I}]^{+}$, with Cu-$C_{aromatic}$ distances higher than 3 Å.

Conclusion

In conclusion, we have theoretically studied here the first example of a reversible intramolecular H/D exchange promoted by Cu^{I}. The process is finely controlled by the precise coordination distance required to form the agostic interaction between the Cu^{I} and the aromatic C-H_a bond, and thus the reactivity is sharply modified by the coordination effect exerted by the solvent used. Indeed, the reactivity can also be tuned by the electronic effects on the aromatic ring and also on the amine substitution.

References

1. J. M. Thomas, R. Raja, G. Sankar,; R. G. Bell, *Acc. Chem. Res*. **2001**, *34*, 191-200.

2. S. S. Stahl, J. A. Labinger, J. E. Bercaw, *Angew. Chem.* **1998**, *110*, 2298-2311; *Angew. Chem. Int. Ed.* **1998**, *37*, 2180-2192.
3. a) A. E. Shilov, G. B. Shul'pin, *Chem. Rev*. **1997**, *97*, 2879-2932. b) M. Q. Slagt, G. Rodríguez, M. M. P. Grutters, R. J. M. Klein Gebbink, W. Klopper, L. W. Jenneskens, M. Lutz, A. L. Spek, G. van Koten, *Chem. Eur. J*. **2004**, *10*, 1331-1344.
4. a) M. Gozin, A. Weisman, Y. Ben-David, D. Milstein, *Nature* **1993**, *364*, 699-701. b) M. E. van der Boom, D. Milstein, *Chem. Rev*. **2003**, *103*, 1759-1792. c) M. Albrecht, G. van Koten, *Angew. Chem*. **2001**, *113*, 3866-3898; *Angew. Chem. Int. Ed.* **2001**, *40*, 3750-3781.
5. a) M. Stepien, L. Latos-Grazynski, *Acc. Chem. Res*. **2005**, *38*, 88-98. b) J. Cámpora, P. Palma, D. Río, M. M. Conejo, E. Álvarez, *Organometallics* **2004**, *23*, 5653-5655.
6. J. D. Harvey, C. J. Ziegler, *Chem. Commun*. **2004**, 1666-1667.
7. K. Rachlewicz, S.-L. Wang, J.-L. Ko, C.-H. Hung, L. Latos-Grazynski, *J. Am. Chem. Soc*. **2004**, *126*, 4420-4431.
8. D. S. Bohle, W.-C. Chen, C.-H. Hung, *Inorg. Chem*. **2002**, *41*, 3334-3336.
9. a) P. J. Chmielewski, L. Latos-Grazynski, I. Schmidt, *Inorg. Chem*. **2000**, *39*, 5475-5482. b) A. Srinivasan, H. Furuta, *Acc. Chem. Res.* **2005**, *38*, 10-20. c) M. Castro, J. Cruz, H. López-Sandoval, N. Barba-Behrens, *Chem. Commun*. **2005**, 3779-3781.
10. X. Ribas, R. Xifra, T. Parella, A. Poater, M. Solà, A. Llobet, *Angew. Chem. Int. Ed*., in press.
11. a) X. Ribas, D. A. Jackson, B. Donnadieu, J. Mahía, T. Parella, R. Xifra, B. Hedman, K. O. Hodgson, A. Llobet, T. D. P. Stack, *Angew. Chem*. **2002**, *114*, 3117-3120. *Angew. Chem. Int. Ed.* **2002**, *41*, 2991-2994. b) R. Xifra, X. Ribas, A. Llobet, A. Poater, M. Duran, M. Solà, T. D. P. Stack, J. Benet-Buchholz, B. Donnadieu, J. Mahía, T. Parella, *Chem. Eur. J.* **2005**, *11*, 5146-5156.
12. Similar reactivity is found by using CD_3OD with the systems H33m and pMe-H33m, however with faster reaction rates compared to acetone-d^6. In the case of using CD_3OH no disappearance of the H_a signal is observed because the exchange is done between the H of the alcohol group.
13. The addition of 1.5 eq. of $NaBH_4$ to the corresponding organometallic $[Cu^{III}(H33mC)]^{2+}$ compound (reference 11a) leads to the Cu^I complex bearing

the H_a aromatic proton (monitored by ^{1}H-NMR), and thus gives support to the formation of the transient aryl-Cu^{III} hydride.

14. a) W. D. Jones, *Acc. Chem. Res*. **2003**, *36*, 140-146. b) W. D. Jones, F. J. Feher, *J. Am. Chem. Soc*. **1984**, *106*, 1650-1663.
15. The addition of 0.5 eq of CF_3COOD to a solution of $[Cu^I(H33m)]^+$ in CD_2Cl_2 (non-coordinating solvent) causes the formation of a species with broad ^{1}H-NMR signals (probably partial decomplexation and oligomerization due to ligand amine protonation).
16. E. J. Baerends, D. E. Ellis, P. Ros, *Chem. Phys.* **1973**, *2*, 41-51.
17. C. Fonseca Guerra, O. Visser, J. G. Snijders, G. te Velde, E. J. Baerends, *Methods and Techniques for Computational Chemistry*, STEF, Cagliari, 1995, p. 305.
18. G. te Velde, F. M. Bickelhaupt, E. J. Baerends, C. Fonseca Guerra, S. J. A. van Gisbergen, J. G. Snijders, T. Ziegler, *J. Comput. Chem.* **2001**, *22*, 931-967.
19. W. Ravenek, *Algorithms and Applications on Vector and Parallel Computers*, Elsevier, Amsterdam, 1987.
20. G. te Velde, E. J. Baerends, *J. Comput. Phys.* **1992**, *99*, 84-98.
21. ADF2000. E. J. Baerends, J. A. Autschbach, A. Bérces, C. Bo, P. M. Boerrigter, L. Cavallo, D. P. Chong, L. Deng, R. M. Dickson, D. E. Ellis, L. Fan, T. H. Fischer, C. Fonseca Guerra, S. J. A. van Gisbergen, J. A. Groeneveld, O. V. Gritsenko, M. Grüning, F. E. Harris, P. van den Hoek, H. Jacobsen, G. van Kessel, F. Kootstra, E. van Lenthe, V. P. Osinga, S. Patchkovskii, P. H. T. Philipsen, D. Post, C. C. Pye, W. Ravenek, P. Ros, P. R. T. Schipper, G. Schreckenbach, J. G. Snijders, M. Solà, M. Swart, D. Swerhone, G. te Velde, P. Vernooijs, L. Versluis, O. Visser, E. van Wezenbeek, G. Wiesenekker, S. K. Wolff, T. K. Woo, T. Ziegler, Vrije Universiteit Amsterdam: Amsterdam, The Netherlands, 2000.
22. A. D. Becke, *Phys. Rev. A* **1988**, *38*, 3098-3100.
23. J. P. Perdew, *Phys. Rev. B* **1986**, *33*, 8822-8824.
24. J. G. Snijders, E. J. Baerends, P. Vernooijs, *At. Nucl. Data Tables* **1982**, *26*, 483-509.
25. P. Vernooijs, E. J. Baerends, *Slater Type Basis Functions for the Whole Periodic System. Internal Report*, Vrije Universiteit of Amsterdam, The Netherlands, 1981.

26. J. Krijn, E. J. Baerends, *Fit Functions in the HFS Method. Internal Report (in Dutch)*, Vrije Universiteit of Amsterdam, The Netherlands, 1984.
27. The direct coordination of acetone to a metal center has been reported, along with the description of the keto-enol equilibrium (see M. A. Henderson, Langmuir **2005**, *21*, 3451-3458 and J. Ruiz, M. T. Martínez, V. Rodríguez, G. López, J. Pérez, P. A. Chaloner, P. B. Hitchcock, *Dalton Trans*. **2004**, 3521-3527).
28. DFT calculations failed in locating the postulated hydride intermediate $[Cu^{III}(H33mC)(H)]^{+}$, but we are currently investigating the possibility of a solvent-assisted stabilization.
29. a) G. Golub, H. Cohen, P. Paoletti, A. Bencini, L. Messori, I. Bertini, D. Meyerstein; *J. Am. Chem. Soc*. **1995**, *117*, 8353-8361. b) D. Meyerstein, *Coord. Chem. Rev*. **1999**, *185-6*, 141-147. c) P. V. Bernhardt, *J. Am. Chem. Soc*. **1997**, *119*, 771-774. d) P. V. Bernhardt, *Inorg. Chem*. **2001**, *40*, 1086-1092.

Chapter IV: *Electronic Properties of Highly Stable Organometallic Cu^{III} Complexes Containing Monoanionic Macrocyclic Ligands*

Electronic Properties of Highly Stable Organometallic Cu^{III} Complexes Containing Monoanionic Macrocyclic Ligands

Abstract

The structural and spectroscopic properties of a family of highly stable organometallic Cu^{III} complexes with monoanionic triazamacrocyclic ligands (L^i) with general formula $[CuL^i]^+$ have been thoroughly investigated. The HL^i ligands had been designed by the group of Prof. Llobet in order to understand and quantify the electronic effects exerted by electron donor and electron-withdrawing groups on either the aromatic ring or the central secondary amine or on both. In the solid state the Cu^{III} complexes were mainly characterized by single-crystal X-ray diffraction analysis. The UV/Vis spectroscopy has been used to analyze the electronic effects exerted by the ligands on the Cu^{III} metal center. A theoretical analysis of this family of Cu^{III} complexes has been undertaken by DFT calculations to gain a deeper insight into the electronic structure of these complexes, which has in turn allowed a greater understanding of the nature of the UV/Vis transitions as well as the molecular orbitals involved.

Introduction

The controlled activation of small and relatively inert molecules by transition-metal complexes (TMC) under mild conditions is a very active area of research that has made impressive advances over the last 20 years.[1] In particular, the activation of C-H bonds in saturated hydrocarbons is of special interest since these are the major constituents of natural gas and petroleum.[2] However, the full potential of TMC in profitable practical applications, for example, in catalytic conversion to more valuable products, has not yet been realized.[3]

By choosing the appropriate ligands and metal, a remarkable degree of control over the activation processes can be accomplished under mild conditions, which in turn can lead to the improved efficiency and selectivity of the whole process.[4]

In a recent paper it was presented a novel aryl C-H activation process involving Cu^{II} complexes that leads to the formation of relatively unusual and stable Cu^{III} complexes containing a monoanionic ligand.[5] Few d^8 Cu^{III} complexes have been structurally characterized by single-crystal X-ray diffraction and those that have all exhibit a square-planar type of geometry. The higher oxidation state is stabilized either by the presence of a trianionic ligand derived from the deprotonation of tripeptides,[6] corroles[7] or confused porphyrins,[8] or by the participation of several ligands supplying overall at least three negative charges, such as the trifluoromethanate ligand.[9] The different factors that govern Cu^{III} stabilization and its reactivity are of considerable interest in biology since Cu^{III} is the active center of certain metalloproteins[10] and also because Cu^{III} is thought to be responsible for the oxidative degradation and site-specific cleavage of DNA.[11] Furthermore Cu^{III} has been postulated as an intermediate in the oxidation of saturated hydrocarbons using copper complexes as oxygen and/or hydrogen peroxide activators, a variation of the socalled Gif chemistry developed by Barton et al.[12]

Herein we present the characterization of a family of $[Cu^{III}L^i]^{2+}$ macrocyclic complexes, generated via C-H activation using the corresponding $[Cu^{II}(HL^i)]^{2+}$ complexes, containing the ligands displayed in Scheme IV-1. These ligands enable us to gain some understanding of the influence of steric and electronic effects on the properties of the Cu^{III} complexes.

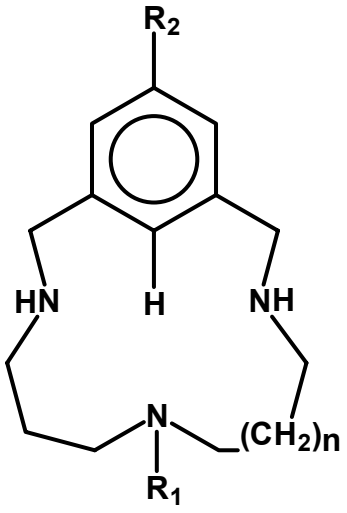

HL1: $R_1 = H$, $R_2 = H$, $n = 0$
HL2: $R_1 = H$, $R_2 = H$, $n = 1$
HL3: $R_1 = H$, $R_2 = Me$, $n = 1$
HL4: $R_1 = H$, $R_2 = NO_2$, $n = 1$
HL5: $R_1 = Me$, $R_2 = H$, $n = 1$
HL6: $R_1 = Me$, $R_2 = Me$, $n = 1$

Scheme IV-1. Triazamacrocyclic ligands HL^i (i = 1-6).

Synthesis and X-ray structures: The triazamacrocyclic ligands used in this work are depicted in Scheme IV-1. In general, these ligands were prepared by the cyclization of the corresponding 1,3-bis(bromomethyl)benzene with the appropriate tosylated triamine following a similar methodology (see Scheme IV-2 for the particular case of HL^3) to that first described by Bencini et al.[13] for related compounds. The tosylated triazamacrocycles were then treated with lithium suspended in liquid ammonia[14] to afford the triazamacrocyclic ligands HL^i in moderate-to-good yields. The ligands HL^3, HL^4, and HL^6, which contain Me- and NO_2-substituted aryl groups, are described and characterized for the first time in the work by Llobet et al.,[15] whereas the other three have been reported previously.[5,16]

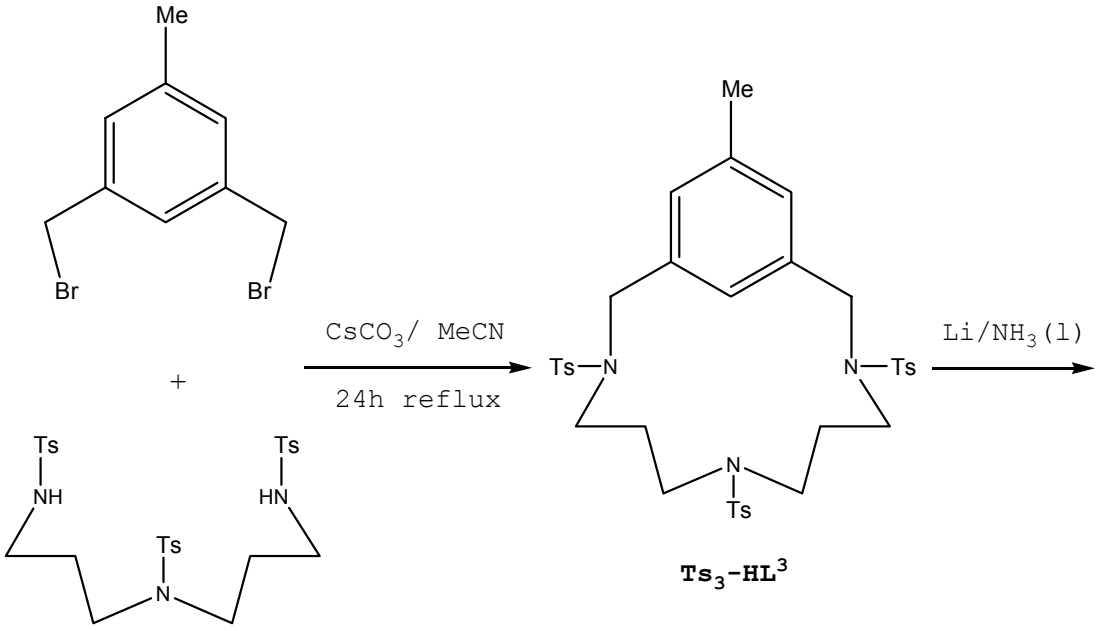

Scheme IV-2. Synthetic strategy for the preparation of the triazamacrocyclic ligand HL^3.

Under anaerobic conditions at room temperature, the HL^i ligands react instantaneously with Cu^{II} salts (triflate or perchlorate) in acetonitrile to afford the corresponding unstable $[Cu^{II}(HL^i)]^{2+}$ complexes, which quantitatively disproportionate to generate a colorless Cu^I and an orange Cu^{III} complex [Eq. (1)], both of which are diamagnetic.

$$2\ [Cu^{II}(HL^i)]^{2+} \xrightarrow{MeCN,\ RT} [Cu^{III}(L^i)]^{2+} + [Cu^{I}(H_2L^i)]^{2+} \quad (1)$$

Diffusion of diethyl ether into the resulting acetonitrile solution overnight results in the precipitation of red microcrystals of $[Cu^{III}(L^{i})]^{2+}$ (**1–6**, i=1–6) in nearly quantitative yield. These six Cu^{III} complexes, **1–6**, are all stable in the solid state and in both protic (H_2O, pH 1–7; MeOH) and aprotic solvents (MeCN, CH_2Cl_2) under aerobic conditions except for **4** which decomposes in solution at room temperature as a result of the strong electron-withdrawing nature of the nitro substituent. Under basic conditions the Cu^{III} complexes readily transform into the corresponding dinuclear diphenoxo complexes of general formula $[Cu_2^{II}(m\text{-}OL^{i})_2]^{2+}$.[15]

^1H NMR spectroscopic analysis of the reaction mixture, performed by using CD_3CN as the solvent, confirms that the reaction proceeded by disproportionation by simple integration of the Cu^{I} and Cu^{III} resonances. Furthermore, optical titration of the reaction mixture with excess phenanthroline also confirms a 50% conversion of Cu^{II} to Cu^{I}. Complex **2** reacts with Cl^- at room temperature to form a pentacoordinate copper complex, $[Cu^{III}(L^{2})Cl]^{+}$, **7**, whose structure will be discussed below. In a similar manner, **4**, which contains the NO_2 electron-withdrawing group, also reacts readily with Cl^- stabilizing the resulting nitro complex $[Cu^{III}(L^{4})Cl]^{+}$, **8**, although its isolation in the solid state still remained elusive as a result of decomposition. Selected bond lengths and angles for complexes **2**, **3**, **6** and **7** of the crystallographic data are reported in Table IV-1. Some ORTEP views of these complexes together with their labeling schemes are shown in Figure IV-1. In complexes **1**, **2**, **3**, **5**, and **6**, the Cu^{III} metal center is coordinated to the three nitrogen atoms of the macrocyclic ligand and a carbon atom of the phenyl ring and adopts a distorted square planar geometry. The shortest coordination distance is always the organometallic Cu1-C1 bond, which ranges from 1.848 Å for **1** to 1.926 Å for **6**. This is in agreement with the fact that the macrocyclic ligand, L^1, of complex **1** has the smallest cavity of this series and also with the fact that the longest Cu1-C1 distance is that of complex **6**, which contains a ligand, L^6, with a tertiary amine. The trans effect produced by the Cu1-C1 bond generates the longest Cu-N distances (Cu1-N2 bond lengths range from 1.995 Å for **3** to 2.048 Å for **6**) and are 0.033–0.095 Å longer than the mean distances of the other two Cu-N bonds (Cu1-N1 and Cu1-N3). This is especially acute for complexes **5** and **6** which contain the macrocyclic ligands L^5 and L^6 with the methylated central amine. This phenomenon has been described in detail previously mainly by Meyerstein and co-workers[17] and by Bernhardt;[18] the M-N bond strength of tertiary amines is weaker than that of secondary amines under

comparable conditions. Herein this phenomenon will from now on be termed the "N-methylation effect". The increase in the steric crowding and strain around the tertiary nitrogen atom of the amine together with solvation effects through hydrogen bonding are identified as the main factors that produce this effect.[19]

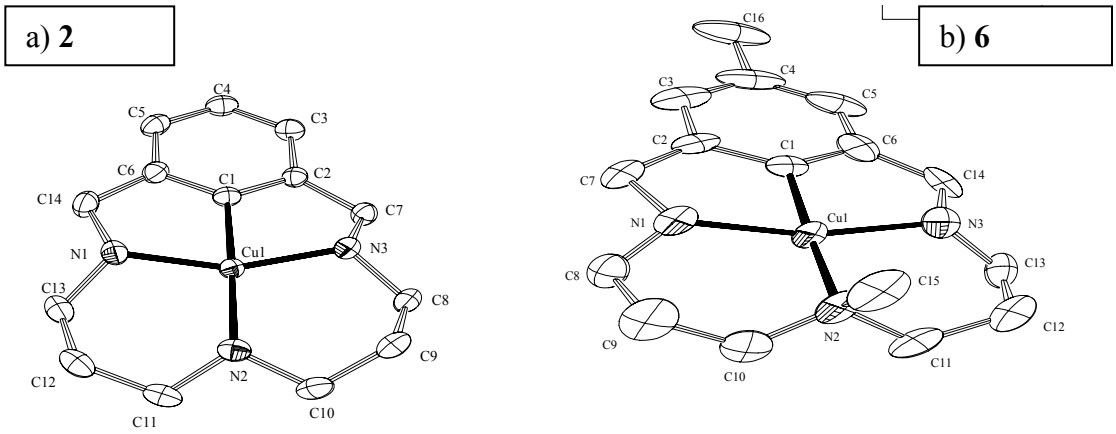

Figure IV-1. ORTEP plot (50% probability) of the cationic moiety of the X-ray crystal structures of complexes a) **2** and b) **6**. Hydrogen atoms have been omitted for clarity.

	1[a]	**2**	**3**[b]	**5**[a]	**6**	**7**
C1-Cu1	1.848(4)	1.901(2)	1.902(2)	1.905(3)	1.926(8)	1.898(6)
N1-Cu1	1.899(4)	1.960(2)	1.961(2)	1.985(3)	1.957(7)	1.958(5)
N3-Cu1	1.911(3)	1.952(2)	1.963(2)	1.961(3)	1.963(7)	1.963(5)
N2-Cu1	2.000(8)	2.002(2)	1.995(2)	2.031(3)	2.048(7)	1.988(5)
C1-Cu1-N1	84.600(2)	82.800(1)	82.000(1)	82.900(2)	84.100(3)	82.200(2)
C1-Cu1-N3	84.400(2)	81.700(1)	82.200(1)	82.300(2)	82.600(4)	81.100(2)
N1-Cu1-N2	105.600(2)	95.600(1)	97.400(1)	96.900(1)	94.300(3)	94.700(2)
N2-Cu1-N3	85.200(2)	99.700(1)	96.400(1)	99.700(1)	97.600(3)	99.300(2)
C1-Cu1-N2	163.500(2)	178.400(1)	173.800(1)	177.600(1)	173.800(3)	171.900(2)
N1-Cu1-N3	169.000(2)	157.200(1)	156.000(1)	160.700(2)	161.000(4)	154.500(2)
Cu-O (short)	2.428(3)	2.408(2)	2.256(2)	2.442(4)	2.279(5)	2.556(2) (Cl)[c]
Cu-O (long)	2.584(3)	2.643(2)	2.835(2)	2.736(4)	3.662(5)	3.301(2) (Cl)[c]
O-Cu-O	170.9(2)	156.6(1)	161.0(1)	177.3(1)	148.01(3)	160.7(2) (Cl)[c]

[a] See reference [5]
[b] There are two different molecules in the unit cell with very similar metric parameters
[c] The values shown here for complex **7** are the shortest Cu-Cl distances and the smallest Cl-Cu-Cl angles (see Figure IV-2 for the other values).

Table IV-1. Selected bond lengths [Å] and angles [º] for complexes **1–3** and **5–7.** All values taken from ref. [16].

The *N*-methylation effect of the tertiary amines, besides the elongation of the Cu-N_{tert} bond, is also structurally manifested in our case through a geometrical distortion. This distortion involves the torsion angles between the best-fitted plane that contains the carbon framework of the aromatic ring and the best-fitted plane that contains the C1, Cu1, N1, and N3 atoms (the first coordination sphere of the copper center with the exception of the nitrogen atom of the tertiary amine). In complexes **5** and **6**, which contain a tertiary amine, this torsion angle is 9.4 and 9.6º, respectively, whereas in complexes **2** and **3** this distortion is reduced to 7.4 and 2.1º, respectively, thus showing a lower degree of distortion.

Note also that in all cases the hydrogen atoms bonded to the secondary amines (**2** and **3**) are oriented in the same direction and thus the macrocyclic ligand adopts a syn conformation. This syn conformation is also adopted by macrocyclic ligands with methylated central amines (**5** and **6**). The non-anionic nature of the nitrogen-coordinating atoms is in line with the longest Cu^{III}-N bonds found in this family of complexes relative to the bond lengths found in other Cu^{III} complexes that contain deprotonated amides as ligands.[6,39] In complexes **1–3**, **5**, and **6** the ClO_4^- or $CF_3SO_3^-$ counteranions or a water molecule (in the case of complex **6**) are weakly associated with the metal center, generating a decompressed tetragonally distorted octahedral environment in which one of the Cu-O distances is substantially longer than the other (see Table IV-1). In all cases, the longer Cu-O distance is located on the same side of the macrocycle as the N-H or N-Me bonds, whereas the shorter Cu-O distance is located on the other side which has a much lower steric encumbrance. This distorted octahedral environment is perhaps the most salient feature of this family of compounds[5] in comparison with Cu^{III} complexes described previously[6-9] and can be attributed to the fact that in this case the higher oxidation state of the copper center is stabilized by a monoanionic ligand. In complex **7**, the Cu^{III} metal center adopts a similar geometry as in the previous cases except that the axial positions are occupied by chlorine instead of oxygen atoms, which at the same time bridge two metal centers. Furthermore, this complex exhibits two crystallographically distinct molecules in its unit cell (their atoms are thus labeled by adding the letters “a” or “b”, for example, the copper atoms are labeled Cu1a and Cu1b), although their parameters are very similar. While the crystal packing in the complexes **1–6** is unremarkable, the chlorine bridge in **7** produces

pseudochains along the z axis with alternating “a” and “b” molecules, as shown in Figure IV-2.

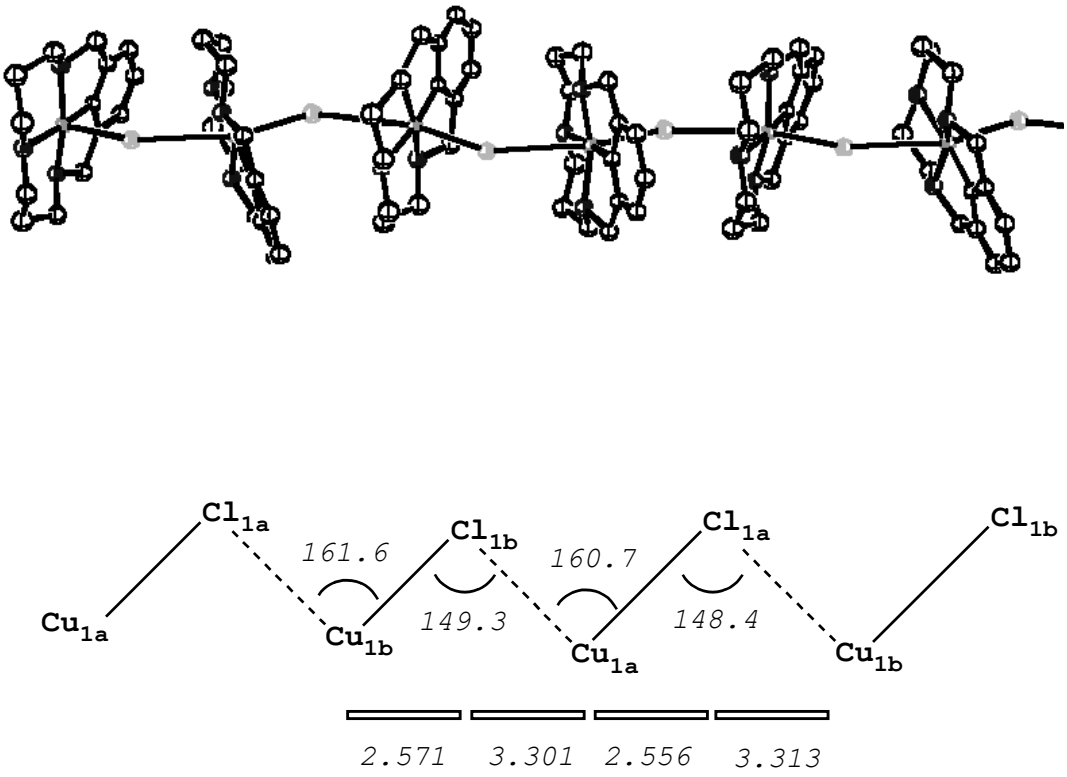

Figure IV-2. Crystal packing for complex **7** showing the formation of a pseudochain through the Cu-Cl bonds; structural parameters are also indicated.

Spectroscopic properties:

The UV/Vis spectra of complexes **2–7** are presented in Figure IV-3. The complexes **2–7** display a very intense band below 300 nm and another less intense but broad band in the range of 370– 520 nm (see Figure IV-3) that can be assigned to two similar $\pi \rightarrow d_{x^2-y^2}$ ligand-to-metal charge transfer (LMCT) transitions.[40] As shown in Figure IV-3, the $\pi_1 \rightarrow d_{x^2-y^2}$ band for complexes **3**, **5**, and **6** is red-shifted relative to **2**, while for complexes **4** and **7** a blue shift is observed.

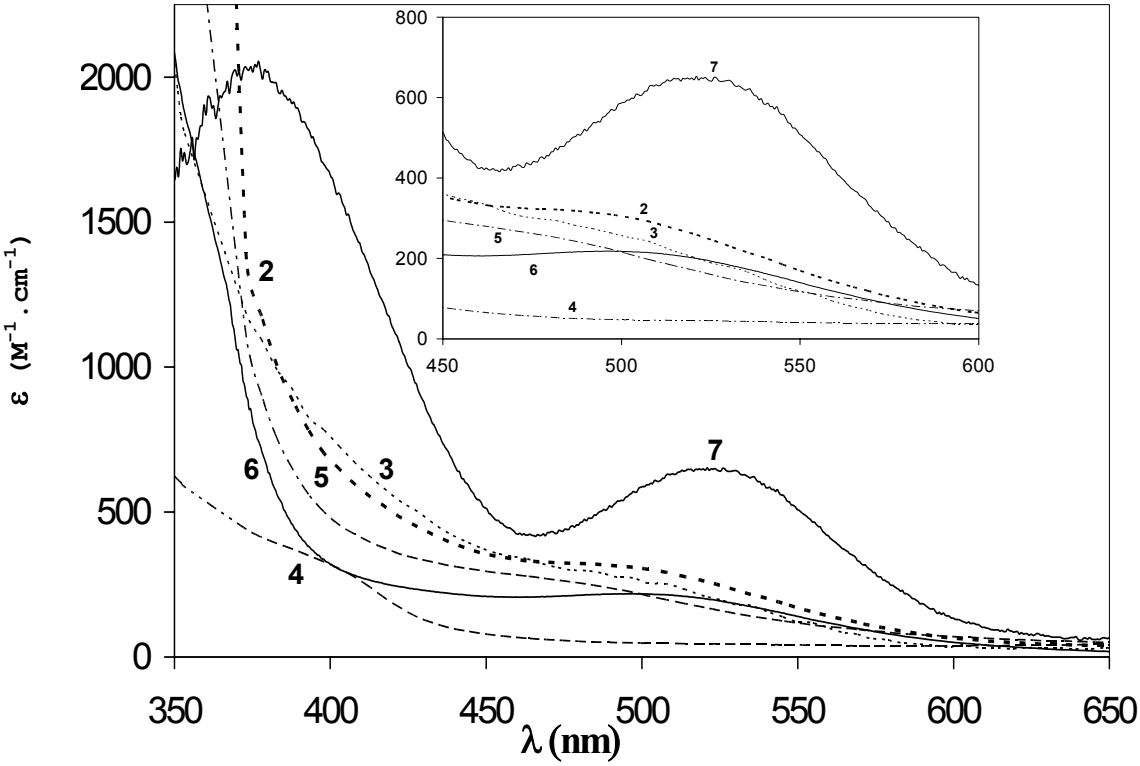

Figure IV-3. UV/Vis spectra for complexes **2–7**. The inset shows an enlargement of the 450–600 nm zone.

Computational details

The reported calculations were carried out by using the Amsterdam density functional (ADF) package developed by Baerends and co workers[20-22] and vectorized by Ravenek.[23] The numerical integration scheme employed was that of te Velde and Baerends.[24] Both geometry optimizations and energy evaluations were performed using a generalized gradient approximation (GGA) that includes Becke's GGA exchange correction[25] and Perdew's GGA correlation correction.[26] Experimentally it was found that these mononuclear species are diamagnetic. For this reason, optimizations were carried out for neutral closed-shell singlet ground-state structures. However, we have checked the relative stabilities of the singlet and triplet states of all the calculated complexes. In all cases, the triplet state has a higher energy. This is in agreement with the sharp peaks in the diamagnetic regions of the NMR spectra. The difference between the two states is around 25 kcal·mol^{-1} in all the cases studied. The UV spectra were simulated by the time-Dependent DFT method (TDDFT),[27] using the LB94 potential of van Leeuwen and Baerends.[28] The 2000.02 release of the ADF package was used for all

geometry optimizations and the calculated UV/Vis spectra were obtained by using the 2002.03 release of the ADF program.[29] In the geometry optimizations we used an uncontracted triple-ζ basis set to describe the 3s, 3p, 3d, 4s, and 4p orbitals of copper. For carbon (2s,2p), nitrogen (2s,2p), oxygen (2s,2p), and hydrogen (1s), double-ζ basis sets were employed. All the basis sets were augmented by an extra polarization function.[30] Electrons in lower shells were treated within the frozen-core approximation.[20] A set of auxiliary s, p, d, f, and g functions, centered in all nuclei, was introduced in order to fit the molecular density and Coulomb potential accurately in each SCF cycle.[32]

To simulate the UV/Vis spectra an uncontracted triple-ζ basis set was used for all the atoms, augmented by an extra polarization function.[30-31] We have checked in several complexes that the inclusion of diffuse functions in the basis set and relativistic effects in the hamiltonian only produce slight changes in the positions of the bands, and therefore to reduce the computational cost these effects have not been taken into account.[33]

The effect of solvent on the UV/Vis spectra was considered by using the conductor-like screening model (COSMO) of Klamt and Schüürmann,[34] as implemented by Pye and Ziegler in the ADF program.[35] The radius chosen of 2.75 Å for acetonitrile (ε=37.50)[36] was obtained by calculating the molecular volume with the Gaussian 98 package.[37] The radii used for the C, N, Cl, H, O, and Cu atoms were 2.00, 1.40, 1.20, 1.18, 1.30, and 1.50 Å, respectively.[35]

All molecular orbitals were constructed by using the MOLEKEL program.[38]

Results

Density functional theory (DFT) calculations were carried out for complexes **2–7** to elucidate the electronic properties of these complexes and thus understand the nature of the transitions observed in the UV/Vis spectra. For complex **2**, the DFT-optimized structure nicely fits the experimental X-ray structure thus validating the adequacy of the theoretical method employed for the geometry optimizations of these particular systems. The experimental and theoretical bond lengths and angles differ by less than 0.07 Å and

3.08º, respectively. The standard deviation for the bond distances is 0.03 Å, and for the angles 1.81º. The standard deviation is calculated using Equation (2),

$$s_{n-1} = \sqrt{\frac{\sum_{i=1}^{N}(CV - EV)^2}{N-1}} \qquad (2)$$

where CV means calculated value, EV experimental value (X-ray data), and N is the number of bond distances or angles taken into account. See Table IV-2 for the bond distances and angles used to calculate s_{n-1}.

Distances	dist(RX)	dist(BP86)
Cu1-C1	1.919	1.901
N1-Cu1	2.006	1.952
N2-Cu1	2.070	2.002
N3-Cu1	2.005	1.960
C6-C14	1.487	1.488
C2-C7	1.487	1.488
C14-N1	1.513	1.494
N1-C13	1.493	1.483
C11-N2	1.500	1.481
N2-C10	1.500	1.487
C8-N3	1.494	1.488
N3-C7	1.514	1.502

Angles	ang(RX)	ang(BP86)
C1-Cu1-N3	82.47	82.79
C1-Cu1-N2	178.44	178.38
C1-Cu1-N1	82.27	81.69
N1-Cu1-N2	97.68	99.73
N1-Cu1-N3	160.33	157.24
N2-Cu1-N3	97.24	95.63
C14-N1-C13	112.18	110.47
C11-N2-C10	109.55	109.85
C8-N3-C7	111.99	109.40

Table IV-2. Comparison between the X-Ray data of complex **2** and the corresponding BP86 geometry (Distances in Å and angles in degrees).

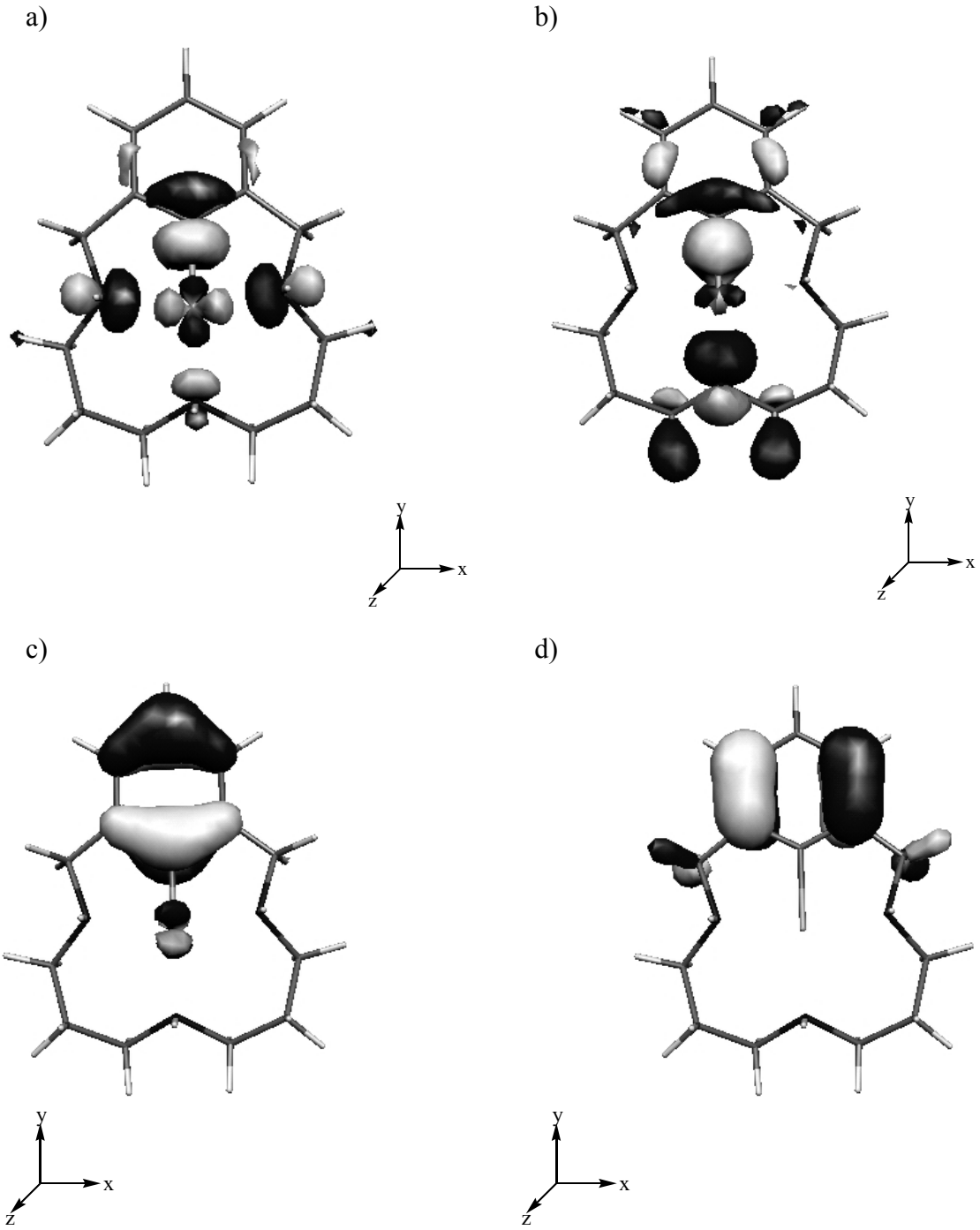

Figure IV-4. 3D representation of the orbitals most involved in the calculated excitations of the UV/Vis spectra of complex **2**: a) the LUMO orbital; b) the starting orbital (σ_1) involved in the highest energy band; c) the starting orbital (π_1) involved in the $\pi_1 \rightarrow d_{x^2-y^2}$ excitation; d) the starting orbital (π_2) involved in the $\pi_2 \rightarrow d_{x^2-y^2}$ excitation. (Isosurface values are -0.05 and 0.05 a.u.)

Time-dependent DFT calculations (TDDFT) show that the most intense band below 300 nm involves the LUMO frontier orbital (Figure IV-4a) as the main arrival orbital for complex **2** (only small differences are observed for complexes **2–7**) and the σ_1 orbital (Figure IV-4b) as the main starting one. The LUMO orbital is mainly a combination of the $d_{x^2-y^2}$ orbital of the copper atom and the p orbitals of the nitrogen atoms and the carbon atom that participates in the Cu-C bond. In **7** there is an extra contribution from the p_z orbital of the chlorine atom.

The σ_1 orbital depicted in Figure IV-4b is composed essentially of the p_y orbitals of the atoms contained in the axis N2-Cu1-C1. This orbital is the HOMO-2 except in complex **4**, in which it is the HOMO-3 owing to the insertion of an orbital with mainly nitro-group character as the HOMO-2 orbital, and in complex **7**, in which the σ_1 orbital is the HOMO-6 because of the intercalation of three orbitals with Cu-Cl antibonding character and another orbital of macrocyclic character related to the Cu-N bonding interaction. The $\pi \rightarrow d_{x^2-y^2}$ LMCT band is composed of two charge transfer excitations, principally from the ligand to the metal. The main arrival orbital is the LUMO (see Figure IV-4a), but the starting orbital changes depending on the system. The first excitation starts from the π_1 orbital (Figure IV-4c), while the second one starts from the π_2 orbital (Figure IV-4d). The π_1 and π_2 orbitals are the HOMO and HOMO-**1** orbitals in complexes **2**, **4**, and **5**. In the other complexes, these two orbitals are exchanged, except in complex **7** in which the π_1 and π_2 orbitals are the HOMO-3 and HOMO-4, respectively. The solvent has a significant effect on the energy of the $\pi \rightarrow d_{x^2-y^2}$ LMCT band and a less strong one on the band below 300 nm. After including this effect in the calculations, the $\pi \rightarrow d_{x^2-y^2}$ LMCT bands are blue-shifted, this shift being more noticeable in solvents with high dielectric constants.

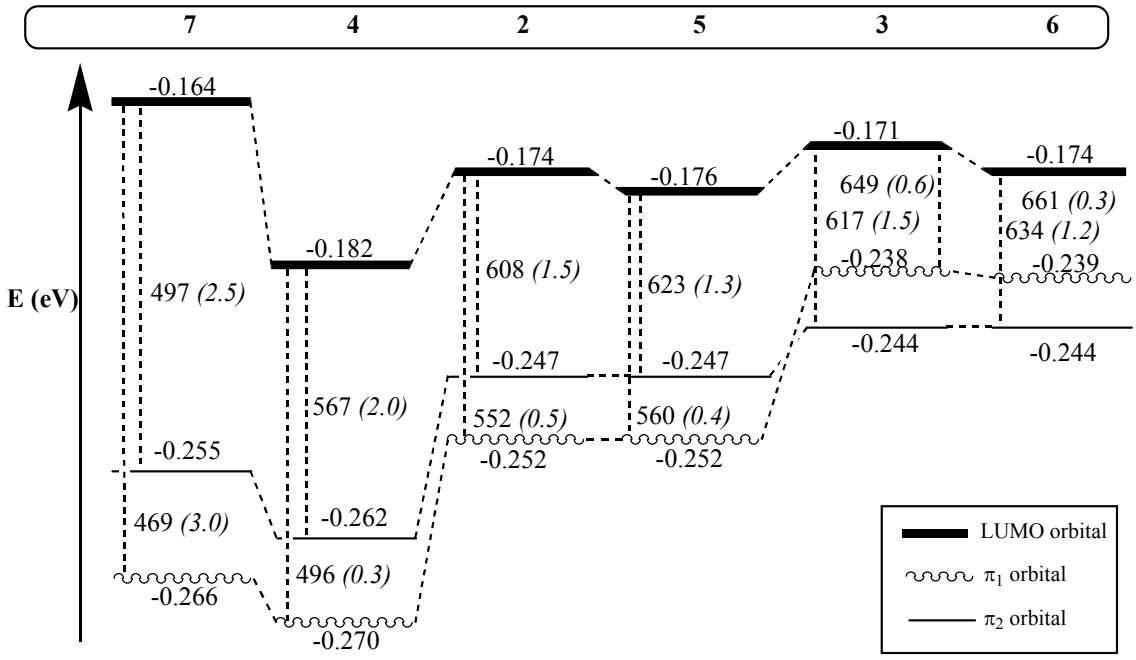

Figure IV-5. Calculated qualitative energy diagram of the orbitals involved in the $\pi \rightarrow d_{x^2-y^2}$ LMCT bands of complexes **2**, **3**, and **5**. The orbital energies are given in atomic units (hartrees) and the wavelengths of the excitations in nm. In parenthesis, the intensities of the bands.

	$\pi_1 \rightarrow d_{x^2-y^2}$		$\pi_2 \rightarrow d_{x^2-y^2}$	
Complex	λ_{max} (exp.[a])	λ_{max} (theor.)	λ_{max} (exp.[a])	λ_{max} (theor.)
2	390(417)	552	463(147)	608
3[b]	487(303)	649	388(559)	617
4	277(325)	496	380(15)	567
5	393(345)	560	478(157)	623
6[b]	503(198)	661	397(285)	634
7	328(630)	469	386(1260)	497

[a] Extinction coefficients are given in parenthesis and are measured in $M^{-1}cm^{-1}$. Experimental values taken from ref. [16]

[b]The energies of the π_1 and π_2 orbitals are inverted compared with the energies of the other complexes; see text, Figure IV-5.

Table IV-3. Calculated and experimental UV-Vis data assigned to $\pi_1 \rightarrow d_{x^2-y^2}$ and $\pi_2 \rightarrow d_{x^2-y^2}$ transitions.

Figure IV-5 shows the energies of the orbitals and the wavelengths of the two calculated excitations with the corresponding oscillator strength values that produce the $\pi \rightarrow d_{x^2-y^2}$ LMCT bands for complexes **2-7**, and reveal the main features of the experimental and calculated LMCT transitions. Table IV-3 contains these theoretical results in comparison with the experimental values (l_{max} values together with the corresponding extinction coefficients). As can be observed from the data in Table IV-3, the experimental $\pi_1 \rightarrow d_{x^2-y^2}$ transition correlates well with the TDDFT calculated one with a shift of 141–167 nm for complexes **2**, **3**, **6**, and **7** and of 219 nm for **4**. Although the absorption wavelengths calculated by TDDFT are clearly overestimated, the errors are comparable to those found in similar studies.[41] These errors may be attributed to the size of the basis set,[42] the inadequate description of solvent effects, which are very relevant in charged species, and the different localized or delocalized character of the initial and final electronic states.[41a] However, we want to emphasize that our main goals are to tentatively assign the observed transitions and to understand the origin of the shifts experienced by the different bands when going from complex **2** to complexes **3–7**. In our opinion, these shifts are well reproduced by our calculations and an understanding of the origin of the shifts is provided by the analysis of the molecular orbitals that are most involved in the electronic transitions. Finally, the $\pi_2 \rightarrow d_{x^2-y^2}$ transition has a similar degree of correlation to that of the $\pi_1 \rightarrow d_{x^2-y^2}$ transition, with the exception of **3** and **6**, which are shifted in opposite directions.

Methylation of the aromatic ring of species **2** to yield complex **3** has a greater effect on the $\pi_1 \rightarrow d_{x^2-y^2}$ LMCT band than the methylation of the central amine in complex **5**. In both cases, the band is red-shifted, but the magnitude of the shift in the former is much larger (exptl: 97 nm, calcd: 97 nm for **3**; exptl: 3 nm, calcd 8 nm for **5**). Methylation in both places (complex **6**) causes a red shift that is nearly the sum of the two shifts described above (exptl: 113 nm, calcd: 109 nm for **6**). By using complex **2** as a reference, it is found that the energies of the π_1 and π_2 orbitals remain almost constant after the methylation of the amine (complex **5**), while the LUMO is slightly stabilized, as expected from the fact that the methyl group behaves as an electron-acceptor group (vide supra) in this particular species (see Figure IV-5). Methylation of the aromatic

ring in complex **3** has the opposite effect on the LUMO, that is, the LUMO is slightly destabilized, which is not surprising if one considers that this methyl group behaves as an electron donor. In line with this, the π_1 and π_2 orbitals in complex **3** are significantly destabilized owing to their proximity to the aromatic group. In fact, the π_1 orbital is destabilized more than the π_2 orbital because the methyl group bonded to the aromatic carbon contributes to the π_1 orbital with an antibonding interaction whereas it does not participate in the π_2 orbital. This effect is responsible for the relative inversion of the energies of the π_1 and π_2 orbitals in complexes **3** and **6** in which the methyl substituent is bonded to the phenyl group. The significant destabilization of the π_1 and π_2 orbitals in complex **3** accounts for the larger red shift observed for complex **3** than for complex **5**.

The presence of a nitro group (complex **4**) in the aromatic ring causes a blue shift of the $\pi_1 \rightarrow d_{x^2-y^2}$ transition relative to complex **2** (exptl: 113 nm, calcd: 56 nm). This blue shift results from a greater stabilization of the π_1 and π_2 orbitals than of the LUMO giving a larger energy difference as a result of the electron-accepting nature of the nitro group. In complex **7**, two bands were found experimentally at 375 and 522 nm. The band at 375 nm splits into two bands centered at 328 nm and 386 nm (Gaussian deconvolution). In this case, theoretical calculations were useful to understand and assign the origin of these transitions. It has been found that the band at 375 nm is a result of a $\pi \rightarrow d_{x^2-y^2}$ LMCT transition similar to that occurring in complexes **2–6** but the band at 522 nm arises from three transitions that start from antibonding σ^* and π^* orbitals of the Cu-Cl bond (HOMO, HOMO-1, and HOMO-2) (see Figure 6) and finish at the LUMO orbital. Our calculations indicate that the $\pi_1 \rightarrow d_{x^2-y^2}$ LMCT transition in complex **7** is blue-shifted relative to the same transition in **2** (exptl: 62 nm, calcd: 83 nm). This blue shift results from the substantial destabilization of the LUMO orbital and at the same time an important stabilization of the π_1 and π_2 orbitals in this complex. The destabilization of the LUMO orbital is a result of the large charge transfer (0.62 e^-) from the chlorine anion to complex **2** that occurs in the formation of complex **7**.

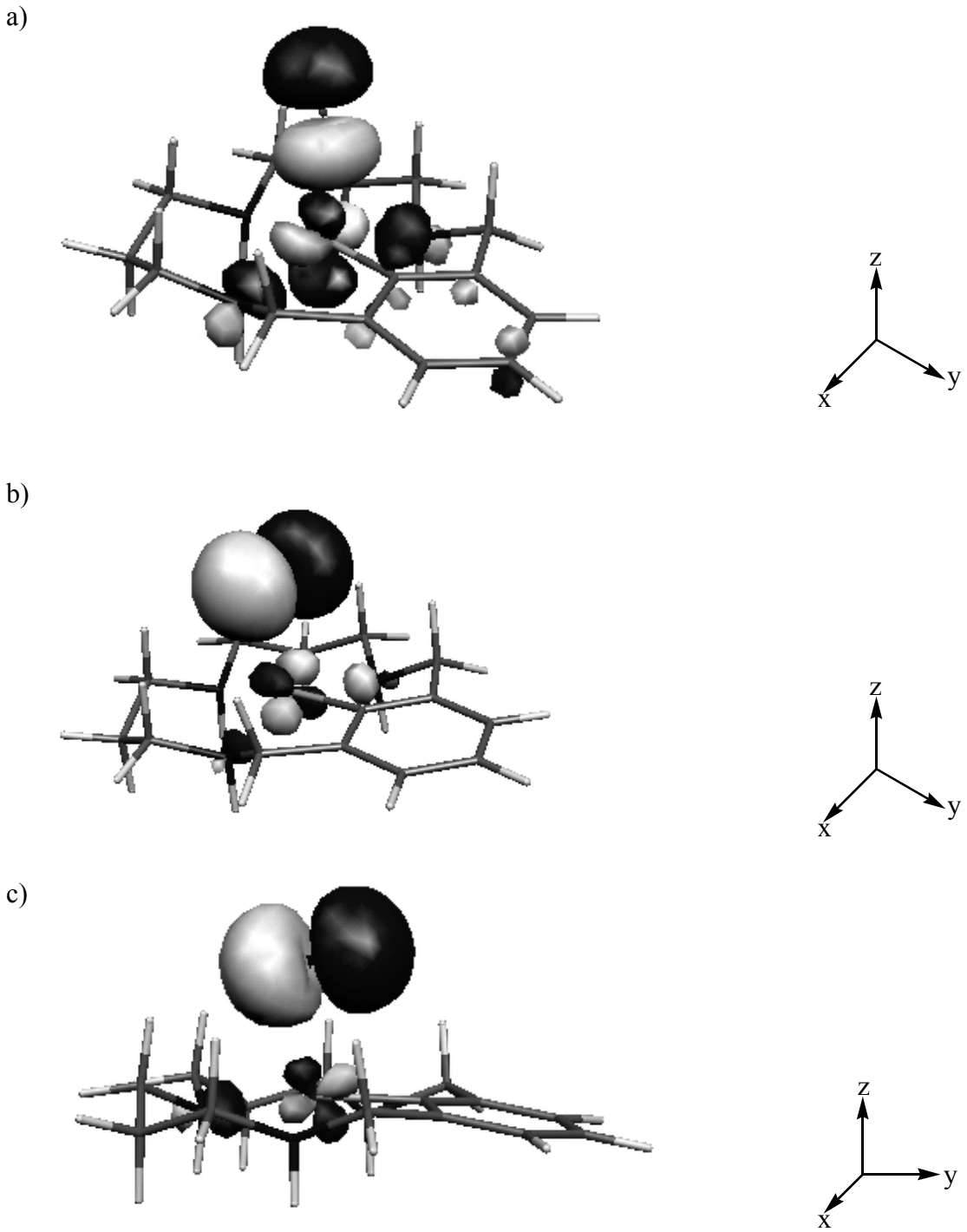

Figure IV-6. 3D representations of the starting orbitals most involved in the excitation at 522 nm in the experimental UV/Vis spectra of complex **7**: a) HOMO; b) HOMO-1; and c) HOMO-2 orbitals. Isosurface values are -0.05 and 0.05 a.u.

Finally, our calculations also correctly predict much higher intensities for the $\pi \rightarrow d_{x^2-y^2}$ bands of the Cu-Cl complex **7** than for complexes **2–6**.

Conclusions

A family of Cu complexes in the unusual oxidation state of +3 and containing triazamacrocyclic ligands has been described and their structural and spectroscopic properties thoroughly investigated by DFT calculations. This has allowed us to unravel the detailed electronic structure of these Cu^{III} complexes which in turn permitted us to rationalize their spectroscopic properties. As a result of this detailed work it has been possible to measure the electronic effects of *N*-methylation in a quantitative manner.

References

1. a) J. P. Collman, L. S. Hegedus, J. R. Norton, R. G. Finke in *Principles and Applications of Organotransition Metal Chemistry*, 2nd ed., University Science, Mill Valley, 1987, Chapter 7. b) A. E. Martell, D. T. Sawyer, *Oxygen Complexes and Oxygen Activation by Transition Metals*, Texas A & M University, 1987. c) M. D. Fryzuk, S. A. Johnson, *Coord. Chem. Rev.* **2000**, *200–202*, 379–409. d) M. Albrecht, G. van Koten, *Angew. Chem. Int. Ed.* **2001**, *113*, 3866–3898; *Angew. Chem. Int. Ed.* **2001**, *40*, 3750-3781. e) W. D. Jones, Acc. Chem. Res. **2003**, *36*, 140-146. f) M. E. van der Boom, D. Milstein, *Chem. Rev.* **2003**, *103*, 1759-1792.
2. a) J. A. Labinger, J. E. Bercaw, *Nature* **2002**, *417*, 507-514. b) J. M. Thomas, R. Raja, G. Sankar, R. G. Bell, *Acc. Chem. Res.* **2001**, *34*, 191-200. c) H. Chen, S. Schlecht, T. C. Semple, J. F. Hartwig, *Science* **2000**, *287*, 1995-1997. d) R. H. Crabtree, *Chem. Rev.* **1995**, *95*, 987-1007. e) A. E. Shilov, G. B. Shul'pin, *Chem. Rev.* **1997**, *97*, 2879-2932.
3. M. J. Gradassi, N. W. Green, *Fuel Process. Technol.* **1995**, *42*, 65-83.
4. M. Gandelman, L. J. W. Shimon, D. Milstein, *Chem. Eur. J.* **2003**, 94295-4300.
5. X. Ribas, D. A. Jackson, B. Donnadieu, J. Mahía, T. Parella, R. Xifra, B. Hedman, K. O. Hodgson, A. Llobet, T. D. P. Stack, *Angew. Chem.* **2001**, *113*, 3117-3120; *Angew. Chem. Int. Ed.* **2002**, *41*, 2991-2994.
6. L. L. Diaddario, W. R. Robinson, D. L. Margerum, *Inorg. Chem.* **1983**, *22*, 1021-1025.

7. I. H. Wasbotten, T. Wondimageng, A. Ghosh, *J. Am. Chem. Soc.* **2002**, *124*, 8104-8116.
8. a) H. Furuta, H. Maeda, A. Osuka, *J. Am. Chem. Soc*. **2000**, *122*, 803-807. b) M. Stepien, L. Latos-Grazynski, *Chem. Eur. J*. **2001**, *7*, 5113-5117.
9. a) M. A. Willert-Porada, D. J. Burton, N. C. Baenziger, *J. Chem. Soc., Chem. Commun.* **1989**, 1633-1634. b) D. Naumann, T. Roy, K. F. Tebbe, W. Crump, *Angew. Chem*. **1993**, *105*, 1555-1556; *Angew. Chem. Int. Ed.* **1993**, *32*, 1482-1483. c) R. Eujen, B. Hoge, D. J. Brauer, *J. Organomet. Chem*. **1996**, *519*, 7-20.
10. a) T. D. P. Stack, *Dalton Trans*. **2003**, 1881-1889. b) N. W. Aboelella, E. A. Lewis, A. M. Reynolds, W. W. Brennessel, C. J. Cramer, W. B. Tolman, *J. Am. Chem. Soc*. **2002**, *124*, 10660-10661.
11. S. K. Burke, Y. Xu, D. W. Margerum, *Inorg. Chem.* **2003**, *42*, 5807-5817.
12. D . H. R. Barton, N. C. Delanghe, H. Patin, Tetrahedron **1997**, *53*, 16017-16028.
13. A. Bencini, M. I. Burguete, E. Garcia-España, S. V. Luis, J. F. Miravet, C. Soriano, *J. Org. Chem*. **1993**, *58*, 4749-4753.
14. C. Bazzicalupi, A. Bencini, A. Bianchi, V. Fusi, E. Garcia-España, P. Paoletti, P. Paoli, B. Valtancoli, *Inorg. Chem*. **1993**, *32*, 4900-4908.
15. R. Xifra, X. Ribas, A. Llobet, A. Poater, M. Duran, M. Solà, T. D. P. Stack, J. Benet-Buchholz, B. Donnadieu, J. Mahía, T. Parella, *Chem. Eur. J.* **2005**, *11*, 5146-5156.
16. a) K. Hiraki, J. Tsutsumida, Y. Fuchita, *Chem. Lett.* 1986, 337-340. b) K. Hiraki, Y. Fuchita, Y. Ohta, J. Tsutsumida, K. I. Hardcastle, *J. Chem. Soc*., Dalton Trans. 1992, 833-836. c) A. Chellini, G. B. Giovenzana, R. Pagliarin, G. Palmisano, M. Sisti, *Helv. Chim. Acta* **2000**, *83*, 793-800.
17. a) G. Golub, H. Cohen, P. Paoletti, A. Bencini, L. Messori, I. Bertini, D. Meyerstein, *J. Am. Chem. Soc*. 1995, 117, 8353-8361. b) D. Meyerstein, *Coord. Chem. Rev*. **1999**, *185–186*, 141-147.
18. a) P. V. Bernhardt, *J. Am. Chem. Soc*. **1997**, *119*, 771-774; b) P. V. Bernhardt, *Inorg. Chem*. **2001**, *40*, 1086-1092. c) P. V. Bernhardt, P. Comba, T. W. Hambley, *Inorg. Chem*. **1993**, *32*, 2804-2809. d) M. M. Bernardo, M. J. Heeg, R. R. Schroeder, L. A. Ochrymowycz, D. B. Rorabacher, *Inorg. Chem*. **1992**, *31*, 191-198.

19. It is important to bear in mind the existence of a certain controversy on the purity of the compounds reported in the work published by Meyerstein (see ref. [17a]) and Bernhardt (see ref. [18a]).
20. E. J. Baerends, D. E. Ellis, P. Ros, *Chem. Phys*. **1973**, *2*, 41-51.
21. C. Fonseca Guerra, O. Visser, J. G. Snijders, G. te Velde, E. J. Baerends, *Methods and Techniques for Computational Chemistry*, STEF, Cagliari, 1995, p. 305.
22. G. te Velde, F. M. Bickelhaupt, E. J. Baerends, C. Fonseca Guerra, S. J. A. Van Gisbergen, J. G. Snijders, T. Ziegler, *J. Comput. Chem*. **2001**, *22*, 931-967.
23. W. Ravenek, *Algorithms and Applications on Vector and Parallel Computers*, Elsevier, Amsterdam, 1987.
24. G. te Velde, E. J. Baerends, *J. Comput. Phys*. **1992**, *99*, 84-98.
25. A. D. Becke, *Phys. Rev. A* **1988**, *38*, 3098-3100.
26. J . P. Perdew, *Phys. Rev. B* **1986**, *33*, 8822-8824.
27. a) E. K. U. Gross, J. F. Dobson, M. Petersilka, *Density Functional Theory* (Ed.: R. F. Nalewajski), Springer, Heidelberg, 1996. b) S. J. A. van Gisbergen, J. G. Snijders, E. J. Baerends, *Comput. Phys. Commun*. **1999**, 118, 119-138.
28. R. van Leeuwen, E. J. Baerends, *Phys. Rev. A* **1994**, *49*, 2421-2431.
29. ADF2002.03, E. J. Baerends, J. A. Autschbach, A. Bérces, C. Bo, P. M. Boerrigter, L. Cavallo, D. P. Chong, L. Deng, R. M. Dickson, D. E. Ellis, L. Fan, T. H. Fischer, C. Fonseca Guerra, S. J. A. van Gisbergen, J. A. Groeneveld, O. V. Gritsenko, M. Grüning, F. E. Harris, P. van den Hoek, H. Jacobsen, G. van Kessel, F. Kootstra, E. van -Lenthe, V. P. Osinga, S. Patchkovskii, P. H. T. Philipsen, D. Post, C. C. Pye, W. Ravenek, P. Ros, P. R. T. Schipper, G. Schreckenbach, J. G. Snijders, M. Solà, M. Swart, D. Swerhone, G. te Velde, P. Vernooijs, L. Versluis, O. Visser, E. van Wezenbeek, G. Wiesenekker, S. K. Wolff, T. K. Woo, T. Ziegler, Vrije Universiteit Amsterdam, Amsterdam, 2002.
30. J. G. Snijders, E. J. Baerends, P. Vernooijs, *At. Nucl. Data Tables* **1982**, *26*, 483-509.
31. P. Vernooijs, E. J. Baerends, *Slater Type Basis Functions for the Whole Periodic System. Internal Report*, Vrije Universiteit of Amsterdam, Amsterdam, 1981.
32. J. Krijn, E. J. Baerends, *Fit Functions in the HFS Method. Internal Report (in Dutch)*, Vrije Universiteit of Amsterdam, Amsterdam, 1984.
33. E. van Lenthe, E. J. Baerends, *J. Comput. Chem*. **2003**, *24*, 1142-1156.

34. A. Klamt, G. Schüürmann, *J. Chem. Soc., Perkin Trans*. *2* **1993**, 799-805.
35. C. C. Pye, T. Ziegler, *Theor. Chem. Acc*. **1999**, *101*, 396-408.
36. *Handbook of Chemistry and Physics*, 83rd ed. (Ed.: D. R. Lide), CRC Press, Boca Raton FL, 2002–2003.
37. Gaussian 98 (Revision A.11), M. J. Frisch, G. W. Trucks, H. B. Schlegel, G. E. Scuseria, M. A. Robb, J. R. Cheeseman, V. G. Zakrzewski, J. A. Montgomery, Jr., R. E. Stratmann, J. C. Burant, S. Dapprich, J. M. Millam, A. D. Daniels, K. N. Kudin, M. C. Strain, O. Farkas, J. Tomasi, V. Barone, M. Cossi, R. Cammi, B. Mennucci, C. Pomelli, C. Adamo, S. Clifford, J. Ochterski, G. A. Petersson, P. Y. Ayala, Q. Cui, K. Morokuma, P. Salvador, J. J. Dannenberg, D. K. Malick, A. D. Rabuck, K. Raghavachari, J. B. Foresman, J. Cioslowski, J. V. Ortiz, A. G. Baboul, B. B. Stefanov, G. Liu, A. Liashenko, P. Piskorz, I. Komaromi, R. Gomperts, R. L. Martin, D. J. Fox, T. Keith, M. A. Al-Laham, C. Y. Peng, A. Nanayakkara, M. Challacombe, P. M. W. Gill, B. Johnson, W. Chen, M. W. Wong, J. L. Andres, C. Gonzalez, M. Head-Gordon, E. S. Replogle, J. A. Pople, Gaussian, Inc., Pittsburgh PA, 2001.
38. MOLEKEL 4.0, P. Flükiger, H. P. Lüthi, S. Portmann, J. Weber, Swiss Center for Scientific Computing, Manno (Switzerland), 2000.
39. a) J. Hanss, H.-J. Krüger, *Angew. Chem*. **1996**, *108*, 2989-2991; *Angew. Chem. Int. Ed.* **1996**, *35*, 2827-2830. b) J. Hanss, A. Beckmann, H.-J. Krüger, *Eur. J. Inorg. Chem*. **1999**, 163-172.
40. E. I. Solomon, M. E. Hanson in *Inorganic Electronic Structure and Spectroscopy, Vol. 2* (Eds.: E. I Solomon, A. B. P. Lever), Wiley, 1999, Chapter 1.
41. a) L. Bernasconi, J. Blumberger, M. Sprik, R. Vuilleumier, *J. Chem. Phys*. **2004**, *121*, 11885-11899. b) X. Ribas, J. C. Dias, J. Morgado, K. Wurst, E. Molins, E. Ruiz, M. Almeida, J. Veciana, C. Rovira, *Chem. Eur. J*. **2004**, *10*, 1691-1704. c) Y. Yamaguchi, S. Yokoyama, S. Mashiko, *J. Chem. Phys*. **2002**, *116*, 6541-6548. d) Z.-L. Cai, K. Sendt, J. R. Reimers, *J. Chem. Phys*. **2002**, *117*, 5543-5549.
42. S. J. A. van Gisbergen, A. Rosa, G. Ricciardi, E. J. Baerends, *J. Chem. Phys*. **1999**, *111*, 2499-2506.

Chapter V: *C-C bond Activation in Square Planar Triazamacrocyclic Copper Complexes*

C-C bond Activation in Square Planar Triazamacrocyclic Copper Complexes

Abstract

The synthesis by the experimental group of Llobet et al. of square planar copper complexes, including a triazamacrocyclic ligand with a C-C bond interacting with the metal induced us to study the possible activation of this C-C bond. The available X-ray data indeed reveal that such a C-C bond activation in square planar complexes is possible, especially for a C-C bond where one of the carbon atoms belongs to an aromatic ring. DFT calculations have confirmed these C-C bond activations both for Cu and Ni.

Introduction

The saturated hydrocarbons that contain only C-H and C-C bonds are usually considered as inert products. The activation of these bonds through agostic interactions with transition metals is well-documented and it occurs mainly in solution and in soft conditions.[1] Whereas several agostic interactions of C-H bonds have been reported (for instance, the metallic complexes with agostic C-H bond activations are found as intermediates of oxidative C-H additions),[2] examples of agostic interactions with C-C are scarce.[3] The metallic complexes with agostic C-H bond activations are found as intermediates of oxidative C-H additions. The so-called "*pincer*" systems for the activation of C-H and C-C bonds by rhodium complexes occur for a series of species having similar electronic requirements.[4]

In a previous work, Llobet et al. had treated the same triaaza ligands,[5] nevertheless, the intermediates of oxidative C-H additions could not be located. In this system, the C-H bond of the aromatic carbon placed nearer to the metal was replaced by a C-C bond. The new Cu^{II} complex presents a violet colour, and was well characterized, especially by X-ray diffraction analysis (see Figure V-1). The results demonstrate the formation of a C-C agostic intermediate. The ligand used was characterized by X-ray diffraction analysis, but with the amines protonated (see Figure V-2), making difficult the geometrical comparison with the real ligand present in the C-C activated bond complex.

In the previous Chapter III we show how DFT can be used to determine C-H agostic intermediates with similar triazamacrocyclic ligands. From an experimental point of view, the higher strength of the C-C with respect to the C-H bond allowed to characterize better this C-C agostic intermediate. The activation reaction is not so fast, allowing a longer half-life time of the C-C agostic intermediate. In this chapter, we analyze theoretically the C-C bond activation in the complex of Figure V-1 using DFT methods.

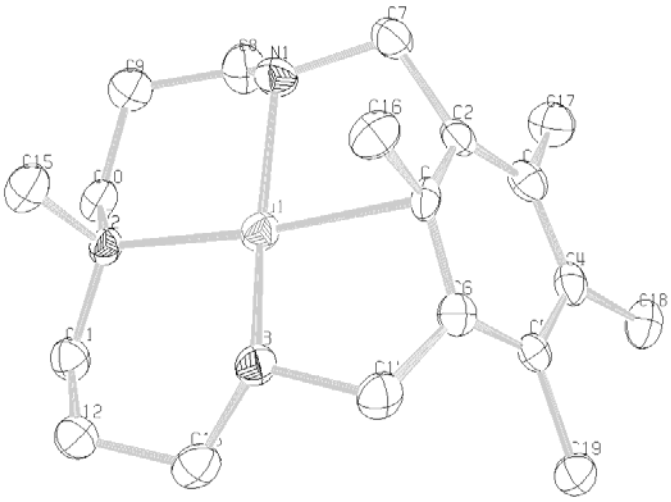

Figure V-1. Ortep view of the C-C bond activated complex (hydrogen atoms have been omitted for clarity).

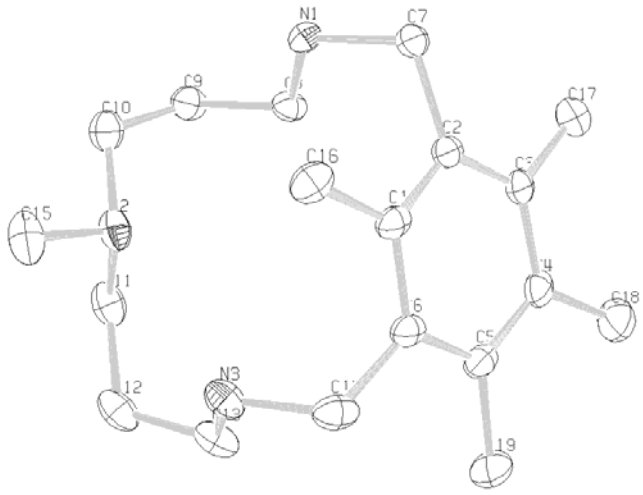

Figure V-2. Ortep view of the protonated ligand of the C-C bond activated complex (hydrogen atoms have been omitted for clarity).

Computational details

The geometry optimizations have been performed without symmetry constraints at the B3LYP level,[6] using the standard 6-31G** basis set[7] with the Gaussian03 package.[8] The nature of the extrema was checked by analytical frequency calculations. The energies discussed throughout the text are electronic energies without ZPE corrections.

The number of electrons of each metal and their oxidation state lead to complexes having even or odd number of electrons. The singlet or the duplet ground-state structure must not be necessarily the most stable states. For this reason, optimizations were done checking all the possible multiplicities, either neutral closed-shell singlet ground-state structures and also triplet, quintuplet, and septuplet or duplet, tetraplet, sextuplet, and octet open-shell ground-state structures.

Results

To confirm the C-C bond activation DFT calculations were performed for the ligands, with the amines biprotonated or only monoprotonated, and the metallic complex in which the monoprotonated ligand interacts either with M^{I} or M^{II} (M = Cu and Ni). The doubly protonated ligand has the N1 and N3 atoms connected to two protons, and the monoprotonated has only one proton at each nitrogen atom. The optimized copper structures and the ligands are depicted in Figure V-3, and the structural data in Table V-1. The labelling is given in Scheme V-1.

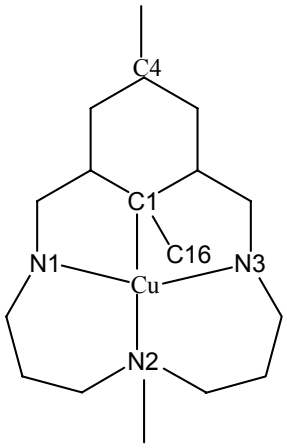

Scheme V-1. Labelling of the optimized structures (hydrogen atoms have been omitted for clarity).

$L_{monoprotonated}$

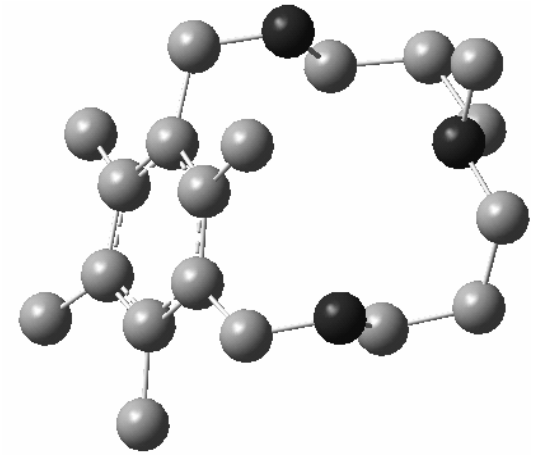

$L_{biprotonated}$

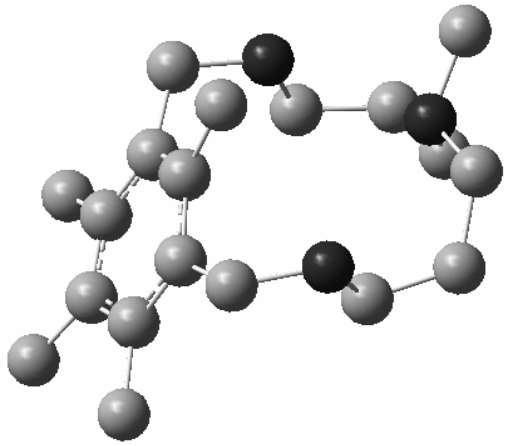

Cu^{I}

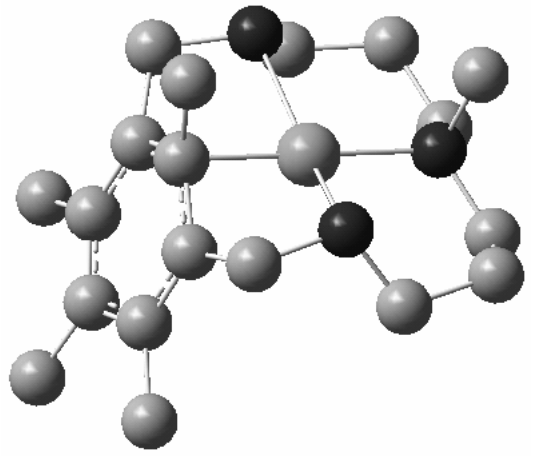

Cu^{II}

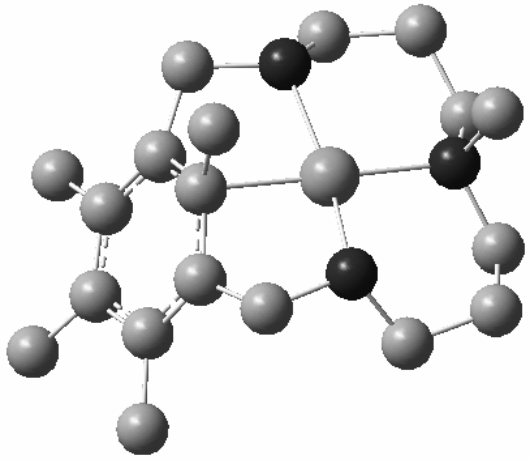

Ni^{I}

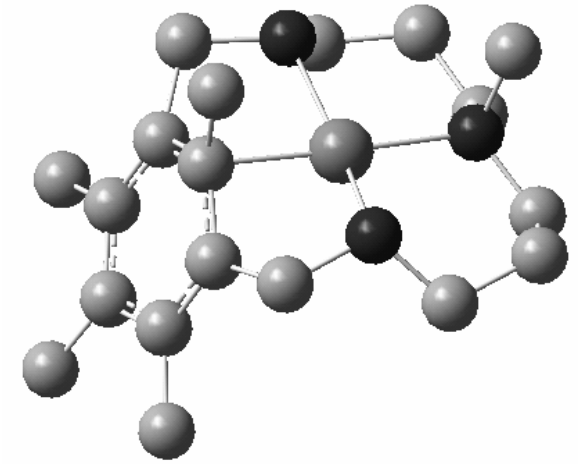

Ni^{II}

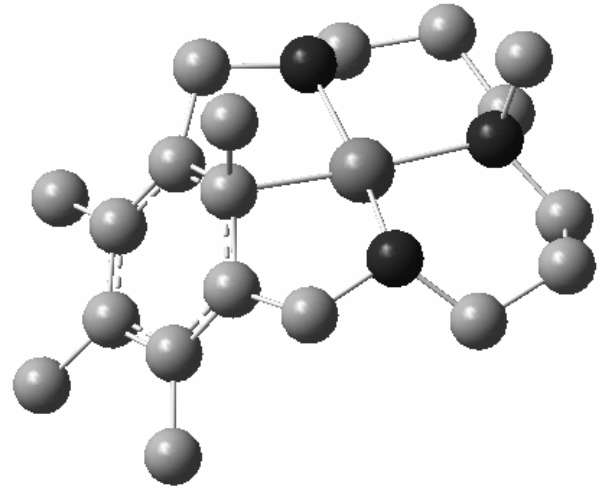

Figure V-3. Optimized copper structures and ligands.

	M-C1	M-C16	C1-C16	M-N1	M-N2	M-N3	M-C1-C16	C4-C1-C16
$L_{monoprotonated}$	-	-	1.513	-	-	-	-	174.1
$L_{biprotonated}$	-	-	1.523 (1.506)[a]	-	-	-	-	170.7 (176.3)[a]
Cu^{I}	1.996 (2.353)[a]	2.701 (2.762)[a]	1.534 (1.531)[a]	2.264 (2.155)[a]	2.043 (2.137)[a]	2.259 (2.128)[a]	99.0 (88.0)[a]	154.8 (159.2)[a]
Cu^{II}	2.113 (2.200)[a]	2.690 (2.736)[a]	1.545 (1.549)[a]	2.062 (2.035)[a]	2.049 (2.025)[a]	2.063 (2.041)[a]	93.4 (92.1)[a]	150.2 (160.8)[a]
Ni^{I}	2.084	2.693	1.534	2.077	2.073	2.102	95.0	154.7
Ni^{II}	2.021	2.708	1.552	1.984	2.010	1.988	97.7	141.9

[a] X-ray data

Table V-1. Main structural data of optimized complexes.

Table V-1 lists the values for all the optimized structures. The parameters for Cu^{II} structure and $L_{biprotonated}$ ligand can be compared because there are available X-ray data. To observe the activation of the C-C bond we must compare the Cu^{II} values with respect to the values for the $L_{monoprotonated}$ ligand. This bond is elongated by 0.032 Å.

To predict the possible C-C bond activation for Ni^{II} complexes, the copper atom was replaced by Ni^{II}, obtaining a stronger activation, as it happens experimentally and computationally for the C-H bond activation. These values are included in Table V-1.

The higher activation of the aromatic C-C bond by Cu^{II} and Ni^{II} with respect to Cu^{I} and Ni^{I} can be explained because of the electron density donation of the ligands towards the empty *d* orbitals of the metal, allowing a higher interaction with the C-C bond.

Conclusion

DFT calculations have confirmed the C-C bond activation either by Cu or Ni. The C-C-C bond belongs to an aromatic ring of a triazamacrocyclic ligand

References

1. a) R. G. Bergman, *Science* **1984**, *223*, 902-908. b) R. H. Crabtree, *Chem. Rev*. **1985**, *85*, 245-269. c) R. H. Cabtree, In *The Chemistry of Alkanes and Cycloalkanes*; S. Patai, Z. Rappoport, Eds. Wiley: New York, 1992.
2. a) C. Hall, R. N. Perutz, *Chem. Rev*. **1996**, *96*, 3125-3146. b) P. Dani, T. Karlen, R. A. Gossage, W. J. J. Smeets, A. L. Seck, G. van Roten, *J. Am. Chem. Soc*. **1997**, *119*, 11317-11318. c) H Urtel, C. Meier, F. Eisenträger, F. Rominger, J. P. Joschek, P. Hofmann, *Angew. Chem. Int. Ed*. **2001**, *40*, 781-784.
3. a) Y. –H. Kiang, G. B. Gardner, S. Lee, Z. –T. Xu, E. Lobkovsky, *J. Am. Chem. Soc*. **1999**, *121*, 8204-8215. b) S. Noro, S. Kitagawa, M. Kondo, K. Seki, Angew. *Chem. Int. Ed.* **2000**, *39*, 2081-2084. c) C. J. Kepert, T. J. Prior, M. J. Rosseinsky, *J. Am. Chem. Soc.* **2000**, *122*, 5158-5168. d) T. Kurahashi, A. de Meijere, *Angew. Chem. Int. Ed*. **2005**, *44*, 7881-7884.
4. B. Rybtchinski, S. Oevers, M. Montag, A. Vigalok, H. Rozenberg, J. M. L. Martin, D. Milstein, *J. Am. Chem. Soc*. **2001**, *123*, 9064-9077.
5. a) X. Ribas, D. A. Jackson, B. Donnadieu, J. Mahía, T. Parella, R. Xifra, B. Hedman, K. O. Hodgson, A. Llobet, T. D. P. Stack, *Angew. Chem. Int. Ed.* **2002**, *41*, 2991-2994. b) R. Xifra, X. Ribas, A. Llobet, A. Poater, M. Duran, M. Solà, T. D. P. Stack, J. Benet-Buchholz, B. Donnadieu, J. Mahía, T. Parella, *Chem. Eur. J.* **2005**, *11*, 5146-5156.
6. a) A. D. Becke, *J. Chem. Phys.* **1993**, *98*, 5648-5652. b) C. Lee, W. Yang, R. G. Parr, *Phys. Rev. B* **1988**, *37*, 785-789. c) P. J. Stevens, F. J. Devlin, C. F. Chablowski, M. J. Frisch, *J. Phys. Chem*. **1994**, *98*, 11623-11627. d) J. P. Perdew, Y. Wang, *Phys. Rev. B* **1992**, *45*, 13244-13249.
7. W. J. Hehre, R. Ditchfield, J. A. Pople, *J. Chem. Phys*. **1972**, *56*, 2257-2261.
8. Gaussian 03, M. J. Frisch, G. W. Trucks, H. B. Schlegel, G. E. Scuseria, M. A. Robb, J. R. Cheeseman, J. A. Montgomery, Jr., T. Vreven, K. N. Kudin, J. C. Burant, J. M. Millam, S. S. Iyengar, J. Tomasi, V. Barone, B. Mennucci, M. Cossi, G. Scalmani, N. Rega, G. A. Petersson, H. Nakatsuji, M. Hada, M. Ehara, K. Toyota, R. Fukuda, J. Hasegawa, M. Ishida, T. Nakajima, Y. Honda, O. Kitao, H. Nakai, M. Klene, X. Li, J. E. Knox, H. P. Hratchian, J. B. Cross, C. Adamo, J. Jaramillo, R. Gomperts, R. E. Stratmann, O. Yazyev, A. J. Austin, R. Cammi, C. Pomelli, J. W. Ochterski, P. Y. Ayala, K. Morokuma, G. A. Voth, P. Salvador, J. J.

Dannenberg, V. G. Zakrzewski, S. Dapprich, A. D. Daniels, M. C. Strain, Ö. Farkas, D. K. Malick, A. D. Rabuck, K. Raghavachari, J. B. Foresman, J. V. Ortiz, Q. Cui, A. G. Baboul, S. Clifford, J. Cioslowski, B. B. Stefanov, G. Liu, A. Liashenko, P. Piskorz, I. Komaromi, R. L. Martin, D. J. Fox, T. Keith, M. A. Al-Laham, C. Y. Peng, A. Nanayakkara, M. Challacombe, P. M. W. Gill, B. Johnson, W. Chen, M. W. Wong, C. Gonzalez, J. A. Pople, Gaussian, Inc., Pittsburgh PA, 2003.

Chapter VI: Cu(II) Hexaaza Macrocyclic Dinuclear Complexes Obtained from the Reaction of their Cu(I) Derivates and Molecular Oxygen. An Example of How Subtle Ligand Variations Can Lead to Major Differences in Reactivity

Cu(II) Hexaaza Macrocyclic Dinuclear Complexes Obtained from the Reaction of their Cu(I) Derivates and Molecular Oxygen. An Example of How Subtle Ligand Variations Can Lead to Major Differences in Reactivity

Abstract

DFT calculations have been carried out for a series of Cu(I) complexes bearing N-hexadentated macrocyclic dinucleating ligands, and their corresponding peroxo intermediates (**1c**-**8c**) generated by their interaction with molecular oxygen. For complexes **1c**-**7c** it has been found that the side-on peroxo is the favored structure with regard to the bis-oxo. For these complexes the singlet state has also been shown to be more stable than the triplet state. In the case of **8c** the most favored structure is the *trans*-peroxo due to *para* substitution and the steric encumbrance produced by the methylation of the aminic N atoms. The evolution of complexes **1c**-**8c** towards their oxidized species has also been rationalized by DFT calculations based mainly on their structure and electrophilicity.

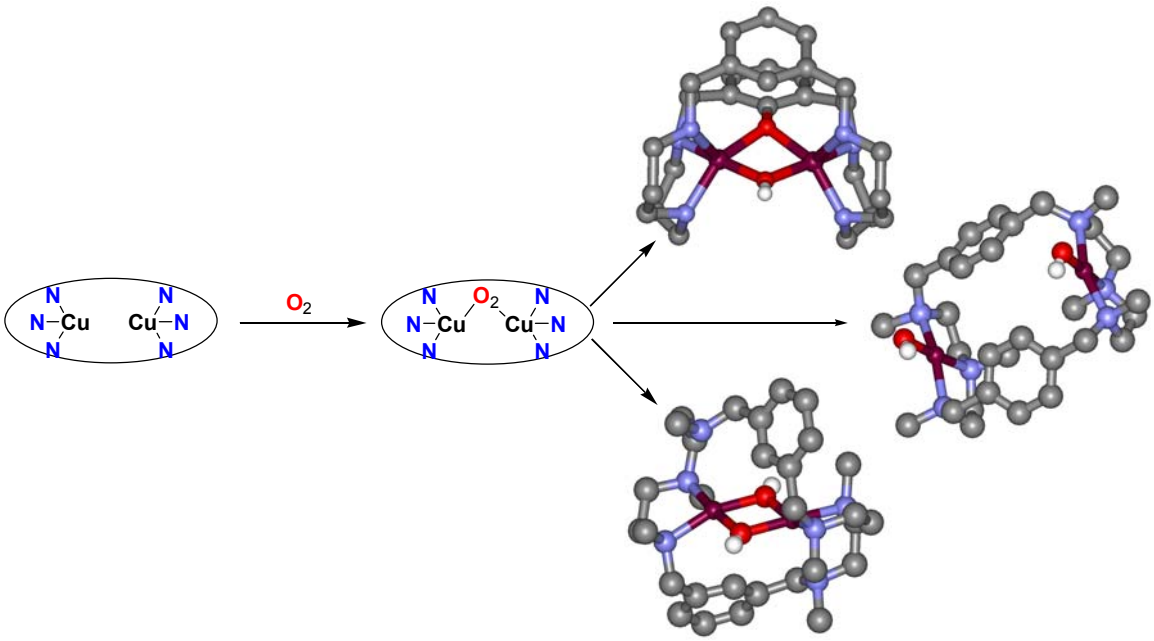

Introduction

Polynuclear complexes have been intensively investigated in fields that range from studies of their physical properties, with special attention to magnetic interactions,[1-3] to unique chemical reactivity patterns.[4-7] In both cases the relative disposition of the metal centers as well as the bridging ligands are key issues that determine their physical and chemical behavior.

A first approach towards the understanding and mastering of chemical metal cooperation involves the use of simple dinuclear metal complexes. A recent work by Bosnich et al. elegantly shows how a substrate bound to a single metal center can be reduced using the reducing power of multiple metals.[7]

Nature also benefits from metal cooperation in a number of metalloproteins whose functions range from small molecule activation (N_2, O_2, H_2)[8-12] to hydrolysis.[13] Of special interest are those iron and copper metalloproteins containing a dinuclear active site and whose function is the processing of molecular oxygen. In particular hemocyanine and tyrosinase possess a very similar active site consisting of a dinuclear copper complex but their biological role is completely different.[11,14-16]

Low molecular weight models have been of great help for understanding the spectroscopic and structural properties of the active site of these proteins.[17,18] From a reactivity viewpoint model compounds have shown how subtle variations in ligand design strongly affect their reactivity toward oxygen, and of the corresponding oxygenate complex towards its intramolecular oxidation or towards the oxidation of an external substrate.[19-25]

Modeling of the oxyform active center of dinuclear oxygen processing metalloproteins such as tyrosine or hemocyanin has been carried out by mononuclear complexes that upon reaction with dioxygen form the dinuclear complexes or with dinuclear complexes containing a dinucleating ligand.[129,26-32] The latter strategy allows prearranging two metal centers with a particular M-M distance.

It has been recently shown that the family of dinucleating hexaaza macrocyclic ligands containing tertiary amines depicted in Chart VI-1 allows exerting a certain control of the metal center local geometry as well as their relative disposition.[26-33] In this text it is reported how those subtle variations exemplified in this family of ligands strongly influence the reactivity of their corresponding dinuclear Cu(I) complexes towards molecular oxygen and of their oxidative evolution.

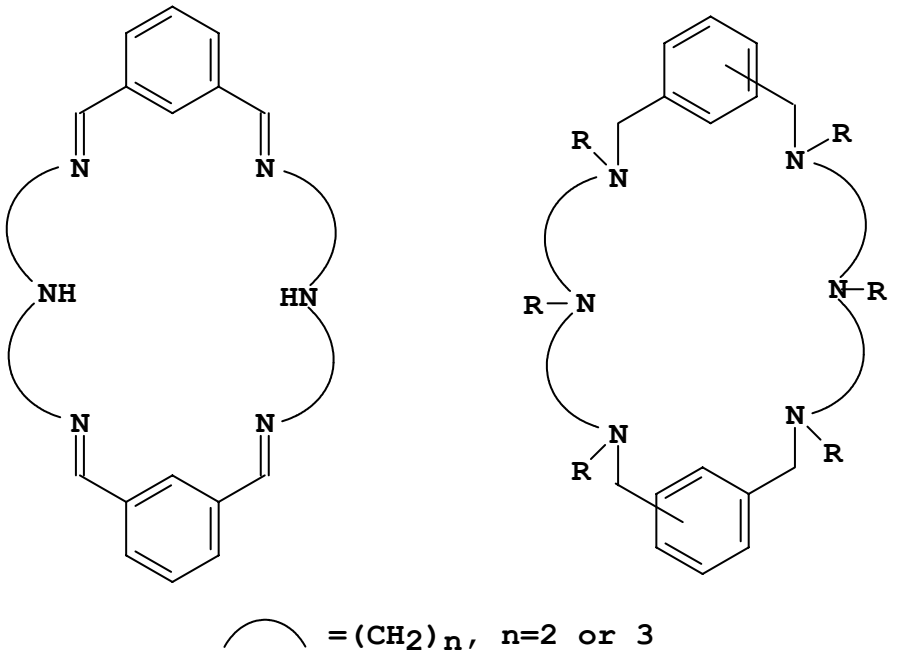

LIGANDS		COMPLEXES				LIGANDS		COMPLEXES
n=2,	*sb2m*	$[Cu_2(O_2)(sb2m)]^{2+}$, **1c**	m=*meta*	R=H	n=2,	*H2m*	$[Cu_2(O_2)(H2m)]^{2+}$, **3c**
n=3,	*sb3m*	$[Cu_2(O_2)(sb3m)]^{2+}$, **2c**			n=3,	*H3m*	$[Cu_2(O_2)(H3m)]^{2+}$, 4**c**
				R=Me	n=2,	*Me2m*	$[Cu_2(O_2)(Me2m)]^{2+}$, **5c**
					n=3,	*Me3m*	$[Cu_2(O_2)(Me3m)]^{2+}$, **6c**
			p=*para*	R=H	n=2,	*H2p*	$[Cu_2(O_2)(H2p)]^{2+}$, **7c**
				R=Me	n=2,	*Me2p*	$[Cu_2(O_2)(Me2p)]^{2+}$, **8c**

Chart VI-1. Drawing of the macrocyclic ligands together with the abbreviations used.

Synthesis and Structure of Oxidized Complexes. Hydroxo dinuclear Cu(II) complexes with the ligands H2m, Me2m, and Me2p were generated from the corresponding colorless Cu(I)-carbonyl complexes (which are easily generated from their respective Cu(I) complex by bubbling CO into the solution)[26] upon oxidation with molecular oxygen at room temperature. For the case of the Me2m ligand the final product obtained is a blue-green bis(μ-hydroxo) dinuclear Cu(II) complex, **5e**,

$$[Cu^{I}_2(Me2m)(CO)_2]^{2+} + O_2 + 2H^+ + 2e^- \xrightarrow{RT} [Cu^{II}_2(\mu\text{-}OH)_2(Me2m)]^{2+} + 2\,CO$$

5e

If the dinuclear Cu(I) complex containing the isomeric Me2p ligand is used then the product obtained is also a bis(hydroxo) dinuclear Cu(II), $[Cu^{II}(Me2p)(OH)_2]^{2+}$, **8e**, but now with the hydroxo ligands acting in a terminal manner.

Alternatively, hydroxocomplexes **5e** and **8**e could be directly prepared by reaction in acetonitrile of the macrocyclic ligand, $Cu(CF_3SO_3)_2$ and NaOH in molar ratio 1:2:2.

Finally, for the dinuclear Cu(I) complex containing the H3m ligand, its oxygenation leads to intramolecular oxygen insertion into the phenyl ring generating a dinuclear Cu(II) complex with both phenoxo and hydroxo bridges, $[Cu^{II}(H3m\text{-}O)(\mu\text{-}OH)]^{2+}$, **4e,** where H3m-O represents the deprotonated/oxygenated H3m ligand. This new heptadentate phenolic ligand was obtained as a free ligand, H3m-OH, by treating **4e** with aqueous ammonia and extracting it with dichloromethane.

The crystal structures of complexes **4e**, **5e**, and **8e**, have been determined by means of single crystal X-ray diffraction analysis. Figure VI-1 display the ORTEP diagrams obtained for the cationic molecular structures of complexes **4e**, **5e**, and **8e.**

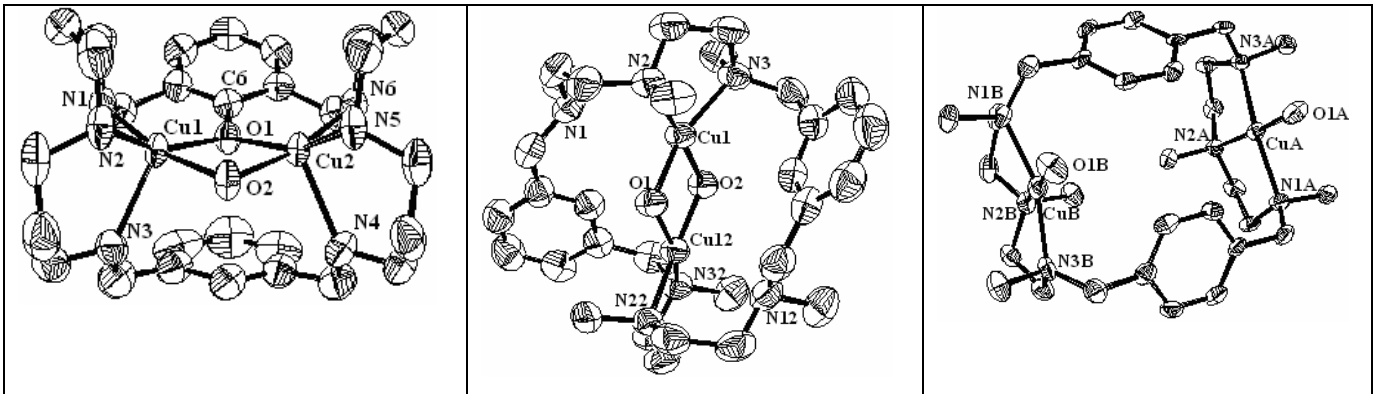

4e	**5e**	**8e**

Figure VI-1. X-ray crystal structure of **4e**, **5e**, and **8e**

The cationic part of **5e** consists of the macrocyclic ligand, binding two copper atoms and two OH molecules acting in a bridging fashion. The molecule has a C2 axis that runs through the oxygen atoms of the aromatic bridging ligands and converts half of the molecule into the other half. The copper atoms can be considered to have a distorted square pyramidal geometry with a τ factor of 0.23.[34] The two bridging aromatic ligands and the two nitrogen atoms from the macrocyclic ligand (N2 and N3) occupy the base of the pyramid forming a five member chelate ring whereas the apical position is occupied by N1. The distance Cu-N1 is 3.02 Å indicating that there is no formal covalent bond but only a slight contact, since the free nitrogen pair is pointing out towards the Cu metal center. The two pyramids are relatively arranged so that they share a basal edge, constituted by the two bridging oxygen atoms, with the apical vertexes pointing out in opposite directions. The Cu_2O_2 core is virtually planar and has a rhomboidal arrangement with one Cu-O distance slightly longer than the other (Cu-O1, 1.922(4) Å; Cu-O2 1.935(4) Å) and as consequence it generates two different CuOCu angles (CuO1Cu, 103.16^o; CuO2Cu 102.19^o). The O1CuO2 angle is 77.3^o and the Cu-N distances are slightly different (Cu-N2, 2.014(4); Cu-N3, 2.054(4)). The base of the pyramid is strongly distorted while N2 is relatively close to the plane defined by the Cu_2O_2 core the N3 is widely off as evidenced by the following torsion angles: O2CuO1N2 is 175.7^o, O1CuO2N3 is 161.0^o. Finally the methyl groups bonded to the tertiary amines of each square base point out in opposite directions.

The cationic part of **8e** consists of the macrocyclic ligand, binding two copper atoms and now with two OH ligands acting in a terminal fashion. The copper atoms can be considered to have a distorted square planar geometry with the benzylic amine atoms N1a and N3b slightly off the plane and with bond distances within the values measured for related compounds.[35-40] The Cua-O1a and Cub-O1b bond distances are 1.857(5) and 1.846(5) Å respectively which are within the values obtained in the literature for terminal Cu(II)-OH bonds.[41-46] The two planes defined by the square planar copper coordination are oriented in a nearly parallel manner (angle of 8.91^o) with a Cu···Cu distance of 6.60 Å. The copper coordination produces a ligand folding producing an angle between aromatic rings of 61.58^o. Finally the methyl groups bonded to the tertiary amines are oriented in an *anti* fashion with regard to other adjacent methyl groups.

The structure of **4e** consists of the macrocyclic ligand acting as a heptadentate ligand. Six amino groups are bonded to the two copper atoms together with a μ-phenoxo group also from the macrocyclic ligand and an external μ-hydroxo ligand. The molecule has a pseudo plane of symmetry that bisects the two aromatic rings and contains the two oxygen bridging atoms. The copper atoms can be considered to possess a slightly distorted trigonal bipyramid geometry with $\tau = 0.90$[34] and with the two bipyramids sharing an axial edge (O2 occupies an axial vertex whereas O1 an equatorial one in both trigonal bipyramids). N6 and N1 occupy the other axial positions while N2, N3 and N4, N5 occupy the two other equatorial positions respectively. Cu-N bond distances are comparable to those measured for **5e** and **8e**, and within the observed values for related complexes,[35-40] except for Cu1-N3 and Cu2-N4 that are 2.320(6) and 2.340(5) Å respectively which are a bit longer due to the constrain imposed by the macrocyclic ligand (these N atoms are the benzylic ones that belong to the non phenolic aromatic ring). The Cu_2O_2 core is non planar with a hinge type of distortion (the hinge angle is 139.4°) adopting a roof shape. The Cu_2O_2 metric parameters show two longer Cu-O bond distances for the equatorial oxygen atoms (Cu1-O1, 2.033(4) Å; Cu2-O1, 2.022(3) Å) and two shorter Cu-O distances for the axial oxygen atoms (Cu1-O2, 1.918(4) Å; Cu2-O2, 1.920(4) Å). Finally the CuOCu core angles (Cu1O1Cu2, 97.40°; Cu1O2Cu2, 105.02°) are significantly different while the OCuO are relatively similar (O1Cu1O2, 77.12°; O1Cu2O2, 77.33°). The hydrogen and the carbon atoms bonded to the oxygen bridging atoms are also bended in opposite directions with regard to the core planes intersection formed by those two oxygen atoms (O1O2H1a, 164.74°; O2O1C6 165.11°). Upon coordination to the Cu metal center the N atoms of the macrocyclic ligand form six member rings. While the ones formed by the benzylic N of the phenoxy moiety have typical chair conformation, the ones formed by the phenolic moiety are clearly distorted manifesting again the constraint imposed by the rigidity of the macrocyclic ligand. Finally, the molecule has two PF_6^- counterions associated with the cationic moiety of the complex, which are disordered and an acetonitrile molecule of crystallization per molecule of **4e**.

The influence of the macrocyclic ligand on the magnetic properties displayed by the dinuclear copper complexes 4e, 5e, and 8e. In complex **8e**, the geometry of the Me2p ligand does not allow the formation of either phenoxo or hydroxy bridging

ligand; as a consequence there is no efficient magnetic coupling between metal centers and therefore it behaves as a typical uncoupled Curie magnet. The square-pyramidal geometry around each copper metal center is manifested in the ESR parameters obtained from the spectrum where $g_z = 2.20 > g_x = 2.05 \sim g_y = 2.05$ and the magnetic equivalence of each center is in agreement with the presence of only one signal in the ESR.

From a magnetic viewpoint, complexes **4e** and **5e** belong to the broad and largely studied family of dinuclear Cu(II) complexes doubly bridged by O-ligands. Several magnetostructural correlations and theoretical studies have been carried out[47-60] for this type of compounds where it is shown that the major factor influencing the exchange is the angle of the Cu-O-Cu bridge (α). However, there are other significant factors that may contribute to increase the ferromagnetic (F) character and that can effectively reduce any AF term generally associated with the bridges (for instance for angles $\alpha \sim 97.6^{\circ}$ the AF contribution could be compensated by the F contribution leading to a coupling constant $J \sim 0$). Distortions of the geometry generally produce a decrease in |J| values; the most usual distortions are in the coordination geometry the Cu(II) metal, from square-planar to tetrahedral for tetracoordianted complexes or from square pyramidal to trigonal bipyramid for pentacoordinated ones.[61] Other usual distortions include the deviation of the Cu_2O_2 planar core towards a roof-shape.[56-59,62,63] Deviation of the Cu-OH or Cu-OR bonds from the Cu_2O_2 plane produce an increase of the F term.[57,58] Finally, another factor affecting the magnetic properties of this kind of compounds is the basicity of the terminal ligands: the more basic the ligands the more AF coupling is observed. Even though these trends can be generally applied to Cu_2O_2 cores, there are significant differences for bis-μ-hydroxo and bis-μ-phenoxo complexes;[64] empirical magnetostructural correlations yield $-J = 74.53\alpha - 7270$ cm^{-1} for hydoxo complexes and $-J = 31.95\alpha - 2462$ cm^{-1} for phenoxo complexes with lower $|J|$ values generally for the former. Thus, for phenoxo compounds, the effect of the CuOCu angle seems to be weaker compared to the hydroxo analogues. Moreover the accidental orthogonality ($J = 0$ cm^{-1}) for phenoxo complexes is obtained for $\alpha \sim 77^{\circ}$ whereas for hydroxo complexes is at $\alpha \sim 97^{\circ}$. Furthermore the replacement of OH by OR generates a reduction of the electronic density in the bridging O atom,[62,63] due to the presence of a more electronegative C atom, that is significantly enhanced for the case of the phenoxo

ligands. Compounds **5e** and **4e** show an important AF coupling, larger for the mixed hydroxo-phenoxo bridging ligands, **4e**, than for the bis–hydroxo, **5e**. The CuOCu average angle is quite similar for both compounds (101.2º for **4e** and 102.7º for **5e**) and as it could be expected the substitution of one hydroxo bridging ligand by a phenoxo bridging ligand should considerably increases the AF interaction.

For compound **5e**, with two hydroxo bridging ligands, the expected *J* value from the empirical correlation reported by Hatfield et al.[47] would be -384 cm^{-1}, which is much larger than the found value, -286 cm^{-1}. The decrease in the predicted AF character in our case could be due to the structural distortion of the Cu_2O_2 core imposed by the Me2m ligand as well as the deviation of the Cu-N bond angles from the planar Cu_2O_2 core (Cu-N3, 19.0^o). Another factor that can also produce a certain decrease of the AF character is the basicity of the amines.[57,58]

To the best of our knowledge complex **4e** is the third trigonal byramidal phenoxo-hydroxo complex with its magnetic properties reported in the literature. In complex **4e** however, there are other geometrical factors, imposed by the nature of the macrocyclic ligand, that have been described to lower the AF character, which are the following: a) the hinged nature of the Cu_2O_2 core, b) the bending of the OH and OC bonds with regard to the O -- O axis, c) the trigonal bipyramidalic geometry of the Cu centers.

Viewing that experimentally only intermediates **1c** and **4c** can produce intramolecular C-H bond activation, the knowledge of why only these two compounds suffer this kind of process has been achieved by DFT calculations. Moreover no intermediate has been characterized experimentally.

Computational Details.

The reported calculations were carried out by using the Amsterdam density functional (ADF) package developed by Baerends *et al*.[65-67] and vectorized by Ravenek.[68] The numerical integration scheme employed was that of te Velde *et al*.[69] An uncontracted triple-ς basis set was used for describing the 3s, 3p, 3d, 4s, and 4p orbitals of copper. For carbon (2s,2p), nitrogen (2s,2p), oxygen (2s,2p), and hydrogen (1s), double-ς basis sets were employed. All these basis sets were augmented by an extra polarization

function.[70,71] Electrons in lower shells were treated within the frozen core approximation.[65-67] A set of auxiliary s, p, d, f, and g functions, centered in all nuclei, was introduced in order to fit the molecular density and Coulomb potential accurately in each SCF cycle.[72] Closed and open-shell systems were studied within the restricted and unrestricted formalism, respectively. Geometries were fully optimized within the local density approximation (LDA), which includes the X_α exchange (α=2/3),[73] together with the electron gas correlation functional in the Vosko-Wilk-Nusair (VWN) parametrization.[74] The analytical gradients implemented by Versluis and Ziegler[75] were employed to perform geometry optimizations. Energies were evaluated at the LDA molecular geometries using a generalized gradient approximation (GGA) that includes a GGA exchange correction of Becke[76] and the GGA correlation correction of Perdew.[77] This method is labeled throughout this work as BP86//VWN. Several authors have shown that this scheme of calculation provides excellent results for geometries and bond dissociation energies.[78-83] Furthermore, in a previous work it has been shown that the Density Functional Theory (DFT) approaches, such as used in the present work, efficiently incorporate the dynamic correlation needed to describe accurately the complexes studied in this work.[84] Finally, ligand conformation energy plays an important role in fine-tuning the energetic balance so that models which ignore these effects cannot describe the energetics correctly.[85] For this reason, calculations presented in this work correspond to the full real molecules, without any futher modelling. The 2000.02 release of the ADF package was used for all calculations.[86]

In open-shell systems, the energy of the highest α or β semioccupied molecular orbital (SOMO) was taken as the energy of the HOMO orbital.

To analyze the origin of the binding energy between the ground state of molecular O_2 and the binuclear macrocycle to form the μ–η^2:η^2-peroxo compounds, the binding energy has been decomposed into deformation energy and interaction energy. The deformation energy (ΔE_{def}) is the energy needed to modify the geometry of the ground state free fragments to attain the geometry that they have in the intermediate. It can be divided into the deformation energy of the dinuclear complex ($\Delta E_{def\ complex}$) and the deformation energy of the oxygen molecule ($\Delta E_{def\ O_2}$). On the other hand, the

interaction energy (ΔE_{int}) is the energy released when the two free deformed fragments in their ground states are brought to the position that they have in the intermediate.

Results

Starting structures for geometry optimization. Due to the presence of the methyl groups or hydrogen atoms coordinated to nitrogen atoms that can adopt up and down positions and because of the boat and chair conformations of the methylene chain connecting nitrogen atoms in the ligand, a large number of possible conformers for each isomer are possible. Since available computational resources do not allow for a complete study of all possible conformers, a single conformer for each isomer was studied.

For complex **5c**, bearing the Me2m ligand, the geometry optimization was started from the available X-ray coordinates of **5e** (which is the corresponding evolved complex; see next section and Figure VI-1C) with the minimum modifications required to achieve a rhombic structure for the Cu_2O_2 core (see chart VI-2). From **5c**, the starting point for the geometry optimization for complex **3c**, containing the H2m ligand, was obtained by replacing the methyl groups bonded to the N atoms by H atoms. Further, by removing one hydrogen atom from the CH_2 benzylic groups and the hydrogen atom of all benzylic amines, an initial geometry was obtained for the optimization of the complex **1c** containing the bs2m Schiff base ligand. Overall the Schiff base bs2m ligand has eight hydrogen atoms less than the corresponding secondary amine H2m ligand.

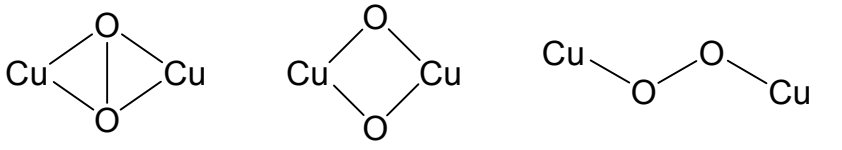

μ-η²:η²-peroxo bis–μ–oxo μ-trans-1,2-peroxo

Chart VI-2. Cu_2O_2 core structures discussed in the present work.

For the complex **8c** containing the Me2p ligand, the geometry optimization was started from the available X-ray coordinates of complex **8e**. The two hydrogen atoms coordinated to the oxygen atoms were eliminated, and disposed them separated by 1.3 Å

in the center of the molecule forming a rhombic structure with the copper atoms, which were separated by 3.6 Å. From the starting geometry of **8e**, an initial structure for **7c** was also obtained, containing the corresponding secondary amine H2p ligand, by replacing the methyl groups bonded to the N atoms by H atoms.

Finally, for the complex **4c**, containing H3m, the calculations were started from the geometry corresponding to the X-ray structure of **4e**, by removing the hydrogen atom coordinated to the oxygen atom and attaching it to the carbon atom of the phenyl group nearest to the other oxygen atom, and at the same time by reducing the distance between both oxygen atoms to 1.3 Å. The distance between both copper atoms was augmented by 0.5 Å with respect to the one of the X-ray data. The insertion of a methyl group in each nitrogen yielded complex **6c** that bears the Me3m ligand. From **4c** an initial geometry was obtained for **2c** that contains the bs3m ligand in a similar manner as in the previous Schiff base case.

To validate the method of calculation, a geometry optimization for **5e** was made, excluding the molecules of solvent. The results show good agreement between the experimental and the theoretical data. The standard deviation for the bond distances is 0.067 Å and for the angles is 1.5º; thus providing confidence on the reliability of the chosen method to reproduce geometries of the intermediate complexes.

Singlet vs. Triplet State. The optimized structures obtained for the peroxo complexes **1c**-**8c** are depicted in Figure VI-2. All attempts to optimize the bis-oxo $Cu^{III}_2(\mu\text{-}O)_2$ complexes starting from complexes **3c** and **4c** by increasing the O-O distance have reverted to the peroxo species. Thus, it is concluded that in the present complexes the peroxo form is favored with respect to the isomeric bis-μ-oxo (see Chart VI-2 for a drawing of core structures). It is worth mentioning that stabilization of the bis-μ-oxo isomer can be achieved by the addition of anionic ligands.[32]

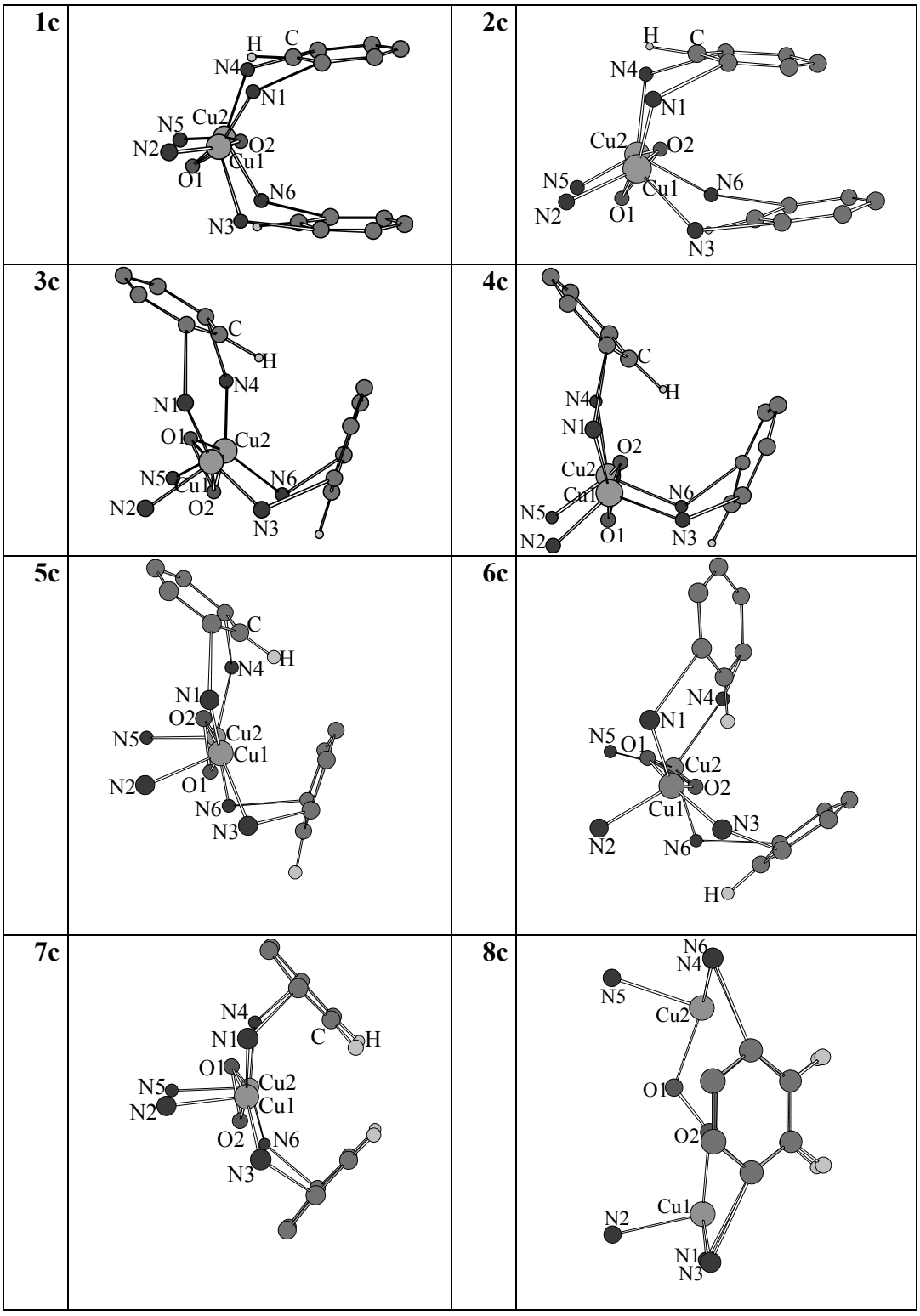

Figure VI-2. Calculated structures for μ–η^2:η^2–peroxo side-on complexes **1c**-**7c** and *trans*-μ–1,2-peroxo **8c**. The methylenic units linking amines or phenyl units as well as most of the hydrogen atoms have been omitted for clarity.

Optimizations were carried out for the charged +2 closed-shell singlet ground state structures. However, since it has been found for similar species that the triplet state is quite close in energy to the singlet[87,88] (or even for some particular cases it can be more stable[89]) it has been checked in all compounds the relative stability of both states by optimizing the triplet state. In all cases, except for **8c**, the optimized triplet state structure presents a higher energy than the optimized singlet state geometry. The difference between these two states ranges from 0.7 kcal·mol^{-1} for the peroxo species **3c** and **4c,** containing respectively the H2m and H3m ligands, to 11.2 kcal·mol^{-1} for **5c** that contains the Me2m ligand. Spin-unrestricted broken-symmetry calculations for the singlet diradical state have also been performed. Starting from unsymmetric wavefunctions, it has been observed in all cases reconvergence to the restricted solution. This means, that, at least at the present BP86//VWN level of theory, the restricted singlet is the ground state. It has been shown by different authors[90-94] that delocalized states are overstabilized with present pure density functionals as a result of a bad cancellation of the self-interaction included in the Coulomb energy by the exchange-correlation functional. As a result, closed-shell singlet states are favored with respect to open-shell diradical singlet states by DFT. Additionally and related to this effect, it has been shown that the spin density and the DFT orbitals for Cu(II) binuclear complexes are excessively delocalized on the ligands.[95,96] This over delocalization is partially corrected when using hybrid functionals, especially those that incorporate a large percentage of exact Hartree-Fock exchange. For this reason, the relative stability of the restricted closed-shell and diradical singlets has been further analyzed with the hybrid functionals B3LYP[97-99] and BHLYP[100] at the VWN optimized geometries using Gaussian03[101] and the 6-31G** basis set.[102] Convergence to the open-shell diradical singlet state for our systems were not achieved and in all cases spin-unrestricted broken-symmetry calculations reverted to the restricted solution. Thus, the present results clearly favor the closed-shell singlet state as the ground state of complexes **1c**-**7c**. However, because of the multideterminantal character of the diradical singlet state, sophisticated post-Hartree-Fock calculations are still needed to reach a conclusive answer about the relative stability of closed-shell and the open-shell diradical singlet states in the peroxo complexes.[103,104] Although high level post-Hartree-Fock methods provide better and more reliable results, they remain prohibitive for molecules containing more than 6 or 7 heavy atoms. In this sense, DFT methods offer a better

compromise between the accuracy of results and the computation time required for large systems such as those analyzed in this work.

It is worth noting that **8c**, which contains the Me2p ligand, represents a special case as far as the ground state multiplicity is concerned. For this compound a *trans*-μ-1,2-peroxo structure with the copper atoms separated by 4.7 Å was optimized (see Figure VI-2). This is probably due to the presence of the methyl groups and the para substitution in the aromatic linkers of Me2p, which force the copper atoms to be particularly distant. In its optimized ground state geometry the rhombic structure of the $Cu^{II}_2(\mu\text{-}\eta^2\text{:}\eta^2\text{-}O_2)$ core is lost, resulting in a complex that is more stable in the triplet rather than in the singlet state. Consequently, this complex has the same multiplicity as the free dioxygen molecule and to a large extent retains its molecular character. This is corroborated by the short distance between oxygen (1.301 Å) atoms, which is significantly shorter than in **7c**. It should be mentioned here that experimentally characterized *trans*-μ-1,2-peroxo dicopper(II) complexes described so far in the literature are diamagnetic (singlet state).[105] However, one has to take into account that in **8c** the much longer Cu•••Cu distance and the much shorter O-O bond length (4.677 and 1.301 Å, respectively) as compared to the structurally characterized *trans*-μ-1,2-peroxo dicopper(II) complex described by Karlin et al. (4.359 and 1.432 Å, respectively)[105] favor the triplet state.

Structure of Calculated Peroxo Complexes. For complexes **1c**-**7c** a distorted side-on core is obtained where the Cu centers adopt a highly distorted square pyramidal geometry as depicted in Figure VI-2. Selected metric parameters for structures **1c**-**8c** are displayed in Table VI-1.

Intermediate	d(Cu1-Cu2)	d(O1-O2)	d(Cu1-O1)	d(Cu1-O2)	d(Cu2-O1)	d(Cu2-O2)	d(Cu1-N)	d(Cu2-N)	d(O-C) (d(O-H))[a]	dihedral angle Cu1O1O2Cu2
1c	3.595	1.414	2.034	1.867	2.050	1.864	1.972 2.016 2.097 1.956	2.997 1.994 2.085 1.980	2.553 (2.202)	167.8
2c	3.568	1.429	2.008	1.886	1.998	1.879	1.996 2.118 2.012	1.967 2.158 2.015	2.346 (2.364)	164.7
3c	3.455	1.435	1.910	1.942	1.912	1.931	2.219 2.024 2.017	2.025 2.015 2.004	2.643 (2.626)	150.9
4c	3.605	1.429	1.984	1.910	2.009	1.897	1.994 2.174 2.092	2.009 2.168 2.015	2.522 (2.041)	169.2
5c	3.582	1.418	1.951	1.969	1.922	1.953	2.290 2.103 2.169	2.177 2.182 2.191	2.452 (2.468)	161.3
6c	3.738	1.412	1.946	2.033	2.115	1.904	2.013 2.119 2.047	2.098 2.021 2.043	2.578 (2.800)	175.1
7c	3.574	1.420	1.951	1.946	1.943	1.956	2.219 2.036 2.074	2.215 2.034 2.112	2.959 (3.519)	159.9
8c	4.677	1.301	2.938	1.878	1.922	2.840	2.099 2.123	2.166 2.107	2.724 (2.800)	162.5

[a] these values correspond to the distance between the O1 or O2 oxygen atoms, from the Cu_2O_2 core, to the closest aromatic C-H bond of the macrocyclic ligand.

Table VI-1. Selected Metric Parameters for Calculated Structures **1c**-**8c**.

The complexes with two methylenic units bonding the N atoms all adopt a square pyramidal geometry where the central aminic nitrogen atoms occupy the apical positions except for **1c** that are occupied by the benzylic N atoms of one of the phenylic rings. The latter geometry is also obtained for the complexes **2c** and **4c** that contain three methylenic units between their N atoms. Complex **6c** possesses a completely different arrangement: one of the Cu centers has a benzylic N atom in the apical position whereas in the other one is occupied by the central aminic N atom. Complex **8c,** as mentioned in the previous sections, adopts a *trans*−μ−1,2-peroxo structure where the Cu centers display a distorted tetrahedral geometry.

For complexes **1c** and **2c,** containing the Schiff base ligands sb2m and sb3m, their corresponding peroxo complexes adopt a relatively similar global conformation where the aromatic rings are situated nearly parallel, presenting values of 4.4º and 13.4º, respectively, for the dihedral angle between the planes defined by the two aromatic

rings in each complex. This suggests that the geometry imposed by the imine bonds are a key factor influencing the overall geometry of the complex whereas the number of methylenic groups linking the amine-imine N atoms exerts only a fine tuning effect to the relative disposition of the Cu_2O_2 core with regard to the aromatic rings. In this situation the closest O···C_{ar} and O···H_{ar} distances (O atom from the peroxo core and H and C atoms from the closest C-H group of the aromatic rings) for complexes **1c** and **2c** are relatively similar (see Table VI-1).

For complexes **3c** and **4c**, with the *meta* substituted secondary amines, the general geometry is very similar between them but completely different from the previous cases. Now the aromatic rings are situated nearly perpendicular to one another and the number of methylenic units bonding secondary amines strongly influences the relative orientation of the Cu_2O_2 core. The O···C_{ar} and O···H_{ar} distances are particularly short for complex **4c**. It is important to mention here that in the **1c**-**4c** cases just described, the six N atoms bonding the two metal centers adopt an eclipsed disposition thus resembling a trigonal pyramidal geometry.

For the complexes bearing tertiary amines **5c** and **6c** their relative geometry is completely different. The geometry adopted by the **5c** complex is similar to its secondary amine analogue **3c** and thus the potential geometric distortion exerted by the encumbrance of the six methyl groups of the tertiary amines is nearly negligible. In sharp contrast the structure of complex **6c** is strongly influenced by the steric effects produced by the six methyl groups. Complex **6c**, adopts a completely different geometry with the six coordinated N atoms situated in an alternate manner and thus displaying an octahedral type of geometry. In these two cases the O···C_{ar} and O···H_{ar} distances are relatively large.

Complex **7c** substituted in the *para* position presents a global conformation relatively similar to its *meta* isomer **3c**. However, the *para* substitution of the aromatic ring generates a relative disposition of their aromatic C-H bonds that end up much farther away from the oxygen core atoms than in the previous cases. In complex **8c**, the steric effects produced by the methyl groups inhibit the formation of the side-on peroxo core leading to the less sterically demanding *trans*–μ–1,2-end-on coordination.

Bonding Energies and Electrophilic Character of the Cu_2O_2 Core. The energies released when molecular O_2 binds the binuclear macrocycles to form the $\mu-\eta^2:\eta^2$–peroxo intermediates are given in Table VI-2. It is found that the energy released when the O_2 molecule interacts with the binuclear macrocyclic complexes to yield the corresponding $\mu-\eta^2:\eta^2$–peroxo complexes decreases in the order **1c** > **2c** > **3c** > **4c** > **6c** > **5c** > **7c**. In general, when the basic character of the macrocyclic ligand increases, the absolute value of the binding energy is reduced. Thus, there is a slight diminution when going from the complex **1c** bearing the sb2m Schiff base ligand to the **3c** bearing the H2m. There is also a decrease when going from the secondary amine ligands to the corresponding tertiary amine ones (compare **3c** with **5c** and **4c** with **6c**). Finally, a reduction was also found when a methylenic group is added to the aliphatic chain of the macrocycle (compare complexes bearing ligands sb2m with sb3m and H2m with H3m) with the exception of **5c** and **6c** containing tertiary amine ligands. These results can be understood from the correlation diagram that describes the orbitals most involved in the bonding between the copper dimer and the oxygen molecule depicted in Figure VI-3. As can be seen, the key interaction is the one involving the $(d_{xy})_1+(d_{xy})_2$ orbital of the copper dimer with the π_x^* orbital of the O_2 molecule. One can expect that the smaller the energy difference between these two orbitals, the larger the interaction energy. When the basicity of the macrocycle increases, the energy of the $(d_{xy})_1+(d_{xy})_2$ orbital of the copper dimer raises and consequently the energy released in the interaction between the copper dimer and the O_2 molecule decreases. Factors such as the Cu···Cu distance may also have an important effect. Indeed, an increase of the Cu···Cu distance should stabilize the $(d_{xy})_1+(d_{xy})_2$ orbital of the copper dimer and produce an increase of the absolute value of the binding energy. However, this effect is partially compensated by a reduction of the overlap between the $(d_{xy})_1+(d_{xy})_2$ orbital of the copper dimer and the π_x^* orbital of the O_2 molecule. The low (in absolute value) binding of **7c** containing the H2p ligand as compared to **3c** containing H2m is related to the larger deformation energy needed to modify the geometry of the $[Cu_2(H2p)]^{2+}$ complex without O_2 to reach the structure that this fragment has in the $\mu-\eta^2:\eta^2$–peroxo form (*vide infra*).

Intermediate	$\Delta E_{def\ O2}$	$\Delta E_{def\ Complex}$	ΔE_{def}	ΔE_{int}	BE
1c	16.5	12.8	29.3	-48.8	-19.7
2c	18.9	12.7	31.7	-51.3	-19.6
3c	19.8	28.2	48.0	-67.1	-19.1
4c	18.9	28.6	47.6	-61.5	-13.9
5c	17.3	22.4	39.7	-48.5	-8.8
6c	16.3	24.3	40.6	-52.2	-11.6
7c	17.5	42.9	60.4	-62.9	-2.5

Table VI-2. Decomposition energy analysis (kcal·mol^{-1}) of the Cu–μ–η^2:η^2–O_2 intermediates.

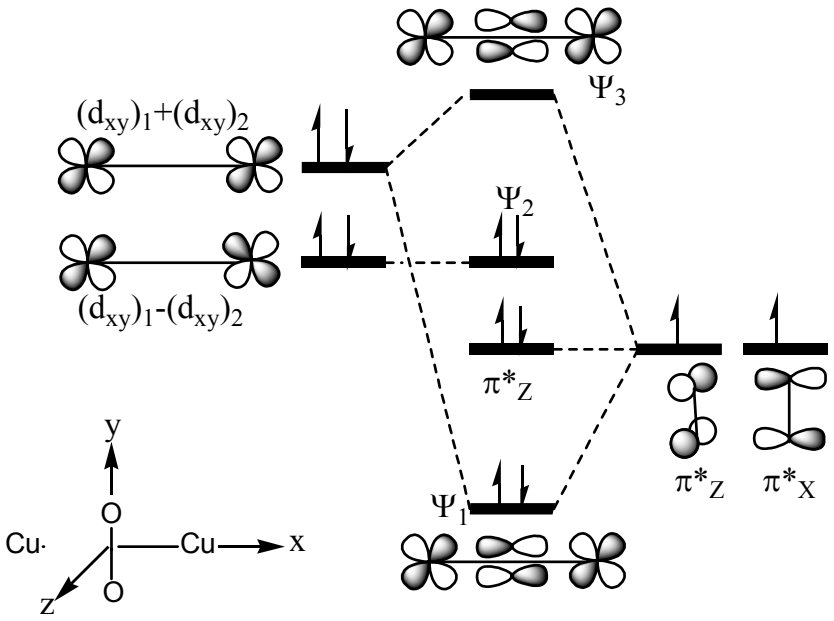

Figure VI-3. Correlation diagram which describes the main orbitals involved in the bonding between the copper dimer and the oxygen molecule in the ground state.

To gain a deeper insight into the nature of bond energy of the O_2 molecule to the copper complex, the binding energy has been split up of all μ–η^2:η^2–peroxo intermediates into the deformation energy term (ΔE_{def}) and the interaction energy term

(ΔE_{int}). The results are gathered in Table VI-2. The ΔE_{def} total values range from 29.3 kcal·mol^{-1} (**1c**) to 60.4 kcal·mol^{-1} (**7c**). The deformation energy of the oxygen molecule is almost constant for all complexes (from 16.3 to 19.8 kcal·mol^{-1}), being somewhat larger for **3c** (19.8 kcal·mol^{-1}) which is the complex with the most activated O-O bond and largest O-O bond length. The large ΔE_{def} of complex **7c** is due to the fact that this molecule possesses the initial unreacted dinuclear complex suffering the most important changes, when going from the geometry that it has without the O_2 molecule to the final structure. This is reflected in the shortening of the distance between the copper atoms from 6.172 Å to 3.574 Å. Interestingly, the complexes bearing more rigid ligands undergo less deformation in their original structures and thus lead to lower deformation energies, and, in general, more negative binding energies. The ΔE_{int} terms take values from –48.5 kcal·mol^{-1} (**5c**) to -67.1 kcal·mol^{-1} (**3c**).

Table VI-3 contains the values of the highest occupied molecular orbital (ε_H) and the lowest unoccupied molecular orbital (ε_L) energies, and the μ, η, and ω. It is important to notice that the value of electrophilicity is especially low for complex **2c** as compared to that of complex **1c**. The main difference comes from the hardness value, i.e., the HOMO-LUMO gap which is larger for the **2c** case.

Intermediate	ε HOMO	ε LUMO	μ	η	ω	q Cu1+Cu2	q O1+O2
1c	-247.5	-229.5	238.5	9.0	3163.1	1.647	-0.993
2c	-250.1	-226.1	238.1	12.0	2364.5	1.546	-1.017
3c	-243.4	-225.3	234.4	9.1	3033.7	1.607	-1.018
4c	-242.6	-222.2	232.4	10.2	2648.4	1.456	-1.016
5c	-243.2	-226.5	234.8	8.3	3309.5	1.772	-0.963
6c	-241.1	-223.9	232.5	8.6	3138.5	1.745	-0.956
7c	-243.8	-227.2	235.5	8.3	3330.9	1.547	-0.962
8c	-241.3	-225.2	233.3	8.0	3387.5	1.329	-0.579

Table VI-3. HOMO and LUMO energies, chemical potencial, hardness, and electrophilicity for the different complexes analyzed together with Mulliken charges of copper and oxygen atoms. Units for energies, chemical potential, hardness, and electrophilicity are kcal·mol^{-1} and electrons for charges.

Finally, the Mulliken charge distribution has also been collected for the Cu_2O_2 core in Table VI-3. Qualitatively, the results are the same using the Hirshfeld or Voronoi charges. The charges on the C atom and the H atom of the C-H bonds with high probability of being attacked are very similar. The main differences are observed in the charges of the oxygen and the copper atoms for the different complexes. Interestingly, complexes showing larger electrophilicities are also those that have less negative oxygen atoms.

Theoretical prediction of the influence of the macrocyclic ligand on the formation of the Cu_2O_2 cores and their evolution. Previous work by Karlin, Tolman, Stack, and others has shown that using different didentate or tridentate alkylamine ligands and depending on solvent and/or counterions a given Cu(I) complex interacts with molecular oxygen to form both the μ-η^2:η^2-peroxo or the bis-μ-oxo dicopper cores, and that this species might be in rapid equilibrium.[19,106,107] In a recent work, Karlin and coworkers,[108] using simple bis-propylenetriamine type of ligands, have illustrated once more the delicate equilibrium between the isomeric forms of the Cu_2O_2 core structures, by simply changing a coordinating secondary amine for a tertiary amine. In the present case the corresponding peroxo or bis-μ-oxo dicopper intermediates bearing the macrocyclic ligands displayed in Chart VI-1 were not detected, even at low temperatures. However, theoretical calculations have revealed that in our case the side-on peroxo isomer is likely to be the only possible isomer since, as indicated previously, no optimized structures for the bis-μ-oxo isomers of **3c** and **4c** were located.

The formation of the side-on complexes **1c-7c** from the corresponding dinuclear Cu(I) complexes and molecular oxygen is accompanied with an enlargement of the O-O distance with regard to the free O_2 molecule in its ground state (1.218 Å at the VWN/DZP level of theory) together with a shortening of the Cu···Cu distance with regard to the initial unreacted copper complexes. Interestingly, there is a strong correlation between the O-O bond length and the Cu···Cu distance ($d_{O\text{-}O} = -0.1114\ d_{Cu\text{-}Cu} + 1.8222$, $R^2 = 0.9794$) for complexes **1c-7c** with the μ-η^2:η^2-peroxo structure (Table VI-1).

For the series of complexes studied containing the macrocyclic ligands displayed in Chart VI-1, the aromatic substitution in the *meta* or *para* position strongly influences the nature of the intermediate formed. Complex **7c** containing the H2p ligand, has the lowest bonding energy (Table VI-2) mainly due to the unfavorable contribution of a large ΔE_{def} factor. This is a consequence of relative disposition of the Cu centers imposed by the *para* substitution together with the increase by two units of the internal macrocyclic member ring (the largest cycle that contains the metal centers in the initial copper complex) with regard to its *meta* isomer. In complex **8c** that contains the Me2p ligand, a further increase of the steric crowding with regard to **7c**, is provided by the methyl groups of the tertiary amines. This provokes the instability of the *side-on* peroxo intermediate and now only the *end-on* peroxo isomer is obtained. Thus providing an example of how steric factors allow controlling the nature of the reactive intermediate.

For the *meta side-on* complexes **1c**-**6c**, the number of methylenic units as well as the nature of the linking N atoms strongly influences the electronic properties of the generated side-on peroxo core as can be seen in Tables VI-2 and -3. The ligands also influence the spatial arrangement of the Cu_2O_2 core with regard to the phenyl ring which is also a key factor that will determine the performance of these complexes especially from an intramolecular viewpoint.

There is experimental evidence that only the complexes bearing the bs2m and H3m ligands possess reactive species that leads towards the intramolecular hydroxylation of an aromatic C-H bond.[109,110] A reaction that has been shown to take place via a nucleophilic attack of the aromatic ring towards the electrophilic *side-on* peroxo Cu_2O_2 core.

It is worth noting that complexes **1c** and **4c** are among the ones having the smallest distances between the C-H_{ar} group and one of the two oxygen atoms. Thus, as a possible rule of reactivity, based only on geometric factors, is that a system will be reactive if the sum of the two shortest O···H and O···C distances in the μ–η^2:η^2–peroxo form is smaller than 4.75 Å. This requirement is only accomplished by **1c**, **2c**, and **4c** and except for **2c** fully coincides with the experimental evidence.

However, complex **2c** as shown in Table VI-3 has by far the lowest electrophilicity (mainly due to a large hardness value; the HOMO-LUMO gap) that prevents its Cu_2O_2 core to undergo an aromatic nucleophilic attack. Thus it constitutes an example of how the electronic factors transmitted by the macrocyclic ligand predominate over the geometric factors also established by these ligands. In addition, the orientation of the aromatic rings in **4c** suggests hydroxylation occurs through a σ* mechanism according to the classification by Decker *et al*.[111]

Complex **6c** possesses an unique structure in this family of complexes in the sense that each copper center has two different type of apical coordinating amines and that the relative disposition of the six N atoms is octahedral instead of trigonal prismatic. Thus this comparison of the structure of **4c** with **6c** reveals how the steric effect of the six methyl groups can strongly influence the geometry of the complex.

Conclusions

Theoretical analyses based on DFT calculations have shown that the intermediates obtained from the oxidation of the macrocyclic Cu(I) complexes and molecular oxygen, generates a variety of side on Cu_2O_2 motifs. Those Cu_2O_2 intermediates evolve towards the formation of radically different Cu(II) complexes which depending on the macrocyclic ligand are obtained as a μ-bis-hydroxo complex **4e**, a μ-hydroxo-μ-phenoxo complex **5e** with intramolecular oxidation of the initial ligand, and a terminal bis-hydroxo complex **8e** in the *para* substitution of the phenyl rings. The latter being the first example of its kind described in the literature.

DFT calculations for dinuclear copper complexes (**1c**-**8c**), containing the macrocyclic ligands shown in Chart VI-1 and the Cu_2O_2 core, have proven to be an excellent tool to envisage reactive intermediates that can not be detected and characterized experimentally. Furthermore, these DFT calculations have also provided an excellent guide to unravel their potential reactivity based on the relative disposition of the aromatic rings and the Cu_2O_2 core and also based on their electronic properties mainly their electrophilicity. This has allowed rationalizing the nature of the evolved oxidized species based on the nature of the macrocyclic ligand that could not have been understood otherwise.

References

1. R. L. Carlin, *Magnetochemistry*; Springer-Verlag: Berlin, Heidelberg, 1986.
2. O. Kahn, In *Modular Chemistry*; Michl, J., Ed.; Kluwer Academic: Dordrecht, 1997; Vol. 499, pp 287-302.
3. A. Cornia, D. Gatteschi, R. Sessoli, *Coord. Chem. Rev.* **2001**, *219*, 573-604.
4. M. Suzuki, H. Furutachi, H. Okawa, *Coord. Chem. Rev.* **2000**, *200-202*, 105-129.
5. A. L. Gavrilova, B. Bosnich, B. *Chem. Rev.* **2004**, *104*, 349-384.
6. A. L. Gavrilova, C. J. Qin, R. D. Sommer, A. L. Rheingold, B. Bosnich, *J. Am Chem. Soc.* **2002**, *124*, 1714-1722.
7. C. Incarvito, A. L. Rheingold, A. L. Gavrilova, C. J. Qin, C., B. Bosnich, *Inorg. Chem.* **2001**, *40*, 4101-4108.
8. J. B. Howard, D. C. Rees, *Chem. Rev.* **1996**, *7*, 2965-2982.
9. B. J. Wallar, J. D. Lipscomb, *Chem. Rev.* **1996**, *96*, 2625-2658.
10. R. K. Thauer, A. R. Klein, G. C. Hartmann, *Chem. Rev.* **1996**, *7*, 3031-3042.
11. E. I. Solomon, P. Chen, M. Metz, S.-K. Lee, A. E. Palmer, *Angew. Chem. Int. Ed.* **2001**, *40*, 4570-4590.
12. C. Belle, J.-L. Pierre, *Eur. J. Inorg. Chem.* **2003**, 4137-4146.
13. D. E. Wilcox, *Chem. Rev.* **1996**, *96*, 2435-2458.
14. N. Kitajima, Y. Moro-oka, *Chem. Rev.* **1994**, *94*, 737-757.
15. K. A. Magnus, H. Ton-That, J. E. Carpenter, *Chem. Rev.* **1994**, *94*, 727-735.
16. E. I. Solomon, U. M. Sundaram, T. E. Machonkin, *Chem. Rev.* **1996**, *96*, 2563-2605.
17. M.-A. Kopf, K. D. Karlin, In *Biomimetic Oxidations Catalyzed by Transition Metal Complexes*; Meunier, B., Ed.; Imperial College Press: London, 2000, pp 309-362.
18. S. Schindler, *Eur. J. Inorg. Chem.* **2000**, 2311-2326.
19. W. B. Tolman, *Acc. Chem. Res.* **1997**, *30*, 227-237.
20. L. Que Jr., W. B. Tolman, *Angew. Chem. Int. Ed.* **2002**, *41*, 1114-1137.
21. V. Mahadevan, J. L. DuBois, B. Hedman, K. O. Hodgson, T. D. P. Stack, *J. Am. Chem. Soc.* **1999**, *121*, 5583-5584.

22. V. Mahadevan, M. J. Henson, E. I. Solomon, T. D. P. Stack, *J. Am. Chem. Soc.* **2000**, *122*, 10249-10250.
23. M. Taki, S. Itoh, S. Fukuzumi, *J. Am. Chem. Soc.* **2001**, *123*, 6203-6204.
24. M. Taki, S. Teramae, S. Nagatomo, Y. Tachi, T. Kitagawa, S. Itoh, S. Fukuzumi, *J. Am. Chem. Soc.* **2002**, *124*, 6367-6377.
25. C. X. Zhang, H.-C. Liang, E.-I. Kim, J. Shearer, M. E. Helton, E. Kim, S. Kaderli, C. D. Incarvito, A. D. Zuberbühler, A. L. Rheingold, K. D. Karlin, K. D. *J. Am. Chem. Soc.* **2003**, *125*, 634-635.
26. M. Costas, R. Xifra, A. Llobet, M. Solà, J. Robles, T. Parella, H. Stoeckli-Evans, M. Neuburger, M. *Inorg. Chem.* **2003**, *42*, 4456-4468.
27. S. Mahapatra, V. G. Young Jr., S. Kaderli, A. D. Zuberbühler, W. B. Tolman, *Angew. Chem. Int. Ed. Engl.* **1997**, *36*, 130-133.
28. S. Mahapatra, S. Kaderli, A. Llobet, Y.-M. Neuhold, T. Palanche, J. A. Halfen, V. G. Young Jr., T. A. Kaden, L. Que Jr; A. D. Zuberbühler, W. B. Tolman, *Inorg. Chem.* **1997**, *36*, 6343-6356.
29. J. E. Bol, W. L. Driessen, R. Y. N. Ho, B. Maase, L. Que Jr., L. Reedijk, *Angew. Chem. Int. Ed.* **1997**, *36*, 998-1000.
30. R. Menif, A. E. Martell, *J. Chem. Soc., Chem. Commun.* **1989**, *20*, 1521-1523.
31. R. Menif, A. E. Martell, P. J. Squattrito, C. Clearfield, *Inorg. Chem.* **1990**, *29*, 4723-4729.
32. L. M. Mirica, M. Vance, D. J. Ruud, B. Hedman, K. O. Hodgson, E. I. Solomon, T. D. P. Stack, *Science* **2005**, *308*, 1890-1892.
33. M. Costas, C. Anda, A. Llobet, T. Parella, H. Stoeckli Evans, E. Pinilla, *Eur. J. Inorg. Chem.* **2004**, *4*, 857-865.
34. A. W. Addison, T. N. Rao, J. Reedijk, J. Van Rijn, G. C. Verschoor, *J. Chem. Soc., Dalton Trans.* **1984**, *7*, 1349-1346.
35. M. Becker, F. W. Heinemann, F. Knoch, W. Donaubauer, G. Liehr, S. Schindler, G. Golub, H. Cohen, D. Meyerstein, *Eur. J. Inorg. Chem.* **2000**, *4*, 719-726.
36. M. Becker, F. W. Heinemann, S. Schindler, *Chem. Eur. J.* **1999**, *5*, 3124-3129.
37. S. J. Barlow, S. J. Hill, J. E. Hocking, P. Hubberstey, W.-S. Li, *J. Chem. Soc., Dalton Trans.* **1997**, *24*, 4701-4704.
38. C. Bazzicalupi, A. Bencini, A. Bianchi, V. Fusi, C. Giorgi, P. Paoletti, A. Stefani, B. Valtancoli, B. *Inorg. Chem.* **1995**, *34*, 552-559.
39. M. J. Scott, S. C. Lee, R. H. Holm, *Inorg. Chem.* **1994**, *33*, 4651-4662.

40. N. A. Bailey, D. E. Fenton, M. S. L. Gonzalez, *Inorg. Chim. Acta* **1984**, *88*, 125-134.
41. H. Arii, Y. Funahashi, K. Jitsukawa, H. Masuda, *J. Chem. Soc., Dalton Trans.* **2003**, *11*, 2115-2116.
42. M. Harata, K. Jitsukawa, H. Masuda, H. Einaga, *Bull. Chem. Soc. Jpn.* **1998**, *71*, 637-645.
43. W. E. Allen, T. N. Sorrell, *Inorg. Chem.* **1997**, *36*, 1732-1734.
44. L. M. Berreau, S. Mahapatra, J. A. Halfen, V. G. Young Jr., W. B. Tolman, *Inorg. Chem.* **1996**, *35*, 6339-6342.
45. G. Fusch, E. C. Fusch, A. Erxleben, J. Hüttermann, H.-J. Scholl, B. Lippert, *Inorg. Chim. Acta* **1996**, *252*, 167-178.
46. S. C. Lee, R. H. Holm, *J. Am. Chem. Soc.* **1993**, *115*, 11789-11798.
47. V. H. Crawford, H. W. Richardson, J. R. Wasson, D. J. Hodgson, W. E. Hatfield, *Inorg. Chem.* **1976**, *15*, 2107-2110.
48. D. J. Hodgson, *Prog. Inorg. Chem.* **1975**, *19*, 173-241.
49. M. Handa, N. Koga, S. Kida, *Bull. Chem. Soc. Jpn.* **1988**, *61*, 3853-3857.
50. K. Nieminen, *Ann. Acad. Sci. Fennicae A II* **1982**, *197*, 1-60.
51. L. Walz, H. Paulus, W. Haase, *J. Chem. Soc., Dalton Trans.* **1985**, 913-920.
52. A. Bencini, D. Gatteschi, *Inorg. Chim Acta* **1978**, *31*, 11-18.
53. P. J. Hay, J. C. Thibault, R. Hoffman, *J. Am. Chem. Soc* **1975**, *97*, 4884-4889.
54. O. Kahn, *Inorg. Chim. Acta* **1982**, *62*, 3-14.
55. J. Coomarmond, P. Plumere, J. M. Lehn, Y. Agnus, P. Louis, R. Weiss, O. Kahn, I. Morgenstern-Badarau, *J. Am. Chem. Soc.* **1982**, *104*, 6330-6340.
56. H. Astheimer, W. Haase, *J. Chem. Phys.* **1986**, *85*, 1427-1432.
57. E. Ruiz, P. Alemany, S. Alvarez, J. Cano, *J. Am. Chem. Soc.* **1997**, *119*, 1297-1303.
58. E. Ruiz, P. Alemany, S. Alvarez, J. Cano, *Inorg. Chem.* **1997**, *36*, 3683-3688.
59. C. Blanchet-Boiteux, J. M. Muesca, *J. Phys. Chem. A.* **2000**, *104*, 2091-2097.
60. L. Merz, W. Haase, *J. Chem. Soc., Dalton Trans.* **1980**, 875-879.
61. R. J. Butcher, E. Sinn, *Inorg. Chem.* **1976**, *15*, 1604-1608 and references therein.
62. M. F. Charlot, Y. Journaux, O. Kahn, A. Bencini, D. Gatteschi, C. Zanchini, *Inorg. Chem.* **1986**, *25*, 1060-1063.
63. M. F. Charlot, S. Jeannin, Y. Jeannin, O. Kahn, J. Lucrece-Abaul, J. Martin-Frere, *Inorg. Chem.* **1980**, *19*, 1410-1411.

64. L. K. Thompson, S. K. Mandal, S. S. Tandon, J. N. Bridson, M. K. Park, *Inorg. Chem.* **1996**, *35*, 3117-3125.
65. E. J. Baerends, D. E. Ellis, P. Ros, *Chem. Phys.* **1973**, *2*, 41-51.
66. C. Fonseca Guerra, O. Visser, J. G. Snijders, G. te Velde, E. J. Baerends, *Methods and Techniques for Computational Chemistry*; STEF: Cagliari, 1995.
67. G. te Velde, F. M. Bickelhaupt, E. J. Baerends, C. Fonseca Guerra, S. J. A. van Gisbergen, J. G. Snijders, T. Ziegler, *J. Comput. Chem.* **2001**, *22*, 931-967.
68. W. Ravenek, H. J. J. te Riele, in *Algorithms and Applications on Vector and Parallel Computers*. T. J. Dekker, H. A. van de Vorst, Eds.; Elsevier: Amsterdam, 1987.
69. G. te Velde, E. J. Baerends, *J. Comp. Phys.* **1992**, *99*, 84-98.
70. J. G. Snijders, E. J. Baerends, P. Vernooijs, *At. Nucl. Data Tables* **1982**, *26*, 483-509.
71. P. Vernooijs, J. G. Snijders, E. J. Baerends, *Slater Type Basis Functions for the Whole Periodic System. Internal Report*; Vrije Universiteit of Amsterdam: The Netherlands, 1981.
72. J. Krijn, E. J. Baerends, *Fit Functions in the HFS Method. Internal Report (in Dutch)*; Vrije Universiteit of Amsterdam: The Netherlands, 1984.
73. J. C. Slater, *Quantum Theory of Molecules and Solids*; McGraw-Hill: New York, 1974; Vol. 4.
74. S. H. Vosko, L. Wilk, M. Nusair, *Can. J. Phys* **1980**, *58*, 1200-1211.
75. L. Versluis, T. Ziegler, *J. Chem. Phys.* **1988**, *28*, 322-328.
76. A. D. Becke, *Phys. Rev. A* **1988**, *38*, 3098-3100.
77. J. P. Perdew, *Phys. Rev. B* **1986**, *33*, 8822-8824.
78. J. Li, G. Schreckenbach, T. Ziegler, *J. Phys. Chem.* **1994**, *98*, 4838-4841.
79. F. M. Bickelhaupt, M. Solà, P. v. R. Schleyer, *J. Comput. Chem.* **1995**, *16*, 465-477.
80. M. Torrent, L. Deng, M. Duran, M. Solà, T. Ziegler, *Organometallics* **1997**, *16*, 13-19.
81. M. Torrent, L. Deng, M. Duran, M. Solà, T. Ziegler, *Can. J. Chem.* **1999**, *77*, 1476-1491.
82. L. Deng, T. Ziegler, *Organometallics* **1997**, *16*, 716-724.
83. L. Deng, T. Ziegler, *Organometallics* **1996**, *15*, 3011-3021.

84. F. Bernardi, A. Bottoni, R. Casadio, P. Fariselli, A. Rigo, *Int. J. Quantum Chem.* **1996**, *58*, 109-116.
85. A. Bérces, *Inorg. Chem.* **1997**, *36*, 4831-4837.
86. ADF2000. E. J. Baerends, J. A. Autschbach, A. Bérces, C. Bo, P. M. Boerrigter, L. Cavallo, D. P. Chong, L. Deng, R. M. Dickson, D. E. Ellis, L. Fan, T. H. Fischer, C. Fonseca Guerra, S. J. A. van Gisbergen, J. A. Groeneveld, O. V. Gritsenko, M. Grüning, F. E. Harris, P. van den Hoek, H. Jacobsen, G. van Kessel, F. Kootstra, E. van Lenthe, V. P. Osinga, S. Patchkovskii, P. H. T. Philipsen, D. Post, C. C. Pye, W. Ravenek, P. Ros, P. R. T. Schipper, G. Schreckenbach, J. G. Snijders, M. Solà, M. Swart, D. Swerhone, G. te Velde, P. Vernooijs, L. Versluis, O. Visser, E. van Wezenbeek, G. Wiesenekker, S. K. Wolff, T. K. Woo, T. Ziegler, Vrije Universiteit Amsterdam: Amsterdam, The Netherlands.
87. M. Flock, K. Pierloot, *J. Phys. Chem. A* **1999**, *103*, 95-102.
88. S. Mahapatra, J. A. Halfen, E. C. Wilkinson, G. Pan, X. Wang, V. G. Young Jr., C. J. Cramer, L. Que Jr., W. B. Tolman, *J. Am. Chem. Soc.* **1996**, *118*, 11555-11574.
89. T. Lind, P. E. M. Siegbahn, R. H. Crabtree, R. H. *J. Phys. Chem. B* **1999**, *103*, 1193-1202.
90. B. Braïda, P. C. Hiberty, A. Savin, *J. Phys. Chem. A* **1998**, *102*, 7872-7877.
91. M. Sodupe, J. Bertran, L. Rodríguez-Santiago, E. J. Baerends, *J. Phys. Chem. A* **1999**, *103*, 166-170.
92. H. Chermette, I. Ciofini, F. Mariotti, C. Daul, *J. Chem. Phys.* **2001**, *115*, 11068-11079.
93. M. Grüning, O. V. Gritsenko, S. J. A. van Gisbergen, E. J. Baerends, *J. Phys. Chem. A* **2001**, 105, 9211-9218.
94. J. Poater, M. Solà, A. Rimola, L. Rodríguez-Santiago, M. Sodupe, *J. Phys. Chem. A* **2004**, 120, 6072-6078.
95. J. Cabrero, C. J. Calzado, D. Maynau, R. Caballol, J. P. Malrieu, *J. Phys. Chem. A* **2002**, *106*, 8146-8155.
96. M. A. Aebersold, B. Guillon, O. Plantevin, L. Pardi, O. Kahn, P. Bergerat, I. v. Seggern, F. Tuczek, L. Öhrström, A. Grand, E. Lelièvre-Berna, *J. Am. Chem. Soc.* **1998**, 120, 5238-5245.
97. A. D. Becke, *J. Chem. Phys.* **1993**, *98*, 5648-5652.

98. C. Lee, W. Yang, R. G. Parr, *Phys. Rev. B* **1988**, *37*, 785-789.

99. P. J. Stephens, F. J. Devlin, C. F. Chabalowski, M. J. Frisch, *J. Phys. Chem.* **1994**, *98*, 11623-11627.

100. A. D. Becke, *J. Chem. Phys.* **1993**, *98*, 1372-1377.

101. Gaussian 03, M. J. Frisch, G. W. Trucks, H. B. Schlegel, G. E. Scuseria, M. A. Robb, J. R. Cheeseman, J. A. Montgomery, Jr., T. Vreven, K. N. Kudin, J. C. Burant, J. M. Millam, S. S. Iyengar, J. Tomasi, V. Barone, B. Mennucci, M. Cossi, G. Scalmani, N. Rega, G. A. Petersson, H. Nakatsuji, M. Hada, M. Ehara, K. Toyota, R. Fukuda, J. Hasegawa, M. Ishida, T. Nakajima, Y. Honda, O. Kitao, H. Nakai, M. Klene, X. Li, J. E. Knox, H. P. Hratchian, J. B. Cross, C. Adamo, J. Jaramillo, R. Gomperts, R. E. Stratmann, O. Yazyev, A. J. Austin, R. Cammi, C. Pomelli, J. W. Ochterski, P. Y. Ayala, K. Morokuma, G. A. Voth, P. Salvador, J. J. Dannenberg, V. G. Zakrzewski, S. Dapprich, A. D. Daniels, M. C. Strain, Ö. Farkas, D. K. Malick, A. D. Rabuck, K. Raghavachari, J. B. Foresman, J. V. Ortiz, Q. Cui, A. G. Baboul, S. Clifford, J. Cioslowski, B. B. Stefanov, G. Liu, A. Liashenko, P. Piskorz, I. Komaromi, R. L. Martin, D. J. Fox, T. Keith, M. A. Al-Laham, C. Y. Peng, A. Nanayakkara, M. Challacombe, P. M. W. Gill, B. Johnson, W. Chen, M. W. Wong, C. Gonzalez, J. A. Pople, Gaussian, Inc., Pittsburgh PA, 2003.

102. M. J. Frisch, J. A. Pople, J. S. Binkley, *J. Chem. Phys.* **1984**, *80*, 3265-3269.

103. N. W. Aboelella, S. V. Kryatov, B. J. Gherman, W. W. Brennessel, V. G. Young, Jr., R. Sarangi, E. V. Rybak-Akimova, K. O. Hodgson, B. Hedman, E. I. Solomon, C. J. Cramer, W. B. Tolman, *J. Am. Chem. Soc.* **2004**, *126*, 16896-16911.

104. B. J. Gherman, C. J. Cramer, *Inorg. Chem.* **2004**, *43*, 7281-7283.

105. Z. Tyeklár, R. R. Jacobson, N. Wei, N. N. Murthy, J. Zubieta, K. D. Karlin, *J. Am. Chem. Soc.* **1993**, *115*, 2677-2689.

106. T. D. P. Stack, *J. Chem. Soc., Dalton Trans.* **2003**, *10*, 1881-1889.

107. M. J. Henson, P. Mukherjee, D. E. Root, T. D. P. Stack, E. I. Solomon, *J. Am. Chem. Soc.* **1999**, *121*, 10332-10345.

108. H.-C. Liang, C. X. Zhang, M. J. Henson, R. D. Sommer, K. R. Hatwell, S. Kaderli, A. D. Zuberbühler, A. L. Rheingold, E. I. Solomon, K. D. Karlin, *J. Am. Chem. Soc.* **2002**, *124*, 4170-4171.

109. R. Menif, A. E. Martell, P. J. Squattrito, A. Clearfield, *Inorg. Chem.* **1990**, *29*, 4723-4729.

110. M. Becker, S. Schindler, R. v. Eldik, *Inorg. Chem.* **1994**, *33*, 5370-5371.

111. H. Decker, R. Dillinger, F. Tuczek, *Angew. Chem. Int. Ed.* **2000**, *39*, 1591-1595.

Chapter VII: *O_2 Chemistry of Dicopper Complexes with Alkyltriamine Ligands. Comparing Synergetic Effects on O_2 Binding*

O_2 Chemistry of Dicopper Complexes with Alkyltriamine Ligands. Comparing Synergetic Effects on O_2 Binding

Abstract

Two dicopper(I) complexes containing tertiary *N*-methylated hexaaza ligands, $[Cu_2(L1)](X)_2$ (**1X₂**) and $[Cu_2(L2)](X)_2$ (**2X₂**) (X = CF_3SO_3, SbF_6 and BArF, BArF = $[B\{3,5\text{-}(CF_3)_2\text{-}C_6H_3\}_4]^-$), have been studied. **1** and **2** share structurally related metal coordination sites. Their reactivity towards O_2 exhibits remarkable differences. Acyclic complex **2** reacts with O_2 at low temperatures generating metastable bis(μ-oxo)dicopper(III) species (**3**). Analogous macrocyclic complex **1** did not react with O_2 at 193K. The differences between the O_2 chemistry exhibited by **1**, **2**, and the related mononuclear complex $[Cu(MeAN)]B(C_6F_5)_4$ can be traced to the relative ability of the ligand to promote or impede synergetic effects between two copper ions upon O_2 binding. DFT calculations are useful to explain why Cu(III) species are formed in complex **2** and not in complex **1**. The intramolecular C-H aromatic bond activation is structurally not possible in complex **2**. Nevertheless this type of activation is possible for similar complexes with macrocyclic ligands in complex **1**.

Introduction

A number of proteins involved in dioxygen transport and activation contains a dinuclear Cu active site.[1] The arguably best known are hemocyanin and tyrosinase, which react with O_2 generating O_2-bound species which have been spectroscopically and, in the former case, structurally characterized.[1,2] Traditionally, the mimicking of these dicopper centers was performed either using mononuclear complexes that self-assemble when reacting with O_2, or via dinucleating ligands designed with the purpose of favoring O_2 binding by spatial pre-organization of the dimetallic site.[3] Particularly remarkable are *m*-xylyl linked dinuclear Cu(I) complexes which react with O_2 to form well-characterized (μ-η^2:η^2-peroxo)dicopper(II) species that in selected cases undergo intra-[4] or intermolecular[5] regioselective hydroxylation of an aromatic ring, thus mimicking tyrosinase activity.

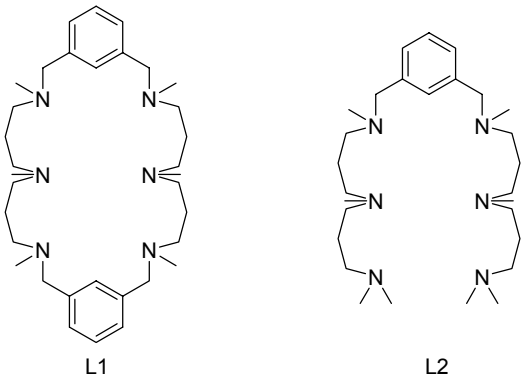

Scheme VII-1. Schematic structure of ligands L1 and L2.

The reactivity with O_2 of two related dinuclear copper(I) complexes supported by two hexaaza ligands (L1[6] and L2, Scheme VII-1) based on a *m*-xylyl spacer, and the comparison with the one recently reported for the mononuclear analogue $[Cu(MeAN)]B(C_6F_5)_4$[7] is different. The three complexes contain ligands which bind copper atoms within very similar coordination environments and give rise to electronically and structurally comparable metal sites. However, they exhibit rather unexpected differences in their reaction with O_2 which may be understood on the basis of the relative ability of the ligand to promote a synergetic role of the two Cu ions along the O_2 binding process.

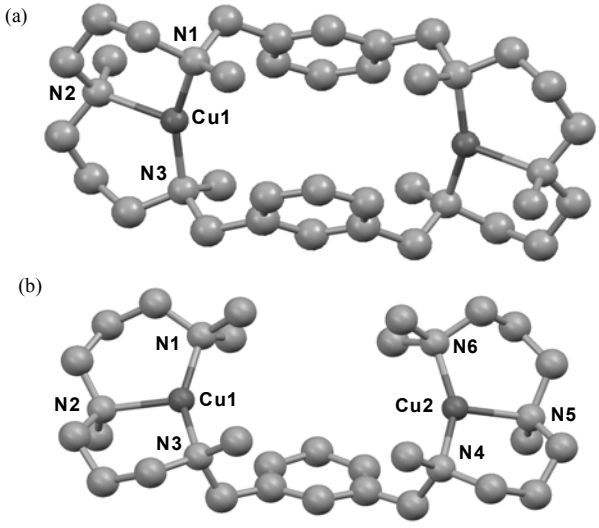

Figure VII-1. Experimental diagrams for the cationic part of (a) **1(BArF)$_2$**; Cu-N1 2.007(3) Å, Cu-N2 2.192(2) Å, Cu-N3 1.999(3) Å, N3-Cu-N1 156.52(10)º, N3-Cu-N2 102.50(10)º, N1-Cu-N2 100.98(10)º and (b) **2(SbF$_6$)$_2$**. Cu1-N1 1.990(3) Å, Cu1-N2

2.120(3) Å, Cu1-N3 1.986(3) Å, Cu2-N4 1.974(2) Å, Cu2-N5 2.100(3) Å, Cu2-N6 1.973(3) Å, N3-Cu1-N1 148.84(11)º, N3-Cu1-N2 105.08(10)º, N1-Cu1-N2 105.59(11)º, N6-Cu2-N4 150.62(13)º, N6-Cu1-N5 104.34(15)º, N4-Cu1-N5 104.95(12)º.[8]

1(BArF)$_2$ and **2(SbF$_6$)$_2$** contain discrete dinuclear cationic complexes (Figure VII-1). The coordination geometry and metrical parameters of the metal sites does not exhibit significant differences. Within each complex, the two Cu sites are pseudo or symmetrically related and the Cu···Cu distances are 7.04 and 7.02 Å, respectively. Each Cu ion contains a N3 coordination set and adopts a distorted trigonal planar geometry. The average Cu-N distance is 2.07 Å for **1(BArF)$_2$** and 2.02 Å for **2(SbF$_6$)$_2$**. The main difference between the two structures can be found in the N1-Cu1-N3 angle which is 156.52(10)º in **1(BArF)$_2$** and 148.84º (150.62º for the pseudo-symmetrically related N4-Cu2-N6 angle) in **2(SbF$_6$)$_2$**, which presumably reflects subtle ligand strains imposed by the more rigid macrocyclic L1 backbone. These structural parameters are in close proximity to the ones found in [Cu(MeAN)]B(C_6F_5)$_4$,[7] where Cu(I) adopts a tricoordinated geometry using a similar nitrogen-based donor-set ligand. The low coordination number and geometry attained in these complexes is particularly interesting because it provides available coordination sites for interaction with external molecules such as O_2 and indeed is the most common coordination structure found in Cu-dependent O_2-processing proteins.[1,2]

Costas et al.[9] studied the vibrational properties of the metal sites studied by FT-IR analyses of the corresponding Cu(I)-CO adducts, generated *in situ* by bubbling CO through CH_2Cl_2 solutions. Remarkably, ν_{str}(CO) frequencies are 2083 and 2085 cm^{-1} in **1** and **2** respectively,[10] which indicates that Cu(I) sites in both complexes are electronically comparable.[11] Cu(I) ions in **1** and **2** possess electronically and structurally analogous properties.

In spite of the structural similarities between the complexes described, they show an unexpectedly different reactivity towards molecular oxygen; reaction of **2** with O_2 in acetone, CH_2Cl_2 or THF at low temperature show the relatively fast formation (within seconds) of a yellow species which was formulated as a bis-μ-oxo dicopper(III) species **3** on the basis of its UV-visible and resonance Raman spectra. The UV-vis spectrum of

3 in THF at -80 ºC exhibits two prominent characteristic bands at 308 nm (ε = 20000 $M^{-1}\cdot cm^{-1}$) and at 413 nm (ε = 28000 $M^{-1}\cdot cm^{-1}$). Resonance Raman experiments carried out in acetone using laser excitation at 413 nm reveals a characteristic Cu_2O_2 breathing vibration peak at 600 cm^{-1} that shows a 23 cm^{-1} downshift when $^{18}O_2$ is used (Figure VII-2). These are common spectral features for a $Cu_2^{III}(\mu\text{-}O)_2$ core allowing to formulate **3** as $[Cu_2^{III}(\mu\text{-}O)_2L2]^{2+}$.[12]

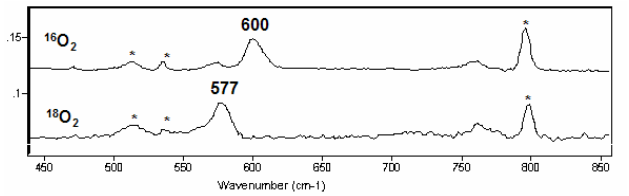

Figure VII-2. Resonance Raman spectra (λ_{ex} = 413 nm) of **3** generated from $^{16}O_2$ (top) and from $^{18}O_2$ (bottom) in frozen acetone (77 K). Solvent peaks are marked with *.

Diffusion rate for **3** measured in acetone-d_6 at -80 ºC is $10^{-9.90\ \pm\ 0.05}$ $m^2\cdot s^{-1}$, which compares well with the values obtained for **1** and **2** and strongly supports the intramolecular nature of O_2 binding. **3** constitutes the first example of a $Cu_2^{III}(\mu\text{-}O)_2$ species formed within a dicopper complex containing a xylyl spacer.[13] Although, it is well established that $Cu_2^{III}(\mu\text{-}O)_2$ species are usually close in energy to their $Cu_2^{II}(\mu\text{-}\eta^2\text{:}\eta^2\text{-}O_2)$ isomeric form,[3,14] the structure of **3** was found to be unperturbed by either the counterion (CF_3SO_3 or BArF) or the solvent (THF, acetone or CH_2Cl_2).

Stopped-flow kinetic analysis of the oxygenation reactions indicates that **2** reacts reversibly with O_2 to generate **3**. At low temperatures (from -80 to -50 ºC), the equilibrium is shifted to the right, and the formation of **3** is essentially quantitative. Under these conditions, the reaction is first-order in $[O_2]$ and first-order in [**2**].

$$v = k_{ox}[\mathbf{2}][O_2]$$

Activation parameters for the oxygenation reactions are characterized by a rather low $\Delta H^{\ddagger}$ = 9.5 $kJ\cdot mol^{-1}$ and a large negative $\Delta S^{\ddagger}$ = -175 $J\cdot K^{-1}\cdot mol^{-1}$. The simple second-order rate law observed at low temperature is consistent with an intramolecular formation of the bis-μ-oxo compound **3.** Even though no reaction intermediates were observed

between **2** and **3,** a stepwise reaction Scheme VII-(Scheme VII-2) similar to the oxygenation mechanisms of other dicopper(I) complexes[3b] can be proposed:[15]

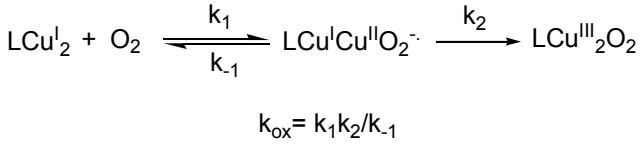

Scheme VII-2.

This mechanistic picture (Scheme VII-2) involves reversible reaction of O_2 with **2** to generate a putative superoxo $Cu^{I}Cu^{II}O_2^{-}$ species in a left-lying preequilibrium process, followed by intramolecular collapse into the final dinuclear $[Cu_2^{III}(\mu\text{-}O)_2L2]^{2+}$ structure.

It is very interesting to point out that k_{ox} in **2** is 8.1 $M^{-1}\cdot s^{-1}$, nearly two orders of magnitude slower than in the related mononuclear $[Cu(MeAN)]^{+}$ complex (690 $M^{-2}\cdot s^{-1}$ in CH_2Cl_2, 183K).[7] Therefore, opposite to expected, pre-organization of the dinuclear site along the order $[Cu(MeAN)]^{+}$ < **2** < **1** results in slowing down of the oxygenation rate. Examination of the kinetic parameters indicate that this is due to a significant increase in the $\Delta H^{\ddagger}$, which is not compensated by the lower $\Delta S^{\ddagger}$ associated to the more organized dinuclear structure.[16] Given the comparable coordination sphere and electronic properties of the Cu(I) ion in $[Cu(MeAN)]^{+}$, **1** and **2**, it is rather unlikely that first O_2 binding to a single Cu(I) ($k_1\cdot k_{-1}^{-1}$) depends on the particular complex and therefore the different O_2 reactivity highlights the important role played by the second metal ion. In complex **2**, the ligand is flexible, allowing copper sites to approach close enough to promote their synergetic role in O_2 binding/reduction. Instead, the rather rigid nature of the macrocyclic ligand L1 poses energetic barriers to this process, slowing down the reaction. The stability of **3**, which allows its spectroscopic characterization, in comparison with the lack of stability of any reaction intermediate formed along the **1** + O_2 pathway may also be explained on the basis of the different structural strains imposed by the ligands.

Computational details

All geometry optimizations calculations have been performed at the B3LYP level,[17] using the standard 6-31G* basis set[18] with the Gaussian03 package.[19] The geometry optimizations were performed without symmetry constraints, and the nature of the extrema was checked by analytical frequency calculations. Furthermore, all the extrema were confirmed by calculation of the intrinsic reaction paths. The energies discussed throughout the text do no contain ZPE corrections.

Results

DFT calculations at B3LYP level for complex **2** after reacting with molecular oxygen, **H3Me**, indicate that the system $Cu_2^{III}(\mu\text{-}O)_2$ is 9.4 kcal·mol^{-1} more stable than $Cu_2^{II}(\mu\text{-}\eta^2\text{:}\eta^2\text{-}O_2)$, thus substantiating the single observation of bis-μ-oxo isomer. These results clearly contrast with the ones reported by Karlin et al. in the oxygenation of mononuclear [Cu(MeAN)]B$(C_6F_5)_4$,[7] where side-on $Cu_2^{II}(\mu\text{-}\eta^2\text{:}\eta^2$-peroxo) species are formed. Although unexpected, this is not surprising since it is well established that very subtle differences in ligand architecture can cause profound changes in the relative stability of the two isomeric species.[3] On the other hand, **1** does not react with O_2 at 198K, but irreversibly reacts with O_2 at 273K to generate copper(II) species. However, experimentally, no accumulation of any apparent intermediate was detected, and therefore we conclude that decomposition of any reaction intermediate is always faster than its formation.

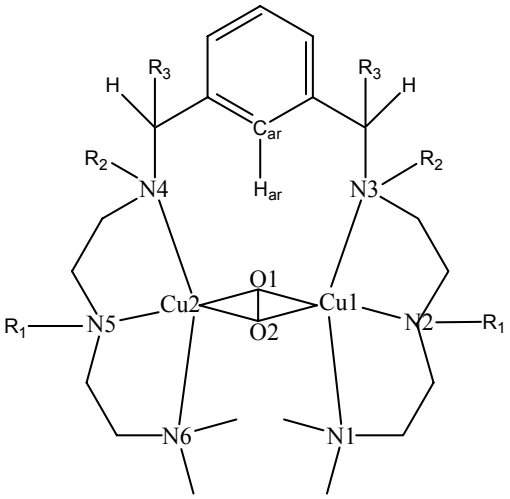

BsH3 $R_1 = H$; $R_2 = -$; $R_3 = -$

H3 $R_1 = R_2 = R_3 = H$

H3Me $R_1 = R_2 = Me$; $R_3 = H$

Scheme VII-3.

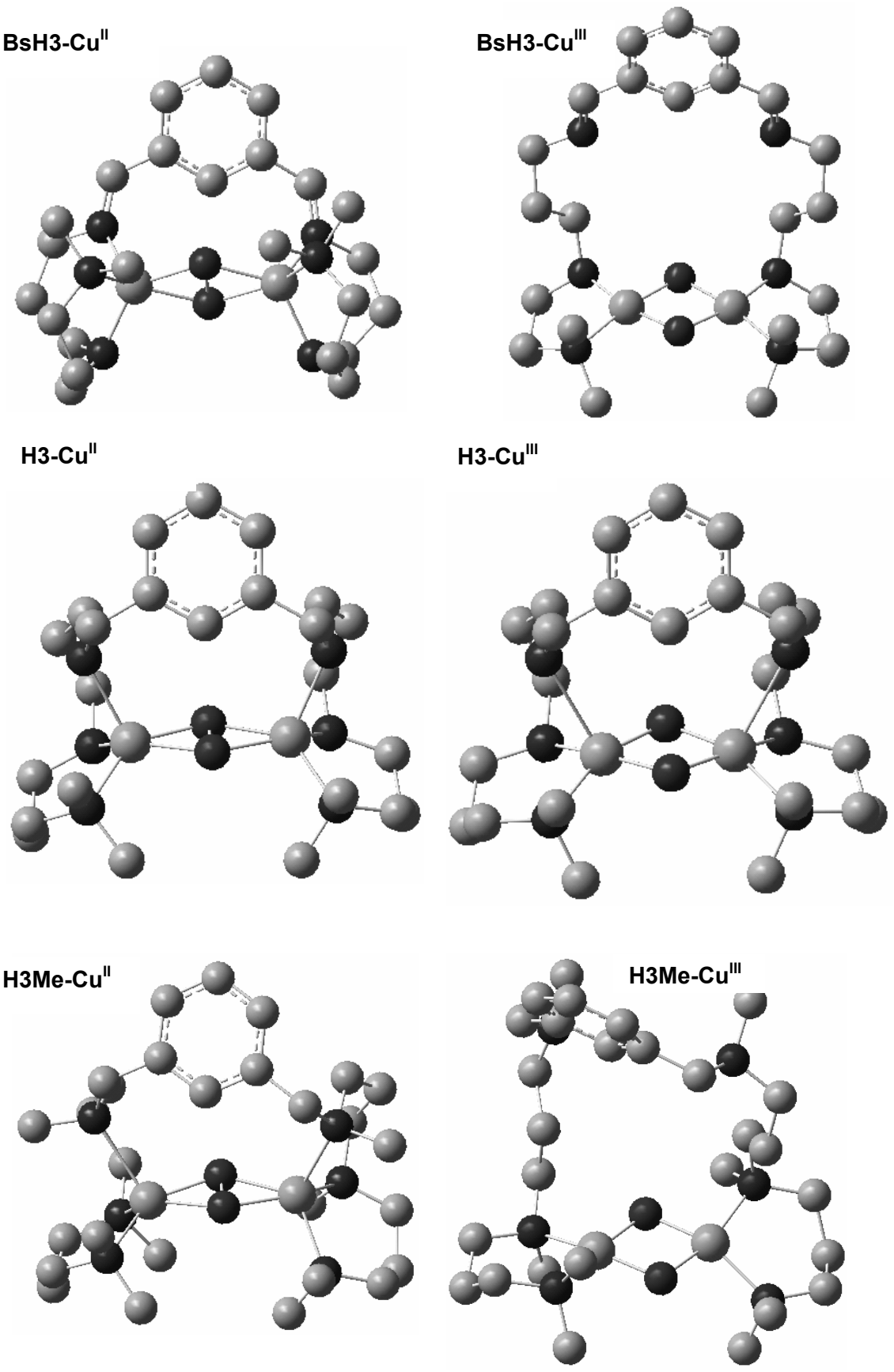

Figure VII-3. $Cu_2^{II}(\mu\text{-}\eta^2\text{:}\eta^2\text{-}O_2)$ and $Cu_2^{III}(\mu\text{-}O)_2$ structures for **BsH3**, **H3**, **H3Me** complexes. See Scheme VII-3 for a schematic representation of these complexes.

Complex **H3Me** was further studied with some changes in the ligand structure, replacing the methyl molecules of the N2, N3, N4, and N5 atoms by protons (**H3**). The exclusion of these methyls in addition to the exclusion of one proton of one methylic group next to the amine groups gives a shift basis (**BsH3**). Scheme VII-3 summarizes this new nomenclature. The most stable $Cu_2^{II}(\mu\text{-}\eta^2\text{:}\eta^2\text{-}O_2)$ and $Cu_2^{III}(\mu\text{-}O)_2$ structures for each system are depicted in Figure VII-3 and the structural data are collected in Table VII-1 (labelling of Scheme VII-3). They all present one minimum for the Cu^{II} oxidation state (I) and two for the Cu^{III} state (II, III). These minima are connected by two transition states (TSI, TSII). The predicted interconversion process between the Cu^{II} and Cu^{III} species is reflected in Scheme VII-4. The most stable Cu^{III} structure for each complex is depicted in Figure VII-3. However, Cu^{III} oxidation state is able to produce different conformations due to the fact that the metal atoms are strongly bonded to only two amine units instead of three as in the Cu^{II} complex. In fact, these nitrogen atoms even for the Cu^{II} species present higher Cu-N bond distances, i. e. 0.3 Å, than the N2, N3, N4, and N5 atoms. The farthest amines with respect to each metal are placed at least at about 2.3 Å in all cases. Therefore, depending on the case either N1 amine or the N6 one are not connected to the Cu1 and Cu2 atoms, respectively. And the absolute no connection of neither the N1 nor the N6 atoms is also possible for Cu^{III} oxidation state. The TSII structures have not been characterized yet.

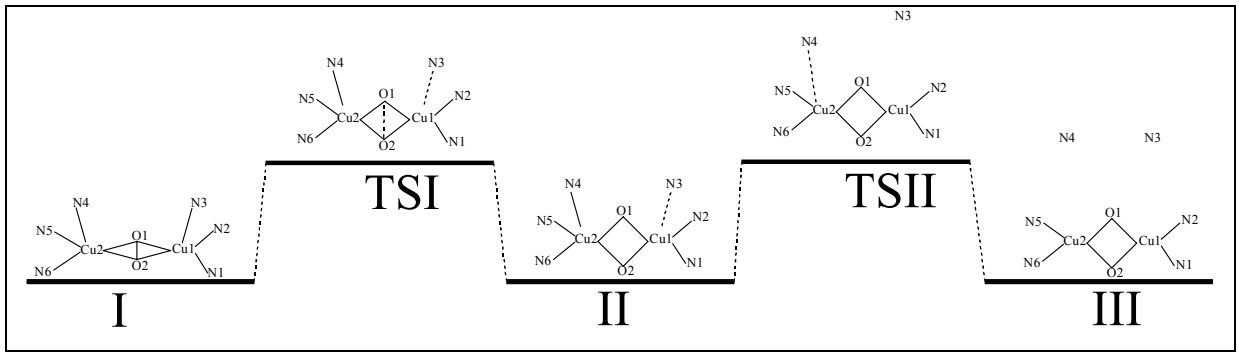

Scheme VII-4.

	BsH3				H3				H3Me			
	I	TSI	II	III	I	TSI	II	III	I	TSI	II	III
Cu1-Cu2	3.625	3.241	2.827	2.755	3.603	3.269	2.837	2.752	3.636	3.270	2.831	2.810
O1-O2	1.436	1.769	2.231	2.287	1.447	1.740	2.234	2.288	1.438	1.723	2.227	2.246
Cu1-N1	2.033	2.056	2.014	1.970	2.045	3.269	2.030	1.970	2.087	2.086	2.014	1.999
Cu1-N2	2.046	2.026	1.986	1.963	2.019	2.030	2.010	1.962	2.044	2.022	2.001	1.992
Cu1-N3	2.211	2.396	2.546	4.827	2.240	2.359	2.564	4.813	2.319	2.338	2.714	5.101
Cu2-N4	2.227	2.418	3.821	4.827	2.242	2.359	2.565	4.819	2.430	3.438	4.500	5.513
Cu2-N5	2.019	2.017	1.994	1.963	2.032	2.030	2.010	1.961	2.056	2.009	2.014	2.004
Cu2-N6	2.058	2.060	1.993	1.970	2.045	2.042	2.031	2.116	2.029	1.995	1.998	1.990
Cu1-O1	1.954	1.850	1.816	1.791	1.943	1.850	1.806	1.791	2.006	1.881	1.810	1.801
Cu1-O2	1.949	1.851	1.801	1.794	1.937	1.856	1.810	1.794	1.938	1.856	1.805	1.798
Cu2-O1	1.962	1.850	1.794	1.791	1.931	1.850	1.806	1.791	1.929	1.833	1.790	1.796
Cu2-O2	1.935	1.846	1.794	1.794	1.958	1.856	1.810	1.793	1.978	1.846	1.800	1.799
C_{ar}-H_{ar}	1.082	1.082	1.084	1.083	1.085	1.085	1.085	1.086	1.084	1.084	1.088	1.085
O1-C_{ar}	3.173	3.319	3.888	5.472	3.456	3.571	3.862	5.072	3.227	3.610	4.265	5.164
O2-C_{ar}	2.813	2.886	3.740	6.225	3.190	3.284	3.381	5.375	3.118	3.450	4.479	5.971
Cu1-O1-Cu2	135.5	122.3	103.1	100.6	136.9	124.1	103.5	100.4	135.0	123.4	103.7	102.7
Cu1-O2-Cu1	137.9	122.5	103.7	100.4	135.4	123.4	103.2	100.2	136.4	124.1	103.5	102.7
O1-Cu1-O2	43.2	57.1	76.2	79.3	43.8	56.0	76.3	79.3	42.7	54.9	76.1	77.2
O1-Cu2-O2	43.2	57.2	76.9	79.3	43.7	56.0	76.3	79.3	43.2	55.8	76.7	77.3
N6-Cu2-N5	104.5	102.5	99.8	100.7	102.6	99.2	98.2	100.8	101.8	103.5	101.2	101.4
N1-Cu1-N2	104.6	102.4	97.6	100.7	100.8	99.2	98.1	100.8	99.7	99.5	99.5	102.1

Table VII-1. Structural data of **BsH3**, **H3**, and **H3Me** optimized structures (distances in Å and angles in degrees). Atom labels are given in Scheme VII-3.

As expected, the O-O bond distance is smaller and the Cu-Cu distance is higher for the Cu^{II} species. Species II present Cu-N bonds that are in some cases large enough to guarantee that the Cu-N bond does not exist, nevertheless there are some Cu-N bond distances, 2.546 or 2.714 Å for **BsH3** and **H3Me** complexes, respectively, that are doubtful as far as the existence of the bond is concerned. The Cu^{II}/Cu^{III} interconversion process supposes an enlargement of the O-O bond distance, from 1.4 to 2.3 Å, with a transition state at about 1.7 Å, i. e. very near to the Cu^{II} minimum, but showing significantly higher Cu-N3 and Cu-N4 distances. Furthermore the Cu-Cu distance suffers a decrease from 3.6, to 3.2 and 2.8 Å from I to TSI and II structures, respectively.

The relative stability between these isomers is depicted in Figure VII-4, where the energy diagrams of the conversion from the Cu^{II} geometry to the Cu^{III} geometries are reflected.

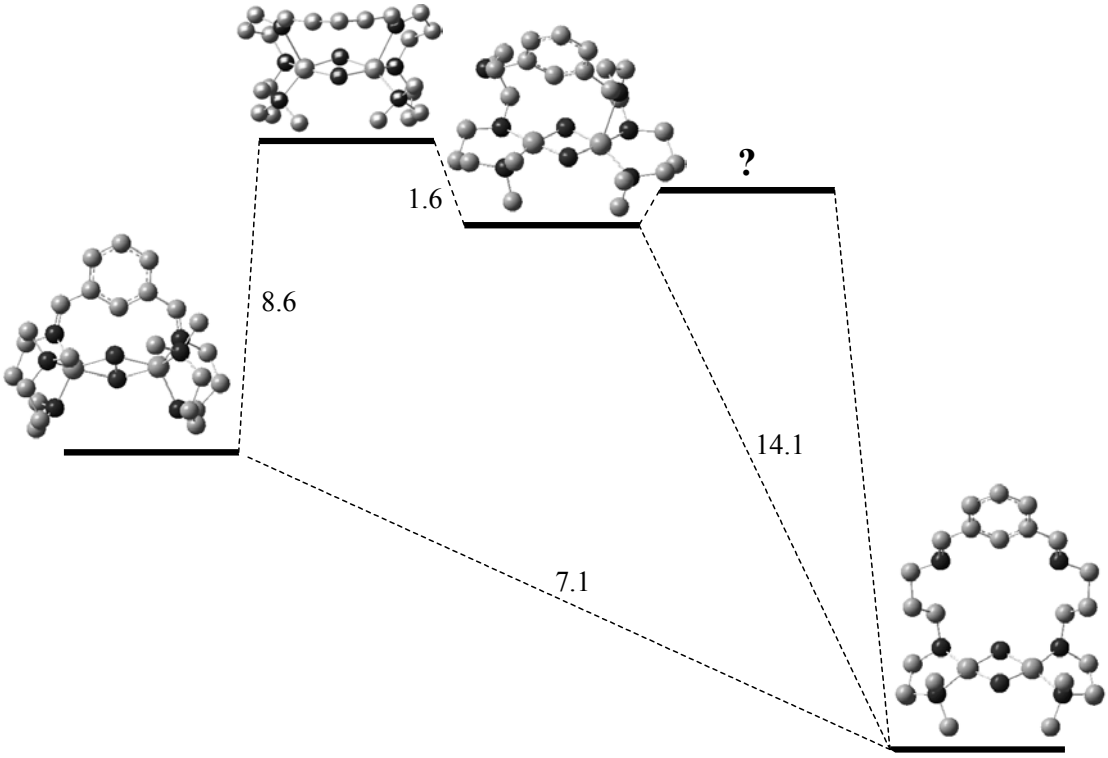

Figure VII- 4a. I, TSII, II, and III structures of complex **BsH3**.

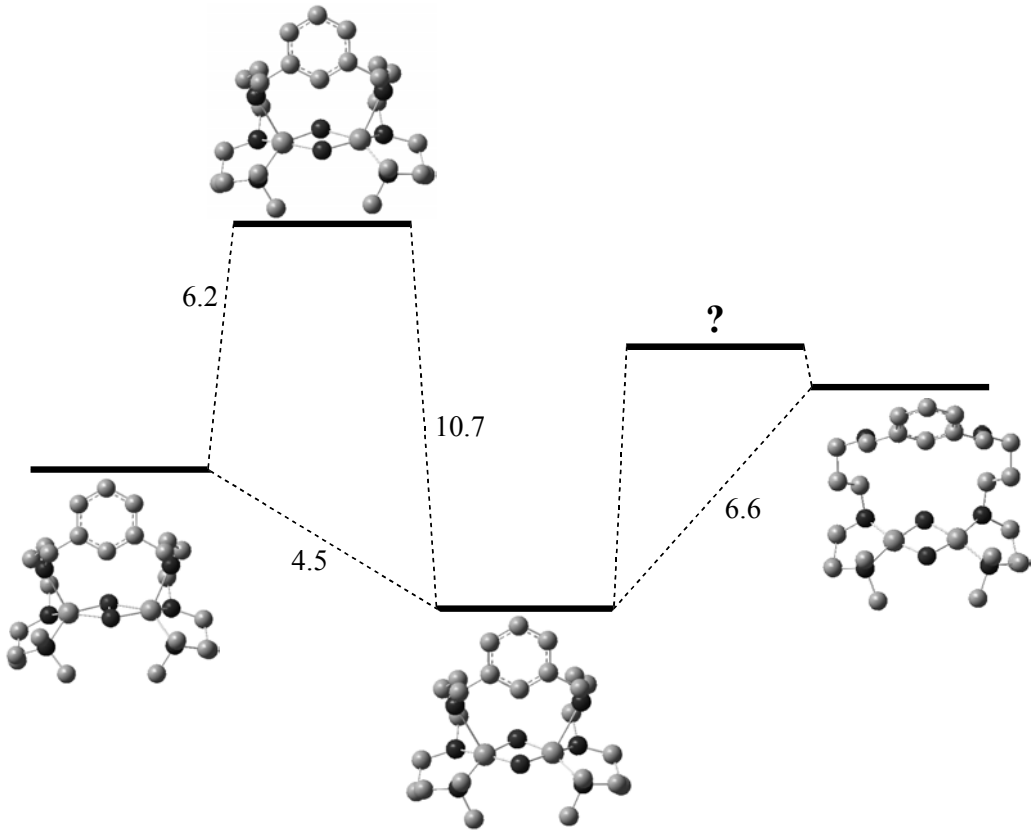

Figure VII- 4b. I, TSII, II, and III structures of complex **H3**.

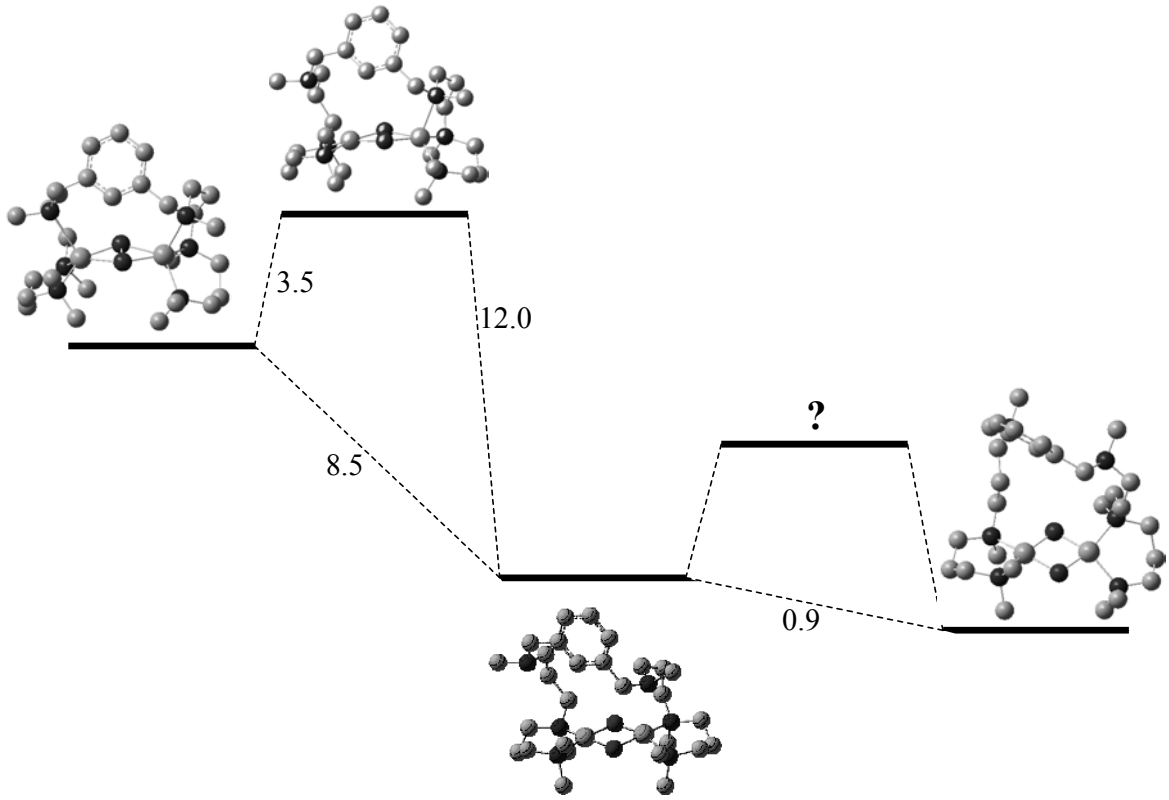

Figure VII- 4c. I, TSII, II, and III structures of complex **H3Me**.

The most stable Cu^{III} species with respect to the Cu^{II} species are stabilized by 7.1 kcal·mol^{-1} for **BsH3** and by 9.4 kcal·mol^{-1} for **H3Me**. Nevertheless for **H3** this difference is even lower, 4.5 kcal·mol^{-1}. Furthermore the species III for **H3**, which presents the three amines of each copper atom bonded to it, is 6.6 kcal·mol^{-1} less stable than II, and even 2.1 kcal·mol^{-1} less stable withrespect to I. The species of **BSH3** present more rigid ligand structures, due to the loss of four protons of this macrocycle with respect to **H3**. Therefore this rigidity is more stabilized when the amines that have lost protons are not bonded to the copper atoms, avoiding a quaternary amine. This explains why the structure with one copper atom bonded to the three amines is 14.1 kcal·mol^{-1} less stable than the isomer with both copper atoms only bonded to two amines each one, and also 6.5 kcal·mol^{-1} less stable than I. **H3Me** present more steric problems than **H3**, therefore II is further stabilized, allowing a better disposal of the methyl units bonded to the amines that only present **H3Me**.

The Cu^{II}/Cu^{III} interconversion barrier is lower for **H3Me** with respect to **BsH3** and **H3** because the species I suffers sterical hindrance due to the permethylation of all the

amines and therefore, only a small amount of energy is necessary to reach the Cu^{III} species.

At present the transition state TSII is being further studied, but it is likely that the limiting step for this Cu^{II} to Cu^{III} conversion will be the transformation of I to II through the transition state TSI.

		O-O	Cu-Cu	Cu1-N1	Cu1-N2	Cu1-N3	Cu2-N4	Cu2-N5	Cu2-N6	Cu1-O1	Cu1-O2	Cu2-O1	Cu2-O2
BSH3	I	0.93	0.23	0.43	0.44	0.38	0.38	0.45	0.42	0.42	0.42	0.44	0.42
	TSI	0.65	0.05	0.43	0.45	0.30	0.29	0.45	0.42	0.59	0.59	0.61	0.59
	II	0.19	-0.17	0.48	0.54	0.25	0.04	0.55	0.55	0.75	0.73	0.75	0.77
	III	0.18	-0.19	0.52	0.57	0.02	0.02	0.57	0.52	0.77	0.77	0.77	0.77
H3	I	0.93	0.24	0.42	0.46	0.38	0.38	0.45	0.42	0.44	0.41	0.42	0.41
	TSI	0.67	0.07	0.42	0.45	0.33	0.33	0.45	0.42	0.57	0.56	0.57	0.56
	II	0.21	-0.21	0.46	0.51	0.24	0.24	0.51	0.46	0.73	0.76	0.73	0.76
	III	0.17	-0.19	0.53	0.58	0.02	0.02	0.58	0.53	0.76	0.77	0.76	0.77
H3Me	I	0.93	0.23	0.39	0.41	0.34	0.29	0.40	0.42	0.42	0.40	0.40	0.41
	TSI	0.68	0.08	0.40	0.42	0.32	0.12	0.44	0.45	0.55	0.50	0.56	0.57
	II	0.19	-0.22	0.48	0.47	0.19	0.04	0.50	0.50	0.68	0.74	0.76	0.80
	III	0.19	-0.17	0.50	0.52	0.00	0.01	0.50	0.51	0.71	0.79	0.77	0.71

Table VII-2. Main MBO for **BsH3**, **H3**, and **H3Me**.

To study further in detail the strength of the bonds from the formation of I to the formation of III a MBO analysis has been made whose main results are displayed in Table VII-2. For **BsH3,** the value of 1.40 for the free oxygen molecule decreases to 0.93 for I, 0.65 for TSI and 0.19 for II. The MBO for III (posar MBO d´oxigen) is 0.18, therefore only slightly lower than for II, showing that the effect of breaking one or two Cu-N bonds does not especially affect the Cu_2O_2 core. Actually, the MBO values follow nearly the same trend as the O-O bond distance. Nevertheless it is useful to note that both oxygen atoms for II and III are not absolutely disconnected despite presenting a

highly elongated O-O distance. In addition, the low and decreasing from I to III for the Cu-Cu MBO values demonstrate that the intermetallic repulsion in II and III is present. The Cu-O MBO increase from I to II, and only a little to III. For I, the MBO for Cu-N3 and the symmetrical Cu-N4 are lower than for the rest, because these two Cu-N pairs present more elongated Cu-N distances. And the path to III supposes an increase of the MBO for Cu-N pairs except for the Cu-N that presented first lower values, which for III will present values tending to null values.

There are no significant differences between the MBO for **BsH3**, **H3**, and **H3Me.**

The electrophilicity analysis displayed in Table VII-2 is key to understand that, in spite of the similarity of **BsH3**, **H3**, and **H3Me** systems, the small structural differences that display are clearly overviewed through this analysis. The electrophilicity decreases deprotonating the amines and increases with the permethylation of the amines, and increases from I to III, except for TSI that presents a lower value than I. The value for III is significantly higher than for II, surely due to the fact that the copper atoms present more freedom to interact with possible reactants. This higher supposed reactivity for III is demonstrated by the chemical hardness values, which are extremely low in comparison to I and II.

		HOMO	LUMO	μ	η	ω
BSH3	I	-0.406	-0.312	-0.359	0.047	1.373
	TSI	-0.427	-0.314	-0.370	0.057	1.211
	II	-0.430	-0.339	-0.385	0.045	1.634
	III	-0.389	-0.342	-0.365	0.024	2.809
H3	I	-0.405	-0.311	-0.358	0.047	1.367
	TSI	-0.415	-0.314	-0.364	0.051	1.308
	II	-0.410	-0.333	-0.371	0.039	1.782
	III	-0.381	-0.342	-0.362	0.019	3.391
H3Me	I	-0.404	-0.315	-0.359	0.044	1.450
	TSI	-0.408	-0.317	-0.362	0.046	1.437
	II	-0.397	-0.332	-0.364	0.033	2.040
	III	-0.365	-0.341	-0.353	0.012	5.014

Table VII-2. HOMO, LUMO, chemical potential (μ), chemical hardness (η), and electrophilicity (ω) values for **BsH3**, **H3**, and **H3Me** (in eV).

The chemical potential increases from I to II, demonstrating the higher stability of Cu^{III} species. Structures III present lower values than II. From I to III the LUMO orbitals are more and more stable, but for HOMO orbitals there is a no clear trend. Therefore HOMO orbitals will be key to understand the different behavior of the structures.

Apart from the study of compounds with the ligand L2, the same methodology has been applied to the compounds presented in Chapter 9. Therefore the calculations for the intermediates **1c-8c** (labelling from Chapter VI) have been repeated, now with Gaussian and at the B3LYP/6-31G* level of theory. In this case, it has been possible to achieve both Cu^{II} and Cu^{III} possible intermediates that have been depicted in Figure VII-5. The structural data are summarized in Table VII-3 (the labeling is the same used in Scheme VII-3. Nevertheless, due to the presence of two aromatic rings, there are some distances, C_{ar}-H_{ar}, O1-C_{ar}, O2-C_{ar} which have been chosen through the criterion of the shortest O-C_{ar} distance. The N-Cu-N angles of Table VII-3 take as the nitrogen atoms the two nearest ones for each copper atom).

	I	II
1c	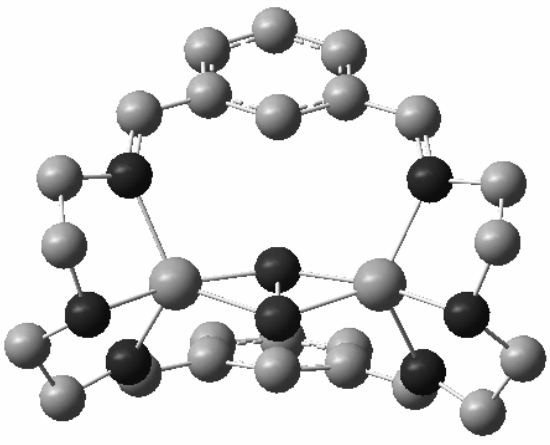	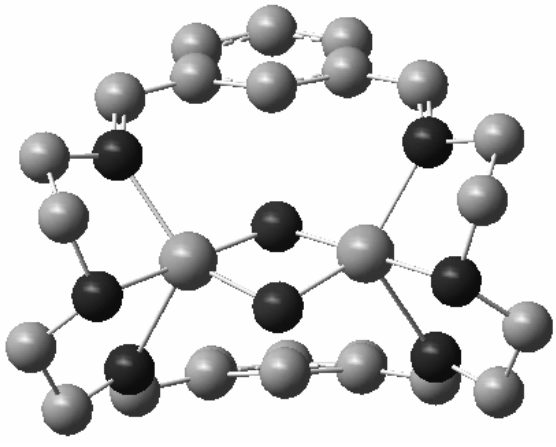

2c	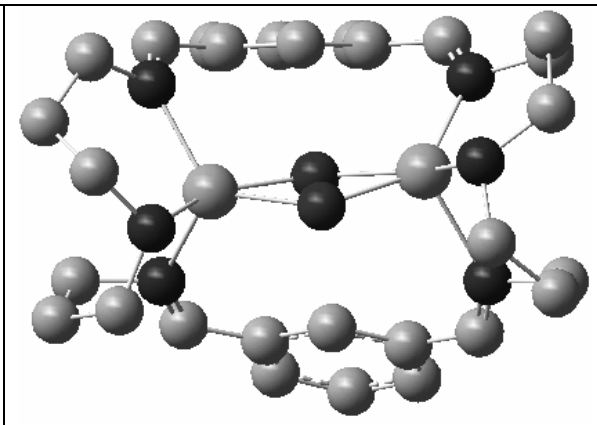	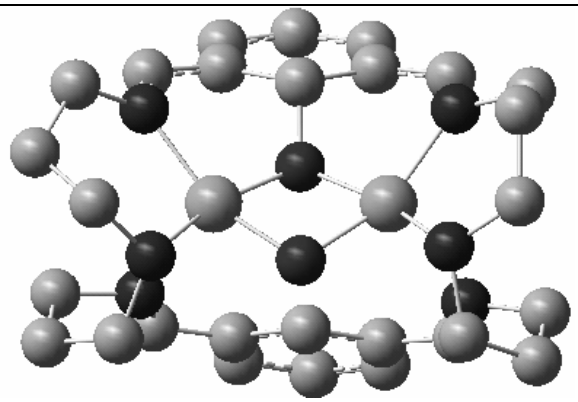
3c	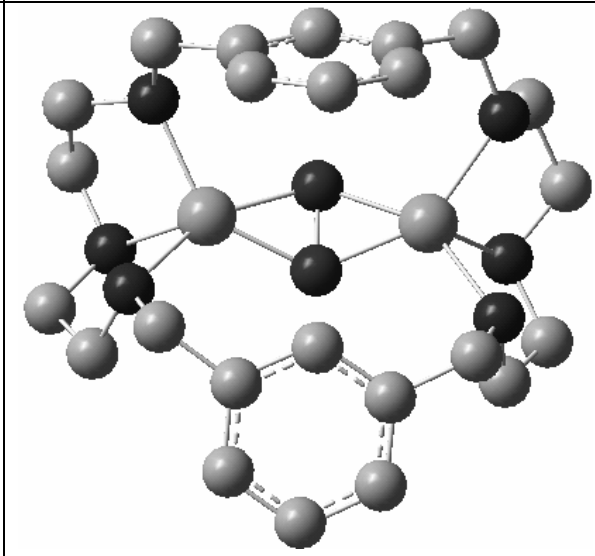	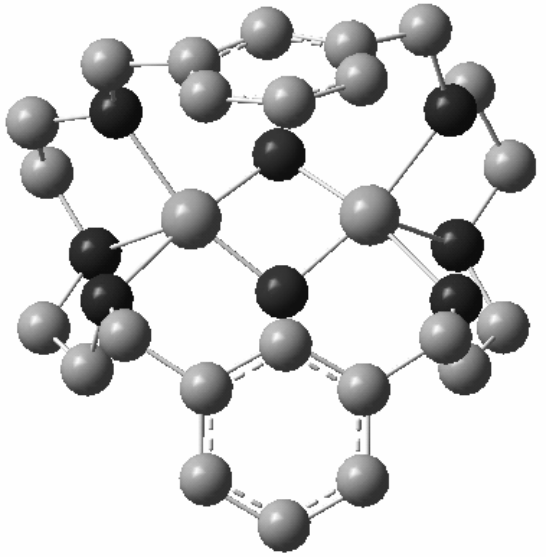
4c	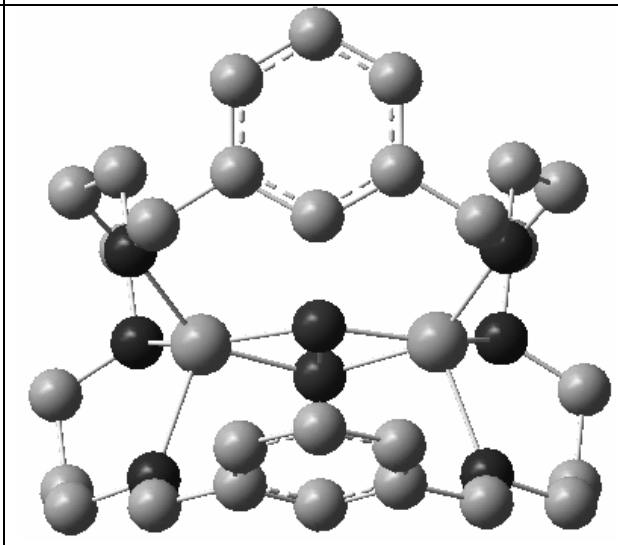	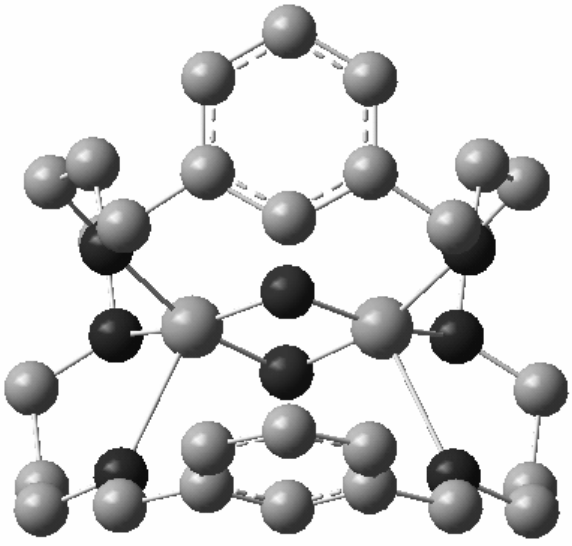

5c	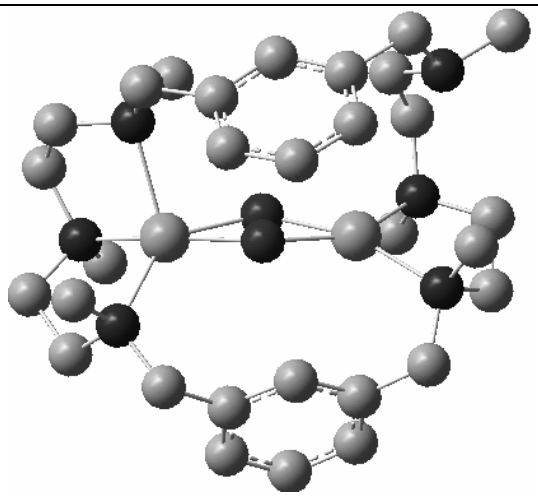	not located
6c	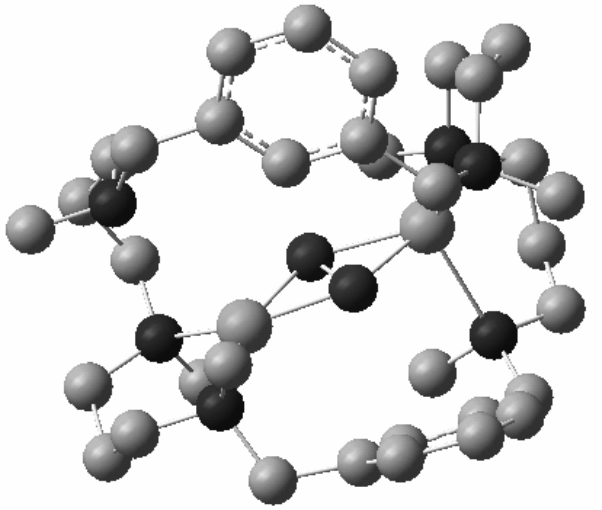	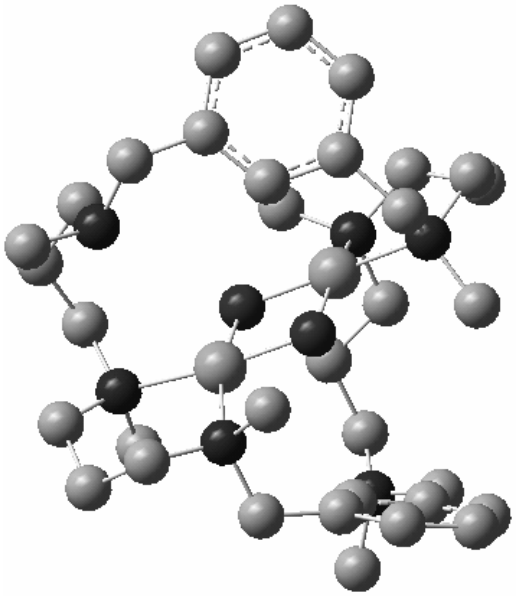
7c	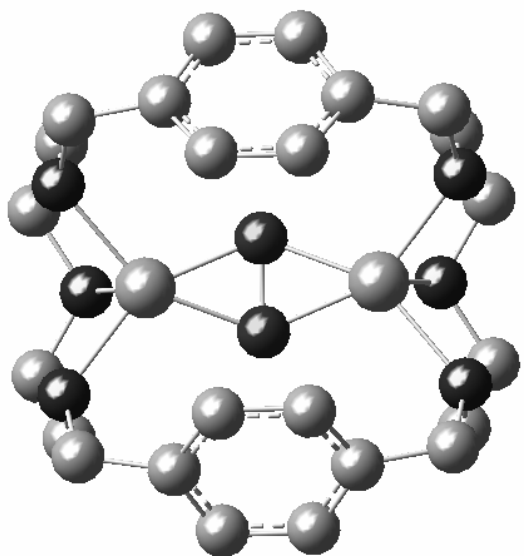	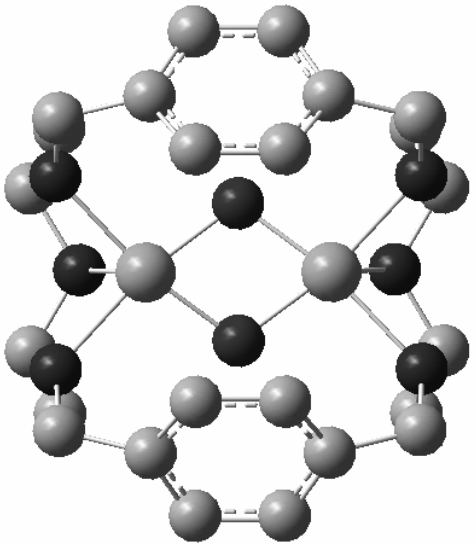

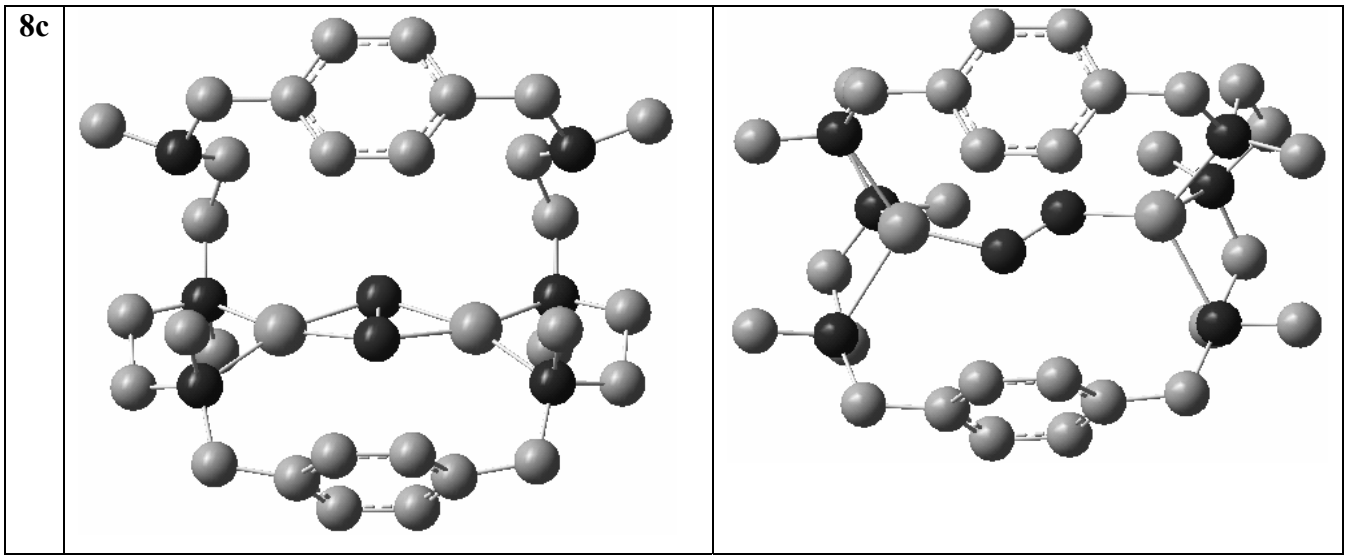

Figure VII- 5. Intermediates **1c-8c**.

	1c-I	**1c**-II	**2c**-I	**2c**-II	**3c**-I	**3c**-II	**4c**-I	**4c**-II	**5c**-I	**6c**-I	**6c**-II	**7c**-I	**7c**-II	**8c**-I	**8c**-II
Cu1-Cu2	3.618	2.860	3.606	2.863	3.485	2.755	3.594	2.848	3.572	3.603	2.810	3.568	2.889	3.480	4.636
O1-O2	1.430	2.197	1.432	2.321	1.447	2.220	1.444	2.210	1.449	1.443	2.230	1.434	2.136	1.475	1.351
Cu1-N1	2.059	2.060	2.019	2.556	2.047	2.012	2.250	2.584	2.030	2.326	4.784	2.073	2.066	2.033	2.196
Cu1-N2	2.012	1.972	2.028	1.952	2.243	2.374	2.035	1.994	1.996	2.026	2.008	2.244	2.361	1.985	2.147
Cu1-N3	2.156	2.369	2.201	1.957	2.060	2.030	2.024	2.017	3.527	2.101	1.998	2.073	2.066	3.657	2.112
Cu2-N4	2.149	2.364	2.156	1.949	2.038	2.032	2.035	2.018	2.242	3.303	3.647	2.073	2.066	3.657	2.108
Cu2-N5	2.004	1.972	2.003	1.986	2.255	2.350	2.024	1.995	2.045	2.013	2.005	2.244	2.361	1.985	2.037
Cu2-N6	2.079	2.063	2.097	2.497	2.045	2.040	2.250	2.579	2.110	2.016	2.011	2.073	2.066	2.033	2.277
Cu1-O1	2.024	1.846	1.975	1.819	1.933	1.792	1.980	1.819	1.877	2.039	1.793	1.940	1.807	1.919	1.873
Cu1-O2	1.884	1.774	1.914	1.889	1.913	1.805	1.901	1.788	1.918	1.892	1.794	1.940	1.807	1.883	2.895
Cu2-O1	2.033	1.847	1.998	1.832	1.925	1.798	1.980	1.820	2.050	1.894	1.798	1.940	1.807	1.919	2.882
Cu2-O2	1.881	1.773	1.901	1.909	1.920	1.801	1.901	1.789	1.890	1.942	1.789	1.940	1.807	1.883	1.856
C_{ar}-H_{ar}	1.079	1.079	1.080	1.101	1.087	1.086	1.083	1.082	1.087	1.083	1.082	1.087	1.087	1.087	1.088
O1-C_{ar}	3.833	4.107	3.759	3.638	3.964	4.310	4.044	4.420	3.728	3.834	3.797	3.150	3.098	4.547	3.949
O2-C_{ar}	2.708	2.262	2.546	1.454	2.750	2.600	2.611	2.211	2.737	2.828	3.092	3.955	4.241	3.122	2.878
O1-H_{ar}	3.076	3.556	3.206	3.751	3.544	3.768	3.553	4.202	3.857	3.566	3.425	3.726	3.749	3.780	4.470
O2-H_{ar}	2.272	2.243	2.324	2.064	2.654	2.601	2.139	2.153	2.580	2.952	2.381	4.206	4.419	3.780	3.330
Cu1-O1-Cu2	126.3	101.5	130.4	103.3	129.2	99.6	130.3	103.0	130.9	132.7	103.0	133.7	106.2	130.1	153.8
Cu1-O2-Cu1	147.9	107.5	141.9	97.8	130.8	100.2	142.0	105.5	139.5	140.0	103.3	133.7	106.2	135.0	154.1
O1-Cu1-O2	42.8	74.7	43.2	77.5	44.2	76.2	43.6	75.6	44.9	42.8	76.9	43.4	72.5	45.6	21.8
O1-Cu2-O2	42.7	74.7	43.0	76.7	44.2	76.2	43.6	75.5	42.9	44.2	76.9	43.4	72.5	45.6	21.9
N-Cu1-N	86.2	84.4	100.5	99.4	106.1	97.4	98.9	94.8	91.4	102.5	100.9	101.5	93.4	90.3	86.2
N-Cu2-N	85.3	84.5	100.9	99.9	108.0	95.6	98.9	94.9	89.2	106.5	100.1	101.5	93.4	90.3	88.0

Table VII-3. Structural data for intermediates **1c-8c**.

For intermediate **8c** we have only found two different Cu^{II} isomers. The isomer depicted in the left part presents each copper atom bonded to two nitrogen atoms, and without any connection with the third amine. Nevertheless it is amazing to observe that copper remains in oxidation state II instead of changing to Cu^{III}. The other isomer shows an asymmetric insertion of the molecular oxygen with a strong O-O bond, very short, 1.351 Å, and it presents a triplet multiplicity. This state is 16.4 $kcal \cdot mol^{-1}$ more stable than the singlet state. Therefore the para substitution of the aromatic rings in addition to the permethylation of the all the six amine groups of the macrocycle makes impossible to obtain similar structures as the ones obtained for **1c-7c**.

Two of these compounds have been found to activate an aromatic C-H bond of the same macrocycle. In principle these structures would have to be intermediates **1c** and **4c**. The key factor to predict the reactivity from a computational point of view was to observe the sum of the $O\text{-}C_{ar}$ and $O\text{-}H_{ar}$ bond distances. If this sum is higher than 5 Å no intramolecular C-H bond activation is possible. Only three compounds follow this rule, nevertheless intermediate **2c** has been experimentally proved to be non reactive.

Intermediate **4c** has been further analyzed to try to find the reaction path that leads to the product that is obtained experimentally. The attack of the molecular oxygen can be either σ or π. The first one gives a similar product to the one obtained experimentally, whereas the second one gives a product that after a flip of one phenyl group and small rearrangements of the macrocycle becomes the same product of the σ reaction path. The details of both mechanisms are depicted in Scheme VII-5.

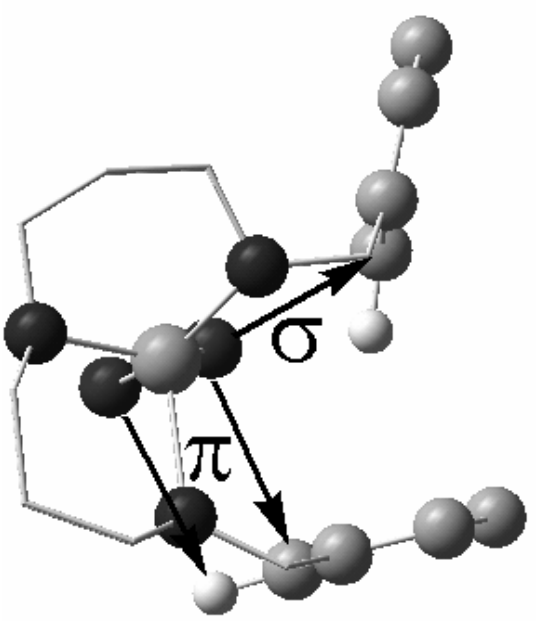

Scheme VII-5. σ and π mechanisms for intermediate **4c** (most of the hydrogen atoms as well as some carbon atoms have been omitted or simplified for clarity).

The mechanism called σ supposes the interaction with the top phenyl ring of the intermediate, based on the direct attack of one oxygen to one aromatic C-H bond, whereas in the π mechanism the attacking oxygen atoms interact with the aromatic ring placed below the Cu_2O_2 core, both oxygen atoms attack simultaneously the C-H bond of the other aromatic ring. In Figure VII-6 there are two views of each minimum and transition state for the σ-mechanism. In spite of the lack of some structures because they have not been characterized by frequencies, we have linear transits that give an upper bound to the actual energy barriers.

4c-I	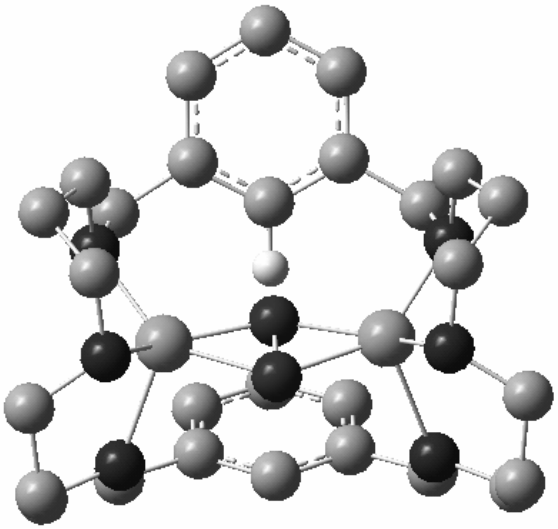	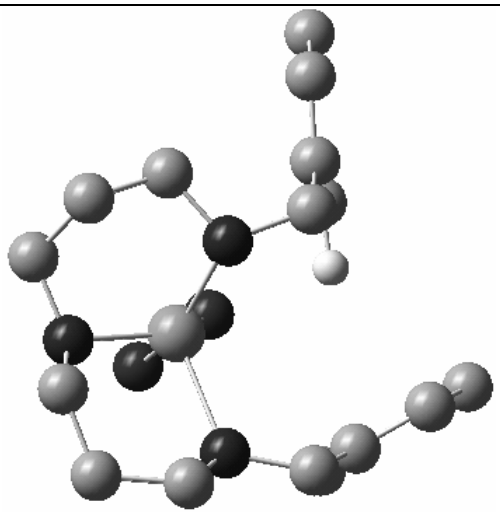
4c-TSI	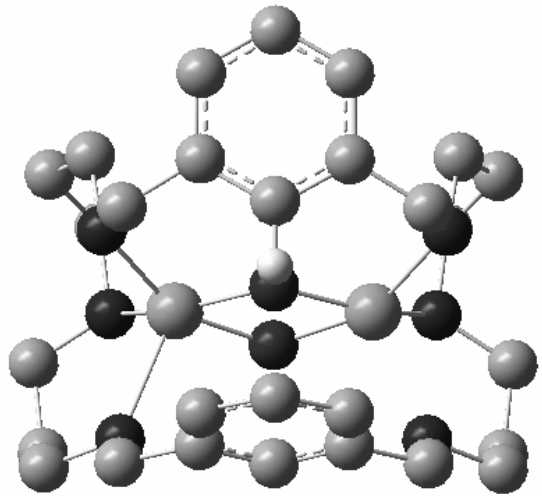	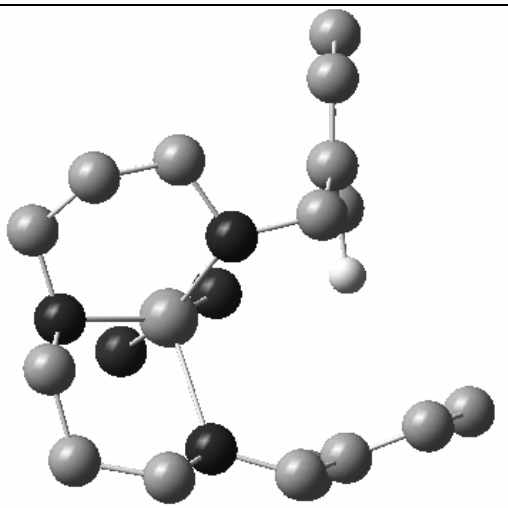
4c-II	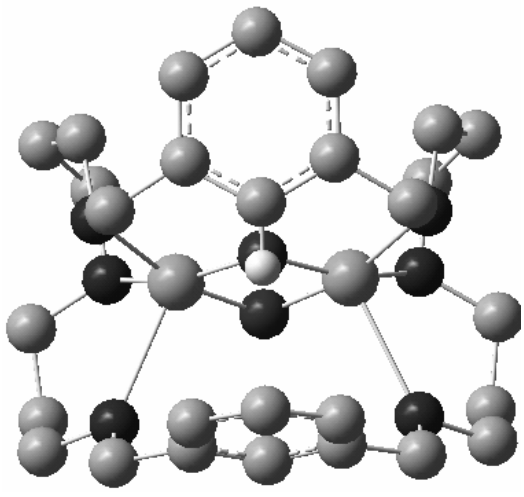	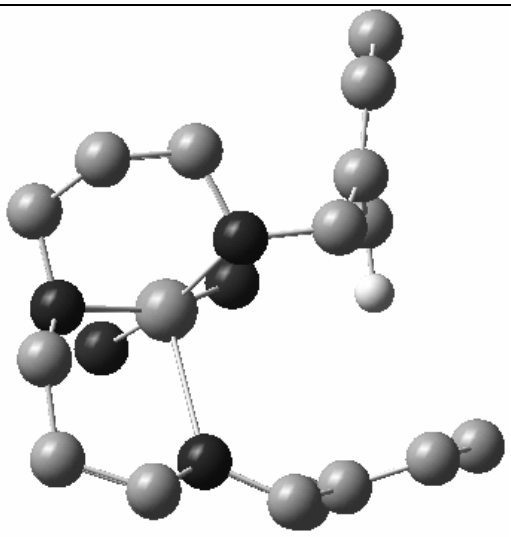

4c-TSII	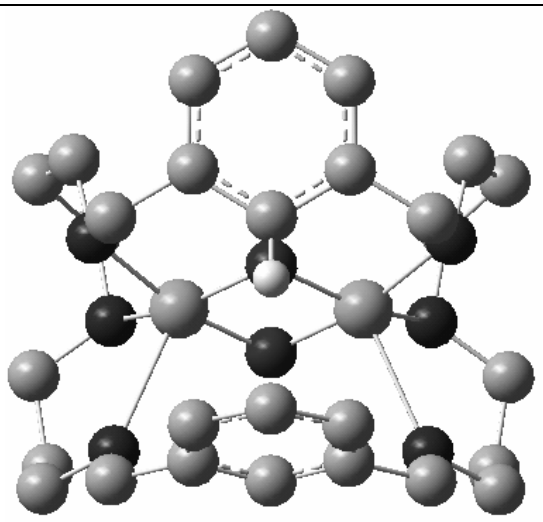	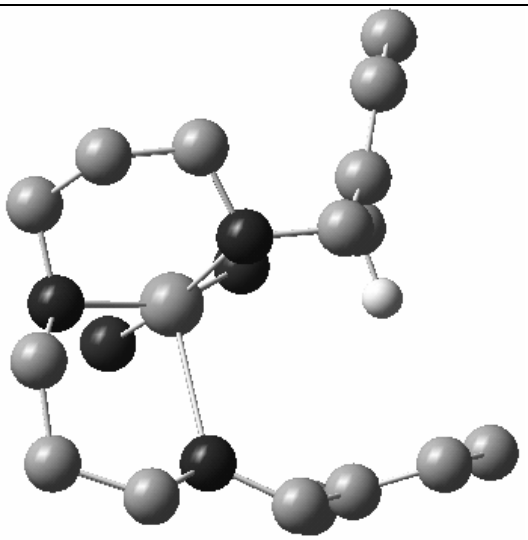
4c-III	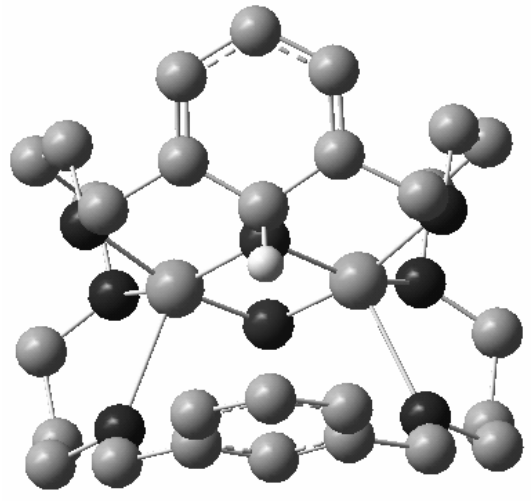	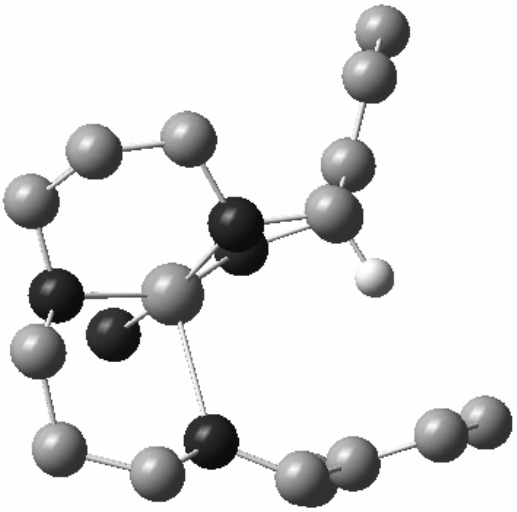
4c-IV	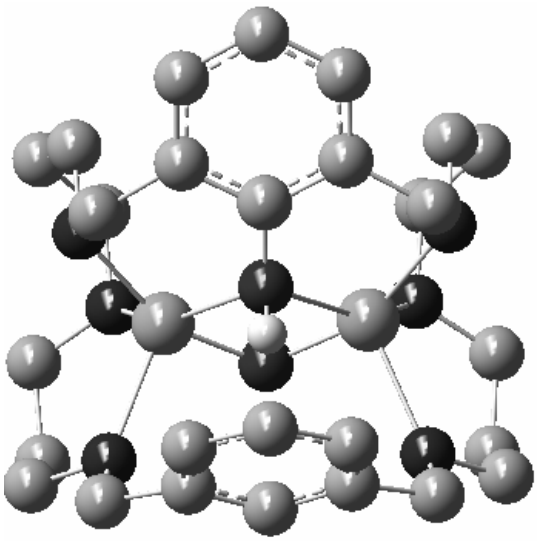	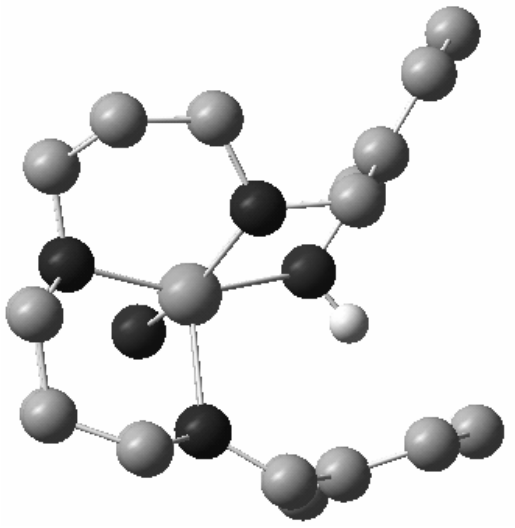

4c-V	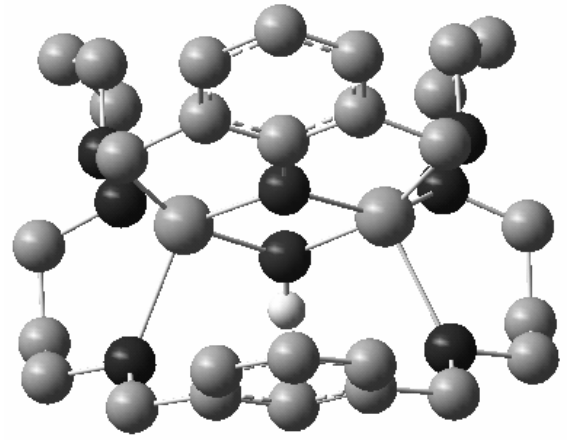	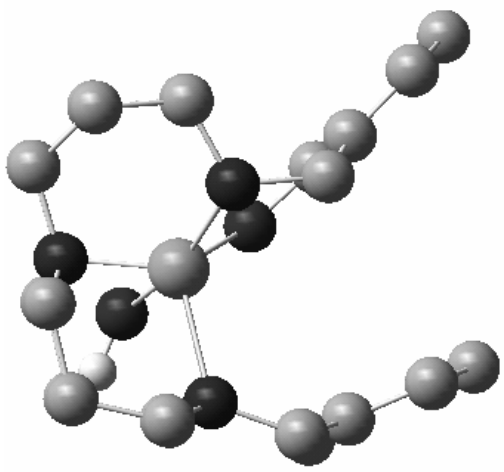

Figure VII- 6. All the characterized (by frequencies) species of **4c** involved in the σ-mechanism (all the hydrogen atoms have been omitted for clarity except the one involved in the reaction mechanism).

The pictures depicted in the right part of Figure VII-6 show that to achieve the intramolecular product the phenyl rings rotate to be at the end nearly in the same plane as the Cu_2O_2 core, which was placed first approximately perpendicular. TSIII and TSIV have not been located yet. Figure VII-7 collects the full energetic diagram from I to V.

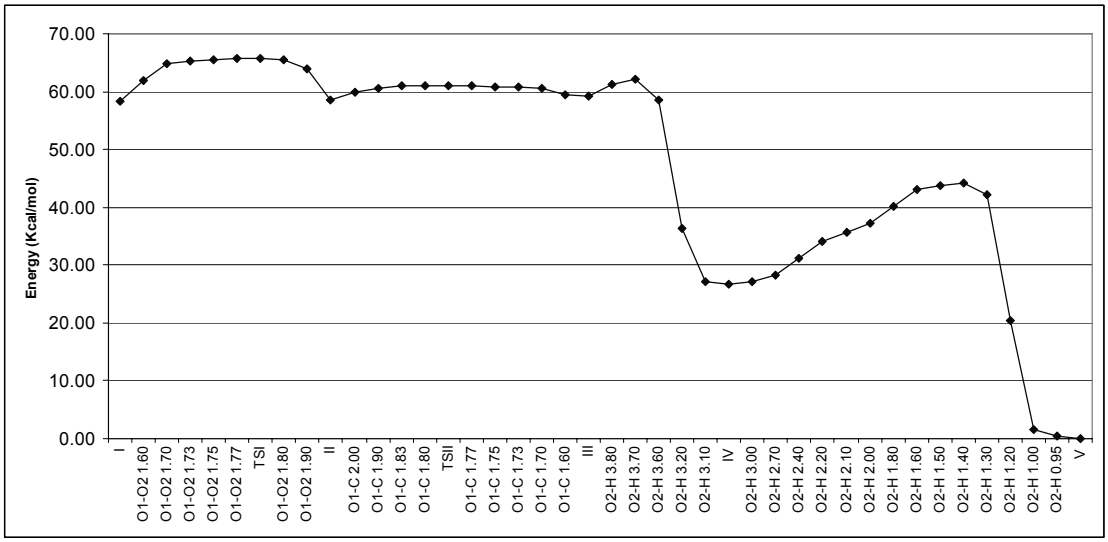

Figure VII-7. Reaction path from I to V species of complex **4** involved in the σ-mechanism.

The intermediates and transition state structures involved in the π-mechanism are depicted in Figure VII-8. The energetic diagram of Figure VII-9 reflects that the most favorable mechanism from an energetic point of view is the σ one because TSI is higher in energy with respect to I for the π-mechanism. Nevertheless the π-mechanism is very similar to the σ-mechanism because the approach of both oxygen atoms in a parallel way to the axis defined by the aromatic C-H bond is not favored energetically. Furthermore, experimentally the structure characterized by X-ray that is the final product of the intramolecular reaction can also be obtained by the product of the π-mechanism but after a rotation of a phenyl ring and some other little molecular rearrangements.

4c-I	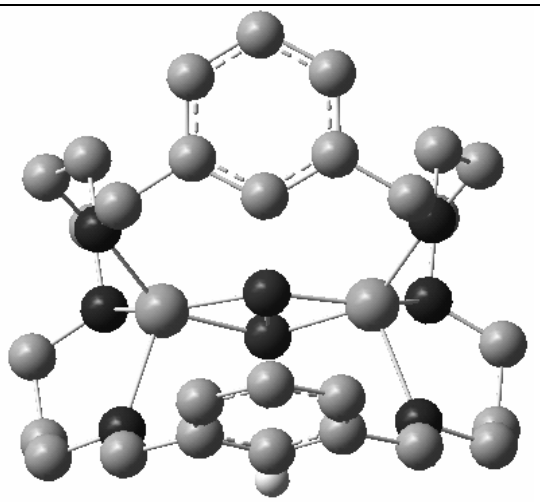	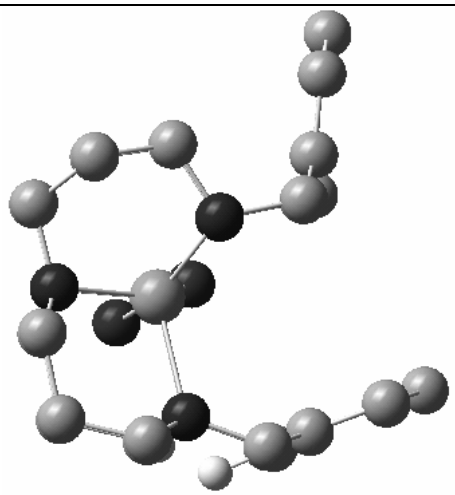
4c-TSI	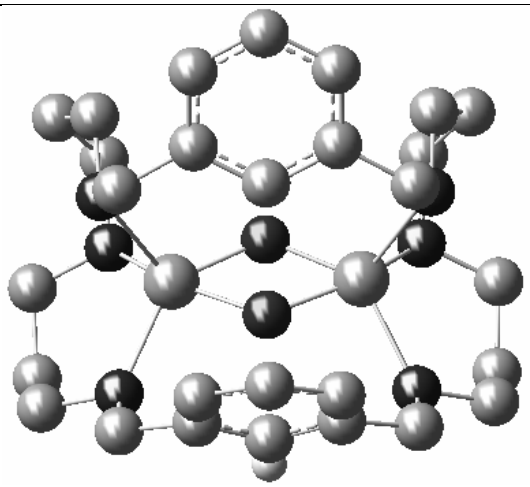	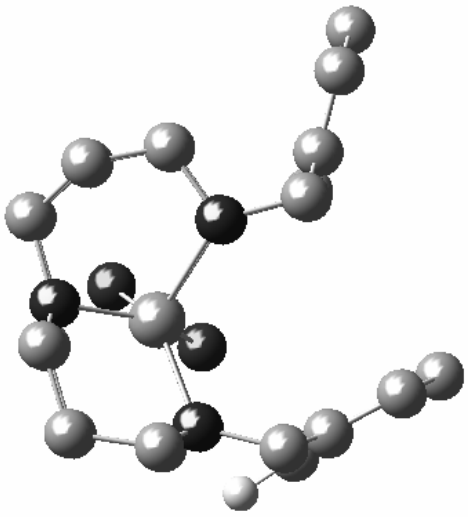

4c-II	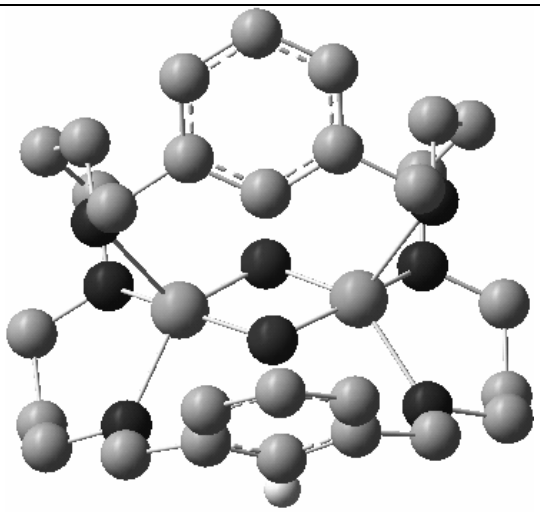	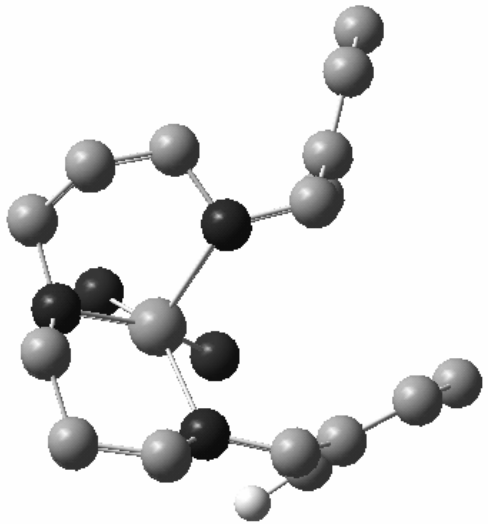
4c-III	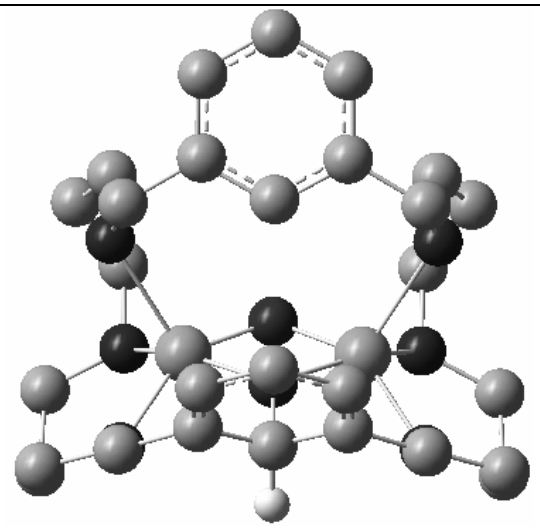	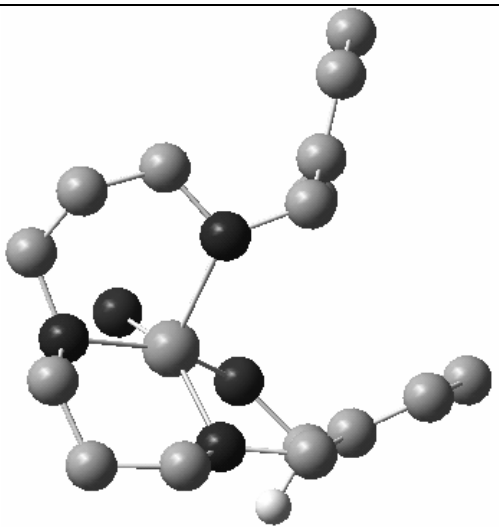
4c-V	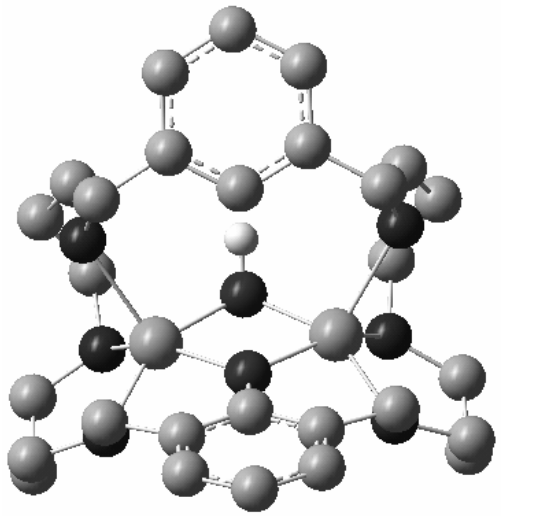	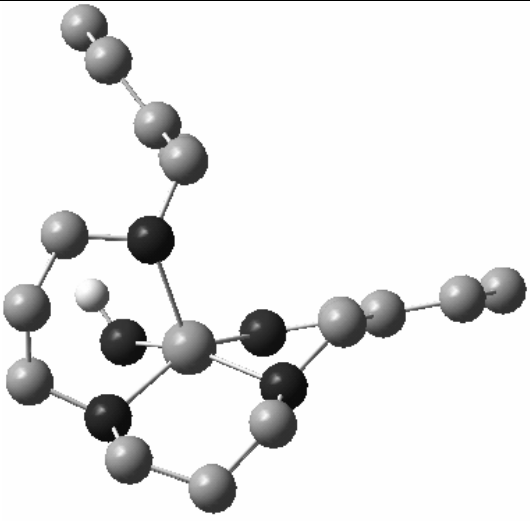

Figure VII-8. All the characterized (by frequencies) species of complex **4** involved in the π-mechanism (all the hydrogen atoms have been omitted for clarity except the one involved in the reaction mechanism).

Figure VII-9 reveals the energy of the species of the reaction path for π-mechanism. Species II is 5.6 kcal·mol^{-1} less stable than the one presented in σ-mechanism. Furthermore, TSI is 10.5 kcal·mol^{-1} higher in energy with respect to I, for the σ-mechanism this difference was smaller, 7.3 kcal·mol^{-1}. These energetic results show that the σ-mechanism is favored with respect to π-mechanism.

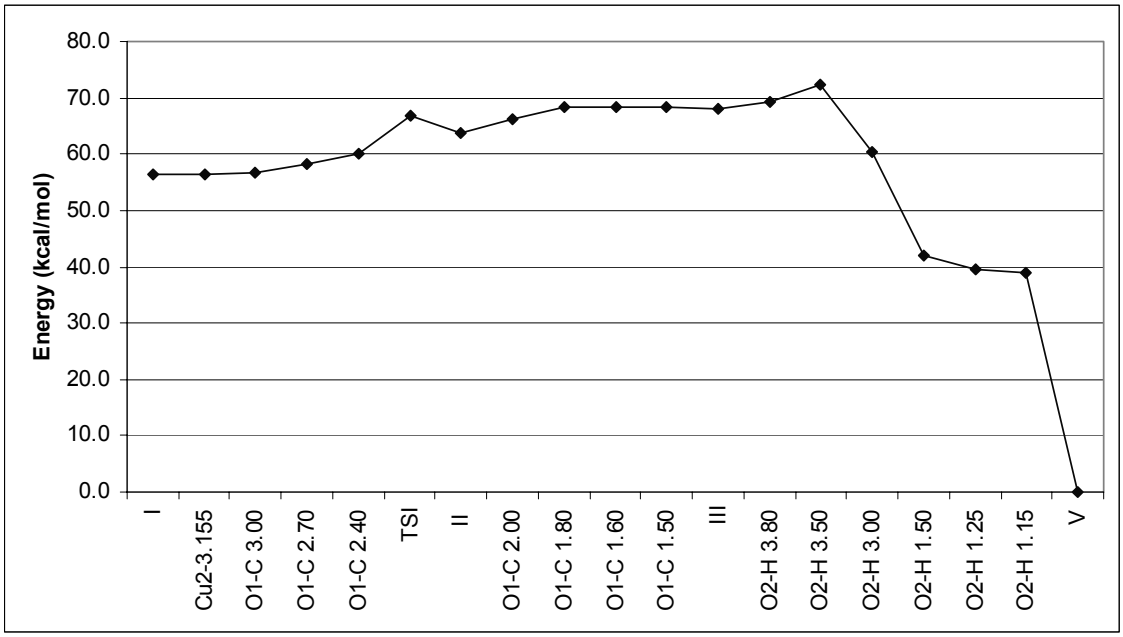

Figure VII-9. Reaction path from I to V species of complex **4** involved in the π-mechanism.

Among **1c**-**8c** intermediates, only another isomer, **1c**, is experimentally able to succeed by the same intramolecular aromatic C-H bond activation as **4c**. The mechanism is depicted in Figure VII-10. And the energetic diagram is represented in Figure VII-11. It is not necessary to study the π-mechanism because of the similarity of the possible attacks of the oxygen atoms for this intermediate. Therefore we have chosen the interaction with the nearest oxygen atom with respect to an aromatic C atom. The achievement of the I, TSI, II, III, and IV structures supposes the same mechanism as for **4c**. After this, the activated aromatic hydrogen atom can go directly to oxygen 2, without being attached to the oxygen 1. Nevertheless the energetic barrier to go directly is very high and this means that the mechanism is favored through different steps, displaying extrema with the hydrogen atom attached to oxygen 1.

1c-I	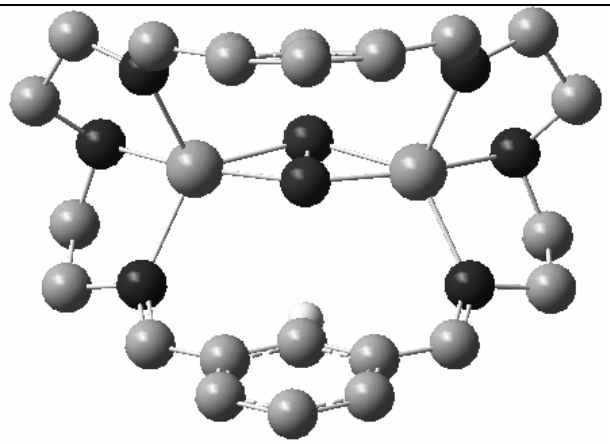	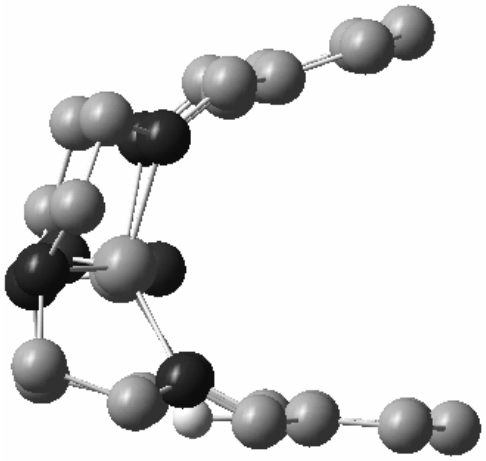
1c-TSI	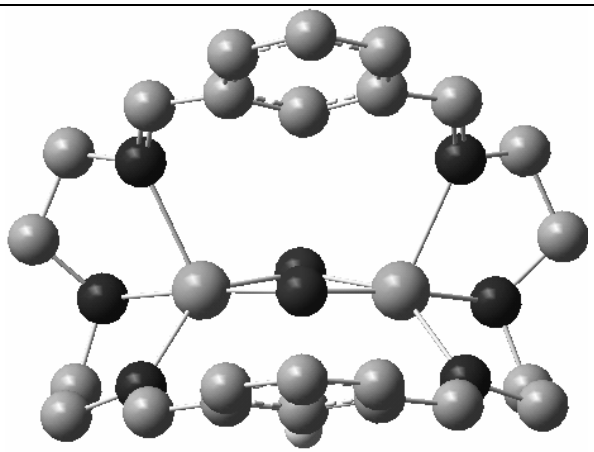	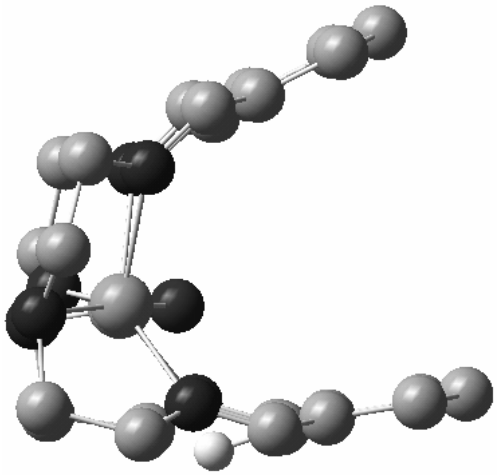
1c-II	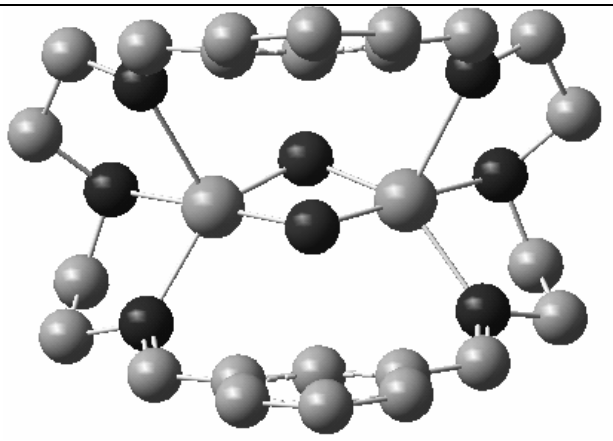	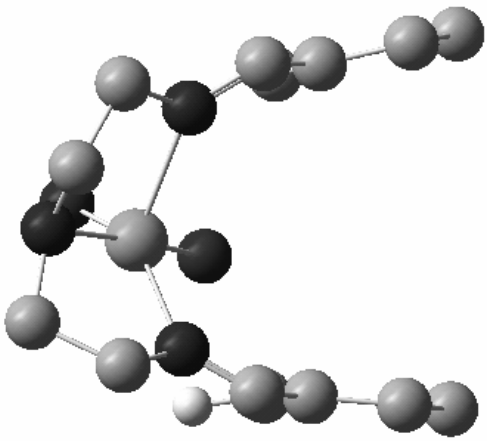

1c-III	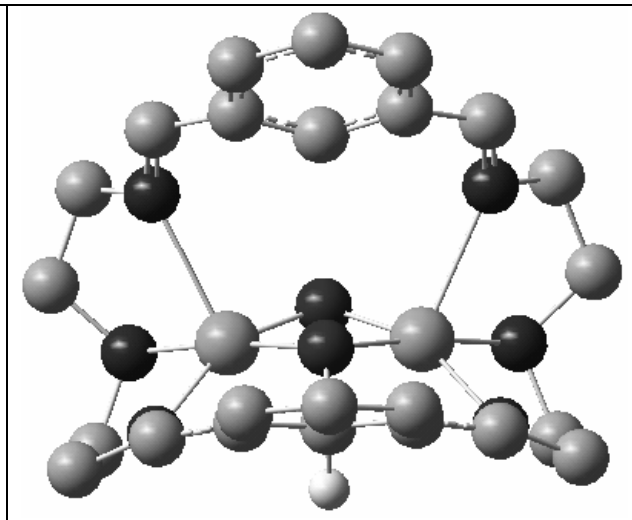	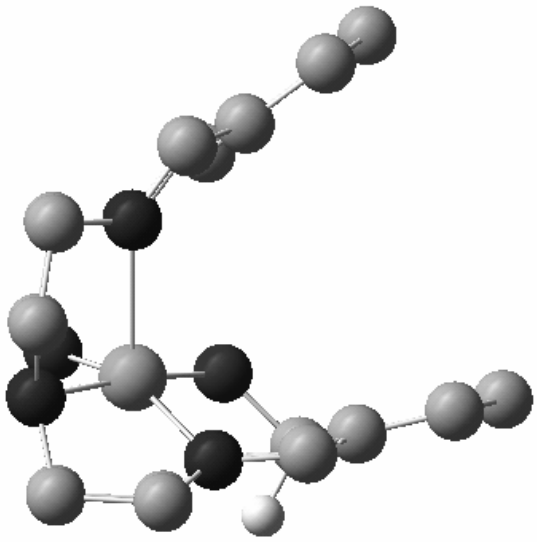
1c-IV	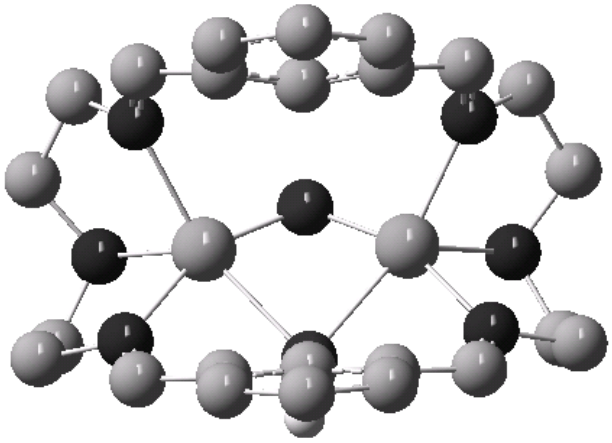	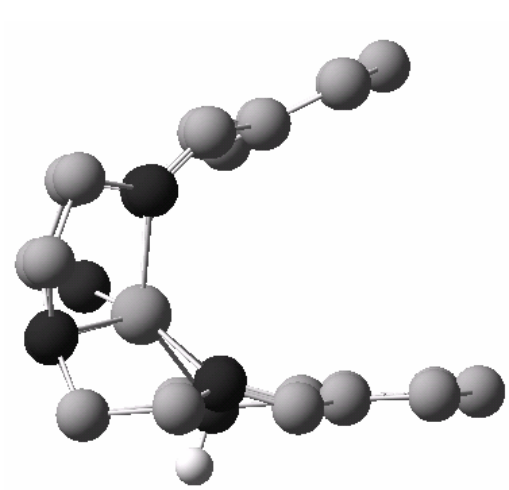
1c-V	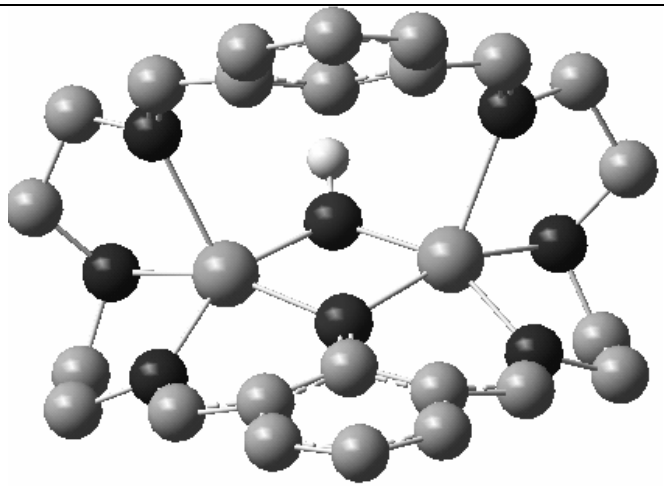	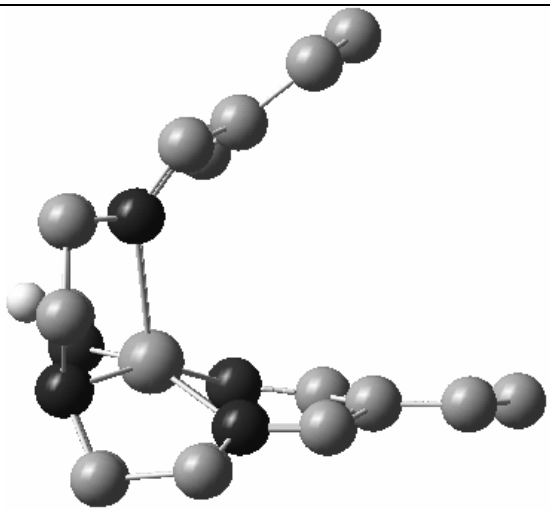

Figure VII-10. All the characterized (by frequencies) species of complex **1c** involved in the σ-mechanism (all the hydrogen atoms have been omitted for clarity except the one involved in the reaction mechanism).

Finally, although there are some structures of the σ-mechanism for **1c** that have not been located, the available results and the attempts to obtain new structures show that the mechanism is similar to the **4c** one. The reaction path is reflected in Figure VII-11.

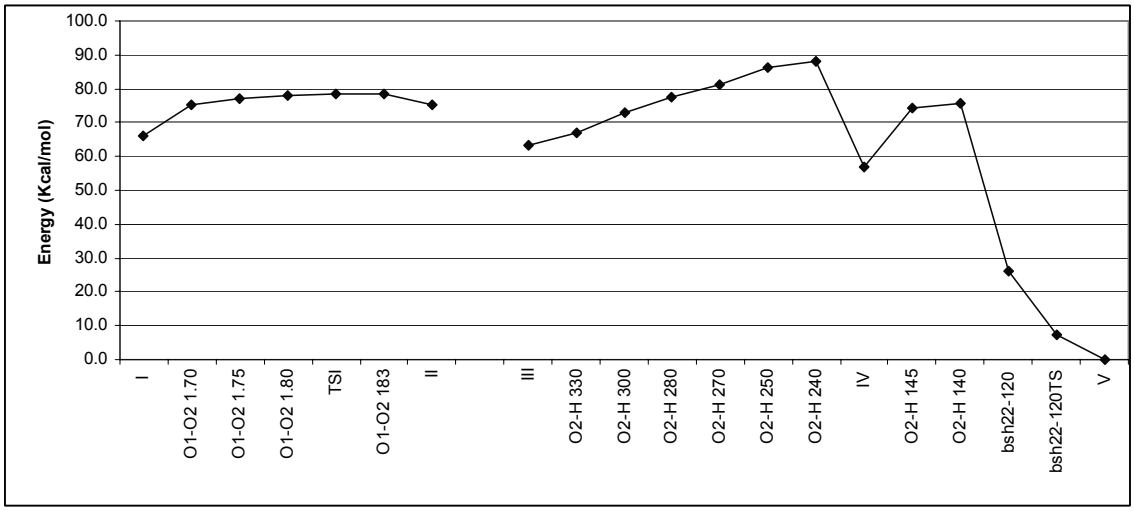

Figure VII-11. Reaction path from I to V species of complex **1c** involved in the σ-mechanism.

All the structures not located for these complexes are now being further studied.

Conclusion

In summary, comparison of the dioxygen chemistry associated to $[Cu(MeAN)]^+$, **1** and **2** constitutes a remarkable example of the importance of the cooperative role of two metal centers in the activation of O_2 and highlights the challenge in designing suitable dinuclear scaffolds for modeling O_2 processing proteins containing a dimetallic active site. Furthermore the intramolecular aromatic C-H bond activation has been shown to proceed through a σ-mechanism for complex **4c**.

References

1. a) E. I. Solomon, U. M. Sundaram, T. E. Machonkin, *Chem. Rev*. **1996**, *96*, 2563-2605. b) E. I. Solomon, P. Chen, M. Metz, S.-K. Lee, A. E. Palmer, *Angew. Chem. Int. Ed*. **2001**, *40*, 4570-4590.
2. K. A. Magnus, H. Ton-That, J. E. Carpenter, *Chem. Rev*. **1994**, *94*, 727-735.

3. a) L. M. Mirica, X. Ottenwaelder, T. D. P. Stack, *Chem. Rev*. **2004**, *114*, 1013-1046. b) E. A. Lewis, W. B. Tolman, *Chem. Rev.* **2004**, *114*, 1047-1076.
4. a) K. D. Karlin, M. S. Nasir, B. I. Cohen, R. W. Cruse, S. Kaderli, A. D. Zuberbühler, *J. Am. Chem. Soc*. **1994**, *116*, 1324-1336. b) E. Pidcock, H. V. Obias, C. X. Zhang, K. D. Karlin, E. I. Solomon, *J. Am. Chem. Soc*. **1998**, *120*, 7841-7847.
5. L. Santagostini, M. Gullotti, E. Monzani, L. Casella, R. Dillinger, F. Tuczek, *Chem. Eur. J*. **2000**, *6*, 519-522.
6. M. Costas, R. Xifra, A. Llobet, M. Solà, J. Robles, T. Parella, H. Stoeckli-Evans, M. Neuburger, *Inorg. Chem*. **2003**, *42*, 4456-4468.
7. H.-C. Liang, C. X. Zhang, M. J. Henson, R. D. Sommer, K. R. Hatwell, S. Kaderli, A. D. Zuberbühler, A. L. Rheingold, E. I. Solomon, K. D. Karlin, *J. Am. Chem. Soc*. **2002**, *124*, 4170-4171.
8. Crystal structure data analysis for $1(BArF)_2$: $C_{98}H_{82}B_2Cu_2F_{48}N_6$, Mf = 2404.40, monoclinic, P21/n, a = 13.073(5), b = 27.978(12), c = 13.464(6) Å, β = 96.633(7), V = 4891 (3) $Å^3$, Z = 2, T = 100(2) K, δ_{calc} = 1.633 $Mg{\cdot}M^{-3}$, μ = 0.578 mm^{-1}, R_1 = 0.0510, WR_2 = 0.1057. $2(SbF6)_2$: $C_{28}H_{56}Cu_2F_{12}N_6Sb_2$, Mf = 1075.37, monoclinic, P21/c, a = 16.264(4), b = 15.169(4), c = 17.642(5) Å, β = 103.776(4), V = 4227(2) Å3, Z = 4, T = 100(2) K, δ_{calc} = 1.690 $Mg{\cdot}M^{-3}$, μ = 2.337 mm^{-1}, R_1 = 0.0305, WR_2 = 0.0772.
9. A. Company, D. Lamata, A. Poater, M. Solà, E. Rybak-Akimova, L. Que, X. Fontrodona, T. Parella, A. Llobet, M. Costas, *Inorg. Chem.*, submitted.
10. When CO was bubbled through an acetone solution with $1(CF_3SO_3)_2$ prepared in situ from $Cu(CH_3CN)_4CF_3SO_3$ and L1 a $\nu_{str}(CO)$ = 2069 cm^{-1} is measured (see ref 6).
11. All the attempts to obtain a Cu(II)/Cu(I) red-ox potential by cyclic voltametry were unsuccessful.
12. a) P. Holland, C. J. Cramer, E. C. Wilkinson, S. Mahapatra, K. R. Rodgers, S. Itoh, M. Taki, S. Fukuzumi, L. Que Jr., W. B. Tolman, *J. Am. Chem. Soc*. **2000**, *122*, 792-802. b) L. Que Jr., W. B. Tolman, *Angew. Chem. Int. Ed*. **2002**, *41*, 1114-1137.
13. $Cu_2^{III}(\mu\text{-}O)_2$ species have been described for xylyl-bridged TACN systems, but resulting from intermolecular interaction of Cu ions. See S. Mahapatra, S. Kaderli,

A. Llobet, Y.-M. Neuhold, T. Palanche, J. A. Halfen, V. G. Young Jr., T. A. Kaden, L. Que Jr., A. D. Zuberbühler, W. B. Tolman, *Inorg. Chem*. **1997**, *36*, 6343-6356.

14. J. A. Halfen, S. Mahapatra, E. C. Wilkinson, S. Kaderli, V. G. Young Jr., L. Que Jr., A. D. Zuberbühler, W. B. Tolman, *Science* **1996**, *271*, 1397-1400.
15. From a kinetic point of view, O_2 binding appears to be essentially irreversible at low temperatures and O_2 release appears to be significant only at higher temperatures. However analysis of these reactions is complicated by the onset of rapid thermal decomposition.
16. See ref 7. Reported kinetic parameters for the oxygenation of $[Cu(MeAN)]^+$ in CH_2Cl_2 are $\Delta H^{\ddagger} = -27$ kJ·mol^{-1} and $\Delta S^{\ddagger} = -335$ J·K^{-1}·mol^{-1}.
17. a) A. D. Becke, *J. Chem. Phys.* **1993**, *98*, 5648-5652. b) C. Lee, W. Yang, R. G. Parr, *Phys. Rev. B* **1988**, *37*, 785-789. c) P. J. Stevens, F. J. Devlin, C. F. Chablowski, M. J. Frisch, *J. Phys. Chem*. **1994**, *98*, 11623-11627. d) J. P. Perdew, Y. Wang, *Phys. Rev. B* **1992**, *45*, 13244-13249.
18. W. J. Hehre, R. Ditchfield, J. A. Pople, *J. Chem. Phys*. **1972**, *56*, 2257-2261.
19. Gaussian 03, M. J. Frisch, G. W. Trucks, H. B. Schlegel, G. E. Scuseria, M. A. Robb, J. R. Cheeseman, J. A. Montgomery, Jr., T. Vreven, K. N. Kudin, J. C. Burant, J. M. Millam, S. S. Iyengar, J. Tomasi, V. Barone, B. Mennucci, M. Cossi, G. Scalmani, N. Rega, G. A. Petersson, H. Nakatsuji, M. Hada, M. Ehara, K. Toyota, R. Fukuda, J. Hasegawa, M. Ishida, T. Nakajima, Y. Honda, O. Kitao, H. Nakai, M. Klene, X. Li, J. E. Knox, H. P. Hratchian, J. B. Cross, C. Adamo, J. Jaramillo, R. Gomperts, R. E. Stratmann, O. Yazyev, A. J. Austin, R. Cammi, C. Pomelli, J. W. Ochterski, P. Y. Ayala, K. Morokuma, G. A. Voth, P. Salvador, J. J. Dannenberg, V. G. Zakrzewski, S. Dapprich, A. D. Daniels, M. C. Strain, Ö. Farkas, D. K. Malick, A. D. Rabuck, K. Raghavachari, J. B. Foresman, J. V. Ortiz, Q. Cui, A. G. Baboul, S. Clifford, J. Cioslowski, B. B. Stefanov, G. Liu, A. Liashenko, P. Piskorz, I. Komaromi, R. L. Martin, D. J. Fox, T. Keith, M. A. Al-Laham, C. Y. Peng, A. Nanayakkara, M. Challacombe, P. M. W. Gill, B. Johnson, W. Chen, M. W. Wong, C. Gonzalez, J. A. Pople, Gaussian, Inc., Pittsburgh PA, 2003.

PART III: Copper Clusters

Chapter VII: *Molecular Structure and Bonding of Copper Cluster Monocarbonyls Cu_nCO (n = 1-9)*

Molecular Structure and Bonding of Copper Cluster Monocarbonyls Cu_nCO (n = 1-9)

Abstract

In this work we analyze CO binding on small neutral copper clusters, Cu_n (n=1-9). Molecular structures and reactivity descriptors of copper clusters are computed and discussed. The results show that the condensed Fukui functions and the frontier molecular orbital theory are useful tools to predict the selectivity of CO adsorption on these small clusters. To get further insight into the CO binding to copper clusters, an energy decomposition analysis of the CO binding energy is performed. The C_s symmetry of the formed Cu_nCO clusters (n=1-8) allows the separation between the orbital interaction terms corresponding to donation and back-donation. It is found that, energetically, the donation is twice as important as back-donation.

Introduction

Transition metal clusters are particularly interesting for their potential use in homogeneous and heterogeneous catalysis and novel optoelectronic materials.[1-3] The number of works devoted to the analysis of metal clusters has grown considerably over the past years as new experimental and theoretical techniques have been developed allowing detailed characterization of this type of systems. These small species are extremely sensitive to the number of atoms, and their properties can sometimes change dramatically with the addition or removal of one or few atoms from the cluster. Most studies in this field have analyzed the dependences of different properties, such as ionization potentials, electron affinities, chemical reactivity, thermochemistry, and ion abundances upon the size of the clusters,[4] and how these properties tend to the bulk values.[5,6]

In particular, copper clusters have been extensively studied both experimentally and theoretically.[7-29] From a theoretical point of view, density functional theory (DFT) calculations for small copper clusters (Cu_n up to n=5) have been performed by Calaminici *et al.*[21] to predict their structures and electronic properties. Jackson has extended this investigation to the electronic properties of the smallest copper clusters,[25] concluding that the participation of the *3d* and *4s* orbitals of copper in the bonding states

of the clusters is significant. Jaque and Toro-Labbé have analyzed the stability and reactivity pattern of the neutral clusters showing that clusters with an even number of copper atoms and a closed-shell electronic structure are more stable than those with an odd number of copper atoms.[29] The static polarizabilities and polarizability anisotropies of copper clusters have been reported by Jackson and Calaminici and co-workers.[23] On the other hand, Jug *et al.* have investigated the electronic and molecular structure of the most stable anionic, cationic, and neutral small copper clusters.[26] Finally, other studies have compared the properties of these small clusters with those of the copper surface.[30,31]

The interaction of metal clusters with small molecules has centered part of the interest of several works.[32-35] For Cu_nCO clusters, Cao *et al.*[32] have observed that the static mean polarizability increases monotonically as the size of the copper cluster carbonyl increases, while the mean polarizability per atom has a decreasing oscillating behavior. In that paper, the authors have also computed the CO binding energies and have discussed the selectivity of CO adsorption on copper clusters. Despite their important contribution, Cao and co-workers[32] did not analyze in their work the nature of the chemical bond in copper cluster monocarbonyls. In particular, the study of the relative importance of donation and back-donation in the binding of CO to Cu_n as a function of the size of the cluster remains to be done yet. Here, we report an accurate structural and electronic characterization of neutral copper clusters Cu_n (n=1-9) and of their monocarbonyls. The binding of CO to Cu_n is analyzed by means of an energy decomposition analysis that allows separating the contributions of donation and back-donation to the total CO binding energy. Previous works have shown the relevance of chemical electronic reactivity descriptors such as the chemical potential (μ), chemical hardness (η), and electrophilicity index (ω), defined within the framework of DFT to understand the reactivity pattern of molecules and molecular aggregates.[5,29-31,36-39] In the present work, we discuss the use of the condensed Fukui functions to predict the selectivity of CO adsorption on copper clusters.

Computational details

The reported calculations were carried out by using the 2002.03 release of Amsterdam density functional (ADF) package[40] developed by Baerends *et al.*[41-43] The numerical

integration scheme employed was that of te Velde and Baerends.[44] Both geometry optimizations and energy evaluations were performed using a generalized gradient approximation (GGA) that includes the GGA exchange correction of Becke[45] and the GGA non-local correlation of Perdew and Wang,[46] that is, the so-called BPW91 functional. The optimization process was based on the gradients scheme developed by Ziegler *et al*.[47] The vibrational harmonic frequencies were calculated by the force constants obtained by the numerical differentiation of the energy gradients.[48] The kinetic relativistic effects are not important for an accurate calculation of copper clusters and they were ignored in our calculations.[49] All calculations were performed using an uncontracted triple-ς basis set augmented with two polarization functions for describing the 3s, 3p, 3d, 4s, and 4p orbitals of copper and the 2s and 2p of carbon and oxygen.[50,51] Electrons in lower shells were treated within the frozen core approximation.[41] A set of auxiliary s, p, d, f, and g functions, centered in all nuclei, was introduced in order to fit the molecular density and Coulomb potential accurately in each SCF cycle.[52] Molecular orbitals were depicted using the Molekel program.[53]

Depending on the number of copper atoms of each cluster, clusters have an even or odd number of electrons. For this reason, optimizations were done checking different multiplicities to characterize the ground-states, either neutral closed-shell singlet and triplet multiplicities for systems with even number of electrons or open-shell doublet and quadruplet multiplicities for clusters with odd number of electrons. Calculations of open-shell species have been performed within the unrestricted methodology, while the closed-shell singlet molecules have been calculated using the restricted formalism.

Results and discussion

This section is organized as follows. First, we validate the methodology employed by computing a series of chemical properties for the Cu_2 cluster, the simplest of the systems studied. Second, we discuss shortly the structures, and the possible reactivity toward the CO molecule. Finally, we analyze the molecular structures and binding energies of CO in the copper cluster carbonyls and we examine the nature of the Cu-CO chemical bond.

A. The Cu_2 cluster. Validation of the Methodology

We start this section by comparing our results for the smallest Cu_2 cluster with previous experimental and theoretical results.[25-27,29,54] Table VIII-1 lists the Cu-Cu bond length (r_0), the harmonic frequency, the binding energy (BE), the ionization potential (IP), the electron affinity (EA). For comparison purposes, Table VIII-1 also contains values from other theoretical and experimental studies. In general, all GGA and hybrid functionals yield results close to the experimental values. It is found that the BPW91/TZ2P performs generally quite well, being slightly superior to the rest of methodologies analyzed in the calculation of the bond length, frequency, and electron affinity. These results provide confidence on the reliability of the chosen method to reproduce the geometry and the electronic structure of copper clusters. Our BE for Cu_2 is close to that obtained with DFT hybrid methodologies and somewhat inferior to those given by the BLYP[55] and PW86//VWN[26] methods. Our BPW91 value of the BE for Cu_2 becomes slightly worse after the inclusion of the zero-point energy (ZPE) and the basis set superposition error (BSSE) corrections. Although the PW86//VWN method provides a best estimation of the Cu-Cu BE,[26] the rest of the calculated parameters are closer to the experimental results when using BPW91 for energy and geometry optimization calculations. For this reason and because the size of the systems treated in the present work prevents the use of higher levels of theory than DFT, we have decided to carry out our study at the BPW91 level.

Property	**LSDA**[a]	**PW91//VWN**[b]	**PBE**[c]	**BLYP**[d]	**B3LYP**[e]	**B3PW91**[c]	**BPW91**	**Exp.**
r_0 (Å)	2.18	2.21	2.27	2.257	2.18	2.254	2.227	2.22[f]
$\nu(cm^{-1})$	292	269	236	263	256	260	267	265[f]
BE (eV)[g]	2.72	2.22 (2.08)	2.21	2.1	2.02	1.93	1.95 (1.91)	2.08[h]
IP (eV)	8.61	8.73	8.36	/	/	7.80	8.23	7.9042[i]
EA (eV)	0.97	0.96	0.93	/	/	0.59	0.83	0.836[j]

[a] From Ref. 25. [b] From Ref. 26. [c] From Ref. 29. [d] From Ref. 55. [e] From Ref. 32. [f] From Ref. 27. [g] In parentheses there are the BE values corrected by BSSE and ZPE [h] From Ref. 28. [i] From Ref. 17. [j] From Ref. 15.

Table VIII-1. Theoretical and experimental results for some of the structural and electronic properties of Cu_2.

B. Bare Copper Clusters Cu_n (n=2-9)

1. Molecular Structures and Stabilities. The optimized structures of the ground state of the studied neutral copper clusters are depicted in Figure VIII-1. If the number of copper atoms is even, the ground state is singlet, and doublet otherwise. In the particular case of the Cu_2 cluster the triplet excited state is 38.8 kcal·mol^{-1} less stable than the singlet ground state. From Cu_3 to Cu_6 the most stable clusters are planar, and the rest are tridimensional (3D). These nine structures apart from being energy minima represent the most stable structure for each n. Other structures of Cu_5* and Cu_6* are also depicted in Figure VIII-1. These are not the most stable structures for the bare copper clusters, but they become the most stable in the corresponding copper cluster carbonyls.

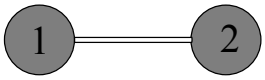

Cu_2	$D_{\infty h}$
r_{12}	2.227

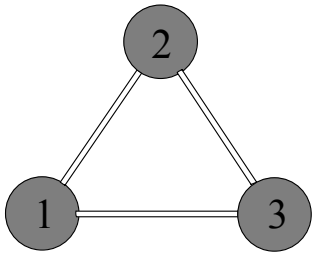

Cu_3	C_{2v}
r_{12}	2.290
r_{13}	2.585

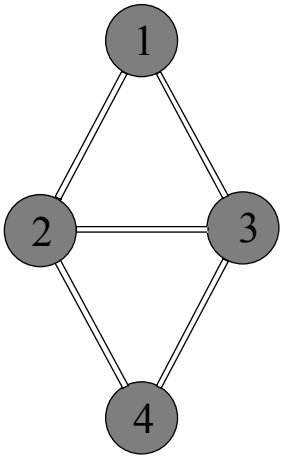

Cu_4	D_{2h}
r_{12}	2.398
r_{23}	2.266

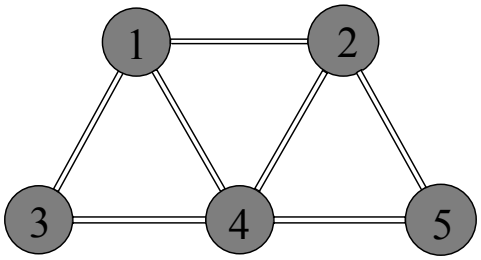

Cu_5	C_{2v}
r_{12}	2.409
r_{13}	2.370
r_{14}	2.405
r_{34}	2.352

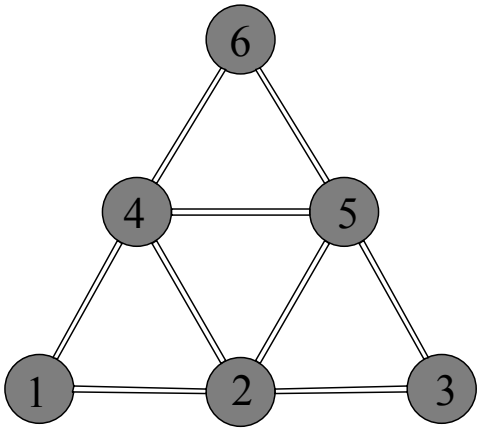

Cu_6	D_{3h}
r_{12}	2.358
r_{25}	2.430

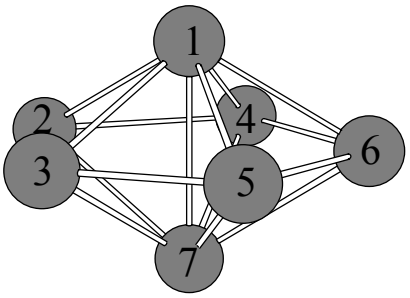

Cu_7	D_{5h}
r_{12}	2.440
r_{17}	2.555
r_{23}	2.444

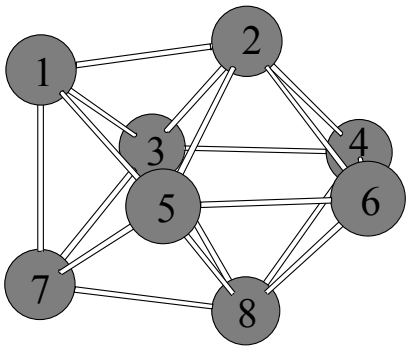

Cu_8	C_{2v}
r_{12}	2.392
r_{15}	2.437
r_{17}	2.534
r_{24}	2.437
r_{25}	2.460
r_{34}	2.392

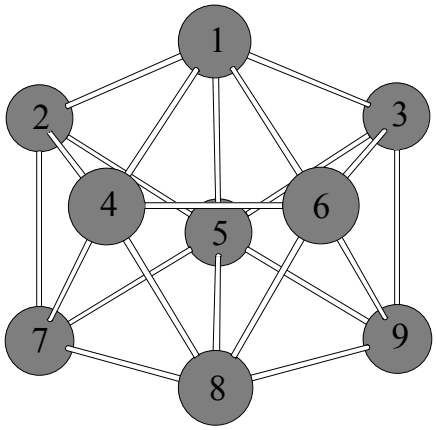

Cu_9	C_{2v}
r_{12}	2.465
r_{14}	2.447
r_{24}	2.475
r_{25}	2.418
r_{27}	2.543
r_{46}	2.434

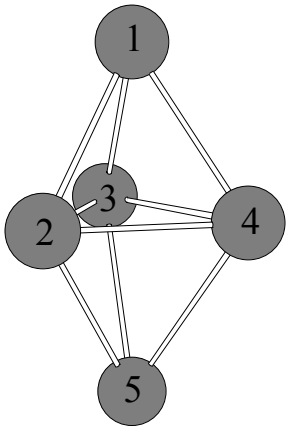

Cu_5*	C_{2v}
r_{12}	2.450
r_{13}	2.422
r_{23}	2.328
r_{24}	2.596

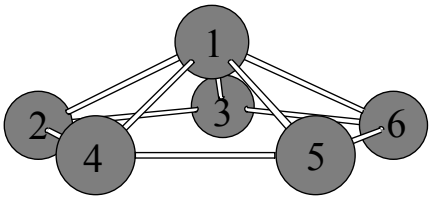

Cu_6*	C_{5v}
r_{12}	2.349
r_{23}	2.469

Figure VIII-1. Structures of the most stable neutral copper clusters Cu_n (n=2-9) (distances in Å).

Table VIII-2 includes the frequencies of the copper clusters, which are similar to those reported in previous works.[26]

Cu_2	Cu_3	Cu_4	Cu_5	Cu_6	Cu_7	Cu_8	Cu_9
266.6	99.9	59.7	41.5	43.6	72.2	69.0	65.7
	162.7	125.2	46.3	46.2	72.5	80.7	70.8
	258.2	143.5	109.8	46.7	119.5	95.8	79.0
		158.5	118.8	109.7	119.9	110.7	98.3
		232.1	148.2	110.5	132.4	110.9	107.5
		269.4	174.2	131.2	136.7	119.7	114.8
			214.2	131.9	137.1	121.7	115.0
			223.8	178.7	150.1	123.1	119.9
			266.3	205.7	168.0	124.2	124.4
				212.1	168.3	139.1	127.6
				267.5	174.0	175.8	130.2
				267.7	174.8	178.0	133.5
					228.9	178.1	152.2
					229.7	192.0	153.0
					244.7	217.9	176.6
						218.3	182.1
						229.6	198.9
						239.3	207.2
							228.0
							231.8
							251.1

Table VIII-2. Frequencies (in cm^{-1}).

It is worth mentioning that the linear Cu_3 copper cluster is 5.1 kcal·mol^{-1} less stable than the triangular conformer. As to Cu_5, the C_{2v} planar isomer of trapezoidal structure is 6.0 and 7.2 kcal·mol^{-1} more stable than the tridimensional clusters of C_{2v} and D_{3h} symmetry, respectively. The interconversion between the C_{2v} trapezoidal Cu_5 cluster and the C_{2v} distorted trigonal bipyramid Cu_5* cluster takes place through a transition state with a very low energy barrier, according to the calculations by Cao and co-workers.[32] For Cu_6, the planar D_{3h} structure is the global minimum in agreement with previous Car-Parinello studies.[61] At the LDA level, three possible geometries of Cu_6 (planar D_{3h} and tridimensional C_{2v} and C_{5v}) lie close in energy.[26] Our BPW91/TZ2P calculations indicate that the planar D_{3h} isomer is 2.3 kcal·mol^{-1} and 5.9 kcal·mol^{-1} more stable than the C_{5v} and C_{2v} species, respectively. We have found in agreement with all studies made before,[26,29,32] that the most stable heptamer of Cu has a 3D structure of D_{5h} symmetry. Planar structures of Cu_7 were found to lie higher in energy. Other 3D structures were also checked, but they were found to be destabilized by at least 5 kcal·mol^{-1}.

The geometry optimizations of the Cu_8 and Cu_9 clusters were started from the most stable Cu_7 structure. The global minima for the Cu_8 and Cu_9 clusters adopt C_{2v}

symmetry. The Cu_8 cluster with C_s symmetry, which was wrongly assigned as the most stable by Cao and co-workers,[32] is 3.2 kcal·mol^{-1} less stable than the C_{2v} one at the BPW91/TZ2P level and 3.7 kcal·mol^{-1} with the B3LYP/DZP method used by Cao *et al.*[32] In addition, the Cu_8 cluster with T_d symmetry appears only 0.1 kcal·mol^{-1} higher in energy with respect to the cluster with C_{2v} symmetry. Two other Cu_9 structures with C_{2v} and C_{3v} symmetry are 1.3 and 5.5 kcal·mol^{-1} less stable than the C_{2v} structure depicted in Figure VIII-1, respectively.

In Figure VIII-2 there are also displayed some other structures: Cu_3*, Cu_6**, Cu_8*, Cu_8**, Cu_9*, and Cu_9** that have also been studied among other less stable copper clusters:

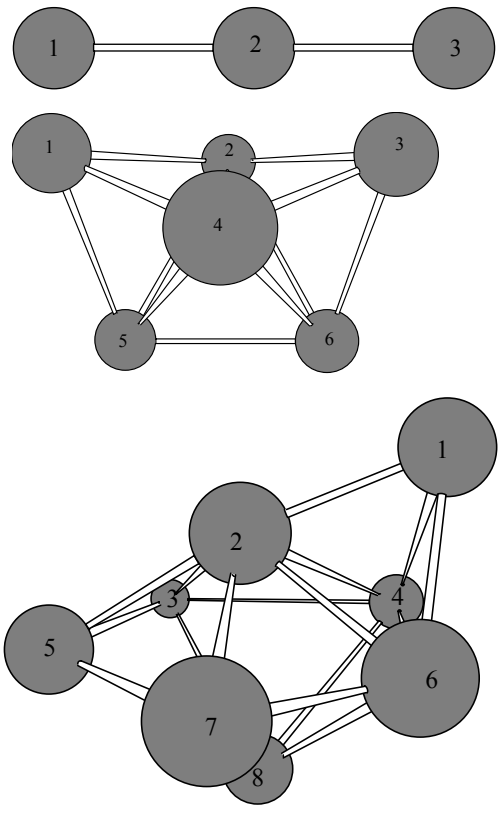

Cu_3*	$D_{\infty h}$
r_{12}	2.301

Cu_6**	C_{2v}
r_{12}	2.401
r_{15}	2.519
r_{24}	2.304
r_{25}	2.483
r_{56}	2.384

Cu_8*	C_s
r_{12}	2.347
r_{14}	2.479
r_{16}	2.442
r_{23}	2.467
r_{24}	2.489
r_{25}	2.348
r_{34}	2.430
r_{35}	2.452
r_{38}	2.420
r_{46}	2.442
r_{48}	2.420
r_{58}	2.603

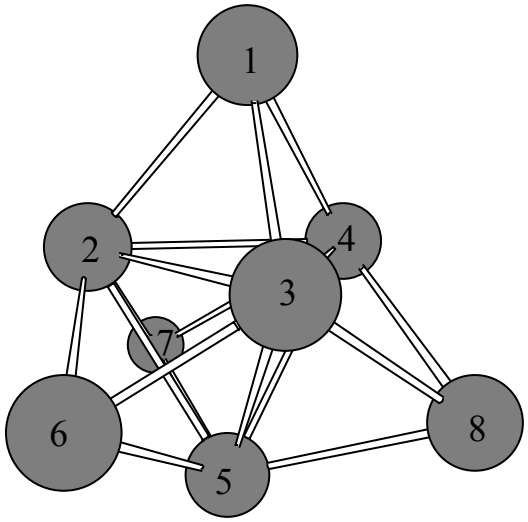

Cu_8**	T_d
r_{12}	2.419
r_{34}	2.486

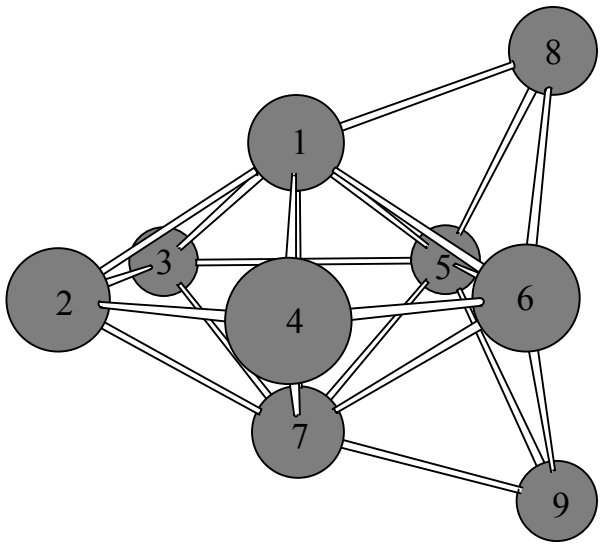

Cu_9*	C_{2v}
r_{12}	2.506
r_{13}	2.430
r_{18}	2.442
r_{23}	2.486
r_{35}	2.454
r_{56}	2.501
r_{58}	2.425

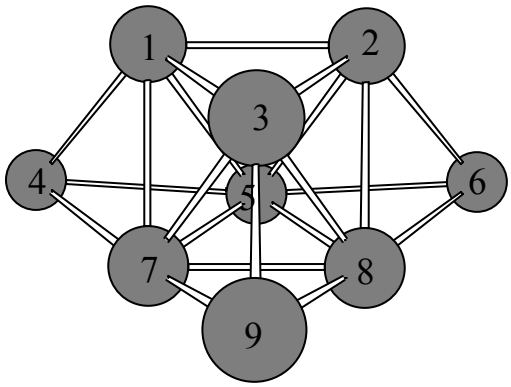

Cu_9**	C_{3v}
r_{12}	2.422
r_{14}	2.412
r_{15}	2.509
r_{45}	2.451
r_{57}	2.406

Figure VIII-2. Structures of other studied copper clusters (the distances are given in Å)

The differences between the higher distance of two copper bonded atoms and the lower distance of a cluster oscillate in increasing the number of copper atoms of the cluster (Table VIII-3). The dependency of r_{Cu-Cu} with respect to n is depicted in Figure VIII-3.

Cluster	r (Å)
Cu_3	0.295
Cu_4	0.132
Cu_5	0.057
Cu_6	0.115
Cu_7	0.115
Cu_8	0.142
Cu_9	0.125

Table VIII-3. Difference between distances Cu-Cu (in Å)

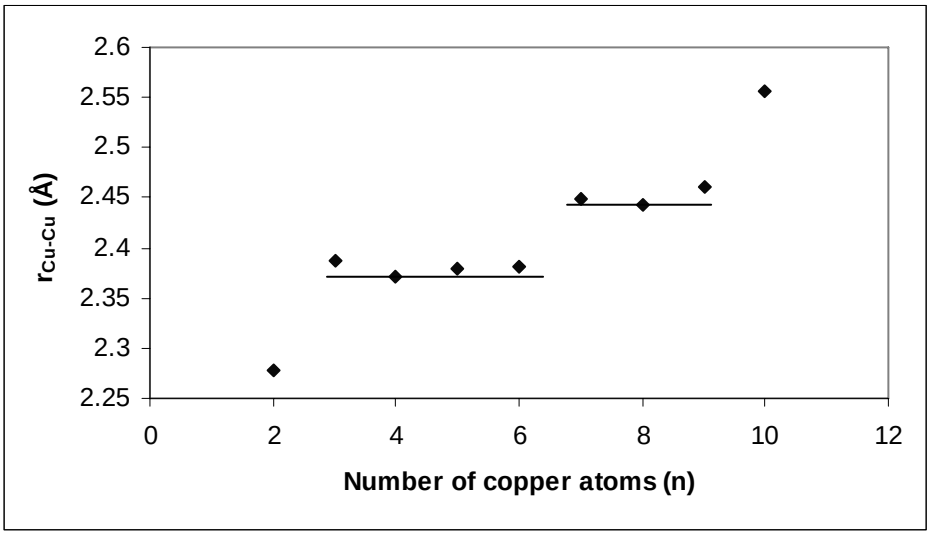

Figure VIII-3. Dependency of r_{Cu-Cu} (Å) with respect to the cluster size (in the value of n=10 there is the experimental data of a copper surface).

Cluster	r_{Cu-Cu}	CN
Cu_2	2.277	1.0
Cu_3	2.388	2.0
Cu_4	2.372	2.5
Cu_5	2.380	2.8
Cu_6	2.382	3.0
Cu_7	2.448	4.3
Cu_8	2.443	4.5
Cu_9	2.460	5.1
Expt. [a]	2.556	12.0

[a] Experimental value for the metallic bulk.

Table VIII-4. Mean value of the Cu-Cu bond distances (Å) and of the coordination numbers (CN) of Cu_n (n=2-9).

The mean values of the Cu-Cu bond distances (r_{Cu-Cu}) and the mean coordination numbers (CN) calculated by the arithmetic mean of the number of bonds of each copper atom in a given cluster are collected in Table VIII-4. Take for instance, the cluster of four copper atoms presents a CN equal to 2.5 due to the presence of two atoms, which form the short diagonal, than have three atoms around them, and the two other atoms, that form the long diagonal, that have two atoms around them. Therefore, the arithmetic mean of 3, 3, 2, and 2 is 2.5. Remarkable structural changes are observed changing from linear to planar and from planar to tridimensional clusters. The r_{Cu-Cu} mean values changes from about 2.28 to 2.38 and 2.45 Å when going from linear to planar and to 3D structures, respectively. As expected, the 3D Cu_n clusters (n=7-9) have Cu-Cu bond distances closer to the experimental Cu-Cu distance of the metallic bulk (2.556 Å).[29] On the other hand, the CN values increases linearly with n,[29] but they are still far from the metallic bulk value.

2. Binding Energies and Physical Properties. Table VIII-5 lists the binding energies (BE) for the copper clusters obtained from the following expression:

$$BE = nE_{Cu} - E_{Cu_n} \quad (1)$$

Table VIII-5 also collects the experimental BE determined by means of a thermodynamic cycle that uses the EA and IP of neutral clusters and the dissociation energies obtained in experiments of collision induced dissociation (CID) carried out over anionic and cationic copper clusters.[9,10] Figure VIII-4 displays the good agreement between the theoretical data with respect to the the experimental data. Another property included in Table VIII-5 is the binding energy per atom (BE/n), that should achieve the experimental cohesion metallic energy of 3.50 eV in the limit of an infinite cluster.[29] It is clear that the studied clusters are too small to give a good prediction of the cohesion energy but, however, the obtained values are between those of the experimental CID for anions and cations,[9,10] and close to the theoretical results previously reported.[29] On the other hand, it is observed that the BE/n increases with the size of the cluster, obtaining the maximum value for Cu_8 and Cu_9. The magnitude of BE/n gives information about the strength of the chemical bonds in the clusters, therefore it can help to determine the stability of the system. The increase of the BE/n value with the size of the system is likely due to a larger electronic delocalization that is present in clusters with higher coordination numbers. From the data of Table VIII-4 and Table VIII-5 a linear relation between BE/n and CN is found (r^2=0.897, see Figure VIII-4). Substituting the value of BE/n=3.50 eV corresponding to the experimental metallic bulk in the plot of the BE/n vs. CN, a CN value close to 12 is obtained.

Cu_n	BE	BE/n	BE[a]	BE(expt) [b]	BE(expt)[c]
Cu_2	1.95	0.98	1.92	2.04 ± 0.17	1.81 ± 0.14
Cu_3	3.11	1.04	3.01	3.19 ± 0.26	2.57 ± 0.27
Cu_4	5.44	1.36	5.23	5.91 ± 0.33	4.60 ± 0.81
Cu_5	7.39	1.48	7.13	7.76 ± 0.37	6.19 ± 1.13
Cu_6	9.92	1.65	9.63	10.32 ± 0.49	7.99 ± 1.37
Cu_7	12.41	1.77	11.85	12.98 ± 0.66	9.04 ± 1.58
Cu_8	14.91	1.86	14.32	15.96 ± 0.75	11.20 ± 1.77
Cu_9	16.71	1.86	15.95		12.22 ± 1.84

[a] B3PW91/LANL2DZ results from Ref. 29.
[b] CID experiments on the anionic clusters.[9]
[c] CID experiments on the cationic clusters.[10]

Table VIII-5. Binding energy (BE) of the copper clusters. BE/n is the binding energy per atom. The values are given in eV.

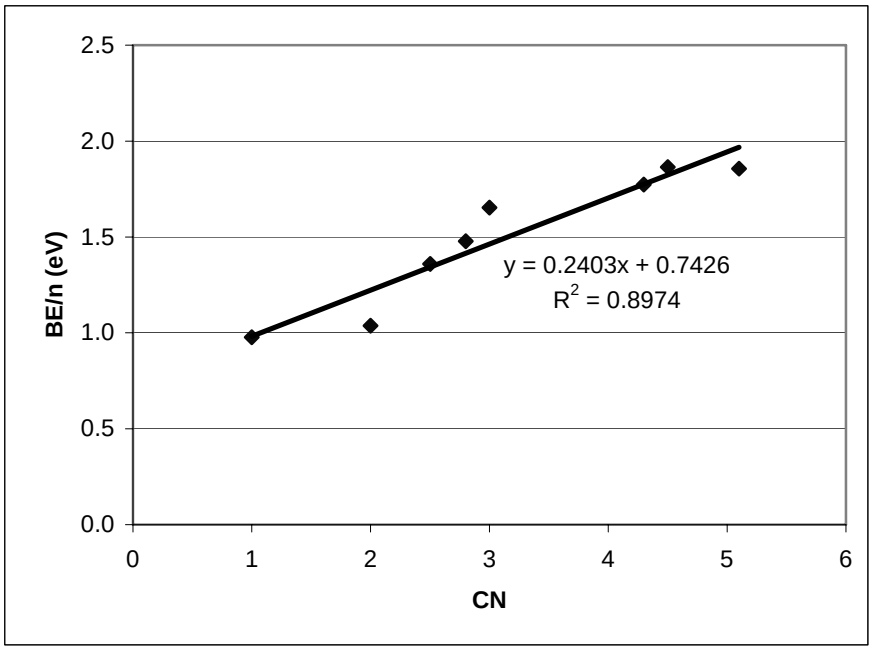

Figure VIII-4. Dependency between BE/n and CN.

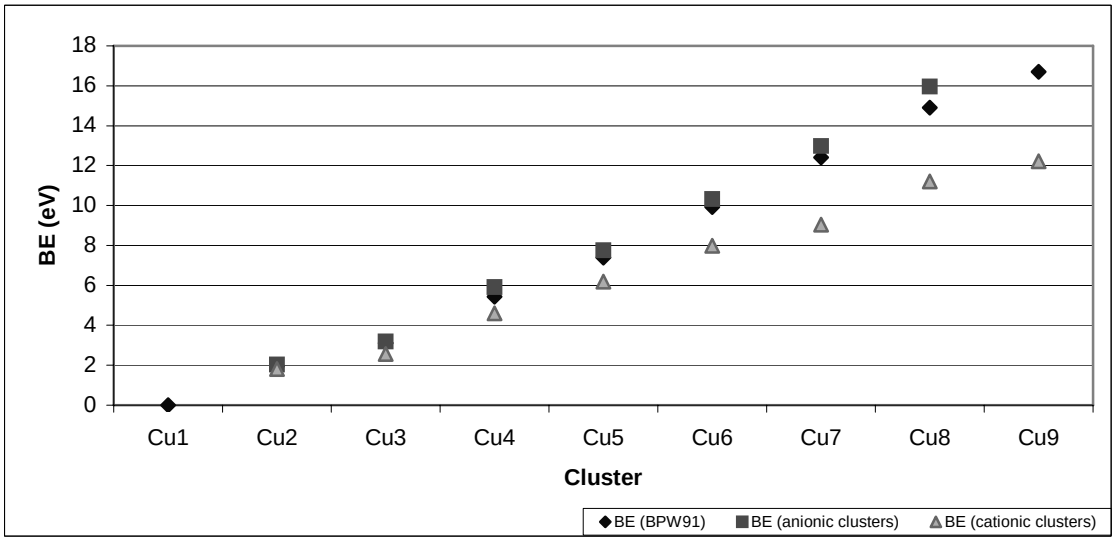

Figure VIII-5. Experimental values (CID) and theoretical ones (BPW91)

The stability of the metallic clusters can also be studied through the following energy difference:

$$\Delta_2 E(n) = E(n+1) + E(n-1) - 2E(n) \qquad (2)$$

where n is the number of atoms of the cluster. This term, named relative binding energy, measures the relative stability of a cluster with n atoms with respect to those with n+1

and n-1 atoms. Positive values of $\Delta_2 E(n)$ show that the cluster Cu_n is more stable than its neighbors Cu_{n-1} and Cu_{n+1}. The plot in Figure VIII-6 of $\Delta_2 E(n)$ as a function of n shows an oscillating behavior, the most stable clusters being those with an even number of copper atoms and closed-shell singlet ground states.[29]

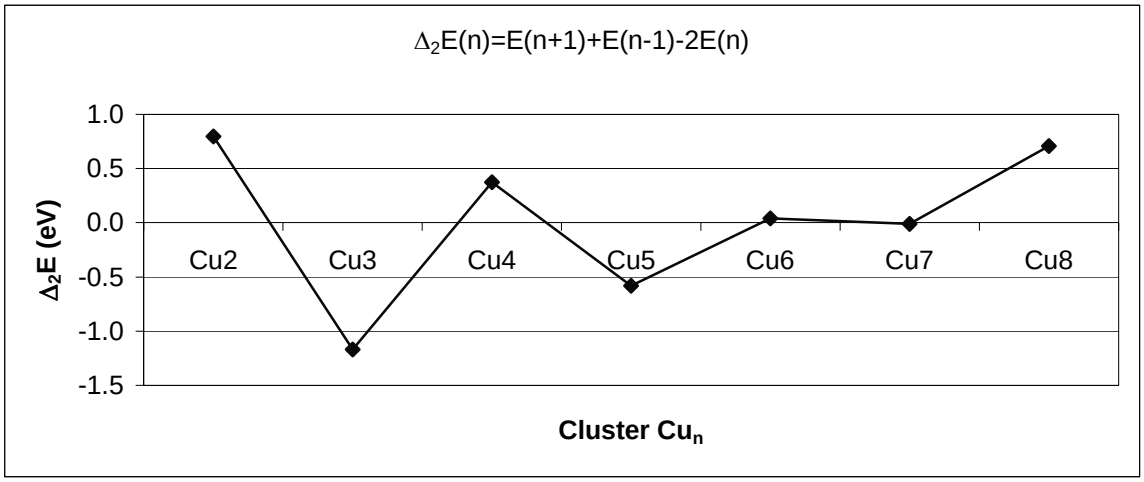

Figure VIII-6. $\Delta_2 E(n)$ in function of the size of the cluster.

Cu_n	ε_H	ε_L	IP	IP (expt) [a]	EA	EA (expt) [b]
Cu_1	-5.06	-3.69	8.25	7.724	1.14	1.235 ± 0.005
Cu_2	-4.72	-2.86	8.23	7.9042 ± 0.0008	0.83	0.836 ± 0.006
Cu_3	-4.90	-3.05	6.18	5.80 ± 0.04	0.98	2.37 ± 0.01
Cu_4	-4.35	-3.32	6.90	7.15 ± 0.75	1.46	1.45 ± 0.05
Cu_5	-4.76	-3.64	6.53	6.30 ± 0.10	1.86	1.94 ± 0.05
Cu_6	-4.71	-2.73	7.25	7.15 ± 0.75	1.24	1.96 ± 0.05
Cu_7	-4.72	-3.54	6.29	6.10 ± 0.05	1.84	2.16 ± 0.10
Cu_8	-4.50	-2.95	6.85	7.15 ± 0.75	1.41	1.57 ± 0.05
Cu_9	-4.40	-3.22	5.72	5.35 ± 0.05	1.68	2.40 ± 0.05

[a] Refs. 7, 8, and 17.
[b] Ref. 15.

Table VIII-6. BPW91/TZ2P HOMO and LUMO energies, ionization potentials, and electron affinities for the copper clusters Cu_n (n=1-9). All energies are given in eV.

Table VIII-6 contains the ionization potentials and electron affinities together with the energies of the HOMO (ε_H) and the LUMO (ε_L) for copper clusters Cu_n (n=1-9). Unsurprisingly, the clusters with an even number of copper atoms tend to present larger HOMO-LUMO gaps, and, therefore, higher hardnesses and lower reactivities. The closed-shell clusters present a higher value of IP and, in general, a lower EA. This reflects the fact that it is more difficult to extract or add an electron in a closed-shell system than in an open-shell one. The same tendency is found in the energy of the HOMO and LUMO orbitals. The values obtained theoretically for the IP differ by less than 0.5 eV as compared to the experimental results. In addition, in general, the studied EAs match the experimental values, especially for the clusters with an even number of copper atoms that possess closed-shell structures. Larger differences between experimental and theoretical values are observed in clusters with an odd number of members. In particular, the experimental and theoretical EAs of the Cu_3 cluster are very different. The generally good correlation between the experimental and theoretical values let us to suggest revision of the experimental EA value for the Cu_3 cluster.

Cu_n	μ	μ^{expt}	η	η^{expt}	ω	ω^{expt}
Cu_1	-4.70	-4.48 ± 0.01	3.55	3.24 ± 0.01	3.11	3.09 ± 0.01
Cu_2	-4.53	-4.37 ± 0.01	3.70	3.53 ± 0.01	2.77	2.70 ± 0.01
Cu_3	-3.58	-4.08 ± 0.04	2.60	1.72 ± 0.04	2.47	4.86 ± 0.14
Cu_4	-4.18	-4.30 ± 0.75	2.72	2.85 ± 0.75	3.22	3.24 ± 1.17
Cu_5	-4.20	-4.12 ± 0.11	2.33	2.18 ± 0.11	3.78	3.89 ± 0.25
Cu_6	-4.24	-4.55 ± 0.75	3.01	2.60 ± 0.75	2.99	3.99 ± 1.49
Cu_7	-4.06	-4.13 ± 0.11	2.23	1.97 ± 0.11	3.70	4.33 ± 0.30
Cu_8	-4.13	-4.36 ± 0.75	2.72	2.79 ± 0.75	3.13	3.41 ± 1.24
Cu_9	-3.70	-3.87 ± 0.07	2.02	1.48 ± 0.07	3.40	5.09 ± 0.28

Table VIII-7. Chemical potentials, chemical hardnesses, and electrophilicity index of Cu_n(n=1-9). The values are given in eV.

3. Chemical Descriptors. Table VIII-7 gathers the chemical potentials (μ), hardnesses (η), and electrophilicities (ω) for the copper clusters obtained with the calculated and experimental values of IPs and EAs given in Table VIII-6.[56-60]

Experimental results present a large imprecision for the Cu_4, Cu_6, and Cu_8 clusters because of the 10% error in the determination of the experimental IPs. In addition, these experimental values have another associated type of error due to the fact that they are not calculated directly as energy derivatives with respect to the number of electrons, but they are obtained from the experimental IP and EA values.

The chemical potentials of the Cu_3 and Cu_9 clusters have the lower absolute values. These clusters also show the lower ionization potentials (Table VIII-6). So, these systems transfer more easily one electron to close the electronic shell becoming systems with 2 and 8 valence electrons, respectively. This is in agreement with the magic number predicted for the stability in the shell jellium model, where the clusters with 2, 8, 18, 20, 40, 58, 92... valence electrons show peaks of high intensity in the mass spectra.[62]

The closed-shell clusters present higher values of chemical hardness than their neighbors with open-shell electronic configuration. This confirms that the stability of the even-numbered clusters follows the principle of maximum hardness.[63] These results agree with those obtained by Mineva *et al*.[4] for a series of sodium clusters and by Jaque and Toro-Labbé for copper clusters.[29]

C. Reactivity Predictors

We have calculated the condensed Fukui functions to predict the selectivity of CO adsorption on copper clusters. With CO characterized as a nucleophilic species, one could expect that the f^+ would be the best Fukui function to predict the CO preferred binding sites. The metal-CO bond is usually[64] discussed in terms of the familiar Dewar-Chatt-Duncanson (DCD) model[65] considering that the two synergistic main bonding interactions are σ donation from the carbon atom lone pair orbital of the CO into the empty d(σ) orbital of the metal, and π back-donation from an occupied d(π) metal atomic orbital to the empty π* orbital of CO. Then, CO acts in copper cluster carbonyls not only as a nucleophile transferring electronic charge to the copper cluster, but also as an electrophile by receiving electrons from the metal cluster. Thus, given the complexity of CO bonding, the f^- and f^0 have been also studied.[66]

The present condensed Fukui function analysis has been carried out using the Mulliken, Hirshfeld, and Voronoi charges. Although there is a general agreement that the Hirshfeld are more accurate than the Mulliken charges,[66a,67] we have included in Table VIII-8 condensed Fukui functions derived from both the Mulliken and Hirshfeld charges to allow for comparisons. The condensed Fukui functions from Voronoi charges are also listed in Table VIII-8. The results from Voronoi charges are completely equivalent to those obtained from the Hirshfeld charges.

n	Atom	f^-			f^+			f^0		
		Mulliken	Hirshfeld	Voronoi	Mulliken	Hirshfeld	Voronoi	Mulliken	Hirshfeld	Voronoi
2	Cu1,2	0,500	0,500	0,507	0,500	0,500	0,510	0,500	0,500	0,500
3	Cu2	0,226	0,225	0,208	0,183	0,221	0,203	0,204	0,223	0,206
	Cu1,3	0,387	0,388	0,395	0,408	0,390	0,399	0,398	0,389	0,397
4	Cu1,4	0,314	0,336	0,350	0,207	0,214	0,202	0,260	0,275	0,276
	Cu2,3	0,186	0,164	0,150	0,293	0,286	0,298	0,240	0,225	0,224
5	Cu3,5	0,175	0,218	0,220	0,307	0,242	0,243	0,241	0,230	0,232
	Cu4	0,156	0,146	0,144	0,082	0,119	0,111	0,119	0,133	0,128
	Cu1,2	0,208	0,209	0,210	0,191	0,199	0,200	0,199	0,204	0,205
6	Cu1,3,6,	0,202	0,209	0,214	0,347	0,259	0,264	0,274	0,234	0,239
	Cu2,4 5	0,131	0,124	0,120	-0,013	0,074	0,070	0,059	0,099	0,095
7	Cu2,3,4,5,6	0,133	0,129	0,124	0,129	0,131	0,126	0,131	0,130	0,125
	Cu1,7	0,167	0,177	0,190	0,179	0,172	0,184	0,173	0,175	0,187
8	Cu1,7	0,141	0,149	0,150	0,227	0,180	0,184	0,184	0,164	0,167
	Cu3,5	0,115	0,095	0,091	0,023	0,070	0,066	0,069	0,083	0,079
	Cu4,6	0,126	0,122	0,120	0,227	0,180	0,184	0,177	0,151	0,152
	Cu2,8	0,118	0,134	0,139	0,023	0,070	0,066	0,070	0,102	0,103
9	Cu5	0,033	0,032	0,025	0,014	0,029	0,021	0,024	0,031	0,023
	Cu4,6	0,074	0,070	0,065	0,066	0,067	0,063	0,070	0,068	0,064
	Cu2,3,7,9	0,161	0,162	0,170	0,177	0,166	0,174	0,169	0,164	0,172
	Cu1,8	0,089	0,089	0,083	0,073	0,087	0,078	0,081	0,088	0,081
5*	Cu3	0,151	0,138	0,128	0,430	0,406	0,455	0,290	0,272	0,292
	Cu2,4	0,247	0,255	0,269	0,119	0,118	0,104	0,183	0,186	0,187
	Cu1,5	0,177	0,176	0,233	0,167	0,180	0,103	0,172	0,178	0,168
6*	Cu2,3,4,5,6,	0,167	0,163	0,159	0,174	0,166	0,160	0,171	0,164	0,160
	Cu1	0,103	0,079	0,071	0,131	0,172	0,197	0,117	0,126	0,134
CO	C	0,759	0,683	0,644	0,866	0,703	0,669	0,812	0,693	0,657
	O	0,241	0,317	0,356	0,134	0,297	0,331	0,188	0,307	0,344

Table VIII-8. Condensed Fukui functions (electrons) for copper clusters Cu_n. For atom numbering see Fig. VIII-1.

The two positions of Cu_2 have obviously the same probability to be attacked and, therefore, the condensed Fukui functions do not provide new information in this case. For Cu_3, the two atoms connected through the longest bond distance are the most reactive in front of a chemical attack. As to Cu_4, condensed Fukui functions point out the copper atoms in the long diagonal of the rhombus as the most easily attacked, except for the f^+ function. The external positions of the large basis of the trapezium in Cu_5 are the most reactive sites for CO binding except for the Mulliken f values, which indicate that the small basis copper atoms are the most reactive. For Cu_6, the most favored sites

are the three vertices of the external triangle, while for Cu_7, the two copper atoms located in the tips of the pentagonal bipyramid have the highest Fukui function values. In Cu_8, the atoms numbered 1 and 7 in Figure VIII-1 are the most reactive in front of any chemical attack. Cu_9 have four positions partially more favored than the rest, which are those closer to the copper atom number 5 forming a rectangle. For Cu_5*, copper number 3 presents the higher values, except for f^-, which yields the other two positions of the basis of the trigonal-pyramid as the most reactive. In Cu_6*, the basis positions are the most favored sites, except for the Hirshfeld f^+ value. It is worth noting that, with some exceptions, the three types of the Fukui condensed functions obtained using three different definitions of atomic charge yield similar predictions as to the selectivity of CO adsorption on copper clusters. In addition, we have verified that the trends in reactivity predicted by the hard and soft acids and bases (HSAB) principle[68] using the local softness values[69] given in Table VIII-9 are the same than those predicted by the condensed Fukui functions with the exception of Cu_3, for which atom 2 is the most reactive according to the HSAB principle prediction.

		s^-			s^+			s^0		
Molecule	Atom	Mulliken	Hirshfeld	Voronoi	Mulliken	Hirshfeld	Voronoi	Mulliken	Hirshfeld	Voronoi
Cu_2CO	Cu1,2	1,722	1,722	1,746	1,722	1,722	1,757	1,722	1,722	1,752
Cu_3CO	Cu2	1,257	1,254	1,160	1,022	1,231	1,132	1,139	1,243	1,146
	Cu1,3	2,159	2,161	2,203	2,277	2,173	2,225	2,218	2,167	2,214
Cu_4CO	Cu1,4	1,380	1,479	1,539	0,909	0,943	0,888	1,144	1,211	1,214
	Cu2,3	0,819	0,720	0,660	1,290	1,256	1,310	1,055	0,988	0,985
Cu_5CO	Cu3,5	1,012	1,257	1,269	1,768	1,394	1,402	1,390	1,325	1,335
	Cu4	0,900	0,844	0,831	0,475	0,684	0,640	0,687	0,764	0,735
	Cu1,2	1,199	1,204	1,211	1,101	1,148	1,154	1,150	1,176	1,182
Cu_6CO	Cu1,3,6,	0,872	0,904	0,924	1,497	1,120	1,140	1,184	1,012	1,032
	Cu2,4 5	0,567	0,535	0,518	-0,057	0,319	0,302	0,255	0,427	0,410
Cu_7CO	Cu2,3,4,5,6	0,845	0,820	0,787	0,815	0,832	0,799	0,830	0,826	0,793
	Cu1,7	1,061	1,122	1,206	1,134	1,093	1,167	1,097	1,107	1,186
Cu_8CO	Cu1,7	0,723	0,767	0,771	1,168	0,924	0,946	0,946	0,846	0,859
	Cu3,5	0,591	0,489	0,468	0,118	0,361	0,339	0,355	0,425	0,404
	Cu4,6	0,649	0,628	0,617	1,168	0,924	0,946	0,909	0,776	0,782
	Cu2,8	0,607	0,687	0,715	0,118	0,361	0,339	0,362	0,524	0,527
Cu_9CO	Cu5	0,234	0,224	0,176	0,101	0,207	0,148	0,167	0,216	0,162
	Cu4,6	0,518	0,490	0,457	0,464	0,470	0,443	0,491	0,480	0,450
	Cu2,3,7,9	1,129	1,143	1,196	1,244	1,168	1,224	1,187	1,155	1,210
	Cu1,8	0,625	0,629	0,584	0,516	0,609	0,549	0,571	0,619	0,566
Cu_5*CO	Cu3	0,646	0,593	0,550	1,844	1,741	1,954	1,245	1,167	1,252
	Cu2,4	1,062	1,095	1,155	0,509	0,505	0,447	0,785	0,800	0,801
	Cu1,5	0,762	0,756	1,000	0,716	0,771	0,442	0,739	0,764	0,721
Cu_6*CO	Cu2,3,4,5,6,	0,647	0,630	0,615	0,673	0,641	0,619	0,660	0,635	0,617
	Cu1	0,398	0,306	0,275	0,508	0,667	0,762	0,453	0,487	0,519
CO	C	1,300	1,170	1,103	1,482	1,203	1,146	1,391	1,186	1,12419
	O	0,413	0,543	0,610	0,230	0,509	0,567	0,322	0,526	0,58821

Table VIII-9. Local softnesses (electrons) for copper clusters Cu_n.

Another approach for predicting the most favorable site for the CO interaction with the copper cluster is the frontier molecular orbital (FMO) theory. For open-shell systems, because of the presence of an unpaired electron, we have taken as the HOMO the highest α occupied orbital and as the LUMO the lowest β unoccupied orbital.

The representation of the frontier molecular orbitals of copper clusters (n=1-9) allows us to make a prediction of the more favorable adsorption sites. Due to the dominant donor character of the monoxide molecule in this interaction (*vide infra*), the most important orbitals to be considered are the LUMO of the cluster and the HOMO of the CO molecule. At the same time, in the DCD scheme, there is back-donation of the copper cluster toward CO. Therefore, it is necessary to take into account also, as a secondary important interaction, that between the HOMO of the cluster and the LUMO of CO. The representation of the HOMO and LUMO orbitals of the CO and the Cu_n clusters is displayed in Figure VIII-7.

From the LUMO orbitals in Figure VIII-7 it is possible to predict the copper atoms in a given cluster that, in theory, will interact better with CO, which are those having larger contributions to the LUMO orbital. Following this criterion, the central copper would be the most reactive atom of Cu_3, but the significant component of the LUMO corresponding to the external atoms indicates that these atoms may also interact favorably with CO. The copper atoms of the short diagonal of the rhombus of Cu_4 and the atoms of the short basis of the trapezium in Cu_5 are expected to be the most reactive, while the three vertices of the external triangle in Cu_6, the tips of the pentagonal bipyramid in Cu_7, two the most external positions of Cu_8, and one of the four extreme positions in Cu_9 are predicted to be the most suitable for the CO nucleophilic attack according to the shape of the LUMO orbitals. As to the less stable clusters, any position of the basis and the vertex of the pentagonal pyramid are the most reactive sites in Cu_5* and Cu_6*, respectively.

	HOMO	LUMO
CO	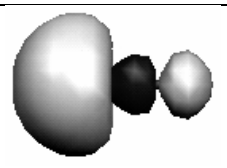	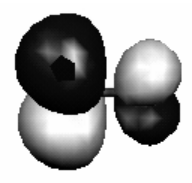
	-9.03	-1.99
Cu_1		
	-5.06	-3.69
Cu_2	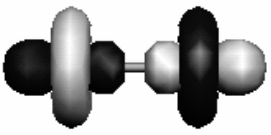	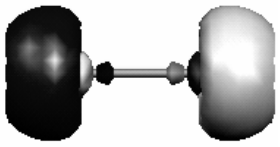
	-4.72	-2.86
Cu_3	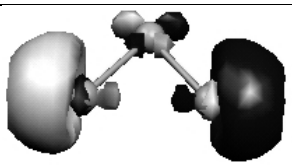	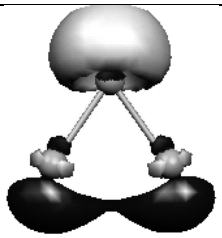
	-4.90	-3.05
Cu_4	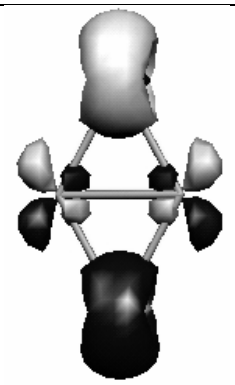	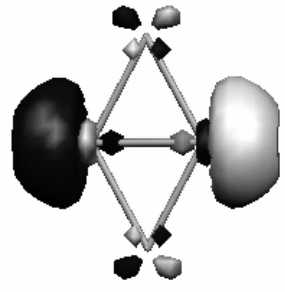
	-4.35	-3.32

Cu_5	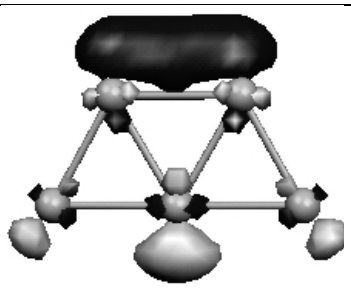	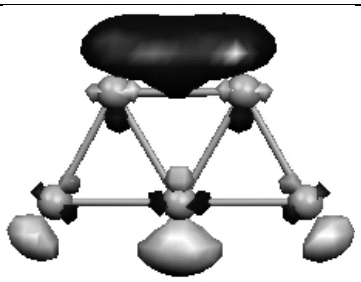
	-4.76	-3.64
Cu_6	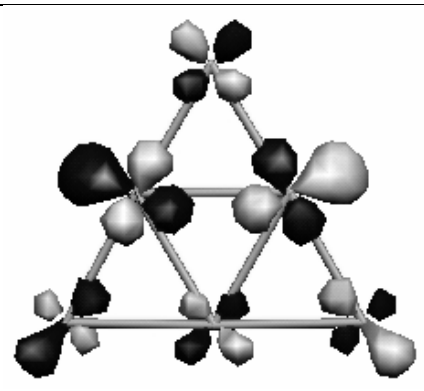	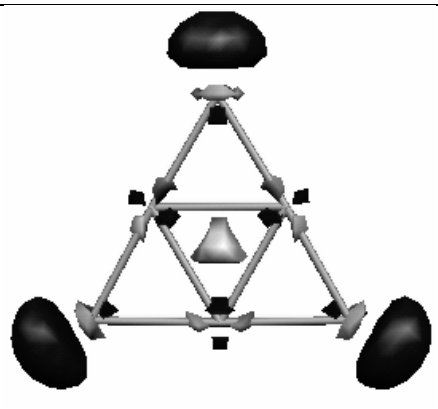
	-4.71	-2.73
Cu_7	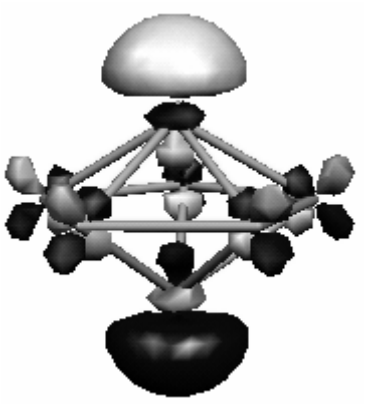	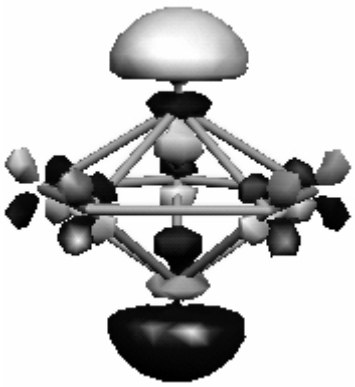
	-4.72	-3.54
Cu_8		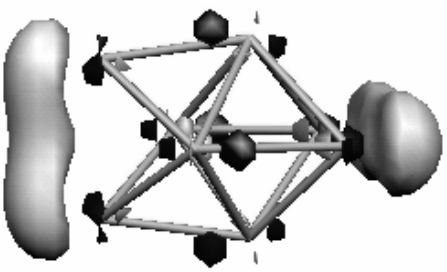
	-4.50	-2.95

Cu_9	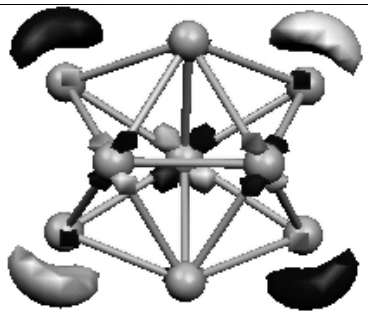	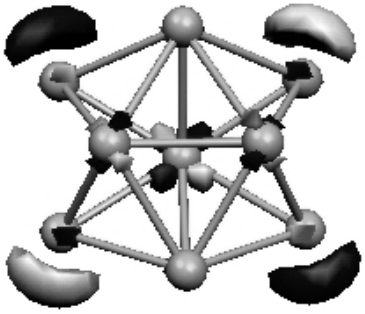
	-4.40	-3.22
Cu_5*		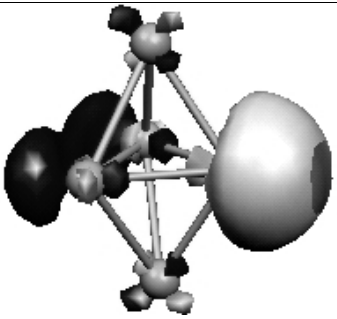
	-4.38	-3.46
Cu_6*	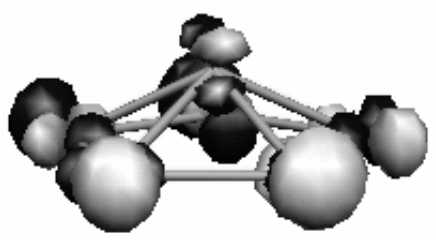	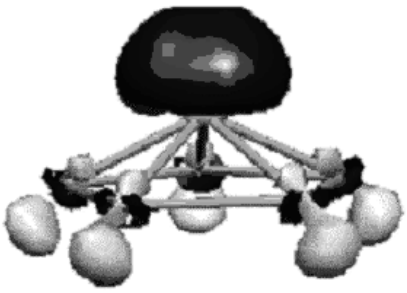
	-4.58	-2.89

Figure VIII-7. Representation of the HOMO and LUMO orbitals of CO and the copper clusters Cu_n. The different grey and black tones of the orbitals represent the negative and the positive regions. Isosurface values are 0.05 and –0.05 a.u. Below each orbital there is its corresponding energy in eV.

It is worth noting that a comparison between the predicted results from the condensed Fukui functions and the frontier orbitals shows that, although the theoretical background is slightly different for both approaches, the results are nearly the same, especially when the cluster presents an even number of copper atoms.

D. Copper Cluster Carbonyls Cu_nCO (n=1-9)

1. Structures and Stabilities. The CO molecules can be adsorbed on the copper surfaces with terminal or bridge coordination. Although we focus our study only on the former, we have checked that the bond bridge coordination is either unattainable or less stable in all cases. Figure VIII-8 depicts the most stable geometrical structures of copper cluster carbonyls for each n (n=1-9). In the clusters with five and six copper atoms, the CO binding results in important geometrical changes of the initially most stable planar copper cluster structure. Thus, the Cu_5CO cluster adopts a trigonal-bipyramidal (tbp) structure with the CO attached to a copper atom of the triangular base while the Cu_6CO species takes a pentagonal-pyramidal arrangement with the CO bonded to the tip of the pyramid.

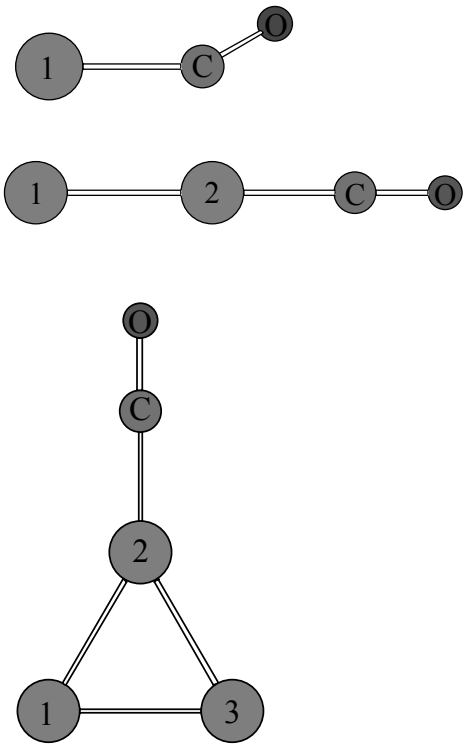

Cu_1CO	C_{2v}
r_{Cu-C}	1.880
r_{C-O}	1.156

Cu_2CO	$C_{\infty v}$
r_{Cu-C}	1.826
r_{C-O}	1.145
r_{12}	2.246

Cu_3CO	C_{2v}
r_{Cu-C}	1.808
r_{C-O}	1.151
r_{12}	2.344
r_{13}	2.382

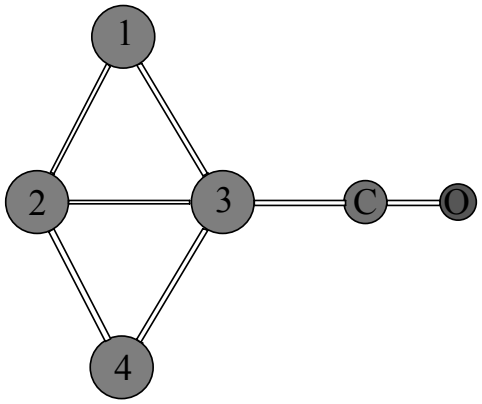

Cu_4CO	C_{2v}
r_{Cu-C}	1.807
r_{C-O}	1.149
r_{12}	2.349
r_{13}	2.435
r_{23}	2.326

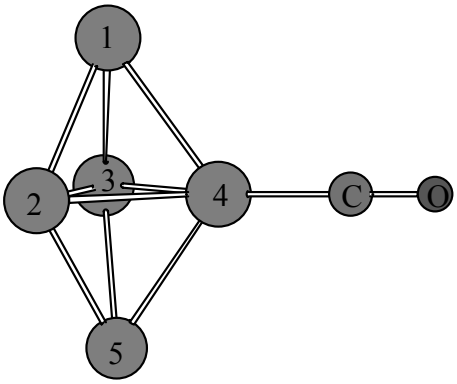

Cu_5CO	C_{2v}
r_{Cu-C}	1.800
r_{C-O}	1.150
r_{12}	2.413
r_{23}	2.489
r_{24}	2.383
r_{45}	2.493

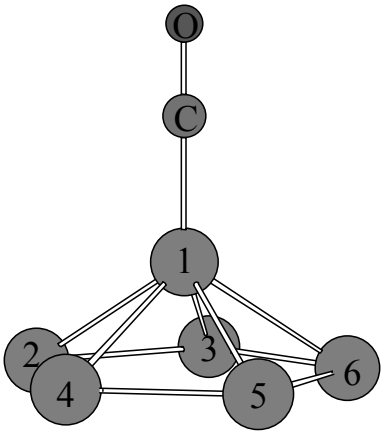

Cu_6CO	C_{5v}
r_{Cu-C}	1.819
r_{C-O}	1.149
r_{12}	2.440
r_{23}	2.386

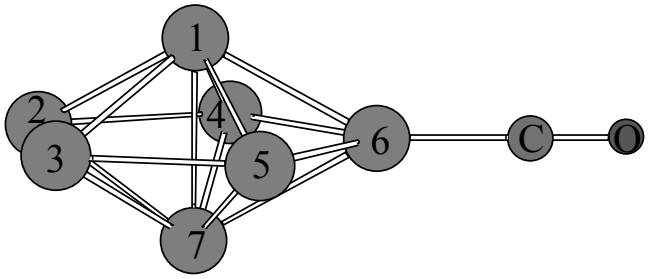

Cu_7CO	C_{2v}
r_{Cu-C}	1.842
r_{C-O}	1.148
r_{23}	2.392
r_{24}	2.499
r_{46}	2.528
r_{56}	2.528
r_{17}	2.455
r_{27}	2.466
r_{47}	2.404
r_{67}	2.500

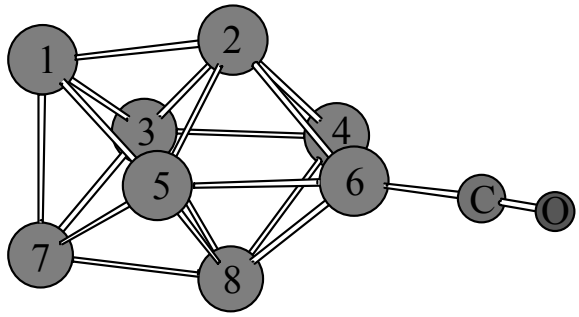

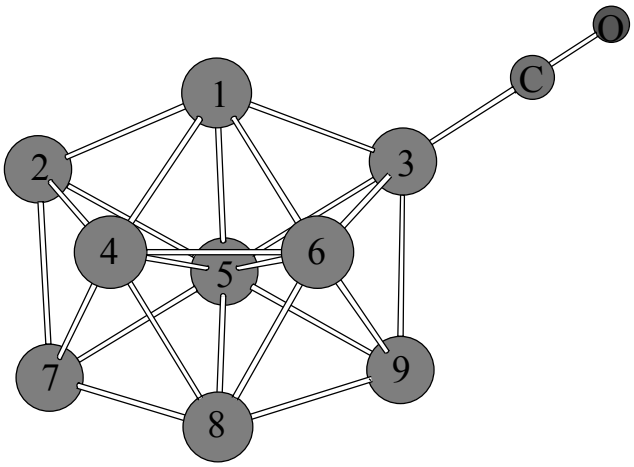

Cu_8CO	C_s
r_{Cu-C}	1.844
r_{C-O}	1.147
r_{12}	2.413
r_{13}	2.422
r_{15}	2.491
r_{17}	2.472
r_{23}	2.481
r_{24}	2.414
r_{25}	2.399
r_{26}	2.490
r_{34}	2.414
r_{46}	2.625
r_{56}	2.469
Cu_9CO	C_1
r_{Cu-C}	1.831
r_{C-O}	1.151
r_{12}	2.492
r_{13}	2.506
r_{14}	2.479
r_{15}	2.413
r_{16}	2.475
r_{24}	2.439
r_{25}	2.486
r_{27}	2.452
r_{35}	2.468
r_{36}	2.536
r_{39}	2.462
r_{45}	2.628
r_{46}	2.422
r_{47}	2.470
r_{48}	2.471
r_{56}	2.573
r_{57}	2.423
r_{58}	2.485
r_{59}	2.425
r_{68}	2.439
r_{69}	2.475
r_{78}	2.417
r_{89}	2.530

Figure VIII-8. Geometries of the Cu_nCO copper cluster carbonyls (n=1-9). (distances in Å).

Cu_1CO does not present a linear structure because the overlap between the HOMO orbital of the copper and the $2\pi^*$ LUMO orbital of CO favors a nonlinear arrangement. The BPW91/TZ2P optimized geometry of Cu_2CO is linear. This is in contradiction with the angular structure reported by Cao and co-workers.[32] All attempts to optimize an angular structure with the BPW91/TZ2P method reverted to the present linear one.

Repeating the calculations made by Cao *et al*.,[32] with the same functional and basis set used by these authors (B3LYP/DZP), we found that the nonlinear structure is only 0.08 kcal·mol^{-1} more stable than the linear arrangement. This means that the difference between linear and angular structures for Cu_2CO is very small, and that little changes in the method and basis set used may lead to different optimized structures. Unexpectedly, after the interaction with CO, the Cu_3 cluster adopts an almost equilater triangle geometry with the shortening of the Cu1-Cu3 bond that before the introduction of CO was the longest. We also found a stable linear structure for Cu_3CO, which is 16.8 kcal·mol^{-1} higher in energy as compared to the triangular arrangement. The CO can interact with Cu_4 in two different ways, either through the main or the short diagonals, the latter being the most favorable.

While the bare Cu_5 cluster presents a planar trapezoidal structure, this fragment in the most stable Cu_5CO species adopts tbp geometry. For the trapezoidal structure, the two copper atoms of the short basis are favored. As a result of the CO interaction this basis becomes markedly elongated, thus anticipating future likely distortions of this planar Cu_5CO structure that would lead to the D_{3h} tbp geometry. A similar phenomenon is found in the copper cluster carbonyl with six copper atoms. The initial planar structure of the Cu_6 cluster changes in the Cu_6CO complex to a pentagonal-pyramidal geometry of C_{5v} symmetry. The most favorable interaction takes place at the tip of the pentagonal-pyramid. The CO interaction at one of the three vertices of the planar triangular D_{3h} Cu_6 cluster leads to a Cu_6CO species with C_s symmetry. The Cu_5 and Cu_6 clusters adopt a 3D structure after the interaction with a CO molecule confirming the predictions by Jug, Zimmermann, and Köster[70] made from the shape of the frontier molecular orbitals.

Unlike in Cu_6, the CO binding in Cu_7 in the positions of the pentagonal bipyramid basis to yield a Cu_7CO species of C_s symmetry is 4.5 kcal·mol^{-1} favored over the interaction with the tips that results in a C_{2v} Cu_7CO cluster, in contradiction with the results reported by Cao *et al*.[32] It is worth noting that at the level of theory used by Cao and co-workers[32] (B3LYP/DZP) the C_{2v} Cu_7CO cluster is more stable than the C_s Cu_7CO complex by 2.2 kcal·mol^{-1} and by 4.5 kcal·mol^{-1} when using B3LYP/6-31G*. Thus, the trend in the relative stability of the C_s and C_{2v} Cu_7CO clusters changes significantly depending on the method and basis set used, showing that the two structures have similar stabilities. In Cu_8 the most favorable copper atoms to be attacked

are those numbered 1 and 7 in Figure VIII-1. In Cu_9, the attack occurs to any of the copper atoms numbered 2, 3, 7, and 9. The most favorable site for CO binding in Cu_9 found by Cao *et al*.[32] is less stable than our predicted position by about 0.1 kcal·mol^{-1} and 0.7 kcal·mol^{-1} at the BPW91/TZ2P and B3LYP/6-31G* levels of theory, respectively.[32] These two structures are found very close in energy. Indeed, the relative stability of the two structures changes if we perform the calculations using the same method and basis set of double-ξ quality containing pseudopotentials (B3LYP/DZP) employed by Cao *et al*.[32]

Some of the other studied Cu_nCO structures are displayed in Figure VIII-9.

Cluster+CO	energies (kcal·mol^{-1}) bond distances (Å)
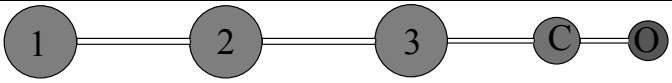	Cu_3CO $C_{\infty v}$ r_{Cu-C} 1.835 r_{C-O} 1.144 r_{13} 2.335 r_{23} 2.316
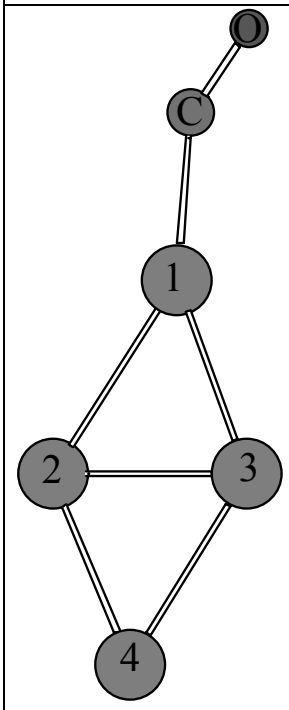	Cu_4CO C_s r_{Cu-C} 1.885 r_{C-O} 1.152 r_{12} 2.622 r_{13} 2.361 r_{23} 2.243 r_{24} 2.351 r_{34} 2.522

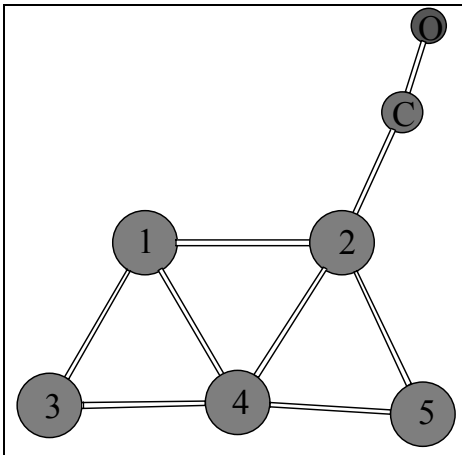

Cu_5CO	C_s
r_{Cu-C}	1.830
r_{C-O}	1.150
r_{12}	2.485
r_{13}	2.397
r_{14}	2.363
r_{24}	2.417
r_{34}	2.373
r_{35}	2.409
r_{45}	2.331

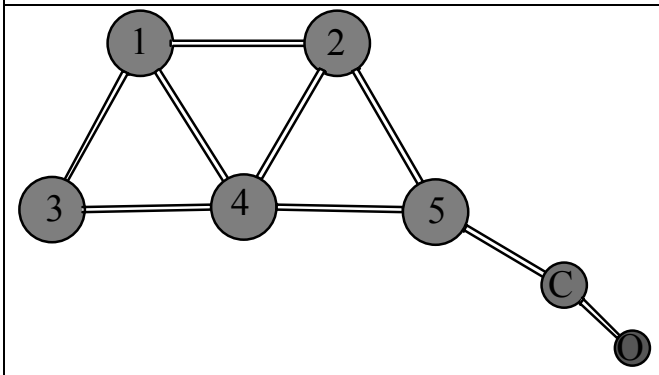

Cu_5CO	C_s
r_{Cu-C}	1.845
r_{C-O}	1.148
r_{12}	2.450
r_{13}	2.348
r_{14}	2.402
r_{24}	2.362
r_{25}	2.434
r_{34}	2.385
r_{45}	2.392

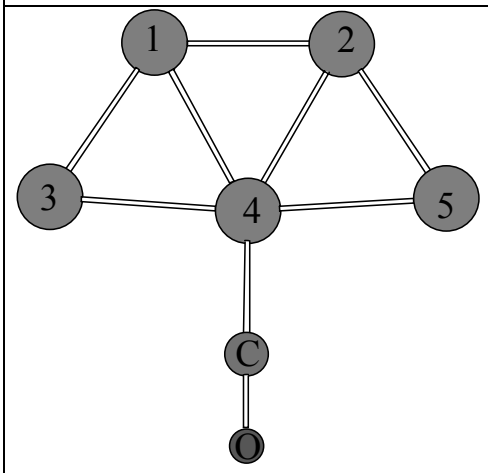

Cu_5CO	C_{2v}
r_{Cu-C}	1.834
r_{C-O}	1.148
r_{12}	2.353
r_{13}	2.350
r_{14}	2.420
r_{34}	2.496

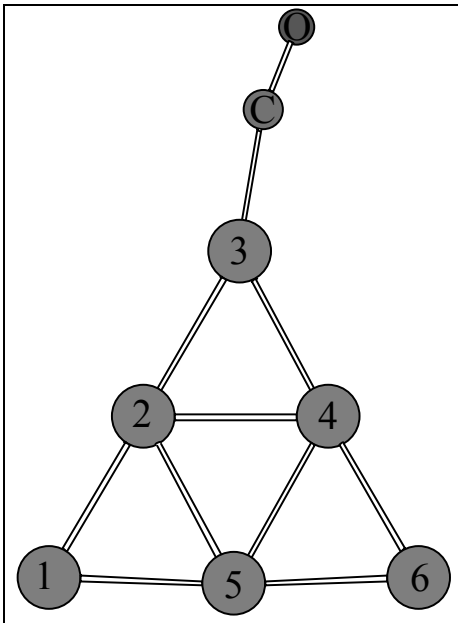

Cu_6CO	C_s
r_{Cu-C}	1.858
r_{C-O}	1.145
r_{12}	2.381
r_{15}	2.359
r_{23}	1.421
r_{24}	2.338
r_{25}	2.450
r_{34}	2.430
r_{45}	2.451
r_{46}	2.381
r_{56}	2.355

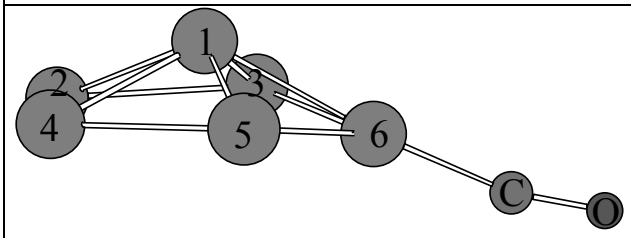

Cu_6CO	C_s
r_{Cu-C}	1.844
r_{C-O}	1.148
r_{36}	2.575
r_{23}	2.560
r_{24}	2.408
r_{45}	2.548
r_{56}	2.570
r_{16}	2.356
r_{13}	2.298
r_{12}	2.360
r_{14}	2.363
r_{15}	2.303

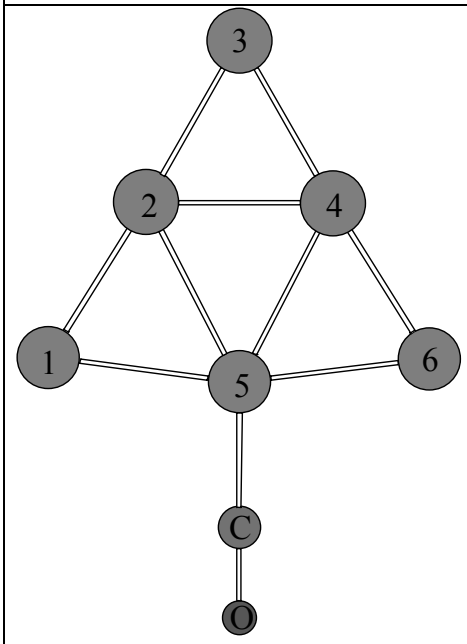

Cu_6CO	C_{2v}
r_{Cu-C}	1.861
r_{C-O}	1.148
r_{56}	2.420
r_{46}	2.330
r_{45}	2.563
r_{34}	2.375
r_{24}	2.342

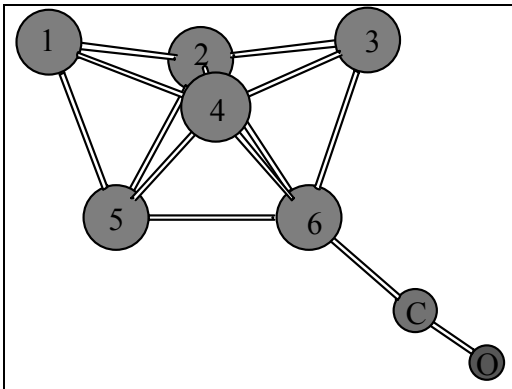

Cu_6CO	C_s
r_{Cu-C}	1.876
r_{C-O}	1.154
r_{36}	2.461
r_{15}	2.498
r_{24}	2.373
r_{56}	2.475
r_{12}	2.432
r_{23}	2.414
r_{25}	2.443
r_{26}	2.510

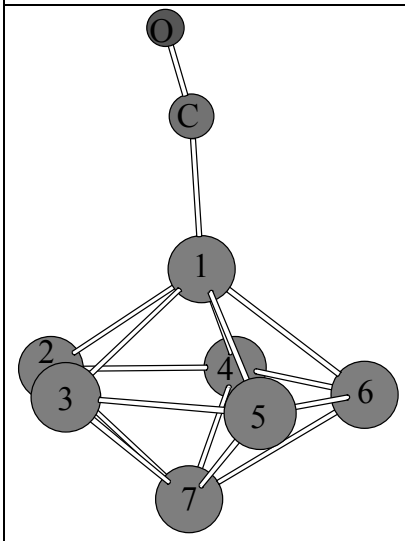

Cu_7CO	C_s
r_{Cu-C}	1.859
r_{C-O}	1.149
r_{12}	2.504
r_{13}	2.505
r_{14}	2.504
r_{15}	2.508
r_{16}	2.506
r_{23}	2.403
r_{24}	2.403
r_{27}	2.444
r_{35}	2.403
r_{37}	2.458
r_{46}	2.404
r_{47}	2.445
r_{56}	2.403
r_{57}	2.456
r_{67}	2.453

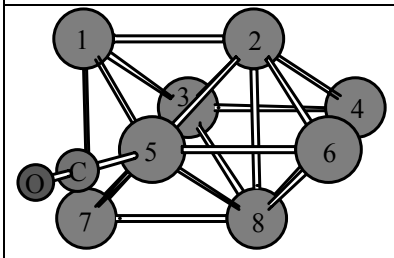

Cu_8CO	C_s
r_{Cu-C}	1.842
r_{C-O}	1.148
r_{15}	2.506
r_{17}	2.530
r_{23}	2.450
r_{26}	2.384
r_{28}	2.523
r_{34}	2.363
r_{37}	2.461
r_{48}	2.457
r_{56}	2.460
r_{58}	2.550
r_{78}	2.374

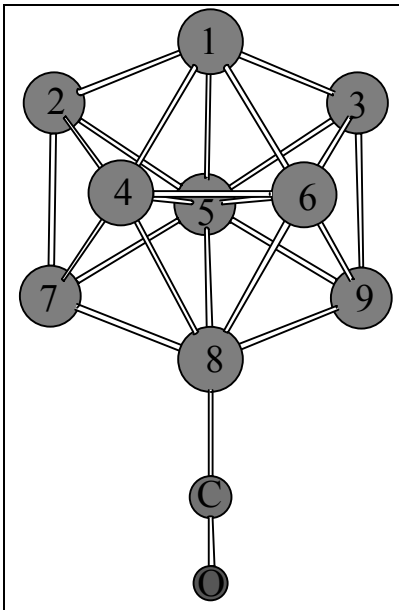

Cu_9CO	C_s
r_{Cu-C}	1.838
r_{C-O}	1.151
r_{12}	2.441
r_{14}	2.493
r_{15}	2.491
r_{24}	2.511
r_{25}	2.403
r_{45}	2.497
r_{46}	2.389
r_{47}	2.440
r_{48}	2.540
r_{57}	2.392
r_{58}	2.569
r_{78}	2.525

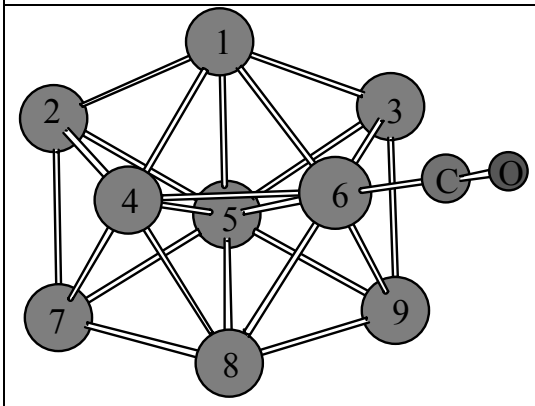

Cu_9CO	C_s
r_{Cu-C}	1.842
r_{C-O}	1.150
r_{12}	2.528
r_{13}	2.473
r_{14}	2.404
r_{15}	2.447
r_{16}	2.539
r_{24}	2.502
r_{25}	2.447
r_{27}	2.486
r_{35}	2.415
r_{36}	2.488
r_{39}	2.528
r_{45}	2.475
r_{46}	2.541
r_{56}	2.664

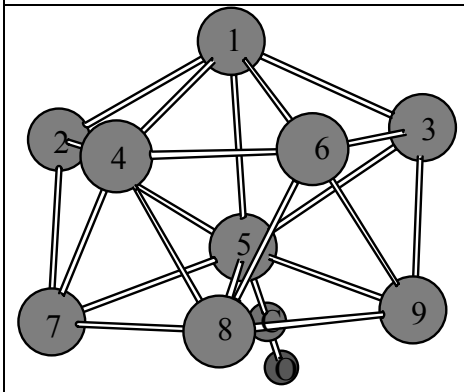

Cu_9CO	C_{2v}
r_{Cu-C}	1.870
r_{C-O}	1.145
r_{15}	2.507
r_{24}	2.436
r_{25}	2.584
r_{27}	2.463
r_{46}	2.367
r_{48}	2.433

Figure VIII-9. Some of the other studied less stable Cu_nCO structures.

In general, the structure of the most stable copper cluster carbonyl for each value of n presents the strongest and shortest Cu-C bond and the weakest and longest C-O bond. This is in line with the DCD bonding scheme for the CO interaction with the copper clusters. In this bonding scheme, donation and back-donation act synergistically. Thus, a larger back-donation to the π^* unoccupied orbital of CO favors the σ donation of CO to the copper cluster, which in turn promotes the back-donation. As a result, a shorter and stronger Cu-C bond and a longer and weaker C-O bond are normally found as observed in Figure VIII-10. The only exception to this general rule is Cu_1CO, which follows a different behavior as compared to the rest of the clusters.[29] Cu-C and C-O frequencies for copper cluster monocarbonyls are listed in Table VIII-10.

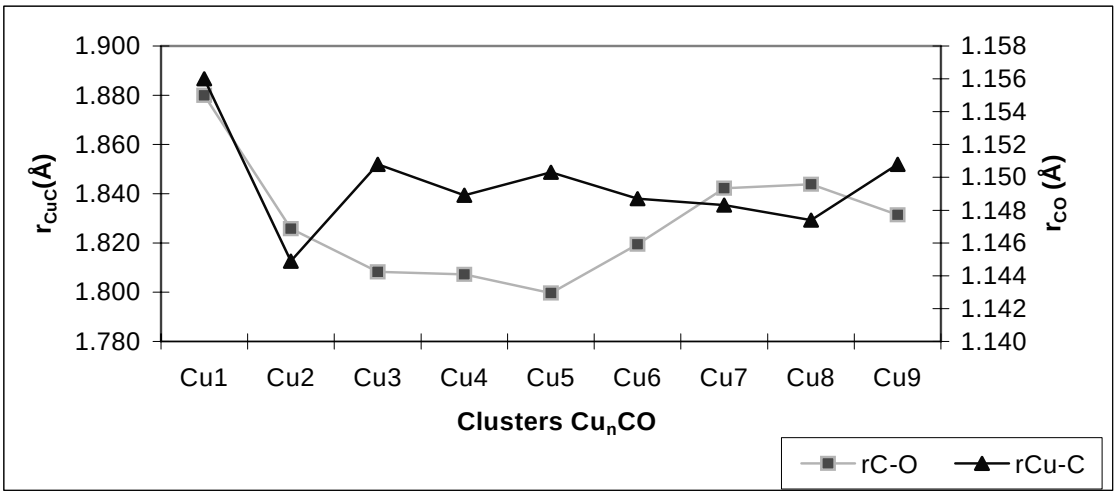

Figure VIII-10. Evolution of the Cu-C and C-O distances (Å) in copper cluster carbonyls.

Cluster	Cu-C	C-O
Cu_2CO	409.7	1961.3
Cu_3CO	427.8	2078.3
Cu_4CO	450.9	2026.8
Cu_5CO	452.4	2044.0
Cu_6CO	465.5	2033.8
Cu_7CO	434.7	2039.3
Cu_8CO	403.5	2032.3
Cu_9CO	403.2	2039.5

Table VIII-10. Frequencies of the most stable Cu_nCO clusters (in cm^{-1}).

Coming back to the results of the condensed Fukui functions, it is observed that most of the predictions done *a priori* have been accomplished. This is particularly true for the f^+ function, which only fails for the prediction of the selectivity in Cu_7. However, the difference between the f^+ condensed Fukui functions for the 1 (7) and 2 (3-6) copper atoms is not large enough to totally discard the interaction through the 2-6 copper atoms, especially if one takes into account that the local reactivity may change by the external field generated by the approaching CO molecule. The f^- and f^o are unsuccessful to predict the correct reactive site of the Cu_4, Cu_6*, and Cu_7 clusters. Thus, the f^+ function is the most suitable for predicting the selectivity of the CO adsorption on copper clusters. Predictions from the shape of the LUMO orbitals of the cluster are also satisfactory except for the Cu_7 cluster.

2. Binding Energies and the Nature of the Chemical Bond. The BE of the CO molecules adsorbed on the copper clusters is calculated as:

$$BE = E^{Cu_nCO}_{Cu_nCO_{multiplicity}} - \left(E^{free}_{CO_{sin\ glet}} - E^{free}_{Cu_{n\,multiplicity}}\right) \qquad (10)$$

where the multiplicity can be either singlet in even-numbered copper clusters or doublet in odd-numbered ones.

The plot of the BE with respect to the size of the cluster is given in Figure VIII-11. The BPW91/TZ2P BEs listed in Table VIII-11 are clearly larger in absolute value than those reported by Cao *et al*.[32] Despite the numerical differences between our BEs and those reported by Cao and co-workers,[32] the trends are exactly the same, except for the fact that the open-shell Cu_3CO cluster has the largest, in absolute value, BE at the BPW91/TZ2P level, while with the B3LYP/DZP method the strongest Cu-C bond corresponds to the Cu_5CO cluster. The BSSE and ZPE corrections do not affect the trends. They are displayed in Table VIII-11 and further in detail in Table VIII-12.

To obtain a deeper insight into the nature of the Cu-CO bond in copper cluster carbonyls, an energy decomposition analysis (EDA) has been carried out. In this analysis, the total BE is divided into preparation energy and interaction energy

($BE=\Delta E_{prep}+\Delta E_{int}$) of the copper cluster with the CO molecule. The preparation energy term (ΔE_{prep}) is the sum of the deformation energy (ΔE_{def}) and the excitation energy (ΔE_{excit}). The deformation energy is the energy needed to modify the geometry of the ground state free fragments to attain the geometry that they have after the insertion of a CO molecule and has two components, the deformation of CO ($\Delta E_{def\ CO}$) and the deformation of the copper cluster ($\Delta E_{def\ Cu_n}$). Due to technical reasons, in the ADF program, this energy decomposition analysis can only be performed only on singlet state fragments. For this reason in clusters having an odd number of copper atoms, it is necessary to correct the interaction energy by adding an energy term, the so-called excitation energy, that accounts for the energy difference between the fictitious singlet state (with half α and β electrons in the HOMO) taken as the reference in the EDA analysis and the real doublet state.[71]

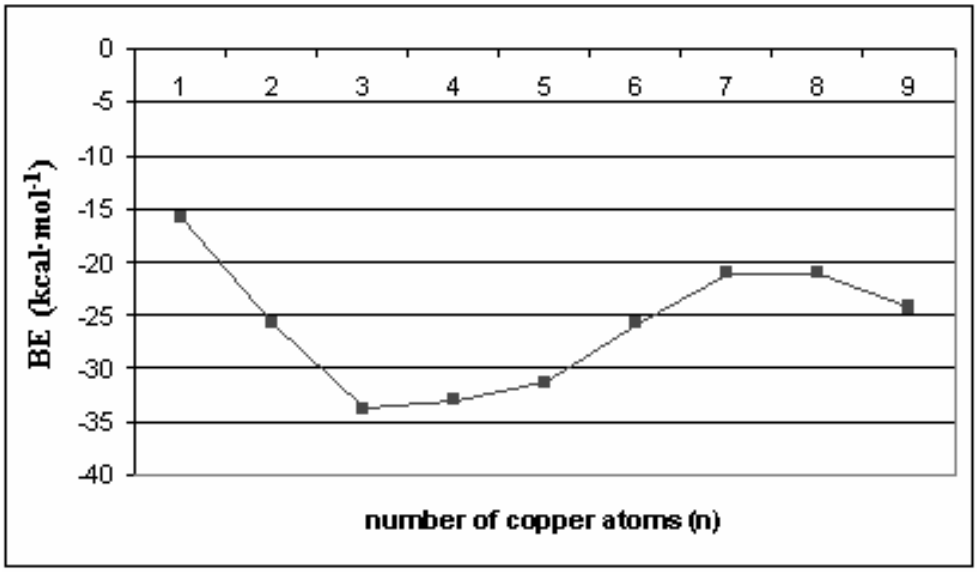

Figure VIII-11. Plot of the CO binding energy (BE, kcal·mol^{-1}) with respect to the number of copper atoms in the copper cluster carbonyls.

Table VIII-11 collects the results of the EDA. For the different copper cluster carbonyls the values of ΔE_{def} do not exceed 1.4 kcal·mol^{-1}, except for Cu_5CO and Cu_6CO due to the important geometrical changes undergone by the bare cluster geometry with the adsorption of CO. The deformation of the CO molecule is always small, ranging between 0.1 and 0.5 kcal·mol^{-1}. The ΔE_{excit} term decreases with the size

of the cluster. Thus, the energy difference between the fictitious singlet state and the doublet state in Cu_1 is 4.4 kcal·mol^{-1} higher than that of the Cu_9 bare cluster. Extrapolation of this result points out that the ΔE_{excit} term will be close to zero for bigger clusters, and null for the copper surface. Like the ΔE_{excit} term, in general, ΔE_{prep} decreases upon the size of the cluster, indicating that in the limit of the metallic bulk this term will likely become insignificant. The ΔE_{int} ranges between 22 and 44 kcal·mol^{-1}. This term is useful to describe the different behavior of the clusters with respect the interaction with CO. The interaction energy term can be also divided into Pauli repulsion (ΔE_{Pauli}), electrostatic interaction (ΔE_{elstat}), and orbital interaction (ΔE_{oi}). There is a relationship between the Cu-C bond and the different components of the interaction energy. In general, the longer the Cu-C bond length, the smaller (in absolute values) are the ΔE_{int}, ΔE_{Pauli}, ΔE_{elstat}, and ΔE_{oi} terms. The correlation between the Cu-C bond distances and the ΔE_{int} term is quite good with a regression coefficient (r^2) of 0.820. Moreover, if we leave out the value of the Cu_1CO species the r^2 value improves to 0.882. This exclusion is often carried out in the bibliography.[26,29,32] The energy ΔE_{oi} presents a good correlation with the Cu-C and the C-O bond lengths. In this latter case, r^2 is 0.860 if the value of the Cu_3CO cluster is left out.

Cluster	ΔE_{defCO}	ΔE_{defCun}	ΔE_{def}	ΔE_{excit}	ΔE_{prep}	ΔE_{Pauli}	ΔE_{elstat}	ΔE_{oi}	ΔE_{int}	BE[a]	$\%\Delta E_{elstat}$
Cu_1CO	0.5	0.0	0.5	6.6	7.1	165.7	-90.0	-98.8	-23.0	-15.9 (-14.4)	47.69
Cu_2CO	0.1	0.0	0.1	0.0	0.1	130.6	-98.1	-58.3	-25.8	-25.7 (-23.0)	62.73
Cu_3CO	0.3	1.0	1.3	5.5	6.8	231.2	-131.7	-140.1	-40.6	-33.8 (-30.4)	48.45
Cu_4CO	0.2	0.5	0.7	0.0	0.7	132.1	-101.1	-64.7	-33.8	-33.0 (-29.2)	60.98
Cu_5CO	0.3	6.6	6.9	5.6	12.5	212.8	-127.2	-129.4	-43.7	-31.2 (-26.8)	49.58
Cu_6CO	0.3	4.9	5.2	0.0	5.2	133.3	-100.3	-64.0	-31.0	-25.8 (-20.9)	61.03
Cu_7CO	0.2	1.1	1.3	2.5	3.8	140.4	-101.1	-64.2	-24.9	-21.0 (-16.4)	61.17
Cu_8CO	0.2	1.0	1.2	0.0	1.2	139.0	-100.0	-61.2	-22.3	-21.1 (-16.1)	62.03
Cu_9CO	0.3	1.1	1.4	2.2	3.6	160.6	-108.3	-80.3	-27.9	-24.3 (-18.6)	57.42

[a] In parentheses, the BE values corrected by BSSE and ZPE

Table VIII-11. Values of the energy decomposition analysis of Cu-C bond (in kcal·mol^{-1}).

Cluster	BE	ZPE	BSSE	Corrected BE
Cu_1CO	-15.9	0.7	0.8	-14.4
Cu_2CO	-25.7	1.4	1.3	-23.0
Cu_3CO	-33.8	1.6	1.8	-30.4
Cu_4CO	-33.0	1.6	2.2	-29.2
Cu_5CO	-31.2	1.7	2.7	-26.8
Cu_6CO	-25.8	1.8	3.1	-20.9
Cu_7CO	-21.0	1.1	3.5	-16.4
Cu_8CO	-21.1	1.1	3.9	-16.1
Cu_9CO	-24.3	1.3	4.4	-18.6

Table VIII-12. BE of Cu_nCO corrected by ZPE and BSSE (in kcal·mol^{-1})

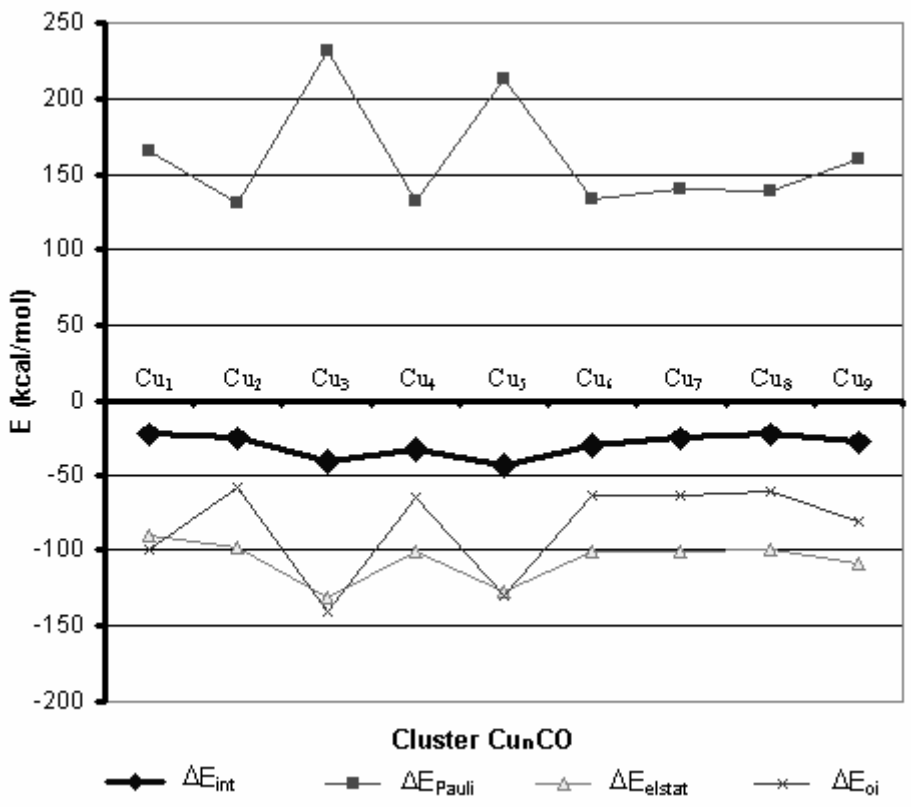

Figure VIII-12. Interaction energy of the Cu_nCO clusters and its components. Energies are given in kcal·mol^{-1}.

Figure VIII-12 plots the values of ΔE_{int} and of its three components for the most stable copper cluster carbonyls. It is worth noting that the values of the components of the

interaction energy as well as the total interaction energy present an oscillating behavior that apparently converges for the largest clusters. As can be seen in this Figure, the behavior of the ΔE_{int} parallels that of the ΔE_{oi} and ΔE_{elstat} terms, while the ΔE_{Pauli} follows an opposite trend. Indeed, the correlation between the ΔE_{Pauli} and ΔE_{oi} terms is quite good (r^2=0.945). Better orbital interactions (ΔE_{oi}) lead to smaller Cu-C bonds and larger absolute value ΔE_{elstat} and ΔE_{Pauli} interactions. This is particularly true for the Cu_3CO and Cu_5CO species. The percentage of ionic character of the CO interaction in the copper cluster carbonyls ranges between the 50 and 60%, approximately. It is smaller for open-shell clusters with an odd number of copper atoms than for closed-shell clusters due to the fact that the former present better orbital interactions because of the presence of a semioccupied molecular orbital (SOMO) that can participate in the bonding as a high-lying HOMO or low-lying LUMO.

Cluster	ΔE_{oi}	ΔE_{σ}	ΔE_{π}	% σ	% π
Cu_1CO	-98.8	-88.3	-10.5	89.4	10.6
Cu_2CO	-58.3	-42.4	-15.9	72.8	27.2
Cu_3CO	-140.1	-126.1	-14.0	90.0	10.0
Cu_4CO	-64.7	-43.3	-21.4	66.9	33.1
Cu_5CO	-129.4	-110.9	-18.5	85.7	14.3
Cu_6CO	-64.0	-47.1	-16.9	73.6	26.4
Cu_7CO	-64.2	-45.6	-18.6	71.1	28.9
Cu_8CO	-61.2	-46.2	-15.0	75.5	24.5

Table VIII-13. ΔE_{oi} decomposition for Cu_nCO (n=1-8) (energies in kcal·mol^{-1}).

To analyze further the orbital interaction energy term, we have taken advantage of the symmetry plane of the Cu_nCO clusters from n = 1 to 8 to separate the σ and π orbital interaction energy parts. From the results in Table VIII-13, we can see that, first, the donation (ΔE_{σ}) linked to the HOMO of CO and LUMO of Cu_n interaction in the DCD bonding scheme (*vide supra*) is more than twice as large as the term associated with back-donation (ΔE_{π}), and, second, there is not a clear-cut relationship between the ΔE_{σ} and ΔE_{π} values. Thus, higher ΔE_{σ} energies do not imply also larger ΔE_{π} values. In fact, a higher value of ΔE_{oi} is only reflected in ΔE_{σ} (r^2=0.992). Finally, back-donation is

especially high in the smallest clusters with an odd number of copper atoms. And there is a clear relationship between rCu-C and ΔE_π, displayed in Figure VIII-13. We note in passing that the fact that donation is more important than back-donation was also found for the interaction of carbene in Fischer carbene complexes.[72]

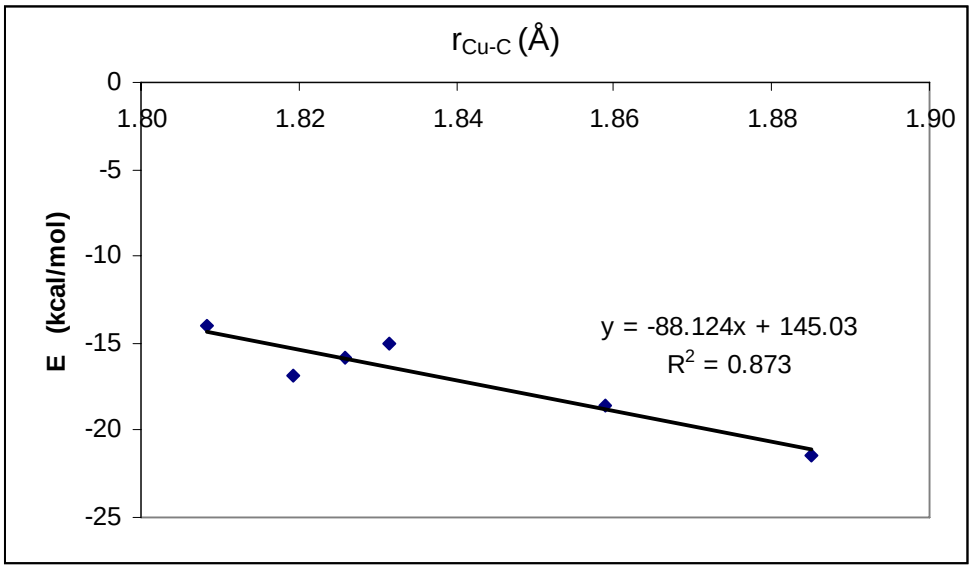

Figure VIII-13. Correlation between $r_{Cu\text{-}C}$ (in Å) and ΔE_π (in kcal·mol^{-1}).

The Mayer bond orders (MBOs) for the most stable Cu_nCO structures are listed in Table VIII-14. The MBO values for Cu_1CO reflect the particular behavior of this copper cluster carbonyl as compared to the other clusters. The MBOs point out that Cu_1CO has the strongest Cu-C bond and the weakest C-O bond. In general, the odd-numbered copper clusters have higher Cu-C and lower C-O MBOs when compared to the even-numbered ones. This is in line with the better orbital interactions found in the EDA analysis for the copper clusters with an odd number of copper atoms. The C-O MBO value for the free CO molecule is 2.28. Therefore, the C-O is clearly activated in copper cluster carbonyls as the MBO decreases when the CO is coordinated to a copper cluster. When the size of the cluster increases, the oscillator behavior of the Cu-C and C-O MBOs tends to disappear.

Cluster	Cu-C	C-O
Cu_1CO	1.02	2.11
Cu_2CO	0.87	2.18
Cu_3CO	0.91	2.13
Cu_4CO	0.88	2.15
Cu_5CO	0.92	2.13
Cu_6CO	0.89	2.15
Cu_7CO	0.88	2.16
Cu_8CO	0.87	2.17
Cu_9CO	0.88	2.14

Table VIII-14. Mayer bond orders for the most stable Cu_nCO (n=1-9).

Table VIII-15 collects the Hirshfeld charge values of the CO fragment in the copper cluster carbonyls. The charge values close to zero for the CO fragment show that, from the Hirshfeld charge analysis viewpoint, the Cu_n back-donation of charge to CO is as important as the donation of CO toward the copper cluster. Although one might expect a larger charge donation than back-donation according to the EDA analysis, the Mulliken charge lost by the HOMO of CO (about 0.3-0.4 a.u.) and the Mulliken charge acquired by the LUMO and LUMO+1 of CO (0.3-0.4 a.u.) in the metal cluster carbonyls supports the conclusion that donation and back-donation are equally important from a charge analysis point of view. Differences in the trends given by the EDA and charge analysis are not completely unexpected[73] because energetically not only the attractive interactions between orbitals are important, but also the repulsive ones (from the charge point of view only the favorable orbital interactions contribute to the charge transfer). The elongation of the C-O bond distance is correlated with the LUMO and LUMO+1 occupations of the CO fragment in the copper cluster monocarbonyls (r^2=0.814, see Figure VIII-14).

Cluster	CO charge	donation	back-donation
Cu_1CO	-0.079	0.29	0.40
Cu_2CO	0.013	0.29	0.26
Cu_3CO	-0.046	0.33	0.38
Cu_4CO	-0.037	0.33	0.35
Cu_5CO	-0.048	0.36	0.38
Cu_6CO	-0.042	0.36	0.34
Cu_7CO	-0.032	0.33	0.33
Cu_8CO	-0.020	0.33	0.31
Cu_9CO	-0.054	0.35	0.36

Table VIII-15. CO Hirshfeld charges in Cu_nCO and reduction of the CO HOMO Mulliken charge (donation) and increase of the CO LUMO and LUMO+1 Mulliken charge (back-donation) in the Cu_nCO clusters (charges in electrons).

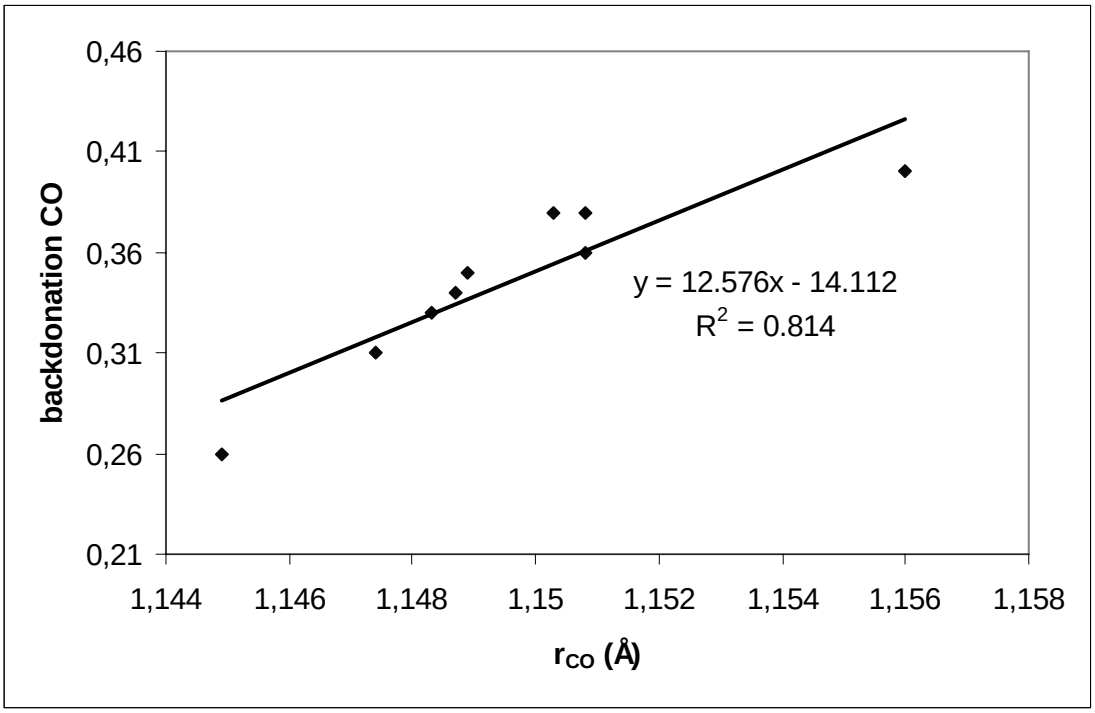

Figure VIII-14. Correspondence between the LUMO and LUMO+1 occupations of CO with r_{C-O}

3. The Binding of CO through the Oxygen Atom. According to our calculations, the coordination of the CO molecule to the copper clusters through the oxygen atom is only possible for the copper clusters with n=2-5. The molecular structure of these clusters together with their CO BE is given in Figure VIII-15. The Cu-O bond distances are about 2 Å for all optimized Cu_nOC clusters, somewhat larger than the Cu-C bond lengths of the Cu_nCO clusters. The CO binding through the oxygen atom energies are about 25-30 kcal·mol^{-1} lower in absolute value than those that come from the interaction through the carbon atom. The BE difference between the CO binding through the carbon as compared to through the oxygen atom increases with the size of the cluster. Indeed, for the higher members of the series the binding of CO is an endothermic process and the geometry optimization of the initial Cu_nOC clusters leads to the Cu_n and CO separated fragments. Extrapolating this result to a copper surface, we conclude that coordination of CO through the oxygen atom is not possible. In fact, the Mulliken condensed Fukui function analysis of the CO molecule gives values of 0.759 and 0.241 for the f^- function of the carbon and the oxygen atoms, respectively, and of 0.866 and 0.134 for the f^+ function. Therefore, an electrophilic or nucleophilic attack through the oxygen atom of CO is not favored according to the condensed Fukui values.

	Distances (Å)	BE_{Cu_nOC}	BE_{Cu_nCO}
Cu_2OC	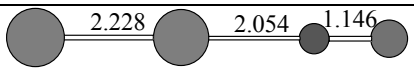	-1.1	-25.7
Cu_3OC	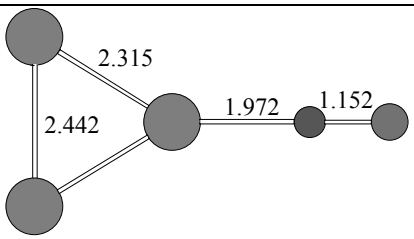	-4.2	-33.8

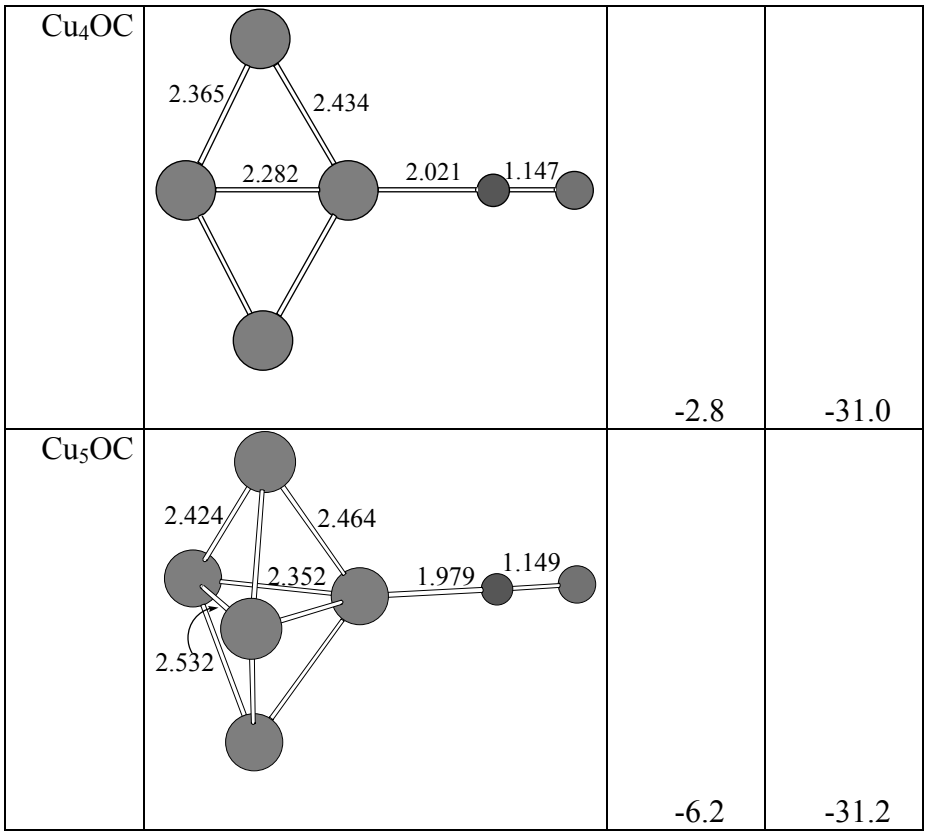

Figure VIII-15. Molecular geometries and binding energies for the Cu_nOC clusters (energies in kcal·mol^{-1}).

Conclusions

This study has analyzed the adsorption of CO on small copper clusters, Cu_n (n=1-9). It has been confirmed that the bare copper clusters with even number of copper atoms are more stable than those with an odd number of copper atoms. The latter are the most reactive and, in fact, they show the higher CO binding energies. We have found that the nucleophilic condensed Fukui function and the shape of the LUMO orbitals are useful tools to predict the regioselectivity of the CO insertion, with the only exception being the Cu_7 cluster. The energy decomposition analyses of the CO binding energy in the copper cluster carbonyls have shown that the σ donation is about twice as important as π back-donation. From an electron charge point of view, however, donation and back-donation are equally important. Finally, we have shown that the coordination of CO through the oxygen is energetically unfavorable as compared to CO binding through the carbon atom, especially for the larger copper clusters.

References

1. M. D. Morse, *Chem. Rev*. **1986**, *86*, 1049-1109.
2. A. G. Zacarias, M. Castro, J. M. Tour, J. M. Seminario, *J. Phys. Chem. A* **1999**, *103*, 7692-7700.
3. J. M. Seminario, J. M. Tour, *Int. J. Quantum. Chem*. **1997**, *65*, 749-758.
4. T. Mineva, N. Russo, M. Toscano, *Int. J. Quantum Chem*. **2000**, *80*, 105-109.
5. P. Jaque, A. Toro-Labbé, *J. Phys. Chem. B* **2004**, *108*, 2568-2574.
6. a) G. M. Koretsky, M. B. Knickelbein, *J. Chem. Phys*. **1997**, *106*, 9810-9814. b) W. D. Knight, K. Clemenger, W. A. de Heer, W. A. Saunders, *Phys. Rev. Lett*. **1984**, *52*, 2141-2143. c) V. Kreibeg, M. Vollmer, *Optical Properties of Metal Clusters*, Springer, Berlin, 1995. d) Y. Zhao, W. Xu, W. Li, Y. Xie, H. F. Schaefer III, *J. Comput. Chem*. **2004**, *25*, 907-920. e) K. R. S. Chandrakumar, T. K. Ghanty, S. K. Ghosh, *J. Phys. Chem. A* **2004**, *108*, 6661-6666. f) R. Fournier, *J. Chem. Phys*. **2001**, *115*, 2165-2177.
7. M. B. Knickelbein, *Chem. Phys. Lett.* **1992**, *192*, 129-134.
8. D. E. Powers, S. G. Hansen, M. E. Geusic, D. L. Michalopoulos, R. E. Smalley, *J. Chem. Phys*. **1983**, *78*, 2866-2881.
9. V. A. Spasov, T.-H. Lee, K. M. Ervin, *J. Chem. Phys*. **2000**, *112*, 1713-1720.
10. O. Ingólfsson, U. Busolt, K. Sugawara, *J. Chem. Phys*. **2000**, *112*, 4613-4620.
11. J. Holmgren, H. Gronbeck, M. Andersson, A. Rosen, *Phys. Rev. B* **1996**, *53*, 16644-16651.
12. B. J. Winter, B. E. K. Parks, S. J. Riley, *J. Chem. Phys*. **1991**, *94*, 8618-8621.
13. V. Lammers, G. Borstel, *Phys. Rev. B* **1994**, *49*, 17360-17377.
14. P. Fuentealba, Y. Simón-Manso, *Chem. Phys. Lett*. **1999**, *314*, 108-113.
15. J. Ho, K. M. Ervin, W. C. Lineberger, *J. Chem. Phys*. **1990**, *93*, 6987-7002.
16. H. Aakeby, I. Panas, L. G. M. Pettersson, P. E. M. Siegbahn, U. Wahlgren, *J. Phys. Chem*. **1990**, *94*, 5471-5477.
17. P. Balbuena, P. Derosa, J. M. Seminario, *J. Phys. Chem. B* **1999**, *103*, 2830-2840.
18. L. Padilla-Campos, A. Toro-Labbé, J. Maruani, *Surf. Sci*. **1997**, *384*, 24-36.
19. L. Padilla-Campos, A. Toro-Labbé, *J. Mol. Struct. (THEOCHEM)* **1997**, *390*, 183-192.
20. L. Padilla-Campos, A. Toro-Labbé, *J. Chem. Phys*. **1998**, *108*, 6458-6465.

21. P. Calaminici, A. M. Köster, N. Russo, D. R. Salahub, *J. Chem. Phys*. **1996**, *105*, 9546-9556.
22. P. Calaminici, K. Jug, A. M. Köster, *J. Chem Phys*. **1998**, *109*, 7756-7763.
23. a) P. Calaminici, A. M. Köster, A. Vela, *J. Chem. Phys*. **2002**, *113*, 2199-2202. b) M. Yang, K. A. Jackson, *J. Chem. Phys*. **2005**, *122*, 184317.
24. C. Mossobrio, A. Pasquarello, A. Dal Corso, *J. Chem. Phys*. **1998**, *109*, 6626-6630.
25. K. A. Jackson, *Phys. Rev. B* **1993**, *47*, 9715-9722.
26. K. Jug, B. Zimmermann, P. Calaminici, A. M. Köster, *J. Chem. Phys*. **2002**, *116*, 4497-4507.
27. K. P. Huber, G. Herzberg, *Molecular Spectra and Molecular Structure*, Vol. IV, Van Nostrand-Reinhold, New York, 1989.
28. E. A. Rohlfing, J. J. Valentini, *J. Chem. Phys.* **1986**, *84*, 6560-6566.
29. P. Jaque, A. Toro-Labbé, *J. Chem. Phys*. **2002**, *117*, 3208-3218.
30. X. Crispin, C. Bureau, V. Geskin, R. Lazzaroni, J.-L. Brédas, *Eur. J. Inorg. Chem.* **1999**, 349-360.
31. G. Schmid, *Chem. Rev*. **1992**, *92*, 1709-1727.
32. Z. Cao, Y. Wang, J. Zhu, W. Wu, Q. Zhang, *J. Phys. Chem. B* **2002**, *106*, 9649-9654.
33. a) M. A. Nygren, P. E. M. Siegbahn, *J. Phys. Chem*. **1992**, *96*, 7579-7584. b) M. A. Nygren, P. E. M. Siegbahn, C. Jin, T. Guo, R. E. Smally, *J. Chem. Phys*. **1991**, *95*, 6181-6184.
34. K. J. Taylor, C. L. Pettiette-Hall, O. Cheshnovsky, R. E. Smalley, *J. Chem. Phys*. **1992**, *96*, 3319-3329.
35. S. E. Wheeler, K. W. Sattelmeyer, P. v. R. Scheleyer, H. F. Schaefer III, *J. Chem. Phys*. **2004**, *120*, 4683-4689.
36. P. K. Chattaraj, P. Fuentealba, P. Jaque, A. Toro-Labbé, *J. Phys. Chem. A* **1999**, *103*, 9307-9312.
37. S. Gutiérrez-Oliva, P. Jaque, A. Toro-Labbé, *J. Phys. Chem. A* **2000**, *104*, 8955.-8964.
38. A. Toro-Labbé, *J. Phys. Chem. A* **1999**, *103*, 4398-4403.
39. P. Jaque, A. Toro-Labbé, *J. Phys. Chem. A* **2000**, *104*, 995-1003.
40. ADF2002.03, E. J. Baerends, J. A. Autschbach, A. Bérces, C. Bo, P. M. Boerrigter, L. Cavallo, D. P. Chong, L. Deng, R. M. Dickson, D. E. Ellis, L.

Fan, T. H. Fischer, C. Fonseca Guerra, S. J. A. van Gisbergen, J. A. Groeneveld, O. V. Gritsenko, M. Grüning, F. E. Harris, P. van den Hoek, H. Jacobsen, G. van Kessel, F. Kootstra, E. van -Lenthe, V. P. Osinga, S. Patchkovskii, P. H. T. Philipsen, D. Post, C. C. Pye, W. Ravenek, P. Ros, P. R. T. Schipper, G. Schreckenbach, J. G. Snijders, M. Solà, M. Swart, D. Swerhone, G. te Velde, P. Vernooijs, L. Versluis, O. Visser, E. van Wezenbeek, G. Wiesenekker, S. K. Wolff, T. K. Woo, T. Ziegler, Vrije Universiteit Amsterdam, Amsterdam, 2002.

41. E. J. Baerends, D. E. Ellis, P. Ros, *Chem. Phys*. **1973**, *2*, 41-51.
42. C. Fonseca Guerra, O. Visser, J. G. Snijders, G. te Velde, E. J. Baerends, *Methods and Techniques for Computational Chemistry*, STEF, Cagliari, **1995**, p. 305.
43. G. te Velde, F. M. Bickelhaupt, E. J. Baerends, C. Fonseca Guerra, S. J. A. van Gisbergen, J. G. Snijders, T. Ziegler, *J. Comput. Chem.* **2001**, *22*, 931-967.
44. G. te Velde, E. J. Baerends, *J. Comput. Phys*. **1992**, *99*, 84-98.
45. a) A. D. Becke, *Phys. Rev. A* **1988**, *38*, 3098-3100. b) A. D. Becke, *J. Chem. Phys.* **1986**, *84*, 4524-4529. c) A. D. Becke, *Int. J. Quantum Chem*. **1983**, *23*, 1915-1922.
46. a) J. P. Perdew, *Phys. Rev. B* **1986**, *33*, 8822-8824. b) J. P. Perdew, W. R. Wang, *Phys. Rev. B* **1992**, *45*, 13244-13249.
47. a) L. Versluis, T. Ziegler, *J. Chem. Phys.* **1988**, *88*, 322. b) L. Fan, T. Ziegler, *J. Chem. Phys.* **1991**, *95*, 7401-7408. c) G. Schreckenbach, J. Li, T. Ziegler, *Int. J. Quantum Chem.* **1995**, *56*, 477-488.
48. L. Fan, L. Versluis, T. Ziegler, E. J. Baerends, W. Ravenek, *Int. J. Quantum Chem. Symp.* **1988**, *22*, 173-181.
49. H. Jacobsen, G. Schreckenbach, T. Ziegler, *J. Phys. Chem.* **1994**, *98*, 11406-11410.
50. J. G. Snijders, E. J. Baerends, P. Vernooijs, *At. Nucl. Data Tables* **1982**, *26*, 483-509.
51. P. Vernooijs, E. J. Baerends, *Slater Type Basis Functions for the Whole Periodic System. Internal Report*, Vrije Universiteit of Amsterdam, The Netherlands, 1981.
52. J. Krijn, E. J. Baerends, *Fit Functions in the HFS Method. Internal Report* (in Dutch), Vrije Universiteit of Amsterdam, The Netherlands, 1984.

53. MOLEKEL 4.0, P. Flükiger, H. P. Lüthi, S. Portmann, J. Weber, Swiss Center for Scientific Computing, Manno (Switzerland), 2000.
54. a) N. E. Schultz, Y. Zhao, D. G. Truhlar, *J. Chem. Phys*. **2000**, *109*, 4388-4403. b) C. J. Barden, J. C. Rienstra-Kiracofe, H. F. Schaefer III, *J. Chem. Phys*. **2000**, *113*, 690-700.
55. E. Florez, W. Tiznado, F. Mondragón, P. Fuentealba, *J. Phys. Chem. A* **2005**, *109*, 7815-7821.
56. J. Rienstra-Kiracofe, G. Tschumper, H. F. Schaefer III, S. Nandi, G. B. Ellison, *Chem. Rev*. **2002**, *102*, 231-282.
57. L. Curtiss, P. Redfern, K. Raghavachari, J. Pople, *J. Chem. Phys*. **1998**, *109*, 42-55.
58. X. Li, Z. Cai, M. D. Sevilla, *J. Phys. Chem. A* **2002**, *106*, 1596-1603.
59. N. Russo, M. Toscano, A. Grand, *J. Comput. Chem.* **2000**, *21*, 1243-1250.
60. P. W. Ayers, R. C. Morrison, R. K. Roy, *J. Chem. Phys*. **2002**, *116*, 8731-8744.
61. C. Massobrio, A. Pasquarello, A. Dal Corso, *J. Chem. Phys*. **1998**, *109*, 6626-6630.
62. a) M. Brack, *Rev. Mod. Phys*. **1993**, *65*, 677-732. b) W. A. de Heer, Rev. *Mod. Phys*. **1993**, *65*, 611-676.
63. a) R. G. Parr, R. G. Pearson, *J. Am. Chem. Soc*. **1983**, *105*, 7512-7516. b) R. G. Pearson, *Chemical Hardness: Applications from Molecules to Solids*; Wiley-VCH: New York, **1997**.
64. Ch. Elschenbroich, A. Salzer, In *Organometallics: A Concise Introduction*, 2nd ed.; VCH: Weinheim, Germany, 1992.
65. a) M. J. S. Dewar, *Bull. Soc. Chim. Fr.* **1951**, *18*, C71-9. b) J. Chatt, L. A. Duncanson, *J. Chem. Soc.* **1953**, 2939-2947.
66. a) S. Arulmozhiraja, P. Kolandaivel, *Mol. Phys*. **1997**, *90*, 55-62. b) P. Fuentealba, P. Pérez, R. Contreras, *J. Chem Phys*. **2000**, *113*, 2544-2551. c) R. K. Roy, K. Hirao, *J. Chem. Phys*. **2001**, *115*, 2901-2907. d) F. De Proft, C. van Alsenoy, A. Peeters, W. Langenaeker, P. Geerlings, *J. Comput. Chem*. **2002**, *23*, 1198-1209. e) R. K. Roy, S. Pal, K. Hirao, *J. Chem. Phys*. **1999**, *110*, 8236-8245.
67. C. Fonseca Guerra, J.-W. Handgraaf, E. J. Baerends, F. M. Bickelhaupt, *J. Comput. Chem.* **2004**, *25*, 189-210.

68. a) P. K. Chattaraj, H. Lee, R. G. Parr, *J. Am. Chem. Soc.* **1991**, *113*, 1855-1856. b) Y. Li, J. N. S. Evans, *J. Am. Chem. Soc.* **1995**, *117*, 7756-7759. c) R. G. Parr, R. G. Pearson, *J. Am. Chem. Soc*. **1983**, *105*, 7512-7516.
69. a) S. K. Ghosh, M. Berkowitz, *J. Chem. Phys.* **1985**, *83*, 2976-2983. b) M. Berkowitz, S. K. Ghosh, R. G. Parr, *J. Am. Chem. Soc.* **1985**, *107*, 6811-6814. c) M. Berkowitz, R. G. Parr, *J. Chem. Phys*. **1988**, *88*, 2554-2557.
70. K. Jug, B. Zimmermann, A. M. Köster, *Int. J. Quantum Chem*. **2002**, *90*, 594-602.
71. O. González-Blanco, V. Branchadell, K. Monteyne, T. Ziegler, *Inorg. Chem*. **1998**, *37*, 1744-1748.
72. a) S. F. Vyboishchikov, G. Frenking, G. *Chem. Eur. J.* **1998**, *4*, 1428-1438. b) M. Cases, G. Frenking, M. Duran, M. Solà, *Organometallics* **2002**, *21*, 4182-4191.
73. G. Frenking, M. Solà, S. R. Vyboishchikov, *J. Organometallic Chem.* **2005**, *690*, 6178-6204.

PART IV: Ruthenium Complexes

Chapter IX: *New Aqua Ruthenium Complex Containing the Tridentate [9]aneS$_3$ and the Didentate 1,10-Phenanthroline Ligands*

New Aqua Ruthenium Complex Containing the Tridentate *[9]aneS$_3$* and the Didentate 1,10-Phenanthroline Ligands

Abstract

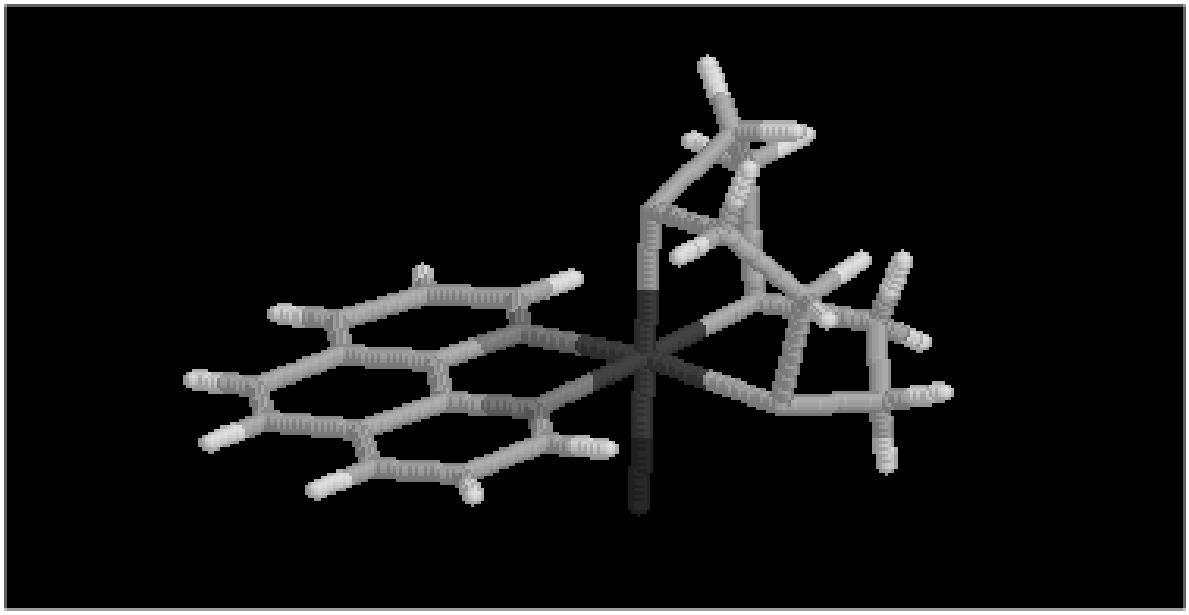

The synthesis of a new Ru-H_2O complex [Ru(*phen*)(H_2O)(*[9]aneS$_3$*)](ClO_4)$_2$, **2**, (*phen* = 1,10-phenanthroline, *[9]aneS$_3$* = 1,4,7-trithiacyclononane) is described. The complex is characterized by UV/Vis and 1-D and 2-D NMR spectroscopy in solution. The complex has been further characterized in the solid-state by X-ray diffraction analysis which displays a distorted octahedral coordination geometry around the Ru metal center. The cyclic voltammetric experiments of the complex show a pH-dependent chemically irreversible wave at $E_{p,a}$ = 0.82 V, at pH = 7.0, indicating the low stability of the higher oxidation states. Nevertheless, before the complex decomposes, it is capable of electrocatalytically oxidizing benzyl alcohol (BzOH) to benzaldehyde with a second-order rate constant of 19.8 $M^{-1}s^{-1}$.

Introduction

Over the last two decades a large number of ruthenium polypyridyl complexes containing a water molecule directly bonded to the metal has emerged.[1] The $[Ru(trpy)(bpy)(H_2O)]^{2+}$ (*trpy* = 2,2′:6′,2″-terpyridine and *bpy* = 2,2′-bipyridine) complex described by Meyer et al.[1a] constitutes a paradigm of this type of complexes, both from a structural and a reactivity point of view.

The Ru^{II}-H_2O complexes are of interest since the corresponding higher oxidation states can be reached within a relatively narrow potential range by sequential electron and proton loss, as shown in Eq.(1) and (2) for $[Ru(trpy)(bpy)(H_2O)]^{2+}$.

$$Ru^{II}(trpy)(bpy)(H_2O)]^{2+} \underset{+1H^+,\,+1e^-}{\overset{-1H^+,\,-1e^-}{\rightleftharpoons}} [Ru^{III}(trpy)(bpy)(OH)]^{2+} \qquad (1)$$

$E_{1/2}(Ru^{III/II}$ at pH = 7) = 0.49 V vs. SSCE

$$[Ru^{III}(trpy)(bpy)(OH)]^{2+} \underset{+1H^+,\,+1e^-}{\overset{-1H^+,\,-1e^-}{\rightleftharpoons}} [[Ru^{IV}(trpy)(bpy)(O)]^{2+} \qquad (2)$$

$E_{1/2}$ ($Ru^{IV/III}$ at pH = 7) = 0.62 V vs. SSCE

These higher oxidation states, especially Ru^{IV}=O, are active catalysts for a variety of oxidative reactions such as the oxidation of alkenes to epoxides,[2] sulfides to sulfoxides,[3] phosphane to phosphane oxides,[4] alcohols to aldehydes,[5] and even saturated alkanes to alcohols.[6] Furthermore, from a bioinorganic perspective, they have also been shown to be able to selectively bind and cleave DNA molecules.[7]

A challenging aspect associated with the chemistry of Ru-H_2O type of complexes is the understanding of how electronic factors transmitted by the ligands can influence the stability of the different oxidation states, and as a consequence its reactivity.[8] With this purpose several Ru-H_2O complexes have been described containing electron-donating and electron-withdrawing substituents in the polypyridylic ligands,[9] as well those that have a variety of ancillary ligands containing oxygen donors such as picolinate or acetylacetonate and phosphorus donors such as phosphanes.[10]

In this paper we report on the synthesis, structural and spectroscopic characterization of the first example of a Ru-H_2O polypyridylic complex containing a thioether type ligand, $[Ru(phen)(H_2O)([9]aneS_3)]^{2+}$ (*phen* = 1,10-phenanthroline. *[9]aneS₃* = 1,4,7-trithiacyclononane). The electronic properties exerted by the thioether ligand to the metal center are discussed, together with its influence on the redox and catalytic properties.

Results

Synthesis and Solid-State Structure. The synthesis of the complex $[Ru(phen)(H_2O)([9]aneS_3)](ClO_4)_2$ (**2**) is straight forward and consists of the addition of Ag^I to the corresponding Ru^{II}-Cl complex according to Equation (3).

$$[Ru(Cl)(phen)([9]aneS_3)]^+ + Ag^+ + H_2O \longrightarrow [Ru(phen)(H_2O)([9]aneS_3)]^{2+} + AgCl \quad (3)$$

The crystal structure of complex **2·2H₂O** was solved by means of single-crystal X-ray diffraction analysis and its crystallographic data, as well as selected bond lengths and angles are presented in Tables IX-1 and -2, respectively. Figure IX-1 presents the ORTEP diagram for the cationic moiety of the molecule, including the corresponding labeling scheme.

Empirical formula	$C_{18}H_{26}Cl_2N_2O_{11}RuS_3$
Formula weight	714.56
Crystal system, space group	Triclinic, *P*1bar
a, Å	8.143(3)
b, Å	9.137(8
c, Å	18.754(7)
α,º	99.46(5)
β,º	91.52(3)
γ,º	107.77(5)
V, Å^3	1306.3(13
Formula Units/Cell	2
Temperatura, K	298
λ Mo-K$_\alpha$, Å	0.71073
$\rho_{calc.}$, g cm^{-3}	1.817
μ, mm^{-1}	1.104
R_1[a]	0.0386
WR_2[b]	0.0580

[a] $R_1 = \Sigma||F_o| - |F_c||/\Sigma|F_o|$

[b] $wR_2=[\Sigma\{w(F_o^2-F_c^2)^2\}/\Sigma\{w(F_o^2)^2\}]^{½}$, where $w=1/[\sigma^2(Fo^2)+(0.0042P)^2]$, $P=(F_o^2+2F_c^2)/3$

Table IX-1. Crystal data for complex **2**.

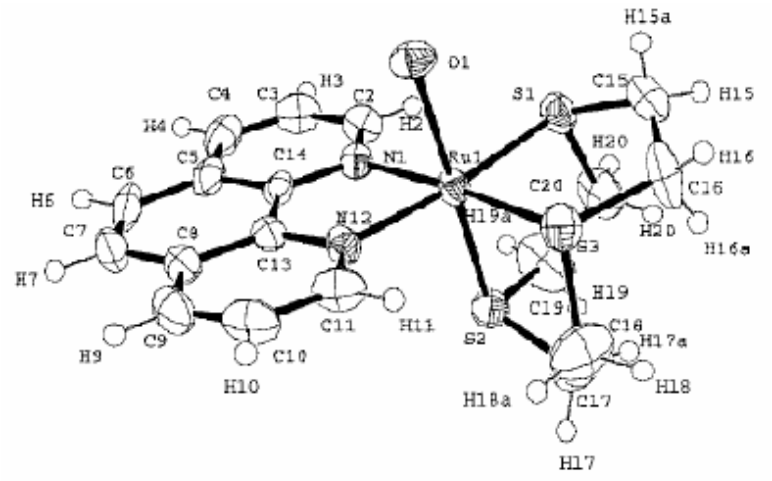

Figure IX-1. An ORTEP view (50% probability) of the molecular structure of cation **2**, including the atom labeling scheme.

The molecular structure of **2** shows that the Ru metal center has a distorted octahedral coordination environment. The *[9]aneS₃* ligand coordinates facially through its sulfur atoms in an endodentate manner, while the *phen* ligand is chelated through its N atoms. The sixth coordination site is occupied by the oxygen atom of the aqua ligand. Bond lengths and angles are within the expected values for this type of complexes.[11,12] It is interesting to note here that the Ru-S bond lengths *trans* to the N atoms of the *phen* ligand are about 4 pm larger than the Ru-S distance *trans* to the aqua ligand, denoting the stronger *trans* effect of the former ligand with respect to the latter. The S-Ru-S *cis* angles are close to 90° indicating the good facial fit of the ligand for an octahedral type of geometry with no steric distortions from the other ligands.[13] In sharp contrast, the *[9]aneS₃* ligand exerts a strong steric interaction over both the *phen* and the aqua ligands, which is clearly manifested, for instance, in the *trans* bonding angles that are all significantly smaller than 180°, ranging from 173.59(12)° to 177.54(10)°, thus producing a sort of umbrella folding [all *cis* X-Ru-S, X = N or O, angles are significantly larger than 90°, ranging from 91.03(10)° to 97.84(12)°, with a mean value for the six angles of 94.21(10)°]. Two disordered perchlorate anions balance the cationic charge. Finally, there are two waters of crystallization per complex that form an intricate network of hydrogen-bonds. O1w forms a strong hydrogen-bond with the aqua ligand bound to the Ru metal center and with the other crystallization water molecule (O2w). It also interacts weakly with one of the perchlorate counteranions. The other perchlorate ion interacts weakly with both the hydrogen atoms of the *phen* and the *[9]aneS₃* ligands, whereas O2w interacts only with O1w and one of the perchlorate ions.

Ru1-N1	2.086(4)	N1-Ru1-N12	78.08(15)	O1-Ru1-S1	91.03(10)
Ru1-N12	2.101(4)	N1-Ru1-O1	85.97(14)	S2-Ru1-S1	88.61(6)
Ru1-O1	2.183(3)	N12-Ru1-O1	83.78(13)	N1-Ru1-S3	174.20(11)
Ru1-S2	2.2636(18)	N1-Ru1-S2	91.67(11)	N12-Ru1-S3	96.16(12)
Ru1-S1	2.2986(17)	N12-Ru1-S2	96.41(11)	O1-Ru1-S3	94.21(10)
Ru1-S3	2.300(2)	O1-Ru1-S2	177.54(10)	S2-Ru1-S3	88.21(7)
N12-Ru1-S1	173.59(12)	N1-Ru1-S1	97.84(12)	S1-Ru1-S3	87.95(7)

Table IX-2. Selected Bond Lengths (Å) and Angles (º) for Complex **2**.

Complex[b]	[d]$E_{1/2}$ (IV/III)	[d]$E_{1/2}$ (III/II)	PK_a(II)	Ref	Complex[c]	[b]$E_{1/2}$ (III/II)	Ref
$[Ru^{II}(acac)(trpy)\ OH_2)]^{2+}$	0.56	0.19	11.2	8	$[Ru^{II}(phen)([9]aneS_3)(Cl)]^{+}$	1.15	e
$[Ru^{II}(bpea)(bpy)(OH_2)]^{2+}$	0.46	0.34	11.1	1g	$[Ru^{II}(tpm)(phen)(Cl)]^{+}$	0.67	1f
$[Ru^{II}(trpy)(tmen)(OH_2)]^{2+}$	0.59	0.36	10.8	8	$[Ru^{II}(py)(phen)([9]aneS_3)]^{2+}$	1.62	17
$[Ru^{II}(tpm)(bpy)(OH_2)]^{2+}$	0.71	0.40	10.8	1f	$[Ru^{II}(tpm)(py)(bpy)]^{2+}$	1.15	24
$[Ru^{II}(tpm)(phen)(OH_2)]^{2+}$	0.71	0.41	10.7	1f	$[Ru^{II}(py)_3([9]aneS_3)]^{2+}$	1.44	25
$[Ru^{II}(trpy)(bpy)(OH_2)]^{2+}$	0.62	0.49	9.7	1a	$[Ru^{II}(tpm)(py)_3]^{2+}$	1.02	26
$[Ru^{II}([9]aneS_3)(phen)(OH_2)]^{2+}$	-	0.77	10.2	e			
$[Ru^{II}(trpy)(dppene)(OH_2)]^{2+}$	1.53	1.17	-	8			

[a] ligand abbreviations used: *acac* = acetylacetonate; *dppene* = cis-1,2-bis(diphenylphosphino)ethylene; *tmen* = N,N,N',N'-tetramethylethylenediamine; *bpea* = N,N-bis(2.pyridyl)ethylamine. *tpm* = tris(1-pyrazolyl)methane

[b] complexes in H_2O at pH=7, μ = 0.1 phosphate buffer solution

[c] complexes in acetonitrile with 0.1 M tetraalkyilammonium hexafluorophosphate

[d] redox potentials are reported with regard to the SSCE reference electrode

[e] this work

Table IX-3. pK_a and Electrochemical Data at pH = 7.0 in μ = 0.1 Phosphate Buffer Solution or in Acetonitrile for Related Ru Complexes.[a]

Spectroscopic properties. The 1-D and 2-D NMR spectra for the aqua complex **2** were recorded in D_2O. The ^1H NMR spectrum of **2** is shown in Figure IX-2 (assignments are shown in the Exp. Sect.). All the resonances in the NMR spectra were unambiguously identified and are consistent with the same structure found in the solid-state. It is worth mentioning here that the cationic part of complex **2** is asymmetric. Nevertheless, from a magnetic point of view, at room temperature, it can be considered as having a plane of symmetry that bisects the *[9]aneS₃* and the *phen* ligands in two halves, and which contains the Ru1, O1, and S2 atoms. The spectrum consists of a series of resonances in the δ = 2.4-3.6 ppm region that can be assigned to the thioether ligand, and a series of resonances in the δ = 5.8-9.6 ppm region arising from the *phen* ligand. There are three key NOESY effects together with the COSY map that allows for the unmistakable assignment of all the resonances observed in the ^1H NMR spectrum. The first two are interligand NOE effects observed between H11 (*phen*) and H17 (strong NOE effects,

hydrogen atoms situated at a distance of 2.64 Å in the X-ray structure) and H18a (4.45 Å), which allows for the identification of the hydrogen atoms of the *[9]aneS$_3$* ligand directed towards *phen* relative to those that are pointing away from the *phen* ligand. The third key NOE effect is also strong and is observed between H18 and H16a (2.47 Å), which allows for the clear differentiation of the H atoms of C17 from those of C18. Finally, the geminal protons can be assigned easily using the HETCOR ^{1}H-^{13}C map, and thus a complete assignment of the *[9]aneS$_3$* ligand is achieved. With regard to the *phen* ligand, the resonances at δ = 7.95 and 8.15 ppm can be assigned to H10 and H7, respectively, based on their multiplicity. The doublet at 9.40 ppm is assigned to H11 based on the above-mentioned interligand NOE effects, and finally, the doublet at δ = 8.67 ppm is assigned to H9. The assignments for the *phen* ligand are consistent with the COSY map.

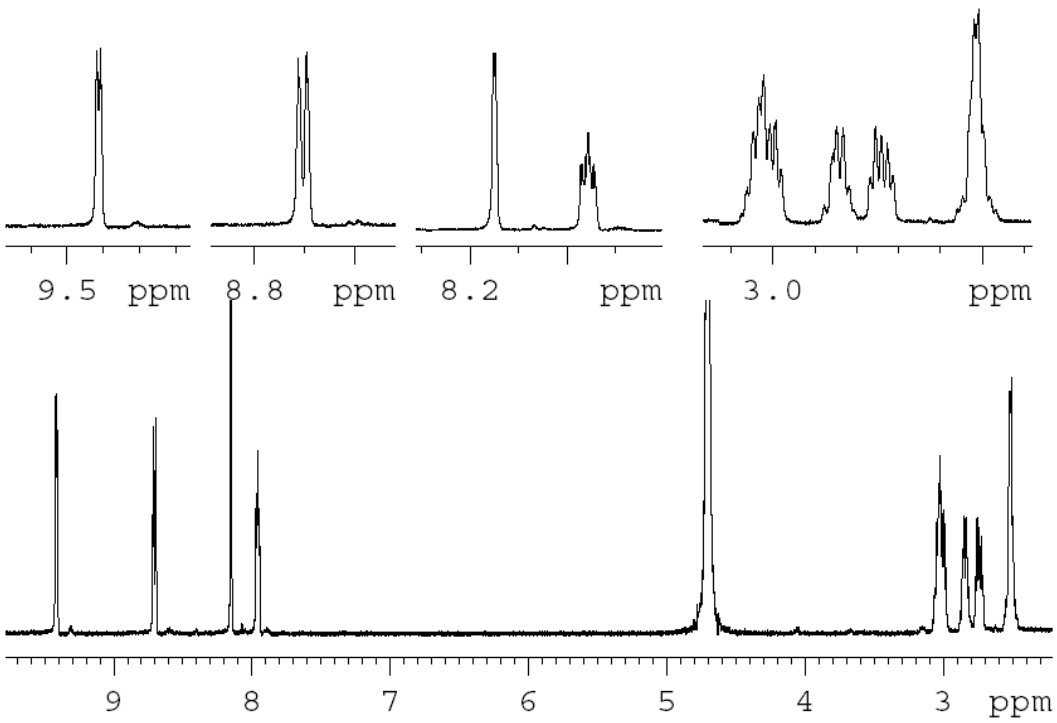

Figure IX-2. ^{1}H NMR spectrum of **2**.

The electronic spectrum of the aqua complex **2** at pH 7.0 is shown in Figure IX-3. Below 300 nm two predominantly ligand based π-π* transitions appear at λ_{max} = 259 nm (ε = 39750 cm^{-1}M^{-1}) and 288 nm (15355 cm^{-1}M^{-1}); above 300 nm two bands appear at 353 nm (6766 cm^{-1}M^{-1}) and 410 nm (6578 cm^{-1}M^{-1}) that can be assigned to a series of MLCT dπ-π*(Ru-*phen*) transitions and their vibronic components, based on previous

literature for related complexes.[1g,11,14] Under basic conditions complex **2** deprotonates generating the corresponding hydroxy derivative, $[Ru^{II}(OH)(phen)([9]aneS_3)]^+$ (**3**). For the hydroxo complex **3**, the two MLCT bands are shifted to higher wavelengths relative to those of the corresponding Ru-aqua complex **2** [410 nm (6816 $cm^{-1}M^{-1}$) and 432 nm (6811 $cm^{-1}M^{-1}$)] due to the relative destabilization of $d\pi$ (Ru) levels prompted by the hydroxo ligand.[1g,15] A pK_a of 10.1 is obtained from the acid-base spectrophotometric titration of **2** (shown as an inset in Figure IX-3), giving one isosbestic point at 379 nm, see Equation (4).

$$[Ru^{II}(phen)(H_2O)(9aneS_3)]^{2+} \longrightarrow [Ru^{II}(OH)(phen)(9aneS_3)]^+ + H^+ \qquad (4)$$

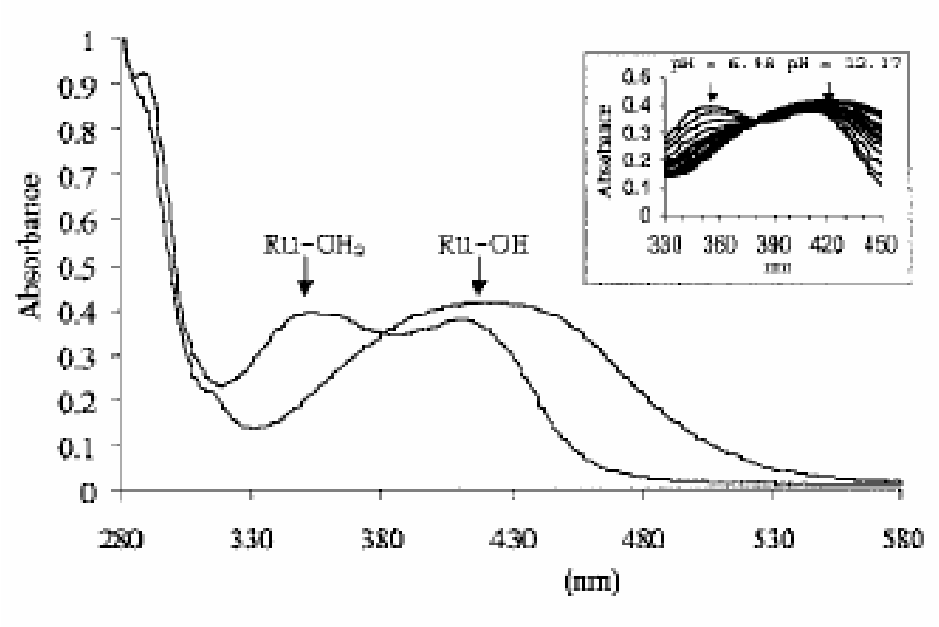

Figure IX-3. UV/Vis spectra of complex **2** at pH 7.0 phosphate buffer and of complex **3** at pH 12.2. The inset shows the acid-base spectrophotometric titration of a $5 \cdot 10^{-5}$ M solution of **2** in the 330-450 nm region (the pH of the different spectra are 7.0, 9.2, 9.6, 9.9, 10.15, 10.3, 10.5, 10.7, 211.2, 11.3, 11.7, 10.05, and 12.2).

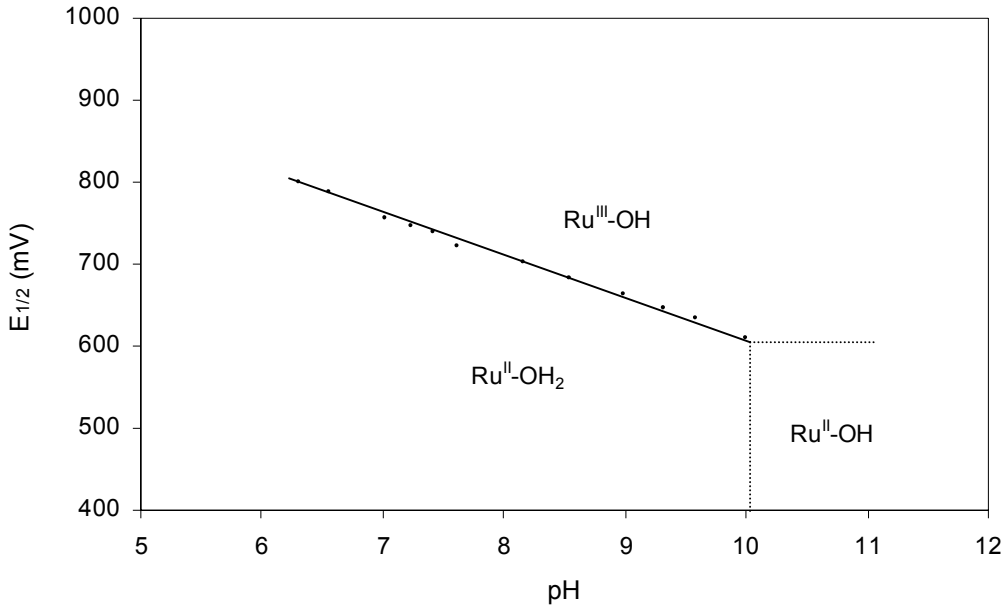

Figure IX-4. Pourbaix diagram of **2**.

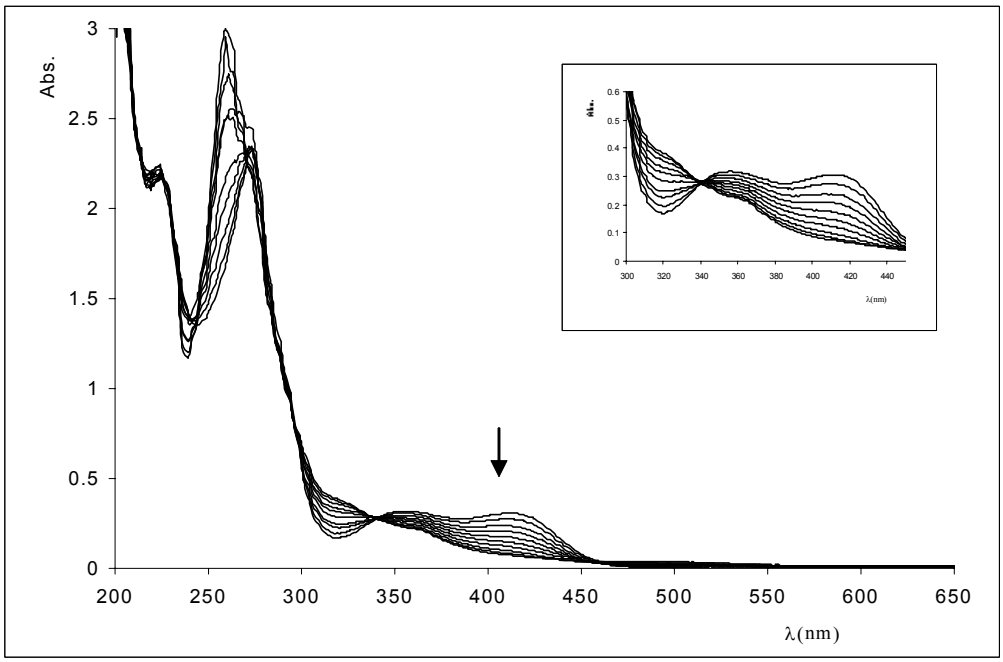

Figure IX-6. Redox spectrophotometric titration of 5 x 10^{-5} M **2**, at pH = 2.5 performed by sequential additions of 5 μl of 9.09 x 10^{-3} M NaOCl.

Redox Chemistry and Catalytic Properties. The redox properties of the aqua complex **2** were investigated by means of cyclic voltammetric and coulometric techniques. Figure IX-6 shows the cyclic voltammograms of complex **2** at pH = 7.0, in the presence and absence of benzyl alcohol, BzOH, and their mathematical simulation has been performed using the software DIGISIM.[16] As can be observed, a chemically irreversible wave is obtained at pH = 7.0 and at a scan rate of 100 mV/s, with $E_{p,a}$ = 0.82 V and a small returning wave at $E_{p,c}$ = 0.72 V ($E_{1/2}$ = 0.77 V; ΔE = 100 mV); these redox processes have been tentatively assigned to the Ru^{III}/Ru^{II} redox couple based on electronic arguments (vide infra) and whilst taking into consideration that the charge under the anodic wave is similar to that of the Ru^{III}/Ru^{II} couple of $[Ru^{II}(py)(phen)([9]aneS_3)]^{2+}$ [17] which behaves in a reversible manner. No further electrochemical processes are observed under these conditions for potentials up to 1.7 V. In sharp contrast, the homologous Ru-Cl complex **1** displays a reversible wave due to the Ru^{III}/Ru^{II} couple with $E_{1/2}$ = 1.15 V ($E_{p,a}$ = 1.19 V, $E_{p,c}$ = 1.11 V, ΔE = 81 mV), in acetonitrile. For the Ru-OH_2 complex, **2**, the reduction potential observed varies with pH with a slope of 56.0 mV per pH unit, as expected for this type of compound. The corresponding Pourbaix diagram in the pH range from 6 to 10 is shown in Figure IX-4. Several attempts have been undertaken to further characterize the Ru^{III}/Ru^{II} couple by performing CV experiments at different temperatures and at different scan rates, but the results did not give further meaningful information. The instability of the Ru^{III}-OH species manifested in the CV is also displayed when it is oxidized using NaOCl as the oxidant at pH = 2.5, as expected. The process was followed spectrophotometrically and is shown in Figure IX-5. In the UV/Vis spectrum the initial bands of **2** at 353 and 410 nm progressively disappear on addition of NaOCl, generating a spectrum with new bands of low intensity at 320 and 370 nm, with two isosbestic points at 280 and 330 nm. Given this chemically irreversible behavior two possibilities arise: the formation of a μ-oxo species or disproportionation to Ru^{II} and Ru^{IV}, followed by the oxidation of the *[9]aneS₃* ligand to the corresponding sulfoxide. The former is ruled out since Ru-O-Ru species have a very characteristic band in the 550-650 nm range[18] that is not observed in the present case, whereas strong evidence for the latter is obtained. The addition of NaOCl to **2** was also followed by NMR spectroscopy. A shift to lower field is observed for the signals of all the methylenic protons of *[9]aneS₃*, in agreement with the oxidation to their corresponding sulfoxide species. This statement is also supported by the fact that no electroactivity of the oxidized species is observed in the 0.0-1.2 V

potential window at pH = 7.0, due to the strong electron-withdrawing capacity of the sulfoxide species which prevents further oxidations of the newly generated diamagnetic Ru^{II} complex.

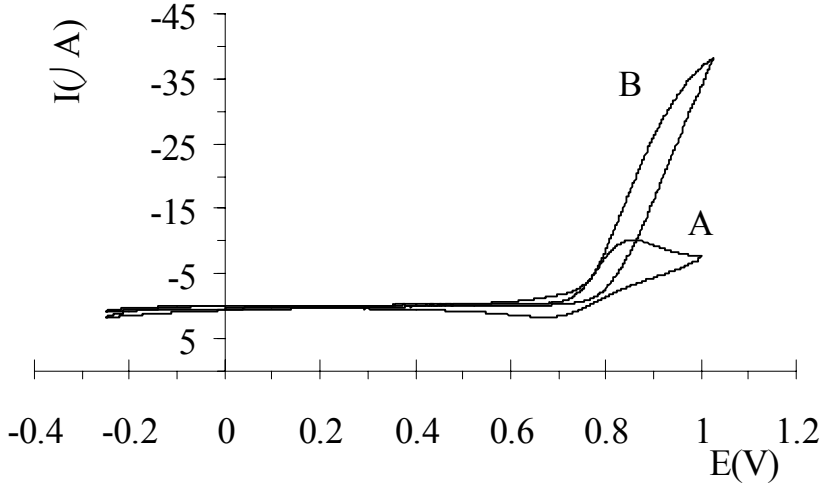

Figure IX-6. Cyclic voltammograms at a scan rate of 20 mV/s of complex **2** at pH = 7.0 in the absence (A) and presence of 0.2 M BzOH (B)

Table IX-3 presents the pK_a and electrochemical information of several polypyridylic Ru-Cl, Ru-OH_2, and Ru-*py* (*py* = pyridine). As can be seen, the redox properties of the Ru-H_2O type of complexes are highly sensitive to the nature of the ancillary ligands. Strong σ-electron donors stabilize the Ru^{III} oxidation state and thus a decrease in the Ru^{III}/Ru^{II} reduction potential is observed. The opposite effect is observed with good π-electron acceptor ligands which increase the Ru^{III}/Ru^{II} redox potential due to the stabilization of Ru^{II} by dπ-π* back-bonding.[10]

For **2**, comparison of the redox potentials can be made with $[Ru(tpm)(N\text{-}N)(L)]^{2+}$ (*tpm*, tris(1-pyrazolyl)methane; N-N is *bpy* or *phen*; L = H_2O, Cl, or *py*). The *tpm* complexes are a convenient choice since, like *[9]aneS₃*, *tpm* is a tridentate facial ligand, and therefore the influence of geometrical aspects on redox potentials is minimized. Thus, when comparing the Ru^{III}/Ru^{II} redox potential of the aqua complexes, $[Ru(T)(N\text{-}N)(H_2O)]^{2+}$ (T = *tpm* or *[9]aneS₃*), it is found that the thioether ligand produces an increase of 360 mV with regard to the corresponding *tpm* complex, due to both a much weaker σ-donor capacity and a stronger π-acceptor ability of the former ligand.[19] A similar phenomenon is also found for the Ru-Cl and Ru-*py* complexes where, as shown

in Table IX-3, an increase of 480 and 420-470 mV in the Ru^{III}/Ru^{II} redox potential is observed, respectively.

The combination of σ- and π-electronic perturbations exerted by the *[9]aneS₃* ligand over the ruthenium metal center results in an increase in the Ru^{III}/Ru^{II} redox potential for the Ru-aqua complex **2**, that in turn is responsible for the instability of the corresponding Ru^{III}-OH species, which undergoes a decomposition process. This increase in the redox potentials is also manifested by the fact that the corresponding Ru^{IV}/Ru^{III} redox wave is not found throughout the entire pH range, on scanning up to 1.7 V. The high reactivity of the Ru^{III}-OH species is also shown by its ability to oxidize BzOH. This is illustrated in Figure IX-6, where the cyclic voltammograms are recorded both in the presence and absence of BzOH. When the alcohol is present, there is a strong enhancement of the anodic peak current due to the electrocatalytic oxidation of the alcohol forming benzaldehyde.[20] Meyer and co-workers[20b] have previously proposed a Ru^{III}-OH species that is capable of oxidizing BzOH, even though it is usually the Ru^{IV} species that is capable of carrying out such an oxidation reaction. In our study, the strong electron-withdrawing nature of the *[9]aneS₃* ligand results in a high increase in the Ru^{III}/Ru^{II} redox potential, and thus it is plausible that the +3 oxidation state is sufficiently reactive so as to oxidize BzOH.

Increasing amounts of BzOH (0.10, 0.18, 0.20 M) were added to the solution and a series of cyclic voltammograms were recorded with a scan rate of 20 mV/s (see Figure IX-6). At this scan rate, the system behaves in a steady-state condition, and thus the limiting current is predicted to be independent of scan rate.[21] A second-order rate constant, k_{cat} = 19.3 $M^{-1}s^{-1}$, is experimentally determined using the equation described by Shain et al.[21] A similar value is also obtained, k_{cat} = 19.8 $M^{-1}s^{-1}$, from the mathematical simulation of the process using DIGISIM. This value is of the same order of magnitude as for the polypyridylic Ru^{IV}=O complexes described previously in the literature,[22] which are capable of oxidizing the same substrate under similar conditions, with k_{cat} values ranging from 6.0 to 30.8 $M^{-1}s^{-1}$. The formation of benzaldehyde as the only product was corroborated in a bulk experiment using the following conditions: 1.46 mM **2**/0.145 M BzOH/$9.09 \cdot 10^{-3}$ M NaOCl/pH 6.9 phosphate. This system yields 8.55 mM benzaldehyde after 15 minutes at 22.0 °C.

Conclusion

In summary, a new Ru-aqua complex, **2**, containing the soft *[9]aneS$_3$* ligand has been prepared and its structural, spectroscopic and redox properties are described. The bonding of the facial thioether ligand by the Ru metal center results in a high anodic shift of the Ru^{III}/Ru^{II} couple relative to the complex $[Ru(tpm)(phen)(H_2O)]^{2+}$, due to the weaker σ- and stronger π-bonding capacities exerted by *[9]aneS$_3$* over the Ru metal center relative to the pyrazolylic ligand. These electronic interactions are also responsible for the instability of the corresponding Ru^{III}-OH species. However, the decomposition reaction coupled to the Ru^{III}-OH species is slower than the oxidation of BzOH that yields the initial Ru^{II}-OH_2 and benzaldehyde, thus generating a catalytic cycle.

Experimental section

Materials: All reagents used in the present work were obtained from Aldrich Chemical Co and were used without further purification. Reagent grade organic solvents were obtained from SDS, and high purity deionized water was obtained by passing distilled water through a nanopure Mili-Q water purification system. The complex $[Ru^{II}(Cl)(phen)(\textit{[9]aneS}_3)]Cl$, **1**, was prepared according to literature procedures and recrystallized twice from methanol prior to its use.[11]

Preparations: All synthetic manipulations were routinely performed under a nitrogen atmosphere using Schlenk tubes and vacuum line techniques in the dark. Electrochemical experiments were performed in the dark under a N_2 or Ar atmosphere with degassed solvents.

Caution! The complex described in this section contains the perchlorate ion as a counteranion; perchlorate salts are potentially explosive.

$[Ru^{II}(phen)(OH_2)(\textit{[9]aneS}_3)](ClO_4)_2 \cdot 2H_2O$ ($2 \cdot 2H_2O$): A sample of **1** (35 mg, 0.051 mmol) was added to a solution of $AgClO_4$ (27.0 mg, 0.130 mmol) dissolved in water/acetone (1:1) (15 mL). The resulting mixture was refluxed for 2 h. AgCl was filtered through a frit containing celite and the volume was reduced using a rotary

evaporator under reduced pressure until the solution started to become turbid. A pale orange solid precipitated. The solid was washed with hexane and diethyl ether and dried under vacuum. Yield: 23.5 mg (53%). $C_{18}H_{22}Cl_2N_2O_9RuS_3 \cdot 2H_2O$: found (calcd.) C 30.47 (30.25), H 3.72 (3.64), N 4.03 (3.92), S 13.30 (13.44). ^{1}H NMR (500 MHz, D_2O, 25 °C): δ, 2.50 (m, H17, H17a), 2.75 (m, H18), 2.85 (m, H16), 3.00 (m, H18a), 3.05 (m, H16a), 7.95 (dd, $J_{9\text{-}10}$ = 7.7, $J_{10\text{-}11}$ = 3.8 Hz, H10), 8.15 (d, $J_{7\text{-}9}$ = 0.5 Hz, H7), 8.67 (d, $J_{9\text{-}10}$ = 7.7 Hz, H9), 9.40 (d, $J_{11\text{-}10}$ = 3.8 Hz, H11) ppm. ^{13}C NMR (500 MHz, D_2O, 25 °C): δ, 32.5 (C18), 33.02 (C16), 35.07 (C17), 127.34 (C10), 129.07 (C7), 132.2 (C8), 139.8 (C9), 148 (C13), 155.1 (C11). For the NMR spectroscopic assignments we have used the same labeling scheme as those used in the X-ray structure shown in Figure IX-1. $E_{1/2}$ (pH, 7.0 phosphate buffer) = 0.77 V vs. SSCE. UV/Vis (pH, 7.0 phosphate buffer) λ_{max}, nm (ε, $M^{-1}cm^{-1}$), assignment: 259 (39750) π-π*; 288 (15355) π-π*; 353 (6766) dπ-π*(*phen*); 410 (6578) dπ-π*(*phen*).

Instrumentation and Measurements: UV/Vis spectroscopy was performed on a Cary 50 Scan (Varian) UV/Vis spectrophotometer using 1 cm quartz cells. pH measurements were performed using a Micro-pH-2000 instrument from Crison. Cyclic voltammetric (CV) experiments were performed with a PAR 263A EG&G potentiostat or an IJ-Cambria IH-660 using a three electrode cell. A glassy carbon disc electrode (3 mm diameter) from BAS was used as the working electrode, platinum wire as auxiliary and SSCE as the reference electrode. All cyclic voltammograms presented in this work were recorded under a nitrogen atmosphere. The pH was adjusted from 0-2 with HCl, adding sodium chloride to keep a minimum ionic strength of 0.1 M. From pH 2-10, 0.1 M phosphate buffers were used, and from pH 10-12 diluted CO_2 free NaOH was used. All $E_{1/2}$ values reported in this work were estimated from cyclic voltammetry as the average of the oxidation and reduction peak potentials ($E_{p,a}$ + $E_{p,c}$)/2. Unless explicitly mentioned, the concentrations of the complexes were approximately 1 mM.

Catalytic studies at neutral pH have been performed in phosphate buffer solution. The conversion of benzyl alcohol to benzaldehyde was followed by GC using Shimadzu GC-17A gas chromatography apparatus in a TRA-5 Column (30 m × 0.25 mm diameter) incorporating a FID detector. GC conditions: initial temperature 80 °C for 1 min, ramp rate 10 °/min, final temperature 220 °C, injection temperature 220 °C, detector temperature 250ºC, carrier gas He at 25 mL/min. Under these conditions, the

retention times for benzaldehyde and benzyl alcohol are 3.9 and 4.9 minutes, respectively.

NMR spectroscopy was performed on a Bruker 500 MHz or a Bruker DPX 200 MHz spectrometer. Samples were run in deuterium oxide. Elemental analyses were performed using a CHNS-O Elemental Analyser EA-1108 from Fisons.

X-ray Structure Determination: Suitable crystals of [Ru(*phen*)(H_2O)(*[9]aneS$_3$*)](ClO_4)$_2$·2H_2O (**2·2H_2O**) were grown from water as yellow blocks. A prismatic crystal (0.1 × 0.1 × 0.2 mm) was selected and mounted on an Enraf-Nonius CAD4 four-circle diffractometer. Unit-cell parameters were determined from automatic centering of 25 reflections ($12 < \theta < 21°$) and refined by least-squares methods. Intensities were collected with graphite monochromatized Mo-$K\alpha$ radiation, using the $\Psi/2\theta$ scan-technique. 7668 reflections were measured in the range $2.21 \leq \theta \leq 29.97°$, of which 7617 were independent (R_{int} = 0.010), and 3557 reflections were assumed as observed applying the condition $I > 2\sigma(I)$. Three reflections were measured every two hours as orientation and intensity controls, significant intensity decay was not observed. Lorentz-polarization but no absorption corrections were made.

The structure was solved by Patterson synthesis, using the SHELXS computer program[23a] and refined by full-matrix least-squares methods with the SHELXL-97 computer program,[23a] using 7617 reflections. The function minimized was $\Sigma w||F_o|^2 + |F_c|^2|^2$, where $w = [\sigma^2(I) + (0.0440P)^2]^{-1}$ and $P = (F_o^2 + 2\,F_c^2)/3$; f, f′, and f″ were taken from International Tables of X-ray Crystallography.[23b] All H atoms were computed and refined, using a riding model, with an isotropic temperature factor equal to 1.2 times the equivalent of the temperature factor of the atoms which are linked. The final R (on F) factor was 0.0386, wR (on F^2) = 0.0580 and the goodness of fit was 0.845 for all observed reflections. The number of refined parameters was 298. Max. shift/esd = 0.014, mean shift/esd = 0.002. Max. and min. peaks in the final difference synthesis was 0.538 and -0.677 e·Å^{-3}, respectively.

Crystallographic data for the structure included in this paper have been deposited with the Cambridge Crystallographic Data Centre as supplementary publication no. CCDC-204307. These data can be obtained free of charge at http://www.ccdc.cam.ac.uk/conts/

retrieving.html [or from the Cambridge Crystallographic Data Centre, 12 Union Road, Cambridge CB2 1EZ, UK; Fax: (internat.) +44-1223-336-033; E-mail: deposit@ccdc.cam.ac.uk].

References

1. a) R. A. Binstead, T. J. Meyer, *J. Am. Chem. Soc.* **1987**, *109*, 3287-3297. b) C. M. Che, T. F. Lai, K. Y. Wong, *Inorg. Chem.* **1987**, *26*, 2289-2299. c) J. H. Muller, J. H. Acquaye, K. J. Takeuchi, *Inorg. Chem.* **1992**, *31*, 4552-4557. d) A. Gerli, J. Reedijk, M. T. Lakin, A. L. Spek, *Inorg. Chem.* **1995**, *34*, 1836-1843. e) X. Hua, M. Shang, A. G. Lappin, *Inorg. Chem.* **1997**, *36*, 3735-3740. f) A. Llobet, P. Doppelt, T. J. Meyer, *Inorg. Chem.* **1998**, *27*, 514-520. g) M. Rodríguez, I. Romero, A. Llobet, A. Deronzier, M. Biner, T. Parella, H. Stoeckli-Evans, *Inorg. Chem.* **2001**, *40*, 4150-4156. h) M. Shiotsuki, H. Miyai, Y. Ura, T. Suzuki, T. Kondo, T. Mitsudo, *Organometallics* **2002**, *21*, 4960-4964. i) M. H. V. Huynh, L. M. Witham, J. M. Lasker, M. Wetzler, B. Mort, D. L. Jameson, P. S. White, K. J. Takeuchi, *J. Am. Chem. Soc.* **2003**, *125*, 308-309.
2. a) J. C. Dobson, W. K. Seok, T. J. Meyer, *Inorg. Chem.* **1986**, *25*, 1513-1514. b) A. S. Goldstein, R. H. Beer, R. S. Drago, *J. Am. Chem. Soc.* **1994**, *116*, 2424-2429. c) L. K. Stultz, R. A. Binstead, M. S. Reynolds, T. J. Meyer, *J. Am. Chem. Soc.* **1995**, *117*, 2520-2532. d) W. C. Cheng, W. Y. Yu, K. K. Cheung, S. M. Peng, C. K. Poon, C. M. Che, *Inorg. Chim. Acta* **1996**, *242*, 105-113. e) C. Ho, C. M. Che, T. C. Lau, *J. Chem. Soc., Dalton Trans.* **1990**, 967-970. f) D. Carmona, C. Cativiela, S. Elipe, F. J. Lahoz, M. P. Lamata, M. Pilar, M. L. R. Deviu, L. A. Oro, C. Vega, F. Viguri, *Chem. Commun.* **1997**, 2351-2352. g) W. H. Fung, W. Y. Yu, C.-M. Che, *J. Org. Chem.* **1998**, *63*, 7715-7726.
3. a) L. Roecker, J. C. Dobson, W. J. Vining, T. J. Meyer, *Inorg. Chem.* **1987**, *26*, 779-781. b) J. H. Acquaye, J. G. Muller, K. J. Takeuchi, *Inorg. Chem.* **1993**, *32*, 160-165. c) X. Hua, A. G. Lappin, *Inorg. Chem.* **1995**, *34*, 992-994. d) L. F. Szczepura, S. M. Maricich, R. F. See, M. R. Churchill, K. J. Takeuchi, *Inorg. Chem.* **1995**, *34*, 4198-4205. e) X. Hua, M. Shang, A. G. Lappin, *Inorg. Chem.* **1997**, *36*, 3735-3740.

4. a) B. A. Moyer, B. K. Sipe, T. J. Meyer, *Inorg. Chem.* **1981**, *20*, 1475-1480. b) W. K. Seok, Y. J. Son, S. W. Moon, H. N. B. Lee, *Kor. Chem. Soc.* **1998**, *19*, 1084-1090.
5. a) M. S. Thompson, T. J. Meyer, *J. Am. Chem. Soc.* **1982**, *104*, 4106-4115. b) L. E. Roecker, T. J. Meyer, *J. Am. Chem. Soc.* **1987**, *109*, 746-754. c) M. E. Marmion, K. J. Takeuchi, *J. Am. Chem. Soc.* **1988**, *110*, 1472-1480. d) R. A. Binstead, M. E. MacGuire, A. Dovletoglou, W. K. Seok, L. E. Roecker, T. J. Meyer, *J. Am. Chem. Soc.* **1992**, *114*, 173-186. e) C. M. Che, C. Ho, T. C. Lau, *J. Chem. Soc., Dalton Trans.* **1991**, 1259-1263. f) V. J. Catalano, R. A. Heck, C. E. Immoos, A. Ohman, M. G. Hill, *Inorg. Chem.* **1998**, *37*, 2150-2157. g) C. M. Che, K. W. Cheng, M. C. W. Chan, T. C. Lau, C. K. Mak, *J. Org. Chem.* **2000**, *65*, 7996-8000.
6. a) T. C. Lau, C. M. Che, W. O. Lee, C. K. Poonl, *J. Chem. Soc., Chem. Commun.* **1988**, 1406-1407. b) C. M. Che, V. W. W. Yam, T. C. W. Mak, *J. Am. Chem. Soc.* **1990**, *112*, 2284-2291. c) N. Grover, S. A. Ciftan, H. H. Thorp, *Inorg. Chim. Acta* **1995**, *240*, 335-338. d) C. Morice, P. Lemaux, C. Moinet, G. Simonneaux, *Inorg. Chim. Acta* **1998**, *273*, 142-150. e) K. Jitsukawa, Y. Oka, H. Einaga, H. Masuda, *Tetrahedron Letters* **2001**, *42*, 3467-3469.
7. a) A. H. Krotz, L. Y. Kuo, J. K. Barton, *Inorg. Chem.* **1993**, *32*, 5963-5974. b) T. M. Santos, B. J. Goodfellow, M. G. B. Drew, J. Pedrosa de Jesus, V. Félix, *Metal Based Drugs* **2001**, *8(3)*, 125-136. c) S. Delaney, M. Pascaly, P. K. Bhattacharya, J. K. Barton, *Inorg. Chem.* **2002**, *41*, 1966-1674. d) O. Schiemann, J. K. Barton, N. J. Turro, *J. Phys. Chem. B* **2000**, *104*, 7214-7220.
8. A. Dovletoglou, S. Ajao Adeyemi, T. J. Meyer, *Inorg. Chem.* **1996**, *35*, 4120-4127.
9. A. Llobet, *Inorg. Chim. Acta* **1994**, *221*, 125-131.
10. a) R. A. Leising, K. J. Takeuchi, *Inorg. Chem.* **1987**, *26*, 4391-4393. b) C. A. Bessel, R. A. Leising, K. J. Takeuchi, *J. Chem. Soc., Chem. Commun.* **1991**, 833-835.
11. B. J. Goodfellow, V. Félix, S. M. Pacheco, J. Pedrosa de Jesus, M. G. B. Drew, *Polyhedron* **1997**, *16*, 393-401.
12. a) C. Landgrafe, W. S. Sheldrick, *J. Chem. Soc., Dalton Trans.* **1994**, 1885-1895. b) B. J. Goodfellow, S. M. Pacheco, J. Pedrosa de Jesus, V. Félix, M. G. B. Drew, *Polyhedron* **1997**, *16*, 3293-3304. c) T. M. Santos, B. J. Goodfellow, J.

Madureira, J. Pedrosa de Jesus, V. Félix, M. G. B. Drew, *New J. Chem.* **1999**, *23*, 1015-1025. d) J. Madureira, T. M. Santos, B. J. Goodfellow, M. Lucena, J. Pedrosa de Jesus, M. G. Santana-Marques, M. G. B. Drew, V. Félix, *J. Chem. Soc., Dalton Trans.* **2000**, 4422-4431.

13. G. J. Grant, S. S. Shoup, C. L. Baucom, W. N. Setzer, *Inorg. Chim. Acta* **2001**, *317*, 91-102.
14. a) J. Z. Wu, B. H. Ye, L. Wang, L. N. Ji, J. Y. Zhou, R. H. Li, Z. Y. Zhou, *J. Chem. Soc., Dalton Trans.* **1997**, 1395-1401. b) B. J. Coe, S. Hayat, R. L. Bedoes, M. Helliwell, J. C. Jeffrey, S. R. Batten, P. S. White, *Dalton Trans.* **1997**, 591-599.
15. K. J. Takeuchi, H. S. Thompson, D. W. Pipes, T. J. Meyer, *Inorg. Chem.* **1984**, *23*, 1845-1851.
16. DigiSim for Windows 95. Version 3.05. File type: CV. Bioanalytical Systems.
17. X. Sala, I. Romero, M. Rodríguez, A. Llobet, G. González, M. Martínez, J. Benet-Buchholz, *Inorg. Chem*., **2003**, *43*, 5403-5409.
18. a) A. Llobet, M. E. Curry, H. T. Evans, T. J. Meyer, *Inorg. Chem.* **1989**, *28*, 3131-3137. b) T. R. Weaver, T. J. Meyer, S. A. Adeyemi, G. M. Brown, R. P. Eckberg, W. E. Hatfield, R. W. Murray, D. J. Untereker, *J. Am. Chem. Soc.* **1975**, *97*, 3039-3048.
19. a) G. J. Grant, T. Salupo-Bryant, L. A. Holt, D. Y. Morrissey, M. J. Gray, J. D. Zubkowski, E. J. Valente, L. F. Mehne, *J. Organomet. Chem.* **1999**, *587*, 207-214. b) S. R. Cooper, *Acc. Chem. Res.* **1988**, *21*, 141-146.
20. a) T. J. Meyer, *J. Electrochem. Soc.* **1984**, *131*, C221-C228. b) L. K. Stultz, M. H. V. Huynh, R. A. Binstead, M. Curry, T. J. Meyer, *J. Am. Chem. Soc.* **2000**, *25*, 5984-5996.
21. Under steady-state conditions, the limiting current is predicted to be independent of scan rate, and the second-order rate constant is given by the expression, *i*L _ *n·F·A·C*o·(*D·k*cat·*C*s)1/2 where *i*L is the limiting current, *n* is the number of electrons transferred, *A* is the electrode area, *C*o is the concentration of RuII, *D* is the diffusion coefficient, and *C*s is the substrate concentration. a) D. S. Polcyn, I. Shain, *Anal. Chem.* **1966**, *38*, 376-382. b) A. J. Bard, L. R. Faulkner, in: *Electrochemical Methods; Wiley*; New York, 1980.
22. E. L. Lebeau, T. J. Meyer, *Inorg. Chem.* **1999**, *38*, 2174-2181.

23. a) G. M. Sheldrick, 1997. Univer. Göttingen, Germany. b) International Tables of X-ray Crystallography, 1974, Ed. Kynoch Press, vol. IV, pp. 99-100 and 149.

Chapter X: *Ru^{II} Complexes Containing C2 Didentate Chiral 1,2-bis(oxazolinyl)benzene Ligands. Structure and Atropisomeric Discrimination*

Ru^{II} Complexes Containing C_2 Didentate Chiral 1,2-bis(oxazolinyl)benzene Ligands. Structure and Atropisomeric Discrimination

Abstract

A new family of Ru^{II} complexes containing the tridentate meridional 2,2':6',2''-terpyridine (trpy) ligand, a C_2 didentate chiral oxazolinic ligand 1,2-bis[4'-alkyl-4',5'-dihydro-2'-oxazolyl]benzene (Phbox-R, R = Et or *i*Pr) and a monodentate ligand, of general formula $[Ru(Y)(trpy)(Phbox\text{-}R)]^{n+}$ (Y = Cl, H_2O, py, MeCN or 2-OH-py (2-hydroxypyridine)) have been prepared and thoroughly characterized. DFT calculations have been performed with these complexes to interpret and complement experimental results. The oxazolinic ligand Phbox-R has free rotation along the phenyl-oxazoline axes. Upon coordination the mentioned rotation is restricted by a barrier of 26.0 $kcal{\cdot}mol^{-1}$ for the case of $[Ru(trpy)(Phbox\text{-}iPr)(MeCN)]^{2+}$ thus preventing its potential interconversion. Furthermore due to steric effects the two atropisomers differ by 5.7 $kcal{\cdot}mol^{-1}$ and as a consequence only one of them is obtained in the synthesis. Subtle but important structural effects are encountered upon changing the monodentate ligands that are interpreted thanks to their calculated DFT structures.

Introduction

Ruthenium polypyridyl complexes have been extensively studied over the years because they enjoy a combination of unique chemical, electrochemical and photochemical properties[1] that has allowed exploring a wide variety of fields including photochemistry and photophysics,[2] bioinorganics[3] and catalysis.[4] Recently, the dynamic behavior of Ru polypyridyl complexes has played a key role in the understanding of artificial molecular-level machines[5] as well as in the elucidation of the factors implicated in their binding to DNA.[6]

The generation, control and induction of chirality is another extraordinarily important field for the scientific and technological community.[7] Of special interest is atropisomerism, in which chirality is generated by the formation of two or more stable (non-interconverting) rotational isomers,[8] since it is potentially applicable to many different fields such as nanoscale

information storage, chiral sensors, optoelectronics as well as biomimetic and asymmetric catalysis among others.[9]

With all this in mind it has been designed atropisomeric Ru complexes where the chirality can be easily generated, controlled and detected. Here on, we present a theoretical study on a new family of pure atropisomeric ruthenium complexes with general formula $[Ru(Y)(trpy)(Phbox\text{-}R)]^{n+}$ (Y = Cl, H_2O, py, MeCN or 2-OH-py; trpy is 2,2':6',2''-terpyridine, Phbox-R is the chiral C_2 didentate ligand 1,2-bis[4'-alkyl-4',5'-dihydro-2'-oxazolyl]benzene and 2-OH-py is 2-hydroxypyridine; see Chart 1 for ligand drawings), which signifies a step forward towards our efforts related on the preparation of new Ru complexes containing N-heterocyclic ligands.[10]

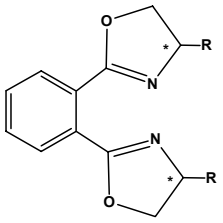

Phbox-**R**
(R = Et, (R_cR_c)-**a**; R = *i*Pr, (S_cS_c)-**b**)

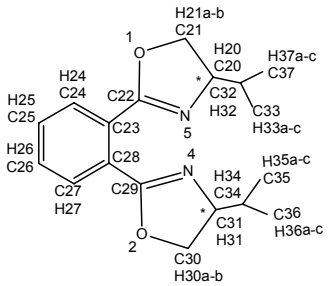

Phbox-*i*Pr, (S_cS_c)-**b**

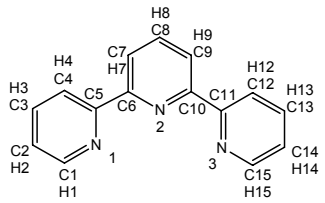

trpy

Chart 1. Drawing of trpy and bis(oxazoline) ligands used in this work together with labeling scheme.

The synthetic strategy followed for the preparation of the compounds described in the present paper is outlined in Scheme 1. The synthesis of complexes **2-6** was carried out following slightly modified methods, previously described in the literature,[11] using the didentate chiral bisoxazolinic ligands Phbox-R instead of 2,2'-bipyridine. The chiral ligands were prepared following Bolm's synthesis.[12] In the ligands nomenclature used, the capital letters refer to the absolute configuration of the two carbon stereocenters of the ligand and the

"c" subindex indicates in each case that the stereochemistry is carbon-centered, in order to clearly establish a difference with the chirality origined by ligand coordination to the ruthenium center, denoted as "a" (see below for the complexes nomenclature).

In the ligands syntheses, whereas the S_cS_c-**b** ligand is obtained in high optical purity, a mixture of two diastereoisomers, (R_cR_c)-**a**/(R_cS_c)-**a** (4/1), is obtained for the ligand **a** case. These two isomers can be separated out by repeated recrystallization of the [Ni(Phbox-Et)$_2$](ClO$_4$)$_2$ complex followed by nickel decomplexation.[13]

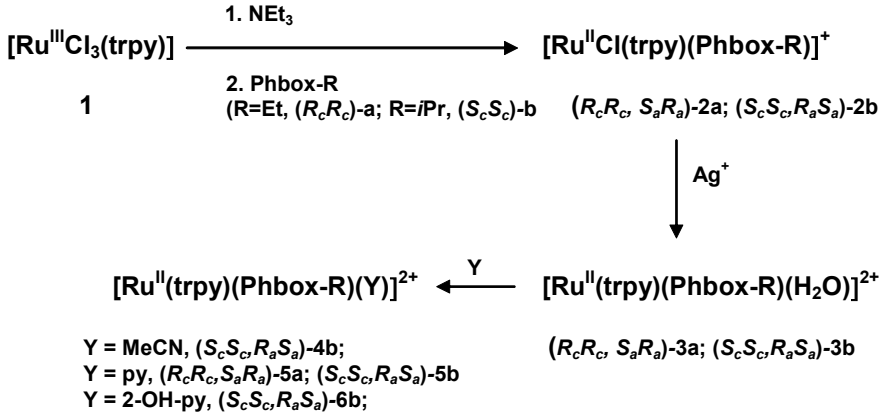

Scheme 1. Synthetic strategy for complexes **2**-**6** and their nomenclature.

As displayed in Scheme 1, the Ru-aqua complexes (R_cR_c,S_aR_a)-**3a** or (S_cS_c,R_aS_a)-**3b** (in the nomenclature used here, the first two letters indicate the absolute configuration of the two carbon stereocenters of the oxazolinic ligand whereas the other two indicate the configuration of the rotation axes, see Figure X-2), that are obtained from the corresponding Ru-Cl complexes, (R_cR_c,S_aR_a)-**2a** and (S_cS_c,R_aS_a)-**2b** respectively, can be used as starting materials for the preparation of the Ru-MeCN ((S_cS_c,R_aS_a)-**4b**) and Ru-pyridino ((R_cR_c,S_aR_a)-**5a,** (**(**S_cS_c,R_aS_a)-**5b** and (S_cS_c,R_aS_a)-**6b**) complexes. In the case of (R_cR_c,S_aR_a)-**5a** and (S_cS_c,R_aS_a)-**5b**, the reaction was carried out at room temperature since higher temperatures produce the substitution of the oxazolinic ligand, besides the aqua ligand, yielding the [Ru^{II}(trpy)(py)$_3$]$^{2+}$ complex.[14] For the case of (S_cS_c,R_aS_a)-**6b**, which contains the 2-hydroxy-pyridine ligand, the reaction was carried out in the presence of molecular sieves otherwise small amounts of water displace this ligand to generate the initial (S_cS_c,R_aS_a)-**3b** Ru-aqua complex due to the steric hindrance generated by the hydroxyl group.

Crystallographic data for complexes (R_cR_c,S_aR_a)-**2a** and (S_cS_c,R_aS_a)-**4b** are presented in Table X-1 whereas Figure X-1 shows an ORTEP view of their cationic moieties. In the Ru-Cl complex (R_cR_c,S_aR_a)-**2a,** the Ru metal atom presents a distorted octahedral coordination with the trpy ligand tricoordinated with its N atoms in a meridional fashion while the oxazolinic ligand coordinates also through its N atoms in a chelate manner. The remaining sixth coordination position is occupied by the chloro ligand. The bond distances and angles involved in the first coordination sphere between the Ru^{II} metal center and the trpy, oxazoline and Cl ligands are similar to related complexes previously described in the literature.[15] The bis(oxazoline) ligand forms a seven-membered chelate ring upon coordination to the Ru metal center with a bite angle of 82.4°[16] and with the two oxazolinyl rings being nearly perpendicular to one another (81.2°). Finally the dihedral angle between the adjusted best planes defined by each oxazolinic ring and the phenyl group are 40.9° and 55.5° for the oxazolinic groups containing N5 and N4 atoms respectively. The phenyl group is situated over the N3 peripheral pyridyl group of the trpy ligand with a dihedral angle between the best adjusted planes defined by these aromatic groups of 22.6°. The other atropisomer (R_cR_c,R_aS_a)-**2a** can be potentially obtained through a partial rotation around the chiral axes (see below for a more detailed description of the different stereoisomers), This involves a simultaneous inverse rotation of two sigma C-C bonds (C29-C28 and C22-C23) that link the phenyl group with the oxazolinic moieties, driving the phenyl group of the (R_cR_c)-**a** ligand over the other N1 peripheral trpy pyridylic ring. It is interesting to note here that the steric demands of the (R_cR_c)-**a** oxazolinic moiety situated over the N3 trpy pyridyl group, produces a significant dihedral angle between the mentioned N3-peripheral pyridyl group and the central N2-pyridyl of 9.6°. In sharp contrast, the measured equivalent dihedral angle for the other pyridyl group containing N1, which is not directly affected by the steric demands of the (R_cR_c)-**a** ligand, is 4.4°. This value is comparable to other Ru-trpy complexes where no steric effects are exerted over the trpy ligand as is the case of the [$Ru^{III}Cl_3$(trpy)] complex, which presents a medium dihedral angle between the peripheral and central pyridyl groups of 4.2°.[14]

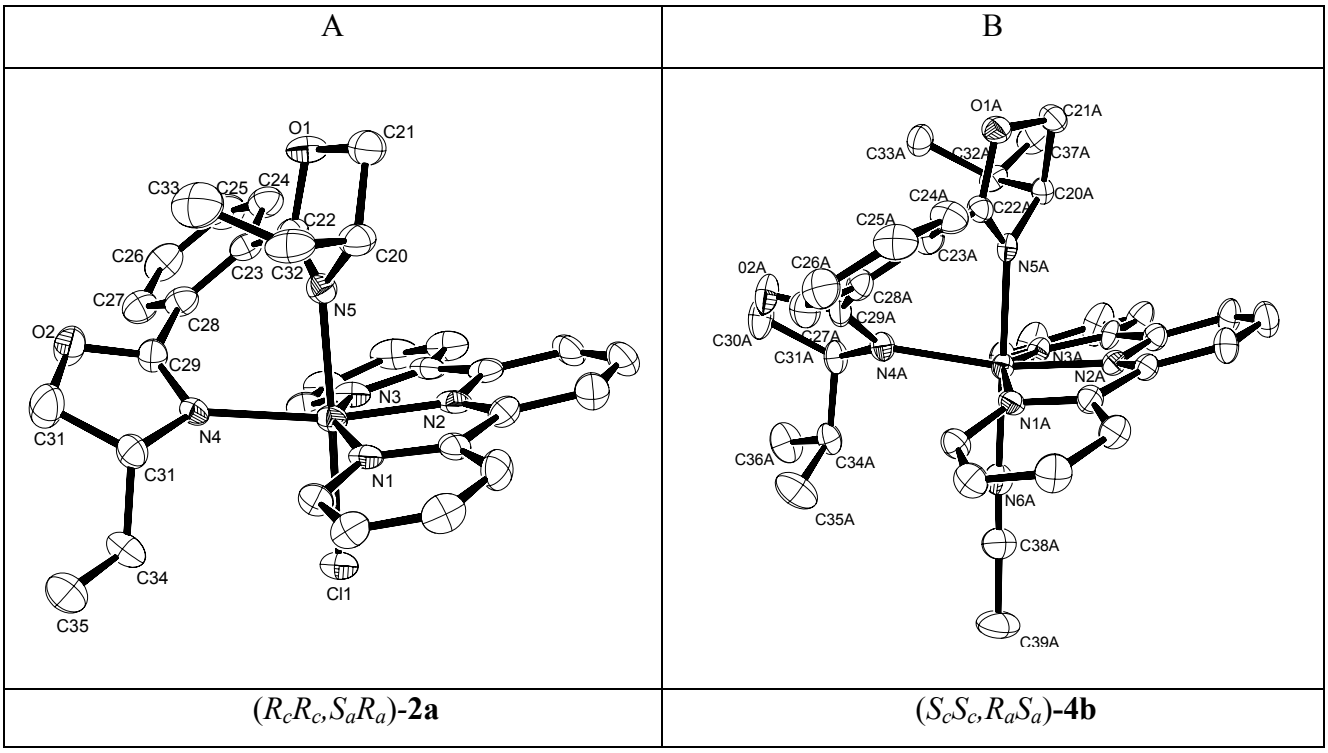

(R_cR_c,S_aR_a)-**2a** (S_cS_c,R_aS_a)-**4b**

Figure X-1. ORTEP diagram (50% probability) for the cationic moieties of complexes (R_cR_c,S_aR_a)-**2a** (A) and (S_cS_c,R_aS_a)-**4b** (B).

	(R_cR_c,S_aR_a)-**2a**	(S_cS_c,R_aS_a)-**4b**
Empirical formula	$C_{31}H_{31}ClF_6N_5O_2PRu$	$C_{70}H_{76}B_4F_{16}N_{12}ORu_2$
Formula weight	787.1	1650.81
Crystal system, space group	orthorhombic, $P2_12_12_1$	Triclinic, $P1$
A, Å	10.4726(6)	8.8020(5)
B, Å	13.0304(9)	11.0777(6)
C, Å	23.0450(13)	19.1883(11)
α,°	90	88.844(3)
β,°	90	82.570(2)
γ,°	90	79.829(2)
V, Å^3	3144.8(3)	1826.10(18)
Formula Units/Cell	1	1
$\rho_{calc.}$, g cm^{-3}	1.663	1.501
μ, mm^{-1}	0.055	0.507
Absolute structure parameter	-0.03(3)	0.05(2)
R_1[a] (I>2σ(I))	0.0337	0.0551
wR_2[b] (all data)	0.0563	0.1282

[a] $R_1 = \Sigma||F_o| - |F_c||/\Sigma|F_o|$.

[b] $wR_2 = [\Sigma\{w(F_o^2-F_c^2)^2\}/\Sigma\{w(F_o^2)^2\}]^{1/2}$,

where $w = 1/[\sigma^2F_o^2+(m)^2+n\mathrm{P}]$ and $\mathrm{P} = (F_o^2 + 2F_c^2)/3$.

Table X-1. Crystal data for X-ray structures of (R_cR_c,S_aR_a)-**2a** and (S_cS_c,R_aS_a)-**4b.**

All F atoms of the PF_6^- counteranions are interacting with the C-H bonds of the trpy and (R_cR_c)-**a** ligands of the $[Ru^{II}Cl(trpy)(Phbox\text{-}Et)]^+$ cation through extensive, moderate to weak

hydrogen bonding, forming a 3D network over the crystal. There are also relatively strong π-π stacking interactions[17] within neighboring cations through their peripheral pyridyl groups.

The crystal structure of complex (S_cS_c,R_aS_a)-**4b** presents two independent but very similar molecules; only the "A" labeled molecule will be discussed in the present paper. The structures are very similar to that of (R_cR_c,S_aR_a)-**2a** except for: a) the coordination of the monodentate ligand and b) the fact that the other atropisomer is obtained due to the opposite chiral configuration of the oxazolinic ligand.

Computational details

The reported density functional theory (DFT) calculations were carried out by using the Amsterdam density functional (ADF)[18] program system, developed by Baerends *et al.* The numerical integration scheme employed was that of te Velde and Baerends.[19] An uncontracted triple-ς basis set[20] was used for describing the 4s, 4p, 4d, 5s, and 5s orbitals of ruthenium. For carbon (2s,2p), nitrogen (2s,2p), oxygen (2s,2p), and hydrogen (1s), double-ς basis sets were employed. Both basis sets were augmented by an extra polarization function.[20] Electrons in lower shells were treated within the frozen core approximation.[18c] A set of auxiliary s, p, d, f, and g functions,[21] centered in all nuclei, was introduced in order to fit the molecular density and Coulomb potential accurately in each SCF cycle. Both geometry optimizations and energy evaluations have been fully carried out within a DFT generalized gradient approximation (GGA) functional that includes the GGA exchange and correlation corrections of Becke[22] and Perdew and Wang,[23] respectively (BPW91).

The solvent effect was included in the calculation of the relative energy of complexes *in*-(S_cS_c,R_aS_a)-**6b** and *out*-(S_cS_c,R_aS_a)-**6b** through single point energy calculations by the conductor-like screening model (COSMO) of Klamt and Schüürmand,[24] implemented by Pye and Ziegler into the ADF program.[25] The radius chosen for the solvent (3.02 Å) was obtained with the GAUSSIAN98 package[26] from the calculated molecular volume of acetone (ε=21.01),[27] the solvent used in the NMR characterization. The radii used for C, O, N, H, and Ru were 1.53, 1.36, 1.48, 1.08, and 2.30 Å, respectively.[28] Finally the dihedral angle between the best adjusted planes defined by two groups of atoms was measured by the Spartan'02 program.[29]

Results

The C_2 symmetrical free ligands, (R_cR_c)-**a** and (S_cS_c)-**b**, possess free rotation around the C-C bonds that link the aromatic ring with the oxazolinic moieties. Upon coordination to the metal center, the rotation is restricted leading to two limit orientations as shown in Figure X-2, thus generating two interdependent chiral axes that lead to atropoisomerism. For the case of the (R_cR_c)-**a** ligand one could potentially obtain two diastereoisomers: the (R_cR_c,S_aR_a)- and the (R_cR_c,R_aS_a)-[[Ru^{II}(Y) (trpy)(Phbox-Et)]$^{n+}$ (Y = Cl, H_2O or py). Experimental evidence, both in the solid state (X-ray diffraction, vide supra) and in solution (NMR spectroscopy, vide infra) indicates the existence of only the (R_cR_c,S_aR_a) isomer in all complexes containing the (R_cR_c)-**a** ligand and the other atropisomeric (S_cS_c,R_aS_a) complex for the case of the (S_cS_c)-**b** ligand. In both cases, the atropisomer obtained is the one that points the R groups of the oxazolinic rings away from the trpy plane, as expected from steric arguments. The fact that only one atropisomer is found in each case is in agreement with a large rotational barrier to interconvert the two atropisomers as it can be further inferred from molecular models.

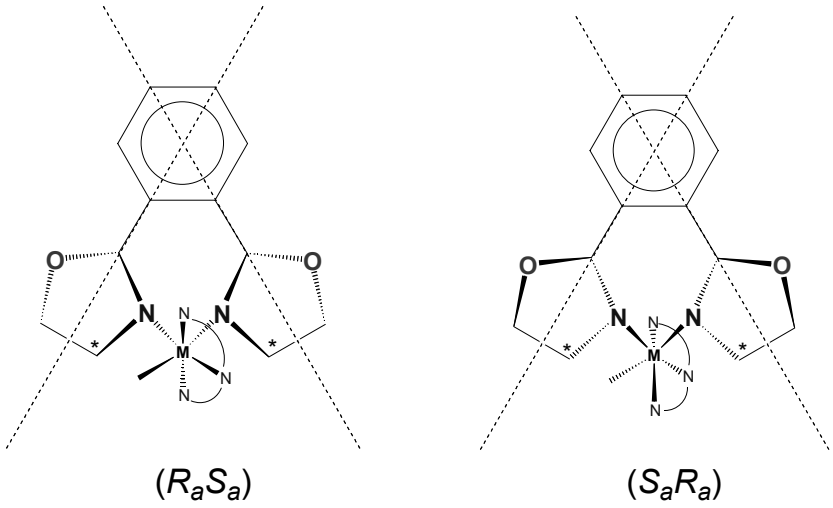

Figure X-2. Drawing of the two atropisomeric forms generated by the bisoxazolinic ligand (Phbox-R) bonded to the Ru metal center. The chiral rotational axes are depicted with broken lines.

DFT calculations for a series of complexes containing the oxazolinic ligand (S_cS_c)-**b** were performed in order to further deepen our structural understanding of these complexes and to obtain the energy barriers of the atropisomeric interconversion. A comparison between the X-

ray data of complex *SS,RS*-**4b** and the corresponding BPW91 optimized geometry (distances in Å and angles in degrees) optimization is given in Table X-2.

dist	Exp.	Calc.	angles	Exp.	Calc.
Ru-N3	2.100	2.148	N3-Ru-N2	78.64	78.06
Ru-N2	1.954	1.991	N3-Ru-N1	156.13	154.94
Ru-N1	2.057	2.125	N2-Ru-N1	79.62	78.28
Ru-N4	2.146	2.191	N2-Ru-N4	167.30	169.89
Ru-N5	2.083	2.127	N4-Ru-N5	83.25	82.99
Ru-N6	2.018	2.040	N3-Ru-N6	88.15	88.63
N6-C	1.148	1.145	N2-Ru-N6	95.42	94.30
N5-C(O1)	1.283	1.286	N1-Ru-N6	84.21	85.01
N5-C	1.488	1.486	N4-Ru-N6	96.62	99.57
N4-C(O2)	1.288	1.288	N5-Ru-N6	179.40	178.35
N4-C	1.487	1.484	N3-Ru-N5	92.41	92.51
O1-C(N5)	1.351	1.352	N2-Ru-N5	84.66	87.11
O1-C	1.453	1.453	N1-Ru-N5	95.24	94.44
O2-C(N4)	1.345	1.347	O1-N5-Ru	157.63	156.11
O2-C	1.452	1.450	O2-N4-Ru	156.45	155.50

Table X-2. Comparison between the X-ray data of complex *SS,RS*-**4b** and the corresponding BPW91 optimized geometry (distances in Å and angles in degrees) optimization.

As shown in Table X-2, the experimental and theoretical bond lengths and angles for (S_cS_c,R_aS_a)-**4b**, differ by less than 0.07 Å and 3.0°, respectively. The standard deviation for the distances is 0.043 Å and for the angles 0.25°.[30] This result validates the adequacy of the theoretical method employed for the geometry optimization of these particular systems.

Table X-3 lists selected structural parameters obtained from X-ray data for (R_cR_c,S_aR_a)-**2a** and (S_cS_c,R_aS_a)-**4b,** together with the computed counterpart for (S_cS_c,R_aS_a)-**4b**. It also contains the computed (S_cS_c,S_aR_a)-**4b**, *TS*-**4b** (the transition state (TS) connecting the two isomers), (S_cS_c,R_aS_a)-**5b** and two different conformers of (S_cS_c,R_aS_a)-**6b**, labeled *in* and *out* depending on the relative orientation of the hydroxyl group versus the phenyl group of the oxazolinic ligand (towards N3 or N1 of the trpy ligand respectively, see Figure X-4).

	(R_cR_c,S_aR_a)-**2a** (X-ray)	(S_cS_c,R_aS_a)-**4b, A** (X-ray)	(S_cS_c,R_aS_a)-**4b**	(S_cS_c,S_aR_a)-**4b**	*TS*-**4b**	(S_cS_c,R_aS_a)-**5b**	*in*-(S_cS_c,R_aS_a)-**6b**	*out*-(S_cS_c,R_aS_a)-**6b**
Ru-N1	2.122(3)	2.057(4)	2.125	2.126	2.122	2.114	2.115	2.094
Ru-N2	1.947(4)	1.954(4)	1.991	1.986	1.981	1.985	1.978	1.977
Ru-N3	2.087(4)	2.100(4)	2.148	2.124	2.104	2.166	2.146	2.151
Ru-N4	2.180(4)	2.146(4)	2.191	2.184	2.230	2.218	2.215	2.208
Ru-N5	2.086(4)	2.083(4)	2.127	2.149	2.149	2.141	2.157	2.147
Ru-Z[a]	2.415(1)	2.018(4)	2.040	2.041	2.050	2.203	2.222	2.231
N3-Ru-N2	79.52(15)	78.64(14)	78.06	78.57	79.39	77.90	78.04	78.01
N3-Ru-N1	156.27(14)	156.13(14)	154.94	156.78	158.65	156.41	157.13	157.30
N2-Ru-N1	78.08(14)	79.62(14)	78.28	78.31	79.27	78.75	79.09	79.30
N2-Ru-N4	169.12(15)	167.30(14)	169.89	178.45	176.71	170.14	172.09	171.60
N4-Ru-N5	82.37(14)	83.25(14)	82.99	91.02	93.68	82.76	84.68	84.82
N3-Ru-Z[a]	87.22(9)	88.15(15)	88.63	88.51	90.55	88.65	91.38	86.29
N2-Ru-Z[a]	94.82(12)	95.42(16)	94.30	88.41	80.28	93.13	89.95	92.36
N1-Ru-Z[a]	86.95(11)	84.21(15)	85.01	88.72	85.30	89.31	88.52	94.51
N4-Ru-Z[a]	96.01(10)	96.62(16)	99.57	90.12	96.50	96.43	97.78	97.78
N5-Ru-Z[a]	177.89(12)	179.40(17)	178.35	178.05	168.99	178.86	177.55	175.39

[a] For (R_cR_c,S_aR_a)-**2a**, Z is Cl; for the other complexes, Z is N6.

Table X-3. Selected geometrical parameters for X-ray structures of (R_cR_c,S_aR_a)-**2a** and (S_cS_c,R_aS_a)-**4b** complexes and for BPW91 optimized geometries of (S_cS_c,R_aS_a)-**4b**, (S_cS_c,S_aR_a)-**4b**, *TS*-**4b**, (S_cS_c,R_aS_a)-**5b,** *in*-(S_cS_c,R_aS_a)-**6b**, and *out*-(S_cS_c,R_aS_a)-**6b** complexes.

DFT calculations for the two atropisomeric **4b** complexes yield a 5.7 kcal·mol^{-1} energy difference in favor of the (S_cS_c,R_aS_a)-**4b** in agreement with the experimental findings. A quick glance over the calculated structures (Figure X-3) of the two isomers shows that the oxazolinic alkyl groups have a lower steric hindrance with the trpy ligand for the most stable isomer. Figure X-3 depicts the relative energies of the **4b** isomers including the TS that can be attained through the simultaneous inverse rotation of the chiral axes (see Figures X-2 and -3). The high computational cost has prevented us to fully characterize this stationary point as a TS by calculating the harmonic frequencies. However, it has been checked that geometry optimization after a slight movement of the ring in both directions starting from the TS leads to the two initial atropisomers, one for each direction. The 26.0 kcal·mol^{-1} energy barrier to interconvert the two atropisomers further agrees with the experimental finding that no interconversion is taking place in solution from one isomer to the other at room temperature. The relatively large energy barrier is due to the highly tensioned nearly planar seven-membered chelating ring that the oxazoline ligand adopts in the TS as depicted in Figure X-3.

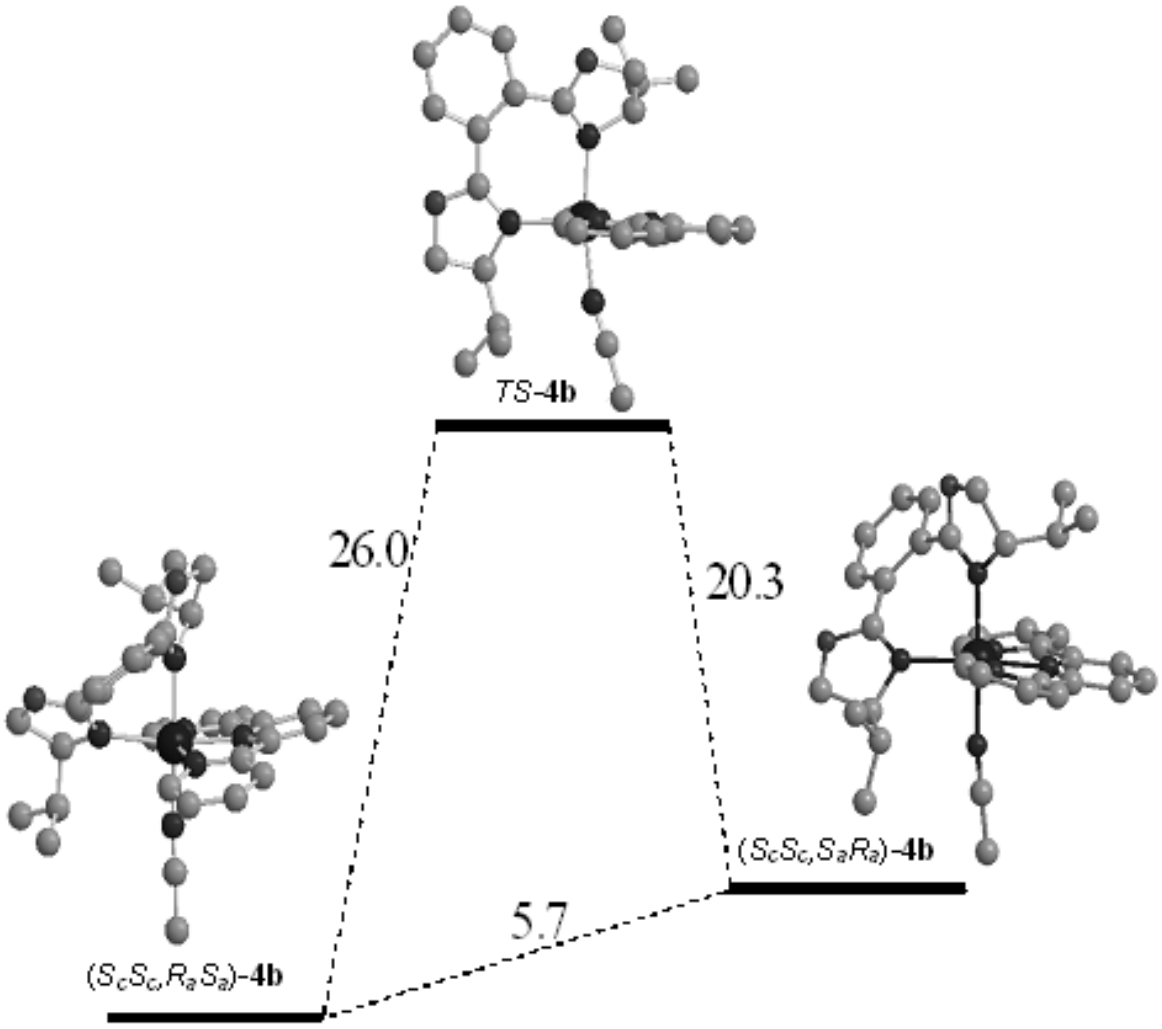

Figure X-3. Relative energy diagram for the two possible atropisomers, (S_cS_c,R_aS_a)**-4b** and (S_cS_c,S_aR_a)**-4b,** and the transition state connecting them, *TS*-**4b**. Energies are given in kcal·mol^{-1}.

Drawings of the calculated gas phase structures for the 2-hydroxypyridine complexes *out*-(S_cS_c,R_aS_a)**-6b** and *in*-(S_cS_c,R_aS_a)**-6b** are displayed in Figure X-4 A and B respectively. The most prominent difference from the Ru-(2-OH-py) (S_cS_c,R_aS_a)**-6b** and the Ru-MeCN (S_cS_c,R_aS_a)**-4b** structures just described is the fact that in the Ru-(2-OH-py) complexes the trpy pyridylic rings are more coplanar due to the steric encumbrance of the perpendicular pyridine ligand. The energy difference between the *in*-(S_cS_c,R_aS_a)**-6b** and *out*-(S_cS_c,R_aS_a)**-6b** isomers is only of 0.6 kcal·mol^{-1} in the gas phase. It has been found that this energy difference remains almost unaltered (0.5 kcal·mol^{-1}) when the solvent effect is considered in our calculations and thus it can be inferred that in solution they will easily interconvert since the barrier for the rotation of pyridine through the Ru-N bond is expected to be low.

A	B
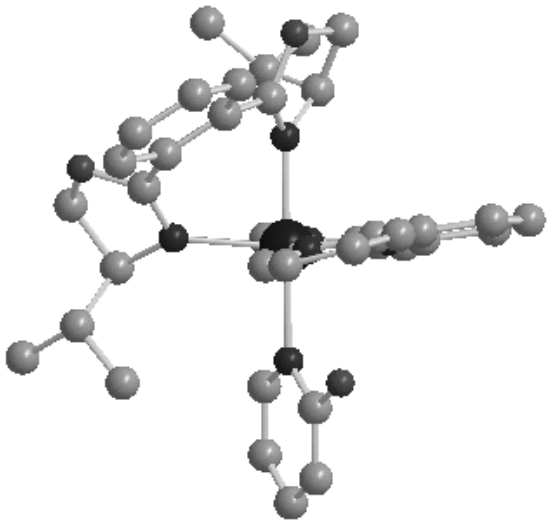	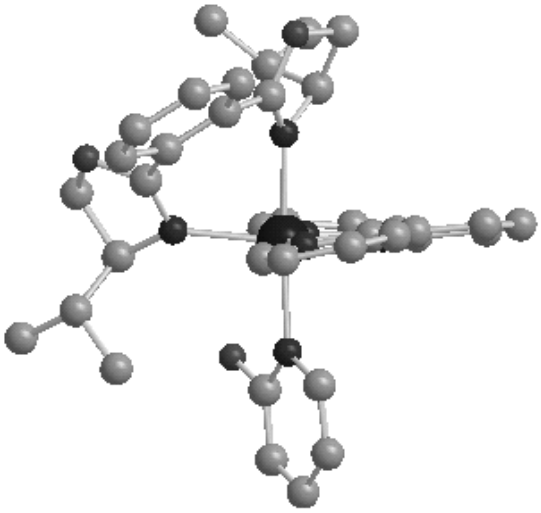
out-(S_cS_c,R_aS_a)-**6b**	*in*-(S_cS_c,R_aS_a)-**6b**

Figure X-4. BPW91 optimized geometries of the cationic moieties of two (S_cR_c,S_aS_a)-**6b** conformers with relatively similar energy but with different orientations of the 2-hydroxypyridine group, *in*-(S_cS_c,R_aS_a)-**6b** and *out*-(S_cS_c,R_aS_a)-**6b**.

Solution structure and NMR spectroscopy. NMR data for complexes **2**-**6** are listed in the experimental section and the most significant chemical shifts and NOEs are reported in Table X-4. All the labels used in the NMR are keyed with regard to the labels used in the crystal structure of (S_cS_c,R_aS_a)-**4b**. The numbering scheme is detailed in Chart 1.

		(S_cS_c,R_aS_a)-**2b**	(S_cS_c,R_aS_a)-**3b**	(S_cS_c,R_aS_a)-**4b**	(S_cS_c,R_aS_a)-**5b**	(S_cS_c,R_aS_a)-**6b**
trpy[a]	H1	7.95	7.97	7.92	8.10	8.97
	H15	9.41	9.46	9.35	9.32	9.00
		(H31, H34, H32)	(H31, H34, H32)	(H31, H34, H32, H36)	(H31, H34, H36)	(H31)
Ph-Ox	H24	7.26	7.25	7.31	7.33	6.27
	H25	7.57	7.58	7.60	7.65	7.22
	H26	7.90	7.95	7.92	7.98	5.83
	H27	8.13	8.20	8.21	8.20	6.12
CH-Ox5	H20	2.97	2.91	3.15	3.14	3.58
CH_2-Ox5	H21a	4.31	4.29	4.43	4.39	3.91
CH_2-Ox5	H21b	3.82	3.84	3.99	3.92	4.35
CH-*i*Pr5	H32	1.11	1.06	1.18	1.03	1.50
Me-*i*Pr5	H33a-c	0.28	0.25	0.28	0.28	0.67
Me-*i*Pr5	H37a-c	0.53	0.57	0.58	0.55	0.70
CH-Ox4	H31	5.56	5.67	5.64	5.4	4.58
CH_2-Ox4	H30a	5.16	5.20	5.14	5.20	4.54
CH_2-Ox4	H30b	5.00	5.11	5.12	5.07	4.13
CH-*i*Pr4	H34	3.72	2.88	3.04	1.51	3.54
Me-*i*Pr4	H36a-c	1.13	1.18	1.30	1.02	0.85
Me-*i*Pr4	H35a-c	1.18	1.21	1.30	1.20	1.17

[a] In brackets, the most significant NOE contacts are indicated.

Table X-4. Selected ^{1}H-NMR chemical shifts (ppm) for (S_cS_c,R_aS_a)-**2b**, (S_cS_c,R_aS_a)-**3b**, (S_cS_c,R_aS_a)-**4b,** (S_cS_c,R_aS_a)-**5b**, and (S_cS_c,R_aS_a)-**6b** complexes.

The absence of symmetry in the ruthenium complexes described in the present work renders all their hydrogen atoms magnetically different. However thanks to the fine structure of their monodimensional ^{1}H-NMR spectra together with their 2D-NMR spectra, the assignment of all the resonances observed was possible. It is important to underline here the importance of the chirality of the C_2 symmetrical Phbox-R ligands, in order to detect and characterize the atropisomeric complexes through NMR spectroscopy. With R = H, the corresponding achiral oxazolinic ligand, the two enantiomeric atropisomers would have been magnetically indistinguishable.

The ^{1}H-NMR spectrum of the Ru-Cl complex, (S_cS_c,R_aS_a)-**2b**, clearly supports that in solution the structure is very similar to the one obtained in the solid state, as expected for this type of Ru d^6 complexes. The most interesting feature of the structure is the fact that one of the oxazoline groups of the Phbox-*i*Pr ligand, (S_cS_c)-**b**, containing N5 and termed from now on Ox5 (see also Table X-4 for the general terms used to described the different groups of the ligands), is situated very close to the N3 peripheral pyridylic group and thus suffers a strong anisotropic current field effect producing a significant upfield displacement of all their resonances (compare Ox5 with Ox4 in Table X-4). The most affected resonance corresponds to the CH group of the *i*Pr substituent, termed CH-*i*Pr5, which is shifted by ca. 2.6 ppm relative to CH-*i*Pr4. Another important feature of the NMR study of complex (S_cS_c,R_aS_a)-**2b** are the interligand NOE contacts observed between H15 from the N3 peripheral pyridylic ring of the trpy ligand and H31 and H34 from CH-Ox4 and CH-*i*Pr4 respectively (see Table X-4), which also indicate the relative position of the Ox4 group with regard to the trpy ligand.

Table X-4 reveals that nearly all the resonances and NOE contacts of complexes (S_cS_c,R_aS_a)-(**2b-5b**) are very similar, and thus it can be concluded that they must present the same type of structure in solution. However some differences are found; for instance it is worth noting that for the Ru-pyridine complex (S_cS_c,R_aS_a)-**5b** the CH-*i*Pr4 resonance is significantly upfield shifted with regard to the (S_cS_c,R_aS_a)-(**2b-4b**) complexes due to the pyridine ligand current field. The fact that the resonances for the Me-*i*Pr4 are not sensibly shifted suggests that the *i*Pr4 group is not freely rotating but, on the contrary, it remains relatively frozen due to the steric congestion generated by the pyridine ligand. This statement is further supported by the fact that the pyridine ligand is rapidly rotating along the Ru-N bond as deduced from the magnetic equivalence of their ortho and meta H atoms, under the NMR experiments conditions, given the asymmetry of the rest of the complex. Furthermore those ortho and meta H atoms present NOE contacts with both H1 and H15 from trpy, which corroborates the previous statement.

As mentioned in the previous section DFT calculations show the existence of two conformers with relatively close energies, suggesting again that in solution the 2-OH-pyridine ligand is also rotating through the Ru-N bond. An interesting feature of the *in*-(S_cS_c,R_aS_a)-**6b** and *out*-(S_cS_c,R_aS_a)-**6b** structures, and particularly acute for the *in* case, is that the angle between the best planes that describe the two oxazolinic rings is significantly increased with regard to the other complexes described in this work including the Ru-py complex

(S_cS_c,R_aS_a)-**5b** (73.4° for (S_cS_c,R_aS_a)-**5b**, 89.6° for *in*-(S_cS_c,R_aS_a)-**6b** and 78.9° for *out*-(S_cS_c,R_aS_a)-**5b**; see Table X-5 for other angles between different rings). This angle increase, with regard to the Ru-py case, is due to the large steric hindrance produced by the OH group of the 2-OH-py ligand against the *i*Pr4 group that in turn generates a slight rotation of the chiral axes to accommodate itself. This produces a synchronized inverse rotation of the oxazolinic rings bringing the *i*Pr4 group farther from the Ru center and the trpy ligand, and moving the phenyl oxazolinic group closer to the peripherical N1 pyridylic trpy group. The former effect is also corroborated by the non existence of the NOE between H15-H34 in (S_cS_c,R_aS_a)-**6b** (see Figure X-5) in sharp contrast with the fact that it is observed for all the other complexes described in this work. The latter is also corroborated by the chemical shift of H26 and H27 (Table X-4) that reverse their increasing tendency and thus decrease by roughly 2 ppm with regard to their related pyridine complex, suggesting an anisotropic influence of the trpy aromatic field towards these two H atoms.

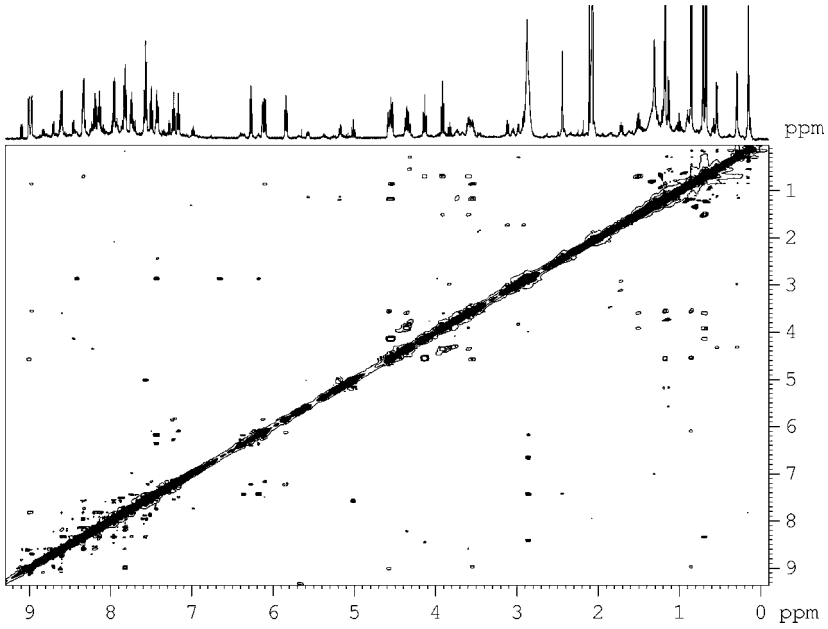

Figure X-5. NOESY NMR spectrum of (S_cS_c,R_aS_a)-**6b**.

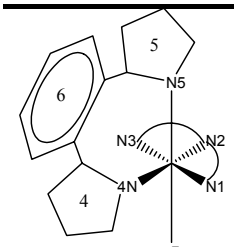	(*RR,SR*)-**2a** (X-ray)	(*SS,RS*)-**4b, A** (X-ray)	(*SS,RS*)-**4b**	(*SS,SR*)-**4b**	*TS*-**4b**	(*SS,RS*)-**5b**	*in*-(*SS,RS*)-**6b**	*out*-(*SS,RS*)-**6b**
plane N1-plane N2	4.44	14.68	13.27	12.24	7.28	7.53	8.20	9.58
plane N1-plane N3	13.24	20.00	20.58	23.13	8.32	13.11	12.79	16.64
plane N2-plane N3	9.62	6.10	8.64	14.06	3.65	7.90	10.24	11.63
phenyl-plane N3	22.58	17.59	26.43	32.73	78.42	31.13	37.40	36.65
phenyl-plane N2	25.50	18.31	24.55	37.82	79.20	27.06	27.38	25.06
phenyl-plane N1	24.73	31.02	34.18	50.04	86.38	32.27	26.92	25.54
plane N4-plane N5	81.15	80.61	75.00	39.84	23.09	73.38	89.60	78.89
phenyl-plane N4	55.45	46.58	50.43	39.57	8.86	49.83	35.06	63.17
phenyl-plane N5	40.88	52.56	38.73	37.48	31.94	35.19	69.07	32.54
phenyl-*trpy*	23.34	19.03	23.67	39.54	81.22	28.52	30.71	29.08
trpy-py						78.65	89.79	89.32

Table X-5. Angles between planes for the X-ray structures of complexes *RR,SR*-**2a** and *SS,RS*-**4b** and BPW91 optimized geometries of complexes *SS,RS*-**4b**, *SS,RS*-**5b**, *SS,SR*-**4b**, *TS*-**4b,** *in-SS,RS*-**6b**, and *out-SS,RS*-**6b**.

Conclusions

In conclusion, the chirality of the 1,2-bis(oxazolinyl)benzene ligand Phbox-R, either (R_cR_c) or (S_cS_c), allows to prepare and isolate pure atropisomeric complexes due to the highly restricted rotation along the oxazolinic-phenyl axes upon coordination to a Ru metal center. A family of atropisomeric complexes has thus been isolated and fully characterized, in the solid state by X-ray diffraction analysis, in solution by mainly NMR spectroscopy and in the gas phase thanks to DFT calculations. This thorough structural characterization yields a very complete and coherent vision of this type of complexes with a surprisingly detailed intimate description of mononuclear ligand effects towards both bis(oxazolinic) and trpy coordinated ligands.

Thus, the coordination of a 1,2-bis(oxazolinyl)benzene ligand to a Ru metal center produces rotationally restricted isomers. These isomers show significantly different energy values due

to steric effects between the oxazolinic and the auxiliary ligands, thus allowing the direct synthesis of pure atropisomers.

References

1. a) A. G. Lappin, R. A. Marusak, *Coord. Chem. Rev*. **1991**, *109*, 125-180. b) W. P. Griffith., *Chem. Soc. Rev.* **1992**, *21*, 179-185. c) J. Wing-Sze Hui, W-T. Wong, *Coord. Chem. Rev.* **1998**, *172*, 389-436. d) M. J. Clarke, *Coord. Chem. Rev.* **2002**, *232*, 69-93. e) T. J. Meyer, M. H. V. Huynh, *Inorg. Chem*. **2003**, *42*, 8140-8169.
2. a) D. W. Thompson, J. R. Schoonover, D. K. Graff, C. N. Fleming, T. J. Meyer, *J. Photochem. Photobiol. A: Chemistry.* **2000**, *137*, 131-134. b) H. E. Toma, R. M. Serrasqueiro, R. C. Rocha, G. J. F. Demets, H. Winnischofer, K. Araki, P. E. A. Ribeiro, C. L. Donnici, *J. Photochem. Photobiol. A: Chemistry.* **2000**, *135*, 185-191. c) M. H. Keefe, K. D. Benkstein, H. T. Hupp, *Coord. Chem. Rev.* **2000**, *205*, 201-228. d) D. S. Tyson, C. R. Luman, X. Zhou, F. N. Castellano, *Inorg. Chem.* **2001**, *40*, 4063-4071. e) V. Valzani, A. Juris, *Coord. Chem. Rev.* **2001**, *211*, 97-115. (f) D. M. Dattelbaum, C. M. Hartshorn, T. J. Meyer, *J. Am. Chem. Soc*. **2002**, *124*, 4938-4939. g) C. N. Fleming, L. M. Dupray, J. M. Papanikolas, T. J. Meyer, *J. Phys. Chem. A* **2002**, *106*, 2328-2334. h) R. Lomoth, T. Haupl, O. Jahansson, L. Hammarstrom, *Chem. Eur. J.* **2002**, *8*, 102-110.
3. a) S. O. Kelly, J. K. Barton, *Science* **1999**, *238*, 375-381. b) D. B. Hall, R. E. Holmlin, J. K. Barton, *Nature* **1996**, *384*, 731-735. c) C. J. Burrows, J. G. Muller, *Chem. Rev.* **1998**, *98*, 1109-1152. d) G. B. Schuster, *Acc. Chem. Res.* **2000**, *33*, 253-260. e) S. C. Weatherly, I. V. Yang, H. H. Thorp, *J. Am. Chem. Soc.* **2001**, *123*, 1236-1237.
4. a) S. I. Murahashi, H. Takaya, T. Naota, *Pure Appl. Chem.* **2002**, *74*, 19-24. b) T. Naota, H. Takaya, S.-I. Murahashi, *Chem. Rev.* **1998**, *98*, 2599-2660. c) M. Rodríguez, I. Romero, A. Llobet, A. Deronzier, M. Biner, T. Parella, H. Stoeckli-Evans, *Inorg. Chem*. **2001**, *40*, 4150-4156. d) U. J. Jauregui-Haza, M. Dessoudeix, Ph. Kalck, A. M. Wilhelm, H. Delmas, *Catal. Today*. **2001**, *66*, 297-302.
5. a) R. Ballardini, V. Balzani, A. Credi, M. T. Gandolfi, M. Venturi, *Int. J. Photoenergy* **2001**, *3*, 63-77. b) P. R. Ashton, R. Ballardini, V. Balzani, A. Credi, K. R. Dress, E. Ishow, C. J. Kleverlaan, O. Kocian, J. A. Preece, N. Spencer, J. F. Stoddart, M. Venturi, S. Wenger, *Chem. Eur. J*. **2000**, *6*, 3558-3574. c) E. Baranoff, J. –P. Collin, J.

Furusho, Y. Furusho, A. –C. Laemmel, J. –P. Sauvage, *Inorg. Chem*. **2002**, *41*, 1215-1222. d) T. Kojima, T. Sakamoto, Y. Matsuda, *Inorg. Chem.* **2004**, *43*, 2243-2245.

6. A. H. Velders, A. C. G. Hotze, J. G. Haasnoot, J. Reedijk, *Inorg. Chem*. **1999**, *38*, 2762-2763.
7. a) E. Yashima, K. Maeda, Y. Okamoto, *Nature*, **1999**, *399*, 449-451. b) L. J. Pins, J. Huskens, T. de Jong, P. Timmerman, D. N. Reinhoudt, *Nature*, **1999**, *398*, 498-502. c) B. L. Feringa, R. A. van Delden, N. Komura, E. M. Geertsema, *Chem. Rev*. **2000**, *100*, 1789-1816. d) P. Hayoz, A. Von Zelewsky, H. Stoeckli-Evans, *J. Am. Chem. Soc.* **1993**, *115*, 5111-5114. e) A. Von Zelewsky, *Coord. Chem. Rev.* **1999**, *190-192*, 811-825. f) U. Knof, A. Von Zelewsky, *Angew. Chem. Int. Ed.* **1999**, *38*, 302-322. g) A. Von Zelewsky, O. Mamula, *J. Chem. Soc., Dalton Trans.*, **2000**, 219-231. h) J. W. Canary, S. Zahn, *Trends in Biotechnology*, **2001**, *19*, 251-255. i) J. Lacour, A. Londez, *J. Organomet. Chem.* **2002**, *643-644*, 392-403. j) P. D. Knight, P. Scott, *Coord. Chem. Rev.* **2003**, *242*, 125-142.
8. A. Von Zelewsky, *Stereochemistry of coordination compounds*. John Wiley and sons Ltd.: West Sussex 1996.
9. a) D. S. Hesek, Y. Inoue, S. R. L. Everitt, H. Ishida, M. Kunieda, M. D. Drew, *Inorg. Chem.* **2000**, *39*, 317-324. b) D. Hesek, G. A. Hembury, M. D. Drew, S. Taniguchi, Y. Inoue, *J. Am. Chem. Soc*. **2000**, *122*, 10236-10237. c) R. A. Sheldon, *Chirotechnology* Marcel Dekker: New York, 1993.
10. a) A. Llobet, *Inorg. Chim. Acta* **1994**, *221*, 125-131. b) I. Romero, M. Rodríguez, A. Llobet, M. -N. Collomb-Dunand-Sauthier, A. Deronzier, T. Parella, H. Stoeckli-Evans, *J. Chem. Soc., Dalton Trans.* **2000**, 1689-1694. c) C. Sens, M. Rodríguez, I. Romero, A. Llobet, T. Parella, B. P. Sullivan, J. Benet-Buchholz, *Inorg. Chem.* **2003**, *42*, 2040-2048. d) M. Rodríguez, I. Romero, A. Llobet, C. Sens, A. Deronzier, *Electrochim. Acta* **2003**, *48*, 1047-1054. e) X. Sala, M. Rodríguez, I. Romero, A. Llobet, G. González, M. Martínez, J. Benet-Buchholz, *Inorg. Chem*. **2004**, *43*, 5403-5409. f) C. Sens, I. Romero, M. Rodríguez, A. Llobet, T. Parella, J. Benet-Buchholz, *J. Am. Chem. Soc*. **2004**, *126*, 7798-7799. g) X. Sala, A. Poater, I. Romero, M. Rodríguez, A. Llobet, X. Solans, T. Parella, T. M. Santos, *Eur. J. Inorg. Chem.* **2004**, *3*, 612-618.
11. a) A. Llobet, P. Doppelt, T. J. Meyer, *Inorg. Chem*. **1988**, *27*, 514-520. (b) K. Barqawi, A. Llobet, T. J. Meyer, *J. Am. Chem. Soc*. **1988**, *110*, 7751-7759.

12. C. Bolm, K. Weickhardt, M. Zehnder, D. Glasmacher, *Chem. Ber*. **1991**, *124*, 1173-1180.
13. A. El Hatimi, M. Gómez, S. Jansat, G. Muller, M. Font-Badía, X. Solans, *J. Chem. Soc., Dalton Trans.* **1998**, 4229-4236.
14. F. Laurent, E. Plantalech, B. Donnadieu, A. Jiménez, F. Hernández, M. Martínez-Ripoll, M. Biner, A. Llobet, A. *Polyhedron* **1999**, *18/25*, 3321-3331.
15. a) H. Kurosawa, H. Asano, Y. Miyaki, *Inorg. Chim. Acta* 1998, *270* ,87-94. b) C. Sens, M. Rodríguez, I. Romero, A. Llobet, T. Parella, B. P. Sullivan, J. Benet-Buchholz, *Inorg. Chem*. **2003**, *42*, 8385-8394. c) L. F. Szczpura, S. M. Maricich, R. F. See, M. R. Churchill, K. J. Takeuchi, *Inorg. Chem*. **1995**, *34*, 4198-4205.
16. M. Gómez, S. Jansat, G. Muller, M. A. Maestro, J. Mahia, *Organometallics* **2002**, *21*, 1077-1087.
17. R. Cini, C. J. Pifferi, *J. Chem. Soc., Dalton Trans*. **1999**, 699-710.
18. a) ADF2002.03, E. J. Baerends, J. A. Autschbach, A. Bérces, C. Bo, P. M. Boerrigter, L. Cavallo, D. P. Chong, L. Deng, R. M. Dickson, D. E. Ellis, L. Fan, T. H. Fischer, C. Fonseca Guerra, S. J. A. van Gisbergen, J. A. Groeneveld, O. V. Gritsenko, M. Grüning, F. E. Harris, P. van den Hoek, H. Jacobsen, G. van Kessel, F. Kootstra, E. van Lenthe, V. P. Osinga, S. Patchkovskii, P. H. T. Philipsen, D. Post, C. C. Pye, W. Ravenek, P. Ros, P. R. T. Schipper, G. Schreckenbach, J. G. Snijders, M. Solà, M. Swart, D. Swerhone, G. te Velde, P. Vernooijs, L. Versluis, O. Visser, E. van Wezenbeek, G. Wiesenekker, S. K. Wolff, T. K. Woo, and T. Ziegler, Vrije Universiteit Amsterdam: Amsterdam, The Netherlands, 2000. b) G. te Velde, F. M. Bickelhaupt, E. J. Baerends, C. Fonseca Guerra, S. J. A. van Gisbergen, J. G. Snijders, T. Ziegler, *J. Comput. Chem.* **2001**, *22*, 931-967. c) E. J. Baerends, D. E. Ellis, P. Ros, *Chem. Phys.* **1973**, *2*, 41-51. d) E. J. Baerends, Ph. D. Thesis, Vrije Universiteit, Amsterdam, 1975. e) W. Ravenek, *Algorithms and Applications on Vector and Parallel Computers*, H. J. J. te Riele, Th. J. Dekker, H. A. van de Vorst, Eds., Elsevier, Amsterdam, 1987.
19. G. te Velde, E. J. Baerends, *J. Comp. Phys.* **1992**, *99*, 84-98.
20. a) J. G. Snijders, E. J. Baerends, P. Vernooijs, *At. Nucl. Data Tables* **1982**, *26*, 483-509. b) P. Vernooijs, J. G. Snijders, E. J. Baerends, *Slater Type Basis Functions for the Whole Periodic System. Internal Report*, Vrije Universiteit of Amsterdam, The Netherlands, 1981.

21. J. Krijn, E. J. Baerends, *Fit functions in the HFS method. Internal Report (in Dutch)*, Vrije Universiteit of Amsterdam, The Netherlands, 1984.
22. A. D. Becke, *Phys. Rev. A* **1988**, *38*, 3098-3100.
23. J. P. Perdew, Y. Wang, *Phys. Rev. B* **1992**, *45*, 13244-13249.
24. A. Klamt, G. Schüürmann, *J. Chem. Soc. Perkin. Trans*. **1993**, 799-805.
25. C. C. Pye, T. Ziegler, *Theor. Chem. Acc.* **1999**, *1101*, 396-408.
26. Gaussian 98 (Revision A.11), M. J. Frisch, G. W. Trucks, H. B. Schlegel, G. E. Scuseria, M. A. Robb, J. R. Cheeseman, V. G. Zakrzewski, J. A. Montgomery, Jr., R. E. Stratmann, J. C. Burant, S. Dapprich, J. M. Millam, A. D. Daniels, K. N. Kudin, M. C. Strain, O. Farkas, J. Tomasi, V. Barone, M. Cossi, R. Cammi, B. Mennucci, C. Pomelli, C. Adamo, S. Clifford, J. Ochterski, G. A. Petersson, P. Y. Ayala, Q. Cui, K. Morokuma, P. Salvador, J. J. Dannenberg, D. K. Malick, A. D. Rabuck, K. Raghavachari, J. B. Foresman, J. Cioslowski, J. V. Ortiz, A. G. Baboul, B. B. Stefanov, G. Liu, A. Liashenko, P. Piskorz, I. Komaromi, R. Gomperts, R. L. Martin, D. J. Fox, T. Keith, M. A. Al-Laham, C. Y. Peng, A. Nanayakkara, M. Challacombe, P. M. W. Gill, B. Johnson, W. Chen, M. W. Wong, J. L. Andres, C. Gonzalez, M. Head-Gordon, E. S. Replogle, J. A. Pople, Gaussian, Inc., Pittsburgh PA, 2001.
27. Handbook of Chemistry and Physics, D. R. Lide, 83rd Ed., CRC Press LLC, Boca Raton, London, 2002-2003.
28. D. M. Dolney, G. D. Hawkins, P. Winget, D. A. Liotard, C. J. Cramer, D. G. Truhlar, *J. Comp. Chem.* **2000**, *21*, 340-366.
29. SPARTAN'02, 2001 Wavefunction, Inc., Q-Chem, USA.
30. Standard deviations for the distances and for the angles, $s_{n-1} = \sqrt{\frac{\sum_{i=1}^{N}(CV - EV)^2}{N-1}}$, where CV means calculated value, EV experimental value (X-ray data), and N is the number of bond distances or angles taken into account).

Chapter XI: *Ruthenium Complexes Containing the N-tridentate "bpea" and Phosphine Ligands*

Ruthenium Complexes Containing the N-tridentate "*bpea*" and Phosphine Ligands

Abstract

The study of a new Ru-Cl complex [Ru^{II}Cl(*bpea*)(*dppe*)](BF_4), **1**, is described. This complex shows three isomeric Ru^{II} complexes in solution, the *trans-fac*, **1a**, the *cis-fac*, **1b**, and the *cis-mer*, **1c**, that presents the *bpea* ligand in a meridional fashion, unknown for Ru. Complexes **1a** and **1b** display a Ru metal center possessing a distorted octahedral type of coordination, where the "*bpea*" ligand is coordinated in a facial fashion. DFT calculations show that *fac*-**1** isomers are more stable than *mer*-**1** isomers. The different behavior of UV-spectra of the isomers of complex **1** has been explained by theoretical calculations through the Time Dependent-DFT approach.

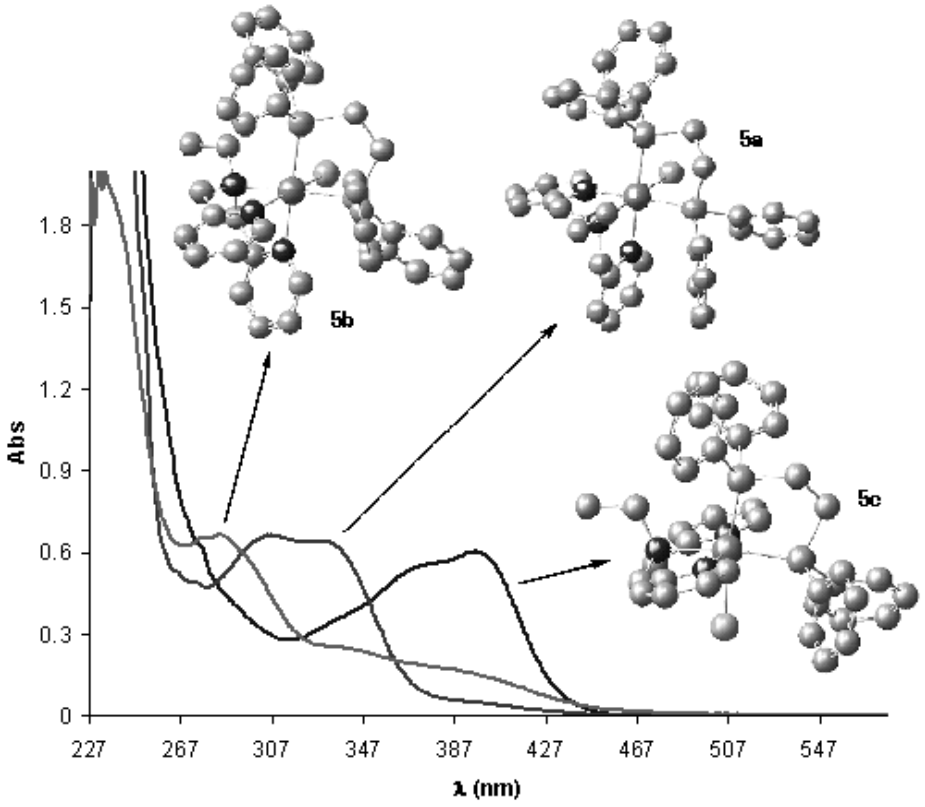

Introduction

Ruthenium complexes are gathering a great deal of attention because of their multiple applications in many fields of science.[1] They are being used extensively as catalyst for a myriad of different processes including oxidative and reductive reactions.[2] The design of new ligands in catalysis generally has been directed by a desire to enhance the reactivity, selectivity and/or thermal stability of homogeneous transition metal-based catalysts. By choosing the appropriate ligand we can control the chemical reactivity due to the steric and electronic properties that the ligand is capable of transmitting to the metal center. Besides, some factors such as the chelate ring size are also important.

Ru(II) complexes containing tertiary phosphines have been extensively studied particularly in connection with their ability to function as catalysts in a variety of reactions,[3] whereas in recent years, there has been increased interest in developing new Ru(II) complexes containing also ligands with nitrogen donor atoms. Thus, synthetic applications involving ruthenium metal and tridentate nitrogen donor ligands have been also developed, such as tris(pyrazolyl)borat,[4] (1-pyrazolyl)metane,[5] 2, 6-bis(oxazolinyl)pyridine,[6] and 1, 4, 7-triazacyclononane.[7] This is in response to the susceptibility of phosphine ligands to undergo degradation such P-C cleavage, oxidation to phosphine oxides, and ortho-metallation reactions, during catalysis, especially under thermal conditions. In addition, ruthenium complexes containing N-donors ligands have been used successfully in catalytic hydrogenation,[8] hydrogen transfer,[9] oxidations,[10] and conversion of terminal alkynes to nitriles.[11]

With the aim to contribute to the elucidation of the influence of steric and electronic properties of the ligands in the catalytic properties, in the present chapter we analyze using DFT methods the structural, energetic, and spectroscopic properties of new Ru-Cl complexes containing a phosphine type of ligand, together with the tridentate polypyridylic ligand N,N-bis(2-pyridylmethyl)ethylamine, commonly known as *bpea*. In particular, theoretical simulations through a Time Dependent-DFT approach have been carried out to understand the nature of the transitions in the experimental UV-Vis spectra.

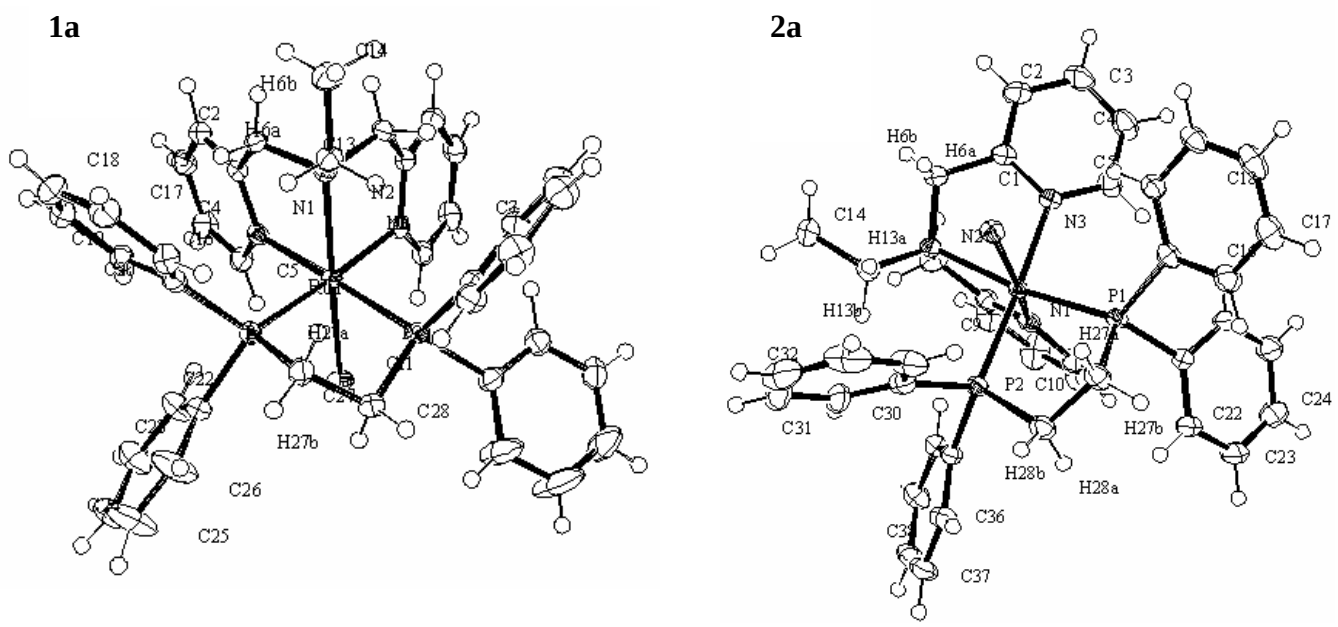

Figure XI-1. X-ray structures (Ortep-plots with ellipsoids at 50% probability level) and labelling scheme for **1a** (left) and **1b** (right).

An ORTEP view together with their labeling scheme is depicted in Figure XI-1 (**1a** and **1b**), respectively. The molecular structure of **1a** shows that the Ru metal atom presents a distorted octahedral environment. The *bpea* ligand coordinates facially through its nitrogen atoms while the diphenyl phosphine ligand, *dppe,* acts in a chelate way through its P atoms, and these P atoms occupy the trans positions with respect to the N atoms of the pyridyl groups of the *bpea* ligand. Finally, the sixth coordination is completed with the chloro ligand that is situated in trans with regard to the aliphatic N atom of the *bpea* ligand.

There is no mirror plane that bisects the molecule due to the spatial disposition of the *dppe* ligand when it is coordinated to the metallic center.

All bond distances and angles between ruthenium and *bpea* and *dppe* ligands are comparable to those of complexes that have been described in the literature with this kind of ligands.[2d,12-14] However, $N_{aromatic}$-Ru bond distances of the *bpea* ligand (Ru(1)-N(3) = 2.1365(18) Å; Ru(1)-N(1) = 2.1389(16) Å) are slightly higher than those in a similar structural complex[10b] where the *dppe* ligand has been substituted by *bpy* ligand

(N(1, 3)-Ru(1) = 2.0680(19)Å). This fact might be due to the higher trans influence of the *dppe* ligand with respect to the *bpy* ligand.

The bond angles deviate from those of the ideal octahedron due to the steric constrains imposed by tridentate and didentate ligands. Thus angles below 90º are obtained for ∠NRuN of the facial *bpea* ligand and for ∠PRuP in the *dppe* ligand, and bond angles above 90º are found for ∠NRuP, whose N atoms belonging to different ligands.

The molecular structure of **1b** shows that the Ru atom presents a distorted octahedral environment. Similar to isomer **1a,** the *bpea* ligand coordinates facially through its nitrogen atoms and the *dppe* ligand acts in a chelate way through its P atoms. Nevertheless, in this isomer one P atom occupies the trans positions with respect to an $N_{aromatic}$ atom of the *bpea* ligand and the other one is placed trans with respect to the $N_{aliphatic}$ of this ligand. Consequently, the chloro ligand is situated trans with regard to the other $N_{aromatic}$ atom of *bpea*.

All bond distances and angles are comparable to those of isomer **1a**, though the Ru-N bond distances are slightly affected by the trans influence of the different chloro and diphosphine ligands. This effect is observed in Ru(1)-N(2), Ru(1)-N(1), and Ru(1)-Cl(1) bond distances. In **1b**, Ru(1)-N(2) = 2.2034(17) Å (P is a trans ligand), therefore higher than Ru(1)-N(2) = 2.1724(17) Å (where Cl is a trans ligand) in **1a**. Similar effects are shown in Ru(1)-N(1) = 2.1389(6) Å (P is a trans ligand, **1a**), and Ru(1)-N(1) = 2.0732(17) Å (Cl is a trans ligand, **1b**).

The *bpea* ligand is a flexible molecule that can adopt either a meridional[15] or a facial[12,16] fashion when coordinated to a transition metal. Chart 1 shows the possible diastereoisomers that could be potentially obtained with *bpea*, and the phosphine ligands coordinating the metal center in an octahedral shape.

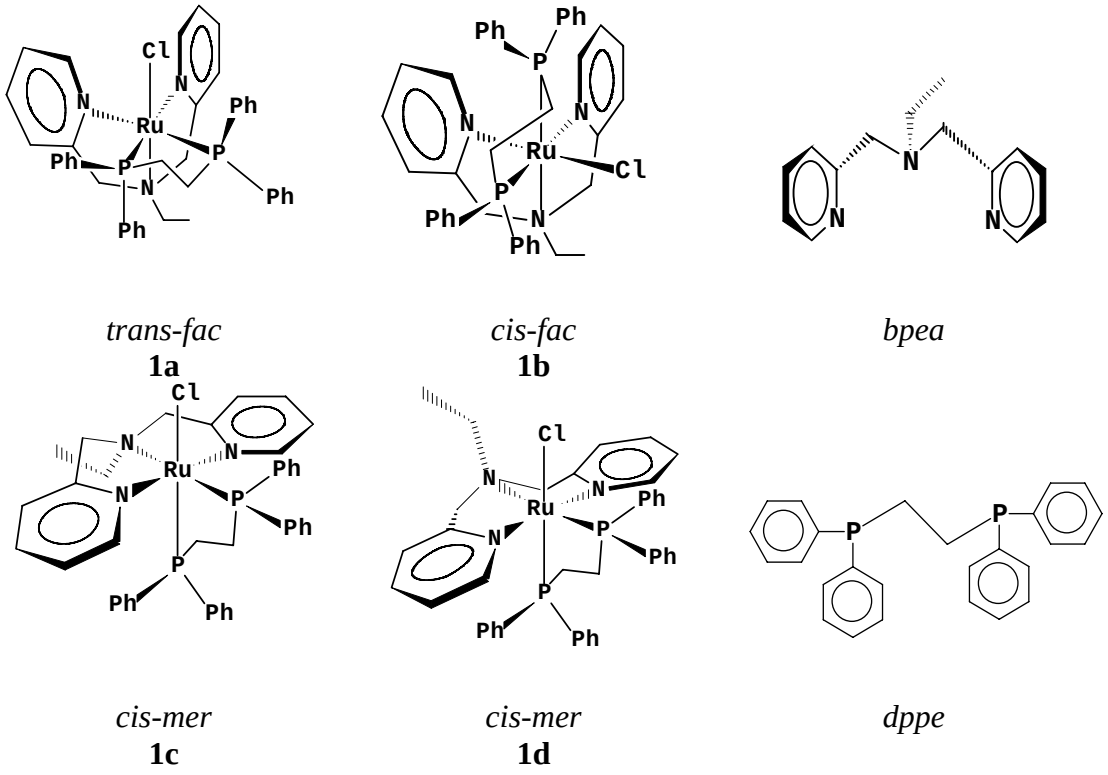

trans-fac **1a** | *cis-fac* **1b** | *bpea*

cis-mer **1c** | *cis-mer* **1d** | *dppe*

Chart 1. Possible diastereoisomers for complex **1.**

X-ray diffraction analysis and NMR spectra shows that for complex **1**, there are only three (**1a**, **1b**, and **1c**) of the four possible diastereoisomers. Isomer **1c** is the first ruthenium complex where the tridentate ligand *bpea* adopts the uncommon meridional mode of coordination around the metal.

Computational Details

The density functional theory (DFT) calculations have been carried out with the hybrid B3PW91 density functional,[17,18] as implemented in the Gaussian03 package.[19] The Ru atoms have been represented with the quasi relativistic effective core pseudo-potentials (RECP) of the Stuttgart group and the associated basis sets augmented with a *f* polarization function (α = 1.235).[20,21] The remaining atoms (C, O, and H) have been represented with 6-31G(*d,p*) basis sets.[22] The B3PW91 geometry optimizations were performed without any symmetry constraints, and the nature of minima was checked by analytical frequency calculations. The energies given throughout the paper are electronic energies without ZPE corrections (inclusion of the ZPE corrections does not

significantly modify the results) or Gibbs free energy values *G* computed with Gaussian 03 at 298 K and *P* = 1 atm. The atomic charges have been calculated using the Natural Population Analysis (NPA) scheme of Weinhold and co-workers.[23] Time-dependent DFT calculations[24] were performed to simulate UV-Vis spectra.

Results

DFT calculations were performed for the four isomers **1a**-**1d**. A geometry optimization of the four gas-phase possible isomers was performed. The optimized structures are drawn in Figure XI-2, and selected bond distances and angles are gathered in Table XI-1 together with the available experimental counterparts for purposes of comparison. The results show good agreement between the experimental and the theoretical data. For isomer **1a**, the standard deviation for the bond distances is 0.019 Å and for the angles is 0.7º, thus providing confidence on the reliability of the chosen method to reproduce geometries of the studied complexes.

	1a (exp.)	**1a** (calc.)	**1b** (exp.)	**1b** (calc.)	**1c** (calc.)	**1d** (calc.)
Ru1-N3	2.1365(18)	2.135	2.1393(18)	2.138	2.097	2.105
Ru1-N1	2.1389(16)	2.126	2.0732(17)	2.092	2.109	2.122
Ru1-N2	2.1724(17)	2.206	2.2034(17)	2.236	2.208	2.215
Ru1-P1	2.3026(6)	2.346	2.3069(5)	2.327	2.326	2.347
Ru1-P2	2.3067(5)	2.344	2.3271(6)	2.372	2.336	2.356
Ru1-Cl1	2.4181(5)	2.418	2.4217(5)	2.425	2.473	2.443
N3-Ru1-N1	81.16(6)	79.9	84.62(7)	79.2	160.0	156.6
N3-Ru1-N2	80.48(7)	79.8	75.89(7)	78.7	80.1	79.4
N1-Ru1-N2	79.38(6)	80.0	81.27(7)	81.0	80.4	77.8
N3-Ru1-P1	177.51(5)	176.1	97.84(5)	97.7	98.4	99.2
N1-Ru1-P1	96.71(5)	96.3	104.08(5)	101.4	100.2	103.2
N2-Ru1-P1	97.88(5)	98.7	171.51(5)	172.3	171.9	175.5
N3-Ru1-P2	97.79(5)	98.6	176.47(5)	150.4	93.2	91.2
N1-Ru1-P2	176.85(5)	176.5	97.62(5)	101.4	95.6	97.6
N2-Ru1-P2	103.42(5)	102.9	101.69(5)	100.4	102.4	99.1
P1-Ru1-P2	84.40(2)	85.2	84.30(2)	83.1	85.6	85.1
N3-Ru1-Cl1	90.59(5)	90.4	89.63(5)	90.7	88.9	91.5
N1-Ru1-Cl1	93.01(5)	93.3	169.92(5)	165.9	85.0	83.4
N2-Ru1Cl1	169.01(5)	169.0	89.32(5)	87.3	85.7	90.2
P1-Ru1-Cl1	90.82(2)	90.7	84.871(18)	85.9	86.4	85.6
P2-Ru1-Cl1	84.02(2)	83.5	87.761(19)	88.5	171.9	170.6

Table XI-1. Selected bond distances and angles for X-ray structures of **1a** and **1b**, and calculated structures **1a**-**1d**.

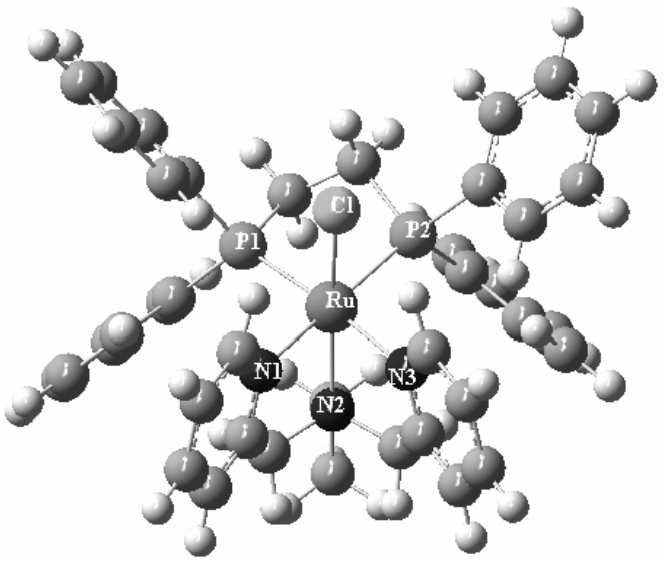

1a

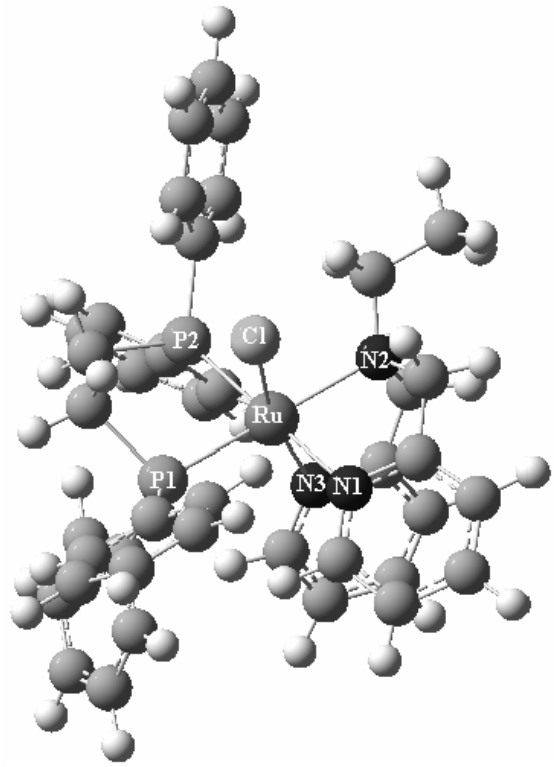

1b

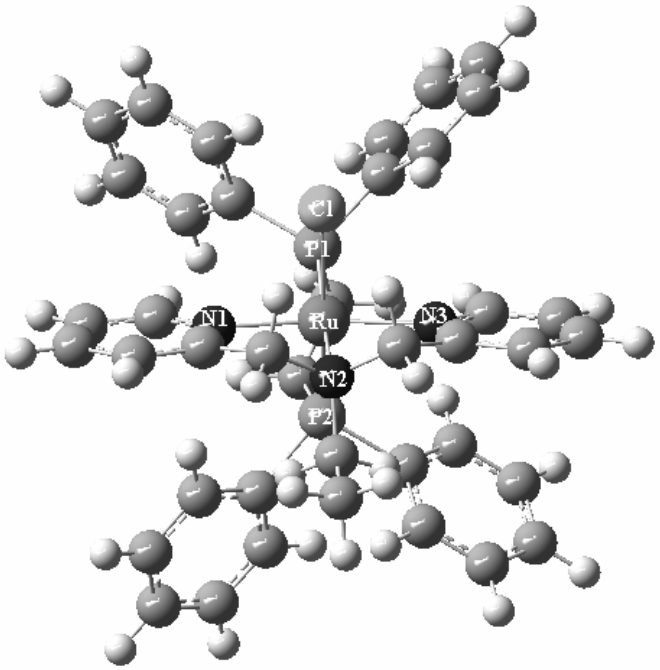

1c

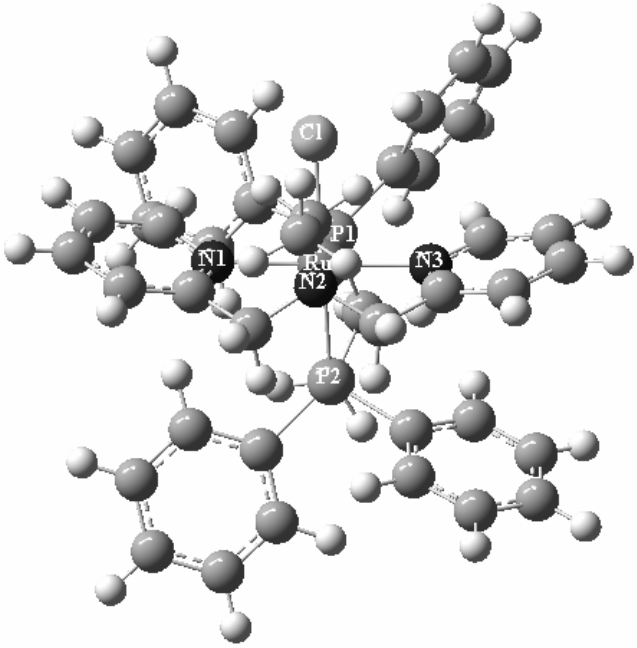

1d

Figure XI-2. B3PW91 optimized geometries of isomers of complex **1**.

In order to simplify the structural discussion for complexes **1a**-**1d**, the plane nearly perpendicular to the Ru-Cl bond, and containing four *cis* coordinating atoms with regard to the mentioned RuCl bond, will be considered as the equatorial plane of these molecules. In the *trans-fac* complex **1a** the pyridyl groups are perpendicular to the equatorial plane, a situation that produces relatively small steric interactions among pyridyl-*bpea* and phenyl-*dppe* groups. For the *cis-fac* complex **1b**, one of the pyridyl-*bpea* rings is perpendicular to the equatorial plane as in the previous case whereas the second pyridyl is nearly parallel to this plane producing significant steric interactions with the closest phenyl-*dppe* rings. In the case of the *mer-down* complex **1c**, now both pyridyl rings are nearly parallel to the equatorial plane and thus producing strong steric interactions with the phenyl-*dppe* groups. This steric repulsion is even more strongly manifested in the case of the isomer **1d** where now the *bpea* ligand needs to bend in order to reduce steric repulsions (the calculated Spartan'02 angles between the best fitted planes defined by each pyridyl group of *bpea* are 3.7 and 24.8º for **1c** and **1d** respectively).[25] The degree of steric repulsions in these isomers is also consistent with the relative energies found for them that are 0.3 (**1b**), 0.8 (**1c**), and 5.3 (**1d**) kcal·mol^{-1} above the energy of the isomer **1a**. It is also consistent with the relative yields obtained in the synthesis; furthermore, the fact that the isomer **1d** is not observed in the present synthesis is also in agreement with its energy being 4.5 kcal·mol^{-1} larger with regard to the energy of any of the other isomers.

A characteristic of this set of isomers is the fact that the Ru-Cl bond is *trans* to N-*bpea* atoms in **1a** and **4b** but is *trans* to P-*dppe* atoms in **1c** and **1d**. The stronger *trans* influence of the P vs. the N donors produces a weakening of the Ru-Cl bond that is manifested through their Ru-Cl bond distances (2.418 Å, **1a**; 2.425 Å, **1b**; 2.473 Å, **1c;** and 2.443 Å, **1d**) and that is also consistent with an increase of Ru(III)/Ru(II) redox potential by 100 mV for **1c** with regard to either **1a** or **1b**. This *trans* influence can also be observed for isomers **1a** and **1b** in the Ru-N(2) aromatic bonds.

It is worth mentioning here that the meridional isomer **1c** constitutes the first example described in the literature of a Ru complex where the *bpea* ligand adopts this geometry. In all the Ru-*bpea* complexes previously described *bpea* adopted a facial geometry.[2d,26] However for other transition metal complexes such as Mn and Fe, both meridional and facial geometries had been described.[27,28]

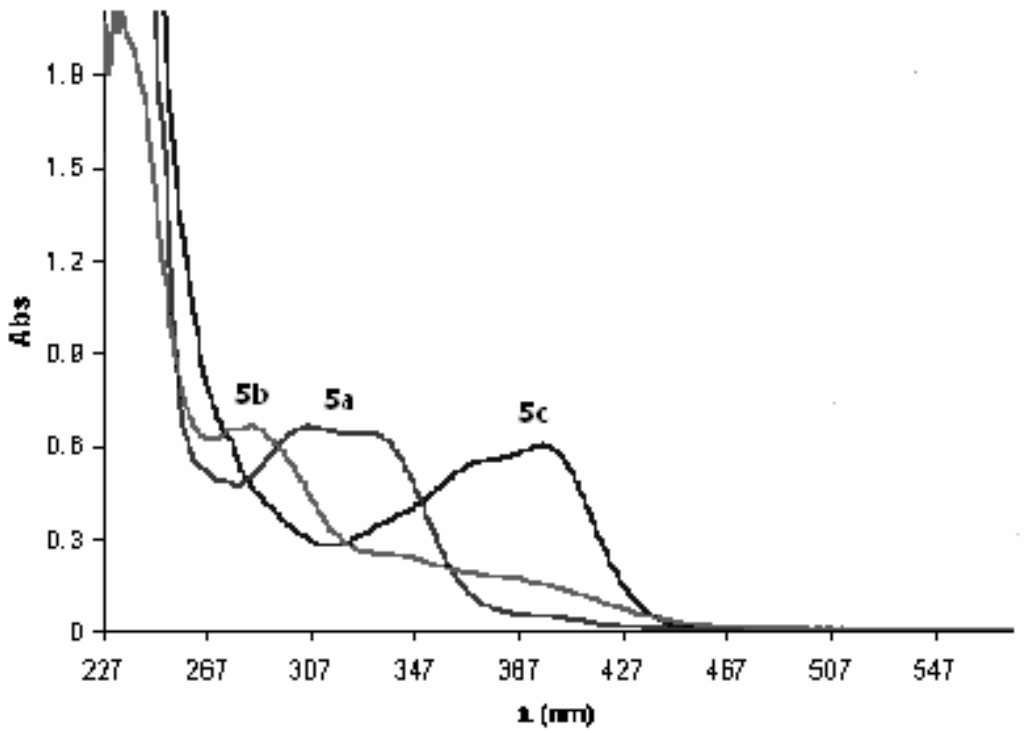

Figure XI-3. UV-Vis spectra for complexes **1**, **1a, 1b**, and **1c**.

The UV-Vis spectra of the chloro complexes **1a, 1b**, and **1c** are shown in Figure XI-3 and their experimental λ_{max} are reported in Table XI-3 that also contains TD-DFT calculated transitions. All these complexes present ligand based π-π* transitions below 300 nm and above 300 nm bands that can be assigned to a series of metal-to-ligand-charge transfer transitions (MLCT), d_{π}-π^*(Ru-*bpea*) and d_{π}-π^*(Ru-*dppe*) *vide infra*.

The presence of a neutral diphosphine ligand in complexes **1a, 1b**, and **1c** leads to a positively charged molecule that is traduced in a shift of the $d_{\pi} - \pi^*$(Ru-*bpea*) MLCT bands to higher energies with respect to the neutral complexes. Similar results have been observed for other ruthenium complexes with terpyridine ligands.[29]

To get insight into the nature of the orbitals involved in the transitions that form these MLCT bands time dependent DFT calculations were performed for the isomers of complex **4**.

Although the *bpea* ligand presents a meridional fashion for isomer **1c**, and a facial coordination for the other two ones, the orbitals of all the isomers of complex **1** are very

similar. The lowest unoccupied molecular orbitals (LUMO) present a strong p_z component of the carbon atoms of the *bpea* aromatic rings and a slight contribution d_{z^2} of the metal only for *fac* isomers. The highest occupied molecular orbitals (HOMO) have a high component of d_{yz} of the metal, in addition with an antibonding contribution p_z of the chloro ligand. In spite of the similarity of the frontier MOs depicted in Figure XI-4 it is observed that the LUMO orbitals for the facial ruthenium complexes are about 0.1 eV more stabilized than that of the meridional complexes.

On the other hand, the Ru-Cl antibonding character present in all the three HOMO orbitals is minor for the meridional ruthenium isomer due to the elongation of the Ru-Cl bond distance from 2.418 Å for isomer **1a** and 2.425 Å for isomer **1b** to 2.473 Å for isomer **1c**. Therefore the HOMO of **1c** is slightly more stable than the *fac*-**1** HOMO orbitals. The HOMO-LUMO gap for isomer **1c** is 0.225 eV larger with respect to that of isomer **1a**. The energies of the HOMO and LUMO orbitals for the **1a**, **1b**, and **1c** species are given in Table XI-2, together with the energies of other orbitals next to the frontier molecular orbitals. The HOMO-1 orbitals present the same lobules as the HOMO, but reoriented 90º, in the plane *xy*. For the same reason as before, the HOMO-1 of **1c** is more stable than those of **1a** and **1c**. HOMO-2 orbital presents d_{xz} contribution. Therefore, HOMO, HOMO-1, and HOMO-2 orbitals comprise the d_{yz}, d_{xy}, and d_{xz} components, respectively. These orbitals are depicted in Figure XI-4.

Orbital	**1a**	**1b**	**1c**
L+3	-3.262	-3.369	-3.363
L+2	-3.667	-3.692	-3.414
L+1	-3.813	-3.900	-3.669
L	-4.106	-4.150	-4.072
H	-7.756	-7.789	-7.947
H-1	-7.876	-7.932	-8.118
H-2	-8.326	-8.534	-8.446
H-3	-8.797	-8.925	-8.870

Table XI-2. Energy (in eV) of the frontier molecular orbitals and other orbitals present in the transitions of the less energetic bands of the UV-Vis spectra.

y x z	**1a**	**1b**	**1c**
L+3	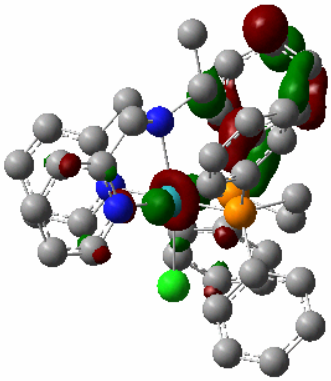	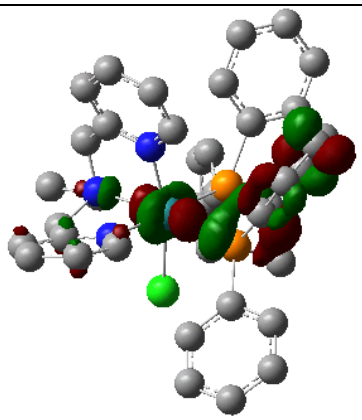	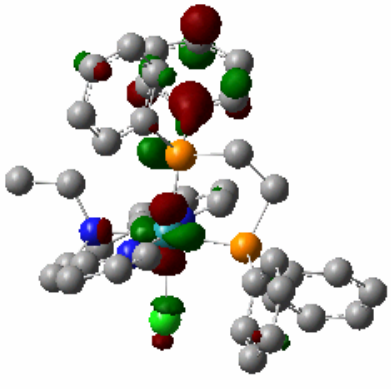
L+2	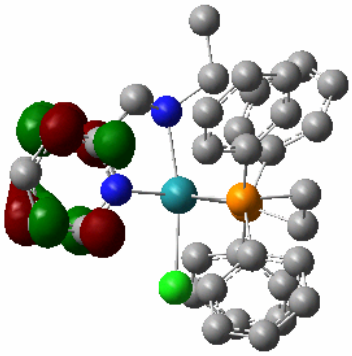	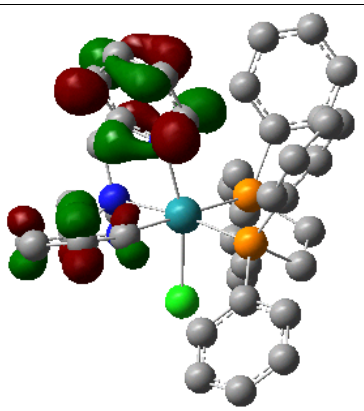	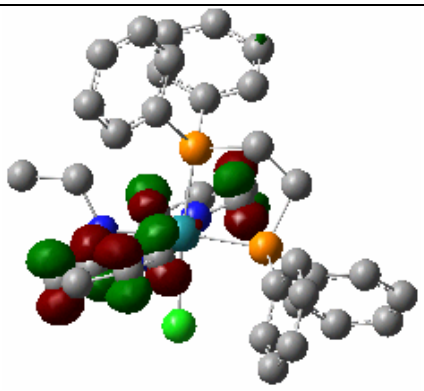
L+1	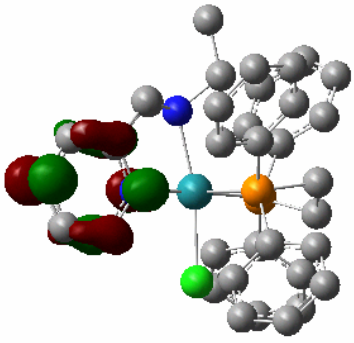	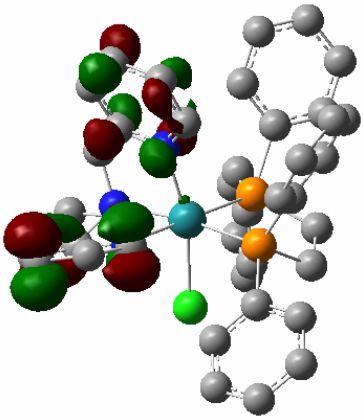	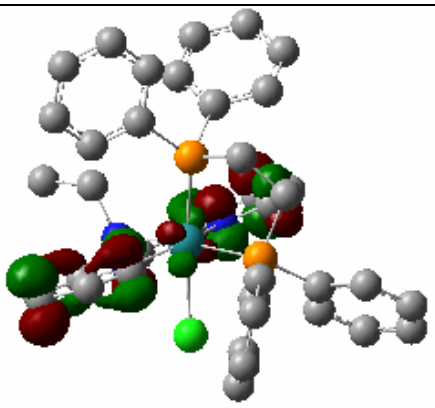

L	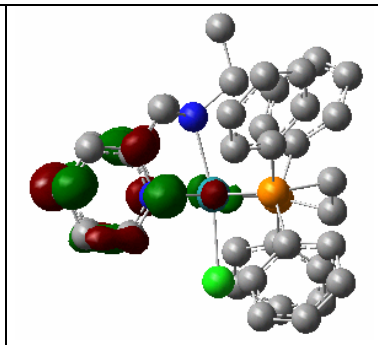	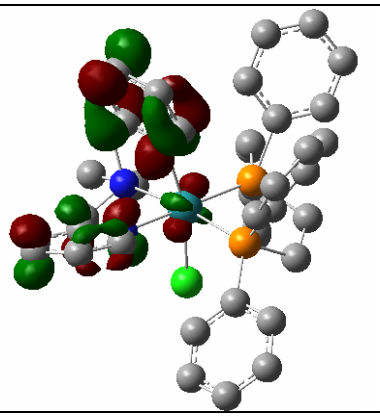	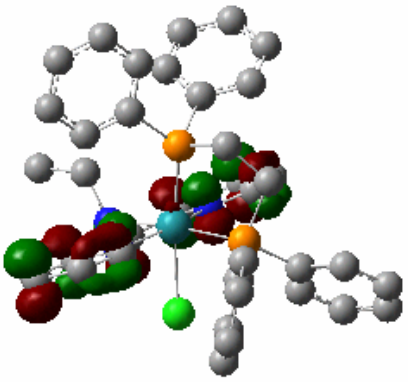
H	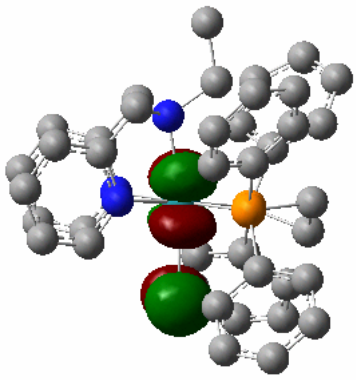	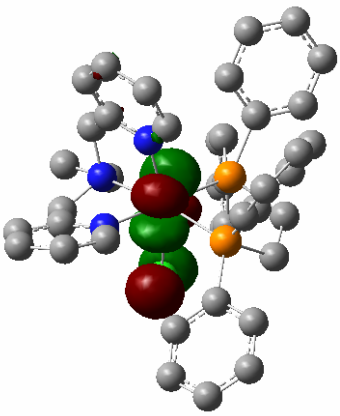	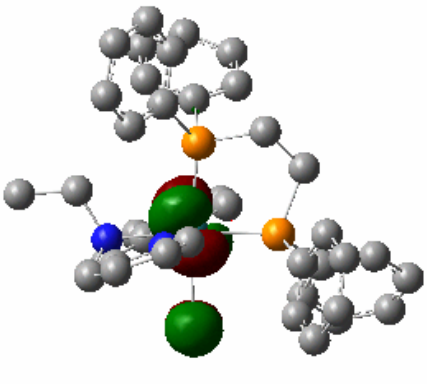
H-1	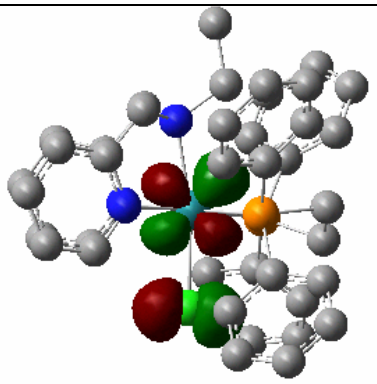	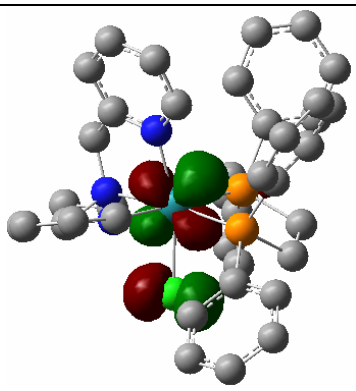	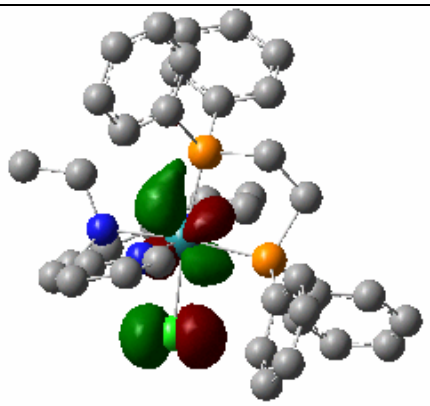
H-2	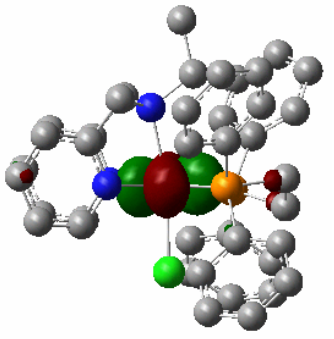	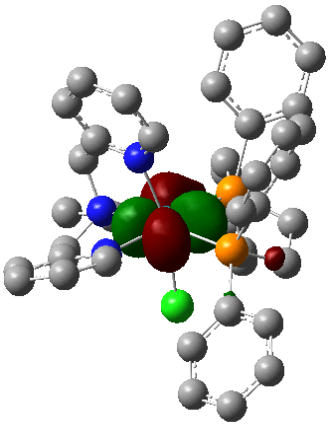	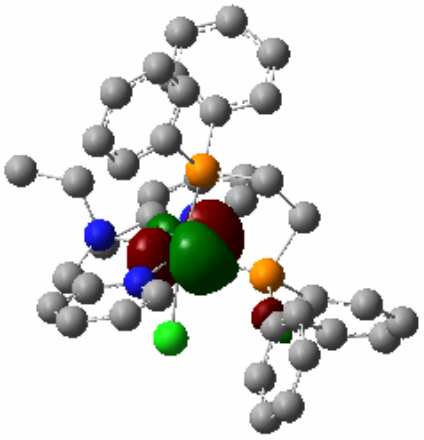

Figure XI-4. Main orbitals involved in the MLCT for isomers **1a-c** (isosurface values are -0.07 and 0.07 a.u.).

Complex	Experimental	Theoretical
1a	267	275
	303	320
	334	345
1b	276	280
	338	334
	343	360
	392	405
1c	275	278
	335	345-358
	371	375
	396	403

Table XI-3. Experimental and theoretical UV-Vis values (in nm) of the MLCT transitions for isomers **1a**, **1b**, and **1c**.

Table XI-3 presents the values of the main less energetic bands of the UV-Vis spectra for isomers **1a-c**. The HOMO-LUMO transition for isomers **1a** and **1b** has no significant intensity. The less energetic bands in isomers **1a** and **1b** involve transitions that present as starting orbitals the HOMO-1 and HOMO-2 orbitals. Thus, for isomer **1a,** the band placed at 345 nm (exp. 334 nm) is mainly the result of a transition that starts at the HOMO-2 orbital and finishes at the LUMO. The gap of this transition, starting at the HOMO-2 orbital, is 0.345 eV larger than the gap of the first transition for isomer **1c** because, for this complex, this transition starts at the HOMO orbital. Thus, the difference between the lowest energetic transition in **1a** and **1c** is not due to a significantly different HOMO-LUMO gap (this difference being 0.225 eV, but in favor of isomer **1c**) but to a different starting orbital for this transition in **1a** with respect to **1c**. The band experimentally placed at 303 nm is computationally found at 320 nm and it is mainly based on the transition from the HOMO-2 orbital to the LUMO+1 orbital, and also the LUMO+2, LUMO+3, and LUMO+4 orbitals. These latter orbitals are mainly composed by p_z orbitals of the carbon atoms corresponding to the phenyl rings of the

bpea and *dppe* ligands. Finally, the less stable band at 275 nm (exp. 265 nm) is related to an ensemble of small contributions of starting and arrival orbitals.

Isomer **1b** presents a band at 405 nm (exp. 392 nm) corresponding to a transition from the HOMO and the HOMO-1 to the LUMO and LUMO+1 orbitals, and furthermore other unoccupied orbitals with contributions of *d* orbitals of the metal and p_z orbitals of the phenyl units of the phosphine ligand and of the aromatic rings of *bpea*. Thus, this band at 405 nm has MLCT nature. At 360 nm (exp. 343 nm) there is a band that goes from the HOMO-2 to the LUMO orbitals and an ensemble of other unoccupied orbitals. The band at 334 nm (exp. 338 nm) is related to the transition that is mainly based on the HOMO-2 as starting orbital and the LUMO+3 as the arrival orbital. The experimental band placed at 276 nm is computationally found at 280 nm.

The first two bands that appear at the less energetic region for **1c** are mainly due to the HOMO to LUMO transition. These bands appear according to our DFT calculations at 375 and 403 nm (exp. 371 and 396 nm, respectively). The arrival orbital of these bands for isomer **1c**, placed at 375 and 403 nm, is mainly the LUMO, but there is also a minor contribution of the LUMO+3 orbital. This latter orbital is composed by the d_{z^2} of the metal and especially p_z of the carbon atoms of a phenyl ring connected to the P1 atom. Another two bands, higher in energy, but much less intense are found at 358 and 345 nm (exp. 335 nm). The first one has as the main starting orbital the HOMO-2 orbital and as the arrival orbitals the LUMO and especially the LUMO+3. The second one, placed at 345 nm, goes from the HOMO and HOMO-1 orbitals to the LUMO+1 orbital. These two bands cannot be well differentiated experimentally despite their relatively high intensity because they are placed near to the band situated at 375 nm, which is very intense with respect to these other two bands. By decombulating the experimental data for this region it would be possible to assign the values of these two bands for the band assigned experimentally to 335 nm. Nevertheless the resulting values would not be accurate enough because it is really a shoulder. The band experimentally placed at 275 nm is computationally found at 278 nm, and it goes from the HOMO orbital to a mixture of orbitals, that have p_z component of the atoms of the ligands, and to a lesser extent d_{z^2} and $d_{x^2-y^2}$ orbitals of the metal.

Conclusion

To summarize, these bands placed in the UV-Vis spectra between 275 and 425 nm are mainly MLCT type of bands because the starting orbital has mainly metallic character, whereas the arrival orbitals present high proportion of the p_z orbitals of the $C_{aromatic}$ atoms of the ligands.

References

1. a) R. Ballardini, V. Balzani, A. Credi, M. T. Gandolfi, M. Venturi, *Int. J. Photoenergy* **2004**, *6*, 1-10. b) E. Baranoff, J. P. Collin, J. Furusho, Y. Furusho, A. C. Laemmel, J. P. Sauvage, *Inorg. Chem.* **2002**, *41*, 1215-1222. c) S. C. Weatherly, I. V. Yang, H. H. Thorp, *J. Am. Chem. Soc.* **2001**, *123*, 1236-1237. d) S. O. Kelly, J. K. Barton, *Science* **1999**, *238*, 375-381. e) G. B. Schuster, *Acc. Chem. Res.* **2000**, *33*, 253-260.
2. a) S. I. Murahashi, H. Takaya, T. Naota, *Pure Appl. Chem.* **2002**, *74*, 19-24. b) T. Naota, H. Takaya, S. I. Murahashi, *Chem. Rev.* **1998**, *98*, 2599-2660. c) D. P. Riley, J. D. Oliver, *Inorg. Chem*. **1986**, *25*, 1825-1830. d) M. Rodríguez, I. Romero, A. Llobet, A. Deronzier, M. Biner, T. Parella, H. Stoeckli-Evans, *Inorg. Chem.* **2001**, *40*, 4150-4156. e) C. W. Chronister, R. A. Binstead, J. Ni, T. J. Meyer, *Inorg. Chem.* **1997**, *36*, 3814-3815. f) U. J. Jauregui-Haza, M. Dessoudeix, P. Kalck, A. M. Wilhelm, H. Delmas, *Catal. Today*. **2001**, *66*, 297-302.
3. K. R. Seddon, E. A. Seddon, *The Chemistry of Ruthenium*. Elsevier, New York, 1984.
4. a) N. W. Alcock, I. D. Burns, K. S. Claire, A. F. Hill, *Inorg. Chem.* **1992**, *31*, 2906. b) B. Buriez, I. D. Burns, A. F. Hill, A. J. P. White, D. J. Williams, J. D. E. T. Wilton-Ely, *Organometallics* **1999**, *18*, 1504-1516. c) K. N. Jayaprakash, T. B. Gunnoe, P. D. Boyle, *Inorg. Chem.* **2001**, *40*, 6481-6486.
5. L. D. Field, B. A. Messerle, L. Soler, I. E. Buys, T. W. Hambley, *J. Chem. Soc., Dalton Trans.* **2001**, 1959-1965.
6. a) Y. Motoyama, O. Kurihara, K. Murata, K. Aoki, H. Nishiyama, *Organometallics* **2000**, *19*, 1025-1034. b) V. Cadierno, M. P. Gamasa, J. Gimeno, L. Iglesias, *Inorg. Chem.* **1999**, *38*, 2874-2879.
7. K. P. Wainwright, *Coord. Chem. Rev.* **1997**, *16*, 35-90.

8. a) K. Abdur-Rashid, S. E. Clapham, A. Hadzovic, J. N. Harvey, A. J. Lough, R. H. Morris, *J. Am. Chem. Soc.* **2002**, *124*, 15104-15118. b) C. A. Sandoval, T. Ohkuma, K. Muñiz, R. Noyori, *J. Am. Chem. Soc.* **2003**, *125*, 13490-13503.
9. a) P. Braunstein, F. Naud, A. Pfaltz, S. J. Rettig, *Organometallics* **2000**, *19*, 2676-2683. b) A. A. Danopoulos, S. Winston, W. B. Motherwell, *Chem. Comm.*, **2002**, 1376-1377. c) C. Sens, M. Rodríguez, I. Romero, A. Llobet, T. Parella, B. P. Sullivan, J. Benet-Buchholz, *Inorg. Chem.* **2003,** *42*, 2040-2048.
10. a) M. E. Marmion, K. J. Takeuchi, *J. Am. Chem. Soc.* **1998**, *110*, 1472-1480. b) M. H. V. Huynh, L. M. Witham, J. M. Lasker, M. Wetzler, B. Mort, D. L. Jameson, P. S. White, K. J. Takeuchi, *J. Am. Chem. Soc.* **2003**, *125*, 308-309.
11. Y. Fukumoto, T. Dohi, H. Masaoka, N. Chatani, S. Murai, *Organometallics* **2002**, *21*, 3845-3847.
12. I. Romero, M. Rodríguez, A. Llobet, M. N. Collomb-Dunand-Sauthier, A. Deronzier, T. Parella, H. Stoeckli-Evans, *J. Chem. Soc., Dalton Trans.* **2000**, 1689-1694.
13. J. R. Polam, L. C. Porter, *J. Coord. Chem.* **1993**, *29*, 109-119.
14. M. Akita, Y. Takahashi, S. Hikichi, Y. Moro-oka, *Inorg. Chem.* **2001,** *40*, 169-172.
15. S. Pal, M. M. Olmstead, W. H. Armstrong, *Inorg. Che*m. **1995**, *3*4, 4708-4715.
16. a) B. K. Das, A. R. Chakravarty, *Inorg. Che*m. **1990**, *2*9, 2078-2083. b) B. K. Das, A. R. Chakravarty, *Inorg. Che*m. **1991**, *3*0, 4978-4986. c) C. Sudha, S. K. Mandal, A. R. Chakravarty, *Inorg. Che*m. **1998**, *3*7, 270-278.
17. A. D. Becke, *J. Chem. Phys*. **1993**, *98*, 5648-5652.
18. J. P. Perdew, Y. Wang, Y.; *Phys. Rev. B* **1992**, *45*, 13244-13249.
19. Gaussian 03, M. J. Frisch, G. W. Trucks, H. B. Schlegel, G. E. Scuseria, M. A. Robb, J. R. Cheeseman, J. A. Montgomery, Jr., T. Vreven, K. N. Kudin, J. C. Burant, J. M. Millam, S. S. Iyengar, J. Tomasi, V. Barone, B. Mennucci, M. Cossi, G. Scalmani, N. Rega, G. A. Petersson, H. Nakatsuji, M. Hada, M. Ehara, K. Toyota, R. Fukuda, J. Hasegawa, M. Ishida, T. Nakajima, Y. Honda, O. Kitao, H. Nakai, M. Klene, X. Li, J. E. Knox, H. P. Hratchian, J. B. Cross, C. Adamo, J. Jaramillo, R. Gomperts, R. E. Stratmann, O. Yazyev, A. J. Austin, R. Cammi, C. Pomelli, J. W. Ochterski, P. Y. Ayala, K. Morokuma, G. A. Voth, P. Salvador, J. J. Dannenberg, V. G. Zakrzewski, S. Dapprich, A. D. Daniels, M. C. Strain, Ö. Farkas, D. K. Malick, A. D. Rabuck, K. Raghavachari, J. B.

Foresman, J. V. Ortiz, Q. Cui, A. G. Baboul, S. Clifford, J. Cioslowski, B. B. Stefanov, G. Liu, A. Liashenko, P. Piskorz, I. Komaromi, R. L. Martin, D. J. Fox, T. Keith, M. A. Al-Laham, C. Y. Peng, A. Nanayakkara, M. Challacombe, P. M. W. Gill, B. Johnson, W. Chen, M. W. Wong, C. Gonzalez, J. A. Pople, Gaussian, Inc., Pittsburgh PA, 2003.

20. D. Andrae, U. Haussermann, M. Dolg, H. Stoll, H. Preuss, *Theor. Chim. Acta* **1990**, *77*, 123-141.
21. A. Bergner, M. Dolg, W. Kuchle, H. Stoll, H. Preuss, *Mol. Phys*. **1993**, *80*, 1431-1444.
22. W. J. Hehre, R. Ditchfield, J. A. Pople, *J. Chem. Phys*. **1972**, *56*, 2257-2261.
23. A. E. Reed, L. A. Curtiss, F. Weinhold, *Chem. Rev*. **1988**, *88*, 899-926.
24. a) M. E. Casida, C. Jamorski, K. C. Casida, D. R. Salahub, *J. Chem. Phys.* **1998**, *108*, 4439-4449. b) R. E. Stratmann, G. E. Scuseria, M. J. Frisch, *J. Chem. Phys.* **1998**, *109*, 8218-8224.
25. J. Kong, C. A. White, A. I. Krylov, C. D. Sherrill, R. D. Adamson, T. R. Furlani, M. S. Lee, A. M. Lee, S. R. Gwaltney, T. R. Adams, C. Ochsenfeld, A. T. B. Gilbert, G. S. Kedziora, V. A. Rassolov, D. R. Maurice, N. Nair, Y. Shao, N. A. Besley, P. E. Maslen, J. P. Dombroski, H. Daschel, W. Zhang, P. P. Korambath, J. Baker, E. F. C. Byrd, T. Van Voorhis, M. Oumi, S. Hirata, C. -P. Hsu, N. Ishikawa, J. Florian, A. Warshel, B. G. Johnson, P. M. W. Gill, M. Head-Gordon, J. A. Pople, *J. Comp. Chem*. **2000**, *21*, 1532-1548.
26. .I. Romero, M. Rodríguez, A. Llobet, M.-N. Collomb-Dunand-Sauthier, A. Deronzier, T. Parella, H. Stoeckli-Evans, *J. Chem. Soc., Dalton Trans.* **2000**, 1689-1694. b) J. R. Polam, L. C. Porter, *J. Coord. Chem.* **1993**, *29*, 109-119. c) M. Akita, Y. Takahashi, S. Hikichi, Y. Moro-oka, *Inorg. Chem.* **2001,** *40*, 169-172.
27. I. Romero, L. Dubois, M.-N. Collomb, A. Deronzier, J. M. Latour, J. Pécaut, *Inorg. Chem.* **2002**, *41*, 1795-1806. b) I. Romero, M.-N. Collomb, A. Deronzier, A. Llobet, E. Perret, J. Pécaut, L. Le Pape, J. M. Latour. *Eur.J. Inorg. Chem.* **2001**, 64-72. c) C. E. Dubé, D. W. Wright, S. Pal, P. J. Bonitatebus, W. H. Armstrong, *J. Am. Chem. Soc.* **1998**, *120*, 3704-3716. d) C. E. Dubé, S. Mukhopadhyay, P. J. Bonitatebus, R. J. Staples, W. H. Armstrong, *Inorg. Chem.* **2005**, *44*, 5161-5175.

28. a) C. Mantel, A. K. Hassan, J. Pécaut, A. Deronzier, M.-N. Collomb, C. Duboc-Toia, *J. Am. Chem. Soc.* **2002**, *125*, 12337-12344. b) S. Pal, M. M. Olmstead, W. H. Armstrong, *Inorg. Chem.* **1995**, *34*, 4708-4715.
29. S. B. Billings, M. T. Mock, K. Wiacek, M. B. Turner, W. S. Kassel, K. J. Takeuchi, A. L. Rheingold, W. J. Boyko, C. A. Bessel, *Inorg. Chim. Acta* **2003**, *355*, 103-115.

Chapter XII: *Ruthenium(II) Isomeric Complexes Containing Dimethyl Sulfoxide, Chloro, and the N-tridentate "bpea" Ligands*

Ruthenium(II) Isomeric Complexes Containing Dimethyl Sulfoxide, Chloro, and the N-tridentate "*bpea*" Ligands

Abstract

Two new isomers *trans-mer*[$Ru^{II}Cl_2$(*bpea*)(*dmso*)], **2a**, and *cis-fac* [$Ru^{II}Cl_2$(*bpea*)(*dmso*)], **2b**, (*bpea* = ligand N,N-bis(2-pyridylmethyl)ethylamine), previously synthesized by Llobet *et al.*, have been studied by DFT calculations. Both isomers display a Ru metal center possessing a distorted octahedral type of coordination where the *bpea* ligand is coordinated in a meridional fashion in **2a** and in a facial fashion in **2b**. The isomer **2a** is the kinetically favored and **2b** is the thermodynamically favored. DFT calculations for these isomers have been performed in order to understand the stability and formation of these isomers and predict the mechanism involved in their interconversion.

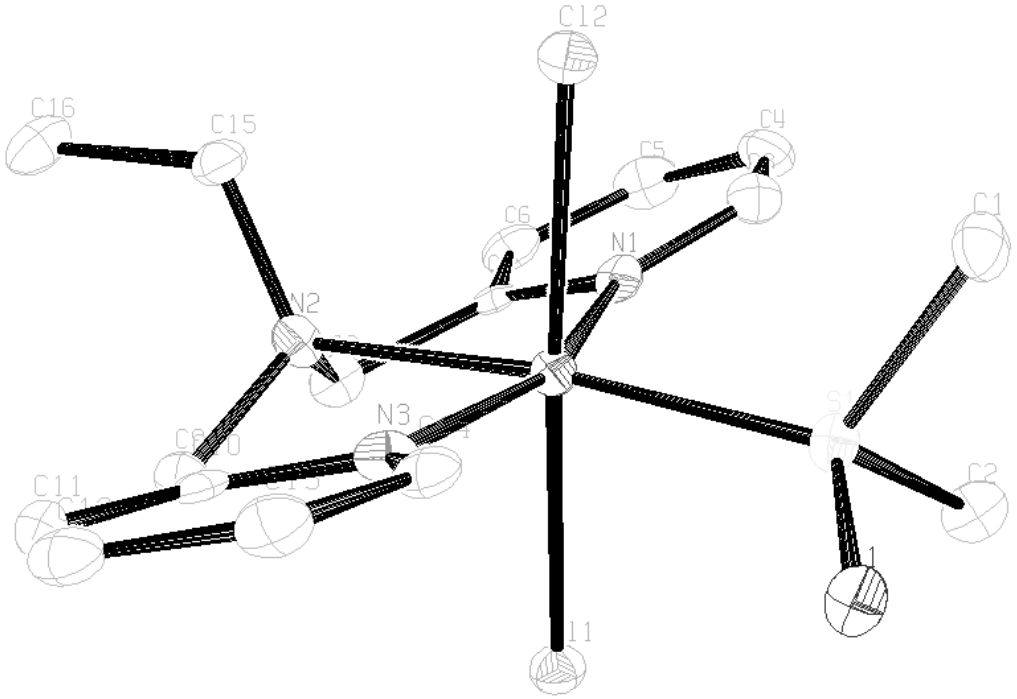

Introduction

Ruthenium complexes have been extensively investigated because of their interesting properties and usefulness in many fields of science, particularly in catalysis including oxidative and reductive reactions,[1] molecular switching devices,[2] including wires and switches,[3] and in biochemistry and clinical diagnosis.[4]

Furthermore, Ruthenium-*dmso* complexes are gathering a great deal of attention because of their applications as antitumoral drugs and the mechanism and scope of their applications is being studied at present.[5] Also, these complexes are widely studied because their present catalytic activity.[6] On the other hand, ruthenium complexes containing N-donors ligands have been used successfully in catalytic hydrogenation,[7] hydrogen transfer,[8] oxidations,[9] and conversion of terminal alkynes to nitriles.[10]

In the last years, the group of Pr. A. Llobet has investigated in detail the chemistry of different chloro and aquo complexes of ruthenium (II), containing polypyridyl ligands, which have been prepared in a classical way starting from $RuCl_3 \cdot nH_2O$ and $[Ru^{III}Cl_3(L)]$, (L = N-tridentate ligand) precursors.[1d,11] For example, the reaction of $[Ru^{III}Cl_3(bpea)]$, (*bpea* = N,N-bis(2-pyridylmethyl)ethylamine) with the diphosphine *dppe* ligand (1,2-Bis(diphenylphosphino)ethane), leads to $[Ru^{II}Cl(bpea)(dppe)]^+$ complex in moderate yield due to the formation of different isomers and other secondary products.

Llobet et al.[11e] found that a new synthetic strategy for the synthesis of this kind of Ru(II) complexes could be developed using new complexes of Ru(II) as starting materials such $[Ru^{II}Cl_2(bpea)(dmso)]$. A few Ru(II) mono-*terpy* species have been previously described using $[Ru^{II}Cl_2(dmso)(terpy)]$ as precursor.[12] They investigated in detail the reaction of $[Ru^{II}Cl_2(dmso)_4]$ with the *bpea* ligand to obtain new Ru-*dmso* isomer complexes containing the tridentate polypyridylic ligand N,N-bis(2-pyridylmethyl)ethylamine (*bpea*), *trans-mer*, **2a**, and *cis-fac*, **2b**, $[Ru^{II}Cl_2(bpea)(dmso)]$, as well as their catalytic activity in hydrogen transfer reactions.

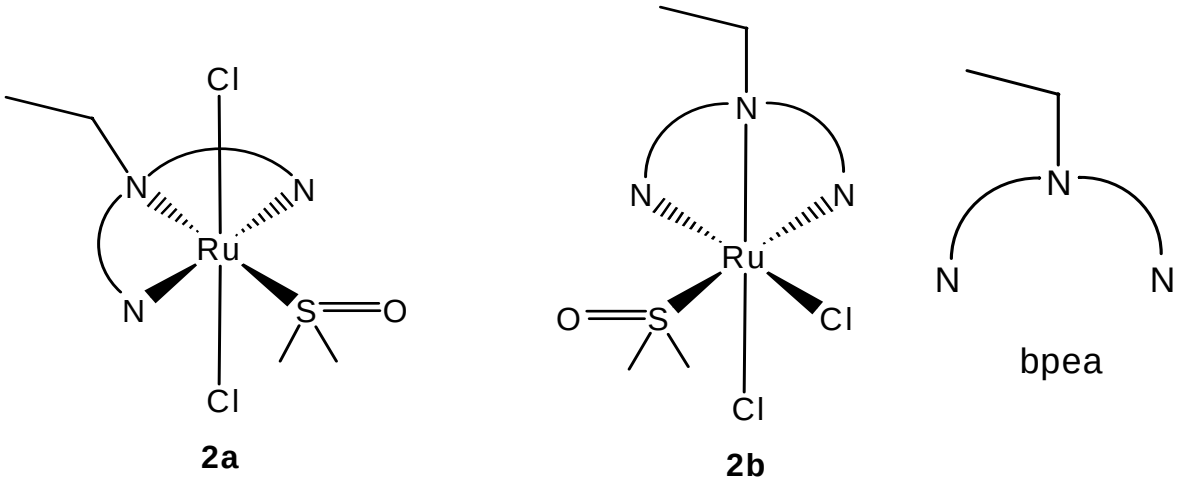

Scheme XII-1. Schematic view of isomers **2a** and **2b**.

The fact that experimentally the symmetric isomer, **2a**, evolves to the unsymmetrical one, **2b**, is indicative that **2a** is the kinetically favored isomer and **2b** is the thermodynamically favored isomer. Isomer **2b** is thermodynamically stable in solution, even when we expose different solutions to sunlight; whereas, isomer **2a** is not stable and a geometrical isomerization process to **2b** takes place. Probably, the hydrogen bond in **2b** (vide infra) produces a stabilization of the *dmso* complex. Ru-S→Ru-O linkage isomerization is not present as in other *dmso*-Ru(II) complexes.[13,14] A similar behavior is observed in similar terpyridine complexes.[12]

Crystallographic data and selected bond distances and angles for complexes **2a** and **2b** are presented by ORTEP views together with their labelling schemes in Figure XII-1.

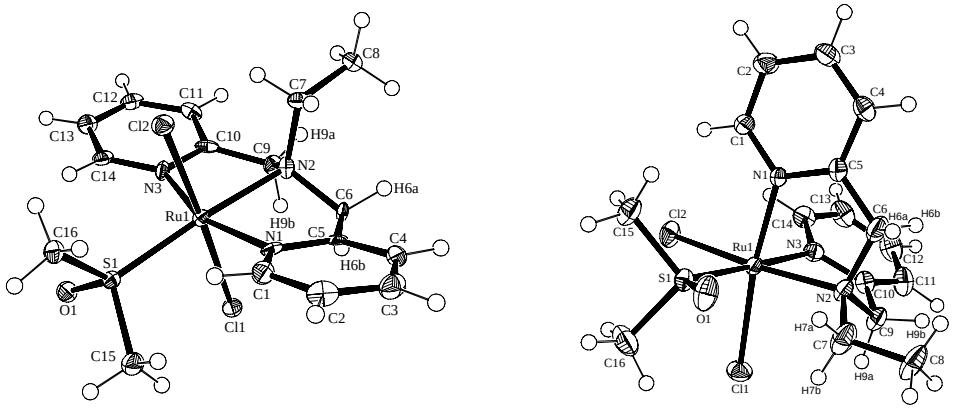

Figure XII-1. X-ray structures (Ortep-plots with ellipsoids at 50% probability level) and labelling scheme for **2a** and **2b.**

Complex **2a** crystallizes in the monoclinic space group P21/c and shows a molecular structure where Ru presents a distorted octahedral environment and the *bpea* ligand adopts the uncommon meridional mode of coordination around the Ru(II). This is the first example of ruthenium complexes where the ligand *bpea* adopts a meridional coordination. This coordination mode has only been observed in some monomer[15] and dimer[16] manganese complexes. The Cl^- ligands are coordinated *trans* and the sixth coordination is completed with the *dmso* ligand that is coordinated to the metal center via the sulfur atom. There is no mirror plane that bisects the molecule due to the spatial disposition of the *dmso* ligand that occupies two positions on each side of the basal plane of the octahedron.

The N-Ru bond distances are comparable to those of complexes where the *bpea* ligand coordinates facially,[1c,11d,11e] the Ru-S (2.2236(13) Å) and Ru-Cl bond lengths (2.4117(13), 2.4378(13) Å) are compared to one similar Ru(II) complex with the terpy ligand, *cis*-[$RuCl_2$(terpy)(*dmso*)].[12] The spatially constrained nature of the tridentate meridional *bpea* ligand produces geometrical distortions manifested in the N(1)-Ru-N(3) angle equal to 160.75(16)º compared to 180º, the theoretical value for a $Ru(NH_3)_6$ complex. The largest bond angles distortions are observed in the basal plane where the *bpea* ligand is contained, N(3)-Ru-N(2), 80.91(16)º, N(2)-Ru-N(1), 80.02(16)º, N(3)-Ru-S(1), 97.23(12)º, and N(1)-Ru-S(1), 103.01(12)º. A weak hydrogen bond is observed between the oxygen atom of the *dmso* ligand and one hydrogen atom of the pyridine ring of the *bpea* ligand, H(14)-O(1), 2.534 Å.

Complex **2b** shows an asymmetric molecular structure where the Ru metal atom presents a distorted octahedral environment. The *bpea* ligand coordinates facially through its nitrogen atoms, the *dmso* ligand is coordinated to the metal center via the sulfur atom and it is located *trans* to one of the $N_{aromatic}$ atoms of the *bpea* ligand, and consequently the two chloro ligands are situated *trans* with respect to the $N_{aliphatic}$ atom and the other $N_{aromatic}$ atom of *bpea* ligand, respectively.

Ru-S (2.2285(7) Å) bond length is slightly shorter than other related complexes previously described in the literature.[17,18] The bonding angles S(1)-Ru(1)-N(1), 93.83(7)º and S(1)-Ru(1)-N(2), 101.95(7)º are bigger than those corresponding to an ideal octahedral geometry, this fact is due probably to the steric effects provoked by the

methyl groups of the *dmso* ligand. A similar effect is observed in the N(2)-Ru(1)-Cl(2), 169.82(7)º and Cl(1)-Ru(1)-N(1), 172.63(6)º angles, both shorter than 180º. This isomer displays a hydrogen bond between the oxygen atom of *dmso* ligand and one hydrogen atom of the *bpea* ligand, H(7a)-O(1), 2.315 Å. The higher stability of **2b** isomer with regard to **2a** could be due to this hydrogen bond.

The ^{1}H-NMR spectrum of isomer **2a** shows in the aromatic region the presence of only one kind of ring, corresponding to pyridyl rings of *bpea*, and in the aliphatic region only one signal corresponding to methyl groups of the bonded *dmso* ligand. This fact reveals the presence of one symmetric isomer; in solution complex **2a** possesses a plane of symmetry that contains the N-aliphatic of the *bpea* ligand, the Ru and the S atom.

In the unsymmetrical isomer all resonances become non-equivalent. The NOESY effect observed between H15 (3.05 ppm) and H1 (9.27 ppm) allows to identify the two methylenic groups of *dmso*. H16 (3.51 ppm) presents also a weak NOE with H7 (4.15 ppm). The rest of the resonances are easily identified through the COSY spectrum.

The electronic spectra of the complexes are shown in Figure XII-2. The complexes present ligand based π-π* transitions below 300 nm and above 300 nm bands that can be assigned to a series of MLCT, $d_{\pi-\pi^*}$(Ru-*bpea*).[1d] A bathochromic shift is observed for the *trans* complex as compared to the *cis* (λ_{max} = 419 nm, ε = 2767 and λ_{max} = 355 nm, ε = 2365, respectively). The same behavior is observed in terpyridine complexes.[12]

(a)

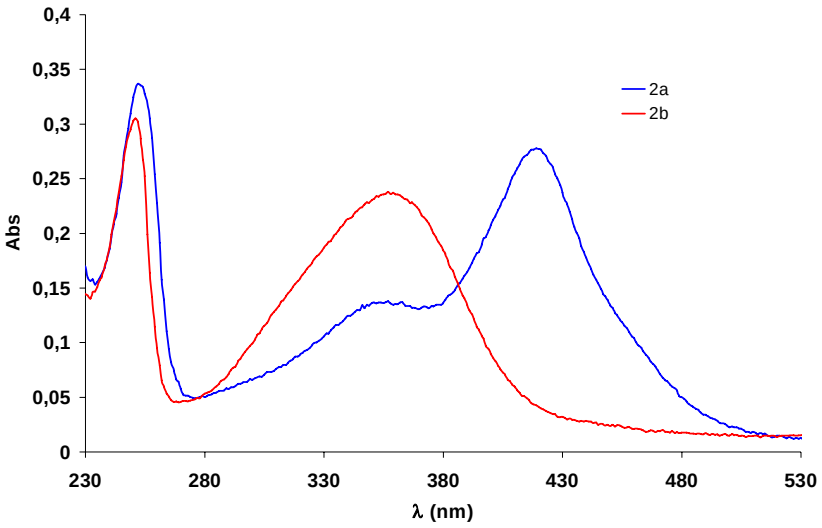

(b)

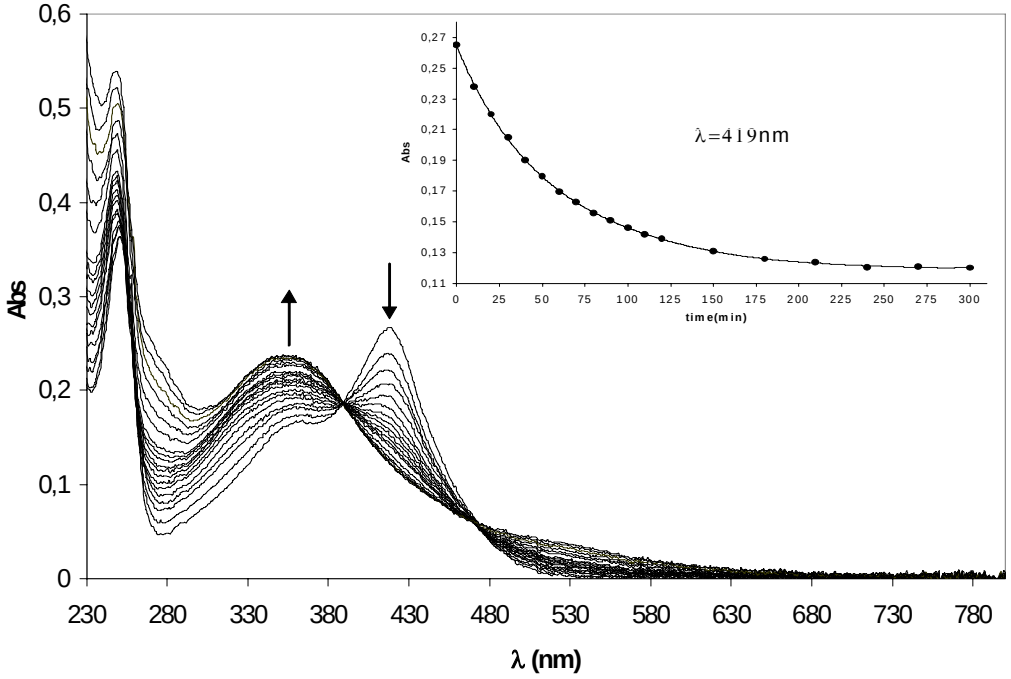

Figure XII-2. a) UV-Visible spectra for complexes **2a** and **2b** in EtOH solution. b) Spectral changes observed during the isomerization of **2a** to **2b** in EtOH solution at 75ºC. The inset shows plots of λ_{max}(419 nm) *vs.* time for the isomerization reaction of **2a** to **2b.**

In ethanol solution and under heating the symmetric isomer **2a** isomerizes to the unsymmetrical **2b**. Figure XII-2b illustrates the spectral changes during the process of isomerization at 75º C where continuous scans of the spectrum in the wavelength range 200-800 nm shown isosbestic points at λ = 388 and λ = 470nm. The rate of the reaction was measured by following the time-dependence of the decay of the absorbance at 419 nm. The kinetics over a range of temperatures, display a first order dependence with regard to the disappearance of the isomer **2a.** Rate constants in EtOH solution at various temperatures are given in Table XII-1, and the activation parameters were calculated using the Eyring plot, $\Delta H^{\neq}$ = 11.53 (± 0.08) kcal·mol^{-1} and $\Delta S^{\neq}$ = -41.86 (± 0.23) cal·K^{-1}·mol^{-1}.

Temp (K)	Solvent	K (min^{-1})	S.D.
348	EtOH	0.018	0.001
353	EtOH	0.023	0.001
363	EtOH	0.037	0.003
373	EtOH	0.059	0.002

Table XII-1. Reaction rates for isomerization reaction from **2a** to **2b** in ethanol (concentration of **2a**, 1.10^{-4}M).

Two possible mechanisms have been proposed for the **2a**->**2b** isomerization process, namely, the dissociative and the intramolecular mechanisms. The dissociative mechanism involves the loss of one ligand at the beginning of the isomerization process. In this chapter we analyze through DFT calculations which is the most feasible mechanism for the **2a**->**2b** isomerization.

Computational Details

Density functional theory (DFT) calculations have been carried out with the hybrid B3PW91 density functional,[19,20] as implemented in the Gaussian03 package.[21] The Ru atoms have been represented with the quasi relativistic effective core pseudo-potentials (RECP) of the Stuttgart group and the associated basis sets augmented with a polarization function (α = 1.235).[22,23] The remaining atoms (C, O, and H) have been represented with 6-31G(d,p) basis sets.[24] The B3PW91 geometry optimizations were performed without any symmetry constraints, and the nature of the extrema (local minima or transition states) was checked by analytical frequency calculations. The energies given throughout the paper are electronic energies *E* without any ZPE corrections (inclusion of the ZPE corrections does not significantly modify the results) or Gibbs free energy values *G* computed with Gaussian 03 at 298 K and *P* = 1 atm. The atomic charges have been calculated using the Natural Population Analysis (NPA) scheme of Weinhold and co-workers.[25]

The solvent effect was introduced by the conductor polarizable calculation model (CPCM).[26] The cavity is created via a series of overlapping spheres.

Results

The optimization of **2a** in the gas phase agrees with the experimental X-ray data. The standard deviation for the bond distances is 0.014 Å and for the angles is 0.8º,[27] thus providing confidence on the reliability of the chosen method to reproduce geometries of the studied complexes. For **2b**, we found only significant differences in the C-C-N and C-N-C angles of the *bpea* ligand. Nevertheless these differences are not important because they are probably due to the packing of the crystal. Figure XII-3 depicts both calculated isomers.

The computation of **2a** and **2b** gives as a result that **2a** is 4.7 kcal·mol^{-1} less stable than **2b** in gas phase and even more in solution, 7.5 kcal·mol^{-1}, using the PCM solvent simulator, taking ethanol as solvent. The only difference between both isomers is the either facial or meridional conformation of the *bpea* ligand. The Gibbs free energy values give an energy difference of 4.5 kcal·mol^{-1}, instead of 4.7 kcal·mol^{-1}, reinforcing the higher stability of isomer **2b**.

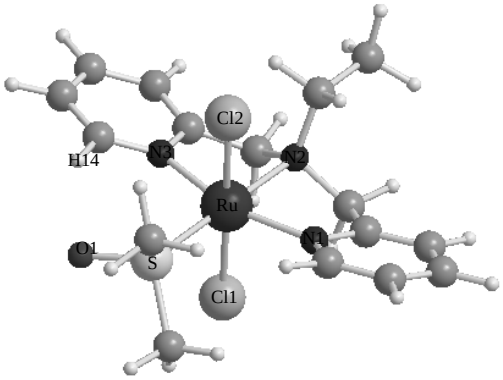

2a

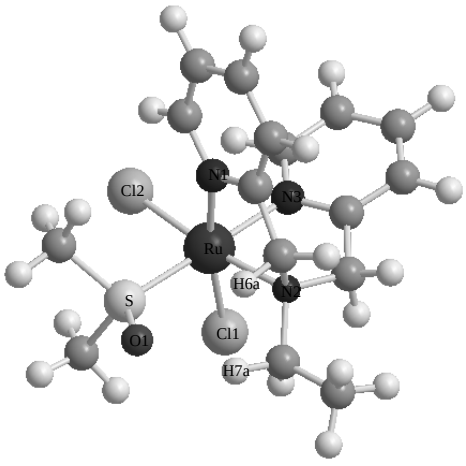

2b

Figure XII-3. B3PW91 optimized structures of isomers **2a** and **2b** (hydrogen atoms have been omitted for clarity).

2a is higher in energy than isomer **2b** by kcal·mol^{-1}. A possible reason for the larger stabilization of **2b** is the formation of H-bonds of the oxygen of the *dmso* group of **2b** and H6a and H7a atoms. One of these H-bonds has an O-H distance of 2.617 Å (O1-H6a), and the other one of 2.138 Å (O1-H7a). For **2a** the O1-H14 bond distance is 2.102 Å, but the O1 lone pairs are not oriented through H14. Furthermore, we would have to take into account the possible H-bonds between the chloro atoms and the hydrogens of the *dmso* fragment.

The optimization of the isolated *bpea* ligand gives as a result that the facial conformation is less stable in 5.7 kcal·mol^{-1} with respect to the meridional conformation; thus the free ligand shows the opposite behavior than that found in the ruthenium complex. However these results are not very reliable because the number of possible conformations of *bpea* are very large, nevertheless the optimizations starting from the X-ray data of both conformations give these results and mean that the facial *bpea* gains energetic stability as compared to the meridional when it complexes a metal, losing entropy. Complex **2b** presents a lower entropy value of about 0.5 cal·mol^{-1}with respect to complex **2a.** The study of the TS between both isolated conformations gives a TS situated only 1.2 kcal·mol^{-1} higher in energy with respect to the meridional *bpea* conformation, which means that the potential energy surface is very flat, and that any conformation can be adopted when the *bpea* ligand is free, and more interestingly, that the interconversion between them is not energetically expensive.

All possible isomers of **2a** and **2b** were studied to try to be sure that the X-ray structures were the most stable ones. In particular, we optimized two new isomers **2a'** and **2a''**, starting for **2a**, and a new **2b'** isomer related to **2b**. The energy diagram represented in Figure XII-4 shows clearly that **2a** and **2b** are most stable isomers among all possible isomers of **2a** and **2b** complexes.

Figure XII-4 confirms that no isomer becomes more stable than the ones corresponding to the X-ray data. Nevertheless due to the fact that the energetic differences are small these structures must not be discarded because they can be part of the interconversion mechanism, and taking into account the solvent effect the differences are close too.

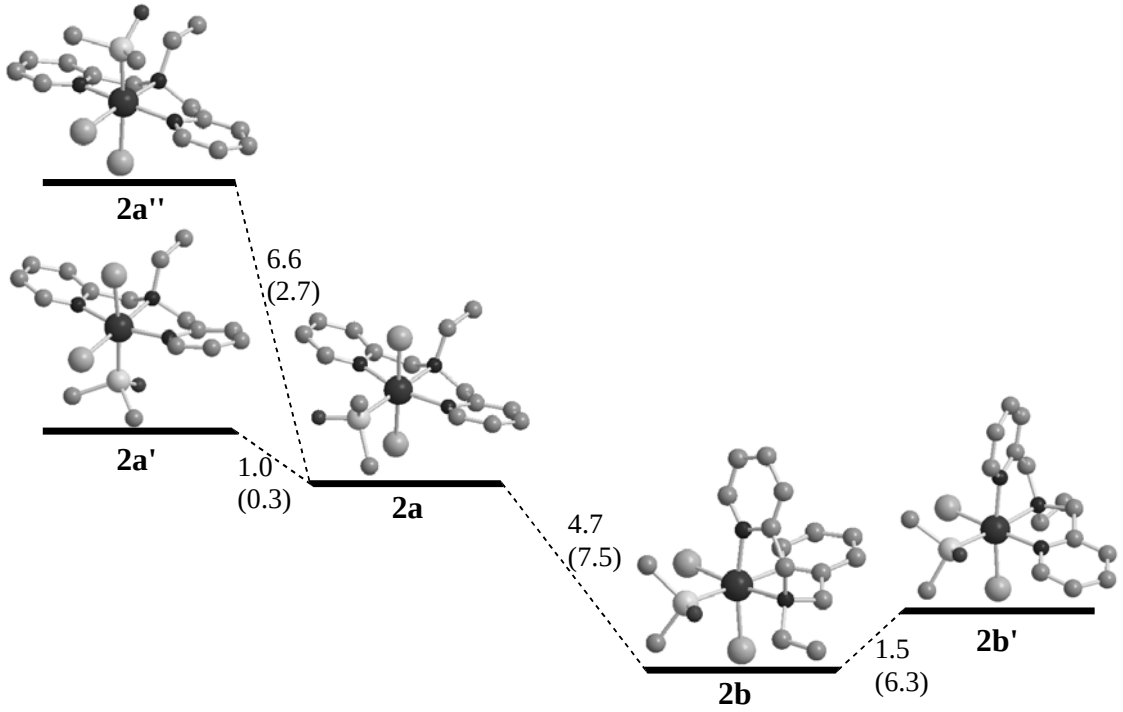

Figure XII-4. Isomers **2a** and **2b** (in parenthesis the energy values (in kcal·mol^{-1}) including solvent effects).

To try to see if the chelate ligand plays a key role, we have replaced the *bpea* ligand by three ammonia units, obtaining $\mathbf{2a_s}$ and $\mathbf{2b_s}$ isomers. The results indicate that now the most stable conformation is the coordination of the three N atoms in a meridional way. These two isomers, $\mathbf{2a_s}$ and $\mathbf{2b_s}$, present more isomers also as **2a** and **2b**, but only the corresponding $\mathbf{2a_s'}$ is different. The solvent effect leaves as a result the same energy difference between $\mathbf{2a_s}$ and $\mathbf{2b_s}$ isomers.

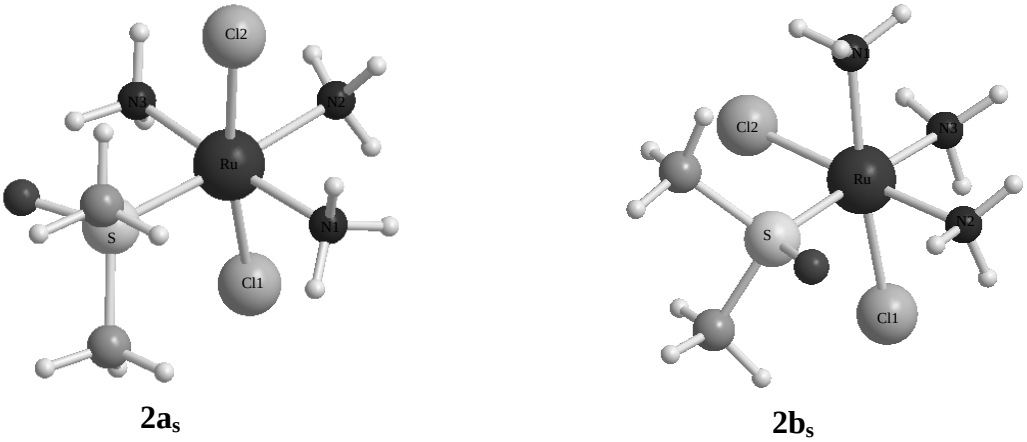

$\mathbf{2a_s}$ $\mathbf{2b_s}$

Figure XII-5. Isomers $\mathbf{2a_s}$ and $\mathbf{2b_s}$.

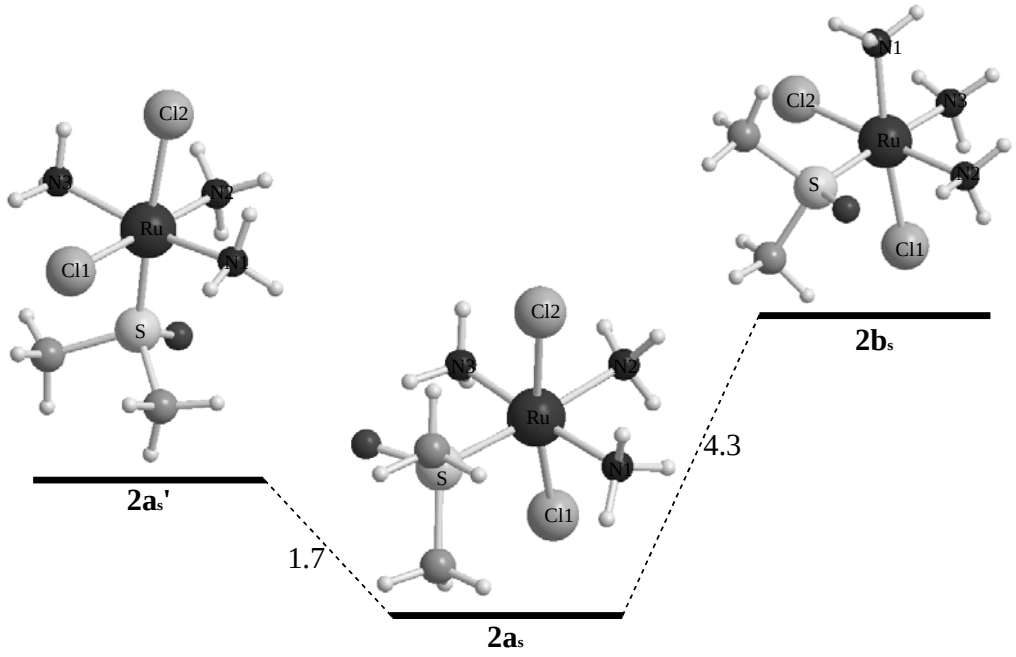

Figure XII-6. Energetic diagram of isomers $\mathbf{2a_s}$, $\mathbf{2b_s}$, and $\mathbf{2a_s'}$ (in kcal·mol^{-1}).

The interconversion mechanism between **2a** and **2b** can be intramolecular. Indeed, the experimental negative value of $\Delta S^{\neq}$ agrees with an intramolecular mechanism in the isomerization process.[17] This intramolecular mechanism has been studied by a linear transit in which the N3-Ru-N2-N1 dihedral angle changes from 180º to 90º. The energy profile presents a maximum at 140º with an upper bound to the energy barrier of 40.2 (38.7) kcal·mol^{-1}. The approximated transition state obtained in the linear transit, **2-TS**, is presented in Figure XII-7 (it has not been characterized by frequencies).

Figure XII-7. Different two views of **2-TS**.

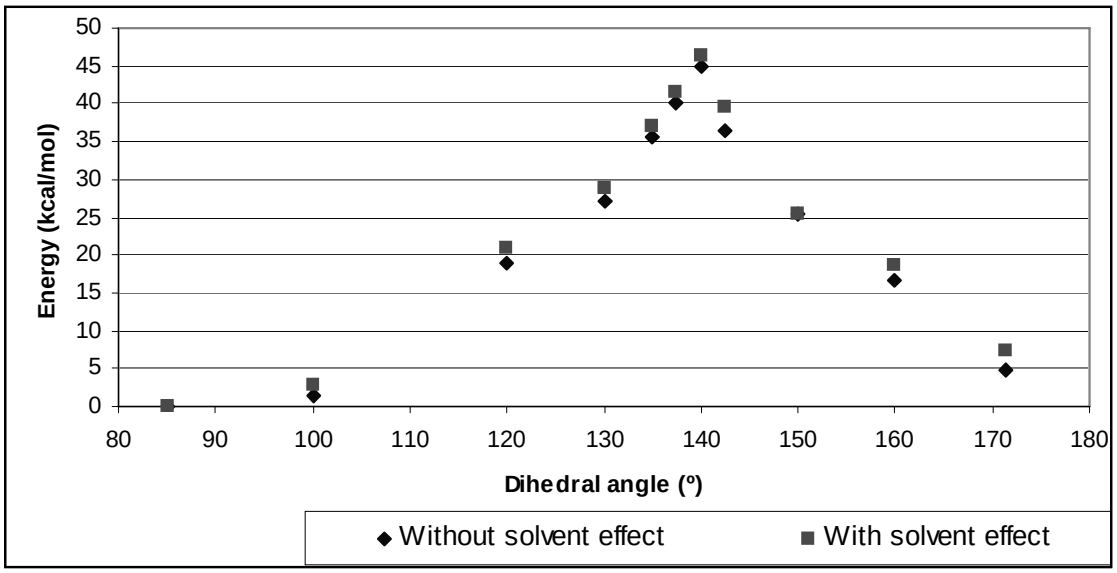

Figure XII-8. Change of the energy by changing the dihedral angle N3-Ru-N2-N1.

Figure XII-8 shows the change of the energy by changing the dihedral angle N3-Ru-N2-N1, taking the energy of the **2b** structure as the reference energy. The solvent effect nearly leaves the values unvariable, because of the fact that Ru atom is octahedrically coordinated not allowing the interaction of solvent molecules in the first coordination shell of the metal. Another reason is that the complex is formally neutral, thus the charge of ruthenium is compensated by the chloro anion charges.

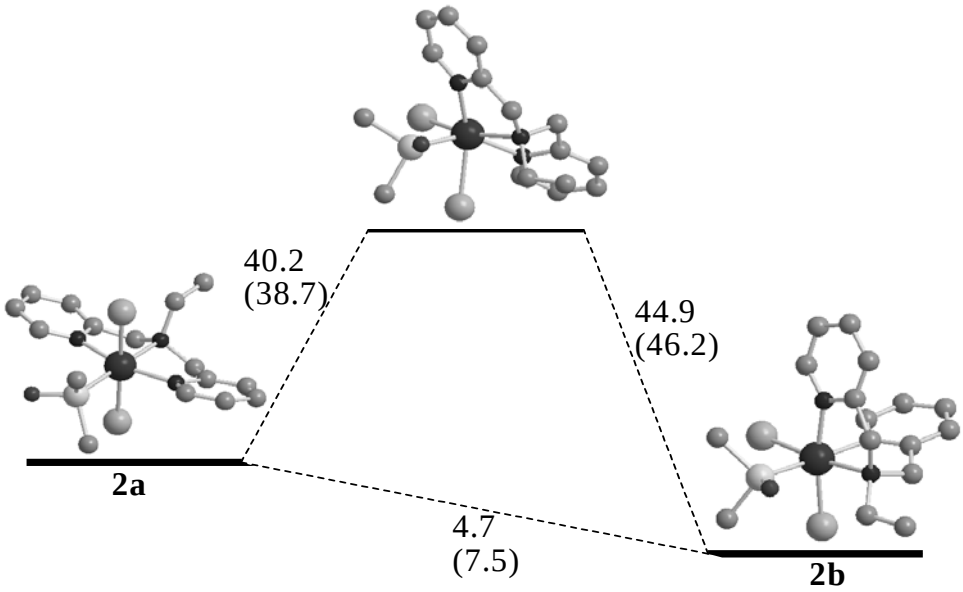

Figure XII-9. Energy diagram of the intramolecular isomerization mechanism with (in parenthesis) and without including solvent effects (energies in kcal·mol^{-1}).

The mechanism could also be dissociative. If first a chloro anion ligand is expelled from the ruthenium first coordination shell, the energetic barrier is very high, but including the solvent effect this barrier decreases due to the fact that after eliminating one chloro anion the ruthenium complex is positively charged and because it has an empty side around its first coordination sphere. In addition, the chloro anion is very stabilized by the presence of the solvent.

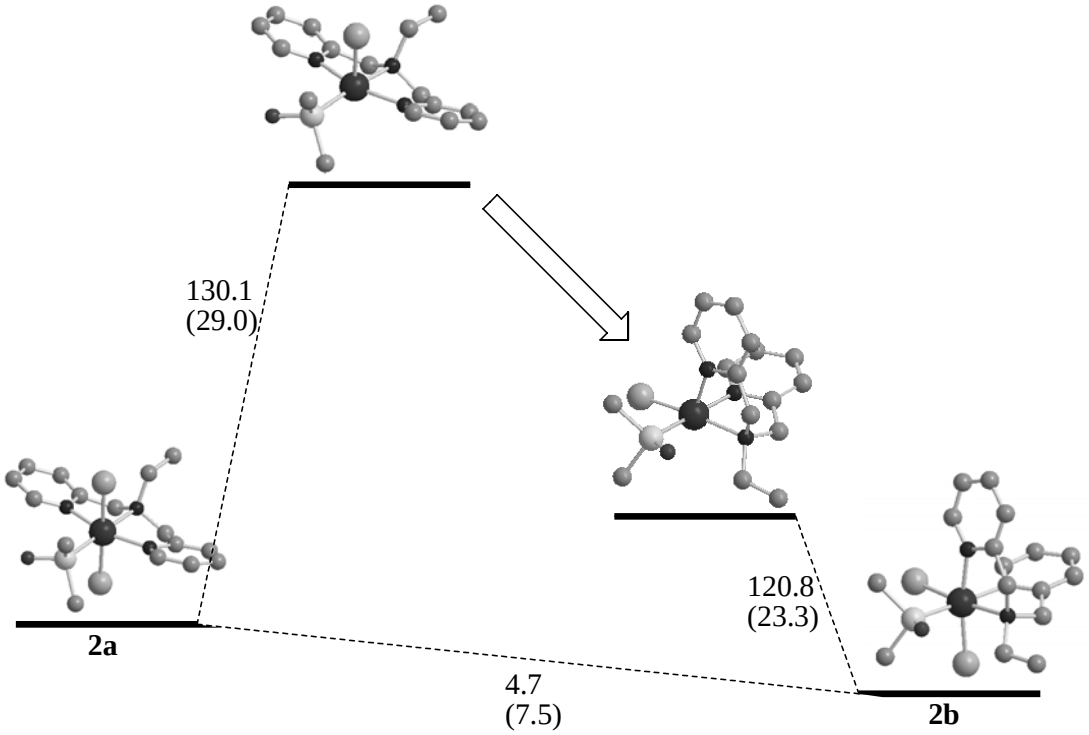

Figure XII-10. Dissociative mechanism by chloro anion elimination with (in parenthesis) and without including solvent effects (energies in kcal·mol^{-1}).

It seems that the dissociation of *dmso* is even easier because the barrier is 33.3 (23.1) kcal·mol^{-1}. The solvent does not stabilize the complex as much as after the chloro ligand loss because after eliminating the *dmso* ligand the molecule is not charged, and the stabilization is mainly due to the empty site of the ruthenium. The same dissociation in the simplified models with ammonia units show a slight increase of the energetic barriers for chloro (32.2 kcal·mol^{-1} compared to 29.0 kcal·mol^{-1}) and *dmso* (33.9 kcal·mol^{-1} compared to 23.1 kcal·mol^{-1}) taking into account the solvent effect.

Considering the dissociative mechanism that involves loss of the *dmso* ligand because it presents the lower energetic cost, the reorganization process from the structure with the meridional *bpea* to the facial *bpea* is depicted in Figure XII-11, including the solvent effect, showing that it is necessary about 17 kcal·mol^{-1} to overcome the barrier of this reorganization, plus the 23.1 kcal·mol^{-1} that supposes the dissociation of the *dmso* ligand. The reorganization takes place in two steps. The first one requires that the two choro ligands are in *trans* position, and the second one is reflected by the dihedral angle N3-Ru-N2-N1, which must go approximately from 180º to 90º. The first step of the reorganization presents a lower barrier compared to the second one. Nevertheless this second one is lower than the intramolecular process studied before because there is less steric hindrance.

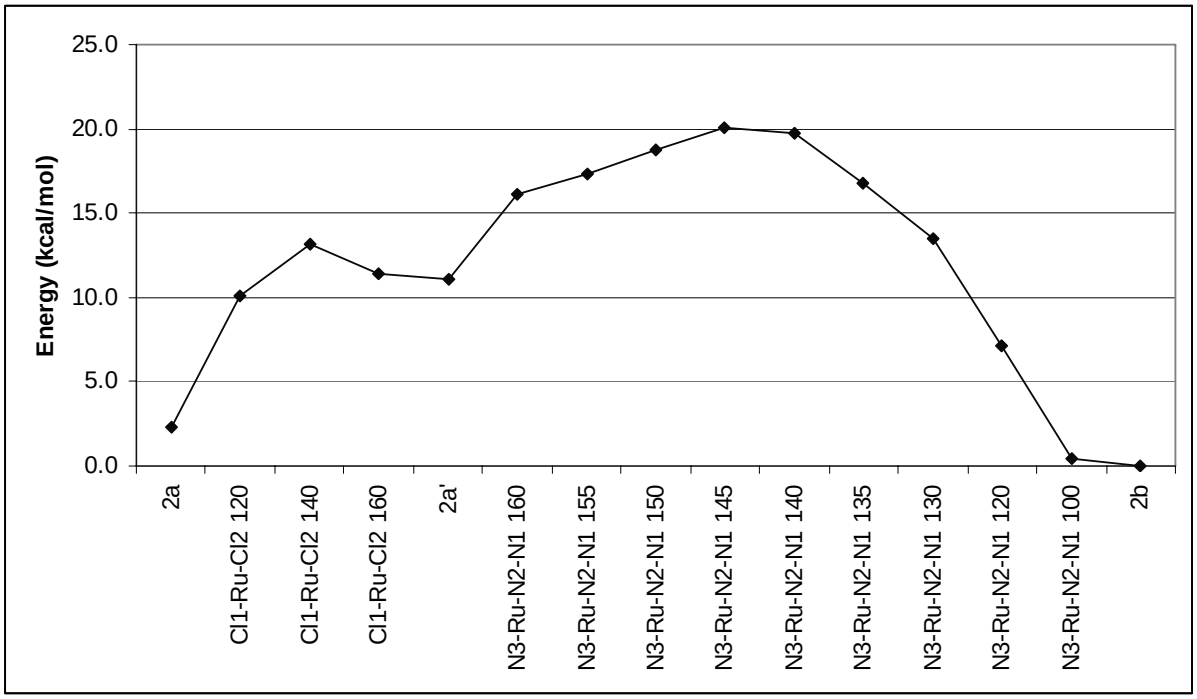

Figure XII-11. Reorganization of the dissociative mechanism by *dmso* elimination including solvent effects.

Conclusion

DFT calculations confirm the experimental results, and give insight into the nature of all the possible isomers. The interconversion process between the ruthenium complex containing the *bpea* ligand with an unknown meridional fashion to the complex with a

facial *bpea* with respect to the metal is supposed to be achieved through an intramolecular mechanism, but without excluding the dissociative mechanism.

References

1. a) S. I. Murahashi, H. Takaya, T. Naota, *Pure Appl. Chem.* **2002**, *74*, 19-24. b) T. Naota, H. Takaya, S. I. Murahashi, *Chem. Rev.* **1998**, *98*, 2599-2660. c) D. P. Riley, J. D. Oliver, *Inorg. Chem*. **1986**, *25*, 1825-1830. d) M. Rodríguez, I. Romero, A. Llobet, A. Deronzier, M. Biner, T. Parella, H. Stoeckli-Evans, *Inorg. Chem.* **2001**, *40*, 4150-4156. e) C. W. Chronister, R. A. Binstead, J. Ni, T. J. Meyer, *Inorg. Chem.* **1997**, *36*, 3814-3815. f) U. J. Jauregui-Haza, M. Dessoudeix, P. Kalck, A. M. Wilhelm, H. Delmas, *Catal. Today*. **2001**, *66*, 297-302.
2. a) A. Hatzidimitriou, A. Gourdon, J. Devillers, J. P. Launay, E. Mena, E. Amouyal, *Inorg. Chem.* **1996**, *35*, 2212-2219. b) V. Balzani, A. Credi, M. Venturi, *Chem. Eur. J.* **2002**, *8*, 5524-5532. c) S. G. Camera, H. E. Toma, *J. Photochem. Photobiol. A: Chem.* **2002**, *151*, 57-65.
3. a) J. P. Sauvage, J. P. Collin, J. C. Chambrón, S. Guillerez, C. Coudret, V. Balzani, F. Barigelletti, L. Decola, L. Flamigni, *Chem. Rev*. **1994**, *94*, 993-1019. b) M. K. Brennaman, J. H. Alstrum-Acevedo, C. N. Fleming, P. Jang, T. J. Meyer, J. M. Papanikolas, *J. Am. Chem. Soc.* **2002**, *124*, 15094-15098.
4. a) A. E. Friedman, J. C. Chambrón, J. P. Savage, N. J. Turro, J. K. Barton, *J. Am. Chem. Soc.* **1990**, *112*, 4960-4962. b) Y. Jenkins, A. E. Friedman, N. J. Turro, J. K. Barton, *Biochemistry* **1992**, *21*, 10809-10816. c) R. E. Holmlin, E. D. A. Stemp, J. K. Barton, *Inorg. Chem*. **1998**, *37*, 29-34. d) L. Li, H. Szmacinski, J. R. Lakowicz, *Biospectroscopy* **1997**, *3*, 155-159. e) L. Li, H. Szmacinski, J. R. Lakowicz, *Anal. Biochem.* **1997**, *244*, 80-85. f) E. Terpetschnig, H. Szmacinski, J. R. Lakowicz, *Anal. Biochem.* **1995**, *227*, 140-147. g) H. J. Youn, E. Terpetschnig, H. Szmacinski, J. R. Lakowicz, *Anal. Biochem.* **1995**, *232*, 24-30. h) Z. Murtaza, Q. Chang, G. V. Rao, H. Lin, J. R. Lakowicz, *Anal. Biochem.* **1997**, *247*, 216-222. i) T. M. Santos, B. J. Goodfellow, M. G. B. Drew, J. Pedrosa de Jesus, V. Félix, *Metal-Based Drugs*, **2001**, *8*(3), 125-136.

5. a) J. Malina, O. Novakova, B. K. Keppler, E. Alessio, B. Brabec, *J. Biol. Inorg. Chem.* **2001**, *6*, 435-445. b) M. J. Clarke, F. C. Zhu, D. R. Frasca, *Chem. Rev*. **1999**, *99*, 2511-2533.
6. a) C. Sens, M. Rodríguez, I. Romero, A. Llobet, T. Parella, B. P. Sullivan, J. Benet-Buchholz, *Inorg. Chem*. **2003**, *42*, 2040-2048. b) R. S. Srivastava, B. Milani, E. Alessio, G. Mestroni, *Inorg. Chim. Acta* **1992**, *191*, 15-17. c) B. R. James, R. S. McMillan, *Can. J. Chem.* **1977**, *55*, 3927-3932. d) B. R. James, R. S. McMillan, K. J. Reimer, *J. Mol. Cat.* **1976**, *1*, 439-441. e) D. P. Riley, *Inorg. Chem*. **1983**, *22*, 1965-1967. f) B. Fontal, A. Anzelotti, M. Reyes, F. Bellandi, T. Suarez, *Catalysis Letters* **1999**, *59*, 187-190.
7. a) K. Abdur-Rashid, S. E. Clapham, A. Hadzovic, J. N. Harvey, A. J. Lough, R. H. Morris, *J. Am. Chem. Soc.* **2002**, *124*, 15104-15118. b) C. A. Sandoval, T. Ohkuma, K. Muñiz, R. Noyori, *J. Am. Chem. Soc.* **2003**, *125*, 13490-13503.
8. a) P. Braunstein, F. Naud, A. Pfaltz, S. J. Rettig, *Organometallics* **2000**, *19*, 2676-2683. b) A. A. Danopoulos, S. Winston, W. B. Motherwell, *Chem. Comm.*, **2002**, 1376-1377. c) C. Sens, M. Rodríguez, I. Romero, A. Llobet, T. Parella, B. P. Sullivan, J. Benet-Buchholz, *Inorg. Chem.* **2003,** *42*, 2040-2048.
9. a) M. E. Marmion, K. J. Takeuchi, *J. Am. Chem. Soc.* **1998**, *110*, 1472-1480. b) M. H. V. Huynh, L. M. Witham, J. M. Lasker, M. Wetzler, B. Mort, D. L. Jameson, P. S. White, K. J. Takeuchi, *J. Am. Chem. Soc.* **2003**, *125*, 308-309.
10. Y. Fukumoto, T. Dohi, H. Masaoka, N. Chatani, S. Murai, *Organometallics* **2002**, *21*, 3845-3847.
11. a) A. Llobet, P. Doppelt, T. J. Meyer, *Inorg. Chem.* **1988**, *27*, 514-520. b) I. Romero, M. Rodríguez, A. Llobet, M. Collomb-Dunand-Sauthier, A. Deronzier, T. Parella, H- Stoeckli-Evans, *J. Chem. Soc., Dalton Trans.* **2000**, 1689-1694. c) C. Sens, M. Rodríguez, I. Romero, A. Llobet, T. Parella, J. Benet-Buchholz, *Inorg. Chem*. **2003**, *42*, 8385-8394. d) I. Serrano, A. Llobet, M. Rodríguez, I. Romero, J. Benet-Buchholz, T. Parella, D. Luna, J. M. Campelo, J. M. Marinas, *submitted to Inorg. Chem.* e) J. Mola, A. Llobet, M. Rodríguez, I. Romero, J. Benet-Buchholz, T. Parella, D. Luna, J. M. Campelo, J. M. Marinas, *submitted to Chem. Eur. J.*
12. R. Ziessel, V. Grosshenny, M. Hissler, C. Stroh, *Inorg. Chem*. **2004**, *43*, 4262.
13. J. J. Rack, N. V. Mockus, *Inorg. Chem.* **2003**, *42*, 5792-5794.
14. J. J. Rack, J. R. Winkler, H. B. Gray, *J. Am. Chem. Soc.* **2001**, *123*, 2432-2433.

15. C. Baffert, I. Romero, J. Pecaut, A. Llobet, A. Deronzier, M. N. Collomb, *Inorg. Chim. Acta* **2004**, *357*, 3430-3436.
16. *Handbook of Metalloproteins*, ed. A. Messerschmidt, R. Huber, T. Poulos, K.Wieghart, Wiley, London, 2001.
17. M. K. Smith, J. A. Gibson, C. G. Young, J. A. Broomhead, P. C. Junk, F. R. Keene, *Eur. J. Inorg. Chem.* **2000**, 1365-1370.
18. R. C. van der Drift, J. W. Sprengers, E. Bouwman, W. P. Mul, H. Kooijman, A. L. Spek, E. Drent, *Eur. J. Inorg. Chem.* **2002**, 2147-2155.
19. A. D. Becke, *J. Chem. Phys*. **1993**, *98*, 5648-5652.
20. J. P. Perdew, Y. Wang, *Phys. Rev. B* **1992**, *45*, 13244-13249.
21. Gaussian 03, M. J. Frisch, G. W. Trucks, H. B. Schlegel, G. E. Scuseria, M. A. Robb, J. R. Cheeseman, J. A. Montgomery, Jr., T. Vreven, K. N. Kudin, J. C. Burant, J. M. Millam, S. S. Iyengar, J. Tomasi, V. Barone, B. Mennucci, M. Cossi, G. Scalmani, N. Rega, G. A. Petersson, H. Nakatsuji, M. Hada, M. Ehara, K. Toyota, R. Fukuda, J. Hasegawa, M. Ishida, T. Nakajima, Y. Honda, O. Kitao, H. Nakai, M. Klene, X. Li, J. E. Knox, H. P. Hratchian, J. B. Cross, C. Adamo, J. Jaramillo, R. Gomperts, R. E. Stratmann, O. Yazyev, A. J. Austin, R. Cammi, C. Pomelli, J. W. Ochterski, P. Y. Ayala, K. Morokuma, G. A. Voth, P. Salvador, J. J. Dannenberg, V. G. Zakrzewski, S. Dapprich, A. D. Daniels, M. C. Strain, Ö. Farkas, D. K. Malick, A. D. Rabuck, K. Raghavachari, J. B. Foresman, J. V. Ortiz, Q. Cui, A. G. Baboul, S. Clifford, J. Cioslowski, B. B. Stefanov, G. Liu, A. Liashenko, P. Piskorz, I. Komaromi, R. L. Martin, D. J. Fox, T. Keith, M. A. Al-Laham, C. Y. Peng, A. Nanayakkara, M. Challacombe, P. M. W. Gill, B. Johnson, W. Chen, M. W. Wong, C. Gonzalez, J. A. Pople, Gaussian, Inc., Pittsburgh PA, 2003.
22. D. Andrae, U. Haussermann, M. Dolg, H. Stoll, H. Preuss, *Theor. Chim. Acta* **1990**, *77*, 123-141.
23. A. Bergner, M. Dolg, W. Kuchle, H. Stoll, H. Preuss, *Mol. Phys*. **1993**, *80*, 1431-1444.
24. W. J. Hehre, R. Ditchfield, J. A. Pople, *J. Chem. Phys*. **1972**, *56*, 2257-2261.
25. A. E. Reed, L. A. Curtiss, F. Weinhold, *Chem. Rev*. **1988**, *88*, 899-926.
26. V. Barone, M. Cossi, *J. Phys. Chem. A* **1998**, *102*, 1995-2001.

27. Standard deviations for the distances and for the angles, $s_{n-1} = \sqrt{\frac{\sum_{i=1}^{N} (CV - EV)^2}{N - 1}}$, where CV means calculated value, EV experimental value (X-ray data), and N is the number of distances or angles taken into account

PART IV: Schrock Catalysts

Schrock Catalysts

Chapter XIII: *Structural and Dynamic Properties of Molybdenum and Tungsten-Based Olefin Metathesis Catalysts, $M(=NR^1)(=CHR^2)(X)_2$*

Structural and Dynamic Properties of Molybdenum and Tungsten-Based Olefin Metathesis Catalysts, $M(=NR^1)(=CHR^2)(X)_2$

Abstract

DFT(B3PW91) and QM/MM (B3PW91:UFF) calculations have been carried out to rationalize the structural and dynamical properties of quasi-tetrahedral imido-alkylidene molybdenum and tungsten complexes $M(NR^1)(CHR^2)(X)_2$ (R^1 = CPh_3, 2, 6-di-isophenyl, R^2 = *t*Bu, X = CH_2*t*Bu, O*t*Bu), which are catalysts for olefin metathesis with efficiency depending on X. The optimized geometries of all complexes are pseudo-tetrahedral and yield *syn* and *anti* isomers. The presence of the C-H agostic interaction in the *syn* isomers is evidenced by geometrical features as well as the ν_{C-H} stretching frequencies and J_{C-H} NMR coupling constants calculated to be lower than in the *anti* isomers, as observed experimentally in the case of the J_{C-H}. Ancillary X ligands that are weak σ-donors and π-donors (OR) compete with the agostic interaction. The calculated *syn/anti* ratios are in good agreement with experimental data. The *syn/anti* interconversion occurs preferentially via the alkylidene rotation, while H transfers between perhydrocarbyl ligands have much higher energy barriers, showing that this process does not compete with alkylidene rotation.

Introduction

Electron-deficient species are potential catalysts for a number of chemical transformations because of their electrophilic behavior towards an incoming organic ligand. For this reason early transition metal d^0 complexes are especially interesting targets. Of these systems, well-defined d^0 nucleophilic alkylidene metal complexes, also known as Schrock alkylidene complexes, can be highly efficient catalysts for olefin metathesis, when proper sets of ligands and metal are used.[1-12] Apart from some Re catalysts,[13-19] molybdenum and tungsten ones have been shown to be more efficient and are most commonly used,[13-19] Catalysts as $Mo(=NR)(=CHR)(X)_2$ are active and usually more compatible with functional groups such as esters (Scheme XIII-1, R = CPh_3 or 2, 6-di-isopropyl, X = CH_2*t*Bu or O *t*Bu). The catalytic efficiency is highly influenced by the nature of the ancillary ligands and the surrounding media. For example, the Mo

complexes are experimentally active.[20] The synthesis of the molecule depicted in Scheme XIII-2 means the knowledge of the existence of this kind of structures for Mo. Furthermore, recently, a well-defined silica-supported Re complex, [(≡OSi)Re(≡C*t*Bu)(=CH*t*Bu)(CH_2*t*Bu)], has been reported, and it has shown unprecedented activity in olefin metathesis even compared with the Mo- and W-based homogeneous catalysts.[21-24]

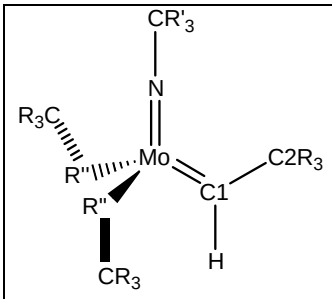	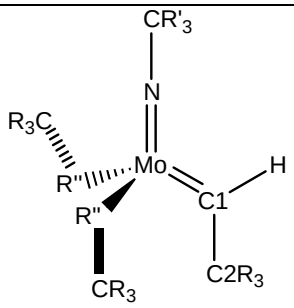
1s$_m$ R=H, R'=H, R''=CH_2 **1s** R=CH_3, R'=Ph, R''=CH_2 **3s$_m$** R=H, R'=H, R''=O **3s** R=CH_3, R'=Ph, R''=O	**1a$_m$** R=H, R'=H, R''=CH_2 **1a** R=CH_3, R'=Ph, R''=CH_2 **3a$_m$** R=H, R'=H, R''=O **3a** R=CH_3, R'=Ph, R''=O
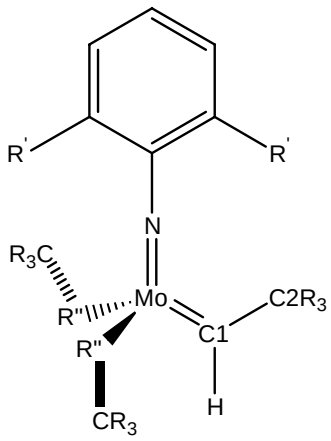	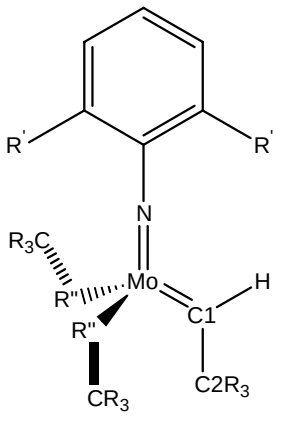
2s$_m$ R=H, R'=H, R''=CH_2 **2s** R=CH_3, R'=$CH(CH_3)_2$, R''=CH_2 **4s$_m$** R=H, R'=H, R''=O **4s** R=CH_3, R'=$CH(CH_3)_2$, R''=O	**2a$_m$** R=H, R'=H, R''=CH_2 **2a** R=CH_3, R'=$CH(CH_3)_2$, R''=CH_2 **4a$_m$** R=H, R'=H, R''=O **4a** R=CH_3, R'=$CH(CH_3)_2$, R''=O

Scheme XIII-1. *syn* (left) and *anti* (right) Isomers for Mo(=NR)(=CHR)$(X)_2$

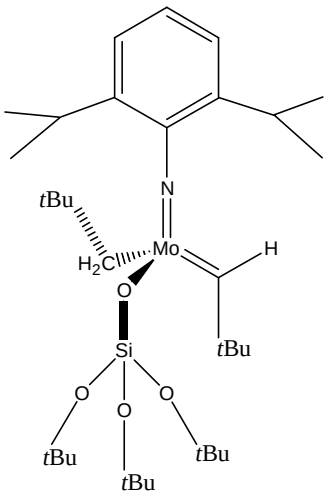

Scheme XIII-2. Experimental Mo catalyst.

These kind of catalyst precursors, $Mo(=NR)(=CHR)(X)_2$, have several common structural characteristics: they have a pseudo-tetrahedral geometry, and they contain both imido and alkylidene ligands with their respective substituents being coplanar. As a consequence, two isomers have been observed in which the alkyl substituent of the alkylidene ligand points either toward or away from the imido, thus leading to *syn* and *anti* isomers, respectively (Scheme XIII-1). The subindex m means that the corresponding molecules are extracted from a simplification of the experimental system.

It has been observed that for Re complexes the *syn* isomers present a much lower $J_{C\text{-}H}$ coupling constant for their alkylidene proton (115-120 Hz) (as compared to that of their respective *anti* isomers: 160-180 Hz),[10,25,26] and this has been associated with an elongation of the C-H bond and therefore with the presence of an α-agostic interaction.[27-29] However, it is currently recognized that an α-agostic C-H interaction is not favored in a tetrahedral complex.[30] Yet, similar low *syn* $J_{C\text{-}H}$ values have been reported for the isolobal $[Mo(=NR)(=CHR)(OR)_2]$ complexes, which lead the authors to suggest the existence of an α-C-H agostic interaction.[31-34]

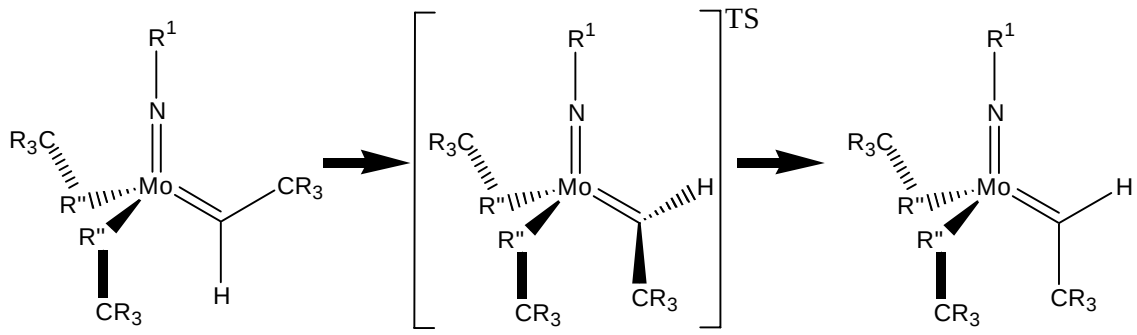

Scheme XIII-3. Schematic representation of the rotation of the imido ligand carbene rotation for $Mo(=NR^1)(=CHR)(X)_2$.

The *syn* and *anti* isomers (rotamers) interconvert slowly for Re complexes, and their thermodynamic ratio, as well as their rate of interconversion, depend on the nature of the substituent X. For example, when X is CH_2tBu, the *syn* isomer is the only one observed,[35] whereas when X is O*t*Bu, the two isomers are present, the *anti* isomer being the major one (75%).[9] For Re(≡C*t*Bu)(=CH*t*Bu)$(OR)_2$, the isomerization requires several hours at 100 ºC or higher temperatures and is attributed to the alkylidene rotation.[20] The high rotation barrier of the alkylidene ligand has been suggested to be associated with the loss of a metal-imido π bond in the transition state: when the alkylidene ligand is rotated by 90º, the imido and alkylidene π orbitals compete for the same metal d orbital.[17] Nevertheless, similar molybdenum complexes, $Mo(=NR)(=CHR)(OR)_2$ present lower experimental barriers, which seems to favour the reactivity of these molybdenum catalysts (Scheme XIII-3). Another characteristic of these complexes is the extremely slow H transfer (weeks) between the alkylidene and imido ligands and between the neopentyl and any of the unsaturated ligands,[11,26,36] which could also be related to *syn-anti* isomerization.

Because these systems are good olefin metathesis catalysts, we have decided to investigate in detail the origin of these special structural features, which are not fully understood. Computational studies at the Hartree-Fock and SCF-Xα-SW levels on the related Mo and W imidoalkylidene systems have been reported and focused on the rotational barrier of the alkylidene ligand.[33,37] A recent study of Solans-Monfort et al. is

a useful tool to make comparisons and evaluate the behaviour of the different kind of metals.[38]

In this paper, we have carried out DFT and some QM/MM studies of the structural and dynamic properties of several Mo(=NR)(=CHR)$(X)_2$ complexes. Computational studies of the agostic interaction have been carried out on numerous systems, and the various factors involved have been discussed. The computational effort on this interaction has recently been reviewed.[39] Despite the relative weakness of the C-H agostic interactions, DFT methods have been shown to be appropriate for geometry optimization. The agostic interaction is sensitive to steric factors, and the need to take into account the full identity of the complexes has been recognized.[39] The QM/MM methods are thus methods of choice for the study of the steric effect of the substituents attached to the carbon responsible of the C-H bond activation.

Computational Details

Two sets of calculations were carried out to represent the experimental molybdenum Mo(=NR^1)(=CH*t*Bu)$(X)_2$ complexes (R^1 = CPh_3 or 2, 6-di-isopropylphenil; X = CH_2*t*Bu or O*t*Bu. To get insight into a more detailed analysis R^1 ligands were simplified by a phenyl group and a methyl group, respectively, and the *t*Bu group was also substituted by a methyl. These simplified complexes were also analysed for tungsten. The Scheme XIII-1 lists all the optimized structures for Mo and W. The hybrid B3PW91[40,41] density functional, as implemented in the Gaussian03[42] package, was used in the QM calculations. The Mo and W atoms were represented with the quasirelativistic effective core pseudopotentials (RECP) of the Stuttgart group and the associated basis sets augmented with a polarization function (α= 1.043, Mo; α= 0.823, W).[43,44] The remaining atoms (H, C, N, and O) were represented with 6-31G(d,p) basis sets.[45]

To test the basis set accuracy, single-point calculations were carried out with the same representation for Mo and a 6-311++G(2df,2pd) basis set for H, C, N, and O.[46] Moreover, geometry optimizations for Mo(=NCH_3)(=$CHCH_3$)$(CH_2CH_3)_2$ were performed with the large basis set. Both tests showed no significant changes in the results with the larger basis sets. Therefore only the results with the smaller basis set are reported.

Apart from the QM calculation the simplified models and the experimental compounds, in order to get insight into the steric influence of the *t*Bu groups, and the aromatic subtituents (CPh_3, 2, 6-di-isopropylphenyl) ONIOM[47] (B3PW91:UFF) calculations were performed on the experimental systems. The inner layer (QM) is the same as described above, indeed similar to the presented ones for the models, and the outer layer (MM) treats the missing groups with molecular mechanics calculations using the UFF force field.[48] To differentiate between QM and QM/MM calculations, all complexes computed at the QM/MM level are designed with an added QM/MM subscript. A further distinction is made according to the position of the alkylidene C-R bond with respect to the imido ligand (**s** for *syn* and **a** for *anti*, see Scheme XIII-1).Test calculations were carried out for complex **1** to assess the reliability of the ONIOM approximation. Single-point calculations on the ONIOM geometries gave a difference in energy between the *syn* and *anti* isomers that differs from that at the QM/MM level by only 0.3 $kcal \cdot mol^{-1}$. Furthermore, the geometry optimizations at the DFT level gave geometrical and energy results similar to that with ONIOM.

The B3PW91 and ONIOM (B3PW91:UFF) geometry optimizations were performed without any symmetry constraints, and the nature of the extrema (local minima or transition states) was checked by analytical frequency calculations. The harmonic $\nu_{C\text{-}H}$ stretching frequency of the alkylidene C-H bond has been identified as an isolated mode in the calculations. The energies discussed throughout the text are electronic energies without any ZPE corrections. Gibbs free energies have been computed from harmonic frequencies at 298.15 K and 1 atm. In addition, the NMR $J_{C\text{-}H}$ coupling constants of the alkylidene C-H bond have only been computed for the QM model at the B3PW91 level using the methodology implemented in the Gaussian03 package, [49] with NMR-optimized basis sets Individual Gauge for Localized Orbital (IGLO) II and III developed by Kutzelnigg and co-workers were used for the calculation of the coupling constants.[50] The natural population analysis (NPA)[51] was used to estimate the atomic charges.

Results and Discussion

Geometrical Structure

We have optimized all the $Mo(=NR^1)(=CHR^2)(X)_2$ structures displayed in Scheme XIII-1. There are two possible imido ligands, either CPh_3 or 2, 6-di-isopropylphenyl; two possibilities of X, C*t*Bu or O*t*Bu. Structures **1-4** have also been computed by QMMM. Furthermore, the QM calculations have been done for the simplified complexes, where the CPh_3 is treated as a CH_3, the 2, 6-di-isopropylphenyl as a phenyl, and the *t*Bu groups as methyls have been repeated replacing Mo by W.

Figure XIII-1 includes the optimized geometries of the *syn* and *anti* isomers of $Mo(=NR^1)(=CHR^2)(Y)_2$ with both the simplified models (**1s$_m$** and **1a$_m$**) and the full systems (**1s** and **1a**, with *t*Bu units). The QM/MM systems have not been displayed because of the similarity with the same systems calculated by QM. Table XIII-1 gives selected spectroscopic properties and Table XIII-2 their relative energies. Species **1s$_m$** and **1a$_m$** present a pseudo-tetrahedral coordination at the metal, the angle between the alkylidene and imido ligands being smaller (ca. 104.2 and 102.2º, respectively for the *syn* and the *anti* isomers) than the idal tetrahedral value of 109.5º. Substituents of the alkylidene and the imido are coplanar; rotating the alkylidene by 90º around the Mo=C bond does not yield a local minimum and the geometries presented in Figure XIII-1 are recovered. The Mo-N distances for the imido and alkylidene ligands are very close to those obtained in the solid state structure for closely related complexes, *anti* Re(≡C*t*Bu)(=CHFc)(OCMe$(CF_3)_2)_2$ (Fc = ferrocenyl).[21-24] Isomer **1s$_m$** presents a small Mo-C1-H angle (98.0º) and a long C1-H bond (1.114 Å), associated with a rather short Mo···H distance of 2.297 Å, which are indicative of a weak α-C-H agostic interaction. Remarkably, the *anti* isomer (**1a$_m$**) exhibits an angle Re-C1-C2 of less than 120º (113.4º), absolutely lower than the *syn* version (145.6º) a longer C1-C2 distance than in **1s$_m$** (1.514 *vs* 1.491 Å) associated with a rather short Mo···C2 distance (2.843 Å as compared with that in **1s$_m$**, i.e., 3.204 Å), suggestive of a weak α-C-C agostic interaction. The lack of bulky ligands in these model complexes suggests that the α-agostic interactions are driven by electronic factors.

These features indicate that these Mo^{VI} complexes have a different electronic structure from the eight-electron tetrahedral complex Cl_3TiCH_3, which does not show

any α-C-H agostic interaction.[30] The C-C agostic interaction is rare in systems without any geometrical constraint.[52,53] The similar behavior of Mo compared to Re allows the observation of a slight higher C1-H bond length with Mo. The tungsten is useful to refuse the idea that the inclusion of *f* electrons has the key role because the results are similar to the molybdenum ones. This higher C-H bond activation for Mo and W should be translated into in presenting higher catalytic capacity. A small angle Re=C_α-C_β, i.e., 114º, in *anti* Re(≡C*t*Bu)(=CHFc)(OCMe$(CF_3)_2)_2$ (Fc = ferrocenyl) has been observed and can be interpreted as a signature of a C-C agostic interaction.[10]

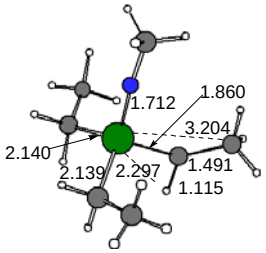	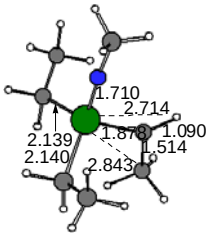
$1s_m$	**$1a_m$**
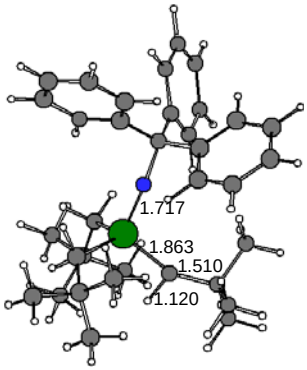	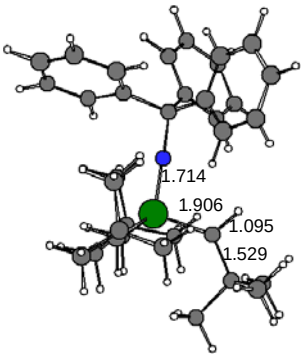
1s	**1a**
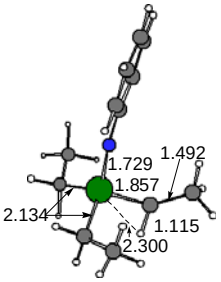	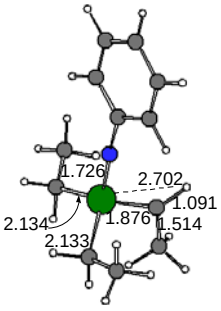
$2s_m$	**$2a_m$**

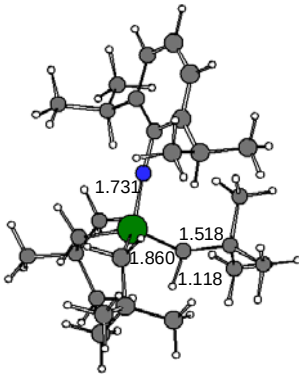

2s

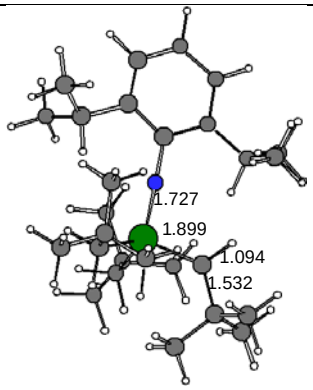

2a

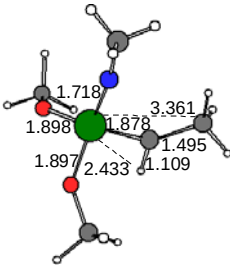

3s$_m$

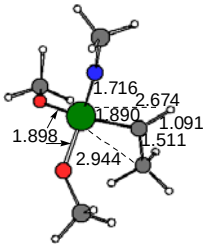

3a$_m$

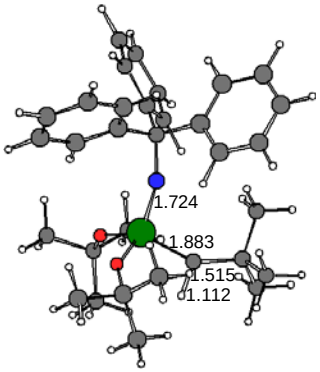

3s

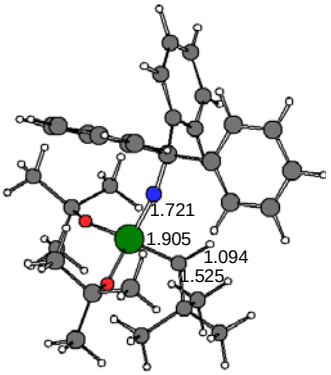

3a

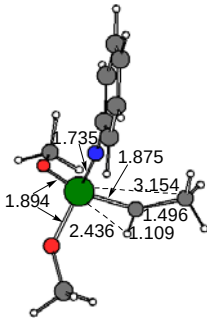

4s$_m$

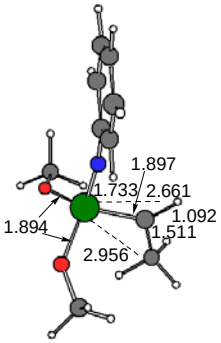

4a$_m$

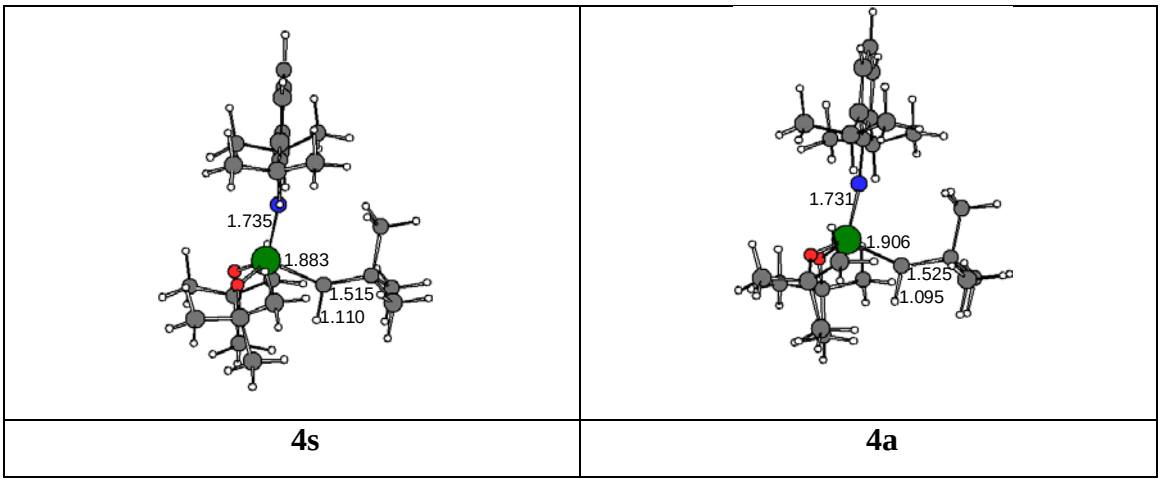

4s	4a

Figure XIII-1. Optimized structures of Mo(=NR[1])(=CHR[2])(X)$_2$ (distances in Å).

The simplified calculated models seem to not change the core structure of the full systems. Furthermore, the treatment by QM/MM of the full systems is not very significative as the single point energy calculations give differences of only 7.8 kcal·mol^{-1} between the **1s$_{QM/MM}$** and the **1s**. These QM/MM calculations let us make comparisons with respect to similar Re complexes that appear in several studies.[38]

The replacement of the ancillary ethyl ligands of **1** by methyl units gives the same results. Indeed the activation of the C1-H bond is exactly the same.

In order to test the steric effect of the alkyl group of the acetilene group a test has been carried out treating the methyl of **1s$_m$** and **1a$_m$** by MM. For **1s$_m$** notorious differences are observed in the C-H bond activation. The C-H bond length decreases from 1.115 Å to 1.098 Å. And thus, the Mo-C1-H angle increases from 97.9º to 114.4º, and the Mo···H from 2.297 Å to 2.539 Å. The C1-C2 bond length of **1a$_m$** also decreases from 1.514 Å to 1.501 Å, nevertheless the Mo···C2 distance is only increased by 0.032 Å. The same trends are observed in the full systems for Mo.

To analyze the effect of the group attached to the imido ligand we have replaced the CPh_3 group by a 2, 6-di-isopropylphenyl unit. Furthermore, to observe the effect of the ancillary ligands X we have replaced the alkyl ligands by weak σ-donor/π-donor OR ligands which does not substantially modify the coordination geometry at metal center, either molybdenum or tungsten. Figure XIII-1 shows the optimized geometries, Table

XIII-1 selected spectroscopic properties and Table XIII-2 the corresponding relative energies for all these species. The alkylidene and imido ligands remain coplanar, and the angle between them is close to 100º for the QM models. The structural changes concern mainly the α-agostic interaction. The agostic interaction becomes weaker when the two alkyl ligands have been substituted by two alkoxy groups. The inclusion of the full ligands for a better representation of the steric bulk strengthens the C-H agostic and weakens the C-C agostic interaction in the *syn* and *anti* isomers, respectively, when compared to the QM models.

Inclusion of the bulky ligands in QM/MM calculations of the full complexes does not alter the main results obtained by QM with the smaller models and even less compared to the same systems treated by QM. The pseudo-tetrahedral geometry is maintained, and the agostic interaction is still present. The most important change for **2s$_{QM/MM}$** is the opening of the N-Mo-C1 angle (116.3º) that comes from steric repulsions between the methyl groups of the alkylidene and imido ligands, but these repulsions are a bit exaggerated taking in account the similar values of **2s** (105.5º) and **2s$_m$** (104.1º). However, the *t*Bu groups mean an enlargement of the N-Mo-C1 that reinforces the α-agostic interaction on the alkylidene: the Mo-C1-H angle decreases from 98.3º for **2s$_m$** to 95.2º for **2s** and till 83.6º for **2s$_{QM/MM}$**. The C-H bond length increases from 1.115 Å for **2s$_m$** to 1.118 Å for **2s** and 1.129 Å for **2s$_{QM/MM}$**. Obviously the Mo···H distance becomes 0.044 Å shorter for **2s** and even shorter for **2s$_{QM/MM}$**, with a decrease of 0.229 Å. For **2a**, an opposite distortion is observed: the Mo-C1-C2 becomes 14.9º (**2as$_{QM/MM}$**) and 17.3º (**2a$_{QM/MM}$**) larger for the complex expected experimentally. This angular change decreases the steric repulsion between the *t*Bu ligands, which results in the loss of the C-C agostic interaction. The Mo=N bond distance remains nearly the same which is different from the *syn* isomer behavior that saw an increase of this distance when the experimental system was taken in account.

Overall there are some relationships for the eight analyzed models that must be taken into account. Taking into account the *syn* and the *anti* isomers, the longer the C1-H bond distance the shorter the C1-C2 one (r^2 = 0.990), the shorter the Mo-H distance (r^2 = 0.988), the smaller the Mo-C1-H angle (r^2 = 0.988). The Mo-C1-C2 and Mo-C1-H angles are correlated perfectly (r^2 = 0.997). If we are based only on *syn* isomers the relationships are quite better. The same can be said for W. The disposition of both C1-H

vs Mo-C1-H regressions for Mo and W show that the origen ordinate is higher for W, demonstrating as above that the W is capable slightly more than Mo.

The complexes presenting a phenyl unit directly attached to the nitrogen atom of the imido ligand are suitable to present a rotation of the aromatic ring, and after doing some tests with **2s** and **2a** isomers the existence of two new isomers for each isomer is proved, exactly the same through a symmetry plane. The corresponding TS are not high in energy, no more than 0.6 kcal/mol with respect to the minima.

The vibrational C-H stretching frequency, $\nu_{C\text{-}H}$, has been calculated (Table XIII-1). The stretching $\nu_{C\text{-}H}$ is isolated from the other modes, and after scaling by 0.9573,[54] to account for both systematic errors on the calculation of the force constant and the lack of anharmonic effects, the resulting values for **Mo-1s$_m$** and **Mo-1a$_m$** are 2921 and 3168 cm^{-1}, respectively. The lack of experimental values for the alkylidene C-H bond does not allow further comparison with these calculated values. The presence of an α-C-H agostic interaction in the *syn* isomer is evidenced by the lower $\nu_{C\text{-}H}$ stretching frequencies (about 240 cm^{-1}) for the syn isomers than those corresponding to *anti* isomers, **1a$_m$** and **1a**, respectively.

The trend is the same for Mo and W species. Nevertheless slight differences can be observed. The $\nu_{C\text{-}H}$ is higher for *anti* isomers of Mo, and the transition state that interconverts both isomers presents even a lower value than the *syn* isomers. The W-anti isomers present higher $\nu_{C\text{-}H}$ than the Mo ones, nevertheless the values for the syn isomers are lower for W, as well as the values for the TS. For $\nu_{C\text{-}C}$ no significant differences exist between both metals.

structure[a]	Mo				W			
	ν_{C-H}	ν_{C-H} scaled	ν_{C-C}	ν_{C-C} scaled	ν_{C-H}	ν_{C-H} scaled	ν_{C-C}	ν_{C-C} scaled
1s$_m$	2921	2796	1149	1100	2906	2782	1151	1101
1a$_m$	3168	3033	1043	998	3173	3037	1041	997
1TS$_m$	2910	2786	1136	1087	2865	2743	1145	1096
2s$_m$	2919	2794	1147	1098	2902	2778	1150	1101
2a$_m$	3163	3028	1048	1003	3167	3031	1046	1001
2TS$_m$	2947	2821	1131	1082	2903	2779	1141	1092
3s$_m$	2972	2845	1143	1094	2962	2836	1144	1095
3a$_m$	3160	3025	1067	1022	3161	3026	1067	1022
3TS$_m$	3057	2927	1119	1071	3045	2915	1123	1075
4s$_m$	2966	2840	1140	1091	2960	2833	1141	1092
4a$_m$	3151	3017	1071	1025	3154	3019	1070	1024
4TS$_m$	3064	2933	1114	1066	3056	2926	1116	1069

[a] See Figure XIII-1

Table XIII-1. Unscaled and scaled stretching frequencies for C1-H (ν_{C-H}) and C1-C2 (ν_{C-C}) in cm^{-1}.

The NMR coupling constants, J_{C-H}, have been calculated. All the NMR values are obtained by IGLO II basis set. Some tests with IGLO III basis set gave similar results. The computed J_{C-H} values show the same trend. The computation of NMR coupling constants is still not frequent for systems of this size and nature,[55] and thus the reliability of the computed DFT J_{C-H} is not well established.[56] The J_{C-H} values are calculated to be 106 and 150 Hz for the *syn* and the *anti* isomers of **Mo-1$_m$**, nearly the same as for **Mo-2$_m$**, 107 and 150 Hz, respectively. Therefore the replacement of the imido ligand does not affect the J_{C-H} value. The value of 107 Hz for **Mo-1s$_m$** can be compared to the experimental one of 108 Hz corresponding to **Mo-1** system. For **Mo-4$_m$** species the values are 114 and 147 Hz for the syn and anti isomers, respectively. The accuracy is high in comparison with the experimental value corresponding to **Mo-4** (115 Hz). Therefore measured J_{C-H} for the *syn* isomer of 114 Hz is only 1 Hz higher than the calculated value (**1s$_m$**).[57] Despite the bibliography illustrates the difficulty in calculating J_{C-H} coupling constants, and it is in particular known that larger basis sets than those used in this work are necessary.[58-60] test J_{C-H} calculations using single-point DFT calculations on QM geometries have given us very good results.

The computed spectroscopic results for species **1$_m$-4$_m$** are similar. The stretching frequencies ν_{C-H} are smaller for the *syn* isomers than for the *anti* isomers. Similarly the

calculated $J_{C\text{-}H}$ values are also smaller for the *syn* isomers. Focusing on the *syn* isomers, the experimental values and the calculations show that the $J_{C\text{-}H}$ coupling constant slightly increases when we replace the alkyl ancillary ligands by alkoxy ligands. The replacement of the imido ligand has almost no effect. The same trend is given for $\nu_{C\text{-}H}$. These two trends indicate the increase of the α-C-H agostic interaction on going from **1**$_m$ to **3**$_m$.The comparison of the Mo and W results shows very insignificant differences.

structure	Mo		W	
	ΔE	ΔG°_{298}	ΔE	ΔG°_{298}
1s$_m$-1a$_m$	2.7	3.7	2.7	3.2
2s$_m$-2a$_m$	2.7	3.0	2.7	3.2
3s$_m$-3a$_m$	1.9	2.1	2.1	1.2
4s$_m$-4a$_m$	2.0	2.3	2.1	2.4

Table XIII-2. Energies and Gibbs free energies, in kcal·mol^{-1}, relative to the more stable isomer.

For Mo, the *syn* isomer of either **1s$_m$** or **2s$_m$** is 2.7 kcal·mol^{-1} more stable than the *anti* isomer (Table XIII-2). The inclusion of the actual substituents at the QM/MM level slightly stabilizes the *syn* isomer, **2s$_{QM/MM}$** being 1.8 kcal·mol^{-1} more stable than **2a$_{QM/MM}$** and this difference is 6.3 kcal·mol^{-1} using only QM. For **1** this difference is 8.3 and 5.9 kcal·mol^{-1} for the QM/MM species and the QM species, respectively. These results are in agreement with the experimental evidence, where the *syn* isomer is the only one observed. Therefore the slight energetic difference observed for the compound **2** calculated by QM/MM is supposed to be a kind of mistake of this method. The energy preference for the syn isomers over the anti isomers can be understood assuming that the α-C-H agostic interaction is stronger than the α-C-C agostic one as the relative elongation of the C-H bond length is larger, the M···H distance is shorter, and the electron density of the C-H bond is more accessible by the metal. The bulky groups in the QM/MM calculations strengthen the α-C-H agostic of the *syn* isomer and suppress the α-C-C agostic interaction, hence increasing the difference in energy between the two rotamers. The barrier for W is similar, only slightly higher by less than 0.1 kcal·mol^{-1}.

For Mo, in the small QM model, the preference for the *syn* isomer is higher for the species that do not contain methoxy ligands. The replacement of the imido substituent does not affect. Taking into account the full nature of the ligands in the QM and QM/MM calculations of the full systems, the anti isomer becomes less stable in the cases of **1** and **2**, in agreement with the experimental data. QM calculations thus show that the decreased preference for the *syn* isomer has an electronic origin and either the QM/MM calculations or the QM calculations show that the steric factors switch the preference between *syn* and *anti* isomers. The differences for QM are slightly smaller. The syn isomer of **1-4** is favored by 5.9, 6.3, 2.6, and 3.9 kcal·mol^{-1}, respectively. Similar remarkable agreements have been previously found in the experimental and computational studies of Nb complexes with competing α- and β-C-H agostic interactions,[61,62] and similar Re studies.[38] This shows a remarkable ability of the DFT calculations in estimating accurately differences between isomers with different agostic interactions.

	$1s_m$	**$TS_{rot}1_m$**	**$2s_m$**	**$TS_{rot}2_m$**	**$3s_m$**	**$TS_{rot}3_m$**	**$4s_m$**	**$4S_{rot}3_m$**
Mo	1.071	1.067	1.084	1.090	1.389	1.457	1.407	1.475
C1	-0.452	-0.547	-0.406	-0.532	-0.461	-0.558	-0.420	-0.531
H[a]	0.222	0.235	0.224	0.237	0.218	0.244	0.219	0.244
N	-0.456	-0.511	-0.472	-0.533	-0.523	-0.600	-0.539	-0.612
X (C,O)	-0.798 / -0.800	-0.740 / -0.702	-0.792 / -0.792	-0.728 / -0.699	-0.729 / -0.731	-0.686 / -0.690	-0.725 / -0.725	-0.677 / -0.689
C3	-0.752	-0.750	-0.755	-0.749	-0.753	-0.751	-0.755	-0.752
$CH_{3,ene}$[a]	0.008	0.005	0.014	0.004	0.005	0.002	0.010	0.006
imido[a]	-0.242	-0.326	-0.303	-0.378	-0.313	-0.416	-0.361	-0.469
X[a]	-0.319 / -0.321	-0.259 / -0.192	-0.308 / -0.306	-0.240 / -0.182	-0.421 / -0.417	-0.364 / -0.264	-0.415 / -0.408	-0.352 / -0.358

[a] H, $CH_{3,ene}$, and imido stand for the alkylidene α-hydrogen and the methyl groups of the alkylidene and the complete imido ligand, respectively. X is each complete ancillary ligand, opposed to X (C, O) that represents only the coordinative atom of the ligand.

Table XIII-3. NPA charges for **$1s_m$-$4s_m$,** and **$TS_{Rot}1s_m$-$TS_{Rot}4s_m$**, for the models of Mo.

Although the changes of properties (E, $\nu_{C\text{-}H}$, $J_{C\text{-}H}$) between **1**, **2**, **3** and **4** are small, they all indicate the same trend. The *syn* isomer has an α-C-H agostic interaction from the alkylidene group, which does not exist in the *anti* isomer. The strength of the agostic interaction decreases as alkyl groups are replaced by alkoxy groups. It is thought that agostic interactions are favored by an electron-deficient metal. There are no differences in charge between the *syn* an the *anti* conformers (see Table XIII-3). The NPA charge on the molybdenum center increases from $\mathbf{2s_m}$ (1.08) to $\mathbf{4s_m}$ (1.41), showing that the charge increases with the number of electronegative atoms in the first coordination sphere of the metal. The same trend is observed from $\mathbf{1s_m}$ (1.07) to $\mathbf{3s_m}$ (1.39). This variation in charge therefore does not rationalize the decrease in the strength of the agostic interaction. In contrast, the π-donating ability of the ligands correlates with the change in the agostic interaction: the alkyl groups in **1** and **2** are pure σ-donor ligands, nevertheless **3** and **4** with the two alkoxy groups present π-donor ligands. Increasing the d_π/p_π interactions from **1** to **3** and from **2** to **4** decreases the weak α-C-H agostic interaction and the *syn*/*anti* ratio. We will discuss later how the π-donating ability of the ligand influences the α-C-H agostic interaction by influencing the shape and energy of the frontier metal d orbitals of the complexes.

Fluxionality of [Mo(=NR)(=CR)$(X)_2$]. It has been established that the interconversion between *syn* and *anti* isomers is slow and that heating is necessary. Interconversion can occur via the rotation of the alkylidene group or via hydrogen transfer between ligands.[9] Nonetheless, isotope labeling has shown that H scrambling occurs very slowly in all Re(≡CR)(=CHR)(X)(Y) complexes.[11,20-26] Scheme XIII-3 shows the different fluxionality paths. The rotation of the alkylidene connects directly *syn* and *anti* isomers, and we studied this process for $\mathbf{1_m}$-$\mathbf{4_m}$. Enthalpies for alkylidene rotation have been established for $\mathbf{2_m}$ 10.8 kcal·mol^{-1}, for $\mathbf{4_m}$ 12.2 kcal·mol^{-1}, for $\mathbf{1_m}$ 11.6 kcal·mol^{-1}, and for $\mathbf{3_m}$ 13.0 kcal·mol^{-1}, indicating an increase of the energy barrier with more electron-withdrawings alkoxy groups,[9] and also the increase of the aromaticity of the ligand attached to the amine. For W there is a similar behavior, but the increase of the barrier for the insertion of the alkoxy ligands is higher because W is a metal more electropositive (11.8, 11.0, 17.2, and 16.5 kcal·mol^{-1} for isomers $\mathbf{1_m}$-$\mathbf{4_m}$ respectively).

All the studies have been limited to the small systems at the QM level due to the high computational cost of calculating TS for the experimental systems **1-4**.

Figure XIII-4 gives the geometries of the transition states $\mathbf{TS_{rot}}\boldsymbol{n}_{\mathbf{q}}$ (*n* = 1, 2, 3, and 4) and the rotational barriers of the alkylidene group in $\mathbf{1_m}$, $\mathbf{2_m}$, $\mathbf{3_m}$ and $\mathbf{4_m}$ for Mo and W. In all cases, the rotation of the alkylidene preserves the tetrahedral coordination at the metal center, but noticeable geometrical changes occur at the imido and alkylidene groups. At the transition states, the Mo-N and Mo-C distances increase for both the imido and the alkylidene ligands. For instance on going from **Mo-1s$_m$** to **Mo-TS$_{rot}$1$_m$**, both bonds elongate by 0.04 and 0.02 Å, respectively. The N-Mo-C1 angle opens and becomes larger than 109º (110.9º). The imido bends significantly with an angle Mo-C1-C2 of 145.2º for $\mathbf{TS_{rot}1_m}$. The energy barrier for the alkylidene rotation is high since $\mathbf{TS_{rot}1_m}$ is 11.6 kcal·mol^{-1} higher in energy than $\mathbf{1s_m}$, supporting a slow *syn*/*anti* interconversion compared to the similar Re complexes where the barrier is approximately the double (22.8 kcal·mol^{-1}). Similar geometrical patterns are obtained for $\mathbf{TS_{rot}3_m}$, and the energy barrier is 13.0 kcal·mol^{-1} (24.3 kcal·mol^{-1} for Re). Therefore the syn/anti interconversion is easier with the presence of alkyl ligands by 1.4 kcal·mol^{-1}. However, the replacement of the methylimido ligand by a phenylimido ligand means a decrease of the barrier of only 0.8 kcal·mol^{-1}. The difference of the barriers are the same attending to the replacement of the imido ligand, nevertheless, the replacement of the alkyl ligands by alkoxy ones supposes a higher increase of the barriers.

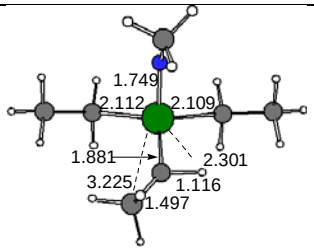

$TS_{rot}1_m$ (11.6)

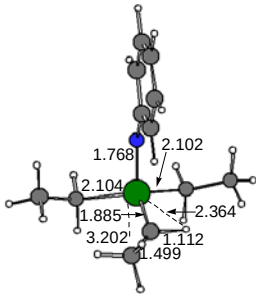

$TS_{rot}2_m$ (10.8)

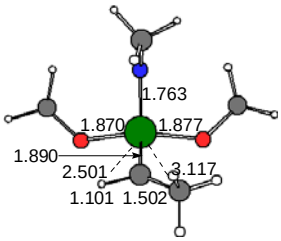

$TS_{rot}3_m$ (13.0)

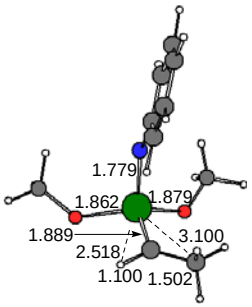

$TS_{rot}4_m$ (12.2)

Figure XIII-4. Transition state structures for the alkylidene rotation in Mo-**1_m**-**4_m** and their energies (kcal·mol^{-1}) relative to the *syn* isomers. Distances in Å and angles in degrees.

Some H transfer processes could be possible but as Solans-Monfort et al. found for Re(≡C-CH_3)(=$CHCH_3$)(C_2H_5)$_2$ where H transfer occurs between all ligands: alkyl / alkylidene, alkylidene /alkylidyne, and alkyl/alkylidyne, the latter forming a tris-alkylidene isomer of the reactant, Re(=CHR)$_3$(CH_2R). The barriers are further larger than the rotational barriers of the alkylidene group (22.8 kcal·mol^{-1}) being 40.5 kcal·mol^{-1}, 43.4 kcal·mol^{-1}, and 45.6 kcal·mol^{-1}. So, this is the reason why we have only analyzed here the rotational barriers of the alkylidene ligand.

It appears that the transfer of hydrogen between any ligand is associated with high-energy barriers, indicating very slow isotope scrambling, in good agreement with experimental data.[11,26] Therefore it is not necessary to calculate these barriers for Mo or W. The rotation around the alkylidene group has a much lower barrier and is the preferred fluxional process, and accounts for the *syn*/*anti* interconversion upon heating.

The high-energy barriers associated with the H transfer between the perhydrocarbyl ligands are in agreement with the rarity and slowness of α-H transfer processes.[36,63-66]

The imido-alkylidene molybdenum or tungsten complex is formally a 14-electron complex and is therefore unsaturated. However, formal electron counting has no relation with the charge at the metal center, which may represent better the properties of the complex. The NPA charge on rhenium increases from 1.07 for **1s$_m$** to 1.39 for **3s$_m$**, and from 1.08 for **2s$_m$** to 1.41 for **4s$_m$**, indicating that the metal is more electron poor in the presence of the alkoxy ligands than in the presence of the alkyl ligands, and the phenyl units of the imido ligand of **2s$_m$** and **4s$_m$** extract negative charge, but the difference is very slight. This shows that the total charge at the metal is driven by the electron-accepting ability of the alkoxy group and not by the d_π /p_π donation from the oxygen lone pair. However, this criterion cannot explain two results: the presence of an α-C-H agostic interaction in the *syn* isomer only and the decrease of the strength of the agostic interaction with an increasing number of OR groups. The lack of relation between the agostic interaction and the charge on the metal shows that the agostic interaction does not have an electrostatic origin. It has been recognized that an agostic interaction requires an empty coordination site with strong acidic Lewis character (i.e., a low lying empty orbital that interacts with the C-H bond acting as a Lewis base),[38] yet a nondistorted tetrahedral complex does not have in principle an empty coordination site.[30] We will thus use a molecular orbital diagram to show that a given structural deformation is favorable to the occurrence of a low lying empty orbital that interacts with the (=C-H) bond in the *syn* geometry only.

An ideal T_d ligand field, set by the four σ bonds between Mo and the four ligands, is used as a reference (Figure XIII-5). From this ideal situation, a Walsh diagram is constructed to follow the energy of the five 5d orbitals as a function of the angle N-M-C1 between the imido and alkylidene ligands. In Figure XIII-6, the π interactions between the metal, the alkylidene, and the imido orbitals are considered in two conformations: the coplanar experimentally preferred conformation (left-hand side) and the perpendicular conformation (right-hand side) corresponding to the transition state for the *syn*/*anti* interconversion. Following the conventions, the alkylidene is a CHR^{2-}

ligand and the imido a NR^{2-} ligand; hence the π orbitals of the two ligands are doubly occupied.

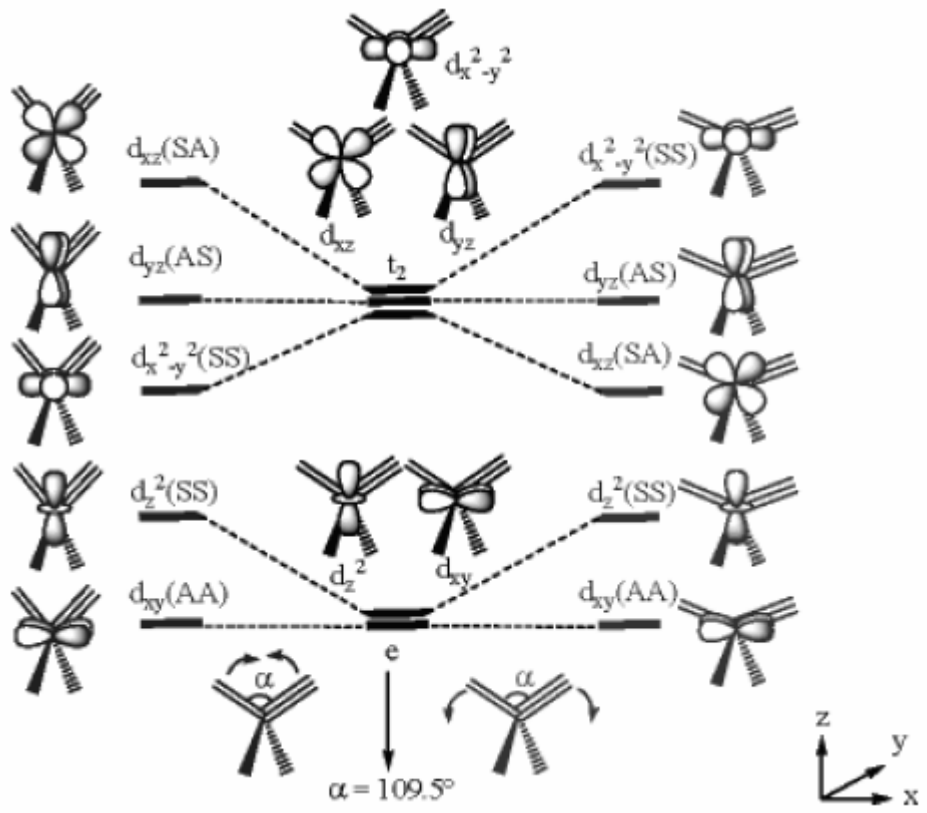

Figure XIII-5. Walsh diagram for the metal d orbitals of a tetrahedral complex as a function of the angle between the alkylidene and imido ligands. The energy scale is qualitative.

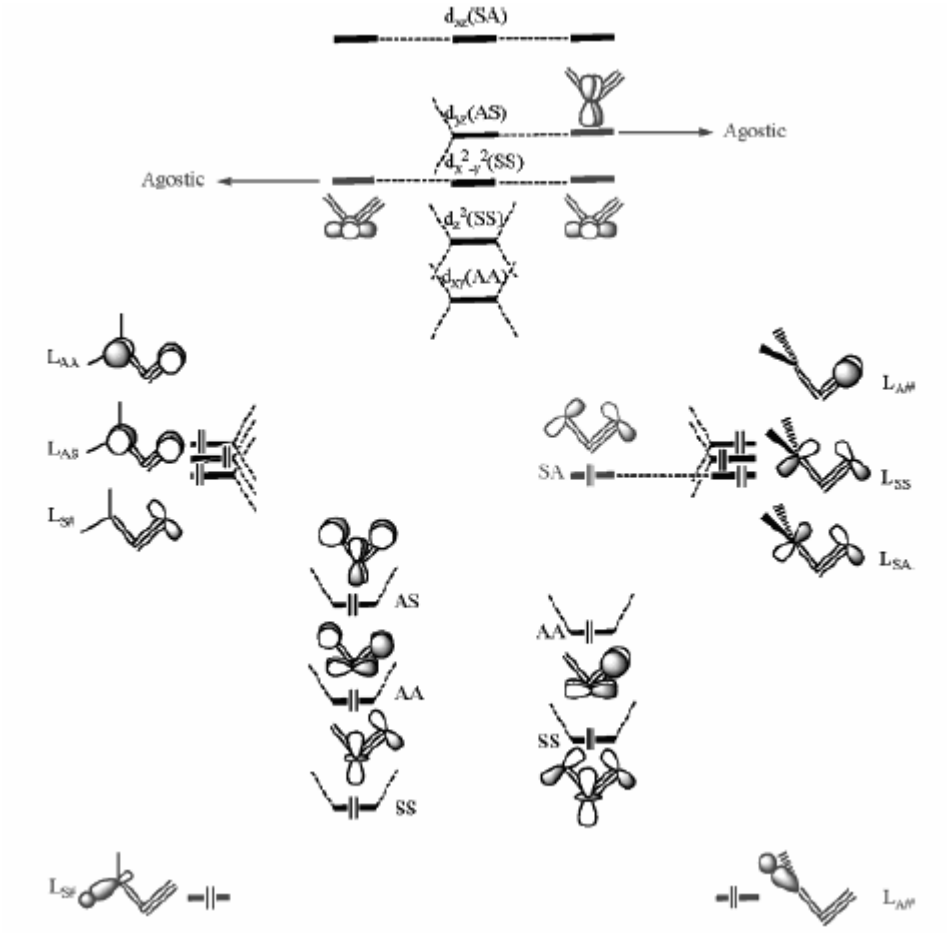

Figure XIII-6. Interaction diagram showing the M-C multiple bonds and the agostic interaction in the coplanar (left) and perpendicular (right) orientation. The energy scale is qualitative.

When the N-M-C1 angle departs from the typical values of a tetrahedral geometry, the degeneracy within the e_g and t_2 orbitals is raised. The $5d_{xy}$ and $5d_{yz}$ orbitals are not affected by a change in the N-M-C1 angle. The decrease of the N-M-C1 angle stabilizes $5d_{x2-y2}$ because the out-of-phase interaction between Mo and the two ligands decreases. For the same angular variation, $5d_{z2}$ and specifically $5d_{xz}$ are destabilized. Conversely, when the N-M-C1 angle increases, $5d_{xz}$ is stabilized, while $5d_{z2}$ and $5d_{x2-y2}$ are destabilized.

The d_π/p_π interaction is added to the metal d orbitals in the coplanar orientation, and the qualitative features do not depend on the N-M-C1 angle. The alkylidene and imido π orbitals mix to be adapted to the approximate symmetry of the complex with respect to the *xz* and *xy* planes. Thus the in-phase and out-of-phase combinations of the p_y

orbitals of the two ligands are L^{C}_{AS} and L^{C}_{AA}, where the labels indicate the symmetry with respect to the *xz*/*yz* planes and C stands for coplanar. The other π orbital of the imido, in the *xz* plane, does not combine in any significant manner with an orbital on the alkylidene ligand and is thus labeled as $L^{C}_{S\#}$. The metal d orbitals combine with the three ligand π orbitals to form three M-C π bonds: $5d_{xy}$ and $5d_{yz}$ combine with L^{C}_{AA} and L^{C}_{AS}, respectively, and $5d_{z2}$ has the nodal properties to fit $L^{C}_{S\#}$. This leaves two metal d orbitals for additional interactions ($5d_{x2-y2}$ and $5d_{xz}$). In the case of a small N-M-C1 angle, $5d_{x2-y2}$ is at relatively low energy and is spatially well adapted to interact with the C-H bond, which lies in the *xz* plane, giving rise to the C-H agostic interaction for the *syn* isomer. In the case of a large N-M-C1 angle, the $5d_{x2-y2}$ is at higher energy and the $5d_{xz}$ is not so well directed to overlap with the C-H bond, so that no C-H agostic interaction can be implemented.

In summary three M-C π bonds can be implemented for the *syn* and *anti* orientations. In addition, for the *syn* isomer, a decrease of the N-M-C1 angle lowers a metal d orbital that is spatially well adapted to be reached by the C-H bond, giving rise to an α-C-H agostic interaction. In the *anti* isomer, the C-C bond can make an agostic interaction, while the C-H bond no longer finds an accessible empty metal d orbital. This molecular orbital analysis shows that the M-C multiple bonds of the imido and alkylidene can be combined with an α-C-H agostic bond in quasi-tetrahedral complexes for a specific orientation of the ligands. This clearly indicates a different electronic situation from that of regular tetrahedral complexes such as Cl_3TiMe, for which no agostic interaction is observed. In the complex with the full substituent set, the steric factors open the N-M-C1 angle to diminish the repulsion between the bulky groups on the imido and alkylidene. This disfavors the C-H agostic interaction, but this is compensated by an increase in the M-C1-C2 angle, which brings the C-H bond of the alkylidene closer to the metal center.

Figure XIII-7 shows the actual orbitals responsible for the three occupied Mo-C π bonds. The close proximity in energy of the two lower orbitals (labeled SS and AA) comes from the relatively close proximity in energy of the $5d_{xy}$ and $5d_{z2}$ orbitals (Figures XIII-5 and -6). The AS orbital is significantly higher because of the higher energy of $5d_{yz}$, which stabilizes less efficiently the ligand π orbitals. The C-H agostic

interaction could be identified only through the out-of-phase combination of the metal orbital (a distorted $5d_{x2-y2}$) and the C-H contribution because the in-phase combination is diluted among many occupied orbitals.

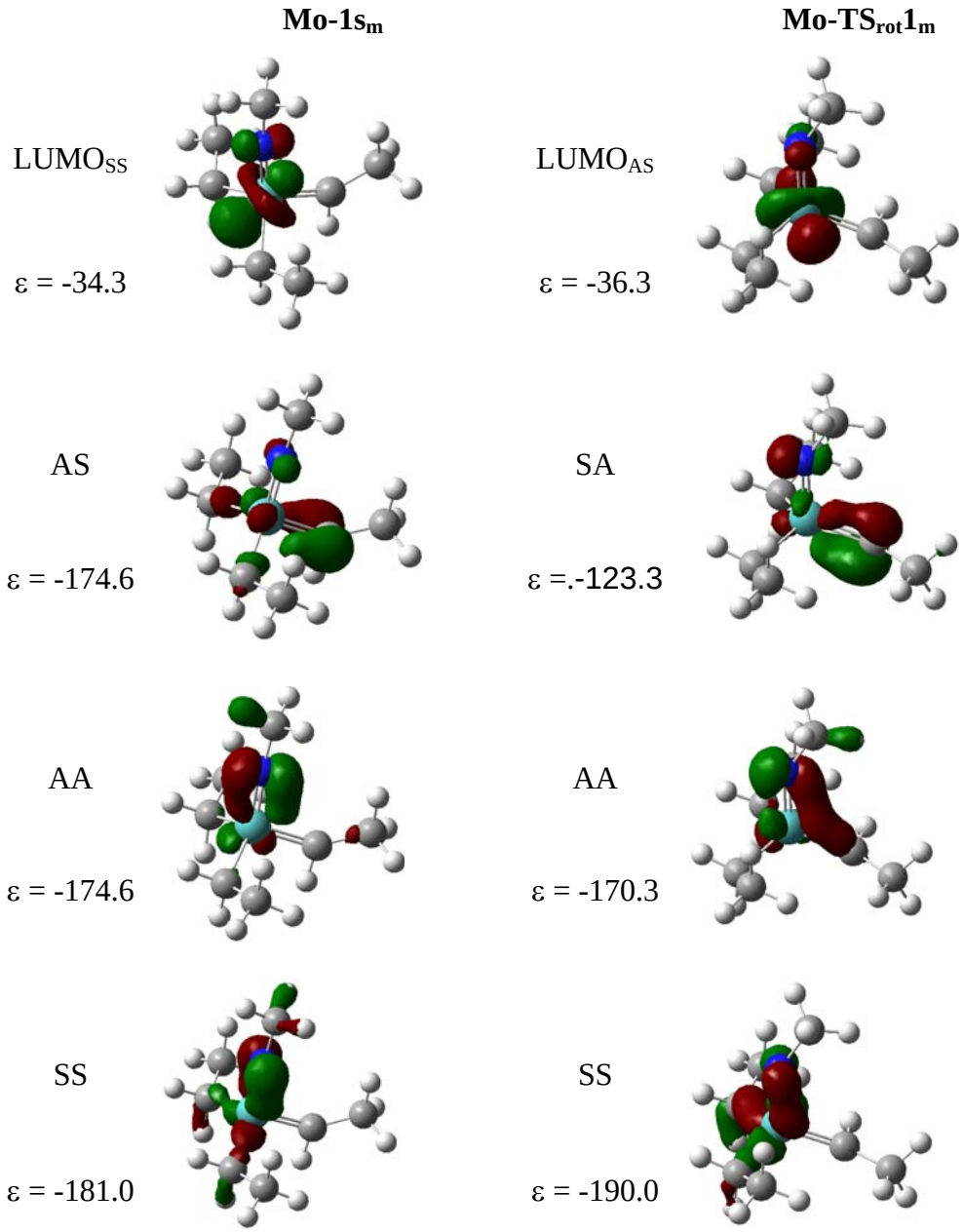

Figure XIII-7. Molecular orbitals for the *syn* isomer (left) and transition state structure for alkylidene rotation (right) of **1s$_m$**.

Rotating the alkylidene group modifies first the M-C π bonding. The in-phase and out-of-phase combinations of the alkylidene and imido π orbitals lie in the *xz* plane and are labeled L^P_{SS} and L^P_{SA} (where P stands for perpendicular). The isolated π orbital of

the imido is perpendicular to the *xz* plane and is labeled $L^{P}_{A\#}$. The L^{P}_{SA} orbital does not find a good match with the metal orbital and thus remains nonbonding with respect to the metal. The two other ligand orbitals L^{P}_{SS} and $L^{P}_{A\#}$ match $5d_{xy}$ and $5d_{z2}$, and four electrons are thus stabilized, giving rise formally to two Mo-C π bonds in place of three π bonds in the coplanar geometry. Thus going from the ground state **1s$_m$** to the transition state **TS$_{rot}$1$_m$** results in the loss of M-C π bonding. The energy barrier for the alkylidene rotation is in fact quantitatively determined by the energy of the M-C π bonds. The sum of the three occupied orbitals describing the π orbitals of the alkylidene and the imido ligands in the coplanar arrangement is 26.6 and 22.7 kcal·mol^{-1} more stable than the sum of the two M-C π orbitals and the nonbonding orbital located on the imido and the alkylidene, for Mo and W respectively. This clearly shows that these three orbitals have a determinant role in the alkylidene rotation barrier. Similar qualitative arguments have been proposed in related isoelectronic imido-alkylidene Re, Mo and W complexes.[33,38a] Nevertheless the energetic difference here is nearly non-existent and this can be explained through the fact that the nonbonding orbital is not really absolutely nonbonding, presenting a strong bonding interaction. Therefore this argument let explain part of the *syn-anti* interconversion barriers. Nevertheless this orbital explanation does not let to see the different barriers for the different metal complexes, either Mo, W, or Re.

The M-imido and the M-alkylidene bonds are both elongated by the alkylidene rotation because the L^{P}_{SA} orbital is delocalized on the two ligands. The L^{P}_{SA} orbital is out-of-phase between the carbons of the alkylidene (C_{ene}) and imido (C_{yne}) ligands, which induces an opening of the N-M-C1 angle to decrease the antibonding interaction. Furthermore, this orbital is also stabilized by mixing in some σ character, especially at the carbon of the imido group, where sp mixing is stronger. This causes the bending of the imido ligand. The C-H agostic interaction is not excluded in the perpendicular orientation **TS$_{rot}$1$_m$** because the C-H bond can interact with the metal d orbital left unused by the d_π/p_π interactions.

The DFT calculations have indicated that the strength of the agostic interaction decreases when the ancillary alkyl ligands are replaced by OR groups. We have seen how the agostic interaction could result from the interaction in the *syn* isomer of the C-

H bond with a relatively low lying $5d_{x2-y2}$ orbital. The C-H bond is a poor electron donor, and therefore the oxygen lone pair, a better electron donor, replaces the α agostic interaction. This is illustrated by the shape of the molecular orbital d_{x2-y2} in $\mathbf{3s_m}$, in which the C-H contribution has been replaced by the oxygen lone pair (Figure XIII-8). A similar behavior has been noted in Tp'Ta(=CH-*t*Bu)(X)(Y) (Tp' = hydrotris(3,5-dimethylpyrazolyl)borate), X = Y = halide, OR, NR_2), where the C-H agostic interaction decreases with increasing π donation.[67]

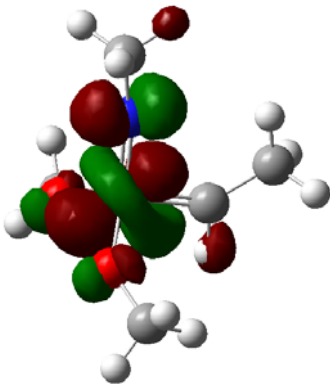

Figure XIII-8. Lowest occupied molecular orbital in $\mathbf{3s_m}$ with the appropriate symmetry to interact with the C-H bond and showing preferred mixing with the oxygen lone pair (out-of-phase combination shown).

We focus on the comparison between $\mathbf{1_m}$ (X = CH_2CH_3) and $\mathbf{3_m}$ (X = OCH_3), and also between $\mathbf{2_m}$ and $\mathbf{4_m}$ species. The higher barrier for $\mathbf{1_m}$ and $\mathbf{3_m}$ agrees with the experimental observation of increasing rotational barriers. An alkyl group is a pure σ-donor group, while an alkoxy group is both a weak σ-donor and a π-donor group. If the weak σ-donor character of the ligand dominates, this reinforces, by synergy, all metal-ligand π bonds and in particular the M-C π bonds because C-based ligands are better electron donors than O-based ligands. If the π-donating effect dominates, this weakens the M-C π bonds. In the first case, the rotational barrier should increase, while it should decrease in the second case. In Table XIII-3 the NPA charges for the simplified complexes are reported. The substitution of X = CH_2CH_3 by the more electron-withdrawing OCH_3 groups leads to an increase of the positive charge at metal, i.e., + $0.4e^-$, and also to an increase of negative charge at the *four* atoms directly bonded to Mo, i.e., $-0.1e^-$. Thus the replacement of CH_2CH_3 by OCH_3 increases the ionic character

of all metal-ligand bonds. No change in electron density is found on atoms not bonded to the metal.

The molecular orbital analysis has shown that rotating the alkylidene group decreases the number of M-C π bonds and forms a high lying molecular orbital essentially located on C_{ene} and N, where C_{ene} (N) is the alkylidene (imido) carbon atom bonded to the metal. This is demonstrated in the NPA analysis by an increased negative charge on both C_{ene} and N centers. This is related to what has been suggested in the related imido Mo and W complexes and alkylidyne Re complexes,[38] where the rotation of the alkylidene group induces a relocalization of the electron density on the sole imido N center due to the difference of electronegativity between C and N.[4]

The charge on the metal does not vary much between $\mathbf{1s_m}$ and $\mathbf{TS_{rot}1_m}$ resulting from a larger donation of electron density from X in the transition state. When X is an alkoxy group, the electron donation from X is smaller and the electron density on C_{ene} is larger. This increased charge separation from ground state to transition state in $\mathbf{3s_m}$ compared to $\mathbf{1s_m}$ is associated with a slightly higher barrier for alkylidene rotation. The same is valid for $\mathbf{4s_m}$ and $\mathbf{2s_m}$.

An AIM analysis of similar Re complexes indicated that the π bond character of the Re-alkylidene bond is increased upon substitution of X = CH_2CH_3 by OCH_3,[38] through the increase of the elipticity of the Re=C bond. Those results suggest a Re-alkylidene π bond more delocalized between Re and C with alkoxy ligands than in alkyl ones, which is consistent with the higher barrier of rotation with alkoxy ligands. By extension, the inclusion of weak σ donor ligands (OR) leads to more ionic Mo-L σ bonds (both M-O and M-C), which is compensated by a reinforcement of M-C and M-N multiple bonds, especially the M-C_{ene} double bond.

Conclusions

The DFT and QM/MM calculations of M(=NR)(=CHR)$(X)_2$ are fully consistent with experimental data. All these complexes adopt a pseudo-tetrahedral structure. An angular distortion at the metal center allows the formation of an α agostic interaction with the bond *anti* to the imido ligand, i. e., the C-H and the C-C bond in the *syn* and *anti*

isomers, respectively. The presence of the C-H agostic interactions in the *syn* isomers is evidenced by geometrical features as well as the ν(C-H) and J_{C-H} coupling constants calculated to be lower than in the *anti* isomers, as observed experimentally in the case of the J_{C-H}.

The C-H agostic interaction is more stabilizing than the C-C agostic interaction, hence a greater stability of the *syn* isomer. Furthermore the higher electrophilicity of *anti* isomers make them be less stable, and confirms the previous fact. Ancillary X ligands that are weak σ-donors and π-donors (OR) compete with the C-H agostic interaction because the oxygen lone pair is a better electron donor to the metal than a C-H bond. Therefore, the *syn* isomer is preferred with ancillary ligands that are pure σ-donors, while the *anti* isomer becomes increasingly preferred with π-donor ligands, and the calculated *syn/anti* ratio is in good agreement with experimental data.

The *syn/anti* inconversion occurs preferentially via the alkylidene rotation, whose energy barrier is high, in agreement with the slow experimental isomerization because of the loss of the Mo-N and Re-C1 π bonds in the transition state. Moreover, H transfers between perhydrocarbyl ligands have much higher energy barriers, showing that these processes do not compete with alkylidene rotation and that α-H scrambling is very slow.

The MO and the electron density analyses show that the strength of the agostic interaction does not increase when the metal becomes more electron poor (ancillary ligands going from alkyl to alkoxy), as indicated by the total charge on the metal center. The agostic interaction is due only to the perturbation of the ligand field away from the tetrahedral geometry.

References

1. R. H. Grubbs, S. Chang, *Tetrahedron* **1998**, *54*, 4413-4450.
2. A. Fürstner, *Angew. Chem. Int. Ed.* **2000**, *39*, 3012-3043.
3. M. R. Buchmeiser, *Chem. Rev.* **2000**, *100*, 1565-1604.
4. R. R. Schrock, A. H. Hoveyda, *Angew. Chem. Int. Ed.* **2003**, *42*, 4592-4633.
5. D. S. Edwards, R. R. Schrock, *J. Am. Chem. Soc.* **1982**, *104*, 6806-6808.

6. D. S. Edwards, L. Vollaro Biondi, J. W. Ziller, M. R. Churchill, R. R. Schrock, *Organometallics* **1983**, *2*, 1505-1513.
7. R. Toreki, R. R. Schrock, *J. Am. Chem. Soc.* **1990**, *112*, 2448-2449.
8. R. Toreki, R. R. Schrock, M. G. Vale, *J. Am. Chem. Soc.* **1991**, *113*, 3610-3611.
9. R. Toreki, R. R. Schrock, W. M. Davis, *J. Am. Chem. Soc*. **1992**, *114*, 3367-3380.
10. R. Toreki, G. A. Vaughan, R. R. Schrock, W. M. Davis, *J. Am. Chem. Soc.* **1993**, *115*, 127-137.
11. A. M. LaPointe, R. R. Schrock, *Organometallics* **1995**, *14*, 1875-1884.
12. R. R. Schrock, *Top. Organomet. Chem.* **1998**, *1*, 1-36.
13. R. R. Schrock, *Acc. Chem. Res.* **1986**, *19*, 342-348.
14. R. R. Schrock, *Acc. Chem. Res.* **1990**, *23*, 158-165.
15. R. R. Schrock, *Polyhedron* **1995**, *14*, 3177-3195.
16. J. Kress, M. Wesolek, J. A. Osborn, *J. Chem. Soc., Chem. Commun.* **1982**, 514-516.
17. J. Kress, J. A. Osborn, *J. Am. Chem. Soc.* **1983**, *105*, 6346-6347.
18. J. Kress, J. A. Osborn, *Angew. Chem., Int. Ed.* **1992**, *31*, 1585-1587.
19. F. Lefebvre, M. Leconte, S. Pagano, A. Mutch, J.-M. Basset, *Polyhedron* **1995**, *14*, 3209-3226.
20. R. R. Schrock, *Chem. Rev.* **2002**, *102*, 145-179.
21. M. Chabanas, C. Copéret, J.-M. Basset, *Chem. Eur. J.* **2003**, *9*, 971-975.
22. C. Copéret, *New J. Chem.* **2004**, *28*, 1-10.
23. M. Chabanas, A. Baudouin, C. Copéret, J.-M. Basset, *J. Am. Chem. Soc.* **2001**, *123*, 2062-2063.
24. C. Copéret, M. Chabanas, R. Petroff Saint-Arroman, J.-M. Basset, *Angew. Chem., Int. Ed.* **2003**, *42*, 156-181.
25. A. Lesage, L. Emsley, M. Chabanas, C. Copéret, J.-M. Basset, *Angew. Chem., Int. Ed.* **2002**, *41*, 4535-4538.
26. M. Chabanas, A. Baudouin, C. Copéret, J.-M. Basset, W. Lukens, A. Lesage, S. Hediger, L. Emsley, *J. Am. Chem. Soc.* **2003**, *125*, 492-504.
27. M. Brookhart, M. L. H. Green, *J. Organomet. Chem.* **1983**, *250*, 395-408.
28. M. Brookhart, M. L. H. Green, L.-L. Wong, *Prog. Inorg. Chem.* **1988**, *36*, 1-124.

29. G. J. Kubas, *Metal Dihydrogen and σ-Bond Complexes: Structure, Theory and Reactivity*; Kluwer Academic Publishers: New York, 2001, and references therein.
30. O. Eisenstein, Y. Jean, *J. Am. Chem. Soc.* **1985**, *107*, 1177-1186.
31. J. H. Oskam, R. R. Schrock, *J. Am. Chem. Soc.* **1993**, *115*, 11831-11845.
32. R. R. Schrock, J. S. Murdzek, G. C. Bazan, J. Robbins, M. DiMare, M. O'Regan, *J. Am. Chem. Soc.* **1990**, *112*, 3875-3886.
33. H. H. Fox, M. H. Schofield, R. R. Schrock, *Organometallics* **1994**, *13*, 2804-2815.
34. R. R. Schrock, W. E. Crowe, G. C. Bazan, M. DiMare, M. B. O'Regan, M. H. Schofield, *Organometallics* **1991**, *10*, 1832-1843.
35. M. Chabanas, PhD Thesis, Université Claude Bernard Lyon I, 2001.
36. K. G. Caulton, M. H. Chisholm, W. E. Streib, Z. Xue, *J. Am. Chem. Soc.* **1991**, *113*, 6082-6090.
37. T. R. Cundari, M. S. Gordon, *Organometallics* **1992**, *11*, 55-63.
38. a) X. Solans-Monfort, E. Clot, C. Copéret, O. Eisenstein, *Organometallics* **2005**, *24*, 1586-1597. b) X. Solans-Monfort, E. Clot, C. Copéret, O. Eisenstein, *J. Am. Chem. Soc.* **2005**, *127*, 14015-14025.
39. E. Clot, O. Eisenstein, In *Structure and Bonding, Computational Inorganic Chemistry*; N. Kaltzoyannis, J. E. McGrady, Eds.; Springer-Verlag: Heidelberg, 2004; pp 1-36, and references therein.
40. A. D. Becke, *J. Chem. Phys.* **1993**, *98*, 5648-5652.
41. J. P. Perdew, Y. Wang, *Phys. Rev. B* **1992**, *45*, 13244-13249.
42. Gaussian 03, M. J. Frisch, G. W. Trucks, H. B. Schlegel, G. E. Scuseria, M. A. Robb, J. R. Cheeseman, J. A. Montgomery, Jr., T. Vreven, K. N. Kudin, J. C. Burant, J. M. Millam, S. S. Iyengar, J. Tomasi, V. Barone, B. Mennucci, M. Cossi, G. Scalmani, N. Rega, G. A. Petersson, H. Nakatsuji, M. Hada, M. Ehara, K. Toyota, R. Fukuda, J. Hasegawa, M. Ishida, T. Nakajima, Y. Honda, O. Kitao, H. Nakai, M. Klene, X. Li, J. E. Knox, H. P. Hratchian, J. B. Cross, C. Adamo, J. Jaramillo, R. Gomperts, R. E. Stratmann, O. Yazyev, A. J. Austin, R. Cammi, C. Pomelli, J. W. Ochterski, P. Y. Ayala, K. Morokuma, G. A. Voth, P. Salvador, J. J. Dannenberg, V. G. Zakrzewski, S. Dapprich, A. D. Daniels, M. C. Strain, Ö. Farkas, D. K. Malick, A. D. Rabuck, K. Raghavachari, J. B. Foresman, J. V. Ortiz, Q. Cui, A. G. Baboul, S. Clifford, J. Cioslowski, B. B.

Stefanov, G. Liu, A. Liashenko, P. Piskorz, I. Komaromi, R. L. Martin, D. J. Fox, T. Keith, M. A. Al-Laham, C. Y. Peng, A. Nanayakkara, M. Challacombe, P. M. W. Gill, B. Johnson, W. Chen, M. W. Wong, C. Gonzalez, J. A. Pople, Gaussian, Inc., Pittsburgh PA, 2003.

43. D. Andrae, U. Häussermann, M. Dolg, H. Stoll, H. Preuss, *Theor. Chim. Acta* **1990**, *77*, 123-141.
44. A. Bergner, M. Dolg, W. Küchle, H. Stoll, H. Preuss, *Mol. Phys.* **1993**, *30*, 1431-1441.
45. W. J. Hehre, R. Ditchfield, J. A. Pople, *J. Chem. Phys.* **1972**, *56*, 2257-2261.
46. R. Krishnan, J. S. Binkley, R. Seeger, J. A. Pople, *J. Chem. Phys.* **1980**, *72*, 650-654.
47. M. Svensson, S. Humbel, R. D. J. Froese, T. Matsubara, S. Sieber, K. Morokuma, *J. Phys. Chem.* **1996**, *100*, 19357-19363.
48. A. K. Rappé, C. J. Casewitt, K. S. Colwell, W. A. Goddard III; W. M. Skiff, *J. Am. Chem. Soc.* **1992**, *114*, 10024-10035.
49. T. Helgaker, M. Watson, N. C. Handy, *J. Chem. Phys.* **2000**, *113*, 9402-9409.
50. W. Kutzelnigg, U. Fleischer, M. Schindler, *NMR-Basic Principles and Progress*; Springer: Heidelberg, 1990.
51. A. E. Reed, L. A. Curtiss, F. Weinhold, *Chem. Rev.* **1988**, *88*, 899-926.
52. J. Jaffart, M. Etienne, M. Reinhold, J. E. McGrady, F. Maseras, *Chem. Commun.* **2003**, 876-877.
53. J. Jaffart, M. L. Cole, M. Etienne, M. Reinhold, J. E. McGrady, F. Maseras, *Dalton Trans.* **2003**, 4057-4064.
54. A. P. Scott, L. Radom, *J. Phys. Chem.* **1996**, *100*, 16502-16513.
55. Selected list: a) J. Khandogin, T. Ziegler, *J. Phys. Chem. A* **2000**, *104*, 113-120. b) G. B. Bacskay, I. Bytheway, N. S. Hush, *J. Am. Chem. Soc.* **1996**, *118*, 3753-3756. c) J. Autschbach, B. Le Guennic, *J. Am. Chem. Soc.* **2003**, *125*, 13585-13593.
56. J. Vaara, J. Jokisaari, R. E. Wasylishen, D. L. Bryce, *Prog. Nucl. Magn. Res. Spectrosc.* **2002**, *41*, 233-304.
57. This $J_{C\text{-}H}$ coupling constant has been measured directly in the ^{1}H NMR of the ^{13}C-labeled compound,[26] which differs from 121 Hz reported by Edwards et al.[6]
58. T. Helgaker, M. Jaszuński, K. Ruud, *Chem. Rev.* **1999**, *99*, 293-352.

59. O. B. Lutnaes, T. A. Ruden, T. Helgaker, *Magn. Reson. Chem.* **2004**, *42*, S117-S127.
60. J. E. Peralta, G. E. Scuseria, J. R. Cheeseman, M. J. Frisch, *Chem. Phys. Lett.* **2003**, *375*, 452-458.
61. J. Jaffart, R. Mathieu, M. Etienne, J. E. McGrady, O. Eisenstein, F. Maseras, *Chem. Commun*. **1998**, 2011-2012.
62. J. Jaffart, M. Etienne, F. Maseras, J. E. McGrady, O. Eisenstein, *J. Am. Chem. Soc.* **2001**, *123*, 6000-6013.
63. S.-H. Choi, Z. Lin, Z. Xue, *Organometallics* **1999**, *18*, 5488-5495.
64. a) T. Chen, Z. Wu, L. Li, K. R. Sorasaenee, J. B. Diminnie, H. Pan, I. A. Guzei, A. L. Rheingold, Z. Xue, *J. Am. Chem. Soc.* **1998**, *120*, 13519-13520. b) L. A. Morton, X.-H. Zhang, R. Wang, Z. Lin, Y.-D. Wu, Z.-L. Xue, *J. Am. Chem. Soc.* **2004**, *126*, 10208-10209.
65. J. D. Fellmann, R. R. Schrock, D. D. Traficante, *Organometallics* **1982**, *1*, 481-484.
66. L. J. Morris, A. J. Downs, T. M. Greene, G. S. McGrady, W. A. Herrmann, P. Sirsch, O. Gropen, W. Scherer, *Chem. Commun.* **2000**, 67-68.
67. J. M. Boncella, M. L. Cajigal, K. A. Abboud, *Organometallics* **1996**, *15*, 1905-1912.
68. D. Cremer, E. Kraka, *Angew. Chem. Int. Ed*. **1984**, *23*, 627-628.
69. S. F. Vyboishchikov, G. Frenking, *Chem. Eur. J.* **1998**, *4*, 1428-1438.

Chapter XIV: *Efficient d^0-Olefin Metathesis Catalysts: which Metal, which Ligands?*

Efficient d^0-Olefin Metathesis Catalysts: which Metal, which Ligands?

Abstract

DFT(B3PW91) calculations on $(MeO)_2Mo(=NMe)(=CHMe)$, $(MeO)_2W(=NMe)(=CHMe)$, and $(MeO)_2Re(\equiv CMe)(=CHMe)$ show that the best olefin metathesis d^0 catalyst results from combining a *4d* metal, which stabilizes the least the metallacyclobutane intermediate, and an imido ligand, which favors the coordination of the olefin.

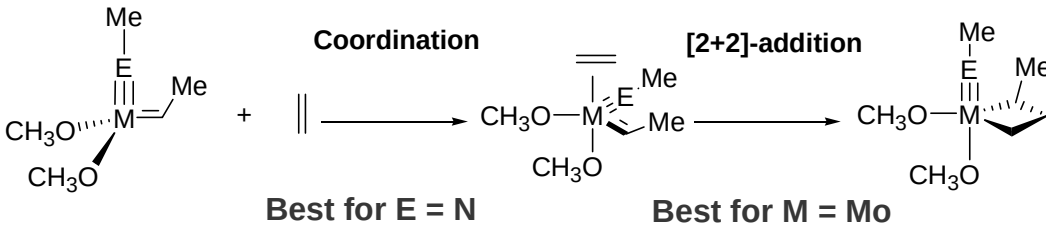

Introduction

Olefin metathesis has become a key process to build carbon-carbon bonds in the development and the synthesis of pharmaceuticals, polymers or basic chemicals.[1] The early mechanistic proposal of Chauvin[2] has lead to the preparation of well-defined metallocarbene catalysts based on early d^0 (groups 6-7)[3-5] or late d^4 transition metals.[6,7]

Experimental works have shown a strong influence of the metal and its ligands on the catalytic activity.[3-7] In the particular case of the catalytic systems developed by Schrock *et al.*,[3-5] the efficiency of the catalysts can be ranked as follows for a set of X alkoxy ligands: $(X)_2Mo(=NR')(=CHR'') > (X)_2W(=NR')(=CHR'') > (X)_2Re(\equiv CR')(=CHR'')$, and it was also shown that the type of alkoxides $\{(CF_3)_2(CH_3)CO > (CH_3)_3CO\}$ and the substituent on the imido moiety (aryl > alkyl) are also critical (Scheme XIV-1). These d^0 systems have attracted the attention of computational chemists,[8-12] but their relative efficiency has not been addressed.

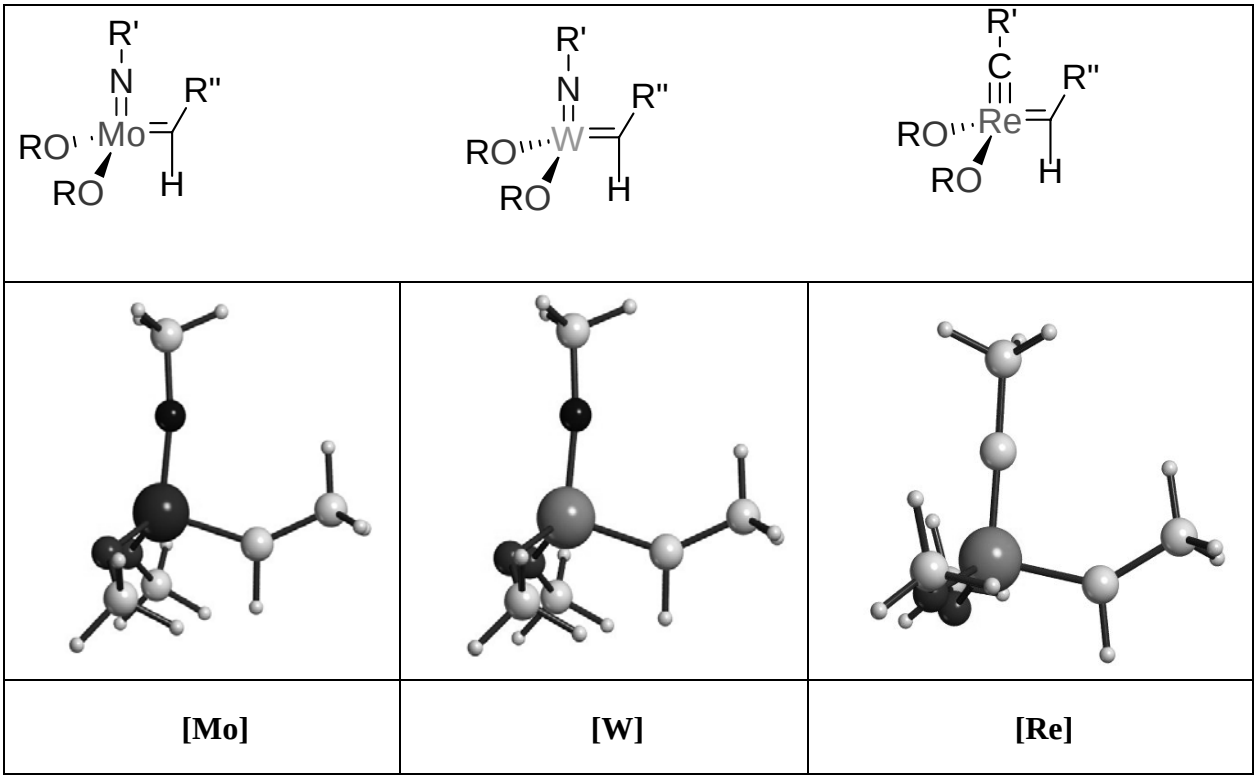

Scheme XIV-1. Calculated structures of **[Mo]** = $(MeO)_2Mo(=NMe)(=CHMe)$, **[W]** = $(MeO)_2W(=NMe)(=CHMe)$, **[Re]** = $(MeO)_2Re(\equiv CMe)(=CHMe)$.

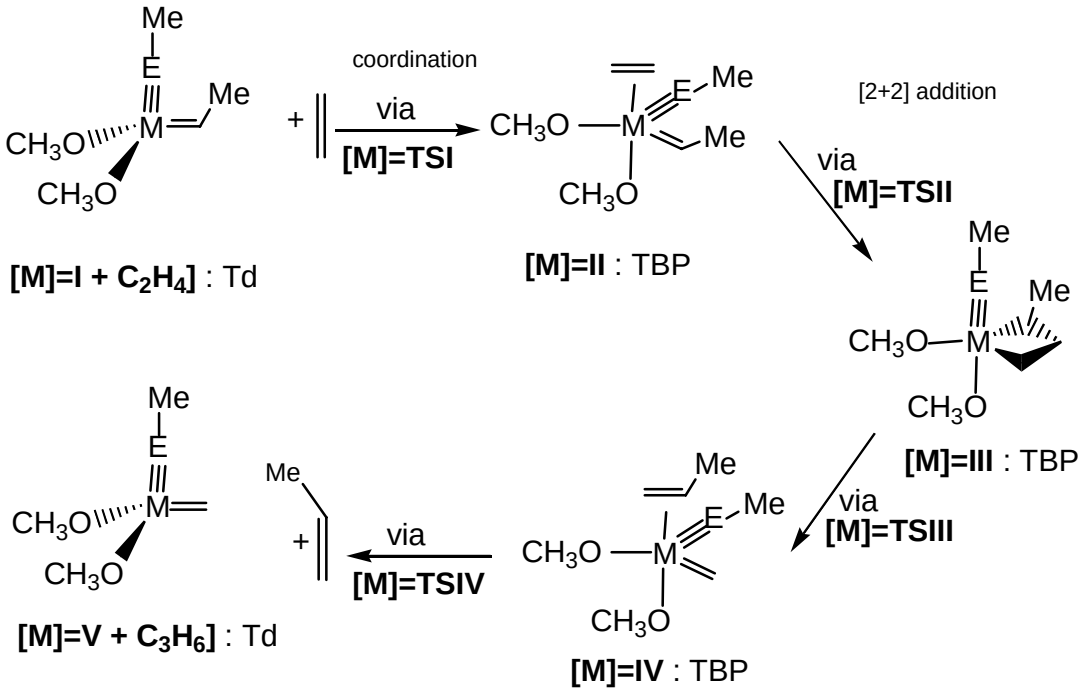

Scheme XIV-2. Olefin metathesis entry and exit pathways of ethylene with $(RO)_2M(\equiv EMe)(=CHMe)$ {**[Mo]** (E = N), **[W]** (E = N) and **[Re]** (E = C)}.

Although the key step has been thought for many years to be the [2+2]-cycloaddition leading to the metallacycle, recent calculations on Re-based systems have shown that the reaction occurs in four elementary steps: the coordination of the entering olefin (a), the metallacycle formation (b) and the corresponding reverse steps (Scheme XIV-2).[12] The energies of the transition states and intermediates are significantly influenced by the nature of the X ligands. In this communication, we study the group 6 imido complexes ([Mo]= $(MeO)_2Mo(=NMe)(=CHMe)$, [W]= $(MeO)_2W(=NMe)(=CHMe)$), we compare them with the isoelectronic group 7 alkylidyne complex ([Re]= $(MeO)_2Re(\equiv CMe)(=CHMe)$) and show how the four elementary step profile is influenced and explains why [Mo] is the most efficient catalyst.

Computational details

Olefin metathesis reaction pathways of ethylene with models of $(RO)_2M(\equiv NR')(=CHR'')$, where M = Mo ([Mo]) and W ([W]); R = R' = R''= Me, have been calculated using DFT(B3PW91)[13,14] methodology with Gaussian03.[15] The Mo, W, and Re atoms were represented with the quasi relativistic effective core pseudo-potentials (RECP) of the Stuttgart group and the associated basis sets augmented with a polarization function.[16] The remaining atoms (C, H, O, and N) were represented with 6-31G(d,p) basis sets.[17] The geometry optimisations were carried out without any symmetry constrain and the nature of the extrema was checked by analytical frequency calculations.

Results

[M]	TSI	II	TSII	III	TSIII	IV	TSIV	V
[Mo]	5.6	0.6	0.8	-13.7	3.4	3.0	5.3	-1.1
[W]	5.9	-[b]	-[b]	-19.5	-[b]	-[b]	4.4	-2.2
[Re]	9.3	-1.2	-[b]	-15.2	2.7	2.3	8.7	-1.7

[a] See text and Scheme XIV-2 for the labelling of extrema. [b] Not located.

Table XIV-1. Energy profiles ($kcal \cdot mol^{-1}$) relative to separated reactants (**[M]-I**+C_2H_4) for the metathesis of ethylene with **[Mo]**, **[W]**, and **[Re]**.[a]

The results summarized in Table XIV-1 are compared to those obtained for $(RO)_2Re(\equiv CR')(=CHR'')$ ([Re]).[12] The structural features of the models for [Mo] and [W]

are similar to those discussed previously for [Re] (Scheme XIV-1).[18] The geometry optimizations are depicted in Figures XIV-1-3.

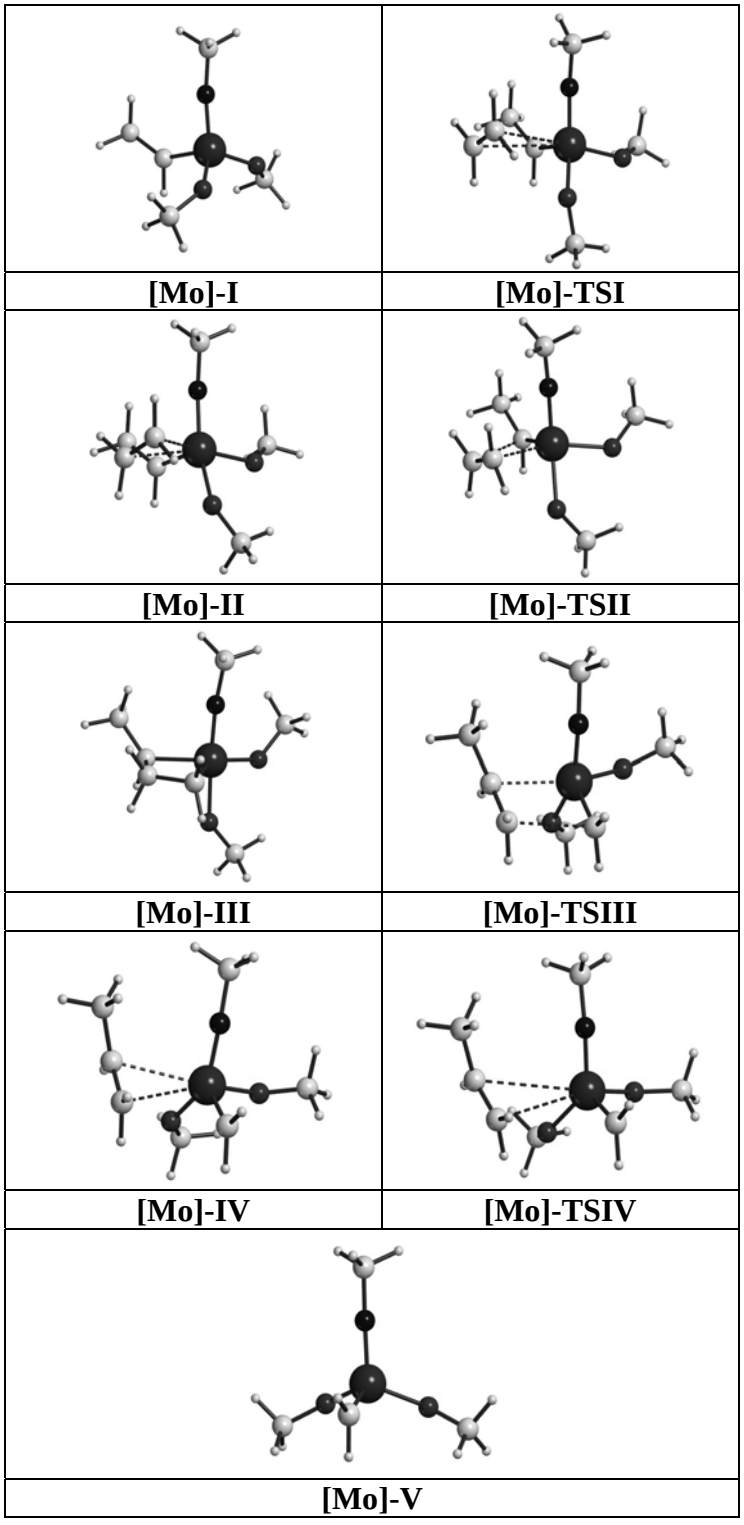

Figure XIV-1. Optimized extrema for the reaction path of ethylene metathesis with $Mo(=NCH_3)(CHCH_3)(OCH_3)_2$.

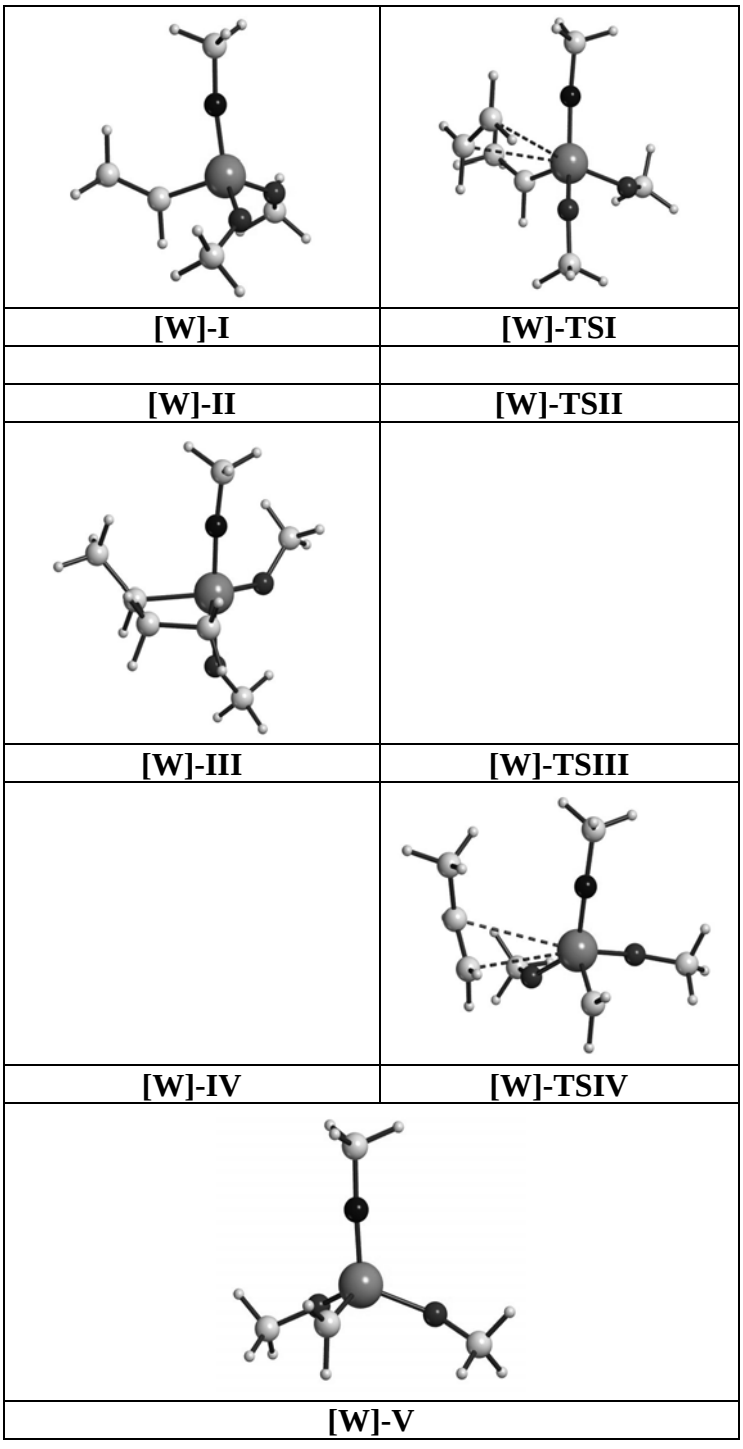

Figure XIV-2. Optimized extrema for the reaction path of ethylene metathesis with $W(=NCH_3)(CHCH_3)(OCH_3)_2$. **[W]-II**, **[W]-TSII**, **[W]-TSIII,** and **[W]-IV** are not located.

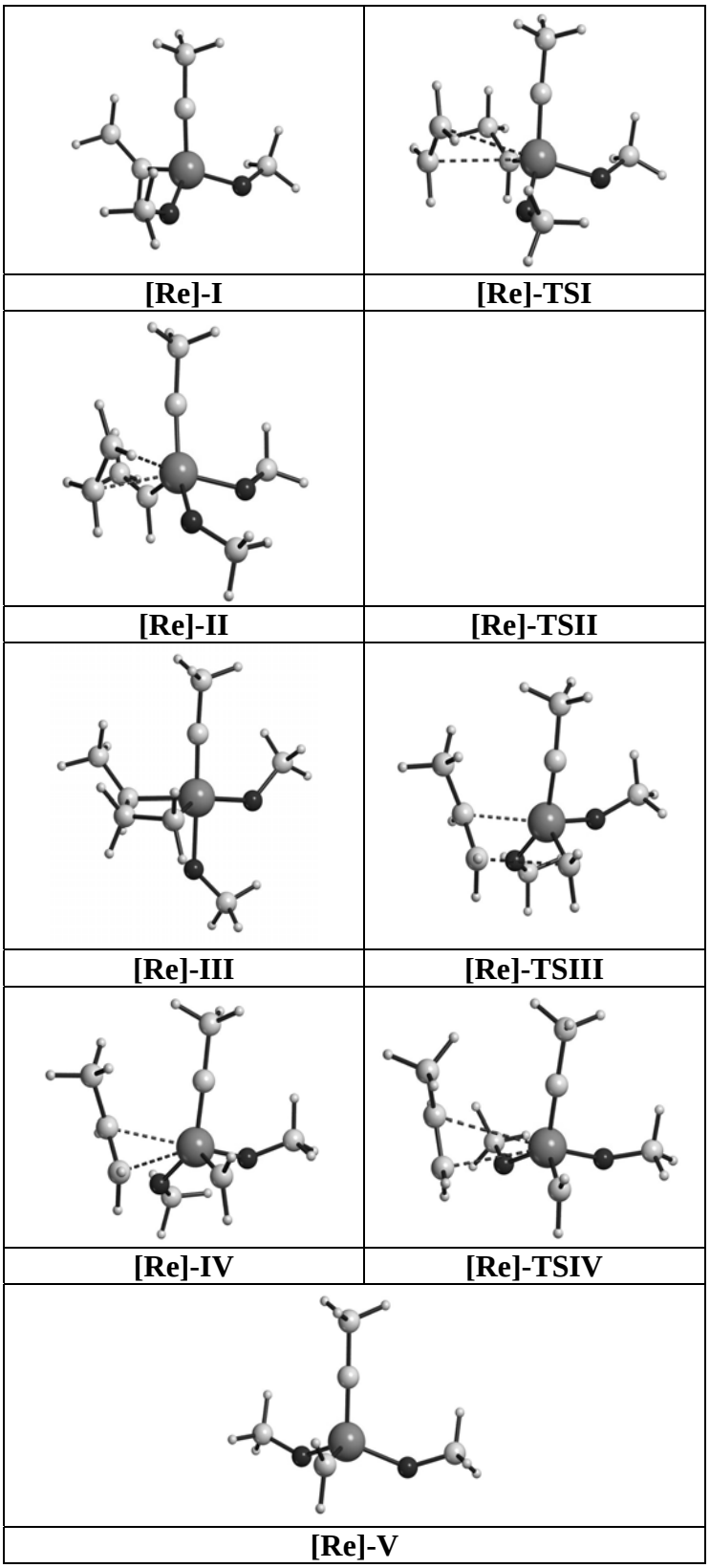

Figure XIV-3. Optimized extrema for the reaction path of ethylene metathesis with $Re(\equiv CCH_3)(CHCH_3)(OCH_3)_2$. **[Re]-TSII** is not located. Oxygen in red sphere.

The four-step mechanism has been found for **[Mo]**.§ The coordination of ethylene (**[Mo]-I**→ **[Mo]-II** via **[Mo]-TSI**) occurs with a distortion of the Mo fragment from a tetrahedral to a trigonal pyramidal geometry with an apical alkoxy group *trans* to the entering olefin (3.21 Å), the three other ligands being in the basal plane, thus constituting an overall trigonal bipyramid (TBP) coordination sphere. From **[Mo]-TSI** to **[Mo]-II**, the N-Mo-O angle opens from 131 to 148°, and the olefin approaches the metal, the distance between Mo and the olefin mid-point varying from 3.21 to 2.38 Å. Then, the [2+2]-cycloaddition (**[Mo]-II** → **[Mo]-III** via **[Mo]-TSII**) yields the metallacyclobutane having a TBP geometry with apical alkoxy and imido groups (N-Mo-O = 175°) through a transition state which has a geometry almost identical to that of **[Mo]-II**. The same structural features are obtained in the following steps of the metathesis process in the exit channel which consists of a cycloreversion (**[Mo]-III** → **[Mo]-IV** via **[Mo]-TSIII**) followed by decoordination of an olefin (**[Mo]-IV** → **[Mo]-V** via **[Mo]-TSIV**).

For **[W]**, the transition states for cycloaddition and cycloreversion (**[W]-TSII** and **[W]-TSIII**) could not be located because of the greater stability of the metallacycle (-19.5 and -13.7 kcal·mol^{-1} for **[W]-III** and **[Mo]-III**, respectively), which is associated with an expected even smaller energy barrier for cycloaddition (< 0.2 kcal·mol^{-1} as found for **[Mo]-II** → **[Mo]-III** via **[Mo]-TSII**). The energy barriers (Table XIV-1) and the geometrical features in **TSI** are very similar for **[Mo]** and **[W]**. In particular, the metal to ethylene mid-point distance is 3.20 Å. Comparing **[Mo]** and **[W]** with **[Re]** shows that the energy barrier of the coordination step is significantly higher for the later (Table XIV-1).

These results show that the coordination step (**[M]-I** → **[M]-II**) is easier for the metal imido complexes (E = N) than for the alkylidyne complex (E = C), but it is similar for **[Mo]** and **[W]**. In contrast, the nature of both the metal and the ligand influences the stability of the metallacycle intermediate as follows: Mo-imido < Re-alkylidyne < W-imido.

Previous work comparing several Re(≡CR)(=CHR)(X)(Y) complexes shows that the energy barrier (ΔE(TSI)) for the first step ([**M]-I** → **[M]-II**) is controlled by the energy

required to distort the tetrahedron to a trigonal pyramid (ΔE_{def}(M)) (Table XIV-2). The olefin is still far from the metal at the transition state leading to a small interaction energy (ΔE_{int}) between the reactants.[12] The same features apply for the three systems: the ΔE_{def}(M) are 6.9, 6.8, and 9.9 kcal·mol^{-1} for **[Mo]**, **[W]**, and **[Re]** respectively, close to the corresponding energy barriers (ΔE(TSI)) of 5.6, 5.9, and 9.3 kcal·mol^{-1}. The distortion energy of the olefin (ΔE_{def}(//)) is negligible. The difference in the ΔE_{def}(M) is not influenced by the metal (*4d vs. 5d*), but is clearly related to the ligand (imido vs. alkylidyne).

In **[Re]-I** and **[Re]-TSI**, there is a Re-C π bond from the alkylidene ligand and two Re-C π-bonds from the alkylidyne ligand. In **[Mo]-I** and **[W]-I** as well as in **[Mo]-TSI** and **[W]-TSI**, there is a M-C π–bond (alkylidene) and two M-N π-bonds (imido). The imido ligand, essentially linear in **[Mo]-I** (171.5°) and **[W]-I** (172.4°), hardly bends in **[Mo]-TSI** (162.4°) and **[W]-TSI** (166.6°). A similar change is seen in the transformation of **[Re]-I** to **[Re]-TSI** where the alkylidyne Re≡C-C angle decreases from 177.7° to 173.2°. While the transformation from **[M]-I** to **[M]-TSI** is not associated with the disappearance of any M-L multiple bonds, an MO analysis of **[M]-I** and **[M]-TSI** shows that the change in the coordination influences the M≡E-R (E-R = N-Me or C-Me) π bonds in the basal plane (see Figures XIV-4-6). The π-bonds in a tetrahedron (**[M]-I**) use metal orbitals that are either nonbonding or slightly antibonding with the other ligands.[19] In a trigonal pyramid, the metal-alkylidene and the M≡E π bond, perpendicular to the basal plane, use nonbonding d_{xz} and d_{yz} orbitals, but the other M≡E π bond, in the basal plane, uses a $d_{x^2-y^2}$ orbital, which is antibonding with the alkoxy ligand (Scheme XIV-3). The resulting destabilization of $d_{x^2-y^2}$ significantly decreases the M≡E π interaction. This is more unfavourable for the less electronegative atom E = C than for E = N. To compensate this loss of M≡E interaction in the basal plane, the M≡E-R angle slightly bends without ever forming a localised lone pair at E. The change in energy of the three molecular orbitals associated with the M=C and M≡E π bonds on going from **[M]-I** to **[M]-TSI** shows that the orbital of the M≡E π bond, in the basal plane, is the only one significantly destabilized and that the destabilization is twice as larger for E = C (**[Re]**) than for E = N (**[Mo]** and **[W]**) (Figures XIV-1-3). Thus, the imido complexes are easier to distort because the energy of the M≡E π bonds are less influenced by change in coordination at the metal centre for E = N.

[M]	$\Delta E(TSI)^a$	$\Delta E_{def}(M)^a$	$\Delta E_{def}(//)^a$	$\Delta E_{int}{}^a$
[Mo]	5.6	6.9	0.0	1.3
[W]	5.9	6.8	0.1	1.0
[Re]	9.3	9.9	0.1	0.7

[a] See text for definitions.

Table XIV-2. Analysis of the energy barrier for [M]-TSI (kcal·mol^{-1}) in terms of distortion and interaction energies of the reactants.

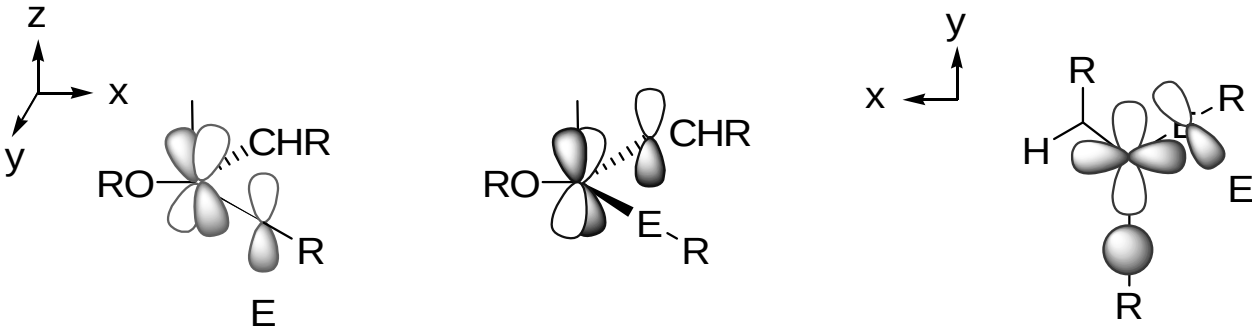

Scheme XIV-3. Schematic molecular orbitals involved in M=C and M≡E π bonds.

[Mo]-I	[Mo] –TSI
	
ε = -0.217	ε = -0.210
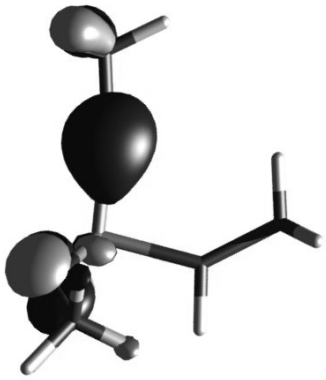	
ε = -0.242	ε = -0.235
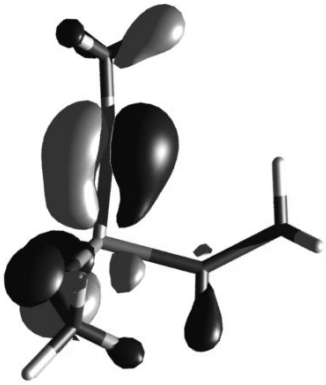	
ε = -0.265	ε = -0.250

Figure XIV-4. Three highest molecular orbitals describing the Mo=C and Mo≡N π bonds in [Mo]-I and [Mo]-TSI. Energies in a.u

[W]-I	[W] –TSI
	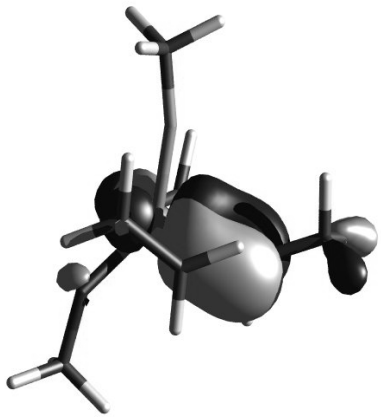
ε = -0.209	ε = -0.203
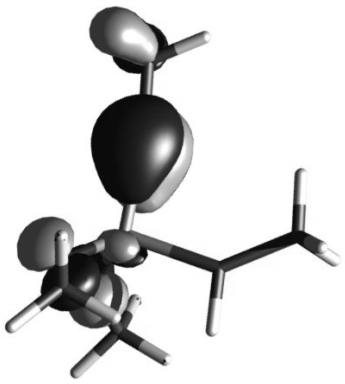	
ε = -0.243	ε = -0.234
	
ε = -0.262	ε = -0.250

Figure XIV-5. Three highest molecular orbitals describing the W=C and W≡N π bonds in **[W]-I** and **[W]-TSI**. Energies in a.u.

[Re]-I	[Re]-TSI
	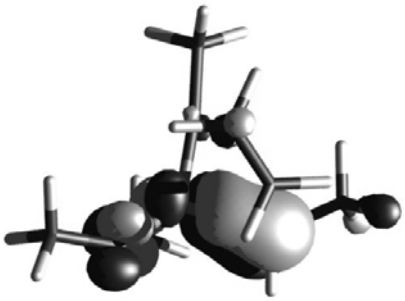
ε = -0.204	ε = -0.201
	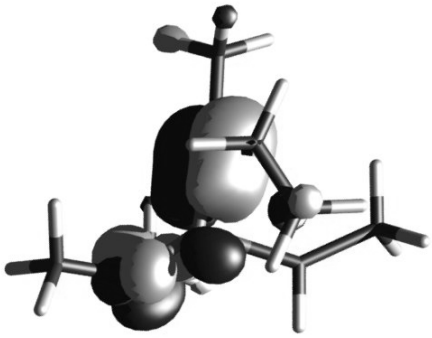
ε = -0.238	ε = -0.227
	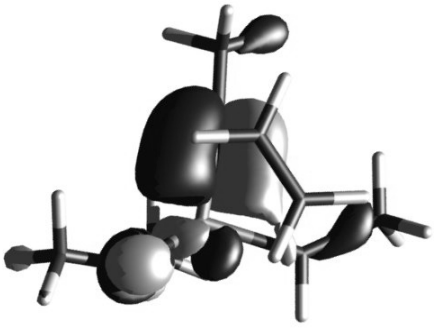
ε = -0.255	ε = -0.231

Figure XIV-6. Three highest molecular orbitals describing the Re=C and Re≡C π bonds in [Re]-I and [Re]-TSI. Energies in a.u.

In the next step (**[M]-II** → **[M]-III**), the formation of the metallacycle **[M]-III** is associated with the disappearance of the M=C and C=C π bonds and the formation of M-C and C-C σ-bonds. Thus, the origin of the relative stability of the metallacyclobutanes was studied using a thermodynamic cycle based on the bond dissociation energies (BDE) of the M=C, C=C π bonds and M-C and C-C σ-bonds (black part of Scheme XIV-4 and Table XIV-3). A similar scheme was used previously

to compare $M(H_2)$ and $M(H)_2$ complexes.[21] In **[M]-I**, the BDE of the M=C π-bond is the energy difference between the triplet and singlet optimized geometries. The π-bond BDE in C_2H_4 is evaluated in a similar way.‡ The M-C and C-C σ-bond BDEs in **[M]-III** are the energy difference between **[M]-III** in its singlet state and the optimised triplet states of **[M]-I** and C_2H_4. The C-C BDE in **[M]-III** is essentially independent of the metal (see Scheme XIV-5 and Table XIV-4). Thus, Scheme XIV-4 shows that the relative stabilities of the metallacycles depends mostly on the BDEs of the alkylidene M=C π bond in **[M]-I** and the M-C σ-bond BDE in the metallacycle.

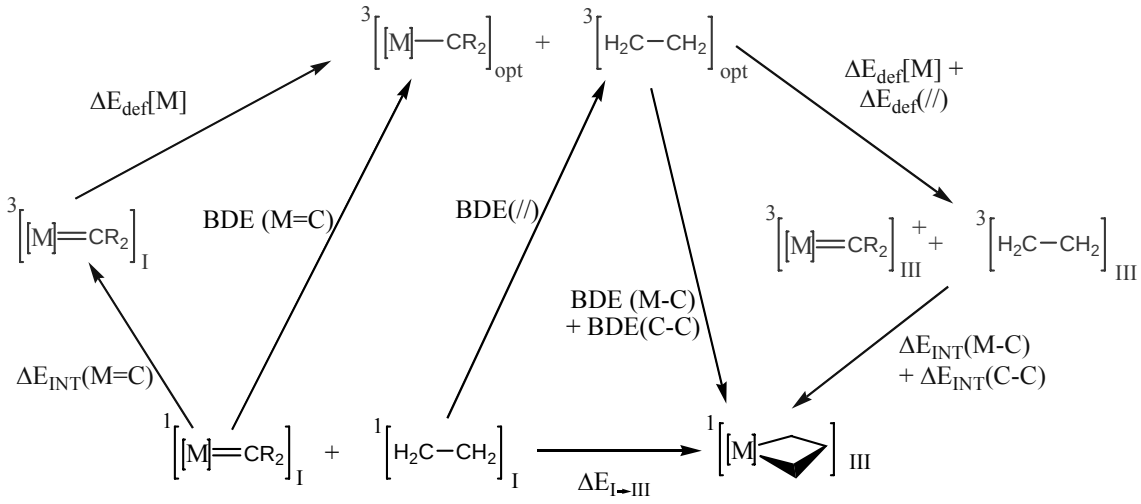

Scheme XIV-4. Analysis of the energy of formation of **[M]-III**.

	[Mo]	[W]	[Re]
ΔE	- 13.7	- 19.5	- 15.2
BDE(M=C)	- 32.0	- 37.5	- 33.6
BDE(C=C)	- 61.8	- 61.8	- 61.8
ΔE_{INT}(M=C)	- 68.8	- 77.1	- 68.8
$-\Delta E_{rel}$[M]	- 36.8	- 39.5	-35.2
BDE (M-C) + BDE(C-C)	-107.5	-118.8	-110.5
ΔE_{def}(//)	+ 24.9	+ 25.1	+25.1
ΔE_{dis}[M]	+ 26.8	+ 22.7	+32.6
ΔE_{INT}(M-C) + ΔE_{INT}(C-C)	- 159.2	- 166.6	-168.2

Table XIV-3. Energies (kcal·mol^{-1}) associated with Scheme XIV-4.

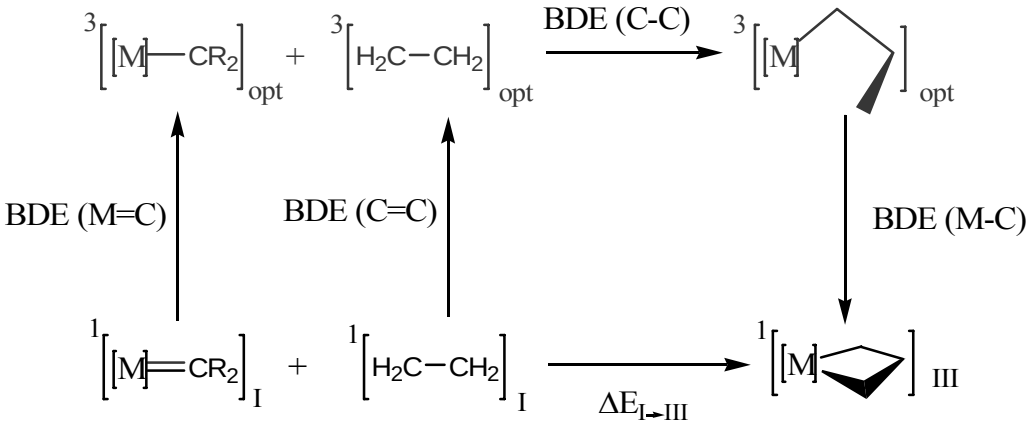

Scheme XIV-5. Analysis of the energy of formation of **[M]-III** to provide a value for C-C bond dissociation energy.

	[Mo]	[W]
$\Delta E_{I \rightarrow III}$	- 13.7	- 19.5
- BDE(//)	+ 61.8	+ 61.8
- BDE(M=C)	+ 32.0	+ 37.5
BDE (C-C)	-77.3	-76.4
BDE (M-C)	-30.2	-42.4

Table XIV-4. Energies (kcal·mol^{-1}) associated with Scheme XIV-5.

Comparing **[Mo]** with **[W]**, **[W]** leads to a stronger W=C π bond and a stronger W-C σ bond, reproducing the stronger M-ligand bonds for *5d* metals.[21] Going from *4d* to *5d* metals has a stronger influence on the M-C σ bond than on the M=C π bonds because of the larger overlap between the metal and the ligand in the former case. Consequently, loosing a M-C π bond and gaining a M-C σ bond is more stabilizing for **[W]** than for **[Mo]**. The differences between **[W]** and **[Re]** are associated with the presence of different E-R groups. To get insight into the role of the E-R group additional thermodynamic cycles (Scheme XIV-4) were designed. Thus, the singlet to triplet excitation of complex **[M]-I** can be decomposed into a vertical singlet to triplet excitation followed by a geometry relaxation of the triplet state. The numerical results show that the vertical and non vertical excitations follow the same trends and that the relaxation energy (ΔE_{def}) is very similar for the three systems. Thus, using several ways

to evaluate the M=C π bond strength gives the same trends: **[Mo]** < **[Re]** < **[W]**. The weaker Re=C π bond is probably associated with the fact that the alkylidyne ligand competes strongly with the alkylidene group for the metal orbitals. In the case of **[W]**, the more electron negative imido group competes less with the alkylidene and leads to a stronger M=C BDE.

The formation of the metallacycle is described by a step where the metal fragment and ethylene in their optimized triplet state are distorted into their geometry in **[M]-III**, followed by a step where the M-C and C-C bonds are formed without relaxation. The first step is associated with the distortion energies of the metal fragment (ΔE_{def}[M]) and ethylene {ΔE_{def}(//)} and the second step with the interaction energy between the two fragments {ΔE_{INT}(M-C) + ΔE_{INT}(C-C)}. The ΔE_{def}[M] is larger for **[Re]-III** than for **[Mo]-III** and **[W]-III** because of the larger trans influence of the alkylidyne ligand at the axial site of the trigonal bipyramidal geometry. The interaction energies are similar for **[W]** and **[Re]** but smaller for **[Mo]** because of the larger M-L overlap for *5d* metals. Thus the greater stabilization associated with the formation of **[W]-III** originates from a larger interaction energy and a smaller distortion energy.

Conclusion

In conclusion, olefin metathesis requires to optimise the coordination of the reactant, the metallacycle formation {[2+2]-cycloaddition}, and the reverse associated steps. In the preparative step, the catalyst needs to acquire a geometry, which opens a coordination site, and the key factor is not the metal but the ligands, which should be preferably electronegative, hence imido > alkylidyne. Noteworthy, the imido ligand does not bend to destroy one of the π M-N bond and localize a lone pair during the reaction path. At the cycloaddition step, the metal is the key factor: *4d* metals are better than *5d* metals because they stabilize less the metallacycle intermediate by making weaker M-C bonds so that overall the best catalyst is the Mo imido complex.

Metathesis is a core reaction for many important industrial processes (triolefin and SHOP processes) and has already been used as a new tool to make carbon-carbon bonds in synthetic organic chemistry. This process is also very likely to be incorporated in the strategy of Research & Development departments of pharmaceutical companies in a

very short term. For these reasons, to understand what makes a good d^0 olefin metathesis catalyst is important and would help to design better systems. In particular, molybdenum imido catalysts have been found to be more efficient than tungsten-imido and rhenium-alkylidyne complexes but the reasons for these differences are yet unknown. We have therefore compared models of three representative d^0 olefin metathesis catalysts, $(CH_3O)_2M(=CHCH_3)(=NCH_3)$ (M = Mo, W) and $(CH_3O)_2Re(=CHCH_3)(CCH_3)$, developed in the group of R.R Schrock, by means of DFT calculations. We have shown that the computed energy profile is indeed best for the Mo-imido complex because it is associated with the lowest energy barriers and the least stable metallacyclobutane intermediate. An analysis of these energy profiles allows understanding these results in terms of everyday chemical concepts, and in particular shows how the nature of the metal and the ligand influences the energy profile.

These results should help to design even more efficient catalysts, which is of immediate interest for a broad audience (organic, organometallic and catalysis communities).

Notes

§ The calculations of ref 11. for the entry channel of the ethylene metathesis with $(CH_3O)_2Mo(=NH)(=CH_2)$ have shown that the two-step process (coordination + cycloaddition) calculated in energy *E* becomes a one-step process in Gibbs free energy G, the unique transition state being associated with the cycloaddition step. For [Mo], the Gibbs free energy profile (298 K and P = 1 atm) still maintains the two step process and in particular shows that $\Delta G_{\mathbf{[Mo]\text{-}TSI}} > \Delta G_{\mathbf{[Mo]\text{-}II}}$.

‡ We verified that the triplet state was associated with a configuration resulting from the breaking of the π bond in each case.

References

1. J. C. Mol, *J. Mol. Catal. A-Chem.* **2004**, *213*, 39-45.
2. J. L. Hérisson, Y. Chauvin, *Makromol. Chem.* **1971**, *141*, 161-176.
3. R. R. Schrock, *J. Mol. Catal. A-Chem.* **2004**, *213*, 21-30.
4. R. R. Schrock, *Polyhedron* **1995**, *14*, 3177-3195.
5. R. R. Schrock, *Top. Organomet. Chem.* **1998**, *1*, 1-36.

6. R. H. Grubbs, S. Chang, *Tetrahedron* **1998**, *54*, 4413-4450.
7. T. M. Trnka, R. Grubbs, H., *Acc. Chem. Res*. **2001**, *34*, 18-29.
8. H. H. Fox, M. H. Schofield, R. R. Schrock, *Organometallics* **1994**, *13*, 2804-2815.
9. Y.-D. Wu, Z.-H. Peng, *J. Am. Chem. Soc*. **1997**, *119*, 8043-8049.
10. Y.-D. Wu, Z.-H. Peng, *Inorg. Chim. Acta* **2003**, *345*, 241-254.
11. T. P. M. Goumans, A. W. Ehlers, K. Lammertsma, *Organometallics* **2005**, *24*, 3200-3206.
12. X. Solans-Monfort, E. Clot, C. Copéret, O. Eisenstein, *J. Am. Chem. Soc*. **2005**, *127*, 14015-14025.
13. A. D. Becke, *J. Chem. Phys*. **1993**, *98*, 5648-5652.
14. J. P. Perdew, Y. Wang, *Phys. Rev. B* **1992**, *45*, 13244-13249.
15. Gaussian 03, M. J. Frisch, G. W. Trucks, H. B. Schlegel, G. E. Scuseria, M. A. Robb, J. R. Cheeseman, J. A. Montgomery, Jr., T. Vreven, K. N. Kudin, J. C. Burant, J. M. Millam, S. S. Iyengar, J. Tomasi, V. Barone, B. Mennucci, M. Cossi, G. Scalmani, N. Rega, G. A. Petersson, H. Nakatsuji, M. Hada, M. Ehara, K. Toyota, R. Fukuda, J. Hasegawa, M. Ishida, T. Nakajima, Y. Honda, O. Kitao, H. Nakai, M. Klene, X. Li, J. E. Knox, H. P. Hratchian, J. B. Cross, C. Adamo, J. Jaramillo, R. Gomperts, R. E. Stratmann, O. Yazyev, A. J. Austin, R. Cammi, C. Pomelli, J. W. Ochterski, P. Y. Ayala, K. Morokuma, G. A. Voth, P. Salvador, J. J. Dannenberg, V. G. Zakrzewski, S. Dapprich, A. D. Daniels, M. C. Strain, Ö. Farkas, D. K. Malick, A. D. Rabuck, K. Raghavachari, J. B. Foresman, J. V. Ortiz, Q. Cui, A. G. Baboul, S. Clifford, J. Cioslowski, B. B. Stefanov, G. Liu, A. Liashenko, P. Piskorz, I. Komaromi, R. L. Martin, D. J. Fox, T. Keith, M. A. Al-Laham, C. Y. Peng, A. Nanayakkara, M. Challacombe, P. M. W. Gill, B. Johnson, W. Chen, M. W. Wong, C. Gonzalez, J. A. Pople, Gaussian, Inc., Pittsburgh PA, 2003.
16. a) D. Andrae, U. Häussermann, M. Dolg, H. Stall, H. Preuss, *Theor. Chim. Acta* **1990**, *77*, 123-141. b) A. W. Ehlers, M. Böhme, S. Dapprich, A. Gobbi, A. Höllwarth, V. Jonas, K. F. Köhler, R. Stegmann, A. Veldkamp, G. Frenking, *Chem. Phys. Lett*. **1993**, *208*, 111-114.
17. W. J. Hehre, R. Ditchfield, J. A. Pople, *J. Chem. Phys*. **1972**, *56*, 2257-2261.
18. X. Solans-Monfort, E. Clot, C. Copéret, O. Eisenstein, *Organometallics* **2005**, *24*, 1586-1597.

19. T. A. Albright, J. K. Burdett, M. H. Whangbo, 'Orbital Interactions in Chemistry', Wiley, 1985.
20. J. Tomàs, A. Lledós, Y. Jean, *Organometallics* **1998**, *17*, 4932-4939.
21. J. A. Martinho Simões, J. L. Beauchamp, *Chem. Rev*. **1990**, *90*, 629-688.

PART VI: Miscellaneous

Miscellaneous

Chapter XV: *Trinuclear Pt(II) Compound with Short Pt-Pt-Pt Contacts. An Analysis of the Influence of π-π Stacking Interactions on the Strength and Length of the Pt-Pt Bond*

Trinuclear Pt(II) Compound with Short Pt-Pt-Pt Contacts. An Analysis of the Influence of π–π Stacking Interactions on the Strength and Length of the Pt-Pt Bond

Abstract

In this work we analize the first example of a trinuclear Pt(II) complex with Pt-Pt-Pt bonds that are not facilitated by direct intervention of bridging ligands but are partially held by the attractive π-π stacking interaction between the phenyl units of the 4,4'-dimethyl-2,2'-bipyridyl ligands. The effect of the π-π stacking interactions on the strength and length of the Pt-Pt bond is discussed using reduced models of the interacting moieties in which the aromatic rings have been removed. The nature of the Pt-Pt bonds is studied through energy decomposition and atoms-in-molecules analyses. The results indicate that the relatively strong (about 40 kcal·mol^{-1}) Pt-Pt metallic bond has similar covalent and ionic contributions.

Introduction

While extensive studies have been carried out on multinuclear complexes of ruthenium, osmium, rhodium, and iridium, much less work has been devoted to multinuclear platinum or palladium complexes.[1] Furthermore, in most of the known Pd(II) and Pt(II) multinuclear complexes, the metal atoms are held together by bridging ligands, making it unclear whether there is metal-metal bonding or the two metals are held together by the chelating ligands.[2] For instance, a crystal structure for a trinuclear complex of formula [M_3(mercaptonicotinic acid)$_3Cl_3$] (M = Pd(II) and Pt(II)) in which the sulphur atom acts as a bridge between two metal (Pd(II) or Pt(II)) atoms was reported in 1999.[3] Homobinuclear platinum complexes, where a bridging aromatic or iminic ligand separates the platinum centres by at least 5 Å, have been reported too,[1] but in this case the interaction of the two platinum centres takes place via its unsaturated π system. Different cases have been described in the literature in which the π-π interaction between the π-conjugated ligands is an important factor in the assemblage of the platinum complexes.[4]

Llobet et al.[5] report here the structural properties of an unexpected trinuclear Pt(II) compound containing the 4,4'-dimethyl-2,2'-bipyridyl ligand. To our knowledge this is the first structure reported for a trinuclear complex of Pt(II) in which intramolecular Pt-Pt-Pt linear contacts are not facilitated by direct intervention of bridging ligands, and with the *trans* disposition for the 2,2'-bipyridine (Bpy) ligand. Although Bpy ligands are commonly used in the formation of different complexes with a great variety of transition metals, the vast majority of metal bis(2,2'-bipyridine) complexes studied by X-ray diffraction possess *cis* geometries.[6-8] Indeed, a general search in the Cambridge Structural Dates Base (CSD) showed that crystal structures of compound type *trans* $M(Bpy)_2$ are not very common, although some cases are described, mainly for ruthenium.[8-9] However, only few cases have been described for bis(bipyridine) complexes of d^8 metal ions (Pd(II), Pt(II)) with this unusual form of the *trans* disposition for bipyridine ligands.[10] In addition, both external platinum atoms present *cis*-platinum structures that might be especially appropriate for antitumoral purposes.[11]

The aim of this work is to study the role played by the π-π stacking interactions between the π-conjugated ligands in the assemblage of this trinuclear Pt(II) compound. To this end we have been applied DFT methods to the real system and to reduced models of the interacting moieties.

Computational details

The reported calculations have been carried out by using the Amsterdam density functional (ADF) package developed by Baerends and coworkers[15] and vectorized by Ravenek.[16] The numerical integration scheme employed has been that of te Velde and Baerends.[17] An uncontracted triple-ς basis set has been used for describing the orbitals of platinum. For carbon, nitrogen, oxygen, and hydrogen, double-ς basis sets have been employed. Both basis sets have been augmented by an extra polarization function.[18] A set of auxiliary s, p, d, f, and g functions, centred in all nuclei, has been introduced in order to fit the molecular density and Coulomb potential accurately in each SCF cycle.[19] Relativistic effects have been included in the energy calculations and geometry optimizations using the ZORA method.[20] This approach gives generally better results than the Pauli formalism. Geometries and energies have been evaluated using a generalized gradient approximation (GGA) that includes a GGA exchange correction of

Becke[21] and the GGA correlation correction of Perdew.[22] This method is labelled throughout this work as BP86. The 2002.03 release of the ADF package has been used for all calculations.[23]

We have also carried out an energy decomposition analysis (EDA).[24] In this EDA, the total binding energy (BE) has been divided into deformation energy and interaction energy ($BE=\Delta E_{def}+\Delta E_{int}$).

In addition, local aromaticity changes have been quantified using two probes of local aromaticity based on structure and magnetic properties, respectively. As a structure-based measure of aromaticity, we have employed the harmonic oscillator model of aromaticity (HOMA) index, defined by Kruszewski and Krygowski.[25] As a magnetic index of aromaticity, we have used the nucleus-independent chemical shift (NICS) measures proposed by Schleyer and co-workers.[26] The GIAO method[27] was used to perform calculations of NICS at ring centres (NICS(0)) determined by the non-weighted mean of the heavy atoms coordinates.

Finally, an Atoms in Molecules (AIM)[28] analysis has been carried out by means of the AIM2000 program.[29] Topological properties of the electron density at the bond critical points (BCP) of the Pt-Pt interactions were analyzed. For the AIM analysis and NICS calculations, the wave function was computed at the BP86 level of theory with the GAUSSIAN03 package[30] using the ADF optimized geometries. The Pt atoms were represented with the relativistic effective core pseudo-potentials (RECP) and the associated basis set[31] augmented with a polarization function (α=0.993, Pt).[32] The remaining atoms (C, H, N, O, and Cl) were represented with the 6-31G(d,p) basis set.[33]

Results

Molecular and electronic structure

The X-ray single crystal structure analysis reported by Llobet et al.[5] shows that the compound $[Pt(Me_2Bpy)_2][PtCl_2(Me_2Bpy)]_2[PF_6]_2.2(CH_3)_2CO$ forms a *tris*-platinum species that crystallises in the monoclinic space group P2(1)/n with Z = 4, and due to the inversion centre there are equivalent atoms. The ORTEP[34] diagram is depicted in Figure XV-1 with selected bond lengths and angles.

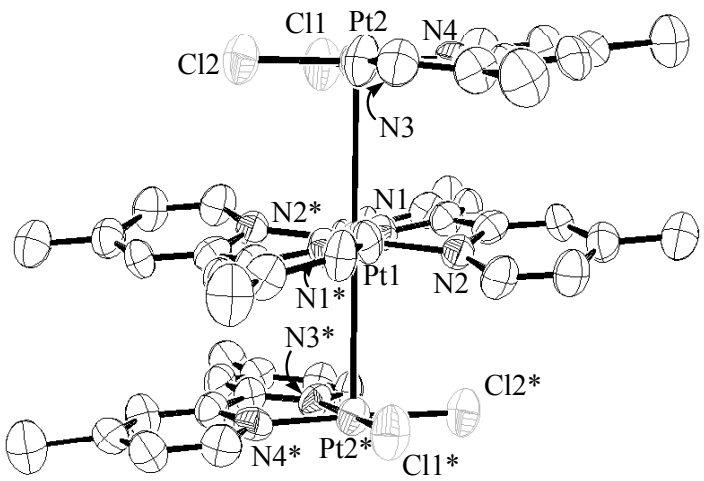

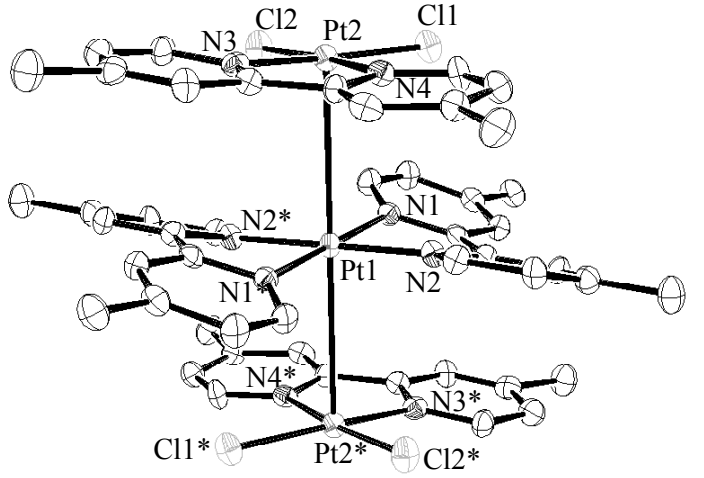

Pt(2)-Cl(1) = 2.294(4)	Pt(1)-Pt(2) = 3.4745(6)	Pt(1)-Pt(2)-Pt(3) = 180.000(17)	N(1)-Pt(1)-N(2) = 78.7(4)
Pt(2)-Cl(2) = 2.290(3)	Pt(1)-N(2) = 2.017(10)	Cl(1)-Pt(1)-Cl(2) = 89.72(13)	Cl(1)-Pt(2)-N(3) = 175.5(3)
Pt(2)-N(3) = 1.990(11)	Pt(1)-N(1) = 2.021(10)	N(3)-Pt(2)-N(4) = 80.6(4)	Pt(2)-Pt(1)-N(2) = 89.7(3)
Pt(2)-N(4) = 1.998(10)		Cl(1)-Pt(2)-N(4) = 95.8(3)	Cl(2)-Pt(2)-N(4) = 174.2(3)

Crystal data for $[C_{27}H_{30}Cl_2N_4O_1Pt_{1.5}][PF_6].(CH_3)_2CO$; Formula weight = 935.06; T = 296(2) K; Crystal system = Monoclinic; Space group = P2(1)/n; Unit cell dimensions = (a = 8.8821(6) Å, b = 12.2768(9) Å, c = 29.030(2) Å, $\alpha = 90°$, $\beta = 97.235(2)°$, $\gamma = 90°$); Volume = 3140.3(4) $Å^3$; Z = 4; Absorption coefficient = 6.969 mm^{-1}; Reflections collected = 16099; Independent reflections = 5513 [R(int) = 0.0713]; Final R indices [$I>2\sigma(I)$] = ($R_1 = 0.0551$, $wR_2 = 0.1412$)

Figure XV-1. Views of the trinuclear crystallographic data with main geometrical parameters. Distances in Å and angles in degrees.

The compound **1** described in the work by Llobet et al.[5] consists of two neutral $[PtCl_2(Me_2Bpy)]$ molecules alternatively stacked with one cationic $[Pt(Me_2Bpy)_2]^{+2}$ moiety, resulting in intramolecular Pt-Pt-Pt linear contacts with a distance of 3.474(6) Å between the adjacent Pt(II) atoms. The existence of M-M contacts between square-planar complexes of Pt(II) in the range 2.7 Å < d > 3.5 Å, shorter than the van der Waals sum, is well-known in the crystal structures of dimers and chains.[1,2,35-38] In complex **1**, the 3.474(6) Å of the Pt-Pt separation between adjacent entities is similar to those reported for the red form of $PtCl_2(Bpy)$ (Bpy = 2,2'-bipyridine) (3.449(1) Å), in which the square-planar complexes stack to form an approximately linear Pt-Pt chain with a spacing of 3.449(1) Å.[37,39]

As it is known in most of the reported cases with complexes of platinum (II),[40] the coordination of each platinum is approximately square planar, but there is a substantial distortion induced by the bidentate ligand that forms a five-membered chelate ring with the Pt atom. The deviations from ideal 90º bond angles, which decrease to 78.7(4)º in the N(1)-Pt(1)-N(2) bond angle and to 80.6(4)º in the N(3)-Pt(2)-N(4) bond angle, may be attributed to a chelate effect. The N-Pt-N chelate angles within each moiety are not identical. This suggests that, in cationic $[Pt(Me_2Bpy)_2]^{+2}$ moiety, the bipyridine ligands considerably more steric crowded within the coordination sphere force towards a smaller N-Pt(1)-N bond angle. For the charged $[Pt(Me_2Bpy)_2]^{+2}$ central fragment, it is interesting to note, as shown in Figure XV-1, that two bipyridine ligands are placed in mutually *trans* position in an inversion centre arrangement around the Pt(1) atom. For the neutral $[PtCl_2(Me_2Bpy)]$ entities, the Cl(1)-Pt(2)-Cl(2) (89.72(13)º), N(3)-Pt(2)-N(4) (80.6(4)º) and N(3)-Pt(2)-Cl(1) (175.5(3)º) bond angles are similar to those reported for the yellow form of $PtCl_2(Bpy)$.[37] The Pt(2)-Cl distances (Pt(2)-Cl(1) = 2.294(4) Å and Pt(2)-Cl(2) = 2.290(3) Å) are similar to those observed for the yellow polymorph too; however the Pt-N bond lengths (Pt(2)-N(3) = 1.990(11) Å, Pt(2)-N(4) = 1.998(10) Å) are somewhat shorter than those found for other Pt(II) compounds.[41] In contrast, all four Pt-N bond distances (Pt(1)-N(1) = 2.021(10) Å and Pt(1)-N(2) = 2.017(10) Å) for the cationic $[Pt(Me_2Bpy)_2]^{+2}$ entity are similar to those found in other similar complexes of platinum(II).[41-43]

To get further insight into the structure of this complex we have performed DFT calculations on complex **1** and related species. The optimized structure is depicted in Figure XV-2a. The Pt-Pt distance in this BP86 optimized structure of 3.184 Å is shorter than the experimental one by 0.290 Å, with a relative error of about 9%. The energetic cost of increasing the Pt-Pt distance by 0.290 Å while keeping the rest of the geometrical parameters fixed in the optimized BP86 complex is 7.6 kcal·mol^{-1}, that is, the elongation of a single Pt-Pt bond by 0.290 Å in this complex costs 3.3 kcal·mol^{-1}. Moreover, reoptimization of the geometry should reduce this value. This shows that the Pt-Pt bond is quite flexible in this molecule. The error in the optimized BP86 Pt-Pt bond length cannot be attributed to the difficulty of generalized gradient approximation (GGA) density functionals for describing π-π stacking interactions because GGA functionals tend to underestimate these interactions.[44] Neither it can be ascribed to a failure in the description of the metal-metal interaction because GGA functionals including relativistic effects describe correctly this kind of interactions.[45] Rather, the error in the theoretical determination of the Pt-Pt bond distance may be the result of packing effects facilitated by a loose Pt-Pt bond. Nevertheless, the possibility that the theoretical study of the present complex requires the use of more sophisticated theoretical methods such as the multireference CI methodologies can not be ruled out, especially if one takes into account the low HOMO-LUMO gap found for this system (*vide infra*). Unfortunately, these methodologies are currently unaffordable for computing large systems such as the present complex.

The Pt-Cl calculated distances are slightly larger (2.387 Å and 2.372 Å) than in the X-ray structure (2.294 Å and 2.290 Å), and the same happens with the Pt-N ones that present values of 2.098 Å and 2.104 Å for both external platinum atoms, and 2.119 Å and 2.128 Å for the central one. As a consequence of the *trans*-influence of the chlorine anions, it is found that the shorter the Pt-Cl bond distance, the larger the Pt-N bond length for the ligand placed in *trans*-position. It is worth noting that the distances between the external pairs of faced hydrogen atoms (H1-H2 and H3-H4 in Figure XV-2a) of the two Me_2Bpy ligands in the central charged entity are 1.908 Å, 0.152 Å shorter than 2.060 Å, the value corresponding to the H1-H2 distance in the optimized geometry of the free charged $[Pt(Me_2Bpy)_2]^{+2}$ entity. The presence of these repulsive interactions explains the distortion of the Bpy ligands out of the molecular plane.

To discuss the π-π stacking effect in the aromatic rings of the Me_2Bpy units, the Me_2Bpy ligands were substituted by ethylendiamines to yield complex **2**. Then, the Me_2Bpy units were replaced by simple amine units (complex **3**) to assess the effect of having a fixed N-Pt-N bite angle in bidentate ligands, as in complexes **1** and **2**. In both simulated complexes an important elongation of the Pt-Pt bond distances took place achieving values of 3.600 Å and 3.660 Å, respectively, confirming that π-π stacking interactions play a significant role on the Pt-Pt bond lengths. Indeed, comparing our experimental results with the reported $[Pt(CN)_4]^{2-}$ chain,[46] we found stronger interactions between the platinum atoms in complex **1** thanks, in part, to the favourable π-π stacking effect of the pyridine units not present in the $[Pt(CN)_4]^{2-}$ chain. Figure XV-2 shows the three calculated structures for complexes **1** to **3**.

a)

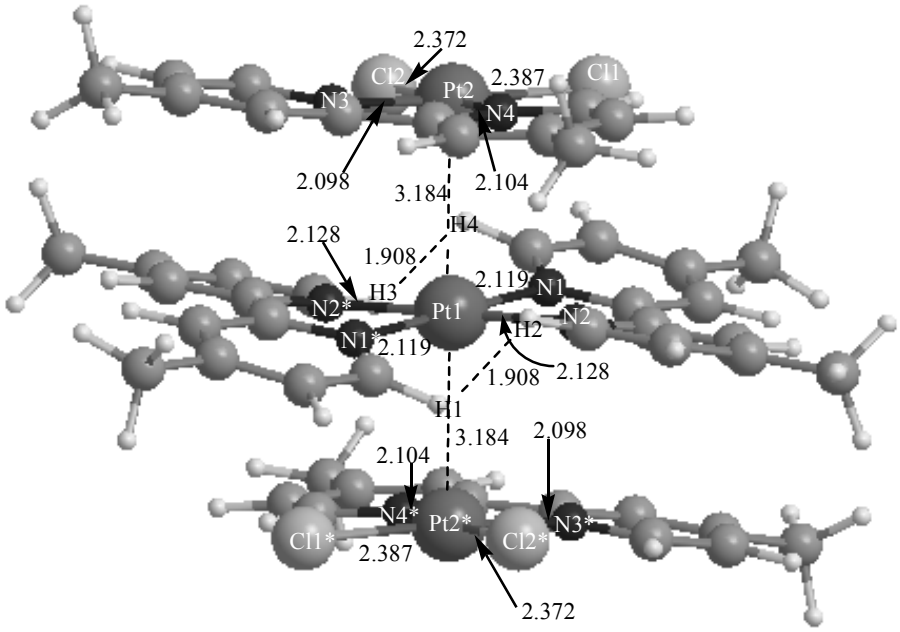

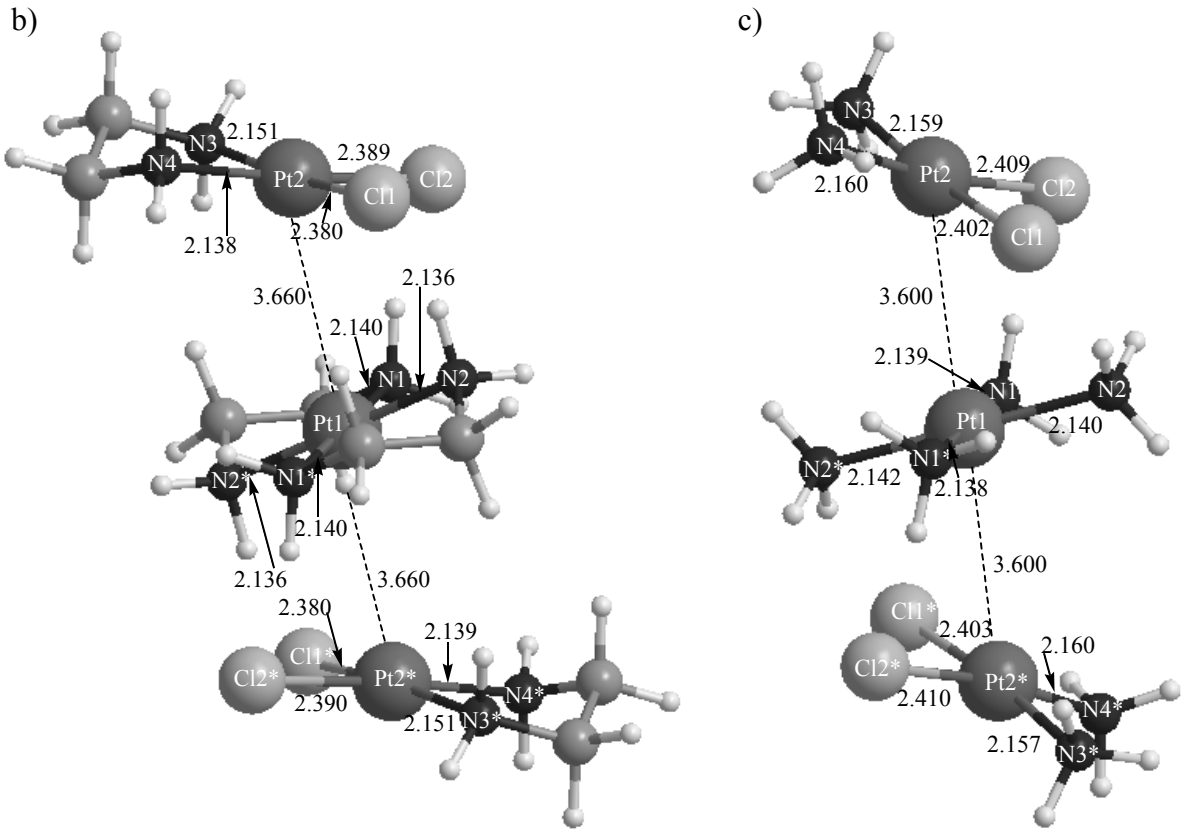

Figure XV-2. BP86 optimized geometries of complexes (a) **1**, (b) **2**, and (c) **3**. Distances in Å and angles in degrees.

The charged square planar central $[Pt(Me_2Bpy)_2]^{+2}$ moiety in **1** is not perfectly planar due to the fact that the Me_2Bpy units suffer in plane and bow distortions.[47] The in-plane effect can be described by the angle θ_P depicted in Figure XV-3a. This angle is near 170º either for the calculated species or the X-ray data for the central charged entity and only slighty smaller for each external neutral entity. The similarity between all these values reflects that it is the size of the metal, the platinum in this case, the main factor that determines this in-plane effect. On the other hand, the so-called bow distortion[6] is the deformation of the Bpy ligand that allows the coordination of the two Bpy units in a single platinum atom in a *trans* disposition. This bow distortion allows the formation of the complex because without this effect the insertion of two Me_2Bpy units in a single platinum atom would not be possible. This distortion, measured with the angle θ_B depicted in Figure XV-3b, is different for the central and external units: 18.2º (exp. 20.6º) and 12.1º (exp. 9.8º), respectively. For the BP86 optimized free central charged $[Pt(Me_2Bpy)_2]^{+2}$ and external neutral $[Pt(M_2Bpy)Cl_2]$ moieties the θ_B values are 21.4º

and 4.3º, respectively. Thus, there is a slight decrease in the bow distortion when going from the free central charged fragment to complex **1** and a remarkable increase for the free external neutral moieties. These changes in the bow angles, which are energetically not very demanding (*vide infra*), help to reduce steric repulsion between the external and the central moieties while at the same time favour the π-π stacking interactions. Indeed, the angle between the central metallic entity and the external metallic entities of **1** is only 7.4º (exp. 6.7º) (this angle corresponds to the angle between the best fitted planes defined by each metal and the four atoms of the ligands bonded to it). This angle increases to 35.8º for **2** and nearly 40º for **3**. In all the complexes the angle between the two external metallic entities is close to zero.

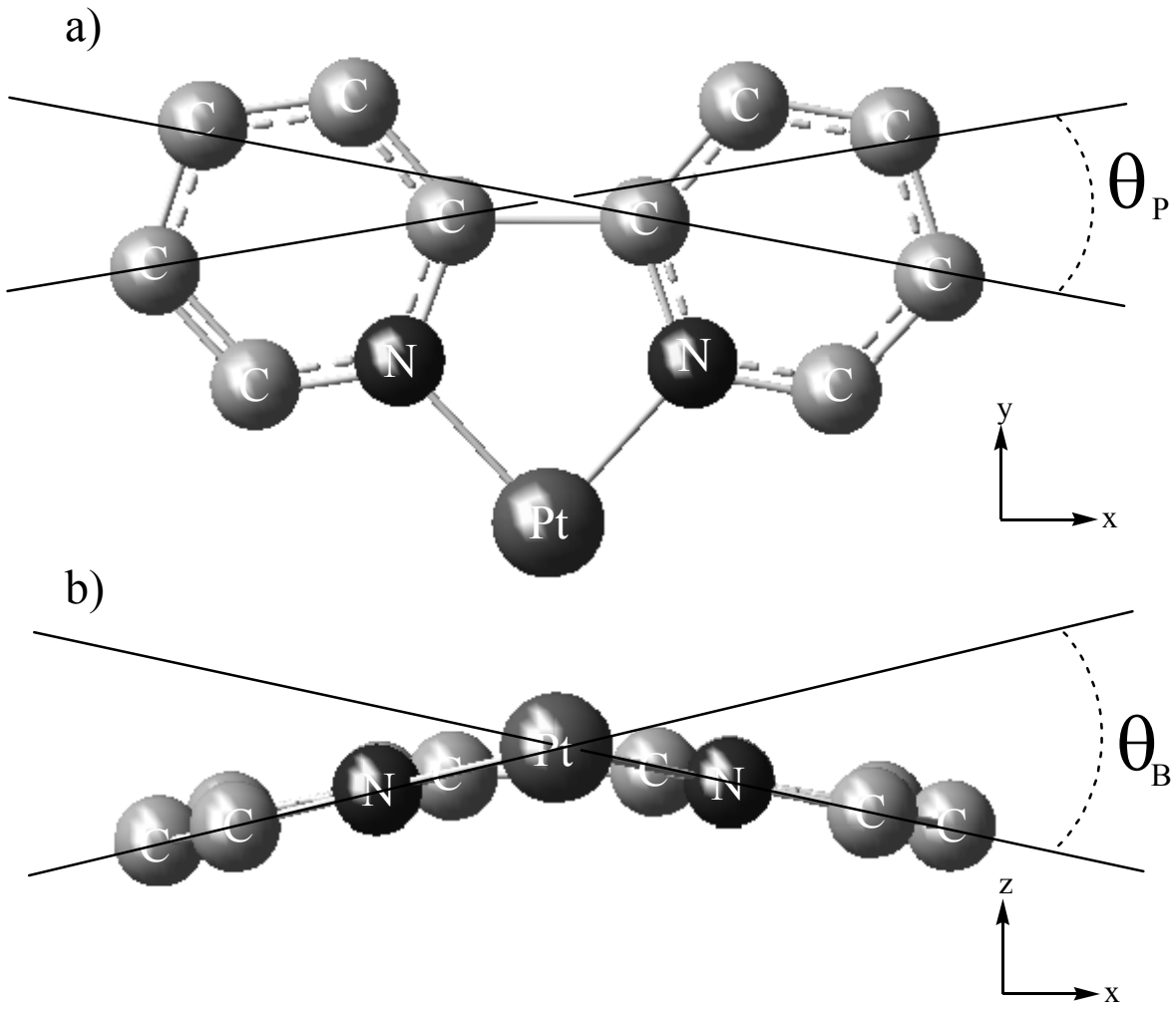

Figure XV-3. Schematic representation of (a) in-plane and (b) bow distortion.

The HOMO-LUMO gap is extremely low for complex **1** (27.5 kcal·mol^{-1}) and somewhat larger for complexes **2** (48.1 kcal·mol^{-1}) and **3** (53.0 kcal·mol^{-1}). Frontier orbitals (see Figure XV-4) are more stable in **2** and **3** as compared to **1**. The HOMO orbitals are mainly based on d_{z^2} contribution of the three metals, through an antibonding interaction. As can be seen in Figure XV-4,[48] the larger overlap between atomic Pt d_{z^2} orbitals in complex **1** because of shorter Pt-Pt bond distances explains its higher HOMO energy. Although the LUMO orbital is slightly different for each calculated complex, it is always related to the Pt-X bonds. The LUMO in complex **1** is mainly located on the central metallic entity, while those of complexes **2** and **3** have larger components on the external metallic units. Finally, the central metal presents a similar Mulliken charge for the three calculated structures (0.88 e$^-$ in **1**, 0.88 e$^-$ in **2**, and 0.86 e$^-$ in **3**), but the external platinum atoms display some differences, thus, in species **1** the external Pt atom presents higher positive Mulliken charges (0.62 e$^-$) than for **3** (0.56 e$^-$) and **2** (0.54 e$^-$) systems.

	1	**2**	**3**
LUMO	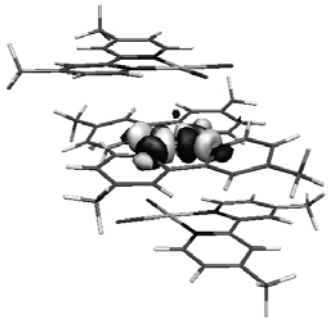		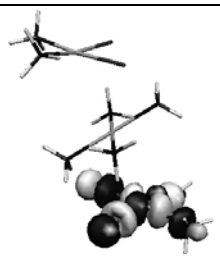
	-0.3015 a.u.	-0.3247 a.u.	-0.3464 a.u.
HOMO	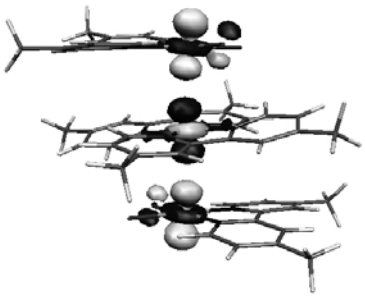	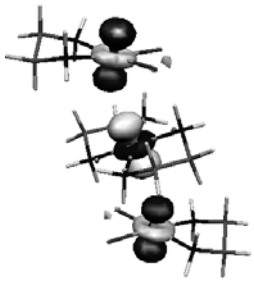	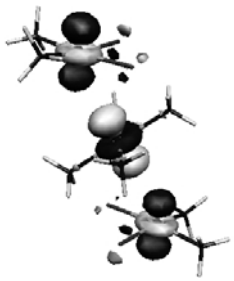
	-0.3454 a.u.	-0.4093 a.u.	-0.4231 a.u.

Figure XV-4. HOMO and LUMO molecular frontier orbitals for complexes **1**, **2**, and **3.** Isosurface values are –0.05 a.u. and 0.05 a.u.

The nature of the Pt-Pt bonds

To discuss the nature of the Pt-Pt chemical bonding and to quantify the degree of ionicity or covalency of the Pt-Pt bonds, a bond energy decomposition analysis (EDA) has been carried out. We have divided complexes **1-3** into two fragments: an external neutral [$PtCl_2X$] moiety and the rest of the molecule. The results are summarized in Table XV-1.

Compound	ΔE_{Pauli}	ΔE_{elstat}	ΔE_{oi}	ΔE_{def}	BE	% covalent
1	52.9	-53.3	-45.4	2.3	-43.5	46.0
2	38.0	-43.9	-46.4	8.3	-43.9	51.4
3	34.8	-49.3	-39.7	11.7	-42.5	44.6

Table XV-1. Energy decomposition analysis (EDA). Energies in kcal·mol^{-1}.

It is found that the binding energy (BE) of the Pt-Pt bond of the two fragments considered does not change significantly (around 43 kcal·mol^{-1}) with the substitution of the ligands in spite of large differences in the Pt-Pt bond lengths. This is apparently in contradiction with the fact that π-π stacking in complex **1** favours the formation of the Pt-Pt bond and one should expect a larger BE for complex **1** than for **2** or **3**. The reason for this discrepancy can be found in the distortion suffered by complexes **2** and **3** that brings the chlorine substituents of the Pt2 and Pt2* groups closer to the central complex Pt1. This kind of distortion allows the formation of hydrogen bonds between the amine hydrogen atoms and the chlorine groups in complexes **2** and **3**. These hydrogen bonds, not present in complex **1,** have an important influence in the calculation of the BE for complexes **2** and **3**. To demonstrate this hypothesis, we have reoptimized complex **2** keeping all Cl-Pt-Pt and N-Pt-Pt angles to 90º and the Pt2-Pt1-Pt2* angle to 180º. The Pt-Pt BE for this new constrained species is reduced by about 9.0 kcal·mol^{-1} as compared to that of the free complex **2**, due to the partial loss of H-bonding interactions. Thus, in the absence of H-bonding interactions, the BE of complex **1** is significantly larger than that of complex **2**, showing that π-π stacking interactions have a remarkable effect both on the Pt-Pt bond length and strength.

The BE is the sum of the interaction energy and the deformation energy. The latter is especially low for the molecules that present bidentate amines, and even lower if there are aromatic systems attached to the nitrogen atoms (11.7 kcal·mol^{-1} for **3**, 8.3 kcal·mol^{-1} for **2**, and 2.3 kcal·mol^{-1} for **1**), perhaps due to a lower flexibility of the bidentate ligands that does not allow for big rearrangements of the coordination sphere of the metal. The Pauli repulsion is higher for **1** (52.9 kcal·mol^{-1}) than for **3** (34.8 kcal·mol^{-1}) and **2** (38.0 kcal·mol^{-1}) as expected from the shorter Pt-Pt bond distances and the size of the ligands in **1**. Not unexpectedly, the electrostatic interaction between the charged $[[Pt(Me_2Bpy)_2][PtCl_2(Me_2Bpy)]_2]^{2+}$ and the neutral $[PtCl_2(Me_2Bpy)]$ fragments is in absolute value larger for the complex having the shortest Pt-Pt distance. Thus, the electrostatic component, related to the ionic character of the bond, is more stabilizing for complex **1** (-53.3 kcal·mol^{-1}) than for **3** (-49.3 kcal·mol^{-1}) and **2** (-43.9 kcal·mol^{-1}). Finally, the orbital component is more negative for **2** (-46.4 kcal·mol^{-1}) and **1** (-45.4 kcal·mol^{-1}) than for **3** (-39.7 kcal·mol^{-1}), thus indicating that the covalent character of the Pt-Pt interactions is favoured in bidentate ligands. The ionic character of the Pt-Pt interaction (measured as $\frac{\Delta E_{elstat}}{\Delta E_{elstat} + \Delta E_{oi}} * 100$) is quite important in **1** (54.0 %), but similar to that of **3** (55.4 %), and not far from **2** (48.6 %).

To further examine the nature of the Pt-Pt bond, we have computed the Mayer bond orders (MBO) for complexes **1-3** (see Table XV-2). The values of Pt-Pt MBOs are relatively low, even for metal-metal bonds that are usually connected to small MBOs.[49] This result shows that the electron sharing between the two Pt atoms is particularly low. Complex **1** with a value of 0.15 presents the largest Pt-Pt MBO in agreement with this complex having the shortest Pt-Pt distance. The Pt-Cl and Pt-N bond orders are similar for all the studied species.

Compound	Pt-Pt	Pt-Cl	Pt-N (external metallic unit)	Pt-N (central metallic unit)
1	0.15	0.72	0.41	0.44
2	0.07	0.71	0.35	0.38
3	0.07	0.69	0.34	0.37

Table XV-2. Mayer bond orders for the BP86 optimized complexes **1-3**.

More information on the Pt-Pt interaction can be achieved from an Atoms in Molecules (AIM)[28] analysis. In the AIM analysis, topological properties of the electron density ($\rho(\mathbf{r})$) are analyzed to define the type of interaction between bonding atoms. A chemical bonding is characterized by the bond critical point (BCP), defined by the AIM theory as the point where $\rho(\mathbf{r})$ becomes a minimum value along the bond path. Table XV-3 summarizes the BCP properties of these Pt-Pt interactions for complexes **1-3**.

Compound	$\rho_{\text{Pt-Pt}}$	$\nabla^2\rho_{\text{Pt-Pt}}$	$H_{\text{Pt-Pt}}$
1	0.0258	-0.0160	-0.0010
2	0.0125	-0.0059	-0.0002
3	0.0133	-0.0069	-0.0001

Table XV-3. BCP properties of the Pt-Pt interactions, in a.u.

The first property of interest is the electron density at the BCP (ρ_{BCP}(Pt-Pt)), which is related to the strength of the interaction. For the three cases, values of ρ_{BCP}(Pt-Pt) are enclosed in the range 0.013 – 0.026 a.u., with the compound **1** presenting the highest ρ_{BCP}(Pt-Pt) in line with the Pt-Pt bond being the shortest for this complex. These ρ_{BCP}(Pt-Pt) values are much lower than for a normal covalent bond[50] but significantly higher than the practical boundary of a molecule ($\rho \approx 0.001$ a.u.), and quite similar to that of typical hydrogen bonds ($\rho_{\text{H-Bond}} \approx 0.002 - 0.040$ a.u.).[50,51] Although ρ_{BCP} for metal-metal bonds is usually small, the ρ_{BCP}(Pt-Pt) is particularly low in line with the small MBO values found for the Pt-Pt interactions. Another important property is the Laplacian of the electron density at the BCP ($\nabla^2\rho_{\text{Pt-Pt}}$), which represents the curvature of the electron density in three-dimensional space at the BCP of the Pt-Pt interaction. In general, a negative value of $\nabla^2\rho$ indicates that the electron density is locally concentrated, while a positive value means that ρ is locally depleted. Therefore, a negative value of $\nabla^2\rho$ at the BCP means of a dominant character of the open-shell (covalent) interactions, whereas a positive value of $\nabla^2\rho$ is related to closed-shell (electrostatic) interactions. From the results of $\nabla^2\rho_{\text{Pt-Pt}}$ in Table XV-3, it can be seen that in all three cases the Pt-Pt interactions present values for $\nabla^2\rho_{\text{Pt-Pt}}$ close to zero quite

common for metal-metal bonds for which neither the covalent nor the electrostatic interactions are favored.[49] The above information extracted from the Laplacian is corroborated by means of the total energy density (H) at the BCP.[52] H is the sum of the electronic kinetic energy density (G) and the electronic potential energy density (V). The Laplacian of complex **1** is depicted in Figure XV-5.

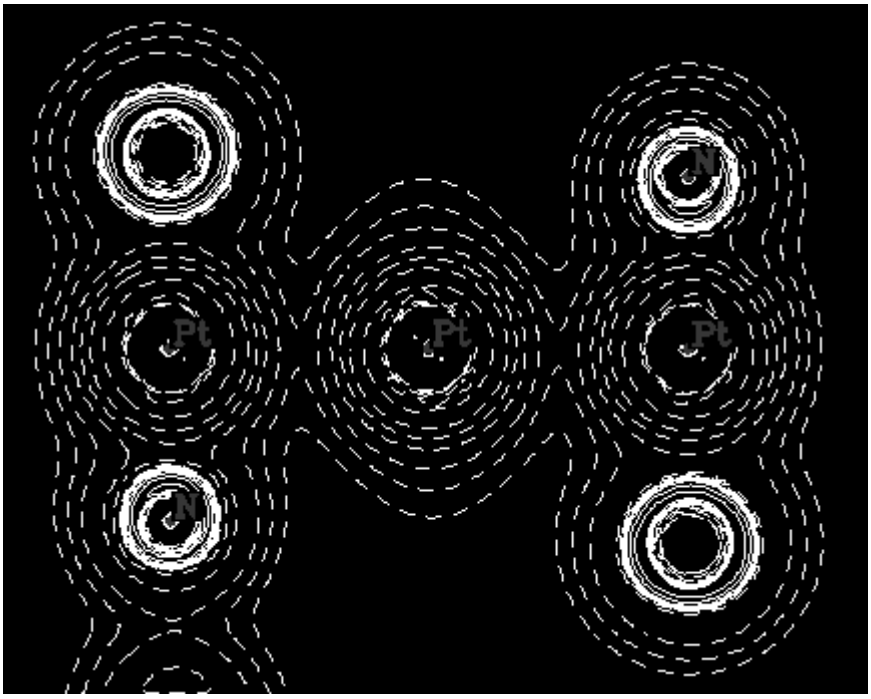

Figure XV-5. Laplacian of the density for complex **1** in the plane defined by the three Pt atoms. Isocontour surfaces go from $-8 \cdot 10^{-6}$ to 0.

Thus, a covalent interaction is characterized by a negative value of H, whereas an electrostatic one is characterized by a positive H value. The negative but close to zero values of $H_{Pt\text{-}Pt}$ in Table XV-3 are usual in metal-metal interactions[49] and are indicative of similar ionic and covalent contributions. Thus, from the EDA and AIM analysis, it can be concluded that the Pt-Pt bond is a metallic bond of intermediate strength and with similar ionic and covalent contributions.

Finally, because of the importance of the π-π stacking interactions in complex **1**, we have decided to analyze the changes in local aromaticity of the aromatic six-membered rings (6-MRs) when complex **1** is formed from the $[PtCl_2(Me_2Bpy)]$ and $[Pt(Me_2Bpy)_2]^{+2}$ fragments by means of the HOMA and NICS indices. The results are

listed in Table XV-4. We have taken as a reference the values for the free Me_2Bpy ligand (HOMA=0.979 and NICS=-6.6 ppm) that have been compared with those of complex **1** and the corresponding free $[PtCl_2(Me_2Bpy)]$ and $[Pt(Me_2Bpy)_2]^{+2}$ fragments. Going from the Me_2Bpy ligand to the $[PtCl_2(Me_2Bpy)]$ and $[Pt(Me_2Bpy)_2]^{+2}$ fragments there is an almost insignificant reduction of aromaticity that must be attributed to the in plane and bow distortions due to coordination of the Me_2Bpy ligands to the metal atoms.

Aromatic ring	HOMA	NICS
Me_2Bpy	0.979	-6.6
N3-N3*	0.976	-6.3
N4-N4*	0.975	-6.0
N2-N2*	0.980	-6.1
N1-N1*	0.982	-6.7
N3-N3* $[PtCl_2(Me_2Bpy)]$	0.978	-5.6
N4-N4* $[PtCl_2(Me_2Bpy)]$	0.975	-5.6
N2-N2* $[Pt(Me_2Bpy)_2]^{+2}$	0.971	-5.5
N1-N1* $[Pt(Me_2Bpy)_2]^{+2}$	0.972	-5.5

Table XV-4. HOMA and NICS (in ppm) local aromaticity indices. Labels of aromatic rings are those in Figure XV-2.

These distortions are more important in the $[Pt(Me_2Bpy)_2]^{+2}$ fragment (*vide supra*) and also the reduction in local aromaticity is somewhat more important in this particular fragment. However, in general, local aromaticity changes are very small as expected from the well-known fact that small distortions of the aromatic rings results in essentially unperturbed local aromaticities.[53] Changes in local aromaticity of the 6-MRs measured by HOMA when going from free $[PtCl_2(Me_2Bpy)]$ and $[Pt(Me_2Bpy)_2]^{+2}$ fragments to complex **1** are also very small, especially for the neutral $[PtCl_2(Me_2Bpy)]$ fragment. For the central charged $[Pt(Me_2Bpy)_2]^{+2}$ fragment there is some increase in local aromaticity as expected from the aforementioned reduction in the bow angle for this fragment in complex **1**. Finally, the significant increase in local aromaticity when going from the free fragments to complex **1** given by NICS is likely an artifact of the

NICS indicator of aromaticity caused by the magnetic couplings between superimposed 6-MRs.[53a] Nevertheless the increase in the NICS values of the N3-N3* rings and especially the N1-N1* rings is clearly another strong argument in favour of the π-π stacking interactions between the pairs of N1-N3* and N1*-N3 rings. As a whole, while π-π stacking interactions are important in the formation of the Pt-Pt bond in complex **1**, aromaticity changes have likely an almost irrelevant influence.

Conclusion

The recently synthesized trinuclear $[[Pt(Me_2Bpy)_2][PtCl_2(Me_2Bpy)]_2]^{2+}$ complex **1** presents short Pt-Pt contacts that indicate the presence of metal-metal bonds. DFT calculations of complexes **1, 2,** and **3** suggest that the π-π stacking interactions between the pyridine units are responsible, in part, for the short Pt-Pt distances found in complex **1**. The Pt-Pt bond has an intermediate strength with a binding energy of about 40 $kcal \cdot mol^{-1}$. As to the nature of Pt-Pt interactions, this is a metallic bond with both covalent and electrostatic components being almost equally important as derived from the AIM and EDA analyses.

References

1. A. Klein, *Reviews in Inorganic Chemistry* **2000**, *20*, 283-303.
2. J. J. Novoa, G. Aullón, P. Alemany, S. Álvarez, *J. Am. Chem. Soc.* **1995**, *117*, 7169-7171.
3. S. Marchala, V. Moreno, G. Aullón, S. Álvarez, M. Quirós, M. Font-Bardia, X. Solans, *Polyhedron* **1999**, *18*, 3675-3682.
4. M. Kato, M. Kozakai, C. Fukagawa, T. Funayama, S. Yamauchi, *Mol. Cryst. Liq. Cryst.* **2000**, *343*, 35-40.
5. A. Poater, S. Moradell, E. Pinilla, J. Poater, M. Solà, M. A. Martínez, A. Llobet, *Dalton Trans*. **2005**, 1188-1196.
6. A. Hazell, *Polyhedron* **2004**, *23*, 2081-2083.
7. M. Bakir, S. Paulson, P. Goodson, B. P. Sullivan, *Inorg. Chem.* **1992**, *31*, 1129-1135.
8. A. W. Cordes, B. Durham, P. N. Swepston, W. T. Pennington, S. M. Condren, R. Jensen, J. L. Walsh, *J. Coord. Chem.* **1982**, *11*, 251-260.
9. a) B. Durham, S. R. Wilson, D. J. Hodgson, T. J. Meyer, *J. Am. Chem. Soc.* **1980**, *102*, 600-607. b) N. R. Weathers, R. C. Sadoski, B. Durham, A. W. Cordes, *Acta Cryst.* **1997**, *C53*, 1047-1049. c) B. J. Coe, T. J. Meyer, P. S. White, *Inorg. Chem.* **1993**, *32*, 4012-4020. d) T. Togano, H. Kuroda, N. Nagao, Y. Maekawa, H. Nishimura, *Inorg. Chim. Acta* **1992**, *196*, 57-63. e) H. Nagao, H. Nishimura, H. Funato, Y. Ichikawa, F. S. Howell, M. Mukaida, H. Kakihana, *Inorg. Chem.* **1989**, *28*, 3955-3959. f) R. Kroener, M. J. Heeg, E. Deutsch, *Inorg. Chem.* **1988**, *27*, 558-566. g) A. J. Blake, A. McA. Marr, D. W.H. Rankin, M. Schröder, *Acta Cryst.* **1988**, *C44*, 935-936.
10. a) A. Hazell, A. Mukhopadhyay, *Acta Cryst.* **1980**, *B36*, 1647-1649. b) A. W. Cordes, B. Durham, P. N. Swepston, W. T. Pennington, S. M. Condren, R. Jensen, J. L. Walsh, *J. Coord. Chem.* **1982**, *11*, 251-260.
11. a) C. Molenaar, J.- M. Teuben, R. J. Heetebrij, H. J. Tanke, J. Reedijk, *J. Biol. Inorg. Chem.* **2000**, *5*, 655-665. b) K. Charalabopoulos, S. Karkabounas, E. Loachim, V. Papalimneou, K. Syrigos, A. Evangelou, N. Agnantis, N. Hadjiliadis, *Eur. J. Clin. Invest.* **2002**, *32*, 129-133. c) B. Lippert, *Coord. Chem. Rev.* 1999, **182**, 263-295. d) L. R. Kelland, N. P. Farrel (eds.), *Platinum-Based*

drugs in Cancer Therapy, Humana Press, Totowa, 2000. e) J. Reedijk, *Proc. Natl. Acad. Sc. (USA)* **2003**, *100*, 3611-3616.

12. S. Moradell, J. Lorenzo, A. Rovira, M. S. Robillard, F. X. Avilés, V. Moreno, R. Llorens, M. A. Martínez, J. Reedijk, A. Llobet, *J. Inorg. Biochem.* **2003**, *96*, 493-502.
13. SHELX97 [Includes SHELXS97, SHELXL97, CIFTAB] - Programs for Crystal Structure Analysis (Release 97-2). G. M. Sheldrick, Institüt für Anorganische Chemie der Universität, Tammanstrasse 4, D-3400 Göttingen, Germany, 1998.
14. G. M. Sheldrick, *Program for Refinement of Crystal Structure*, University of Gottingen, 1997.
15. a) E. J. Baerends, D. E. Ellis, P. Ros, *Chem. Phys*. **1973**, *2*, 41-51. b) C. Fonseca Guerra, O. Visser, J. G. Snijders, G. te Velde, E. J. Baerends, *Methods and Techniques for Computational Chemistry*, STEF, Cagliari, 1995, 305. c) G. te Velde, F. M. Bickelhaupt, E. J. Baerends, C. Fonseca Guerra, S. J. A. van Gisbergen, J. G. Snijders, T. Ziegler, *J. Comput. Chem*. **2001**, *22*, 931-967.
16. W. Ravenek, *Algorithms and Applications on Vector and Parallel Computers*, Elsevier, Amsterdam, 1987.
17. G. te Velde, E. J. Baerends, *J. Comp. Phys.* **1992**, *99*, 84-98.
18. a) J. G. Snijders, E. J. Baerends; P. Vernooijs, *At. Nucl. Data Tables* **1982**, *26*, 483-509. b) P. Vernooijs, E. J. Baerends*, Slater Type Basis Functions for the Whole Periodic System. Internal Report*, Vrije Universiteit of Amsterdam, The Netherlands, 1981.
19. J. B. Krijn, E. J. Baerends, *Fit Functions in the HFS Method. Internal Report* (in Dutch), Vrije Universiteit of Amsterdam, The Netherlands, 1984.
20. a) E, van Lenthe, A. E. Ehlers, E. J. Baerends, *J. Chem. Phys.* **1999**, *110*, 8943-8953. b) E. van Lenthe, E. J. Baerends, J. G. Snijders, *J. Chem. Phys.* **1993**. *99*, 4597-4610. c) E. van Lenthe, E. J. Baerends, J. G. Snijders, *J. Chem. Phys.* **1994**, *101*, 9783-9792. d) E. van Lenthe, J. G. Snijders, E. J. Baerends, *J. Chem. Phys.* **1996**. *105*, 6505-6516. e) E. van Lenthe, E, J. Baerends, J. G. Snijders, *Int. J. Quantum Chem.* **1996**, *57*, 281 -293.
21. A. D. Becke, *Phys. Rev. A* **1988**, *38*, 3098-3100.
22. J. P. Perdew, *Phys. Rev. B **1986***, *33*, 8822-8824.
23. ADF2000. E. J. Baerends, J. A. Autschbach, A. Bérces, C. Bo, P. M. Boerrigter, L. Cavallo, D. P. Chong, L. Deng, R. M. Dickson, D. E. Ellis, L. Fan, T. H.

Fischer, C. Fonseca Guerra, S. J. A. van Gisbergen, J. A. Groeneveld, O. V. Gritsenko, M. Grüning, F. E. Harris, P. van den Hoek, H. Jacobsen, G. van Kessel, F. Kootstra, E. van Lenthe, V. P. Osinga, S. Patchkovskii, P. H. T. Philipsen, D. Post, C. C. Pye, W. Ravenek, P. Ros, P. R. T. Schipper, G. Schreckenbach, J. G. Snijders, M. Solà, M. Swart, D. Swerhone, G. te Velde, P. Vernooijs, L. Versluis, O. Visser, E. van Wezenbeek, G. Wiesenekker, S. K. Wolff, T. K. Woo, T. Ziegler, Vrije Universiteit Amsterdam: Amsterdam, The Netherlands, 2000.

24. a) F. M. Bickelhaupt, N. M. Nibbering, E. M. van Wezenbeek, E. J. Baerends, *J. Phys. Chem.* **1992**, *96*, 4864-4873. b) T. Ziegler, A. Rauk, *Inorg. Chem.* **1979**, *18*, 1558-1565. c) T. Ziegler, A. Rauk, *Inorg. Chem.* 1979, **18**, 1755-1759. d) T. Ziegler, A. Rauk, *Theor. Chim. Acta* **1977**, *46*, 1-10. e) K. Kitaura, K. Morokuma, *Int. J. Quantum Chem.* **1976**, *10*, 325-331.
25. a) J. Kruszewski, T.M. Krygowski, *Tetrahedron Lett.* **1972**, *13*, 3839-3842. b) T. M. Krygowski, *J. Chem. Inf. Comp. Sci.* **1993**, *33*, 70-78.
26. P. v. R. Schleyer, C. Maerker, A. Dransfeld, H. Jiao, N. J. R. van Eikema Hommes, *J. Am. Chem. Soc.* **1996**, *118*, 6317-6318.
27. K. Wolinski, J. F. Hilton, P. Pulay, *J. Am. Chem. Soc.* **1990**, *112*, 8251-8260.
28. R. F. W. Bader, *Atoms in Molecules: A Quantum Theory*; Oxford University Press: Oxford, UK, 1990.
29. F. Biegler-König, J. Schönbohm, D. Bayles, *J. Comput. Chem.* **2001**, *22*, 545-559.
30. Gaussian 03, M. J. Frisch, G. W. Trucks, H. B. Schlegel, G. E. Scuseria, M. A. Robb, J. R. Cheeseman, J. A. Montgomery, Jr., T. Vreven, K. N. Kudin, J. C. Burant, J. M. Millam, S. S. Iyengar, J. Tomasi, V. Barone, B. Mennucci, M. Cossi, G. Scalmani, N. Rega, G. A. Petersson, H. Nakatsuji, M. Hada, M. Ehara, K. Toyota, R. Fukuda, J. Hasegawa, M. Ishida, T. Nakajima, Y. Honda, O. Kitao, H. Nakai, M. Klene, X. Li, J. E. Knox, H. P. Hratchian, J. B. Cross, C. Adamo, J. Jaramillo, R. Gomperts, R. E. Stratmann, O. Yazyev, A. J. Austin, R. Cammi, C. Pomelli, J. W. Ochterski, P. Y. Ayala, K. Morokuma, G. A. Voth, P. Salvador, J. J. Dannenberg, V. G. Zakrzewski, S. Dapprich, A. D. Daniels, M. C. Strain, Ö. Farkas, D. K. Malick, A. D. Rabuck, K. Raghavachari, J. B. Foresman, J. V. Ortiz, Q. Cui, A. G. Baboul, S. Clifford, J. Cioslowski, B. B. Stefanov, G. Liu, A. Liashenko, P. Piskorz, I. Komaromi, R. L. Martin, D. J.

Fox, T. Keith, M. A. Al-Laham, C. Y. Peng, A. Nanayakkara, M. Challacombe, P. M. W. Gill, B. Johnson, W. Chen, M. W. Wong, C. Gonzalez, J. A. Pople, Gaussian, Inc., Pittsburgh PA, 2003.

31. D. Andrae, U. Häussermann, M. Dolg, H. Stoll, H. Preuss, *Theor. Chim. Acta* **1990**, *77*, 123-141.
32. A. W. Ehlers, M. Böhme, S. Dapprich, A. Gobbi, A. Höllwarth, V. Jonas, K. F. Köhler, R. Stegmann, A. Veldkamp, G. Frenking, *Chem. Phys. Lett.* **1993**, *208*, 111-114.
33. P. C. Hariharan, J. A. Pople, *Theor. Chim. Acta* **1973**, *28*, 213-217.
34. C. K. Johnson, ORTEP, Report ORNL-5138, Oak Ridge National Laboratory, Oak Ridge, TN, 1976.
35. S. Komeda, M. Lutz, A. L. Spek, Y. Yamanaka, T. Sato, M. Chikuma, J. Reedijk, *J. Am. Chem. Soc.* **2002**, *124*, 4738-4746.
36. S. Komeda, M. Lutz, A. L. Spek, M. Chikuma, J. Reedijk, *Inorg. Chem.* **2000**, *39*, 4230-4236.
37. W. B. Connick, L. M. Henling, R. E. Marsh, H. B. Gray, *Inorg. Chem.* **1996**, *35*, 6261-6265.
38. B-C. Tzeng, G-H. Lee, S-M. Peng, *Inorg. Chem. Comm.* **2003**, *6*, 1341-1343.
39. R. S. Osborn, D. Rogers, *J. Chem. Soc., Dalton Trans.* **1974**, 1002-1004.
40. D. M. Roundhill, in R.D. Gillard, J. A. McCleverty, G. Wilkinson (eds.), *Comprehensive Coordination Chemistry*, vol.5, Pergamon, Oxford, 1987, Ch 52.
41. H. O. Davies, D. A. Brown, A. I. Yanovsky, K. B. Nolan, *Inorg. Chim. Acta* **1998**, *268*, 313-316.
42. C. Mock, I. Puscasu, M. J. Rauterkus, G. Tallen, J. E. A. Wolf, B. Krebs, *Inorg. Chim. Acta* **2001**, *319*, 109-116.
43. M. Mullaney, S-C. Chang, R. E. Norman, *Inorg. Chim. Acta* **1997**, *265*, 275-278.
44. a) Y. Zhao, D. G. Truhlar, *J. Phys. Chem. A* **2005**, *109*, 5656-5667. b) Y. Zhao, D. G. Truhlar, *J. Chem. Theory Comput.* **2005**, *1*, 415-432.
45. a) P. Belanzoni, M. Rosi, A. Sgamellotti, E. J. Baerends, C. Floriani, *Chem. Phys. Lett.* **1996**, *257*, 41-48. b) T. Ziegler, V. Tschinke, A. Becke, *Polyhedron* **1985**, *6*, 685-693.
46. P. L. Johnson, T. R. Koch, J. M. Williams, *Acta Cryst.* **1977**, *B33*, 1293-1295.

47. a) B. Durham, S. R. Wilson, D. J. Hodgson, T. J. Meyer, *J. Am. Chem. Soc.* **1980**, *102*, 600-607. b) A. W. Cordes, B. Durham, P. N. Swepston, W. T. Pennington, S. M. Condren, R. Jensen, J. L. Walsh, *J. Coord. Chem.* **1982**, *11*, 251-260.
48. MOLEKEL 4.0, P. Flükiger, H. P. Lüthi, S. Portmann, J. Weber, Swiss Center for Scientific Computing, Manno (Switzerland), 2000.
49. P. Macchi, A. Sironi, *Coord. Chem. Rev.* **2003**, *238-239*, 383-412.
50. P. Popelier, *Atoms in Molecules: An Introduction*; Pearson Education: Harlow, 2000.
51. M. Iwaoka, H. Komatsu, T. Katsuda, S. Tomoda, *J. Am. Chem. Soc.* **2004**, *126*, 5309-5317.
52. W. Koch, G. Frenking, J. Gauss, D. Cremer, J. R. Collins, *J. Am. Chem. Soc.* **1987**, *109*, 5917-5934.
53. a) G. Portella, J. Poater, J. M. Bofill, P. Alemany, M. Solà, *J. Org. Chem.* **2005**, *70*, 2509-2521, erratum, íbid **2005**, *70*, 4560-4560 b) P. A. Kraakman, J. -M. Valk, H. A. G. Niederländer, D. B. E. Brouwer, F. M. Bickelhaupt, W. H. De Wolf, F. Bickelhaupt, C. H. Stam, *J. Am. Chem. Soc*. **1990**, *112*, 6638-6646. c) J. E. Gready, T. W. Hambley, K. Kakiuchi, K. Kobiro, S. Sternhell, C. W. Tansey, Y. Tobe, *J. Am. Chem. Soc*. **1990**, *112*, 7537-7540. d) S. Grimme, *J. Am. Chem. Soc*. **1992**, *114*, 10542-10545. e) G. J. Bodwell, J. N. Bridson, T. J. Houghton, J. W. J. Kennedy, M. R. Mannion, *Angew. Chem. Int. Ed.* **1996**, *35*, 1320-1321. f) G. J. Bodwell, J. N. Bridson, T. J. Houghton, J. W. J. Kennedy, M. R. Mannion, *Chem. Eur. J.* **1999**, *5*, 1823-1827. g) G. J. Bodwell, J. N. Bridson, M. K. Cyrañski, J. W. J. Kennedy, T. M. Krygowski, M. R. Mannion, D. O. Miller, *J. Org. Chem*. **2003**, *68*, 2089-2098.

Chapter XVI: *Regioselective Intramolecular Pauson-Khand Reactions of C_{60}: An Electrochemical Study and Theoretical Underpinning*

Regioselective Intramolecular Pauson-Khand Reactions of C_{60}: An Electrochemical Study and Theoretical Underpinning

Abstract

Suitably functionalized fulleropyrrolidines endowed with one or two propargyl groups at the C-2 position of the pyrrolidine ring (1,6-enynes) react efficiently and regioselectively with $[Co_2(CO)_8]$ to afford the respective Pauson-Khand (PK) products with an unprecedented three (**5 a-d**, **7**) pentagonal rings, respectively, fused onto the fullerene sphere. Fulleropyrrolidines with 1,7-, 1,9-, 1,10-, or 1,11-enyne moieties do not undergo the PK reaction and, instead, the intermediate dicobalt complexes formed with the alkynyl group are isolated in quantitative yields. These differences in reactivity have been studied by DFT calculations with a generalized gradient approximation (GGA) functional and several important energy and structural differences were found for the intermediates formed by the interaction between the coordinatively unsaturated Co atom and the π system of C_{60} in 1,6- and 1,7-enynes. The different lengths of the alkyne chains are responsible for the observed reactivities.

Introduction

The [2+2+1] cycloaddition of alkyne, alkene, and carbon monoxide mediated or catalyzed by a transition metal, also known as the Pauson-Khand (PK) reaction, has been widely used in organic synthesis for the construction of biologically active five-membered carbocycles in a convergent approach (Scheme XVI-1).[1] In contrast, the use of this successful reaction has almost been neglected in materials science despite the potential for the construction of complex modified molecules that exhibit nonconventional properties. With this in mind, the experimental group of Nazario Martín recently reported in a preliminary communication the first example of a highly efficient and regioselective intramolecular PK reaction in which fullerene C_{60} was used as the alkene component in the [2+2+1] cycloaddition reaction.[2]

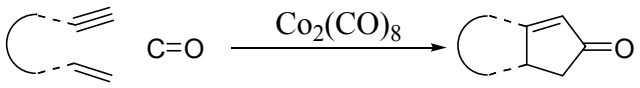

Scheme XVI-1. General scheme for the Pauson-Khand reaction.

Fullerenes are a class of molecule made up of carbon atoms with an unusual hybridization ($sp^{2,3}$)[3] that exhibit a chemical reactivity similar to that of electron-deficient olefins.[4] Although electron-poor alkenes are not suitable substrates for PK reactions as a result of their low reactivity and the competing elimination reaction that can take place to afford 1,3-dienes, a wide variety of inter- and intramolecular PK reactions involving alkenes with electron-withdrawing substituents have been reported in recent years.[5] Therefore, fullerenes have emerged as suitable new substrates for the PK reaction provided that they have a spherical surface with multiple reactive double bonds and, in addition, the competing β-hydride elimination reaction has been overcome due to the absence of hydrogen atoms in their structure.

To carry out a systematic study of the PK reaction of the fullerene sphere Nazario Martín et al. have synthesized a wide variety of novel suitably functionalized fulleropyrrolidines bearing one or two alkyne units on the pyrrolidine ring.[6] Thus, suitably designed 1,6- and 1,7-enynes, as well as other enynes with a larger separation between the alkene and the alkyne groups, with one fullerene double bond as the alkene component, have been prepared (see Schemes XVI-2 and -3). Further, [2+2+1] cobalt-mediated carbonylative cycloaddition of the starting enynes should afford new fullerene *cis*-**1** bisadducts endowed with unprecedented fused cyclopentenone structures. An electrochemical study of the novel modified fullerenes has been carried out by cyclic and square-wave voltammetry at room temperature in order to determine the redox behavior of the starting fulleropyrrolidines and the respective *cis*-**1** bisadducts obtained in the PK reaction.

The PK reaction has a broad scope; it has proved successful with many functional groups (ethers, alcohols, tertiary amines, acetals, esters, amides, and heterocycles) as well as with different promoters, metal catalysts, and experimental conditions.[1] An important disadvantage of the PK reaction is, however, that the intermolecular process is generally limited to strained olefins. Fullerenes are known to have a strained spherical

geometry and, therefore, they appear to be suitable candidates for the PK reaction. However, all attempts to carry out the intermolecular PK reaction with C_{60}, alkynes, and $[Co_2(CO)_8]$ were unsuccessful. Intramolecular PK reactions of fullerenes require the design of new fullerene derivatives suitably functionalized with an alkyne group. With this in mind, fulleropyrrolidines endowed with an alkyne group at the C-2 position of the pyrrolidine ring fulfill the requirements of appropriate geometry and variable length between the fullerene double bond and the alkyne.

Most of the intramolecular PK reactions reported have been carried out with systems derived from hept-1-en-6-ynes or propargyl allyl ethers or amines which afford cyclopentenones fused to a carbo- or heterocyclic pentagonal ring. Enynes connected through aromatic rings have also been successfully used in the PK reaction which has allowed the synthesis of medium-sized rings (six- to eight-membered rings).[7]

To carry out a thorough study of the scope of the PK reaction using C_{60} as the alkene moiety, Martín et al. synthesized a wide variety of suitably functionalized fulleropyrrolidines. The hept-1-en-6-ynes are the most widely used substrates in the PK reaction (Scheme XVI-2).[8]

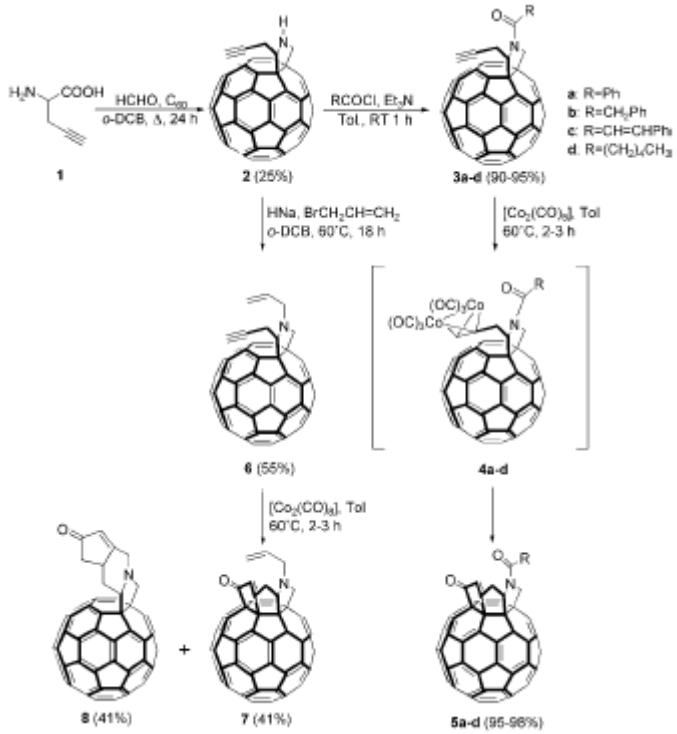

Scheme XVI-2

Fulleropyrrolidine **2** is suitably functionalized to undergo the PK reaction provided that it contains the required 1,6-enyne moiety. However, its reaction with $[Co_2(CO)_8]$ in toluene at 60 °C (or in the presence of molecular sieves) did not afford the PK product owing to the ability of the lone-pair of the pyrrolidine's nitrogen atom to coordinate to the cobalt complex.

The PK products **5a-d** were unambiguously confirmed as the *cis*-**1** biscycloadducts with an unprecedented structure that contains three pentagonal rings fused onto the fullerene surface.

In the light of these results, Martín et al. decided to expand the scope of the PK reaction of the fullerenes to other derivatives with larger enyne moieties. Thus, in addition to the expected *cis*-**1** biscycloadducts, other regioisomeric bisadducts may also be formed depending on the length of the chain connecting the fullerene double bond and the alkyne group. Thus, novel fulleropyrrolidines (**10** and **14**) with a 1,7-enyne moiety, which, under PK reaction conditions were synthesized, should lead to cyclopentenones fused to six-membered carbocyclic rings. Thus, by following Prato's procedure[8] fulleropyrrolidines **10a-g** or **14a-c** could be obtained (Scheme XVI-3).

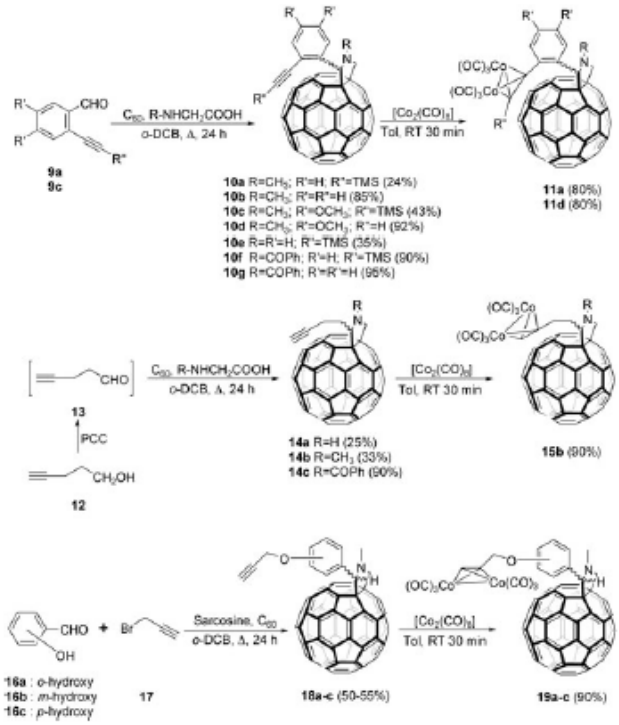

Scheme XVI-3

Further reaction with $[Co_2(CO)_8]$ under the experimental conditions used for the preparation of **5a-d**, **7**, and **8** did not afford, in any case, the corresponding PK products. Thus, the reactions carried out with *N*-substituted (N-CH_3, N-COPh) pyrrolidines or by activating the alkynyl group by introducing electron-releasing methoxy groups onto the benzene ring were futile. Instead, the intermediate dicobalt complexes **11** and **15** were obtained in almost quantitative yields. Further attempts to synthesize the PK products from the intermediate complexes by raising the temperature ($RT \rightarrow 60$ C) either in the presence or absence of molecular sieves also failed. Note that at temperatures higher than 60 C, cobalt atoms were lost to give the precursor fulleropyrrolidines **10** and **14**, together with other uncharacterized products resulting from extensive decomposition.

Note that there are remarkable differences in the reactivities of the fulleropyrrolidines endowed with a 1,6-enyne moiety, which led to PK products in almost quantitative yields, and those with longer-length enynes, which in any case underwent the [2+2+1] cyclization reaction. In particular, fulleropyrrolidines **10** and **14** with the 1,7-enyne moiety seemed to be suitably functionalized to undergo the PK reaction. Since these experimental findings cannot be rationalized in terms of electronic factors, the additional methylene group in the chain linking the olefin and the alkynyl groups must introduce important geometrical differences that are responsible for the observed reactivities.

Electrochemistry: The PK products as well as the precursor fulleropyrrolidines are electroactive molecules that, similarly to the pristine fullerene C_{60}, should behave as electron-accepting species. Therefore, Martín et al. have studied the electrochemical properties of the novel compounds by cyclic voltammetry (CV) in *o*-DCB/MeCN (4:1) as solvent at room temperature and by using tetrabutylammonium perchlorate as the supporting electrolyte. The characteristic shapes of the redox waves and their unequivocal position on the potential scale virtually fingerprint the individual electrochemical properties of the different redox systems. For this reason, CV has been labeled as an electrochemical spectroscopy.[9] In this case, the saturation of one olefinic double bond in the suitably functionalized precursor fulleropyrrolidines should lead, in principle, to different electrochemical behavior to that shown by the related PK products in which two fullerene double bonds are saturated. This should raise the LUMO energy level and, therefore, the reduction waves should be shifted towards more negative

potentials, thus slightly reducing their accepting ability.[10] Therefore, a voltamperometric study of these compounds should allow to determine the electronic effect of the substitution pattern on the electrochemical properties of the compounds obtained and, simultaneously, to use CV as a useful characterization technique.

The redox potentials of some representative novel compounds obtained by Martín et al. are collected in Table 1 together with those of C_{60} as a reference. All the systems studied displayed electrochemically reversible behavior and, therefore, Table 1 gives the half-wave reduction potential values.

Compound	$E^1_{1/2\ red}$	$E^2_{1/2\ red}$	$E^3_{1/2\ red}$	$E^4_{1/2\ red}$
C_{60}	-0.800	-1.209	-1.673	-2.127
2	-0.894	-1.288	-1.818	-2.249
3a	-0.860	-1.253	-1.791	-2.205
3b	-0.852	-1.262	-1.784	-2.215
5a	-0.864	-1.256	-1.908	---
5b	-0.863	-1.265	-1.892	---
5c	-0.857	-1.255	-1.885	---
5d	-0.858	-1.252	-1.888	-2.232
7	-0.891	-1.289	-1.939	---
8	-0.875	-1.279	-1.818	-2.231

Table 1. Half-wave reduction potentials [V versus $Ag/AgNO_3$] of compounds **2**, **3**, **5**, **7**, **8**, and C_{60} (Working electrode: GCE; reference electrode: Ag/Ag^+; counter electrode: Pt; supporting electrolyte: 0.1 M Bu_4NClO_4; scan rate: 100 mV s^{-1}; sample concentrations: $(0.5\text{-}2.0)\times10^{-3}$ M; solvent: *o*-DCB/MeCN (4:1 v/v).

All the compounds studied showed three of four reversible reduction waves that correspond to the reduction steps of the fullerene moiety (Figure XVI-1). A remarkable negative shift in the redox potentials relative to the values for pristine C_{60} was observed in all cases which can be attributed to the saturation of one (**2**, **3a**, **3b**, and **8**) or two (**5a-d** and **7**) fullerene double bonds, which slightly reduces the electron-accepting ability of the fullerene. Fulleropyrrolidine **2** with a free secondary amino group showed

the highest cathodic shift relative to C_{60}. Fulleropyrrolidines **3a,b** with an acyl group linked to the pyrrolidine's nitrogen atom showed a significant anodic shift in comparison with **2** (40 mV) due to the presence of the carbonyl group and the subsequent delocalization of the nitrogen atom's lone-pair (Figure XVI-1 and Table XVI-1).

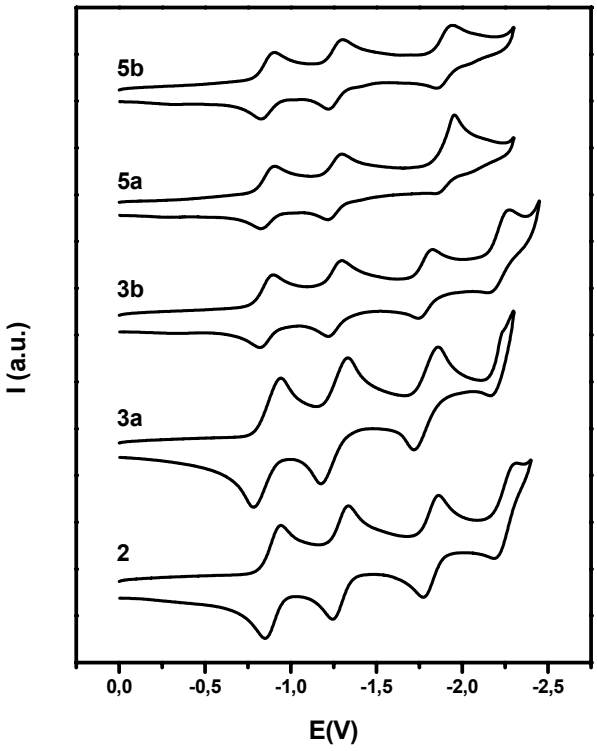

Figure XVI-1. Cyclic voltammograms of compounds **2**, **3a**, **3b**, and **5a, 5b** measured in *o*-DCB/MeCN (4:1) at 100 mV s^{-1}

Computational details

The calculations were carried out by using the 2002.03 release of the Amsterdam density functional (ADF)[11] package developed by Baerends and co-workers.[12,13] The numerical integration scheme of te Velde and Baerends was employed.[14] Both geometry optimizations and energy evaluations of the neutral closed-shell singlet ground-state structures were performed by using a generalized gradient approximation (GGA) which includes Becke's GGA exchange correction[15] and Perdew's GGA correlation correction,[16] the so-called BP86 functional. For geometry optimizations we used an uncontracted double-ζ basis set augmented by an extra polarization function to describe the 3s, 3p, 3d, and 4s orbitals of cobalt, while for the carbon (2s, 2p), nitrogen (2s, 2p),

oxygen (2s, 2p), and hydrogen (1s) atoms, double-ζ basis sets were employed.[17,18] Electrons in lower orbital shells were treated within the frozen core approximation.[12] A set of auxiliary s, p, d, f, and g functions, centered in all nuclei, was introduced in order to fit the molecular density and Coulomb potential accurately in each SCF cycle.[19]

Results

Calculations at the BP86 level were performed on the PK-reactive complex **3e** (complex **3** in Scheme XVI-2 with R=CH_3) and the PK-unreactive species **14b** (Scheme XVI-3). To gain a better understanding of the effect of the curved fullerene surface as well as the length of the chain connecting the alkene and the alkyne functional groups on the PK reaction. From a thermodynamic viewpoint, the reaction **3e**+CO$\rightarrow$**5e** and the equivalent PK reaction for **14b** are exothermic by 73.9 and 64.0 kcal·mol^{-1}, respectively. Apparently, the final product formed from **14b** is more strained than **5e** as indicated by the fact that the fullerene C-C bond length of the centrally formed ring is 1.643 Å in the final product formed from **14b** compared with 1.618 Å in **5e**. However, although the thermodynamics of the PK reaction is about 10 kcal·mol^{-1} more favorable starting from **3e** than from **14b**, the reason for the lack of reactivity in **14b** should not be ascribed to the thermodynamics of the process and must have a kinetic basis.

Previous theoretical studies[20,21] have shown that the most probable rate-determining step in PK reactions is the loss of CO from intermediate dicobalt carbonyl complexes such as complex **4**. This finding is supported by the fact that these are the only intermediates that can be experimentally observed. For this reason we have analyzed the energies and the molecular structures of species **4e** and **15b** obtained from the reaction of **3e** and **14b** with [$Co_2(CO)_8$] and the complexes formed when these intermediates lose a CO ligand, hereafter labeled complexes **4e-CO** and **15b-CO**, in which the coordinatively unsaturated Co atom interacts with the π system of the fullerene. Unfortunately, the sizes of these systems prevented the calculation of the full energy profile.

Figures XVI-2a and -2b show the geometries of complexes **4e** and **15b**, respectively. The differences between the two species are not significant. The shortest distance between a Co atom and the C=C bond on the fullerene to be attacked is about 4.5-5 Å.

The lengths of the C=C double bonds being attacked are almost the same as those of **3e** and **14b** (1.390 and 1.386 Å, respectively, by calculation at the BP86 level of theory). The molecular structures of complexes **4e-CO** and **15b-CO** depicted in Figures XVI-3a and -3b, respectively, are more informative; a clear difference is observed. The distances between the coordinatively unsaturated Co atoms and the C=C bond being attacked are 2.131 and 2.108 Å for complex **4e-CO**, about 0.1-0.2 Å shorter than those found for complex **15b-CO**. This is likely to be due to the fact that the donation and back-donation interactions between the coordinatively unsaturated Co atoms and the π-system of the fullerene are stronger in complex **4e-CO** than in **15b-CO**. The stronger π interaction in **4e-CO** is also reflected by the length of the C=C double bond attacked, which increases by 0.064 Å in the conversion of **4e** into **4e-CO** and by no more than 0.050 Å in the conversion of **15b** into **15b-CO**. Therefore the C=C double bond that interacts with the Co atom is sufficiently well activated in **4e** to continue the PK process. Thus, the differences observed in the two complexes can be attributed to the different lengths of the organic chain containing the alkyne and alkene functional groups. The alkynyl chain in **4e-CO** is of an appropriate length to favor the metal-π interaction.

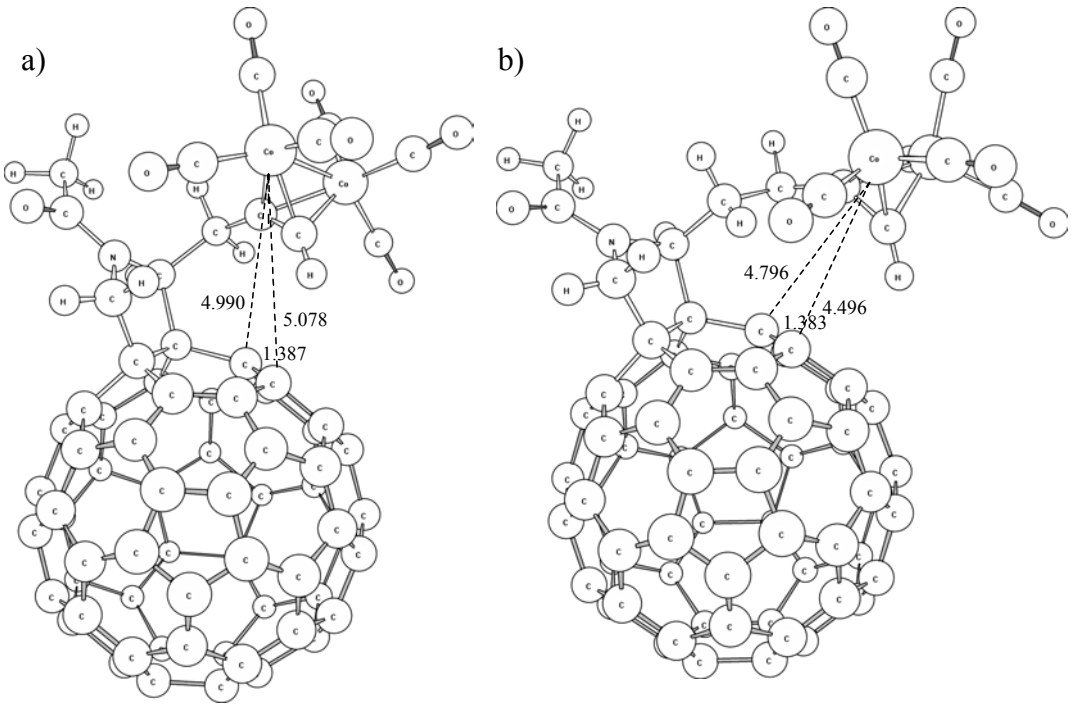

Figure XVI-2. BP86-optimized geometry of complexes a) **4e** and b) **15b** with the most relevant distances given in Å.

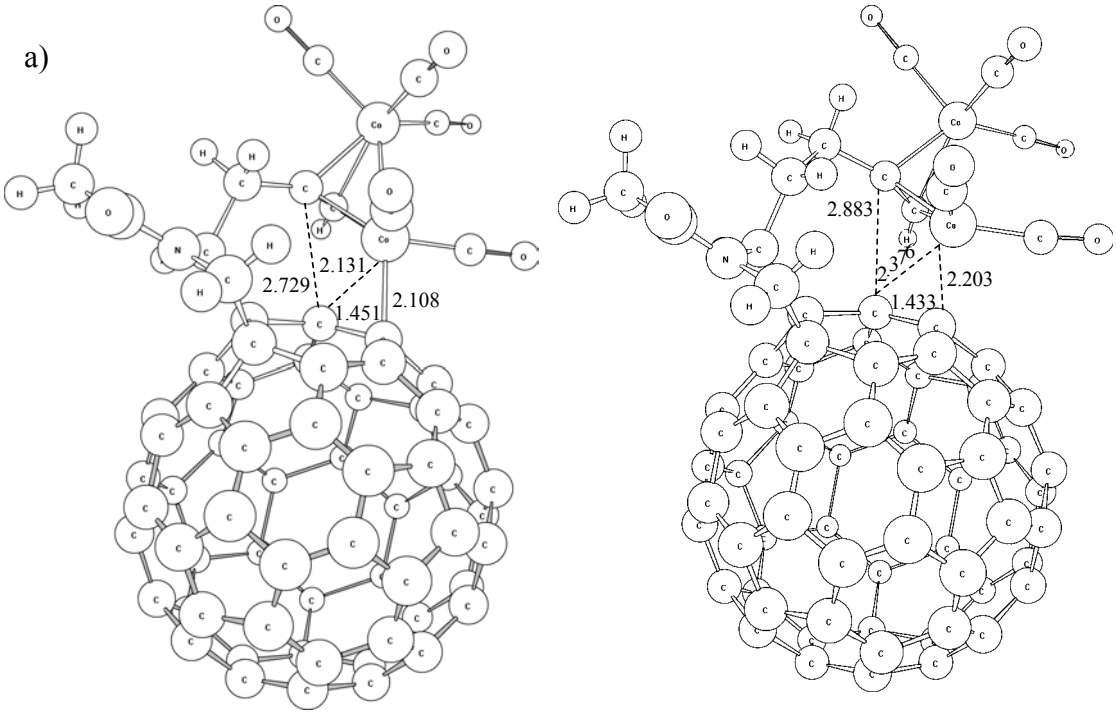

Figure XVI-3. BP86-optimized geometry of complexes a) **4e-CO** and b) **15b-CO** with the most relevant distances given in Å.

Interestingly, this has a relevant effect on the thermodynamics of the formation of **4e-CO** and **15b-CO** by loss of a CO molecule from **4e** and **15b**. While the loss of CO from **15b** (**15b** → **15b-CO**+CO) requires 25.3 kcal·mol^{-1}, the same process starting from **4e** involves only 15.2 kcal·mol^{-1}. Although the transition states of these processes have not been identified owing to high computational costs, it is clear that the loss of CO from **15b** needs more than 25.3 kcal·mol^{-1} and for this reason **15b** does not react further when the temperature is less than 60 °C. As explained before, an increase in the reaction temperature leads to the decomposition of **15b** and so the reaction does not take place at higher temperatures. On the other hand, the loss of CO from **4e** is much more facile. In general terms, the differences in the strength of the interactions between the coordinatively unsaturated Co atom and the π system of the fullerene in the **4e-CO** and **15b-CO** species explain the different reactivities of complexes **3e** and **14b**.

Electrochemistry. *cis*-1 Biscycloadducts **5a-d** and **7** resulting from the PK reaction exhibit half-wave reduction potentials similar to those observed for their precursor fulleropyrrolidines **3** (Figure XVI-1). Although it is known that the reduction potentials of biscycloadducts have a significant cathodic shift relative to related

monocycloadducts,[10,22] in our case the values observed are a result of the electron-withdrawing effect of the carbonyl group of the cyclopentenone ring fused to the fullerene cage. These data are supported by the LUMO energy levels calculated for **3** (-5.795 eV, R=CH_3) and the related PK product **5** (-5.791 eV, R=CH_3) which have almost identical energy values and similar shapes (Figure XVI-4). This finding is in full agreement with previous electrochemical studies carried out on the parent fullerocyclopentenone which exhibited the same reduction potential as pristine C_{60} despite the saturation of one of the double bonds of the fullerene core.[23]

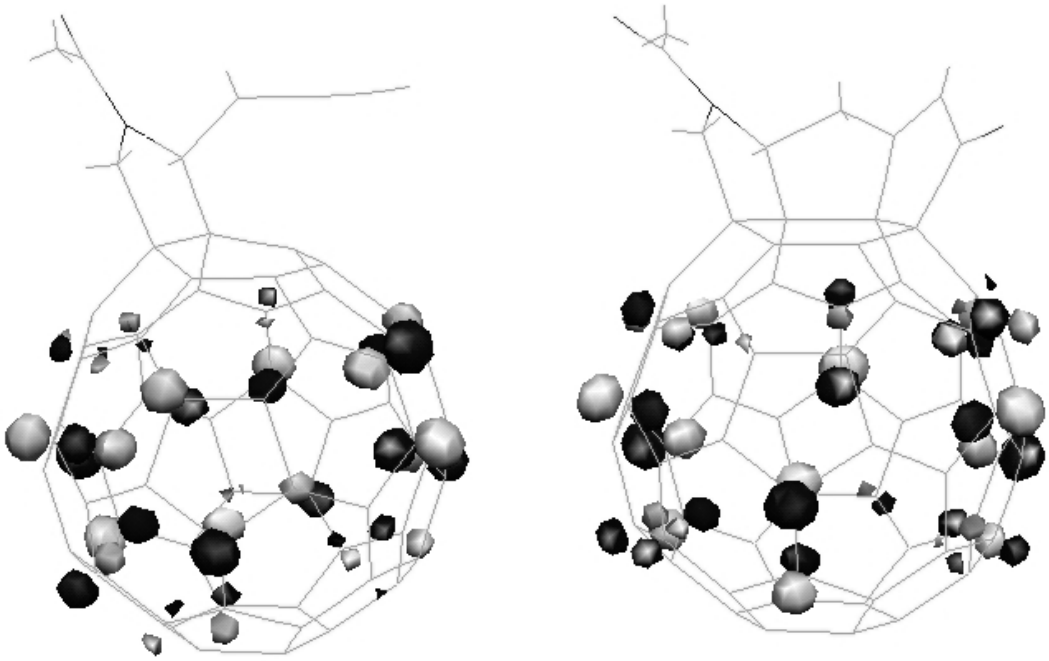

(a) (b)

Figure XVI-4. Three-dimensional representation of the LUMO of a) reactant **3** and b) product **5** with R=CH_3 computed at the BP86 level. Isosurface values are -0.05 and 0.05 a.u.

The above electrochemical data reveal that despite the saturation of two of the double bonds of the fullerene cage in biscycloadducts **5a-d** and **7**, these adducts are remarkable electron acceptors, like their fulleropyrrolidine precursors, as a result of the fused cyclopentenone ring and the electron-withdrawing effect of the carbonyl group directly linked to the C_{60} sphere.

Conclusions

The remarkably different reactivities exhibited by the fulleropyrrolidines endowed with the 1,6-enyne moiety and those with the 1,7-enyne fragment have been rationalized by means of DFT theoretical calculations. The energies and the molecular structures of the intermediates formed through the interaction between the coordinatively unsaturated Co atom and the π system of the fullerene (**4e-CO** versus **15b-CO**) reveal important differences between the two systems and clearly confirm that the interaction in the 1,6-enyne (**4e-CO**) is stronger as a consequence of the different length of the organic chain linking the alkyne and alkene functional groups. These results show that the highly versatile PK reaction can be applied to the spherical molecular surfaces of C_{60} and other fullerenes.

References

1. For recent reviews on the PK reaction, see: a) A. J. Fletcher, S. D. R. Christie, *J. Chem. Soc. Perkin Trans. 1* **2000**, 1657-1668. b) K. M. Brummond, J. L. Kent, *Tetrahedron* **2000**, *56*, 3263-3283. c) T. Sugihara, M. Tamaguchi, M. Nishizawa, *Chem. Eur. J.* **2001**, *7*, 3315-3318. d) S. E. Gibson, A. Stevenazzi, *Angew. Chem.* **2003**, *115*, 1844-1854; *Angew. Chem. Int. Ed*. **2003**, *42*, 1800-1810. e) J. Blanco-Urgoiti, L. Añorbe, L. Pérez-Serrano, G. Domínguez, J. Pérez-Castells, *Chem. Soc. Rev.* **2004**, *33*, 32-42.
2. N. Martín, M. Altable, S. Filippone, A. Martín-Domenech, *Chem. Commun.* **2004**, 1338-1339.
3. R. C. Haddon, *Acc. Chem. Res*. **1992**, *25*, 127-133.
4. a) A. Hirsch, The Chemistry of Fullerenes, Thieme, New York, 1994. b) F. Diederich, C. Thilgen, *Science* **1996**, *271*, 317-323. c) R. Taylor, Lecture Notes on Fullerene Chemistry. A Handbook for Chemists, Imperial College Press, London, **1999**. d) Fullerenes and Related Structures, Topics in Current Chemistry, Vol. 199 (Ed.: A. Hirsch), Springer, Berlin, 1999. e) Fullerenes: From Synthesis to Optoelectronic Properties (Eds.: D. M. Guldi, N. Martín), Kluwer Academic Publishers, Dordrecht, 2002.
5. For a recent review, see: M. R. Rivero, J. Adrio, J. C. Carretero, *Eur. J. Org. Chem.* **2002**, 2881-2889.

6. N. Martín, M. Altable , S. Filippone, A. Martín-Domenech, A. Poater, M. Solà, *Chem. Eur. J.* **2005**, *11*, 2716-2729.
7. a) L. Pérez-Serrano, J. Blanco-Urgoiti, L. Casarrubios, G. Dominguez, J. Pérez-Castells, *J. Org. Chem.* **2000**, *65*, 3513-3519. b) C. J. Lovely, H. Seshadri, B. R. Wayland, A. W. Cordes, *Org. Lett*. **2001**, *3*, 2607-2610.
8. a) M. Prato, M. Maggini, *Acc. Chem. Res*. **1998**, *31*, 519-526. b) M. Maggini, G. Scorrano, M. Prato, *J. Am. Chem. Soc*. **1993**, *115*, 9798-9799. c) N. Tagmatarchis, M. Prato, *Synlett.* **2003**, 768-779.
9. J. Heinze, *Angew. Chem.* **1984**, *96*, 823-840; *Angew. Chem. Int. Ed. Engl.* **1984**, *23*, 831-847.
10. a) L. Echegoyen, L. E. Echegoyen, *Acc. Chem. Res.* **1998**, *31*, 593-601. b) N. Martín, L. Sánchez, B. Illescas, I. Pérez, *Chem. Rev.* **1998**, *98*, 2527-2547.
11. ADF2002, E. J. Baerends, J. A. Autschbach, A. Bérces, C. Bo, P. M. Boerrigter, L. Cavallo, D. P. Chong, L. Deng, R. M. Dickson, D. E. Ellis, L. Fan, T. H. Fischer, C. Fonseca Guerra, S. J. A. van Gisbergen, J. A. Groeneveld, O. V. Gritsenko, M. Grüning, F. E. Harris, P. van den Hoek, H. Jacobsen, G. van Kessel, F. Kootstra, E. van Lenthe, V. P. Osinga, S. Patchkovskii, P. H. T. Philipsen, D. Post, C. C. Pye, W. Ravenek, P. Ros, P. R. T. Schipper, G. Schreckenbach, J. G. Snijders, M. Solà, M. Swart, D. Swerhone, G. te Velde, P. Vernooijs, L. Versluis, O. Visser, E. van Wezenbeek, G. Wiesenekker, S. K. Wolff, T. K. Woo, T. Ziegler, Vrije Universiteit of Amsterdam, The Netherlands, **2002**.
12. E. J. Baerends, D. E. Ellis, P. Ros, *Chem. Phys.* **1973**, *2*, 41-51.
13. G. te Velde, F. M. Bickelhaupt, E. J. Baerends, C. Fonseca Guerra, S. J. A. van Gisbergen, J. G. Snijders, T. Ziegler, *J. Comput. Chem.* **2001**, *22*, 931-967.
14. G. te Velde, E. J. Baerends, *J. Comput. Phys.* **1992**, *99*, 84-98.
15. A. D. Becke, *Phys. Rev. A* **1988**, *38*, 3098-3100.
16. J. P. Perdew, *Phys. Rev. B* **1986**, *33*, 8822-8824.
17. J. G. Snijders, E. J. Baerends, P. Vernooijs, *At. Nucl. Data Tables* **1982**, *26*, 483-509.
18. P. Vernooijs, E. J. Baerends, Slater Type Basis Functions for the Whole Periodic System. Internal Report, Vrije Universiteit of Amsterdam, The Netherlands, 1981.
19. J. Krijn, E. J. Baerends, *Fit Functions in the HFS Method. Internal Report (in Dutch)*, Vrije Universiteit of Amsterdam, The Netherlands, 1984.

20. M. A. Pericàs, J. Balseéis, J. Castro, I. Marchuela, A. Moyano, A. Riera, J. Vázquez, X. Verdaguer, *Pure Appl. Chem.* **2002**, *74*, 167-174.
21. M. Yamanaka, E. Nakamura, *J. Am. Chem. Soc.* **2001**, *123*, 1703-1708.
22. M. Carano, T. Da Ros, M. Fanti, K. Kordatos, M. Marcaccio, F. Paolucci, M. Prato, S. Bofia, F. Zerbetto, *J. Am. Chem. Soc.* **2003**, *125*, 7139-7144.
23. T. Suzuki, Y. Maruyama, T. Akasaka, W. Ando, K. Kobayashi, S. Nagase, *J. Am. Chem. Soc.* **1994**, *116*, 1359-1363.

Chapter XVII: *Stereodiscrimination in Phosphanylthiolato Nickel(II) Complexes*

Stereodiscrimination in Phosphanylthiolato Nickel(II) Complexes

Abstract

The presence of a stereogenic carbon centre (*R* or *S*) in the racemic ligand 1-(diphenylphosphanyl)propane-2-thiol induces a conformational preference (λ or δ) in the five-membered chelate ring of its 2:1 and 2:2 coordination compounds with Ni^{II}: the mononuclear *trans*-[Ni{SCH(CH_3)CH_2PPh_2-*P*,*S*}$_2$] (**1**) and the binuclear *trans*-[Ni{μ-SCH(CH_3)CH_2PPh_2-*P*,*S*}(Cl)]$_2$ (**2**). Both complexes exist as mixtures of two diastereomers: racemic-*trans* (R_λ, R_λ and S_δ, S_δ) and meso-*trans* (R_λ, S_δ), in an equilibrium displaced towards the more stable isomer, the meso-*trans* for **1** (calculated ΔE = < -0.1 kcal·mol^{-1}) and the racemic-*trans* for **2** (calculated ΔE = -5.1 kcal·mol^{-1}). This phenomenon is especially evident for complex **2**, in which an efficient chiral recognition between the two enantiomeric forms of the racemic ligand was observed.

Introduction

The reactivity of 2-phosphanylthiolato nickel(II) complexes has been studied because of their relevance in *S*-alkylation/*S*-dealkylation reactions[1] and their applications in desulfurisation technologies[2] and in understanding the biological pathways of certain sulfur-containing metalloproteins.[3] However, less attention has been given to the importance of the ligand-based stereoelectronic effects in determining the coordination conformations around the metal and the stereochemistries of these compounds.[4] Thus, we decided to focus our attention on these particular aspects. The bis(phosphanylthiolato)nickel(II) complexes *trans*-[Ni($SCH_2CH_2PR_2$-*P*,*S*)$_2$][4,5] exist as mixtures of diastereomers because the five-membered chelate ring can adopt two different conformations (λ and δ) and therefore is able to form three optically isomeric complexes. When both chelate rings are in a λ-conformation, and the two chelate rings of the enantiomer are in a δ-conformation, we have the racemic-*trans* complex and when each chelate ring is in a different conformation, we have the meso-*trans* diastereomer (see Scheme XVII-1). These two stereoisomers can be distinguished when a racemic chiral ligand is present, such as in complex [Ni($SCH_2CH_2PMePh)_2$], which has a racemic ligand chiral at the phosphorus centre. This compound exists in solution

as a mixture of the racemic-*trans* and the meso-*trans* forms that equilibrate slowly ($t_{1/2}$ ca. 12 h) through an intermolecular process to form a 1:1 mixture, since the two diastereomers have very close energies.[4]

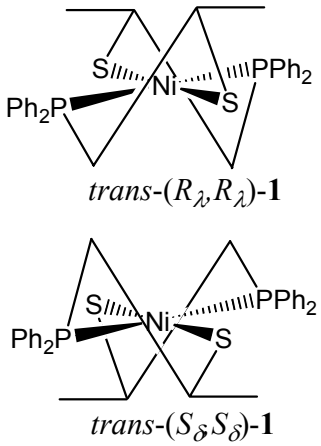

trans-(R_λ,R_λ)-**1**

trans-(S_δ,S_δ)-**1**

racemic-*trans*-**1**

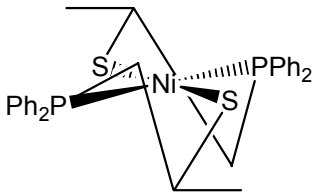

trans-(R_λ,S_δ)-**1**

meso-*trans*-**1**

Scheme XVII-1. Stereoisomers of mononuclear five-member ring bis(phosphanylthiolato)nickel (II) complexes exemplified for complex **1**.

The same stereochemical analysis can be applied to the 2-phosphinothiolato-bridged binuclear nickel (II) complexes $[Ni(\mu\text{-}SCH_2CH_2PR_2)(X)]_2$, which form bent-*syn-endo-trans* structures.[6,7] Theoretical studies have shown that for this class of compounds the stabilization of folded structures with respect to the planar arrangement can be ascribed to the pyramidalization of the sulfur bridge compounded with a weak Ni-Ni interaction. Furthermore, it has been proposed that in a bent structure the chelate ring involving the bridging sulfur would be highly strained in *syn-exo* or *anti* conformations.[7] As in the case of bis(phosphanylthiolato) complexes, the chelate chain introduces some degree of structural variation, also producing the racemic-*trans* and meso-*trans* diastereomers (see Scheme XVII-2). Nevertheless, it should be noted that the *anti* conformation of the bridging sulfur substituents would be necessary for the meso-*trans* isomer to be formed and, for this type of complexes, the bent-*anti* structure has been observed neither in the solid state nor in solution.

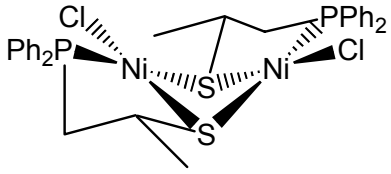

trans-(R_λ,R_λ)-**2**

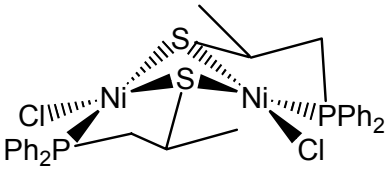

trans-(S_δ,S_δ)-**2**

racemic-*trans*-**2**

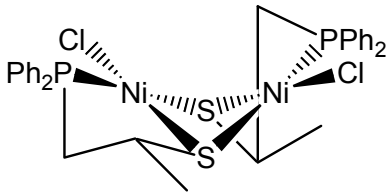

trans-(R_λ,S_δ)-**2**

meso-*trans*-**2**

Scheme XVII-2. Stereoisomers of double 2-phosphanylthiolato-bridged binuclear nickel (II) complexes with bent structures exemplified by complex **2**.

For these reasons, we propose that the energy difference between the racemic-*trans* and meso-*trans* diastereomers of bis(phosphanylthiolato) complexes, and the strong tendency of the phosphanythiolato-bridged binuclear complexes to adopt the folded *syn-endo-trans* conformation, could produce a chiral discrimination between the two enantiomeric conformations of the five-membered chelate ring. In order to demonstrate this hypothesis, the experimental group of Polo et al.[8] synthesized and characterized the 2:1 and 1:1 coordination compounds of the racemic ligand 1-(diphenylphosphanyl)propane-2-thiol[9] with nickel(II). An alternative method to the literature procedures for the syntheses of $[Ni(SCH_2CH_2PPh_2)_2]$[5,10] and $[Ni(\mu\text{-}SCH_2CH_2PPh_2)(Br)]_2$[10] was used to prepare the mononuclear bis-chelate *trans*-$[Ni(SCH(CH_3)CH_2PPh_2)_2]$ **1** and the binuclear *trans*-$[Ni(\mu\text{-}SCH(CH_3)CH_2PPh_2)(Cl)]_2$ **2**. Addition of a CH_2Cl_2 solution of two equiv. of racemic 1-diphenylphosphino-propane-2-thiol to a solution of nikel chloride in methanol resulted in the formation of solid **1**, which was isolated in 85% yield. The same base-free procedure was used for **2**, which was isolated in 80% yield upon addition of one equiv. of the racemic ligand and precipitation with diethyl ether.[11]

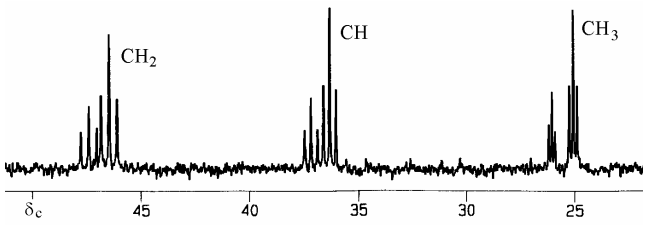

Figure XVII-1. The aliphatic $^{13}C\{^1H\}$ NMR signals of complex **1** appear as triplets owing to virtual coupling with 2 equiv. mutually *trans* phosphorus nuclei.

The *trans* geometry of the mononuclear complex **1** was determined by NMR analysis. In the $^{13}C\{^1H\}$ NMR spectra all aliphatic carbon atoms appear as triplets owing to virtual coupling with two equivalent mutually *trans* phosphorus nuclei (see Figure XVII-1). According to the $^{31}P\{^1H\}$ NMR spectrum, bis-chelate **1** exists as a mixture of two diastereomers: freshly prepared $CDCl_3$ solutions of complex **1** show two resonances at δ_P = 52.6 and 54.2 ppm in about an 11:5 intensity ratio. The similar δ_P values point to two diastereomers with the same configuration but different conformations.

In keeping with the conformational analysis for compound **1** (see Scheme XVII-1), the preferred conformation for the chiral chelate ring depends on the configuration at the stereogenic carbon centre of the ligand.[11a] Thus, the ligand with *R* configuration adopts the λ-conformation, which places the substituent of the chelate ring in the equatorial position. For the same reasons, the ligand with *S* configuration adopts the δ-conformation. As a result of these conformational preferences, complexes carrying two ligands with the same configuration, *trans*-(*R*,*R*)-**1** and *trans*-(*S*,*S*)-**1** are enantiomers (racemic-*trans*-**1**) giving a single $^{31}P\{^1H\}$ NMR signal. The second resonance is then assigned to the diastereomeric complex carrying one ligand in each configuration, *trans*-(*R*,*S*)-**1** (meso-*trans*-**1**). By comparison with the related complex $[Ni(SCH_2CH_2PMePh)_2]$,[4] the major signal could be initially assigned to the racemic-*trans*-**1** stereoisomer, which was claimed to be the kinetic product. However, the intensity ratio of the $^{31}P\{^1H\}$ NMR signals remains constant after 72 h at 50 °C. This behaviour contrasts with that observed for other similar Group VIII metal bis(phosphanylthiolato) complexes, in which the two signals become equal after 24 h at room temperature. In the latter case the two diastereomers have very close energies,[4,11]

suggesting that for complex **1** they have a slight, but significant, difference in energy (experimental ΔE = 0.41 kcal·mol^{-1}).

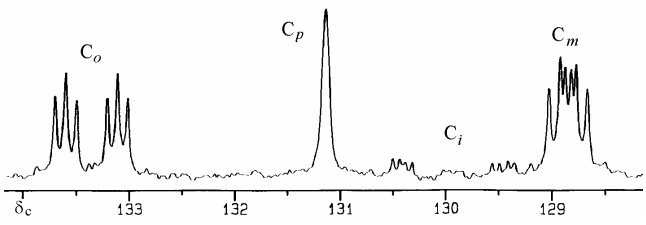

Figure XVII-2. Two of the aromatic $^{13}C\{^1H\}$ NMR signals of complex **2** appear as pseudo-triplets (C_o and C_m), probably owing to a P-Ni-Ni-P coupling; complex **2** is not soluble enough to obtain quality signals for the quaternary carbon atoms, but an unfolded doublet of doublets can be glimpsed in the spectral trace

Binuclear complex **2** adopts a bent *syn-endo-trans* conformation in the solid state and shows a single, sharp resonance in the $^{31}P\{^1H\}$ NMR spectrum at δ_P = 36.3 ppm, both for freshly prepared and aged solutions, pointing to the presence of only one of the possible diastereomers. It is noteworthy that in the $^{13}C\{^1H\}$ NMR spectrum of binuclear **2**, two of the aromatic carbon atoms (C_o and C_m) show two signals each, and all are pseudo-triplets (see Figure XVII-2). The doubling of these signals is assigned to the different surroundings of each phenyl ring in the same diphenylphosphanyl group, while the fine splitting could be ascribed to a somewhat surprisingly similar coupling to both phosphorus nuclei generated by the P-Ni-Ni-P connection, a special case of the known phenomenon of virtual coupling.[7]

The conformational analysis of complex **2** shows, as in the case of **1**, that ligands with *R* and *S* configuration adopt λ and δ conformations, respectively, thereby placing the chelate chain substituent in the equatorial position. Thus, two diastereomeric forms of **2** could exist (racemic-*trans*-**2** and meso-*trans*-**2**: see Scheme XVII-2), but only one of them was observed in solution. The BP86 energy calculations on complex **2** (see below) gave an energy difference of 5.1 kcal·mol^{-1} between the racemic-*trans*-**2** and the meso-*trans*-**2** isomers, in agreement with an equilibrium strongly displaced towards the racemic-*trans*-**2** diastereomer (experimental ΔE = 2.3 kcal·mol^{-1}).[12] Furthermore, the minimum in energy for the meso-*trans*-**2** isomer represents a folded *syn-endo-trans* structure with one of the chelate chain substituents in the equatorial position and the

other in the axial. This result is in agreement with the instability of the bent *anti* conformations predicted for this type of complex.[7]

An XRD study was carried out on crystals of **2**·$CHCl_3$. The crystal structure contains only the racemic-*trans*-**2** diastereomer and reveals an edge-sharing binuclear complex with square-planar coordination geometry around the nickel atoms. The molecule adopts a folded *syn-endo-trans* conformation. Although the Ni-S, Ni-P and Ni-Cl distances are in the range observed for the isostructural $[Ni(\mu\text{-}SCH_2CH_2PPh_2)(X)]_2$ complexes (where X = Cl, Br), the fold angle of the central four-membered Ni_2S_2 cycle is appreciably greater (118.1º *vs*. 100.7-104.1°), increasing the Ni-Ni distance from 2.681-2.695 Å to 2.906 Å.[6] The reason for this geometrical alteration must be attributed to the presence of the substituent in the chelate chain, because there are no other structural changes. In complex **2**, the requirement to locate the methyl group in the equatorial position increases the bending of the tertiary carbon atom away from the S-S hinge (33.6º vs. 27.1-27.8°) and, since this bending is related to the arching of the Ni_2S_2 group,[7] the central core must unfold.

Computational details

The reported calculations were carried out by using the Amsterdam density functional (ADF2002.03) program system,[13] developed by Baerends et al.[14-16] The numerical integration scheme employed was that of te Velde and Baerends.[17] An uncontracted triple-ζ basis set[18] was used for describing the 3s, 3p, 3d, 4s, and 4p orbitals of nickel. For carbon (2s,2p), phosphorus (3s,3p), sulfur (3s,3p), and hydrogen (1s), double-ζ basis sets[18] were employed and augmented by an extra polarisation function. Electrons in lower shells were treated within the frozen core approximation.[15a] A set of auxiliary s, p, d, f, and g functions,[19] centred in all nuclei, was introduced in order to fit the molecular density and Coulomb potential accurately in each SCF cycle. Both geometry optimisations and energy evaluations have been fully carried out within a generalised gradient approximation (GGA) that includes the GGA exchange and correlation corrections of Becke[20] and Perdew (BP86).[21]

The method labeled LDA/VWN was also tested. Geometries were fully optimized within the local density approximation (LDA), which includes the X_α exchange

(α=2/3),[22] together with the electron gas correlation functional in the Vosko-Wilk-Nusair parametrization (VWN).[23]

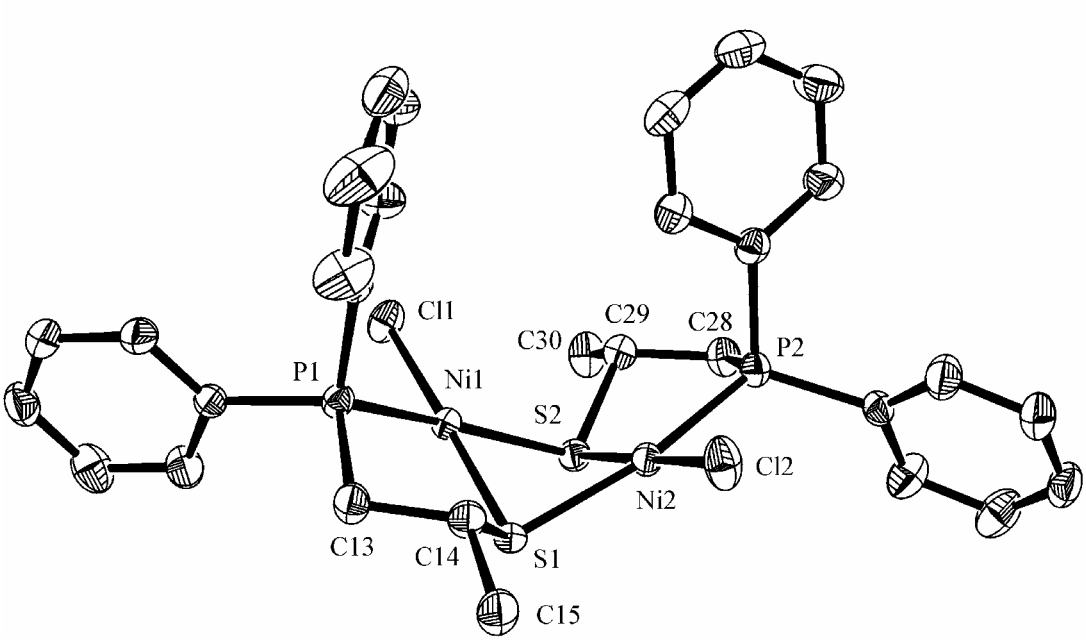

Figure XVII-3. ORTEP plot (50 %) of complex **2**, hydrogen atoms are omitted

In order to validate the method, the XRD data of complex **2** was geometrically optimised by excluding the solvent molecules (see Figure XVII-3). The results show good agreement between the experimental and theoretical data (see Table XVII-1). The experimental and theoretical bond lengths and angles differ by less than 0.08 Å and 3.6°, respectively. The standard deviations for the selected distances and angles listed in Figure XVII-3 were 0.04 Å and 2.1°,[24] respectively, which confirm the validity of the chosen computational method. For LDA//VWN method the standard deviations are 0.06 Å and 3.4º, respectively. As expected, they are worse than BP86 ones. This is the reason why we decided to make the study with GGA for the geometry optimizations.

Distances	RX	LDA	BP86	Angles	RX	LDA	BP86
Ni1-Ni2	2.907	2.898	2.898	S1-Ni1-P1	88.0	89.3	89.1
Ni1-S1	2.156	2.218	2.216	P1-Ni1-Cl1	95.2	94.0	92.3
Ni1-S2	2.224	2.294	2.272	S1-Ni1-S2	79.5	79.9	80.4
Ni1-P1	2.171	2.196	2.188	Cl1-Ni1-S2	97.7	96.8	97.7
Ni1-Cl1	2.191	2.228	2.227	S2-Ni2-P2	88.3	89.1	89.3
Ni2-S1	2.208	2.272	2.293	P2-Ni2-Cl2	92.6	92.3	94.0
Ni2-S2	2.156	2.216	2.218	S2-Ni2-S1	79.8	80.4	79.9
Ni2-P2	2.156	2.188	2.196	Cl2-Ni2-S1	99.1	97.7	96.8
Ni2-Cl2	2.181	2.227	2.228	Ni1-S1-Ni2	83.5	80.4	80.0
S1-C14	1.841	1.868	1.874	C14-S1-Ni1	105.9	104.5	104.0
C13-C14	1.531	1.530	1.540	C14-S1-Ni2	112.7	110.7	109.5
C14-C15	1.516	1.545	1.523	Ni2-S2-Ni1	83.1	80.0	80.4
P1-C13	1.834	1.857	1.853	C29-S2-Ni2	105.4	104.0	104.5
S2-C29	1.854	1.874	1.868	C29-S2-Ni1	112.8	109.5	110.7
C28-C29	1.520	1.540	1.530				
C29-C30	1.521	1.523	1.545				
P2-C28	1.833	1.853	1.857				

Table XVII-1. Comparison between the X-ray data of complex **2** and the corresponding BP86 geometry (Distances in Å and angles in degrees), and also with a LDA//VWN optimization.

Results

All the experimental compounds were analysed computationally. It was found experimentally that both mononuclear and binuclear species are diamagnetic. For this reason, optimisations were carried out for neutral closed-shell singlet ground-state structures. However, since it has been found that the triplet state is close in energy to the singlet state, or it can in some cases be even more stable than the singlet state, we checked the relative stability of both states for all compounds by optimising the triplet state. In all cases the triplet state geometry presented a higher energy, indicating that the singlet states are the most favourable. This is in agreement with the sharp peaks in the

NMR spectra. The difference between these two states is around 20 kcal·mol^{-1} (racemic-*trans*-**1** 22.2 kcal·mol^{-1}; meso-*trans*-**1** 21.4 kcal·mol^{-1}; racemic-*trans*-**2** 19.4 kcal·mol^{-1}; meso-*trans*-**2** 21.6 kcal·mol^{-1}).

Energy calculations predicted a slight stabilisation, by less than 0.1 kcal·mol^{-1} (exp. 0.4 kcal·mol^{-1}), of the meso-*trans*-**1** isomer relative to the racemic-*trans*-**1**, showing that the two isomers have similar energies, in line with the fact that experimentally the two isomers are present as final products. The reasons of the higher stability of the meso-*trans*-**1** isomer are probably the steric interactions between the *pseudo*-axial phenyl groups that are mutually *syn* in racemic-*trans*-**1** and *anti* in meso-*trans*-**1** (see Scheme XVII-3).

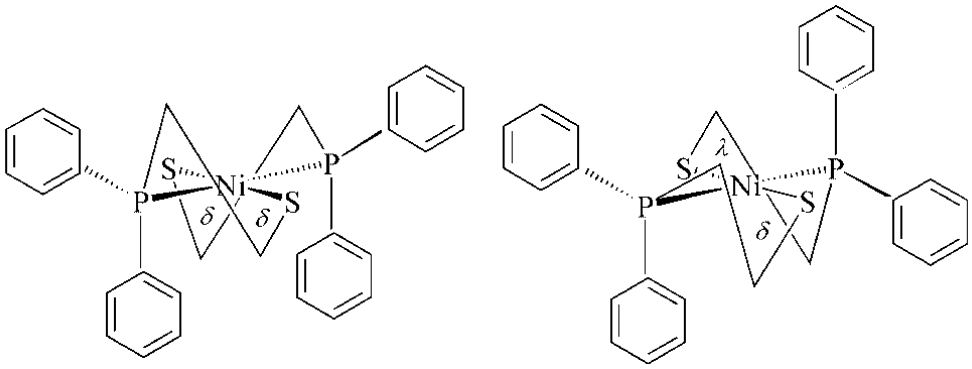

Scheme XVII-3. The pseudo-axial phenyl groups of the *trans*-bis(2-diphenylphosphanylthiolato)nickel(II) complexes are mutually *syn* in the stereoisomers carrying both chelate rings in the same conformation (λ, λ or δ, δ) and *anti* in the stereoisomer with one chelate ring in each conformation (λ, δ)

On the other hand, the energy calculations on complex **2** gave an energy difference of 5.1 kcal·mol^{-1} between the racemic-*trans*-**2** and the meso-*trans*-**2** isomers, the racemic-*trans* isomer being the most stable, in agreement with an equilibrium strongly displaced towards the racemic-*trans*-**2** diastereomer (experimental ΔE = 2.3 kcal·mol^{-1}), explained through the high steric repulsions that the meso-*trans* isomer presents.[12]

We also attempted to optimise an *anti* conformation for the binuclear complex, but the optimisation process evolved towards the racemic-*trans*-**2** species, as the *anti*

conformations are even less stable than the *syn* ones because of the steric requirements of the ligands.

Conclusions

In conclusion, the calculated BP86 energy differences between the racemic-*trans* and meso-*trans* diastereomers of these phosphanylthiolato complexes of Ni^{II} are in agreement with the experimentally observed racemic-*trans*/meso-*trans* ratios and are responsible for the chiral recognition between the two enantiomeric forms of the racemic ligand. This phenomenon is especially important in the binuclear complex **2**, in which a destabilised *anti* conformation of the bridging sulfurs would be necessary for the meso-*trans* isomer to be stable.

References

1. J. S. Kim, J. H. Reibenspies, M. Y. Darensbourg, *J. Am. Chem. Soc.* **1996**, *118*, 4115-4423.
2. D. A. Vicic, W. D. Jones, *J. Am. Chem. Soc.* **1999**, *121*, 7606-7617.
3. a) L. C. Myers, M. P. Terranova, A. E. Ferentz, G. Wagner, G. L. Verdine, *Science* **1993**, *261*, 1164-1167. b) T. Ohkubo, H. Sakashita, T. Sakuma, M. Kainosho, M. Sekiguchi, K. Morikawa, *J. Am. Chem. Soc.* **1994**, *116*, 6035-6036.
4. P. H. Leung, J. W. L. Martin, S. B. Wild, *Inorg. Chem.* **1986**, *25*, 3396-3400.
5. a) Y.-M. Hsiao, S. S. Chojnacki, P. Hinton, J. H. Reibenspies, M. Y. Darensbourg, *Organometallics* **1993**, *12*, 870-875. b) M. Kita, T. Yamamoto, K. Kashiwabara, J. Fujita, *Bull. Chem. Soc. Jpn.* **1992**, *65*, 2272-2274.
6. a) T. Gerdau, W. Klein, R. Kramolowsky, *Acta Crystallogr., Sect. C: Cryst. Struct. Commun.* **1982**, *11*, 1663-1669. b) K. Aurvillius, G. Bertinsson, *Acta Crystallogr., Sect. B* **1982**, *38*, 1295-1298.
7. a) G. Aullón, G. Ujaque, A. Lledós, S. Álvarez, *Chem. Eur. J.* **1999**, *5*, 1391-1410. b) G. Aullón, G. Ujaque, A. Lledós, S. Álvarez, P. Alemany, *Inorg. Chem.* **1998**, *37*, 804-813.
8. J. Duran, A. Polo, J. Real, J. Benet-Buchholz, A. Poater, M. Solà, *Eur. J. Inorg. Chem*. **2003**, 4147-4151.
9. M. Wieber, T. Z. Clarius, *Z. Anorg. Allg. Chem.* **1995**, *621*, 1288-1292.

10. E. Pfeiffer, M. L. Pasquier, W. Marty, *Helv. Chim. Acta* **1984**, *67*, 654-663.
11. a) N. Brugat, J. Duran, A. Polo, J. Real, A. Álvarez-Larena, J. F. Piniella, *Tetrahedron: Asymmetry* **2002**, *13*, 569-577. b) N. Brugat, A. Polo, A. A´ lvarez-Larena, J. F. Piniella, J. Real, *Inorg. Chem.* **1999**, *38*, 4829-4837.
12. The experimental difference of energy between the two diastereomers was calculated from the $^{31}P\{^{1}H\}$ NMR spectra using the relative signal intensities for complex **1** and the signal to noise ratio for complex **2**.
13. ADF2002.03, E. J. Baerends, J. A. Autschbach, A. Bérces, C. Bo, P. M. Boerrigter, L. Cavallo, D. P. Chong, L. Deng, R. M. Dickson, D. E. Ellis, L. Fan, T. H. Fischer, C. Fonseca Guerra, S. J. A. van Gisbergen, J. A. Groeneveld, O. V. Gritsenko, M. Grüning, F. E. Harris, P. van den Hoek, H. Jacobsen, G. van Kessel, F. Kootstra, E. van -Lenthe, V. P. Osinga, S. Patchkovskii, P. H. T. Philipsen, D. Post, C. C. Pye, W. Ravenek, P. Ros, P. R. T. Schipper, G. Schreckenbach, J. G. Snijders, M. Solà, M. Swart, D. Swerhone, G. te Velde, P. Vernooijs, L. Versluis, O. Visser, E. van Wezenbeek, G. Wiesenekker, S. K. Wolff, T. K. Woo, T. Ziegler, Vrije Universiteit Amsterdam, Amsterdam, 2002.
14. G. te Velde, F. M. Bickelhaupt, E. J. Baerends, C. Fonseca Guerra, S. J. A. van Gisbergen, J. G. Snijders, T. Ziegler, *J. Comput. Chem.* **2001**, *22*, 931-967.
15. a) E. J. Baerends, D. E. Ellis, P. Ros, *Chem. Phys.* **1973**, *2*, 41-51. a) E. J. Baerends, PhD Thesis, Vrije Universiteit, Amsterdam, **1975**.
16. W. Ravenek, *Algorithms and Applications on Vector and Parallel Computers* (Eds.: H. J. J. te Riele, Th. J. Dekker, H. A. van de Vorst), Elsevier, Amsterdam, **1987**.
17. G. te Velde, E. J. Baerends, *J. Comput. Phys.* **1992**, *99*, 84-98.
18. a) J. G. Snijders, E. J. Baerends, P. Vernooijs, *At. Nucl. Data Tables* **1982**, *26*, 483-509. b) P. Vernooijs, J. G. Snijders, E. J. Baerends, *Slater Type Basis Functions for the Whole Periodic System. Internal Report*, Vrije Universiteit of Amsterdam, The Netherlands, 1981.
19. J. Krijn, E. J. Baerends, *Fit functions in the HFS method. Internal Report (in Dutch)*, Vrije Universiteit of Amsterdam, The Netherlands, 1984.
20. A. D. Becke, *Phys. Rev. A* **1988**, *38*, 3098-3100.
21. J. P. Perdew, *Phys. Rev. B* **1986**, *33*, 8822-8824.
22. J. C. Slater, *Quantum Theory of Molecules and Solids*; McGraw-Hill: New York, Vol. 4, 1974.

23. S. H. Vosko, L. Wilk, M. Nusair, *Can. J. Phys.* **1980**, *58*, 1200-1211.

24. Standard deviations for the distances and for the angles, $s_{n-1} = \sqrt{\frac{\sum_{i=1}^{N}(CV - EV)^2}{N-1}}$, where CV means calculated value, EV experimental value (X-ray data), and N is the number of distances or angles taken into account.

Chapter XVIII: *Diastereoisomerism in Platinum(II) 2-Phosphino and 2-Aminothiolato Complexes*

Diastereoisomerism in Platinum(II) 2-Phosphino and 2-Aminothiolato Complexes

Abstract

We have carried out DFT calculations to rationalize the diastereoisomerism in Platinum(II) 2-aminothiolato, **1**, and 2-phosphinothiolato, **2**, complexes. The aminothiolato ligand was further studied by attaching a carboxylic group in its alkylic chain. The equilibrium *cis*-trans is experimentally only observed for complex **2**, and for complexes **1** only the *cis* species are formed. Some solutions are possible to obtain only the *trans* isomer, as for instance to enlarge the alkylic chain of the phosphinothiolato chain or attach a chain including an eter and a phenyl group.

Introduction

Chelating diphosphines are the prevalent chiral bidentate ligand for catalytic asymmetric transformations. Many of these diphosphines have two donor atoms with similar electronic and steric properties. Marked differentiation between the coordinating groups can be achieved by changing the chemical nature of one or both atoms, as in the case of 2-aminothiolates and 2-phosphinothiolates. On the other hand, low symmetry platinum complexes are of interest because of their potential as selective catalysts in homogeneous reactions. Despite these promising properties, very few platinum 2-phosphinothiolato and 2-aminothiolato complexes have been described. The low attention given to this class of complexes is due, in our opinion, to the lack of knowledge on the ligand-based stereoelectronic effects in determining the coordination conformations around the metal and stereochemistries of these compounds. In this context, the diastereochemistry of these complexes has particular importance, as different diastereomers should present different activities, regioselectivies, and eneantioselectivies in a given catalytic process.[1]

As a part of a project on the use of this type of complexes as homogeneous catalysts, Polo et al. have previously reported the preparation of low symmetry platinum(II) complexes, with hydrido, phosphine, and *N,S*-2-aminothiolato ligands, by chelate assisted oxidative addition of 2-aminothiols to Pt(0) complexes (see Schemes XVIII-1

and -2).[2] The same method has been used now to prepare the analogous *P,S*-2-phosphinothiolato complexes. Regarding the diastereochemistry of these complexes, the conformation of the chelate rings (λ or δ) can be determined by the presence of a stereogenic carbon center in the chelate chain.[3] However, rather unexpectedly, phosphino and aminothiolato complexes exhibit an opposite geometric-isomerism preference. These geometric differences and the behavior of the complexes in solution were also studied.

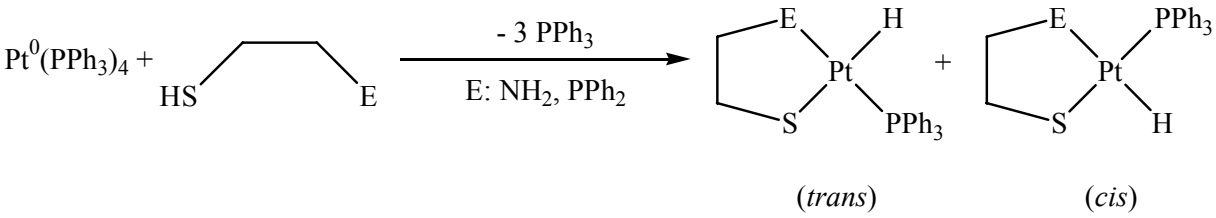

Scheme XVIII-1. General preparation of phosphino and aminothiolato platinum(II) complexes.

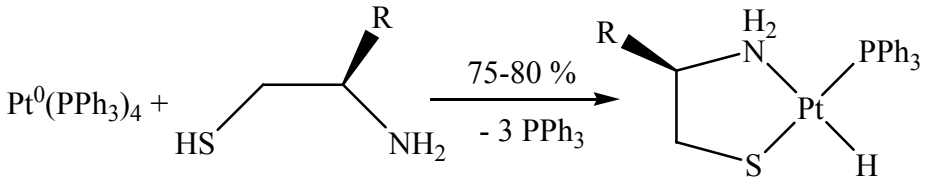

1	/	1	R: H	R: H, **1a**
1	/	1.5	R: COOMe	R: COOMe, **1b**
1	/	1.5	R: COOEt	R: COOEt, **1c**

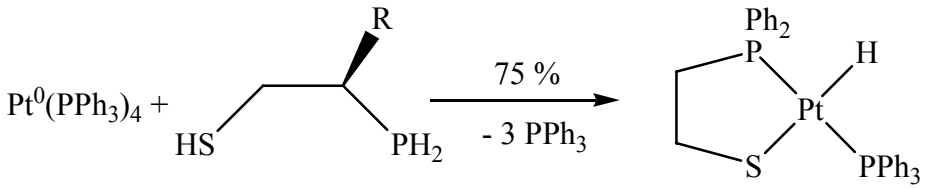

1 / 1 **2**

Scheme XVIII-2. Preparation of the studied phosphino and aminothiolato platinum(II) complexes.

Polo et al. have experimentally characterized by X-ray spectroscopy the four products of the reactions described in Scheme XVIII-2, as Figure XVIII-1 shows.

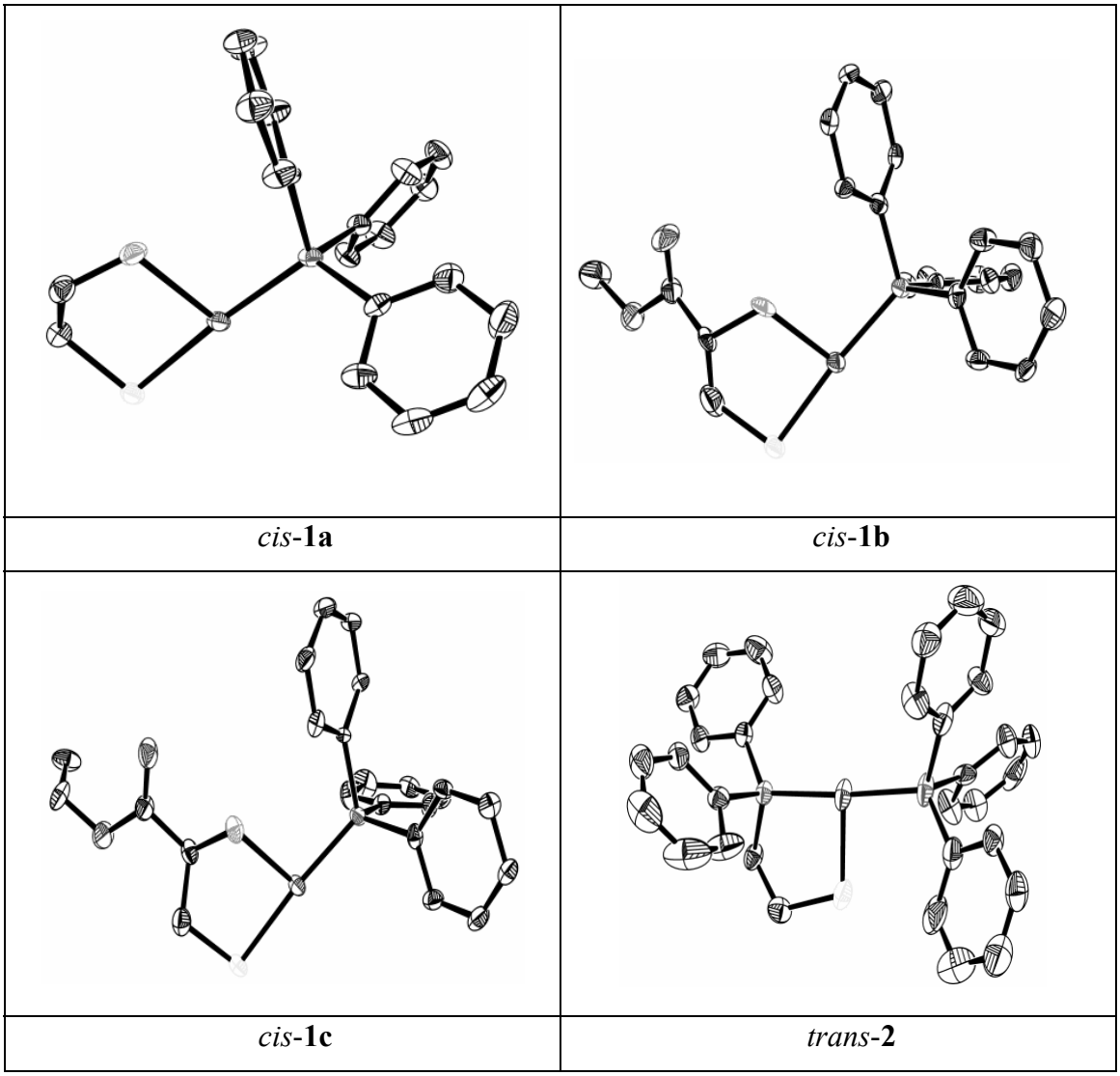

cis-**1a** | *cis*-**1b**

cis-**1c** | *trans*-**2**

Figure XVIII-1. X-ray data of complexes **1a-c** and **2** (hydrogen atoms have been omittd for clarity).

At room temperature, the NMR spectrum for the hydrogen bonded to platinum shows, as expected, a triplet of doublets for complexes **1** ($^{1}J_{^{195}Pt-H}$ = 1180-1112 Hz, $^{2}J_{^{31}P-H}$ (*cis*) ≈ 21 Hz) and a triplet of doublets of doublets for complex **2** ($^{1}J_{^{195}Pt-H}$ = 967.0 Hz, $^{2}J_{^{31}P-H}$ (*trans*) = 182.8 Hz, $^{2}J_{^{31}P-H}$ (*cis*) = 22.0 Hz). At this temperature the hydride NMR spectrum of *trans*-**2** appears as a broad triplet of doublets that resolves in a triplet

of doublets of doublets ($^{1}J_{^{195}Pt-H}$ = 977.9 Hz, $^{2}J_{^{31}P-H}$ (*cis*) = 16.8 Hz, $^{2}J_{^{31}P-H}$ (*cis*) = 9.7 Hz) lowering the temperature to -60 ºC. This observation suggests a rapid intermolecular exchange process for complex *trans*-**2**, owing to the large *trans*-effect of the chelated PPh_2 group. A similar exchange process was previously reported for *trans*-hydridothiolatobis(phosphine)Pt(II) complexes.[8]

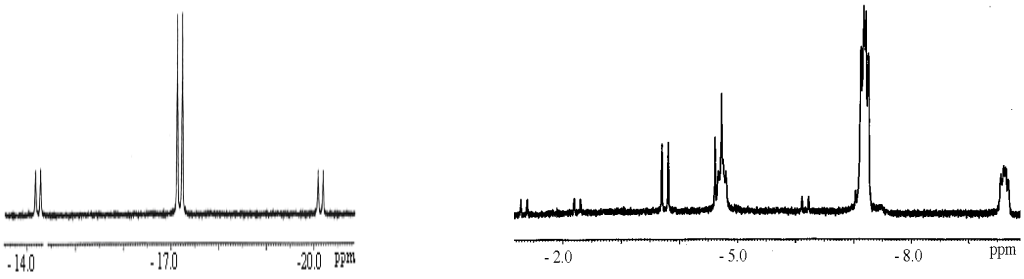

1c **2**

Figure XVIII-2. ^{1}H-NMR data for **1c** and **2**.

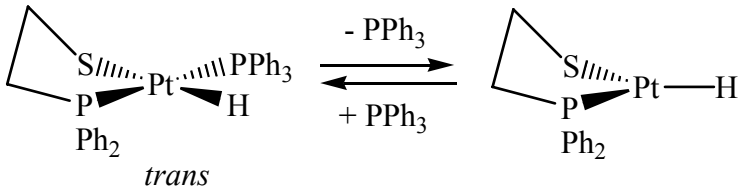

Scheme XVIII-3. Dissociative mechanism for the isomerization of complex **2**.

Although the intermolecular exchange could produce the isomerization process observed for complex **2**, *via* dissociative mechanism (see Scheme XVIII-3), the non-existence of a similar fast exchange for *cis*-**2** isomer (see Scheme XVIII-4), owing to the smaller *trans*-effect of the thiolate *versus* the PPh_2 group, together with the highly displaced equilibrium towards the *trans*-**2** isomer indicates that this process only generates the free PPh_3 needed for the isomerization *via* the most accepted associative mechanism (see Scheme XVIII-5).

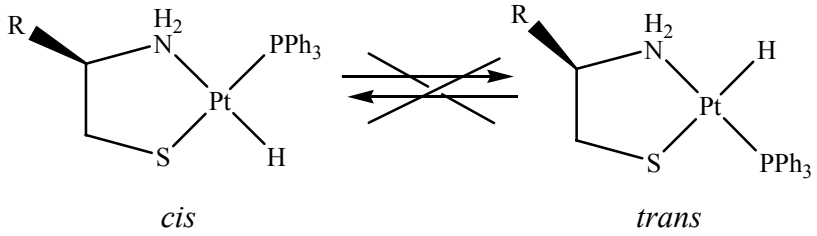

R: H (**1a**), COOMe (**1b**), COOEt (**1c**)

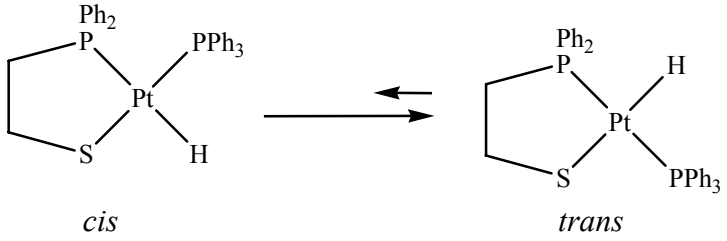

2

Scheme XVIII-4. *Cis*/*trans* exchange

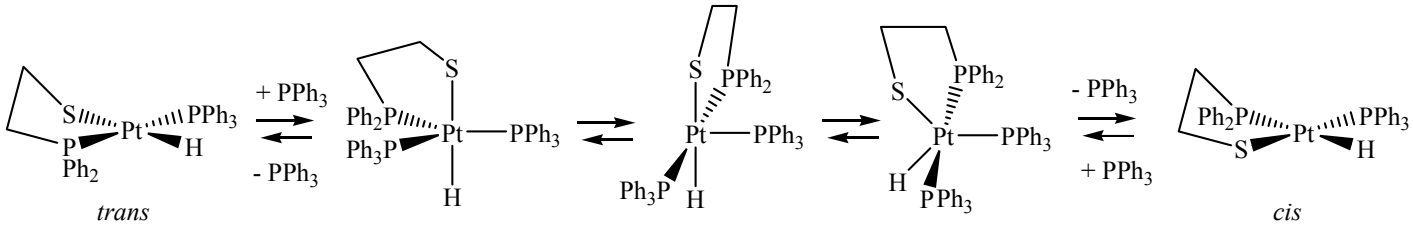

Scheme XVIII-5. Associative mechanism for the isomerization.

For compounds *cis*-**1**, the small *trans*-effect of the thiolato group prevents the dissociation of PPh_3, eliminating the isomerization possibilities.

Further studies by Polo et al., including three methylenic units in the alkylic chain of the phosphinothiolato ligand, give as a result the complex **3**. The ^{1}H-NMR spectrum at r.t. shows two signals at high fields (between -7 and -10.6 ppm) with a relation 1:2 where the corresponding signal of the majority product appears at lower fields (see Figure XVIII-3). The wideness of the signals is due to a dependency of the spectrum with respect to the temperature, which indicates that a dynamical process in solution exists. To know which kind of dynamical process took place a NMR study varying the temperature showed alow value of the ^{1}H-^{31}P coupling constants, demonstrating a *cis* geometry between the hydride ligand and the two phosphorous atoms present in both

isomers **3a** (majority) and **3b** (minority), and therefore presupposes a *trans* geometry between the two phosphorate ligands.

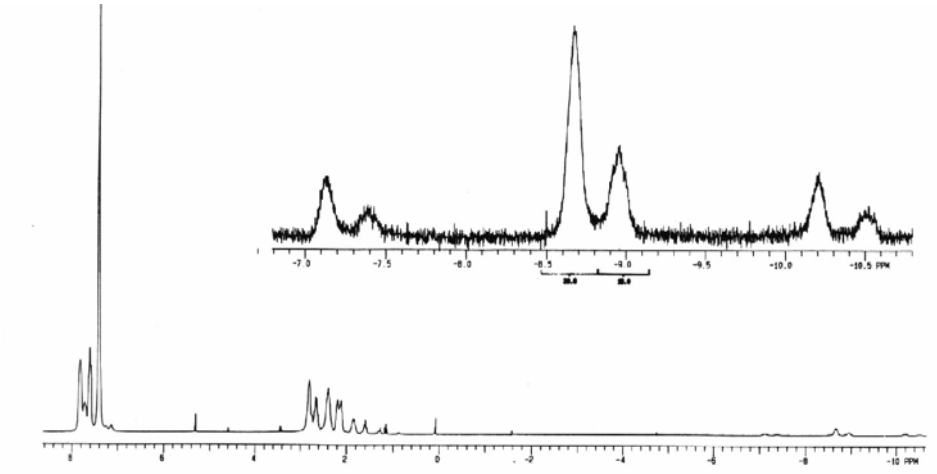

Figure XVIII-3. ^{1}H-NMR data for **3.**

All these spectroscopic data agree with a square planar structure for isomers **3a** and **3b** in which the hydride ligand is placed in cis position with regard to the two phosphino groups, and therefore, in trans with respect to the thiolato group. The difference between the two observed isomers by NMR must be found in the chelate ring. Normally at r.t. the conformations of a six-member cycle interconvert very quickly avoiding the observation by NMR, thus making the acquisition of data be very difficult. This situation, known as fast-exchange limit, at the NMR spectrum the signals of only a compound are observed being the average of the two conformations. The lowering of temperature is traduced as a slow motion of the equilibrium, giving as a result the widening of the signals till the absolute disappearance in the basis line. This point is known as the point of coalescence and takes places at the coalescence temperature.

A higher decrease of the equilibrium speed, by cooling, makes the signals of the two conformers in solution appear. The signals are initially near and very wide and they are more and more separated and being solved while the equilibrium is blocked. In this situation, known as a slow exchange limit, the interconversion speed is lower than the acquisition speed of NMR data, which allows the observation of the signals of both conformers separated.

The aim of the DFT calculations shown in this chapter is to rationalize why the equilibrium *cis-trans* is observed for **2**, and for complexes **1** only the *cis* species are formed. In addition the effect of increasing the length of the alkylic chain of the phosphinothiolato ligand is also studied.

Computational details

The reported calculations have been carried out by using the Amsterdam density functional (ADF) package developed by Baerends and coworkers[9] and vectorized by Ravenek.[10] The numerical integration scheme employed has been that of te Velde and Baerends.[11] An uncontracted triple-ς basis set has been used for describing the orbitals of platinum. For carbon, nitrogen, phosphor, oxygen, sulphur, phosphor, and hydrogen double-ς basis sets have been employed. Both basis sets have been augmented by an extra polarization function.[12] A set of auxiliary *s, p, d, f*, and *g* functions, centered in all nuclei, has been introduced in order to fit the molecular density and Coulomb potential accurately in each SCF cycle.[13] Relativistic effects have been included in the energy calculations and geometry optimizations using the ZORA method.[14] This approach gives generally better results than the Pauli formalism. Geometries and energies have been evaluated using a generalized gradient approximation (GGA) that includes the GGA exchange correction of Becke[15] and the GGA correlation correction of Perdew.[16] This method is labeled throughout this work as BP86. The 2002.03 release of the ADF package has been used for all calculations.[17] We have also carried out an energy decomposition analysis (EDA).[18]

Results

In order to validate the computational method a geometry optimization of the X-ray data of the complex *trans*-**2** was made. The results show good agreement between the experimental and theoretical data as can be seen in Table XVIII-1. The experimental and theoretical bond lengths and angles differ by less than 0.118 Å and 2.6º, respectively. And the standard deviation for the distances is 0.057 Å, and for the angles 1.3º,[19] which confirms the validity of the chosen computational method.

Distances	X-ray	BP86	Angles	X-ray	BP86
Pt-H	1.613	1.627	O-C-O	125.6	126.0
Pt-S	2.400	2.328	S-Pt-H	87.1	86.6
Pt-N	2.252	2.142	H-Pt-P	85.4	87.1
Pt-P	2.323	2.204	P-Pt-S	172.4	173.6
N-C43	1.478	1.481	N-Pt-P	102.3	101.7
S-C44	1.840	1.827	N-Pt-S	85.1	84.4
C43-C44	1.527	1.510	Pt-N-C43	108.2	108.3
P-C12	1.839	1.845	Pt-S-C44	96.2	98.8
P-C22	1.843	1.824	C43-C44-S	112.1	110.3
P-C25	1.837	1.837	C44-C43-N	109.3	108.4

Table XVIII-1. Comparison between the X-ray data of complex and the corresponding BP86 geometry (Distances in Å and angles in degrees). Atoms numbering from X-ray data.

Compounds **1** and **2** were analyzed computationally. Experimentally it is found that these mononuclear species are diamagnetic. For this reason, optimizations were carried out for neutral closed-shell singlet ground-state structures. However, since it has been found that the triplet state is close in energy to the singlet or even it can be more stable we have checked for all compounds the relative stability of both states by optimizing the triplet state. In all cases the triplet state geometry presents a higher energy, indicating that singlet state is the most favourable. This is in agreement with the sharp peaks in the diamagnetic regions of the NMR spectra. The difference between these two states is never lower than 8 kcal·mol^{-1}.

The optimization of the isomers *cis* and *trans* of **1a-1c** and **2** gives as a result for the *cis* isomers **1** a favorable energy difference of at least 2.9 kcal·mol^{-1}. The difference is especially high when the ethylic chain of the aminothiolato ligand has coordinated a methyl carboxyl group. The difference between the *cis* and *trans* isomers for complex **2**,

i. e. with the phosphinothiolato ligand, is low, the *trans* isomer being slightly more stabilized by 1.1 kcal·mol^{-1}. These optimized geometries are displayed in Figure XVIII-2. The results for the compounds with aminothiolato ligands and with phosphinothiolato ligands agree with an equilibrium displaced towards the isomer *cis* for complexes **1** and towards the isomer *trans*-**2**. Experimentally the equilibrium between *cis* and *trans* species for complex **2** is observed, and displaced towards the *trans* species, nevertheless for **1** the equilibrium is not observed which agrees faithfully with the computational results.

compound	*cis*	*trans*
1a	-2.9	0
1b	-4.6	0
1c	-3.6	0
2	0	-1.1

Table XVIII-2. Relative energies for the isomers *cis* and *trans* of **1a-c** and **2**. (kcal·mol^{-1}).

The experimental results in solution absolutely agree with these computational optimizations in gas phase. We included the solvent effect in the calculations of complex **1** to observe if there are any substantial differences between the *cis*/*trans* equilibrium in gas or solution phase. Nevertheless, the solvents that were used in the experimental synthesis were rather non polar, using toluene ($\varepsilon = 2.4$) or dichlorometane ($\varepsilon = 9.1$). The simulated calculation with solvent effect gave nearly the same difference between the *cis* and *trans* isomers as that found in the gas phase.

compound	*cis*	*trans*
1a	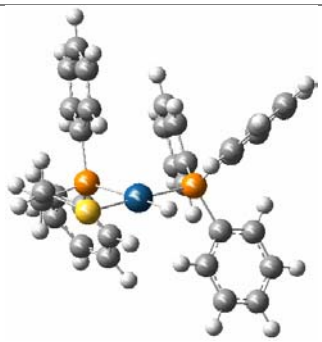	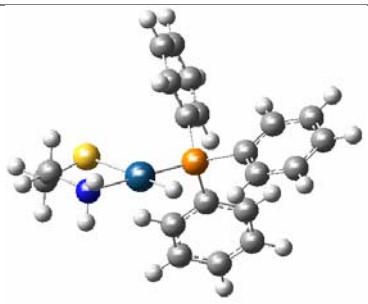
1b	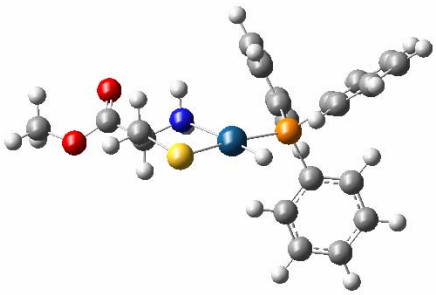	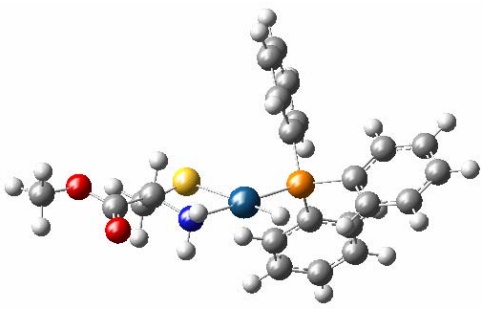
1c	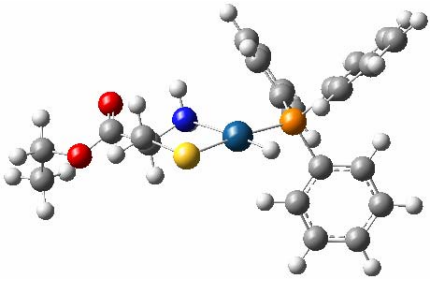	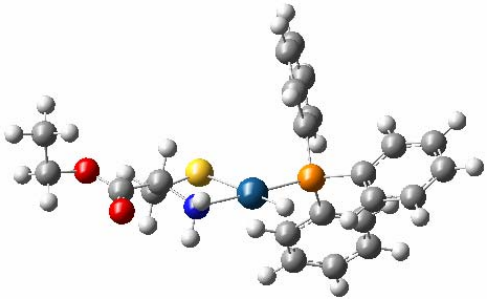
2	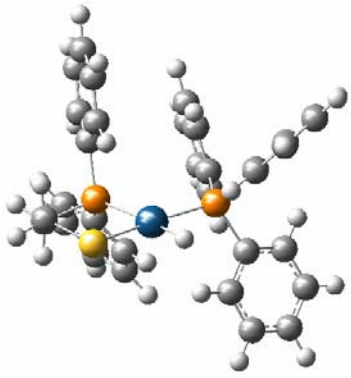	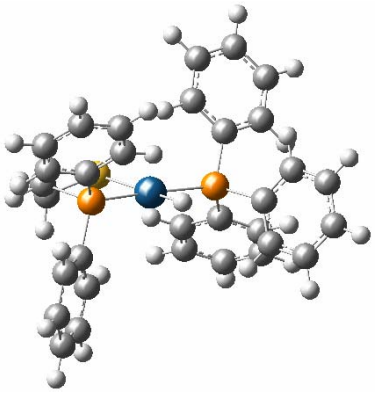

Figure XVIII-2. Optimized geometries for the isomers of **1a-c** and **2**.

	cis-**1a**	*trans*-**1a**	*cis*-**1b**	*trans*-**1b**	*cis*-**1c**	*trans*-**1c**	*cis*-**2**	*trans*-**2**
Pt-H	1.614	1.643	1.613	1.638	1.613	1.639	1.650	1.642
Pt-P	2.325	2.280	2.329	2.282	2.323	2.281	2.347	2.373
Pt-S	2.395	2.476	2.394	2.488	2.400	2.488	2.410	2.498
Pt-N/P	2.257	2.208	2.254	2.206	2.252	2.204	2.405	2.331
∠ P-Pt-H	85.2	86.7	85.5	85.9	85.4	85.9	86.5	84.4
∠ S-Pt-H	86.6	176.6	86.9	176.7	87.1	176.6	85.2	174.6
∠ P-Pt-N/P	102.9	178.6	102.1	177.8	102.3	177.4	102.1	174.2
∠ S-Pt-N/P	85.4	84.8	85.5	84.2	85.1	84.2	86.3	85.4

Table XVIII-3. Geometrical parameters for the isomers *cis* and *trans* of **1a-c** and **2**. (distances in Å, angles in degrees).

The geometrical analysis of these compounds is reflected in Table XVIII-3. The Pt-S bond distance suffers an increase when going from the *cis* isomer to the *trans* one due to the slightly higher *trans* effect of the phosphine with respect to the hydride. For *cis*-**2** isomer this bond is slightly weaker with respect to the *cis*-**1** isomers. The Pt-H bond distances are longer for the *trans* isomers except for **2**, with the possible meaning that the H placed *cis* with respect to the other anionic atom bonded to the metal, i. e. the sulphur, supposes an instability for the *cis*-**2** isomer. The Pt-H bond distance is similar for all the *trans* isomers. The behavior of the Pt-N/P bond distance, depending on the type of thiolato ligand that is inserted, follows a same trend for all the complexes, being larger for the *cis* isomers. So, the effect of the different atom bonded to the metal, in principle, does not imply substantial changes except for the fact that the Pt-N bond distances are much shorter than the Pt-P ones, allowing a best fit of the two phenyl units attached to the phosphorus atom. Furthermore isomer *cis*-**2** implies the presence of the two phosphorus atom groups with bonded phenyl groups, among which there are strong steric repulsions. There are not such repulsive sterical effects in the *trans* isomer. In addition, the longer bond distances between the platinum atom and the coordinated ligands for complex **2** with respect to complexes **1** help to interconvert the *cis* and the *trans* isomers due to the major facility to break any bond.

On the other hand, the ∠S-Pt-N/P shows that the *cis* isomers present a higher angle, thus the packing of the thiolato ligand is higher for the *trans* isomers, and this is better for the phosphinothiolato complex, **2**, because of the two phenyl groups attached to the phosphorus of the thiolato ligand. These additional phenyl groups can also explain that the decrease of the ∠P-Pt-P in order to reduce the steric repulsions between the aromatic hydrogens, achieving an angle different than the ideal 180º. The same comment can be made to explain the ∠S-Pt-H. The reorganization is more difficult in the *cis* isomer. The ∠P-Pt-P is similar to the ∠P-Pt-N.

The differences between the behavior of the aminothiolato and phosphinothiolato complexes can be studied from an electronic point of view. In all cases the energy of the HOMO is more stabilized for the *cis* isomer, except for **2** as can be observed in Table XVIII-4, thus the most stable HOMO agrees with the most stable isomer. For aminothiolato complexes is the *cis* one, however for the phosphinothiolato is the *trans*. The orbitals for **1a** and **2** are depicted in Figure XVIII-4. For LUMO orbitals the *trans* isomers present much higher stabilization in all cases. Thus, the HOMO-LUMO gap defined as the difference between the energies of HOMO and LUMO is lower for all the *trans* species, which for the species **1** is in contradiction with the prediction made by the principle of maximum hardness.

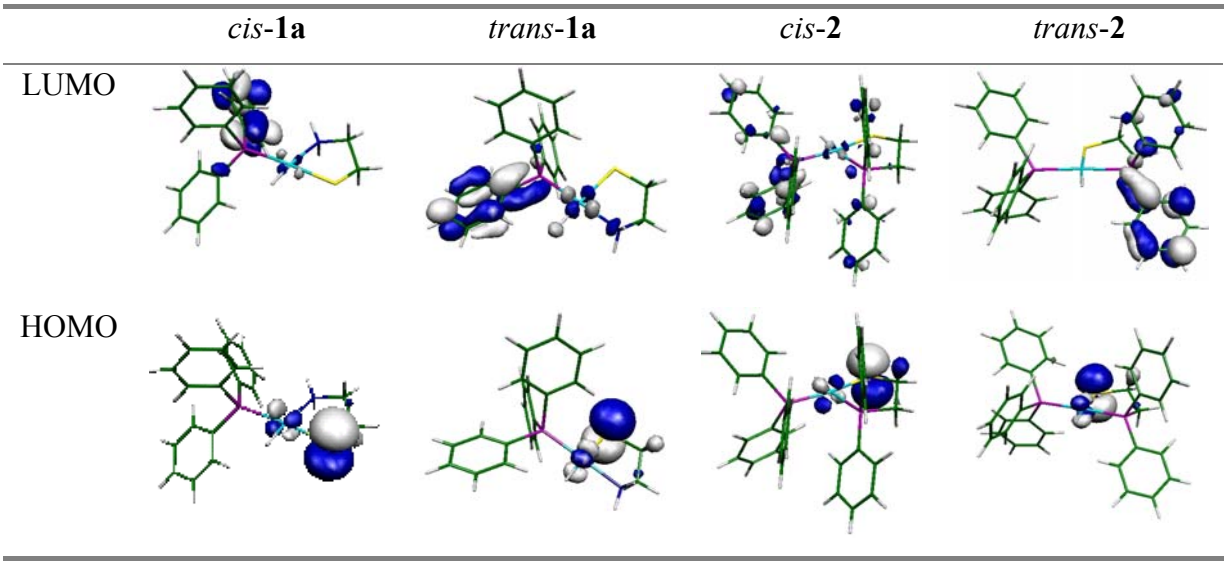

Figure XVIII-4. Frontier molecular orbitals of **1a** and **2**.

	cis-**1a**	*trans*-**1a**	*cis*-**1b**	*trans*-**1b**	*cis*-**1c**	*trans*-**1c**	*cis*-**2**	*trans*-**2**
LUMO	-53.8	-49.2	-53.5	-49.8	-52.9	-49.7	-56.1	-52.7
HOMO	-99.0	-98.5	-101.6	-100.4	-101.0	-99.7	-101.8	-103.4
gap	45.2	49.3	48.1	50.6	48.1	50.0	45.7	50.7

Table XVIII-4. Energies for molecular frontier orbitals of **1a-c** and **2**. (kcal·mol^{-1})

The charge concentrated on the platinum atom is close to zero for the phosphinothiolato complexes as can be viewed in Table XVIII-5. The metallic atom is less positively charged when it has the anionic ligands in *cis* position, although the difference is not quantitatively high. For the sulphur atom, Voronoi charges indicate that the charge is slightly negatively higher for the *trans* isomers. Nevertheless this cannot be proved by Mulliken charges. As to the charge of the phosphorus of the phosphine ligand it is useful to mention that it is always more positive for the *trans* isomers. For the nitrogen atom or the phosphorus atom depending on the thiolato ligand the charge requires some comments. The N atoms present negative charges, and the P atoms positive ones, nevertheless the *trans* isomers are more positively charged.

Atom	Type	*cis*-**1a**	*trans*-**1a**	*cis*-**1b**	*trans*-**1b**	*cis*-**1c**	*trans*-**1c**	*cis*-**2**	*trans*-**2**
Pt	Mulliken	0.290	0.306	0.273	0.306	0.283	0.312	0.017	0.075
	Voronoi	0.067	0.080	0.068	0.080	0.066	0.081	0.045	0.055
S	Mulliken	-0.220	-0.209	-0.213	-0.210	-0.213	-0.214	-0.186	-0.225
	Voronoi	-0.266	-0.275	-0.264	-0.276	-0.266	-0.278	0.262	-0.278
N/P	Mulliken	-0.352	-0.370	-0.331	-0.342	-0.329	-0.342	0.731	0.686
	Voronoi	-0.147	-0.135	-0.147	-0.136	-0.148	-0.136	0.153	0.170
P	Mulliken	0.645	0.677	0.646	0.673	0.647	0.669	0.660	0.677
	Voronoi	0.145	0.179	0.149	0.080	0.148	0.081	0.155	0.166

Table XVIII-5. Charges of the most relevant atoms of complexes **1a-c** and **2** (e^-).

In addition, as BP86(DFT) calculations show in Table XVIII-6, the chemical potential is higher for the *cis* isomers, but the *trans* isomer of **2** is not far from the respective *cis* isomer. The highest difference of chemical hardness between the *cis* and the *trans* isomers is presented for the phosphinothiolato complexes. Thus, this means a minor tendency to come back from the *trans* isomer to the *cis* one. Complexes **1** are less

electrophilic than complex **2** and then, they have smaller tendency to coordinate the fifth ligand necessary to an isomerization *via* associative mechanism. The calculated species of **2** with an extra PPh_3 group are displayed in Figure XVIII-5. The electrophilicity of the *cis* species decreases with the addition of the R group to the alkyl part of the aminothiolato ligand, nevertheless for the *trans* species a slight increase is observed.

(a.u.)	*cis*-**1a**	*trans*-**1a**	*cis*-**1b**	*trans*-**1b**	*cis*-**1c**	*trans*-**1c**	*cis*-**2**	*trans*-**2**
Chemical potential (μ)	-76.4	-73.8	-77.5	-75.1	-77.0	-74.7	-78.9	-78.1
Chemical hardness (η)	22.6	24.6	24.1	25.3	24.1	25.0	22.8	25.3
Electrophilicity (w)	129.1	110.6	124.9	111.5	123.0	111.6	136.3	120.3

Table XVIII-6. Chemical potential, chemical hardness, and elecrophilicity values for **1a-c** and **2** (in kcal·mol^{-1}).

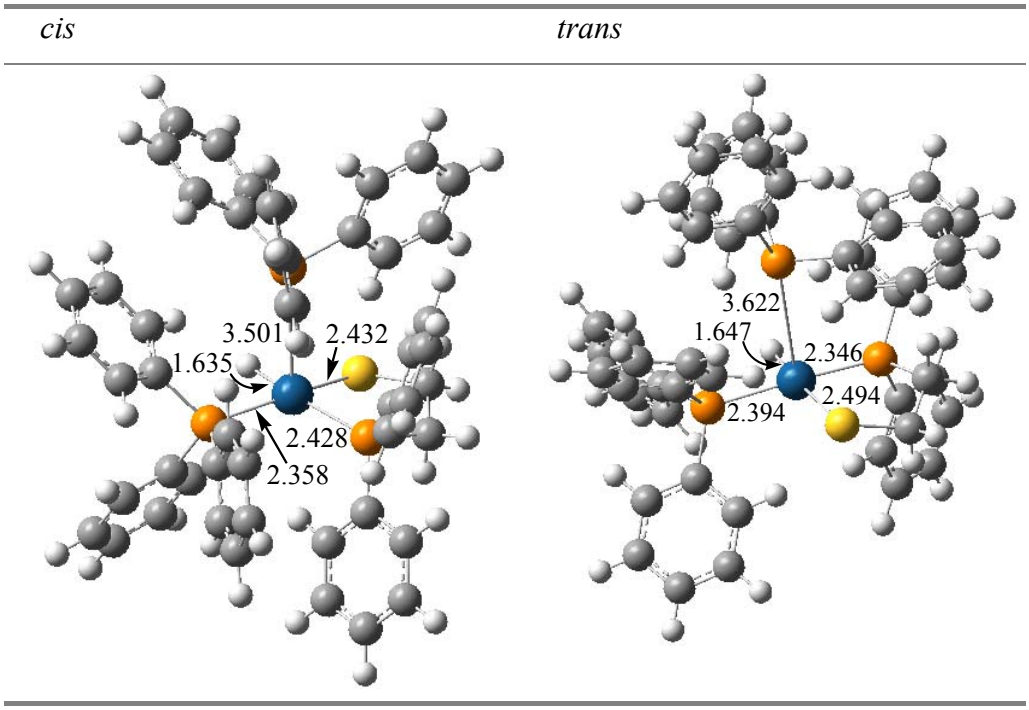

Figure XVIII-5. Addition of an extra PPh_3 group to complex **2**.

Figure XVIII-5 shows that the new inserted ligand cannot be coordinated to the metal as the rest of the atoms that are bonded to the platinum atom achieve a square planar

geometry. This extra phosphine is placed farther than 3.5 Å with respect to the metal either in *cis* or *trans* isomers of **2**. This supposes that the associative mechanism is *a priori* not feasible even for the phosphinothiolato complexes. Nevertheless it is necessary to study the whole mechanism to be sure of this.

To give insight into the bond nature, an energy decomposition analysis (EDA) was developed. The aim is to break the binding energy (BE) into deformation energy (ΔE_{def}) and interaction energy (ΔE_{int}). This last attractive term can also be split into a Pauli repulsion term (ΔE_{Pauli}), an orbital interaction term (ΔE_{oi}), and an electrostatic term (ΔE_{elstat}). The ΔE_{oi} is related to the covalent bond character and the ΔE_{elstat} to the ionic bond character. The deformation energy means the energetic difference between the free optimized fragment with respect to the frozen geometry presented in the EDA.

Decomposition method	Compound	ΔE_{Pauli}	ΔE_{oi}	ΔE_{elstat}	ΔE_{int}	$\Delta E_{def\ frag\ 1}$	$\Delta E_{def\ frag.\ 2}$	ΔE_{def}	BE
1 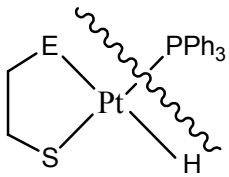	*cis*-**1a**	153.5	-66.4	-136.9	-49.9	0.6	0.8	1.4	-48.5
	trans-**1a**	169.0	-77.9	-153.1	-62.0	0.8	0.7	1.4	-60.6
	cis-**2**	161.3	-72.0	-143.2	-53.9	2.3	1.7	4.0	-49.9
	trans-**2**	140.9	-67.6	-126.4	-53.1	2.3	1.5	3.8	-49.3
2 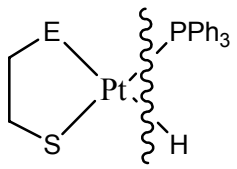	*cis*-**1a**	183.1	-124.5	-255.7	-197.1	8.9	13.7	22.5	-174.6
	trans-**1a**	176.5	-119.4	-251.3	-194.2	8.5	13.9	22.3	-171.9
	cis-**2**	224.8	-147.7	-271.4	-194.3	7.0	9.3	16.3	-177.9
	trans-**2**	222.7	-148.6	-273.9	-199.8	10.3	8.7	19.0	-180.8
3 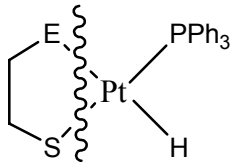	*cis*-**1a**	287.6	-202.7	-341.3	-256.5	3.2	23.3	26.5	-230.0
	trans-**1a**	295.3	-207.6	-346.6	-258.9	4.4	27.2	31.5	-227.4
	cis-**2**	286.0	-189.8	-326.8	-230.6	6.8	24.2	31.0	-199.6
	trans-**2**	290.4	-206.1	-331.9	-247.6	6.4	39.0	45.5	-202.1

Table XVIII-7. Three different methods to analyze the BE by the energy decomposition analysis (EDA) for complexes **1a-c** and **2**.

The decomposition of the molecule has been done in three different ways. The first one is displayed in the four first rows of the Table XVIII-7 and reflects that the BE of the phosphine is similar for all the compounds except for *trans*-**1a**, which presents the highest value. This confirms the geometrical optimized values. For *trans*-**1a** the Pt-P bond distance is 2.280 Å, while it is 2.325, 2.347, and 2.373 Å for *cis*-**1a**, *cis*-**2**, and *trans*-**2** respectively, due to the stronger *trans*-effect of the phosphino groups with respect to the amino groups. The Pauli repulsion is higher in the *cis* isomer with regard to the *trans* isomer for **2**, opposite to what happens for **1a**, because the entrance of the phosphine in *cis* places phenyl groups in close proximity. For **2**, the electrostatic component is also higher for the *cis* isomer. It is generally true that stronger overlap of the charge distributions of the fragments leads not only to higher steric repulsion but also to more attractive electrostatic interaction.[20] It is a general phenomenon that when we let two fragment charge distributions interpenetrate the total electrostatic interaction is attractive since the electron-nucleus attraction outweighs the repulsive terms. The deformation energies are higher for complex **2** obviously due to the phenyl groups of the phosphinothiolato ligand that are more stabilized without the presence of the phosphine ligand.

As to the second method of decomposition, the following four rows decompose the BE of the platinum atom with the thiolato ligand with respect to the two monodentate ligands. The split of the interaction energy confirms that the repulsion is higher in the *cis* conformations according to the Pauli repulsion term, higher in all the *cis* conformations. Furthermore the values are much higher for the phosphinothiolato complexes because of the two extra phenyls of the phosphinothiolato ligand.[20] Nevertheless the energetic difference between both isomers is only 2.1 kcal·mol^{-1} showing that in spite of the higher steric hindrance caused by phenyls, in *cis* conformation there are ways to help to stabilize the system. The similar high Pauli terms of the *cis* and the *trans* isomers reflect that the presence of extra phenyl groups produces an increase of the repulsion, but the proximity between them is not as important as it could be thought *a priori*. The deformation energy is higher because the metal, now, presents one more free position with respect to the extraction of a phosphine ligand. The ΔE_{oi} term is higher for complex **2** due to the higher *trans* effect of the phosphines with respect to the amine group of the thiolato ligands.

The four last rows of Table XVIII-7 reflect the BE presented for the insertion of the thiolato ligand. The results also support the experimental ones. Thus, the *cis*-**1a** and *trans*-**2** complexes present the highest BE values. In this case the deformation energies are even higher because of the free fragment optimizations the empty two positions of the coordinative sphere of the metal supposes a perfect option to stabilize the hydride and the phosphine ligands.

The second and the third methods used to describe the binding energies reflect that there is an increase of the electrostatic term, surely due to the charged fragments that appear in these two methods.

The optimization of the structure with two identical phosphinothiolato ligands bonded to the platinum atom, **4**, produces as the most stable isomer the *cis* one, being the *trans* only at 1.0 kcal·mol^{-1} higher in energy. Despite the low energy differences the *trans* complex has not been observed experimentally. This fact reinforces the idea that the sterical hindrance of the phenyl groups have to be taken in account, but other electronic factors make the *cis* isomer even more stable. The optimizations of both isomers are depicted in Figure XVIII-6.

cis	*trans*
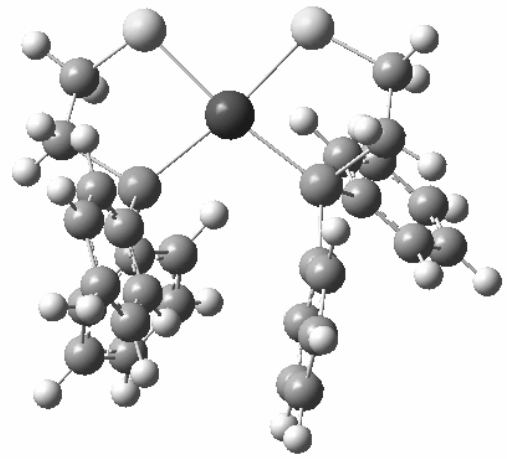	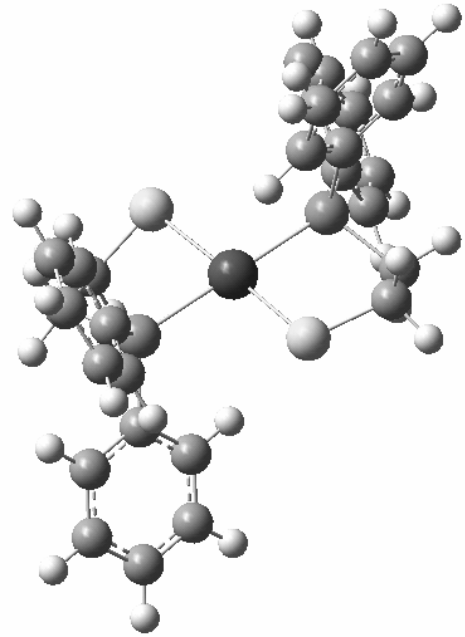

Figure XVIII-6. Optimizations of the bis-phosphinothiolato platinum (II) complex, **3**.

To get insight into the dependency of the length of the alkylic chain of the phosphinothiolato ligand, further studies were done with three methylenic units in this alkylic chain, i. e. optimizing complex **3** displayed in Scheme XVIII-6. These calculations absolutely confirm the experimental results.[4] The available NMR data suggest the existence of two isomers, differentiated by the chelated ring. It is well known that the chelate six-member-rings can adopt three basical conformations: chair, slanting boat, and boat.[5] On the other hand, the boat conformation generally is supposed to be not favored energetically, especially of the square planar complexes. The reasons why is not favored are the repulsive interactions of the substituents of carbon 2 of the chelate chain of Scheme XVIII-6a but especially the disfavored twisting disposition that the structure presents.[6] The boat conformation is not located as a minimum and any optimization starting from a boat conformation leads to the oblique boat conformation. And between the chair and the slanting boat conformations, the first one normally presents more stability due to the respective twisting dispositions of the structures.[7] The experimental results seem to favor the chair conformation, either in solid state or solution.[6]

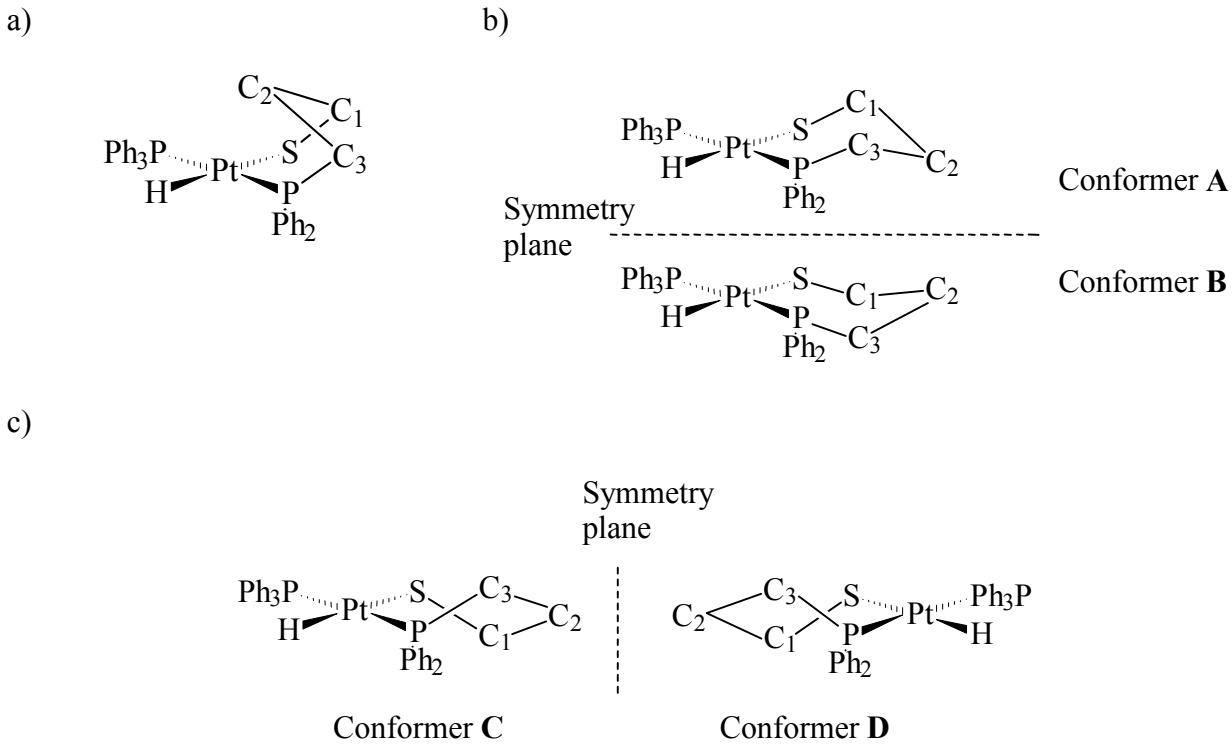

Scheme XVIII-6. Schematic a) boat, b) chair, and c) slanting boat conformations for complex **3**.

Observing the two possible chair conformations in Scheme XVIII-6b, **A** and **B**, the presence of four different substituents bonded to the metal made the two conformers be enantiomeric between them. Thus, they cannot be solved by NMR technique. The same result is obtained if the chelate complex adopts a slanting boat conformation, chiral, and it exists as two enantiomeric forms.[6] Therefore an equilibrium exists between these conformers as Figure XVIII-7 suggests.

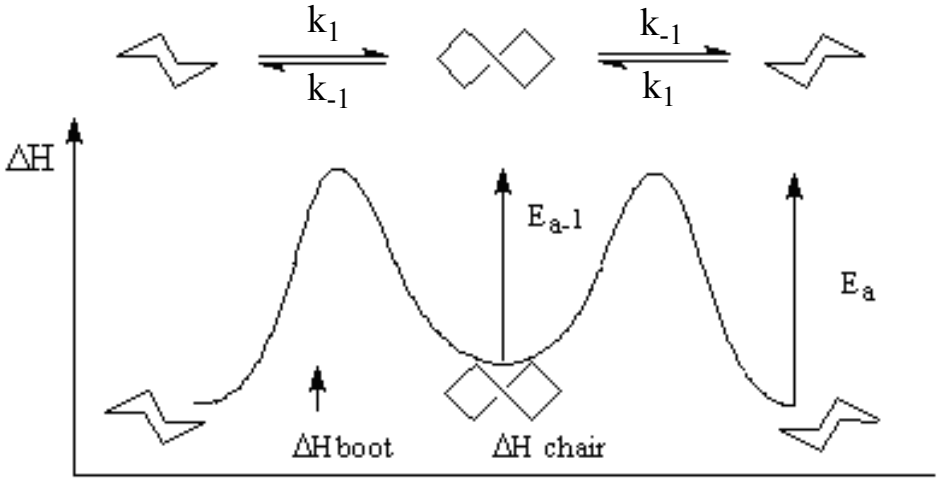

Figure XVIII-7. Conformation equilibrium reaction profiles between two chair forms.

For **3**, always the *trans* conformation is the most stable one by about 4 kcal·mol^{-1}, avoiding the presence of any *cis* isomer. Therefore the *cis* isomer, now, does not exist. Apart from the two chair conformations presenting the same energy, we have achieved one slanting boat, lacking the other slanting conformation, however this is not important because they must present the same energy. Either the chair conformations or the slanting boat ones present exactly the same energy. The interconversion transition states between these conformations must present energetic barriers extremely low. The geometrical parameters are summarized in Table XVIII-8, and Figure XVIII-8 depicts the structures.

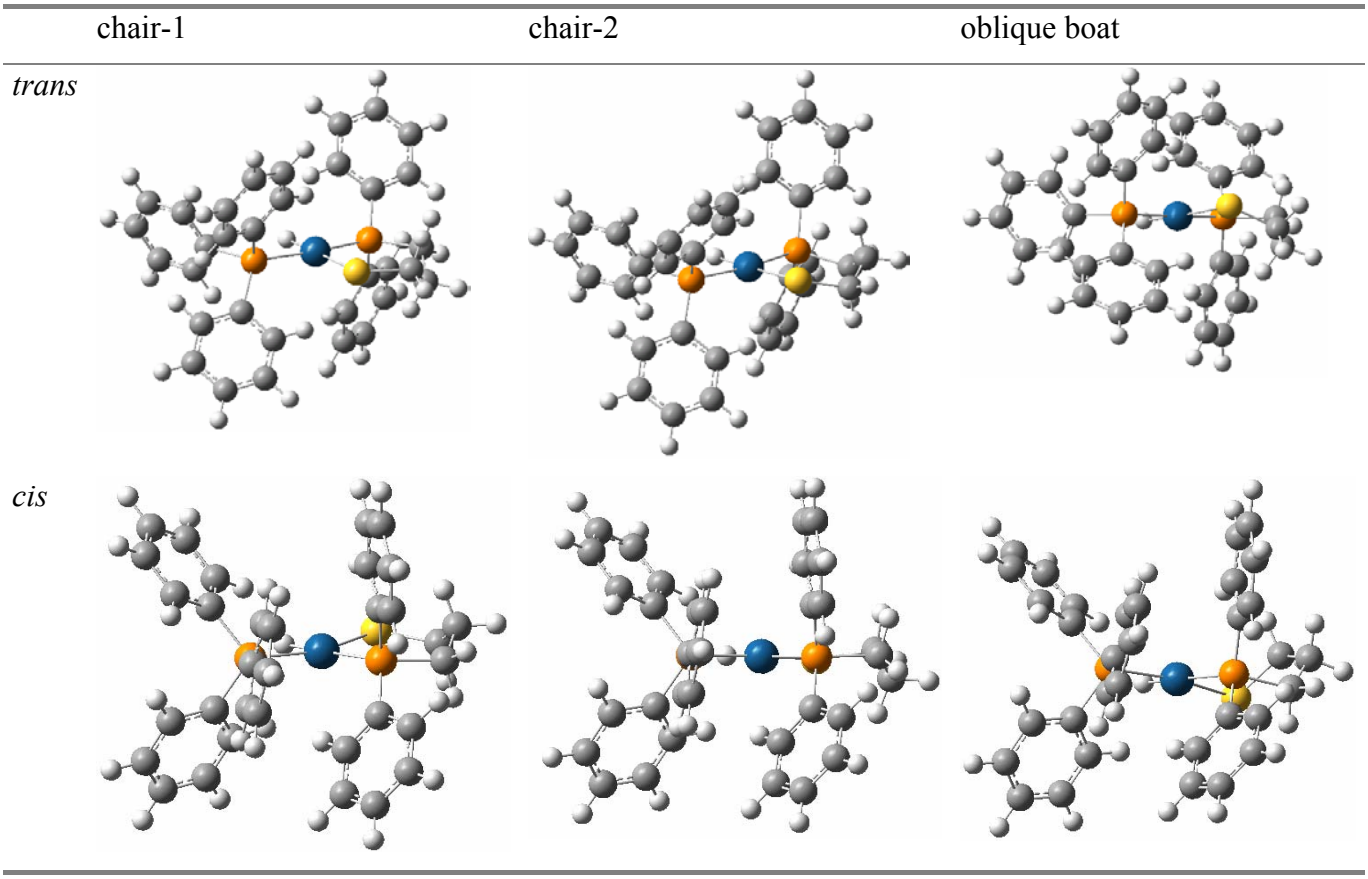

Figure XVIII-8. Optimized geometries of the compounds **3** with an additional methylenic unit in the thiolato ligand.

3	Pt-P	Pt-H	Pt-P	Pt-S	P-Pt-S	P-Pt-H	S-Pt-H	P-Pt-P
trans-chair-1	2.338	1.648	2.387	2.477	96.6	86.9	178.2	171.8
trans-chair-2	2.336	1.646	2.381	2.490	95.9	86.3	177.9	171.2
trans-oblique	2.333	1.644	2.382	2.497	94.0	86.4	177.4	172.3
cis-chair-1	2.416	1.647	2.358	2.408	96.3	82.4	79.8	101.4
cis-chair-2	2.421	1.647	2.359	2.403	97.3	82.2	79.4	101.1
cis-oblique	2.435	1.646	2.361	2.436	89.5	85.2	83.9	101.4

Table XVIII-8. Geometrical parameters for the compounds with an additional methylenic unit in the thiolato ligand.

3	HOMO	LUMO	gap
cis	-99.0	-54.5	44.5
trans	-98.9	-52.4	46.5

Table XVIII-9. Energies of the frontier molecular orbitals of the *cis* and *trans* isomers.

The HOMO-LUMO gap is especially low for the *cis* isomers because of the higher stabilization of the LUMO by about 2 kcal·mol^{-1}. Nevertheless this difference is lower than the 5 kcal·mol^{-1} for complex **2**.

The phosphinothiolato *cis* and *trans* isomers are not energetically differentiated enough to allow only the existence of the most stable isomer, *cis* for **1a-c** and *trans* for **2**. For **2**, an experimental way that has proved to produce only the *trans* isomer has been the utilization of a phosphinothiolato ligand with a replacement of a hydrogen atom of the methylenic unit next to the sulphur by an attachment of a chain. Due to the presence of two hydrogen atoms for the carbon of this methylenic unit both positions have been tested. Obviously the conformation in which this added chain is placed avoiding the axial conformation with respect to the ring that forms the thiolato ligand with the platinum atom is more stable, i. e. the *up* conformation. Nevertheless the difference is not high, only 1.1 kcal·mol^{-1} favoring the *trans-up* isomer, for the *cis* isomers the energetic difference is 2.7 kcal·mol^{-1}. On the other hand, as it was expected, the difference *cis*/*trans* is now increased to 3.5 kcal·mol^{-1} with respect to the 1.1 kcal·mol^{-1} of complex **2**. Both *trans* conformations are depicted in Figure XVIII-9.

trans-up *trans-down*

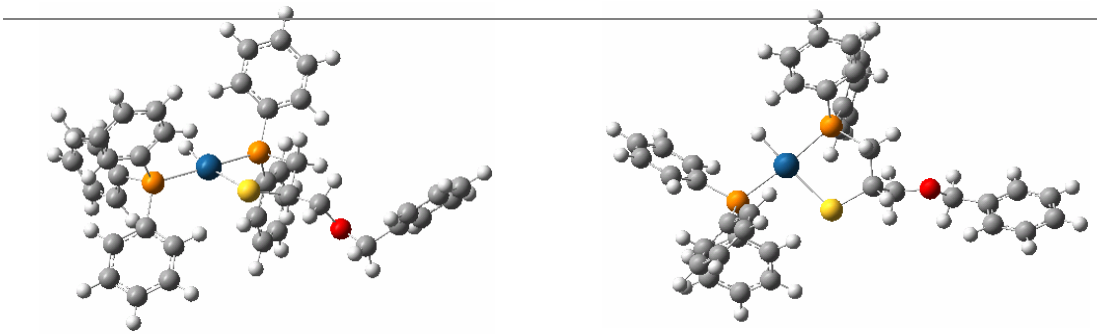

Figure XVIII-9. Isomers of complex **2** with a chain attached to the methylenic group bonded to the sulphur atom.

In addition to the inclusion of a chain attached to the methylenic group bonded to the sulphur atom, the inclusion of an extra methylenic group in the alkylic chain of the phosphinothiolato ligand reinforces the aim of avoiding the *cis* isomers, that are less energetically stable by at least 6.5 kcal·mol^{-1}. The isomers that appear, displayed in Figure XVIII-10, are different from the different shape of the ring that is formed by the platinum atom and the thiolato ligand. This ring can adopt a chair or an oblique boat conformation, not separated by more than 0.5 kcal·mol^{-1}. The boat conformation is not located. As for the thiolato ligands with two methylenic units, the *down* isomers are less stable by about 3 kcal·mol^{-1}.

chair 1-*up*	chair 2-*up*	oblique boat-*up*
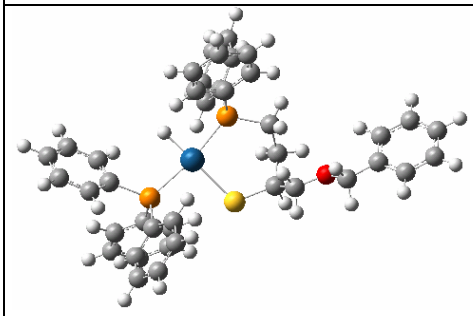	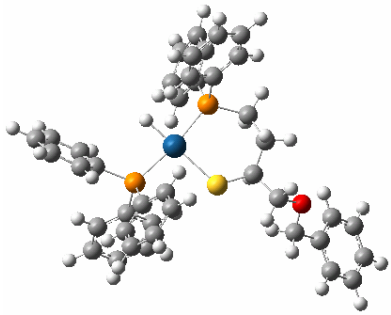	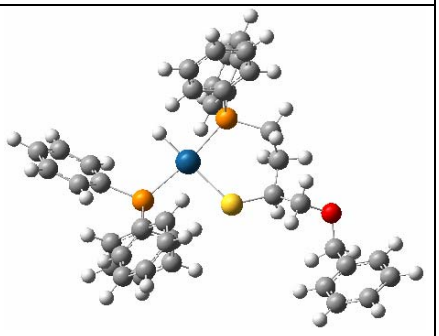
chair 1-*down*	chair 2-*down*	oblique boat-*down*
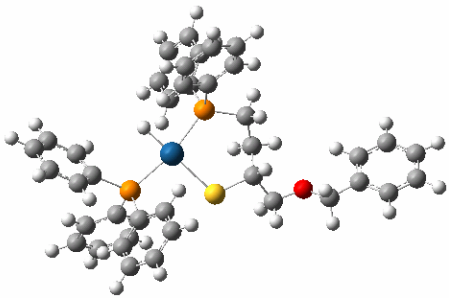	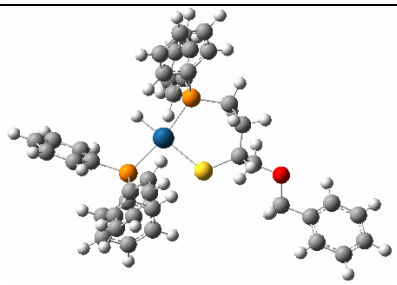	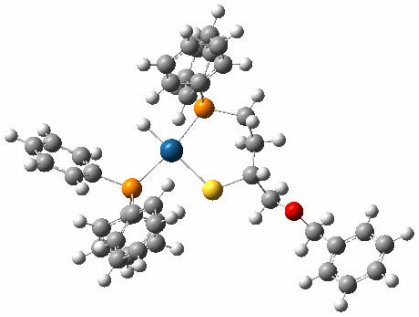

Figure XVIII-10. Isomers of the three methylenic group thiolato complexes, **4**, with a chain attached to the methylenic group bonded to the sulphur atom.

Conclusions

DFT calculations have been key to dilucidate the *cis/trans* equilibriums of aminothiolato and phosphinothiolato platinum complexes. For complexes **1** only the *cis* species are formed. For complex **2** the small amount of *cis* isomer found experimentally

is confirmed with the computational results by the only 1.1 kcal·mol^{-1} that separates this isomer with respect to the *trans* one. The increase of the alkylic chain of the phosphinothiolato chain is useful to form only *trans* isomers, and the inclusion of a chain including an eter and a phenyl group in this alkylic chain also gives as a result only *trans* isomers.

References

1. a) P. W. N. M. van Leeuwen, P. C. J. Kamer, J. N. H. Reek, P. Dierkes, *Chem. Rev.* **2000**, *100*, 2741-2769. b) J. Halpern in *Asymmetric Synthesis* vol. 5. J. D. Morrison, Academic Press, 1985, p41.
2. J. Real, A. Polo, J. Duran, *Inorg. Chem. Commun*. **1998**, *1*, 457-459.
3. N. Brugat, J. Duran, A. Polo, J. Real, A. Álvarez-Larena, J. F. Piniella, *Tetrahedron Asymm*. **2002**, *13*, 569-577.
4. J. Duran, A. Polo, J. Real, A. Poater, M. Solà, J. Benet-Buchholz, to be submitted.
5. C. J. Hawkins, J. A. Palmer, *Coord. Chem. Rev*. **1982**, *44*, 1-60.
6. J. R. Gollogly, C. W. Hawkins, *Inorg. Chem.* **1972**, *11*, 156-161.
7. G. R. Brubaker, D. W. Johnson, *Coord. Chem. Rev.* **1984**, *53*, 1-36.
8. A. E. Keskinen, V. Senoff, *J. Organomet. Chem*. **1972**, *37*, 201-208.
9. a) E. J. Baerends, D. E. Ellis, P. Ros, *Chem. Phys*. **1973**, *2*, 41-51. b) C. Fonseca Guerra, O. Visser, J. G. Snijders, G. te Velde, E. J. Baerends, *Methods and Techniques for Computational Chemistry*, STEF, Cagliari, 1995, 305. c) G. te Velde, F. M. Bickelhaupt, E. J. Baerends, C. Fonseca Guerra, S. J. A. van Gisbergen, J. G. Snijders, T. Ziegler, *J. Comput. Chem*. **2001**, *22*, 931-967.
10. W. Ravenek, *Algorithms and Applications on Vector and Parallel Computers*, Elsevier, Amsterdam, 1987.
11. G. te Velde, E. J. Baerends, *J. Comput. Phys.* **1992**, *99*, 84-98.
12. a) J. G. Snijders, E. J. Baerends; P. Vernooijs, *At. Nucl. Data Tables* **1982**, *26*, 483-509. b) P. Vernooijs, E. J. Baerends*, Slater Type Basis Functions for the Whole Periodic System. Internal Report*, Vrije Universiteit of Amsterdam, The Netherlands, 1981.
13. J. B. Krijn, E. J. Baerends, *Fit Functions in the HFS Method. Internal Report* (in Dutch), Vrije Universiteit of Amsterdam, The Netherlands, 1984.
14. a) E, van Lenthe, A. E. Ehlers, E. J. Baerends, *J. Chem. Phys.* **1999**, *110*, 8943-8953. b) E. van Lenthe, E. J. Baerends, J. G. Snijders, *J. Chem. Phys.* **1993**, *99*, 4597-4610. c) E. van Lenthe, E. J. Baerends, J. G. Snijders, *J. Chem. Phys.* **1994**, *101*, 9783-9792. d) E. van Lenthe, J. G. Snijders, E. J. Baerends, *J. Chem. Phys.* **1996**, *105*, 6505-6516. e) E. van Lenthe, E. J. Baerends, J. G. Snijders, *Int. J. Quantum Chem.* **1996**, *57*, 281-293.

15. A. D. Becke, *Phys. Rev. A* **1988**, *38*, 3098-3100.
16. J. P. Perdew, *Phys. Rev. B* **1986**, *33*, 8822-8824.
17. ADF2002.03, E. J. Baerends, J. A. Autschbach, A. Bérces, C. Bo, P. M. Boerrigter, L. Cavallo, D. P. Chong, L. Deng, R. M. Dickson, D. E. Ellis, L. Fan, T. H. Fischer, C. Fonseca Guerra, S. J. A. van Gisbergen, J. A. Groeneveld, O. V. Gritsenko, M. Grüning, F. E. Harris, P. van den Hoek, H. Jacobsen, G. van Kessel, F. Kootstra, E. van Lenthe, V. P. Osinga, S. Patchkovskii, P. H. T. Philipsen, D. Post, C. C. Pye, W. Ravenek, P. Ros, P. R. T. Schipper, G. Schreckenbach, J. G. Snijders, M. Solà, M. Swart, D. Swerhone, G. te Velde, P. Vernooijs, L. Versluis, O. Visser, E. van Wezenbeek, G. Wiesenekker, S. K. Wolff, T. K. Woo, T. Ziegler, Vrije Universiteit Amsterdam, Amsterdam, 2002.
18. a) F. M. Bickelhaupt, N. M. Nibbering, E. M. van Wezenbeek, E. J. Baerends, *J. Phys. Chem.* **1992**, *96*, 4864-4873. b) T. Ziegler, A. Rauk, *Inorg. Chem.* **1979**, *18*, 1558-1565. c) T. Ziegler, A. Rauk, *Inorg. Chem.* **1979**, *18*, 1755-1759. d) T. Ziegler, A. Rauk, *Theor. Chim. Acta* **1977**, *46*, 1-10. e) K. Kitaura, K. Morokuma, *Int. J. Quantum Chem.* **1976**, *10*, 325-331.
19. Standard deviations for the distances and for the angles, $s_{n-1} = \sqrt{\frac{\sum_{i=1}^{N}(CV - EV)^2}{N-1}}$, where CV means calculated value, EV experimental value (X-ray data), and N is the number of distances or angles taken into account.
20. J. Poater, M. Solà, M. Bickelhaupt, *Chem. Eur. J.* **2006**, *12*, 2889-2895.

PART VII: Conclusions

Chapter XIX: *Conclusions*

➢ We have theoretically studied the first example of a reversible intramolecular H/D exchange promoted by Cu^{I}. The process is finely controlled by the precise coordination distance required to form the agostic interaction between the Cu^{I} and the aromatic C-H_a bond, and thus the reactivity is sharply modified by the coordination effect exerted by the solvent used. Indeed, the reactivity can also be tuned by the electronic effects on the aromatic ring and also on the amine substitution.

➢ A family of Cu complexes in the unusual oxidation state of +3 and containing triazamacrocyclic ligands has been described and their structural and spectroscopic properties thoroughly investigated by DFT calculations. This has allowed us to unravel the detailed electronic structure of these Cu^{III} complexes which in turn permitted us to rationalize their spectroscopic properties. As a result of this detailed work it has been possible to measure the electronic effects of *N*-methylation in a quantitative manner.

➢ Theoretical analyses based on DFT calculations have shown that the intermediates obtained from the oxidation of the macrocyclic Cu(I) complexes and molecular oxygen, generates a variety of side on Cu_2O_2 motifs. Those Cu_2O_2 intermediates evolve towards the formation of radically different Cu(II) complexes which depending on the macrocyclic ligand are obtained as a μ-bis-hydroxo complex, a μ-hydroxo-μ-phenoxo complex with intramolecular oxidation of the initial ligand, and a terminal bis-hydroxo complex in the *para* substitution of the phenyl rings. The latter being the first example of its kind described in the literature. In addition, DFT calculations for dinuclear copper complexes containing the macrocyclic ligands and the Cu_2O_2 core have proven to be an excellent tool to envisage reactive intermediates that can not be detected and characterized experimentally. Furthermore, these DFT calculations have also provided an excellent guide to unravel their potential reactivity based on the relative disposition of the aromatic rings and the Cu_2O_2 core and also based on their electronic properties mainly their electrophilicity. This has allowed rationalizing the nature of the evolved oxidized species based on the nature of the macrocyclic ligand that could not have been understood otherwise.

➢ The comparison of the dioxygen chemistry associated to $[Cu(MeAN)]^{+}$ constitutes a remarkable example of the importance of the cooperative role of two metal centers in

the activation of O_2 and highlights the challenge in designing suitable dinuclear scaffolds for modeling O_2 processing proteins containing a dimetallic active site.

➢ The adsorption of CO on small copper clusters, Cu_n (n=1-9) has been analyzed. It has been confirmed that the bare copper clusters with even number of copper atoms are more stable than those with an odd number of copper atoms. The latter are the most reactive and, in fact, they show the higher CO binding energies. We have found that the nucleophilic condensed Fukui function and the shape of the LUMO orbitals are useful tools to predict the regioselectivity of the CO insertion, with the only exception of the Cu_7 cluster. The energy decomposition analysis of the CO binding energy in the copper cluster carbonyls have shown that the σ donation is about twice as important as π backdonation. From an electron charge point of view, however, donation and backdonation are equally important. Finally, we have shown that the coordination of CO through the oxygen is energetically unfavorable as compared to CO binding through the carbon atom, especially for the larger copper clusters.

➢ The chirality of the 1,2-bis(oxazolinyl)benzene ligand Phbox-R, either (R_cR_c) or (S_cS_c), allows preparing and isolating pure atropisomeric complexes due to the highly restricted rotation along the oxazolinic-phenyl axes upon coordination to a Ru metal center. A family of atropisomeric complexes has thus been characterized in the gas phase thanks to DFT calculations. Furthermore, the coordination of a 1,2-bis(oxazolinyl)benzene ligand to a Ru metal center produces rotationally restricted isomers.

➢ We have described a new Ru-Cl complex $[Ru^{II}Cl(\textit{bpea})(\textit{dppe})](BF_4)$, showing three isomeric Ru^{II} complexes in solution, the *trans-fac*, the *cis-fac,* and the *cis-mer* that presents the *bpea* ligand in a meridional fashion, unknown for Ru. DFT calculations show that *fac*- isomers are more stabilized that *mer*- isomers. The different behavior of UV-spectra of the isomers of the complex has been explained by theoretical calculations through the Time Dependent-DFT approach. The bands placed in the UV-Vis spectra between 275 and 425 nm are mainly MLCT type of bands because the starting orbital has mainly metallic character, whereas the arrival orbitals present high proportion of the p_z orbitals of the $C_{aromatic}$ atoms of the ligands.

➢ Our results show that the interconversion process between the ruthenium complex containing the *bpea* ligand with an unknown meridional fashion to the complex with a facial *bpea* with respect to the metal is achieved through an intramolecular mechanism, but without excluding the dissociative mechanism.

➢ Olefin metathesis requires to optimise the coordination of the reactant, the metallacycle formation {[2+2]-cycloaddition}, and the reverse associated steps. In the preparative step, the catalyst needs to acquire a geometry, which opens a coordination site, and the key factor is not the metal but the ligands, which should be preferably electronegative, hence imido > alkylidyne. Noteworthy, the imido ligand does not bend to destroy one of the π M-N bond and localize a lone pair during the reaction path. At the cycloaddition step, the metal is the key factor: *4d* metals are better than *5d* metals because they stabilize less the metallacycle intermediate by making weaker M-C bonds so that overall the best catalyst is the Mo imido complex.

➢ The recently synthesized trinuclear $[[Pt(Me_2Bpy)_2][PtCl_2(Me2Bpy)]_2]^{2+}$ complex presents short Pt-Pt contacts that indicate the presence of metal-metal bonds. DFT calculations on models suggest that the π–π stacking interactions between the pyridine units are responsible, in part, for the short Pt-Pt distances.. The Pt-Pt bond has an intermediate strength with a binding energy of about 40 $kcal \cdot mol^{-1}$. As to the nature of Pt-Pt interactions, this is a metallic bond with both covalent and electrostatic components being almost equally important as derived from the AIM and EDA analyses.

➢ The remarkably different reactivities exhibited by the fulleropyrrolidines endowed with the 1,6-enyne moiety and those with the 1,7-enyne fragment have been rationalized by means of DFT theoretical calculations. The energies and the molecular structures of the intermediates formed through the interaction between the coordinatively unsaturated Co atom and the π system of the fullerene reveal important differences between the two systems and clearly confirm that the interaction in the 1,6-enyne is stronger as a consequence of the different length of the organic chain linking the alkyne and alkene functional groups. These results show that the highly versatile PK reaction can be applied to the spherical molecular surfaces of C_{60} and other fullerenes.

- The calculated BP86 energy differences between the racemic-trans and meso-trans diastereomers of phosphanylthiolato complexes of Ni^{II} are in agreement with the experimentally observed racemic-*trans*/meso-*trans* ratios and are responsible for the chiral recognition between the two enantiomeric forms of the racemic ligand. This phenomenon is especially important in a binuclear complex, in which a destabilised anti conformation of the bridging sulphurs would be necessary for the meso-trans isomer to be stable.

- DFT calculations are useful to rationalize the diastereoisomerism in Platinum(II) 2-phosphino and 2-aminothiolato complexes.

Agraïments

Aquest apartat podria ser objecte de llargues dissertacions, no obstant cal acotar la dimensió d'aquest apèndix de la tesi (prou he fet ja sofrir els avaluadors de la tesi). Tinc clar que aquest apartat serà el més llegit, segur, d'aquesta tesi, però per no fer perdre el temps al lector, ja avanço que no està en la meva línia ascendent de brillantina kafkiana.

Aquesta tesi m'ha suposat un esforç considerable. He fet errors com posar capítols i apartats que no eren necessaris i no escriure treballs ja acabats, entre ells el que va ser el començament de la tesi. Però calia temps per escriure i ja se sap, el temps és or, i l'or s'esmuny entre els dits (del teclat en aquest cas).

Per diplomàcia academicista, en primer lloc agrair als meus directors de tesi, "els Miquels", Miquel Duran i Miquel Solà, dels quals he pogut aprendre part del virtuosisme de la ciència. M'han permès estar en un grup punter de química teòrica, segons el meu humil punt de vista, col·locant-lo a les portes de l'avantguarda mundial. D'en Miquel Duran espero haver-ne pogut extreure part del seu pragmatisme i sobretot, a partir del contacte amb ell d'aquests darrers anys, guanyar aptituds en dialèctica i de serenitat. Ell ha estat qui mica en mica, amb paciència ha teixit una institució que ja és, avui, una expressió de qualitat de química teòrica a la península. Segurament la seva mà esquerra i el seu punt de diàleg i, tirar pilotes fora a vegades, han permès crear una comunitat de companys i d'amics, amb diferències, però petites. D'en Miquel Solà haig de lloar que m'hagi inculcat un esperit dinàmic i rigorós. El que més li haig d'agrair és la paciència que ha tingut en mi, en les reunions setmanals i en les meves incursions en el seu despatx. He aconseguit fer-li pujar els colors en més d'una ocasió i per molt que, ja aviat, va poder observar que no tendeixo a amagar la sinceritat, no sempre ha estat preparat per les meves sortides fora de to. Els nostres caràcters tot sovint xoquen, però en el fons tenim algunes maneres de fer pròximes i també ideologies de país semblants. Per tot plegat el seguiment en la ciència no vull que mai es deslligui d'ell. Encara puc aprendre molt d'ell. Sempre es diu que cal anar a buscar a fora perquè el que hi ha a fora és millor: en Miquel seria l'excepció que confirma la regla. Aquesta tesi és meva, cert, però tu n'ets el principal culpable, Miquel.

La meva tesi no solament ha estat fruit dels meus dos directors, a darrere també hi ha una multitud de professors, doctors, i doctorands que m'han tingut despert dia rere dia. En primer lloc, en Toni, que moltes vegades m'ha exacerbat degut a la seva parsimònia a l'hora d'enviar-los a publicar treballs, però també li haig d'agrair l'oportunitat en el seu moment de fer projectes experimentals, dels quals en aquesta tesi exposo un capítol, amés a més de les fructíferes múltiples col·laboracions teòrico-experimentals posteriors, i també perquè tot sovint aquests treballs que s'han dilatat en el temps han acabat publicats en revistes d'alt nivell, degut al seu ric assortiment d'idees. D'ell m'ha entusiasmat la seva passió per la química. Llavors he pogut gaudir de l'enteniment d'una investigadora computacional, i sí, femenina, cosa encara difícil en el món científic fins avui. L'Odile em va voler modelar i fer entrar la recerca per vies més estrictes i de més rigor. Encara recordo els ruixats que em queien quan veia la munió de papers amb resultats que li presentava, i també quan li contestava mails passada la mitjanit (a can IQC no respectem ni el dia ni la nit, i moltes vegades es podria dir que a l'IQC no es colga mai el sol en els seus dominis, o sigui, dia i nit, i caps de setmana inclosos té gent fidel fent guàrdia). L'Odile em va començar a ensenyar l'enteniment orbitalari, i reconec que jo no vaig ser prou bon alumne. Cal que hi torni per millorar.

Sigui com sigui, des del primer moment em vaig adonar que no cal que doni la volta al món per trobar gent amb gran talent investigador. En una universitat "petita" i gens "rimbombant" com la de Montpellier es pot fer química d'alt nivell, envejable per qualsevol altra universitat. Segurament el paral·lelisme de mida amb Girona, i la seva proximitat, em van fer decidir per l'estada i si per alguna estranya raó decideixo seguir en el món de la ciència investigadora, espero que allà m'acullin, enyoro la seva química organometàl·lica i m'agradaria endinsar-me també en el camp de sòlids. L'Odile em va demostrar la teoria que un teòric no ha de ser bo en tot, metodologia, reactivitat, programació, sinó que l'aprofundiment en un dels segments pot ser letal per la qualitat de la recerca. I crec que ningú dubta, a hores d'ara, que ella ha triomfat amb escreix en aquest aspecte. Un altre pseudo-director ha estat l'Alfons Polo, que amb molta paciència em va ensenyar l'art de l'estereoisomeria, segurament ell ha estat el que més passió ha mostrat en la meva ensenyança. De la nostra col·laboració ja n'ha sortit un article i espero que pròximament acabin alguns resultats experimentals per tal de publicar un parell de treballs més, que presento en certa part aquí també. No puc oblidar-me de l'Alejandro de Santiago de Xile, a qui l'estrès no afecta aparentment, el qual em va obrir la via del que seria llavors la meva tesina. Allà vaig començar una via nova a can IQC, fins aleshores inèdita, els clusters. Cal dir que el projecte va anar endavant, i el fet de ser novadors per nosaltres em va fer dedicar-hi més esforços que en altres temes, fruit d'això hi ha un article publicat i dos més en vies de publicació, a més a més d'una idea que deixo per un futur proper. A part de tots aquests doctors, he tingut altra gent amb qui he col·laborat, que cronològicament serien Montserrat Rodríguez (em va començar a pervertir en el món de la ciència i...), Marisa (a qui jo intentava pervertir), Pablo Jaque (company de clusters i amic), Xavi Ribas (magnífic col·laborador), Miquel Costas (el rei del coure, de qui segurament no he pogut gaudir suficientment pel fet que no hi era en la meva primera meitat de tesi), Xavi Sala (company de carrera i amic), Xavi Solans (seguidor i conseller dels meus progressos a Montpellier), Eric Clot (si fos a l'oest americà ningú es voldria batre a un duel amb ell, la lentitud no existeix per ell ja que quan s'ha de fer una cosa ja està feta *ipso facto*), Mª Ángeles (veure't sempre implica esbossar somriures d'alegria).

A en Jean-Seb li haig d'agrair la seva amabilitat, obrint-me les portes per fer un postdoc. A en Fred, Marie-Liesse, Pat,… i tothom de Montpellier. Agraïment a tot el grup de l'Alejandro de Xile, que també em va oferir postdoc. Menció especial mereix l'àrea de química inorgànica de la UdG, a més de la resta d'àrees químiques; els companys de curs de doctorat; els companys d'Economia i ADE, els quals em van fer fruir de seguir estudiant i certes amistats espero que perdurin al llarg del temps.

Un apartat especial mereixen els meu companys d'IQC, Freddy, Giro, Ana, Josep Mª, Pedro, Guillem, Albert, Lluís A., Sílvia, Emili, Josep, Jordi, Ferran, Sílvia, Carme, Joan, Edu, Mts, David, Lluís, David A., Marta, Mireia, Juanma, Quim, Pepe, Pep, Eugeni, Dani, Òscar, Samat, Serguey, Montse, Ferran, Sílvia O., Alexander, Merxe, Marcin, Mattias, Marcel, Cristina, Sean… tots ells m'han fet agradable sigui un dia o un altre l'estada a la UdG. Alguns d'ells m'han ajudat de forma incansable i sense gratificació en molts articles i ja saben que si fos per mi mereixerien estar en molts d'ells, la qual cosa en un futur immediat potser serà possible. No faré mencions especials tot i que de mi és sabut la meva simpatia particular cap a alguns membres i ex-membres de l'IQC. Sé que hauria fet la tesi igualment sense ells (sóc sincer), però sense ells potser no tindria ara més visions de cultura intra i interpersonal.

La colla del club, dins la qual hi ha immersa també la meva colla d'amics que he tingut des de fa 20 anys, un orgull. Qui em coneix sap que sóc profeta de la meva terra i de tot el que m'envolta que em faci fruir només entreveure la imatge. Banyoles, Palamós, i Girona han estat l'enclavament del meu univers.

Menció especial també mereix la meva família, qui ha hagut de suportar-me i veure'm fer horaris intempestius, arribar a casa amb desil·lusions derivades de la recerca (la quantitat de trucades que m'ha fet la meva mare per intentar que tanqués l'ordinador i fes via cap a casa...). Espero tenir més temps a partir d'ara per gaudir de la meva nebodeta, l'Alba. Per raons que ara no vénen al cas vaig anar a parar al mateix grup d'investigació que el meu germà, que tot i que la dialèctica entre nosaltres sembla inexistent a vegades, molts han percebut que per mi representa un estendard. Ell em va dir una vegada: "si estudies, sempre aprovaràs", i així ha succeït. Tot i tardar uns anys, des de fa poc hem iniciat col·laboracions científiques, algunes de les quals encara inacabades.

L'Anna, qui m'ha fet de tot, però no obstant, segueixo deixant que em faci sofrir. El seu somriure i el seu to de veu dolç multitud d'ocasions m'han calmat i en altres moments m'han exaltat, endinsant-me en un mar d'alegria. Em resisteixo a deixar-me induir pels seus aires empordanesos: si almenys fossin baixempordanesos..., però potser el que passa és que la bogeria de la tramuntana no pot amb el meu enginy "Palabanyogí". Agraïment especial també mereix la seva família. A tu, merci per tot "onin"!!

Evidentment no tot ha estat bonic durant aquests anys: articles frustrats, treballs parats, discussions acalorades, treballs no fructífers, contractes foscos, promeses incomplertes, descoratjament per visió de coses suposades injustes per mi… però res no pot tapar l'enorme alegria que han suposat aquests anys, primer per la consecució d'Economia i ADE, i finalment ara amb la culminació de la Tesi. Sobretot espero endur-me amics, i especialment poder seguir fent posar vermell a en Miquel durant molts anys, i no deixar-lo de sorprendre mai (amb algun JACS si pot ser també). És el repte.

La cara més amarga del doctorat me la vaig trobar amb una dissortada notícia pocs dies abans de dipositar en format escrit aquesta tesi, i com bé molts ja podeu entreveure, es tracta de la pèrdua d'un ex-membre de l'IQC, en Giro, amb qui segurament jo potser no vaig congeniar mai massa (ell s'assemblava a mi, en el fet que no sabem simular que ens agrada el que realment no ens agrada), però no per això la seva marxa em va suposar menys trauma. El dia en què es va conèixer la notícia a part dels professors titulars, hi havia ja una nova generació de becaris, que només n'havien sentit a parlar (segurament de les seves dots de programador i de publicador insaciable), i segurament per això la notícia no els va enterrar tant en una trista nostàlgia com a mi, o als que havien compartit més hores de despatx i d'amistat. El record per ell espero que es reflexi amb aquestes paraules. Segurament no he estat l'únic que ha meditat sobre el tema i hi ha donat voltes. A vegades, i no és la primera vegada que ho manifesto, penso que a l'IQC potser estem creant pseudomonstres entre tots, on la competitivitat es presenta com a vencedora, però intrapersonal i per sort no interpersonal. L'IQC funciona tan bé gràcies a que tothom ajuda a tothom, però potser caldria recordar en veu alta de tant en tant aquest fet. Caldria deixar clar que la felicitat ve pels petits gestos, per l'amistat (espero ampliar-la jo a partir d'ara baixant més a esmorzar, en el temps que em quedi en el "convent"). Molta gent de l'IQC només ha viscut una realitat, la de la química teòrica, ja que són tantes les hores passades dins aquestes quatre parets... que

ens manlleven llavors oportunitats d'endinsar-nos en altres enriquidores realitats. En el seu moment, vaig poder fer una incursió en la branca econòmica per exemple, i després de fer-ho crec que convindria de tant en tant fer excursions *ex-muros*. Tinc la sensació que estem dins una bombolla, almenys en quant a quota de publicacions, que molts ho adhueixen a major sort, i potser en part sí, però cal tenir clar que l'èxit ens ve per la quantitat d'hores increïbles que deixem dia rere dia en la recerca, a més d'un equip cohesionat com a grup humà. Però tinc clar que això no ha estat un doctorat, sinó una llançadora per ser investigador en el futur. El que no tinc clar és si això té un "Ítaca", ja que no aconsegueixo entreveure un futur professional amb claredat. Heus ací, per tant, que arribem a la gran paradoxa. Es pot o ens podem exigir tant?

Sens dubte que la tesi l'haig de dedicar a molta gent, però aquesta la puc i la vull dedicar al meu, recentment desaparegut, avi, que costaria descriure'l, però només dient que escrivint aquestes paraules ja em cauen les llàgrimes no em cal afegir res més. Va ser una llum en el meu camí, perenne i perdurable en el temps. Va per tu, avi.